NORTH PACIFIC ENVIRONMENT AND PALEOCLIMATE FROM THE LATE PLEISTOCENE TO PRESENT

EDITED BY: Miriam Jones, Lesleigh Anderson and Dorothy M. Peteet

PUBLISHED IN: Frontiers in Earth Science

frontiers Research Topics

frontiers

ISSN 1664-8714
ISBN 978-2-88963-337-1
DOI 10.3389/978-2-88963-337-1

About Frontiers

Frontiers is more than just an open-access publisher of scholarly articles: it is a pioneering approach to the world of academia, radically improving the way scholarly research is managed. The grand vision of Frontiers is a world where all people have an equal opportunity to seek, share and generate knowledge. Frontiers provides immediate and permanent online open access to all its publications, but this alone is not enough to realize our grand goals.

Frontiers Journal Series

The Frontiers Journal Series is a multi-tier and interdisciplinary set of open-access, online journals, promising a paradigm shift from the current review, selection and dissemination processes in academic publishing. All Frontiers journals are driven by researchers for researchers; therefore, they constitute a service to the scholarly community. At the same time, the Frontiers Journal Series operates on a revolutionary invention, the tiered publishing system, initially addressing specific communities of scholars, and gradually climbing up to broader public understanding, thus serving the interests of the lay society, too.

Dedication to Quality

Each Frontiers article is a landmark of the highest quality, thanks to genuinely collaborative interactions between authors and review editors, who include some of the world's best academicians. Research must be certified by peers before entering a stream of knowledge that may eventually reach the public - and shape society; therefore, Frontiers only applies the most rigorous and unbiased reviews.
Frontiers revolutionizes research publishing by freely delivering the most outstanding research, evaluated with no bias from both the academic and social point of view. By applying the most advanced information technologies, Frontiers is catapulting scholarly publishing into a new generation.

What are Frontiers Research Topics?

Frontiers Research Topics are very popular trademarks of the Frontiers Journals Series: they are collections of at least ten articles, all centered on a particular subject. With their unique mix of varied contributions from Original Research to Review Articles, Frontiers Research Topics unify the most influential researchers, the latest key findings and historical advances in a hot research area! Find out more on how to host your own Frontiers Research Topic or contribute to one as an author by contacting the Frontiers Editorial Office: researchtopics@frontiersin.org

NORTH PACIFIC ENVIRONMENT AND PALEOCLIMATE FROM THE LATE PLEISTOCENE TO PRESENT

Topic Editors:
Miriam Jones, United States Geological Survey (USGS), United States
Lesleigh Anderson, United States Geological Survey (USGS), United States
Dorothy M. Peteet, Goddard Institute for Space Studies (NASA), United States

The vast area of the North Pacific, spanning ~55° longitude, represents a challenge for documenting and understanding the geologic history of ocean, atmosphere, and terrestrial environmental change. Nevertheless, its importance for many issues, including our fundamental understanding of ocean and atmospheric circulation patterns and teleconnections with natural modes of climate variability through time, has led to a steady rise in the numbers of study sites and proxy types.

By bringing together a wide range of proxies and timescales that examine the impacts of paleoclimate on ecosystems, water, carbon, and humans, and interactions between marine and terrestrial processes, this Research Topic contributes to an improved understanding of the region's significance at global, hemispheric, and regional scales.

Citation: Jones, M., Anderson, L., Peteet, D. M., eds. (2020). North Pacific Environment and Paleoclimate From the Late Pleistocene to Present. Lausanne: Frontiers Media SA. doi: 10.3389/978-2-88963-337-1

Table of Contents

frontiers in Earth Science

EDITORIAL
published: 26 November 2019
doi: 10.3389/feart.2019.00293

Editorial: North Pacific Environment and Paleoclimate From the Late Pleistocene to Present

Miriam C. Jones[1]*, *Lesleigh Anderson*[2] and *Dorothy M. Peteet*[3,4]

[1] Florence Bascom Geoscience Center, U.S. Geological Survey, Reston, VA, United States, [2] Geoscience and Environmental Change Science Center, U.S. Geological Survey, Denver, CO, United States, [3] NASA GISS, New York, NY, United States, [4] Lamont-Doherty Earth Observatory, Palisades, NY, United States

Keywords: peatland, lake sediments, thermokarst, ecohydrology, dendrochronology, diatoms, Isotopes, pollen

Editorial on the Research Topic

North Pacific Environment and Paleoclimate From the Late Pleistocene to Present

The vast area of the North Pacific, spanning ∼55° longitude, represents a challenge for documenting and understanding the geologic history of ocean, atmosphere, and terrestrial environmental change. This special issue highlights site-specific analyses to address various questions and provides clues that arise in response to continued North Pacific warming today in a rapidly changing climate (**Figure 1**). The emergence of new methods and novel application of existing methods serve to enhance our fundamental understanding of natural modes of climate variability driven by ocean and atmospheric circulation patterns, including the role of external (e.g., insolation) vs. internal forcing [e.g., El Niño Southern Oscillation (ENSO) and the Pacific Decadal Oscillation (PDO)]. Included in this volume are geographically diverse studies that present new and traditional methods for the interpretation of climate records drawn from pollen, macrofossils, tree rings, diatoms, grain size, and glacial studies. Many provide new geographic comparisons, such as Kamchatka and Hawaii, or emerge from novel geologic archives and environments, such as the marine shelf, a thermokarst lake, and a fossil forest.

Questions of natural variability targeted in the compendium include:

- What are geographic patterns of temperature and moisture variability since deglaciation?
- How does carbon accumulation compare among wetlands throughout the North Pacific, and how does moisture affect the differences in accumulation rates?
- What role does seasonality play in the temperature and moisture balance of a region?
- What are the primary controls on glacial advance in non-tidal glaciers of the North Pacific coast?
- Do productivity patterns in the ocean and land show synchronous response to climate variability?
- What are the relationships between patterns of thermokarst modification and changes in climate, forest growth, and fire regimes?
- How can lake basin morphology affect shifts in mixing depths, which impact diatom paleorecords?

We solicited studies from across the entire North Pacific. The studies range from the Hawaiian Islands in sub-tropical North Pacific (Beilman et al.,), California, and Montana in mid-latitude eastern Pacific (Carlin et al.; Kirby et al.; Stone et al.), Kamchatka in the high-latitude western Pacific (Nichols et al.), and Alaska, in high latitude central North Pacific, with numerous new Holocene records from Kodiak Island (Peteet et al.), southcentral Alaska (Jones et al.), southeastern Alaska coast (Ager; Gaglioti et al.), southern Interior Alaska (Bigelow et al.) to as far north as the Yukon

Edited and reviewed by:
Steven L. Forman,
Baylor University, United States

***Correspondence:**
Miriam C. Jones
miriamjones@usgs.gov

Specialty section:
This article was submitted to Quaternary Science, Geomorphology and Paleoenvironment, a section of the journal Frontiers in Earth Science

Received: *23 October 2019*
Accepted: *28 October 2019*
Published: *26 November 2019*

Citation:
Jones MC, Anderson L and Peteet DM (2019) Editorial: North Pacific Environment and Paleoclimate From the Late Pleistocene to Present. Front. Earth Sci. 7:293. doi: 10.3389/feart.2019.00293

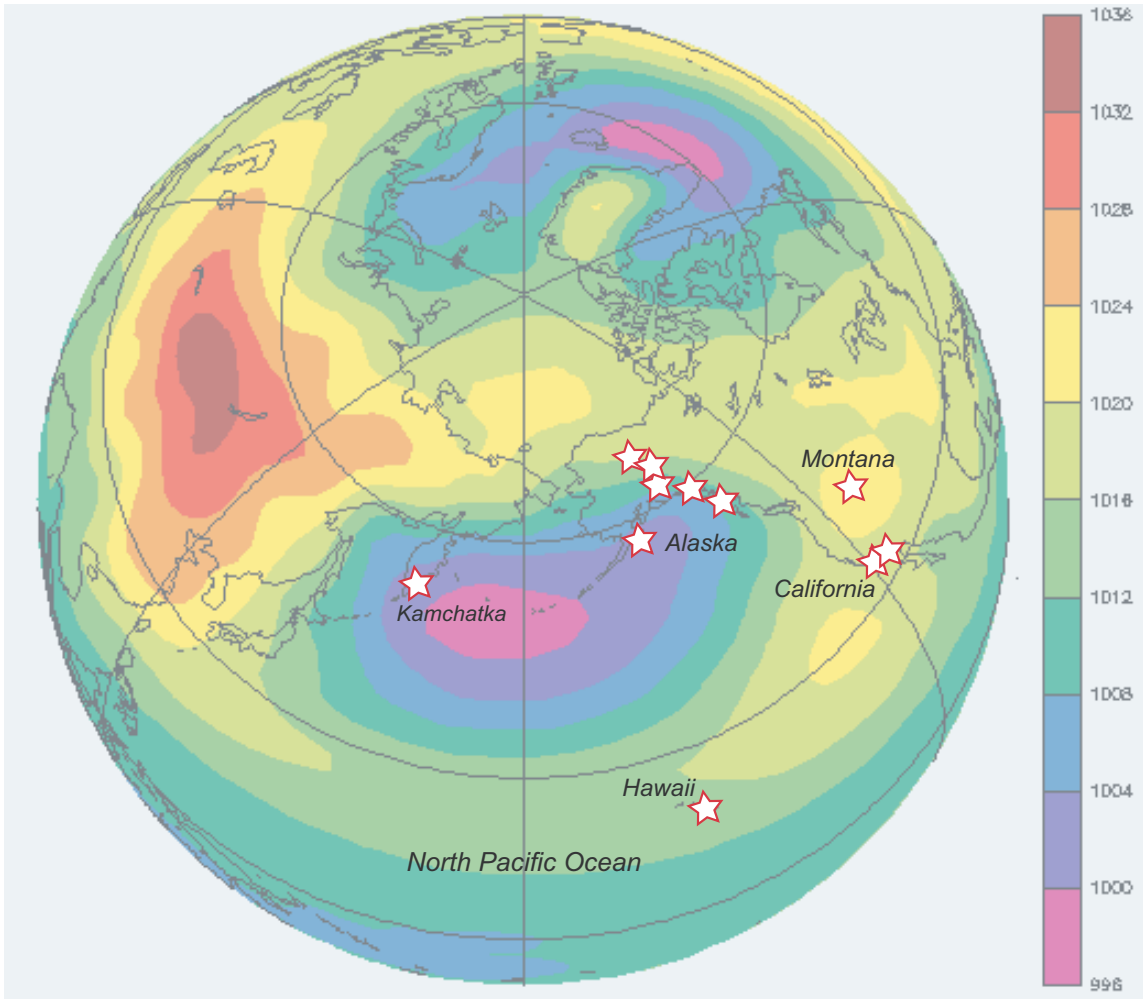

FIGURE 1 | Locations of the North Pacific paleoenvironmental studies included in this volume shown with composite sea level pressure to illustrate their relationship with dominant atmospheric flow patterns. Scale is in millibars (mb) (U.S. National Oceanic and Atmospheric Administration).

Flats in Interior Alaska (Anderson et al.). Evidence of North Pacific climate variability emerges from both the terrestrial and marine realm and connections between them under various modes of climate variability are also explored (Berkelhammer).

Several of the studies spanning the Holocene, employ similar geochemical proxies to elucidate patterns of synoptic responses to both internal and external hydroclimate variability. Early Holocene conditions from southcentral coastal Alaska (Peteet et al.) to Kamchatka, Russia (Nichols et al.) indicate patterns of warm and wet conditions in the early Holocene, before transitioning to drier conditions or more zonal atmospheric flow patterns in the mid-Holocene. The same geochemical proxy employed on a peatland from Hawaii shows climatic shifts occurring on similar timescales (Beilman et al.), suggesting North Pacific-wide changes associated with summer insolation. In the late Holocene, a proposed shift from insolation-dominance to internal influence by ENSO begins to influence the North Pacific, which is manifested as greater extratropical moisture reaching Hawaii and coupled with a trend toward warmer tropical sea-surface temperatures (Beilman et al.). Concurrent with these shifts is gradually increasing moisture in Kamchatka (Nichols et al.). These hydroclimatic shifts are consistent with patterns of vegetation change recorded by pollen and plant macrofossil records from southcentral and southeastern Alaska (Ager; Peteet et al.).

At lower latitudes, severe drought more frequently occurred in southern California relative to modern conditions, during the early to middle Holocene (Kirby et al.), likely in response to higher summer insolation. During the mid-Holocene, Southern California summers and winters were more frequently wet, whereas a late Holocene trend in increasing aridity largely reflects dry summers as winter precipitation increased. Rising lake levels during the late Holocene in the northern Rockies coincides with broad shifts in North Pacific circulation patterns (Stone et al.) related to increased winter precipitation driven by sub-tropical teleconnections, such as ENSO and the PDO. The dominance

of ENSO and the PDO in controlling late Holocene terrestrial hydroclimate variability is apparent from numerous records in this volume. On shorter timescales (years to decades), Carlin et al. explore the relationships between climate, shelf sedimentation, and human impact off the coast of California.

Several studies in this volume address persistent questions about changing precipitation seasonality during the Holocene using a diverse set of proxies. For example, a study from southern California uses grain size to represent pluvials driven by winter changes in precipitation (Kirby et al.), while Gaglioti et al. suggests that winter precipitation increases that expanded coastal Alaskan glaciers were driven by a stronger Aleutian Low during the Little Ice Age.

Hydroclimate variability can impact ecosystem carbon dynamics carbon. Holocene carbon accumulation rates from wetlands are addressed in several studies in this volume, spanning the tropics (Beilman et al.) to the subarctic (Nichols et al.; Peteet et al.). On shorter timescales, the influence of ENSO and the PDO impacts marine and terrestrial productivity and carbon uptake is examined in records from the western coast of North America (Berkelhammer). Climate variability and fire also has major influence on permafrost carbon dynamics and thermokarst in relation to thermokarst lake shoreline expansion, addressed in Anderson et al.. Humans have inhabited the landscape for millennia, and human migration and habitation of North Pacific landscapes are factored into the interpretation of four paleoclimate records in the studies by Ager, Beilman et al., Carlin et al., and Bigelow et al..

A brief summary of each submission to this volume is provided below.

- Beilman et al. document Holocene effective moisture variations from a Hawaiian peatland and relationships with vegetation dynamics and carbon accumulation rates. They utilize leaf wax geochemical methods to generate a novel wetness index and hydrogen isotope proxies of precipitation source and jet stream position. The combined paleoclimatic data with carbon sequestration and vegetation from the north central Pacific provides a new and highly significant point of reference from comparisons with western North America.
- Carlin et al. examine grain size and chronology (^{210}Pb, ^{137}Cs, ^{14}C) in four cores from Monterey Bay, California, in order to investigate shelf sedimentation and ways in which it is affected by climate and humans. They conclude that during dry climatic intervals, sedimentation is dominated by coastal erosion rather than by riverine inputs. In contrast, during wet years more sand was transported from rivers than from coastal erosion to the shelf. They also conclude that dams created by humans contribute to more coastal erosion, and to transport of more littoral sediment offshore.
- Kirby et al. explore Holocene lake level variations in drought sensitive southern California using paleo lake water isotope ratios captured by sedimentary carbonate. In tandem with sediment grain size variations, a proxy for winter precipitation amounts, the extent of water isotope evaporative enrichment indicated by calcite oxygen isotopes is used to provide companion proxies for summer effective moisture. The combined data provide an enhanced record of drought that illustrates the relative effects of changes in seasonal moisture availability.
- Stone et al. utilize diatom-inferred lake mixing depth reconstructions in mountain regions of Montana to explore the extent of regional hydroclimatic variability during the Holocene by examining the influence of individual lake bathymetry. They show that the effects of complex basin morphometry on mixing depth varies with lake levels, thereby complicating interpretation of lake level trends from diatom data. Recognition of unique morphometric effects are found to resolve apparently contradictory late Holocene hydroclimatic trends and provide a new methodological approach that will benefit future work.
- Berkelhammer uses satellite-derived Solar-Induced Florescence and chlorophyll-alpha as proxies for land and sea productivity to determine whether marine-terrestrial synchrony is a widespread phenomenon during modes of climate variability, such as El Nino Southern Oscillation (ENSO) and the Pacific Decadal Oscillation (PDO). Results suggest that marine and terrestrial ecosystems are synchronous across thousands of miles of the North Pacific coastline and that the strength of the synchrony depends on the relative states of the PDO and ENSO.
- Peteet et al. focus on western Kodiak Island peatlands, where a 16,000-year carbon sequestration record is coupled to the vegetational and isotopic history. During cooler, drier climate such as the Younger Dryas, the records show a decline in carbon stored, while the wet and warm early Holocene produces maximum values. A very large deuterium/hydrogen isotopic shift in the mid-Holocene (6,500 years BP) suggests that moisture arrived from cooler waters or a more distal source. Neoglaciation about 3,700 years ago brings cooler conditions as *Artemisia, Betula*, and *Sphagnum* increase, and carbon sequestration increases, all linked to the intensification of the Aleutian Low.
- Jones et al. conduct an oxygen isotope analysis of modern peatland water-plant relationships to better understand the relationship of peatland water to precipitation, and how plant cellulose oxygen isotope differences differ in their offset to peatland water depending on species and location within a peatland. They determined that bryophytes (non-vascular) were not statistically different from one another, but that sedges (vascular) were offset from bryophytes. They use this information to re-evaluate results of a previously published peat oxygen isotope record, which has implications for the deglacial and Holocene evolution of the Aleutian Low in southcentral Alaska. This study also proves the utility of this novel proxy for paleo-hydroclimatic studies in the North Pacific.
- **Ager** provides a comprehensive overview of the southeastern Alaskan paleoecological history, including three new palynological records from the region. Hummingbird Lake, southwestern Baronov Island, begins about 15,000 years ago and mirrors the sequence of vegetational change found in previous regional cores. Two nearby marine records, though

younger, provide similar complementary pollen sequences. His paper elucidates regional links between these records and possible tree refugia, the Queen Charlotte Islands to the south, and early human colonization.

- Gaglioti et al. approach questions about late Holocene glacier activity in the St. Elias Mountains from a recently exposed "ghost," or fossil, forest located on the south-central coast. Utilizing dendrochronological cross-dating methods, comparisons with Little Ice Age chronologies from nearby glaciers, and paleoclimatic data, they explore the climate variables that may have controlled glacier fluctuations in the region. These comparisons are used to examine the prominent differences between the timing of Little Ice Age advances in Alaska and North Atlantic regions to propose the importance of winter precipitation for Gulf of Alaska glaciers during the nineteenth century.
- Bigelow et al. relate the vegetational and climate history from four lakes in the middle Susitna Valley, Alaska, to human occupancy in the region. Their multidisciplinary research includes pollen, diatoms, and geochemistry. Shrub tundra characterized the earliest vegetation about 12,000 years ago, followed by a possible Younger Dryas cooling and aridity, then subsequent warming in the early Holocene as forest advanced beyond present limits. Retreat of spruce after 4,500 years ago indicates late Holocene cooling.
- Anderson et al. explore Holocene thermokarst lake development and evolution in discontinuous permafrost landscape of northern Interior Alaska. The study highlights thermokarst evolution that is characteristic of loess uplands—a landscape that is widespread and yet frequently overlooked for paleoclimatic studies. The authors propose that initial thermokarst lake formation and expansion occurred during early Holocene warmth, corresponding with boreal forest and fire development. Following a period of stabilization, subsequent lake-level rise and fall were influenced by climate via groundwater-surface water dynamics and North Pacific atmospheric circulation variability.
- Nichols et al. use stable isotope geochemical and plant macrofossil record from a peatland in Kamchatka, Russia to examine hydroclimate variability and the controls on that variability in the northwestern Pacific. They find a generally wetter early and late Holocene with a drier, more episodic precipitation regime during the mid-Holocene. These patterns are similar to patterns recorded in the eastern North Pacific, as well as northern Japan. They conclude that the observed patterns can in part be explained by changes in tropical Pacific sea surface temperatures, highlighting the potential influence of the tropics across the broader North Pacific region.

AUTHOR CONTRIBUTIONS

MJ, LA, and DP contributed to writing. LA created the figure. MJ organized and edited.

Conflict of Interest: The authors declare that the research was conducted in the absence of any commercial or financial relationships that could be construed as a potential conflict of interest.

frontiers in Earth Science

ORIGINAL RESEARCH
published: 22 February 2019
doi: 10.3389/feart.2019.00028

The Influence of Fetch on the Holocene Thermal Structure of Hidden Lake, Glacier National Park

Jeffery R. Stone[1], Jasmine E. Saros[2] and Trisha L. Spanbauer[3,4]*

[1] Department of Earth and Environmental Systems, Indiana State University, Terre Haute, IN, United States, [2] Climate Change Institute and School of Biology and Ecology, The University of Maine, Orono, ME, United States, [3] Department of Earth and Atmospheric Sciences, University of Nebraska–Lincoln, Lincoln, NE, United States, [4] Department of Integrative Biology, University of Texas at Austin, Austin, TX, United States

We use three-dimensional modeling of the basin of Hidden Lake, Montana, to assess the influence of effective fetch on diatom-inferred changes in mixing depths throughout the Holocene. The basin of Hidden Lake is characterized by a complex morphometry; for example, three-dimensional modeling of the lake basin indicates that a decrease in lake level of 2 m would result in complete isolation of the deepest part of the lake basin from the rest of the lake. Our model suggests that small changes in the lake surface elevation at Hidden Lake would produce threshold-like responses in effective fetch, which in turn would have a profound influence on average lake mixing depth. The present-day planktic diatom community of Hidden Lake is comprised of three species. Neo-ecological experiments revealed the effect of mixing depth and nutrient levels on growth rates of these species. A sediment core collected from the deepest part of the lake basin and spanning the last 8,640 years was analyzed for diatoms. Here we show how changes in fetch through the Holocene explain changes in the dominant planktic diatom species by modification of the thermal structure of Hidden Lake. Additionally, the timing of diatom-inferred changes in effective moisture and thermal structure from Hidden Lake were compared to late Holocene patterns reconstructed from other regional lake records. Between 8.64 – 7.61 ka the diatom record from Hidden Lake suggests that the lake was deep and fresh, although somewhat lower than the modern lake. After 7.61 ka, water levels rose, expanding the available benthic diatom habitat. Between 6.18 and 4.13 ka, lake level declined and seasonal stratification was enhanced. After 1.4 ka, the lake became deeper and less stratified in response to the effects of enhanced fetch. We argue that changes in effective fetch may play an important, and underexplored, role in planktic diatom community structure over longer time scales and should be more broadly considered in paleolimnological studies.

Keywords: diatoms, fetch, paleolimnology, thermal structure, lakes, lake level, Holocene

OPEN ACCESS

Edited by:
Lesleigh Anderson, United States Geological Survey, United States

Reviewed by:
Jesse C. Vermaire, Carleton University, Canada
David Francis Porinchu, University of Georgia, United States

****Correspondence:***
Jeffery R. Stone
jeffery.stone@indstate.edu

Specialty section:
This article was submitted to Quaternary Science, Geomorphology and Paleoenvironment, a section of the journal Frontiers in Earth Science

Received: *02 October 2018*
Accepted: *05 February 2019*
Published: *22 February 2019*

Citation:
Stone JR, Saros JE and Spanbauer TL (2019) The Influence of Fetch on the Holocene Thermal Structure of Hidden Lake, Glacier National Park. Front. Earth Sci. 7:28. doi: 10.3389/feart.2019.00028

INTRODUCTION

Lakes that are sensitive to changes in effective moisture are highly desirable for paleolimnological studies because variations in lake surface elevation can readily alter the water chemistry, nutrient cycling, and availability of limnobiotic habitats (Stone and Fritz, 2004; Fritz, 2008; Wolin and Stone, 2010). Ideally, limnologic responses faithfully record changing climates and

environmental variables through time by archiving variations in sediment characteristics, geochemistry, and remains of environmentally sensitive organisms (Fritz, 1996).

Morphometric parameters of most lake basins, such as depth, surface area, volume, and basin shape, typically are persistent factors over shorter timeframes. These factors combine with the positional framework components of a basin, such as fetch, aspect, and exposure to wind, to ensure that most lake environments are relatively stable. However, these features of the basin also make the sensitivity to hydroclimate variations over time unique for each lake, even within the same region (Ragotzkie, 1978; Fritz et al., 2000; Håkanson, 2005; Wigdahl et al., 2014).

Physical properties are critical factors that influence the heat budget of a lake (Ragotzkie, 1978). Among other things, they significantly impact the timing of ice formation and breakup, the thermal structure of the lake throughout the season (Davies-Colley, 1988; Gorham and Boyce, 1989; Robertson and Ragotzkie, 1990; Pal'shin et al., 2008), the maximum heat content during the ice free period, and snow coverage (Scott, 1964; Ragotzkie, 1978). Consequently, the influence of physical properties reverberates throughout the limnologic environment. It affects physical limnological settings, such as nutrient cycling (Osgood, 1988), light penetration and turbidity (Bernhardt et al., 2008; von Einem and Graneli, 2010), sediment redistribution (Evans, 1994; Blais and Kalff, 1995; Hamilton and Mitchell, 1996; Bachmann et al., 2000), and sedimentation rates (Lehman, 1975; Anderson, 1990). Hence, it also influences nearly every biological aspect of the ecosystem from phytoplankton production (Fee, 1979; Davies-Colley, 1988; Carrick et al., 1993; Diehl et al., 2002) to availability of fish habitats (Håkanson, 2005).

Despite the relevance of these factors to understanding lake and lake-ecosystem response to climate change, paleolimnological studies rarely examine the effects of changing lake surface elevation on morphometric basin parameters, other than water depth (Mason et al., 1994; Verschuren, 1999). This is somewhat surprising, considering the relative ease and inexpensiveness of generating lake morphometric data (Håkanson, 1981) compared to the potential for utilizing this type of information to improve paleolimnological inferences. From a bathymetric map and software capable of three-dimensional modeling, it is possible to generate all of the morphometric parameters listed above for a modern lake, as well as potential lake morphometries under various lake surface elevations, including conditions substantially deeper and shallower than the modern lake (Stone and Fritz, 2004; Wigdahl et al., 2014).

Fetch, which is the distance that wind blows across a lake surface, is a simple morphometric parameter to measure from a bathymetric map (Håkanson, 1981). Since wind rarely blows in a constant direction, fetch is commonly calculated as *effective fetch*, which takes into consideration a range of possible wind directions and includes the influence of lake width across those directions on wave energy (Smith and Sinclair, 1972; Håkanson and Jansson, 1983). The influence of fetch on most lake systems is profound; fetch is a principle factor affecting wave energy, and as a result, the influence of fetch on seasonal mixing and thermocline development is substantial (Ragotzkie, 1978; Gorham and Boyce, 1989; Håkanson, 2005; von Einem and Graneli, 2010). In shallower areas of a lake, wave energy and the depth of convective mixing controls resuspension of lake sediment (Håkanson and Jansson, 1983; Whitmore et al., 1996; Bachmann et al., 2000). As a result, fetch is also a primary control on macrophyte distribution (Rea et al., 1998; Thomaz et al., 2003). In smaller, temperate lakes, fetch exerts a critical influence over the temperature threshold at which a lake will freeze over and can influence snow coverage, and thus ice thickness and the timing of ice breakup (Scott, 1964; Ragotzkie, 1978). Together, fetch combines with wind strength and duration, air temperature, winter precipitation, average depth, and irradiance/light penetration (Fee et al., 1996; Snucins and Gunn, 2000; Houser, 2006; Persson and Jones, 2008) to control the seasonal progression of the thermal structure of a lake.

In all lakes that are sensitive to changes in effective moisture, as lake levels fluctuate, there is a potential for a change in fetch. Since the lake surface area grows or shrinks with changes in lake volume, the straight-line distance from shore to the shore may be substantially altered. This is particularly true of lakes with a complex bathymetry (multiple-basin lakes), where a relatively small change in lake level may result in a substantial change in lake surface area, for example when lake basins become isolated from each other under shallowing conditions or coalesce when lake levels rise (Stone and Fritz, 2004). These threshold responses in fetch create an intriguing potential for paleolimnological studies, where a series of cascading changes in fundamental lake dynamics may be affected by a fairly minor change in lake surface elevation.

Because of their sensitivity to a variety of changes in the lake environment, particularly changes in lake level, water chemistry, mixing depth, and nutrient conditions, fossil diatom assemblages are used frequently in paleolimnologic studies (Fritz, 1996; Diehl et al., 2002; Wolin and Stone, 2010; Saros et al., 2012; Stone et al., 2016). Saros et al. (2012) explicitly explored the autecology of three planktic diatom species (*Lindavia intermedia, Lindavia comensis, and Discostella stelligera*) that occur in the modern diatom community of Hidden Lake. Using a set of neo-ecological experiments designed to gauge the influence of the interaction of mixing depth and nutrients on growth rates, these three diatom species were determined to express a growth preference reflecting a gradient of mixing depths. These experiments were coupled with the collection of a sediment core from Hidden Lake, which was used to reconstruct the recent (past few centuries) record of changes in mixing depth over time, using the same three diatom species which frequently occur in fossil diatom assemblages of the core.

The modern bathymetry of Hidden Lake is complex (**Figure 1**), and has a linear geometry with multiple sub-basins. Because of the linear geometry, relatively large surface area, and the fact that it is inset into a relatively narrow valley, fetch invariably plays a large role in the energy of the modern lake (Smith and Sinclair, 1972; Håkanson and Jansson, 1983). Additionally, the depth of the sub-basins is highly asymmetric; the basin has one deep sub-basin connected by a relatively shallow arch to the rest of the lake. Over very long timeframes, such as the Holocene, the influence of the basin morphology,

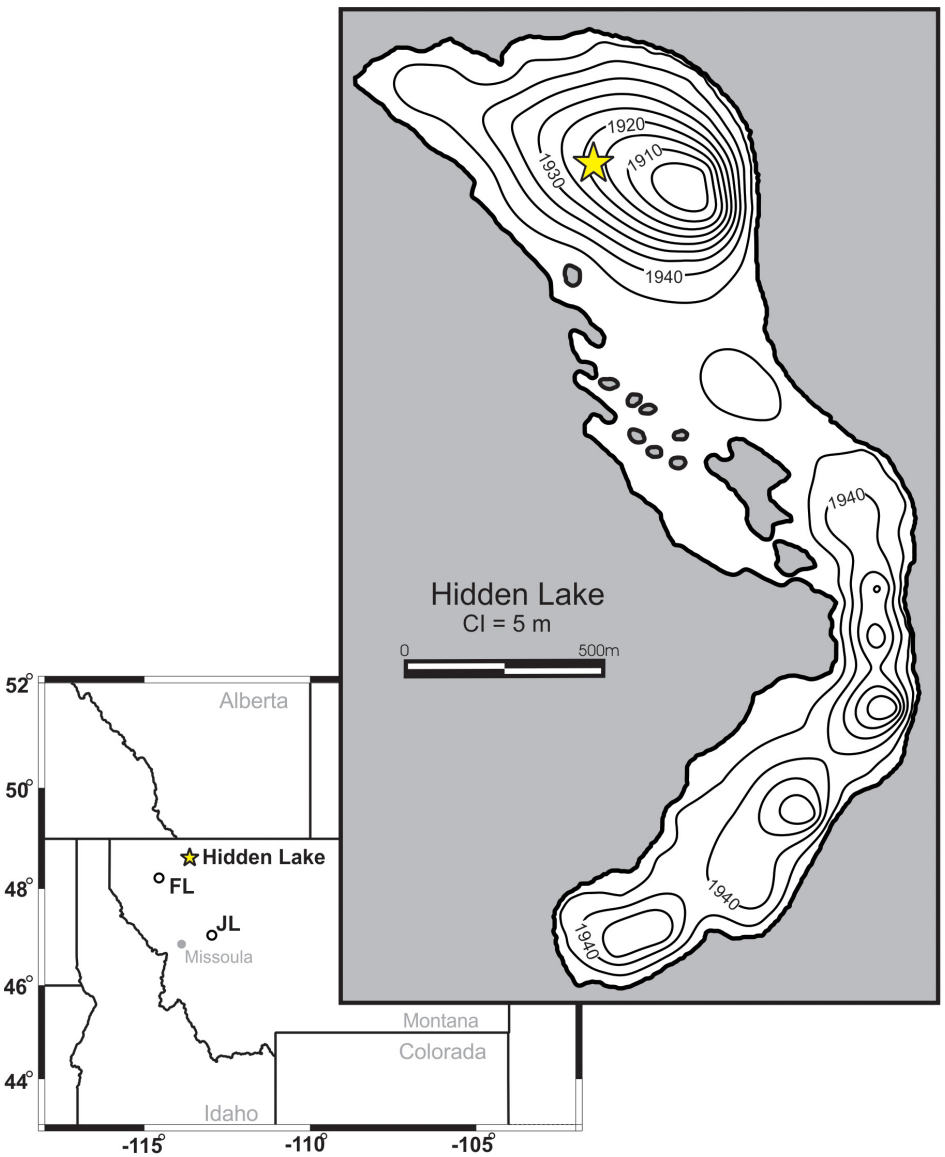

FIGURE 1 | Bathymetric map of Hidden Lake. Core location marked by filled star. Contour intervals shown are in 5 m intervals. Location of Hidden Lake, Foy Lake (FL), and Jones Lake (JL) are marked on inset map.

and its interaction with changes in lake level, are substantially more likely to have played a role in the thermal structure of the lake. To test this hypothesis, we created a three-dimensional model of the lake basin using a bathymetric map we generated by measuring depths throughout the lake. We used this information to calculate lake surface areas across a range of potential lake levels. We then used this information to estimate effective fetch and compared this modeled information against the diatom-inferred mixing depth reconstructed from the sediment record for the last 8,500 years.

Hidden Lake (N48° 40′53″, W113° 44′34.5″) is located in Glacier National Park, immediately west of the Continental Divide (**Figure 1**). Local bedrock is composed of Proterozoic sedimentary rocks, mainly mudstones, of the Belt Supergroup. The lake is inset into a steep-walled basin oriented primarily NW-SE. Talus deposits border the eastern margin of the lake (particularly on the southern end), composed of unsorted and mainly unvegetated, angular rubble. The surrounding basin is primarily exposed bedrock with rocky alpine meadows on flat areas and linear copses of evergreens along moderate slopes.

Hidden Lake is a low-nutrient system [total phosphorus (TP) 1.2 μg/L, Nitrate-N (NO_3^-N) 25 μg/L, dissolved organic carbon (DOC) 0.4 mg/L] with high light penetration [July 1% photosynthetically active radiation (PAR) 34 m]. Consequently, the sedimentation rate is very low (0.08 mm/year). Measurements taken in July 2007 indicated a mixed layer depth of 5 m, with an epilimnion temperature of ∼15°C. This site was selected for analysis because the primary planktic diatom species that occur

in the modern lake system are composed of *Lindavia comensis*, with smaller percentages of *Discostella stelligera*, and *Lindavia intermedia*. The ecology of these three species, within the context of alpine and subalpine lakes of the Northern and Central US Rocky Mountains, were examined in a broader component of this research project in a series of assay experiments performed *in situ*, which found the primary controls on growth to be correlated to (either independently or in combination) NO_3^-N and mixing depth (thickness of the mixed layer) under stratified lake conditions (Saros et al., 2012; Saros and Anderson, 2015).

MATERIALS AND METHODS

Bathymetry and Morphometry

Twenty-seven measurements of the depth to the sediment-water interface were taken with a hand-held depth-finder from a series of transects on Hidden Lake. Depth measurements were overlain onto a topographic map and the basin was digitized using Surfer 10.0 (Golden Software, 2010). A scaled, three-dimensional model of the lake bathymetry (**Figure 1**) and topography of the surrounding basin was generated by gridding the data using a minimum curvature method at a 3 m equant horizontal resolution. Values for lake volume, water surface area, and lake basin (sediment-water) surface area, were calculated within the program Surfer. 3D modeling of the lake basin using Surfer allowed for iterative calculations of every potential lake surface elevation from the modern lake surface elevation down to the minimum potential lake surface in 0.5-m resolution depth steps. Modern Hidden Lake currently overflows via a small stream (Hidden Creek), which would limit significant rise of lake level within the existing basin. Because of this, potential lake surface elevations *above* the modern lake elevation were ignored when modeling. Regions outside the modern lake margin and shallower sub-basins within the lake that became isolated from the deepest basin (where the core was collected) when potential lake elevation surfaces were lower were 'blanked' from the model to remove them from contributing to lake volume and surface area calculations. Mean lake depth was calculated by dividing the total lake volume at a given modeled lake elevation by the total planar surface area for that elevation.

Lake volumes calculated using Surfer were created by averaging the values from three estimation techniques (Trapezoidal Rule, Simpson's Rule, and Simpson's 3/8th Rule), with an average relative error of approximately 0.02% between the three techniques. Values for planar surface area and basin surface area for each contour interval also were calculated within Surfer, using the equation for calculating the area of a polygon with n vertices (where x and y are coordinates in Cartesian space):

$$1/2\sum_{i=1}^{n}(x_i y_i + 1 - x_i + 1 y_i) \quad (1)$$

Average depth values for the lake were calculated for each potential lake elevation by dividing the calculated volume (m^3) by the calculated planar surface area (m^2).

Fetch was calculated at each modeled lake surface elevation from a fixed point in the middle of the deepest basin (near the core site; **Figure 1**). Maximum effective fetch was also calculated for the lake at every potential modeled lake elevation. Effective fetch was calculated using the following formula, after Håkanson and Jansson (1983):

$$L_f = \frac{\sum x_i \cdot \cos\ \gamma_i}{\sum \cos\ \gamma_i} \quad (2)$$

Where x_i is the distance to the shore at angles in increments of $\pm 6^\circ$ (γ) from 0 to 42° from the direction of maximum fetch.

Core Collection, Subsampling, Age-Depth Model

Sediment was collected from an inflatable boat from the deepest basin (~30 mbls) of Hidden Lake (**Figure 1**) with a simple pole-driven (Griffith) piston corer during the summer of 2007. The sediment-water interface was preserved intact, in a polycarbonate barrel that captured a sedimentary sequence 65 cm in length. The complete core was sub-sampled in the field, continuously, in 0.5-cm increments. A set of materials were collected for dating (**Table 1**) using a combination of ^{210}Pb-dating (Appleby and Oldfield, 1978) for near-surface sediments and a series of AMS radiocarbon-dated materials, including wood/plant fragments (Stuiver et al., 1998) that were recovered throughout the core (**Table 1**). ^{210}Pb activities were counted by gamma ray spectroscopy methods; the ^{210}Pb chronology was based on the constant rate of supply (CRS) model. An age model for the core was constructed (**Figure 2**) using the Bayesian age-depth modeling software BACON (version 2.2) (Blaauw and Christen, 2011). All ages reported herein as "ka" are calibrated ages in 1000s of years before 1950.

Fossil Diatom Analysis

One hundred and thirty-one samples were collected from the core for diatom analysis. Each sample was treated with 10% HCl and 35% H_2O_2 at room temperature to digest carbonate and organic material. Known quantities of polystyrene microspheres were added to estimate diatom concentrations (Battarbee, 2003); diatoms were mounted in Zrax, a high-refractive index medium. Diatom frustules were analyzed using a Zeiss AxioSkop2 transmitted light microscope at 1000x magnification under differential interference contrast. Diatom species were identified to the lowest taxonomic level possible using the following taxonomic guides: Foged (1981); Cumming et al. (1995), Lange-Bertalot et al. (1996); Camburn and Charles (2000), Fallu et al. (2000), and Bahls (2004, 2005). Modern taxonomic concepts were applied to diatom identifications (see **Supplementary Data**) using the websites Diatoms of the United States (Spaulding et al., 2010) and AlgaeBase (Guiry and Guiry, 2017). When possible, at least 300 diatom valves were identified from each sample interval. The ratio of planktic to benthic diatoms was calculated for each sample based on autecological information provided in the flora and taxonomic websites listed above. Constrained cluster analysis of the fossil diatom assemblages (CONISS method on square-root

TABLE 1 | Materials used to create the age model for the core collected from Hidden Lake.

Sample	Age	Error	Depth	Method	Material	Cal Age	2-σ Range
HDN-Surf	−57.5	1	0		Surface		
HDN-001	−55.1	1.22	0.25	210-Pb	Sediment		
HDN-002	−48.05	1.21	0.75	210-Pb	Sediment		
HDN-003	−40.05	1.3	1.25	210-Pb	Sediment		
HDN-004	−30.05	1.28	1.75	210-Pb	Sediment		
HDN-005	−15.7	1.79	2.25	210-Pb	Sediment		
HDN-006	5.35	2.22	2.75	210-Pb	Sediment		
HDN-007	33.85	4.88	3.25	210-Pb	Sediment		
HDN-008	68.85	12.03	3.75	210-Pb	Sediment		
HDN-009	101.95	27	4.25	210-Pb	Sediment		
HDN-024	1695	30	11.75	14-C	Plant/Wood	1598	1538–1634 (79.5%) 1649–1695 (20.5%)
HDN-050	3385	30	24.75	14-C	Plant/Wood	3628	3568–3696
HDN-097	5770	35	48.25	14-C	Plant/Wood	6573	6487–6659
HDN-098	6005	30	48.75	14-C	Plant/Wood	6845	6753–6764 (2.4%) 6777–6936 (97.6%)
HDN-105	6060	40	52.25	14-C	Plant/Wood	6915	6791–7009 (98.7%) 7130–7142 (1.3%)

Depth values are given in centimeters below the sediment-water interface. Ages are reported as calendar years (before 1950) for ^{210}Pb dates and uncalibrated radiocarbon years for ^{14}C dates. The calibrated calendar years (median probability) and associated 2-sigma age ranges are included for ^{14}C dates.

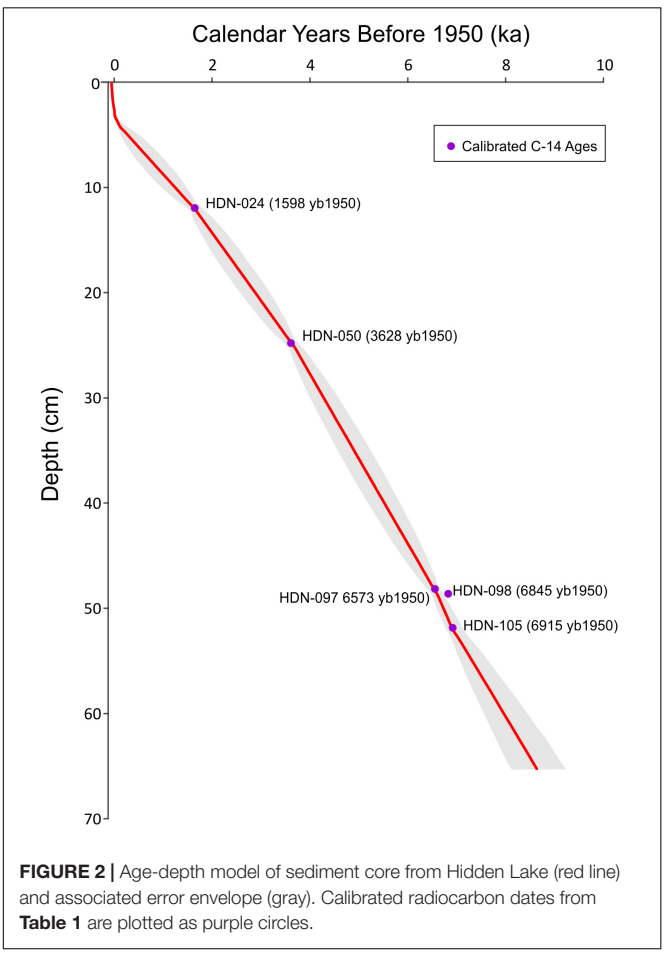

FIGURE 2 | Age-depth model of sediment core from Hidden Lake (red line) and associated error envelope (gray). Calibrated radiocarbon dates from **Table 1** are plotted as purple circles.

transformed data) was performed using the R package rioja (Juggins, 2015). Statistical significance of the constrained clusters was determined using the Broken Stick method.

Diatom-inferred mixing depths (DI-MDs) were reconstructed for each sample using a simple weighted averaging technique applied to the relative abundances of the three dominant planktic diatom species, here extended throughout the length of the core. Optimum mixing depths for each species were shown to be significantly different and, when taken together, form a gradient of species preference for mixing depths: *L. intermedia* (13.8 m), *L. comensis* (9 m), *D. stelligera* (4 m) (Saros et al., 2012). In the sediment record, only one other planktic diatom species was common (*L. radiosa*), occurring in the lower half of the core. However, because it is not a significant component of the modern diatom community of Hidden Lake, was not observed in our original lake calibration dataset, and was not included in neo-ecological experiments presented in Saros et al. (2012), we had no known autecological information regarding mixing depth preferences for this species within this lake system. As a result, this taxon was excluded from the DI-MD reconstructions.

RESULTS

Morphometric Analyses

Three-dimensional modeling of the lake basin produced a series of values for lake surface area, basin surface area, and volume of the lake throughout all potential lake elevations (**Figure 3**). Average lake depth for the modern lake elevation was calculated to be ∼8 m; average lake depth varied non-linearly with maximum depth, reaching a maximum average depth of ∼15 m when the lake level was modeled to be 5 m lower than the modern surface (**Figure 3**).

Three-dimensional modeling of the lake basin under different potential lake surface elevations indicates that the deepest sub-basin in the lake, where the sediment core was collected, would become completely isolated from the remaining lake sub-basins with a drop in lake surface elevation of less than

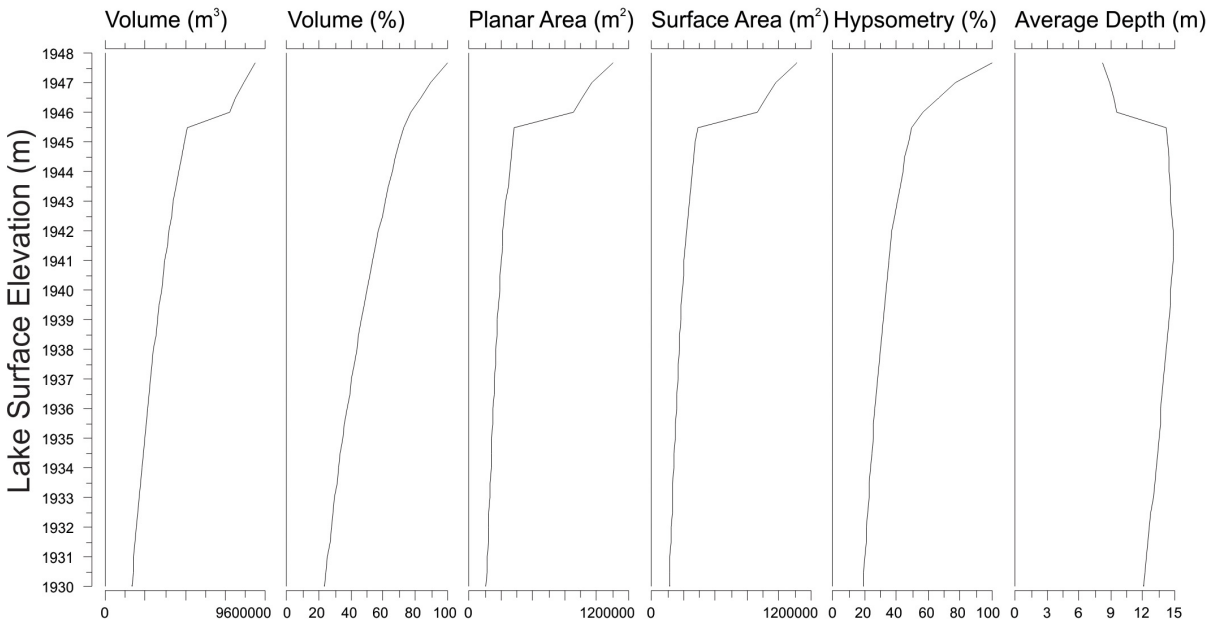

FIGURE 3 | Calculated morphometric parameters at each potential lake surface elevation of Hidden Lake, based upon 3-D modeling of lake bathymetry.

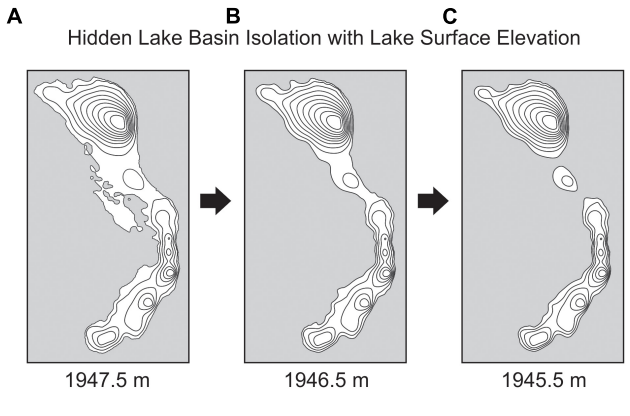

FIGURE 4 | Basin isolation maps showing how small changes in lake surface elevation result in a separation of modern sub-basins for Hidden Lake, based upon 3-D modeling of lake bathymetry. Bathymetry of Hidden Lake at three lake surface elevations: **(A)** 1947.5 m, **(B)** 1946.5 m, and **(C)** 1945.5 m.

2 m (**Figure 4**). Given the complex bathymetry of the lake, it is not surprising that basin surface area, lake surface area, and volume show a threshold response to decreasing lake surface elevation as the deep basin becomes isolated. Modeling the lake elevation to be 2 m shallower decreases the planar lake surface area (within the isolated deepest sub-basin) by nearly 70% (**Figure 3**). At this modeled lake elevation, the potential maximum effective fetch decreases by ∼25% relative to the modern lake system. Potential fetch calculated from the core site produced a slightly larger drop over the same change in lake elevation, decreasing by nearly 35% (**Figure 5**).

Fossil Diatom Analysis

Diatom assemblages for the past 8500 years at Hidden Lake are characterized mostly by the abundance of small colonial tychoplanktic species, primarily *Pseudostaurosira brevistriata* (20–40%) and *Staurosirella pinnata* (5–20%). These species co-occur throughout the core with the most common planktic diatom taxa, *Lindavia comensis* (10 to 60%), found in various combinations with *L. intermedia*, *L. radiosa*, and *Discostella stelligera*, all of which are typically present in relative abundances between 0 and 10% (**Figure 6**). With the exception of one section of the core representing the early Holocene (∼8–6 ka), with unusually high abundances of benthic monoraphid species (*Karayevia suchlandtii*, *K. nitidiformis*, and *Cocconeis* sp.), strictly benthic species were present in low abundances. More commonly, benthic taxa comprised less than 20% of all valves counted.

In general, we interpret the consistent abundance of small colonial tychoplankton (*P. brevistriata*, *P. pseudoconstruens*, *S. pinnata*), which are pervasive throughout the sediment record, to be representative of cold, moderately deep, low nutrient environments within the lake (Lotter and Bigler, 2000; Kingsbury et al., 2012). As discussed above, the most common modern planktic diatom species (*L. intermedia*, *L. comensis*, and *D. stelligera*) were used as part of the selection criteria for this lake. Based upon *in situ* neo-ecological experiments and published autecological information (Saros et al., 2012; Saros and Anderson, 2015) their co-occurrence in the modern lake

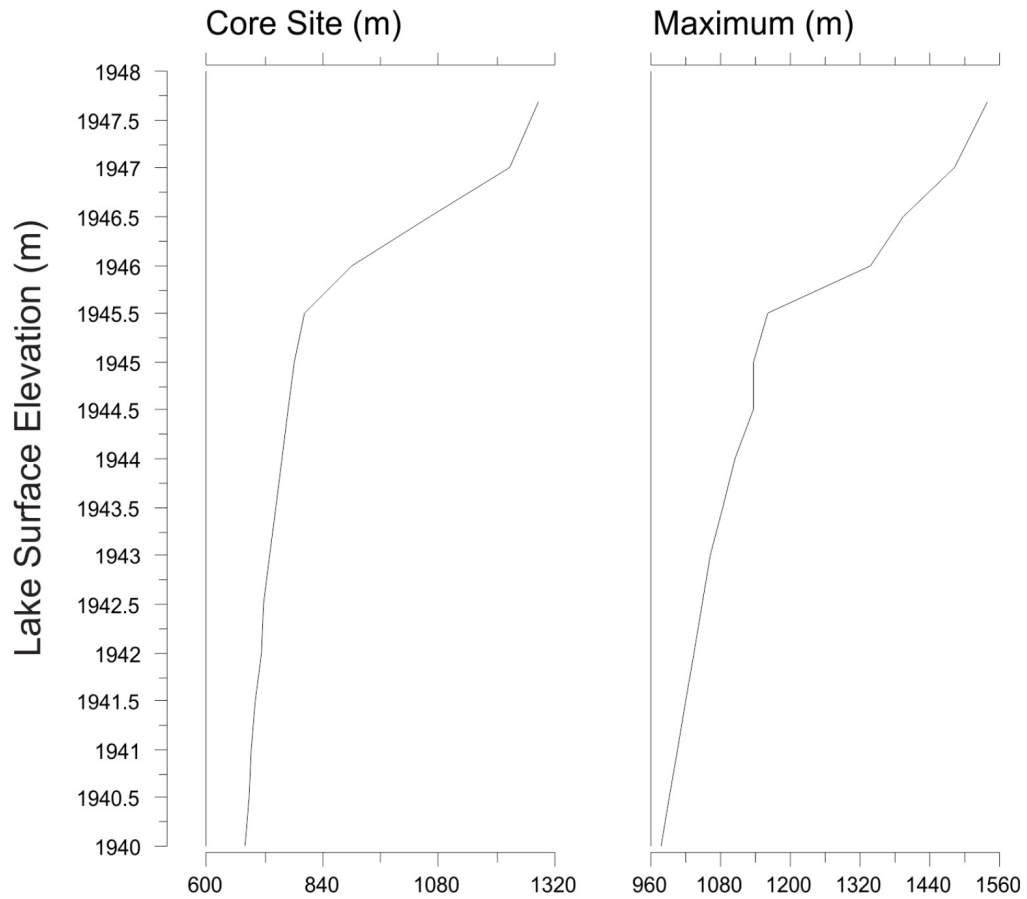

FIGURE 5 | Calculations of effective fetch at the core site and maximum effective fetch for Hidden Lake, based upon 3-D modeling of the lake bathymetry.

most likely reflects seasonal changes in lake mixing depths in Hidden Lake. Because sediment samples average time, changes in their abundances throughout the Holocene are interpreted to represent long-term changes in the average state of mixing depths over time (**Figure 7**). The remaining major diatom species observed preferred strictly benthic habitats (attached to plant, rock, or sediment surfaces); because diatoms are photosynthetic, most benthic diatoms represent the shallow sunlit habitats that mantle the margin of lakes. In clear, oligotrophic, alpine lake systems, photosynthetically active radiation necessary for photosynthesis may penetrate fairly deep into the lake, but most benthic diatom species rapidly decline in relative abundance with depth. In lakes with complex bathymetries, such as Hidden Lake, available surfaces that can be colonized by benthic diatoms may increase or decrease with changing lake levels or light penetration (Stone and Fritz, 2004; Wolin and Stone, 2010; Wigdahl et al., 2014). However, dynamic changes in the ratio of planktic to benthic diatoms through time likely reflect fluctuations in lake level, with the direction of lake level change potentially being uncertain in lakes with complex bathymetries, such as Hidden Lake (Stone and Fritz, 2004).

Based upon the constrained cluster analysis and associated broken stick modeling, statistically significant changes in the fossil diatom assemblages occur at three points in the lake's history: 7.61, 6.18, and 4.13ka (**Figure 6**). These significant changes are defined by the rise of benthic monoraphid diatoms (Diatom Zone 2), the reversal of this transition to dominance by plankton and tychoplankton (Diatom Zone 3), and the eventual disappearance of *Lindavia radiosa* in any substantial abundance from the lake plankton (Diatom Zone 4). Just below the threshold for significance, there are several other important transitions in the fossil diatom assemblages, which we define here as subzones used for descriptive purposes.

Diatom Zone 1 – DZ1 (a: 8.64 – 8.32 ka; b: 8.32 – 7.61 ka)

Diatom sub-zone 1a characterizes the early part of the lake's history as one dominated by plankton (*L. comensis* 20–30%, *L. radiosa*∼5%) and small colonial tychoplankton

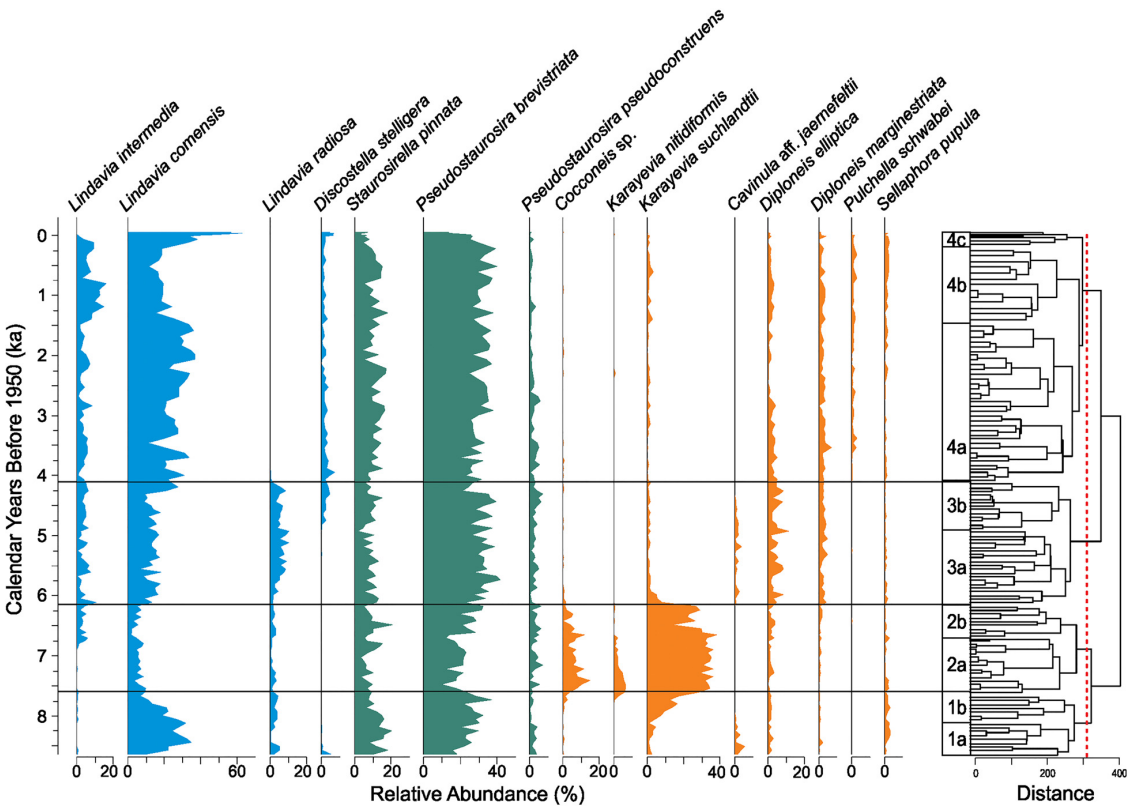

FIGURE 6 | Diatom stratigraphy of Hidden Lake displaying relative abundance of major taxa in the sediment assemblages **(left)**. Constrained cluster dendrogram and associated diatom zones **(right)**. Diatom taxa plots are color coded by habitat type: planktic (blue), tychoplanktic (teal), and benthic (orange). Red dotted line corresponds to clusters defined by Broken Stick Method.

(*P. brevistriata* 20–30%, *S. pinnata* 10–20%) and low abundances (∼20% total) of benthic diatom species. Diatom sub-zone 1b includes the same dominant diatom species as 1a, but is distinguished by the progressive increase (from 8% to ∼30%) in monoraphid benthic diatom species (especially *K. suchlandtii*∼15%), which replaces the dominant planktic species, *L. comensis*, from the base of the sub-zone to the top.

Diatom Zone 2 – DZ2 (a: 7.61 – 6.71 ka; b: 6.71 – 6.18 ka)

This zone is defined by a dominance of monoraphid species (*K. suchlandtii*, *K. nitidiformis*, *Cocconeis* sp.), which typically represent about half of the total assemblage for every sample. Colonial fragilarioid tychoplankton commonly comprise about 25–35% of the assemblage throughout the zone, increasing slightly toward the top of sub-zone 2b. A slight decrease in the relative abundance of the planktic species *L. radiosa* and the presence of uncommon biraphid benthic species, such as *Cavinula* aff. *jaernefeltii* and *Sellaphora pupula*, characterize DZ2. Sub-zone 2b is defined primarily by the gradual disappearance of *K. nitidiformis* and the appearance of the planktic species *Lindavia intermedia*, which represents about 5% of all assemblages throughout sub-zone 2b.

Diatom Zone 3 – DZ3 (a: 6.18 – 4.87 ka; b: 4.87 – 4.13 ka)

This diatom zone is defined by the rapid decline of monoraphid benthic diatoms (which represent < 5% of the total assemblage after DZ2) and a gradual increase in two planktic diatom species (*L. comensis*, *L. radiosa*). Colonial tychoplankton remain common (∼40–50%) throughout this zone. Biraphid benthic diatom species, including *Diploneis elliptica*, *D. marginestriata*, and *C.* aff. *jaernefeldtii*, increase in relative abundance, typically comprising ∼15–20% of the total diatom assemblage in DZ3. Sub-zone 3b is distinguished by the appearance of the planktic species *Discostella stelligera*, which typically occurs as about 5% of the total diatom assemblage throughout the core afterward.

Diatom Zone 4 – DZ4 (a: 4.13 – 1.39 ka; b: 1.39 – 0.122 ka; c: 0.122 – Present)

After about 4ka, the diatom assemblages from Hidden Lake stabilize and for most of the remaining record, the diatom assemblages essentially resemble the modern surface samples. Strictly benthic diatoms usually comprise 15–20% of the total assemblage, tychoplankton make up about 40–50% of the total assemblage, and planktic species typically range from about 30% at the base of DZ4 to about 60% at the top of the zone. The sub-zones in this part of the core are defined entirely by transitions

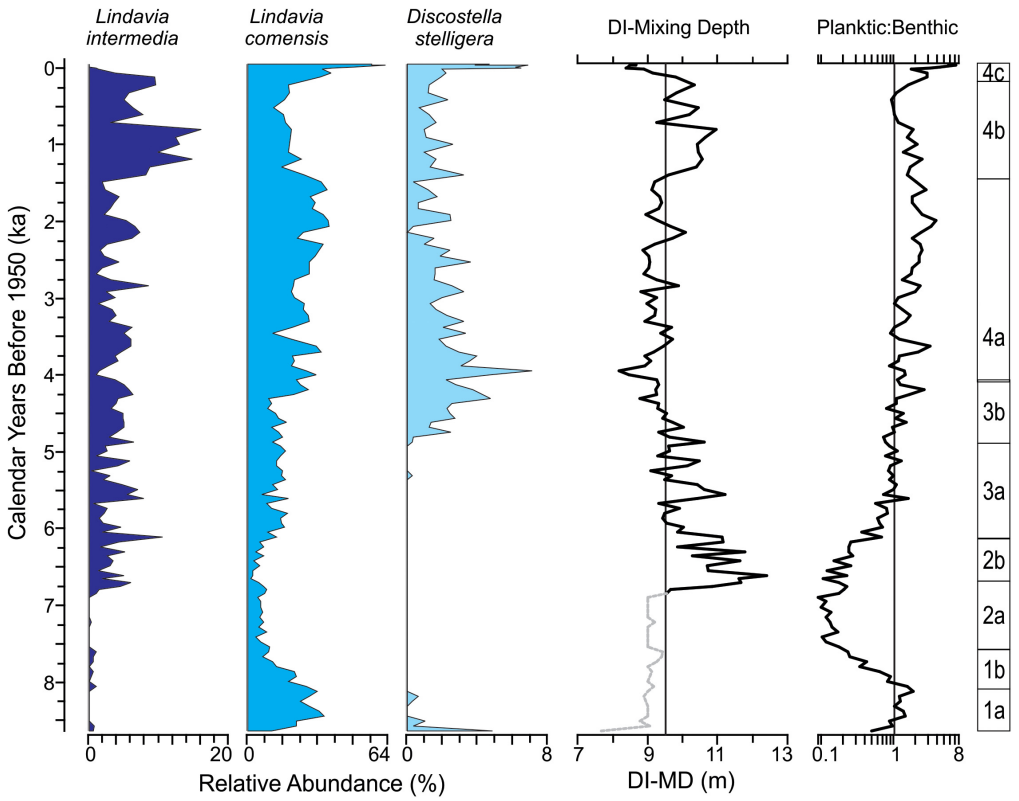

FIGURE 7 | Summary diatom figure for sediment core collected from Hidden Lake. Major planktic diatom taxa used for diatom-inferred mixing depth (DI-MD) plotted **(left)**. DI-MD and planktic to benthic index plotted along with diatom zones **(right)**. DI-MD figure plotted on a reference line indicating average mixing depth in meters; dotted gray line reflect intervals where mixing depth inferences may be less reliable resulting from low diversity in the planktic species used in modeling mixed depths.

between the planktic species *L. comensis* and *L. intermedia*. Subzone 4a is typified by elevated relative abundances of *L. comensis* (∼35% of the assemblage). Sub-zone 4b is marked by an increase in *L. intermedia* (from ∼5% to nearly 20%). Subzone 4c is characterized by a rapid rise in *L. comensis*, which reaches its greatest relative abundance in the last 200 years of the record. The rise in relative abundance of *L. comensis* is subzone 4c occurs at the expense of *L. intermedia* and small colonial tychoplankton, which both rapidly decrease throughout this period.

Diatom-Inferred Mixing Depths

DI-MDs for Hidden Lake ranged from approximately 8–12 m (**Figure 7**) throughout the core. Prior to sub-zone 2b, planktic diatom species occurred with limited relative abundance and are mostly represented by *L. comensis*, and as may not provide consistently reliable information. After this point, however, benthic diatoms become substantially less common in the sediment record and *L. intermedia* becomes much more abundant. Throughout subzone 2b, inferred mixing depths suggest that the lake was mixing fairly deeply, with the thickness of the epilimnion typically ranging between 12 and 10 m. Throughout DZ3, the inferred mixing depths show a progressive decline; the average thickness of the epilimnion decreases by nearly 3 m from the top of sub-zone 2b to the top of sub-zone 3b. Sub-zone 4a represents a period of relatively stable thermal stratification, with the epilimnion averaging around 8.5–9 m in thickness throughout. Through sub-zone 4b, the DI-MD suggests an abrupt deepening of the thermocline, which averages ∼10–10.5 m. This condition abruptly reverses in the final sub-zone, with the epilimnion thickness dropping to approximate 8 m in modern samples.

DISCUSSION

An idealized sequence for dimictic temperate lakes follows a progression with seasonal variation in radiation (Ragotzkie, 1978). Starting from complete ice cover in the winter, dimictic lakes are inversely stratified. As solar irradiance increases in the spring and winter air temperatures warm, this leads to ice break up which culminates with complete mixing of the water column under isothermic water conditions. Through spring and into early summer, thermoclines gradually develop, usually punctuated by short-lived destratification events until the thermocline strengthens. With increasing solar irradiance, thermal stratification is enhanced throughout the summer months. Solar irradiance and air temperatures decline into the fall, where destratification events lead to a return of

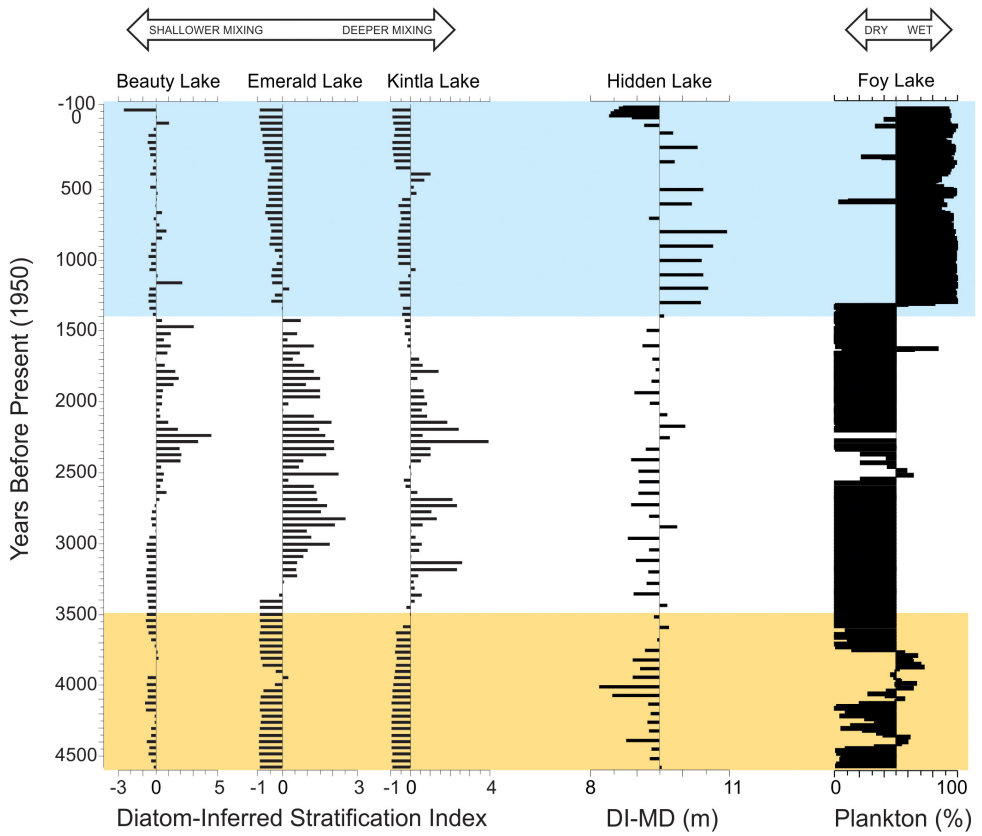

FIGURE 8 | Comparison of Hidden Lake record with other regional diatom records over the past 4.5 ka. Diatom-inferred stratification indices from three nearby lakes (**left**, modified from Stone et al., 2016) and hydroclimate variability inferred from the percent planktic diatoms from Foy Lake (**right**, modified from Stone and Fritz, 2006). Diatom-inferred mixing depth (DI-MD) plotted on a reference line indicating average mixing depth in meters. Yellow bar represents the period before major state changes in stratification observed in Stone et al. (2016) associated with regional glacial advances. Blue bar represents enhanced moisture periods observed in Foy and Jones Lakes (Stone and Fritz, 2006; Shapley et al., 2009).

isothermal lake conditions, eventually leading to sustained cooling of the surface waters and ice cover (Catalan et al., 2002; Ragotzkie, 1978).

In temperate lakes, the thickness of the mixed layer is the result of a complex interaction between multiple factors: solar irradiance, light penetration, wind duration and intensity, and air temperature (Ragotzkie, 1978; Schindler, 1997; Livingstone and Dokulil, 2001; Catalan et al., 2002). The impact of each of these factors upon the thermal structure of any lake is strongly influenced by basin morphometry. For example, the influence of wind intensity and duration is strongly controlled by the surface area and the surface area to depth ratio (Fee et al., 1996; Robertson and Ragotzkie, 1990). Empirical studies have shown that a *primary* control over summer mixing depth is the maximum fetch (Ragotzkie, 1978; Gorham and Boyce, 1989; Håkanson, 2005), which determines the ability of wind energy to induce mixing in stratified lake systems. Water clarity and solar irradiance are also major factors that determine the depth of the mixed layer; however, these elements typically have a larger influence on lakes with smaller surface areas, where fetch is less influential (Ragotzkie, 1978; Sterner, 1990; Fee et al., 1996; Persson and Jones, 2008; von Einem and Graneli, 2010).

While air temperature has limited direct control over lake thermal structure, it can strongly influences the seasonal duration of ice and snow cover. Hence air temperature most commonly influences lake ice phenology, which indirectly influences the timing of light penetration and transference of energy through wind. However, lake ice phenology, particularly freeze-up, is still strongly influenced by basin morphology (Ragotzkie, 1978; Robertson and Ragotzkie, 1990). In alpine lake systems, air temperature can also substantially alter landscape-lake interactions by changing the basin vegetation, soil development rates and frequency of fires. Thus air temperature may also indirectly modify factors that influence water clarity, such as soil erosion, inputs of dissolved organic matter, and nutrient fluxes to lake systems (Wright and Bailey, 1982; Bayley et al., 1992; Fee et al., 1996; Fritz et al., 2004; Rosén and Hammarlund, 2007; Saros et al., 2012).

Below we interpret the observed changes in the diatom assemblages throughout the last 8.5 ka using a combination of inferences based upon the changes in diatom assemblages within each zone, the calculated planktic to benthic ratio, DI-MD, and our modeled three-dimension morphology of the lake basin. It is important to note that while the lake basin has probably

infilled somewhat through the Holocene, sedimentation rates are exceptionally low in Hidden Lake, thus the three-dimensional model we have created based upon modern sediment-water interfaces probably is not substantially different (less than 1 m different) from those that would have been present in the lake throughout the Holocene.

Interpretation of the Diatom Record of Hidden Lake

DZ1 (8.64 – 7.61 ka)

We interpret the earliest part of the diatom assemblage record (DZ1) to represent a deep, alkaline lake. We infer the high proportion of tychoplanktic diatoms in this zone and throughout the core (**Figure 6**) to generally reflect that the lake regularly undergoes seasonal moating during the spring and early summer in response to snow and ice cover (Lotter and Bigler, 2000). Planktic to benthic ratios increase at the base of DZ1, which we interpret as gradually rising lake levels. Hidden Lake occurs in a glaciated basin. This change in lake level probably represents gradual melting of the local glacier systems in response to early Holocene warming. DI-MD through this zone ranges from ∼8 to 9 m and is highly stable throughout most of the zone. Because of the shallow mixing depths inferred, we interpret that DZ1 represented a period when lake elevations were *shallower* than 1945.5 m asl, the lake surface area was substantially smaller in the deep sub-basin than the modern lake, and the effective fetch was lower, resulting in a shallow mixed layer. At lake surface elevations below this depth, our modeled lake suggests that the modern deep sub-basin would have been *completely isolated* from the rest of Hidden Lake (*see* **Figure 4C**).

DZ2 (7.61 – 6.18 ka)

In this zone, we infer a substantial change in lake depth occurred, leading to an abrupt increase in benthic taxa comprised mostly of monoraphid diatoms. The dominant benthic diatom taxa in this zone, represented by *K. suchlandtii*, *K. nitidiformis*, and *Cocconeis* sp., probably reflect an abundance of submerged aquatic macrophytes or other benthic substrates in the lake environment. The strong threshold-like response of the diatom record is probably the result of an interaction between lake elevation and the complex basin morphology, which led to an expansion of benthic diatom habitats. An inferred increase in macrophyte habitat area suggests that water transparency conditions also may have increased relative to those in DZ1. Because of the complex basin morphology, an increase in available benthic habitat might indicate *either an increase or decrease in lake level* (relative to DZ1). For example, modeled surface areas in the lake suggest that the greatest increase in benthic habitat area for the deepest sub-basin actually occurs when the lake surface elevation is around 1946 m asl (∼1.5 m below modern lake levels). We propose two potential models for the transitions observed in DZ2.

Shallow lake DZ2 model

One explanation for the observed trends in the diatom assemblage data in DZ2 is that the deep sub-basin remained isolated throughout the entire period. In this 'shallow lake' model, lake levels were probably low enough (or the water column was clear enough) that the entire lake floor of the deep sub-basin was sunlight, effectively maximizing the benthic habitat of the lake. A compelling argument supporting this idea is that the DZ2 diatom assemblage, dominated by benthic diatoms, is unique to the lower part of the record, suggesting that the lake has not since returned to this state in the entire Holocene. In other words, this was an unusual occurrence and not something that could be reproduced by relatively small changes in regional hydroclimate variability; and thus a fairly large change in lake level (and transparency) must have occurred to produce this change in the assemblage because of deep nature of the lake basin.

Deep lake DZ2 model

An alternative explanation for the abrupt increase in benthic diatom species in DZ2 is that the diatom assemblages in DZ2a represent the joining of all sub-basins to form one continuous lake, but where the available benthic habitat area was substantially higher than it is in the modern lake, perhaps 1–1.5 m below the modern lake level (*see* **Figure 4B**). A compelling argument for this interpretation is that reconstructed DI-MD during DZ1 indicates that the lake was *more stratified* (i.e., shallower mixed layer) than DZ2. A shallower DI-MD would be produced by a lake that had a *smaller maximum effective fetch* (reducing its surface area). Interestingly, the upper part of DZ2 (2b) is defined by the first major occurrence of *L. intermedia* and our DI-MD suggests that the mixing depth was abruptly quite a bit deeper (>11 m) during this interval. Benthic diatom species still dominate the fossil assemblage in DZ2b, but these gradually decline as *L. intermedia* increases and inferred mixing peaks. Given the dependence upon mixing depth for the planktic species in the diatom assemblage, DZ2b could represent a gradual deepening of the lake, resulting in an increase in maximum effective fetch at the core site. Given the relatively small change in lake level required to isolate the deep sub-basin of Hidden Lake, the lake 'deepening DZ2 lake' model described above relies upon the idea that only very small changes in lake level were required to produce a very large change in the mixing depth, because the fetch increased substantially and imparted a greater energy to the upper mixed layer. However, this model also suggested that similar benthic habitat expansion did not recur throughout the remainder of the Holocene, and thus very limited changes in lake level have would have occurred since DZ2b. However, the higher energy state of the lake, resulting from increasing fetch, potentially could have destroyed the potential for macrophyte growth throughout the Holocene, meaning that a return to a similar lake state might not have been possible even if lake levels were at similar elevations at some later point in the Holocene.

The abrupt nature of this transition in both planktic to benthic ratio and DI-MD creates an interesting dilemma. Either lake levels shallowed drastically, exposing the deep sub-basin floor to sunlight, or lake levels simply rose gradually and connected the sub-basins, increasing the benthic habitat in the process and increasing fetch to increase lake mixing depths. We favor the deepening lake DZ2 model, since it relies on less abrupt changes in lake level and might represent a continuation of rising lake

levels resulting from glacial melting in response to warming through the Holocene Climatic Optimum.

DZ3 (6.18 –4.13 ka)

In this period, the lake begins to establish conditions that are more similar to the modern lake. Benthic species become substantially reduced at the transition to DZ3a, suggesting that lake levels initially continued to rise very gradually. Midway through DZ3 (3b), *Discostella stelligera* makes it first substantial appearance in the record. However, the fact that *Lindavia intermedia* does not decline substantially at any point in DZ3 suggests that rather than a major change in lake level, this transition may reflect an enhanced influence of *seasonality* in the thermal structure of the lake. One way this might be produced is by warmer average temperatures during the winter season, resulting in a longer ice-free period. Evidence of increased warming throughout the mid-Holocene period is common from many other lake records from this region of the Rocky Mountains (Bracht et al., 2008; Shapley et al., 2009; Shuman et al., 2009; Whitlock et al., 2012; Slemmons et al., 2015; Stone et al., 2016). Alternatively, it might be the result of the decline in average lake depth with increasing total lake depth, leading to warmer water settings in the epilimnion and accelerated onset of seasonal lake stratification. A similar process might also result from enhanced development of soils in the basin and a concomitant decline in water clarity. Several recent studies (Saros et al., 2014; Malik and Saros, 2016; Malik et al., 2017) have shown a relationship between *L. radiosa* and higher light exposure. Although *L. radiosa* is present in low relative abundance in the sediment record, these observations support the idea that the replacement of *L. radiosa* with *D. stelligera* at the top of this zone may be partially related to a change in water clarity.

DZ4 (4.13 – Present)

The planktic to benthic ratio throughout the upper half of the core expresses a greater level of stability than earlier periods in the sediment record. On average, planktic species are more abundant, tychoplankton is slightly lower. After ∼3 ka, the planktic diatom abundance (particularly *L. comensis*) generally increases. The last 200 years of the record show a sharp rise in species indicative of increased stratification, probably associated with increasing temperatures, which has been previously addressed in Saros et al. (2012). Tychoplanktic species, which in this setting probably represent intermediate lake depths and ice moating conditions (Lotter and Bigler, 2000), rapidly decline in response to 20th century warming, which is also evidenced throughout Glacier National Park by the loss of glaciers and snowpack (Pederson et al., 2004, 2013).

Late Holocene Regional Context

Most regional records suggest that the conditions for the Rocky Mountains in the late Holocene were generally cooler and/or wetter between 3,500 and 1,400 years ago (Osborn and Karlstrom, 1988; Luckman et al., 1993; Palmer et al., 2002; Stevens et al., 2006; Stone and Fritz, 2006; Chase et al., 2008; Walker and Pellatt, 2008; Shuman et al., 2009). Records from nearby paleolimnological sites suggest it was probably mostly warmer but substantially wetter in the past 1,400 years (Stevens et al., 2006; Bracht et al., 2008; Shapley et al., 2009; Shuman et al., 2009). Interestingly, Stone et al. (2016) provided clear evidence of coherent trends of *increased lake mixing* (diametric to inferred changes observed here) across three lakes in the US Rocky Mountains throughout this period, which were interpreted to result from increased winter storms linked to phase changes in the Aleutian Low. Outside of the last 200 years, sedimentation rates within the lake have not undergone major changes, suggesting changes in nutrient loading, which may have substantially affected light penetration, have probably not occurred. Therefore, we interpret the discrepancy between shallower mixing depths and the expected response to cooler climate conditions through this period to suggest that Hidden Lake's thermal structure may have been influenced by the lake basin morphology.

Hidden Lake has a complex basin morphometry, and morphometric parameters that significantly influence mixing depth (particularly surface area and fetch) and are highly dependent upon lake level (**Figure 3**). Three-dimensional modeling indicates that at a lake surface elevation threshold 2–3 m below that of the modern lake, the deep basin of the lake would become isolated from the rest of the lake (**Figure 4**), with a considerably smaller surface area and effective fetch. Since fetch plays a significant role in average lake mixing depth, a substantial decrease in effective fetch as a result of lower lake surface elevation explains the observed shift in mixing depths toward shallower values, even under cooler conditions. A change in effective fetch with lake-level also provides an explanation for the relationship between changes in lake mixing and changing benthic habitats: as the lake level continues to rise to its modern elevation, available benthic habitats expand as the lake begins to flood the surrounding terrain. Ultimately, once the lake surface elevation increases enough that it joins with the adjacent sub-basins, wind intensity picks up considerably with increasing effective fetch, substantially increasing lake mixing, which leads to the sudden increase of *L. intermedia* at the base of sub-zone 4b. This reverses briefly during the period of the Little Ice Age, when plankton losses are generally associated with increases in *S. pinnata,* likely as a result of enhanced snow/ice cover and decreased planktic productivity.

The broader context of these results and their implications for the Late Holocene can best be observed as state changes in the average mixing depth of Hidden Lake in association with changes in hydroclimate (**Figure 8**). The general patterns of lake mixing inferred in the Hidden Lake record tend to be coherent with previously reported regional stratification indicators (Stone et al., 2016) prior to about 3.5 ka. However, after this point, changes in lake level have a profound influence on the response on the thermal structure of Hidden Lake. When other regional records of effective moisture suggest lower lake states associated with the period of glacial advances, between 3.5 and 1.4 ka (Stevens et al., 2006; Shapley et al., 2009; Shuman et al., 2009), the diatom-inferred mixing depth is typically asynchronous with other regional records of lake mixing. We attribute these differences to hydroclimate variability obfuscating the response of lake mixing. Around 1.4 ka, when the records from Foy and Jones Lakes show substantial deepening and freshening,

the diatom-inferred mixing depth from Hidden Lake suggests much deeper mixing (**Figure 8**, blue bar). We associate this change with a pronounced change in lake fetch, associated with the lake at its deepest state. The complexity of the Hidden Lake basin morphology appears to have a distinct impact on the lake response to thermal stratification, but the timing of major changes in variability closely mirrors substantial changes in effective moisture in the region.

Summary and Implications

Between 8.64 and 7.61 ka the diatom record from Hidden Lake suggests that the lake was deep and fresh, with limited benthic habitat, but lower than the modern lake system. After 7.61 ka, the lake level likely rose, inundating the surrounding lake marginal area and expanding the available benthic diatom habitat substantially. Between 6.18 and 4.13 ka, lake level probably declined somewhat, leading to enhanced seasonal stratification. This pattern of enhanced aridity in the mid-Holocene has been observed in many lake records throughout the western US (Shuman et al., 2009; Williams et al., 2009). After 1.4 ka, the record from Hidden Lake suggests that the lake became deeper and less stratified in response to the effects of enhanced fetch.

The results of this research highlight the importance of considering the basin morphology and the potential impacts of fetch when reconstructing changes in lake records that may undergo substantial lake level change. Additionally, this study exemplifies the strengths of using neo-ecological techniques and three-dimensional lake morphometry modeling together when interpreting paleolimnological records using fossil diatom assemblages. The early part of the record is marked by significant changes in lake level that are manifested as changes in the planktic to benthic ratio. Planktic species from the fossil record exhibit long-term changes in mixing depth through the Holocene record from Hidden Lake; the dynamic changes in plankton are particularly helpful for interpreting past lake conditions where the direction of lake level changes are difficult to determine. Because of the complex lake basin morphometry, the interaction of effective fetch and lake level change may be responsible for modifying the lake's response to long-term climatological changes in hydroclimate. Importantly, exploring the interaction between hydroclimate variability and thermal structure showcases how sets of regionally coherent lake records can help to disentangle the signals from records with non-linear responses in complex lake basins.

The influence of changing lake levels on past fetch conditions has not often been the focus of paleolimnological research, but the combination of three-dimensional lake modeling, combined with changes in the planktic to benthic ratio and robust changes in the long-term diatom-inferred mixing depths may provide new opportunities to explore this approach, particularly in lake basins with complex morphologies.

DATA AVAILABILITY

The raw data supporting the conclusions of this manuscript will be made available by the authors, without undue reservation, to any qualified researcher.

AUTHOR CONTRIBUTIONS

JRS was the lead composer of the body of the text. In addition, JRS developed the lake bathymetry, developed the three-dimensional modeling and morphometric analyses, diatom analysis interpretation, statistical analyses, and was responsible for core collection, sub-sampling, and age modeling. JES was the secondary composer of the body of the text, provided a conceptual basis for the research, and was primarily responsible for the design of neo-ecological experiments and their analyses and assisted with diatom interpretation. TS was responsible for diatom analyses and assisted with the concept of the manuscript text.

FUNDING

This work was supported by a grant from the National Science Foundation (Ecology DEB#0639901).

ACKNOWLEDGMENTS

Karlyn Westover and Audrey Bamberg assisted with the collection of sediment cores and bathymetric data. Steve Wooden processed and prepared the diatom slides. Lab preparations and microscope analyses were performed at the Fritz Lab (University of Nebraska–Lincoln). Discussions with David Jewson and comments from Sherilyn C. Fritz, Karlyn Westover, two reviewers, and Lesleigh Anderson improved clarity of the manuscript.

SUPPLEMENTARY MATERIAL

The Supplementary Material for this article can be found online at: https://www.frontiersin.org/articles/10.3389/feart.2019.00028/full#supplementary-material

REFERENCES

Anderson, N. J. (1990). Spatial pattern of recent sediment and diatom accumulation in a small, monomictic, eutrophic lake. *J. Paleolimnol.* 3, 143–160. doi: 10.1007/BF00414068

Appleby, P. G., and Oldfield, F. (1978). The calculation of lead-210 dates assuming a constant rate of supply of unsupported 210Pb to the sediment. *Catena* 5, 1–8. doi: 10.1016/S0341-8162(78)80002-80002

Bachmann, R. W., Hoyer, M. V., and Canfield, D. E. J. (2000). The potential for wave disturbance in shallow Florida lakes. *Lakes Reserv. Manag.* 16, 281–291. doi: 10.1080/07438140009354236

Bahls, L. L. (2004). *Northwest Diatoms: A Photographic Catalogue of Species in the Montana Diatom Collection with Ecological Optima, Associates, and Distribution*

Records for the Nine Northwestern United States. Helena: Montana Diatom Collection, 1.

Bahls, L. L. (2005). *Northwest Diatoms: A Photographic Catalogue of Species in the Montana Diatom Collection with Ecological Optima, Associates, and Distribution Records for the Nine Northwestern United States*. Helena: Montana Diatom Collection, 2.

Battarbee, R. W. (2003). "Diatom analysis," in *Handbook of Holocene Palaeoecology and Palaeohydrology*, eds B. E. Berglund and M. Ralska-Jasiewiczowa (Caldwell, NJ: Blackburn Press), 527–570.

Bayley, S. E., Schindler, D. W., Beaty, K. G., Parker, B. R., and Stainton, M. P. (1992). Effects of multiple fires on nutrient yields from streams draining boreal forest and fen watersheds: nitrogen and phosphorus. *Can. J. Fish. Aquat. Sci.* 49, 584–596. doi: 10.1139/f92-068

Bernhardt, J., Elliott, J. A., and Jones, I. D. (2008). Modelling the effects on phytoplankton communities of changing mixed depth and background extinction coefficient on three contrasting lakes in the English Lake District. *Freshw. Biol.* 53, 2573–2586. doi: 10.1111/j.1365-2427.2008.02083.x

Blaauw, M., and Christen, J. A. (2011). Flexible paleoclimate age-depth models using an autoregressive gamma process. *Bayesian Anal.* 6, 457–474. doi: 10.1214/11-BA618

Blais, J. M., and Kalff, J. (1995). The influence of lake morphometry on sediment focusing. *Limnol. Oceanogr.* 40, 582–588. doi: 10.4319/lo.1995.40.3.0582

Bracht, B. B., Stone, J. R., and Fritz, S. C. (2008). A diatom record of late Holocene climate variation in the Northern Range of Yellowstone National Park. *USA. Quat. Int.* 188, 149–155. doi: 10.1016/j.quaint.2007.08.043

Camburn, K. E., and Charles, D. F. (2000). *Diatoms of Low-Alkalinity Lakes in the Northeastern United States*. Philadelphia: The Academy of Natural Sciences of Philadelphia.

Carrick, H. J., Aldridge, F. J., and Schelske, C. L. (1993). Wind influences phytoplankton biomass and composition in a shallow, productive lake. *Limnol. Oceanogr.* 38, 1179–1192. doi: 10.4319/lo.1993.38.6.1179

Catalan, J., Ventura, M., Brancelj, A., Granados, I., Thies, H., Nickus, U., et al. (2002). Seasonal ecosystem variability in remote mountain lakes: implications for detecting climatic signals in sediment records. *J. Paleolimnol.* 28, 25–46. doi: 10.1023/A:1020315817235

Chase, M., Bleskie, C., Walker, I. R., Gavin, D. G., and Hu, F. S. (2008). Midge-inferred Holocene summer temperatures in Southeastern British Columbia, Canada. *Palaeogeogr. Palaeoclimatol. Palaeoecol.* 257, 244–259. doi: 10.1016/j.palaeo.2007.10.020

Cumming, B. F., Wilson, S. E., Hall, R. I., and Smol, J. P. (1995). "Bibliotheca diatomologica," in *Diatoms from British Columbia Lakes*, Vol. 31, ed. H. Lange-Bertalot (Berlin: J. Cramer).

Davies-Colley, R. J. (1988). Mixing depths in New Zealand lakes. *New Zeal. J. Mar. Freshw. Res.* 22, 517–528. doi: 10.1080/00288330.1988.9516322

Diehl, S., Berger, S., Ptacnik, R., and Wild, A. (2002). Phytoplankton, light, and nutrients in a gradient of mixing depths: field experiments. *Ecology* 83, 399–411. doi: 10.1890/0012-9658(2002)083[0399:PLANIA]2.0.CO;2

Evans, R. D. (1994). Empirical evidence of the importance of sediment resuspension in lakes. *Hydrobiologia* 284, 5–12. doi: 10.1007/BF00005727

Fallu, M.-A., Allaire, N., and Pienitz, R. (2000). *Bibliotheca Diatomologica Band 45: Freshwater Diatoms from northern Québec and Labrador (Canada) - Species-Environment Relationships in Lakes of Boreal Forest, Forest-Tundra and Tundra Regions*. Berlin: J. Cramer.

Fee, E. J. (1979). A relation between lake morphometry and primary productivity and its use in interpreting whole-lake eutrophication experiments. *Limnol. Oceanogr.* 24, 401–416. doi: 10.4319/lo.1979.24.3.0401

Fee, E. J., Hecky, R. E., Kasian, S. E. M., and Cruikshank, D. R. (1996). Effects of lake size, water clarity, and climatic variability on mixing depths in Canadian shield lakes. *Limnol. Oceanogr.* 41, 912–920. doi: 10.4319/lo.1996.41.5.0912

Foged, N. (1981). *Diatoms in Alaska, Bibliotheca Phycologica*, Vol. 53. Port Jervis, NY: Lubrecht & Cramer, Limited.

Fritz, S. C. (1996). Paleolimnological records of climatic change in North America. *Limnol. Oceanogr.* 41, 882–889. doi: 10.4319/lo.1996.41.5.0882

Fritz, S. C. (2008). Deciphering climatic history from lake sediments. *J. Paleolimnol.* 39, 5–16. doi: 10.1007/s10933-007-9134-x

Fritz, S. C., Engstrom, D. R., and Juggins, S. (2004). Patterns of early lake evolution in boreal landscapes: a comparison of stratigraphic inferences with a modern chronosequence in Glacier Bay. Alaska. *Holocene* 14, 828–840. doi: 10.1191/0959683604hl763rp

Fritz, S. C., Ito, E., Yu, Z., Laird, K. R., and Engstrom, D. R. (2000). Hydrologic variation in the Northern Great Plains during the last two millennia. *Quat. Res.* 53, 175–184. doi: 10.1006/qres.1999.2115

Golden Software (2010). *Surfer (Version 10)*. Golden, CO: Golden Software, LLC. Available at: www.goldensoftware.com

Gorham, E., and Boyce, F. M. (1989). Influence of lake surface area and depth upon thermal stratification and the depth of the summer thermocline. *J. Great Lakes Res.* 15, 233–245. doi: 10.1016/S0380-1330(89)71479-9

Guiry, M., and Guiry, G. (2017). *AlgaeBase. World-wide Electronic Publication*. Galway: National University of Ireland.

Håkanson, L. (1981). *A Manual of Lake Morphometry*. Berlin: Springer-Verlag. doi: 10.1007/978-3-642-81563-8

Håkanson, L. (2005). The importance of lake morphometry for the structure and function of lakes. *Int. Rev. Hydrobiol.* 90, 433–461. doi: 10.1002/iroh.200410775

Håkanson, L., and Jansson, M. (1983). *Principles of Lake Sedimentology*. Berlin: Springer. doi: 10.1007/978-3-642-69274-1

Hamilton, D. P., and Mitchell, S. F. (1996). An empirical model for sediment resuspension in shallow lakes. *Hydrobiologia* 317, 209–220. doi: 10.1371/journal.pone.0131431

Houser, J. N. (2006). Water color affects the stratification, surface temperature, heat content, and mean epilimnetic irradiance of small lakes. *Can. J. Fish. Aquat. Sci.* 63, 2447–2455. doi: 10.1139/F06-131

Juggins, S. (2015). *Rioja: Analysis of Quaternary Science Data, R package Version (0.9-9)*. Available at: https://cran.r-project.org/web/packages/rioja/index.html.

Kingsbury, M. V., Laird, K. R., and Cumming, B. F. (2012). Consistent patterns in diatom assemblages and diversity measures across water-depth gradients from eight Boreal lakes from north-western Ontario (Canada). *Freshw. Biol.* 57, 1151–1165. doi: 10.1111/j.1365-2427.2012.02781.x

Lange-Bertalot, H., Kulbs, K., Lauser, T., Norpel-Schempp, M., and Willmann, M. (1996). "Iconographia Diatomologica," in *Diatom Taxa Introduced by Georg Krasske Documentation and Revision*, Vol. 3, ed. H. Lange-Bertalot Koenigstein (Königstein: Koeltz Scientific Books).

Lehman, J. T. (1975). Reconstructing the rate of accumulation of lake sediment: the effect of sediment focusing. *Quat. Res.* 5, 541–550. doi: 10.1016/0033-5894(75)90015-0

Livingstone, D. M., and Dokulil, M. T. (2001). Eighty years of spatially coherent Austrian lake surface temperatures and their relationship to regional air temperature and the North Atlantic Oscillation. *Limnol. Oceanogr.* 46, 1220–1227. doi: 10.4319/lo.2001.46.5.1220

Lotter, A. F., and Bigler, C. (2000). Do diatoms in the Swiss Alps reflect the length of ice-cover? *Aquat. Sci.* 62, 125–141. doi: 10.1007/s000270050002

Luckman, B. H., Holdsworth, G., and Osborn, G. D. (1993). Neoglacial glacier fluctuations in the Canadian Rockies. *Quat. Res.* 39, 144–153. doi: 10.1006/qres.1993.1018

Malik, H. I., Northington, R. M., and Saros, J. E. (2017). Nutrient limitation status of Arctic lakes affects the responses of Cyclotella sensu lato diatom species to light: implications for distribution patterns. *Polar Biol.* 40, 2445–2456. doi: 10.1007/s00300-017-2156-2156

Malik, H. I., and Saros, J. E. (2016). Effects of temperature, light and nutrients on five Cyclotella sensu lato taxa assessed with in situ experiments in arctic lakes. *J. Plankton Res.* 38, 431–442. doi: 10.1093/plankt/fbw002

Mason, I. M., Guzkowska, M. A. J., Rapley, C. G., and Street-Perrott, F. A. (1994). The response of lake levels and areas to climatic change. *Clim. Change* 27, 161–197.

Osborn, G. D., and Karlstrom, E. T. (1988). Holocene history of Bugaboo glacier. *Br. Columbia. Geol.* 16, 1015–1017. doi: 10.1130/0091-7613(1988)016<1015:HHOTBG>2.3.CO;2

Osgood, R. A. (1988). Lake mixis and internal phosphorus dynamics. *Arch. für Hydrobiol.* 4, 629–638.

Palmer, S., Walker, I. R., Heinrichs, M. L., Hebda, R. J., and Scudder, G. (2002). Postglacial midge community change and Holocene palaeotemperature reconstructions near treeline, southern British Columbia (Canada). *J. Paleolimnol.* 28, 469–490. doi: 10.1023/A:1021644122727

Pal'shin, N. I., Efremova, T. V., and Potakhin, M. S. (2008). The effect of morphometric characteristics and geographic zonality on thermal stratification of lakes. *Water Resour.* 35, 191–198. doi: 10.1134/S009780780800 20073

Pederson, G. T., Betancourt, J. L., and McCabe, G. J. (2013). Regional patterns and proximal causes of the recent snowpack decline in the Rocky Mountains. *U.S. Geophys. Res. Lett.* 40, 1811–1816. doi: 10.1002/grl.50424

Pederson, G. T., Fagre, D. B., Gray, S. T., and Graumlich, L. J. (2004). Decadal-scale climate drivers for glacial dynamics in Glacier National Park, Montana, USA. *Geophys. Res. Lett.* 31:L12203. doi: 10.1029/2004GL019770

Persson, I., and Jones, I. D. (2008). The effect of water colour on lake hydrodynamics: a modelling study. *Freshw. Biol.* 53, 2345–2355. doi: 10.1111/j.1365-2427.2008.02049.x

Ragotzkie, R. A. (1978). "Heat budgets of lakes," in *Lakes: Chemistry, Geology, Physics*, ed. A. Lerman (New York, NY: Springer-Verlag), 1–19.

Rea, T. E., Karapatakis, D. J., Guy, K. K., Pinder, J. E. I., and Mackey, H. E. J. (1998). The relative effects of water depth, fetch and other physical factors on the development of macrophytes in a small southeastern US pond. *Aquat. Bot.* 61, 289–299. doi: 10.1016/S0304-3770(98)00069-2

Robertson, D. M., and Ragotzkie, R. A. (1990). Thermal structure of a multibasin lake: influence of morphometry, interbasin exchange, and groundwater. *Can. J. Fish. Aquat. Sci.* 47, 1206–1212. doi: 10.1139/f90-140

Rosén, P., and Hammarlund, D. (2007). Effects of climate, fire and vegetation development on Holocene changes in total organic carbon concentration in three boreal forest lakes in northern Sweden. *Biogeosciences* 4, 975–984. doi: 10.5194/bgd-4-1329-2007

Saros, J. E., and Anderson, N. J. (2015). The ecology of the planktonic diatom Cyclotella and its implications for global environmental change studies. *Biol. Rev.* 90, 522–541. doi: 10.1111/brv.12120

Saros, J. E., Stone, J. R., Pederson, G. T., Slemmons, K. E. H., Spanbauer, T. L., Schliep, A., et al. (2012). Climate-induced changes in lake ecosystem structure inferred from coupled neo- and paleoecological approaches. *Ecology* 93, 2155–2164. doi: 10.1890/11-2218.1

Saros, J. E., Strock, K. E., Mccue, J., Hogan, E., and Anderson, N. J. (2014). Response of Cyclotella species to nutrients and incubation depth in Arctic lakes. *J. Plankton Res.* 36, 450–460. doi: 10.1093/plankt/fbt126

Schindler, D. W. (1997). Widespread effects of climatic warming on freshwater ecosystems in North America. *Hydrol. Process.* 11, 1043–1067. doi: 10.1002/(SICI)1099-1085(19970630)11:8<1043::AID-HYP517>3.0.CO;2-5

Scott, J. T. (1964). *A Comparison of the Heat Balance of Lakes in Winter*. Ph.D. thesis, Wisconsin University, Madison.

Shapley, M. D., Ito, E., and Donovan, J. J. (2009). Lateglacial and Holocene hydroclimate inferred from a groundwater flow-through lake, Northern Rocky Mountains, USA. *Holocene* 19, 523–535. doi: 10.1177/0959683609104029

Shuman, B., Henderson, A. K., Colman, S. M., Stone, J. R., Fritz, S. C., Stevens, L. R., et al. (2009). Holocene lake-level trends in the Rocky Mountains. *U.S.A. Quat. Sci. Rev.* 28, 1861–1879. doi: 10.1016/j.quascirev.2009.03.003

Slemmons, K. E. H., Saros, J. E., Stone, J. R., McGowan, S., Hess, C. T. T., and Cahl, D. (2015). Effects of glacier meltwater on the algal sedimentary record of an alpine lake in the central US Rocky Mountains throughout the late Holocene. *J. Paleolimnol.* 53, 385–399. doi: 10.1007/s10933-015-9829-9823

Smith, I. R., and Sinclair, I. J. (1972). Deep water waves in lakes. *Freshw. Biol.* 2, 387–399. doi: 10.1111/j.1365-2427.1972.tb00378.x

Snucins, E., and Gunn, J. (2000). Interannual variation in the thermal structure of clear and colored lakes. *Limnol. Oceanogr.* 45, 1639–1646. doi: 10.4319/lo.2000.45.7.1639

Spaulding, S. A., Lubinski, D. J., and Potapova, M. G. (2010). *Diatoms of the United States*. Available at: http://westerndiatoms.colorado.edu/ [accessed March 29, 2018].

Sterner, R. W. (1990). Lake morphometry and light in the surface layer. *Can. J. Fish. Aquat. Sci.* 47, 687–692.

Stevens, L. R., Stone, J. R., Campbell, J., and Fritz, S. C. (2006). A 2200-yr record of hydrologic variability from Foy Lake, Montana, USA, inferred from diatom and geochemical data. *Quat. Res.* 65, 264–274. doi: 10.1016/j.yqres.2005.08.024

Stone, J. R., and Fritz, S. C. (2004). Three-dimensional modeling of lacustrine diatom habitat areas: improving paleolimnological interpretation of planktic:benthic ratios. *Limnol. Oceanogr.* 49, 1540–1548. doi: 10.4319/lo.2004.49.5.1540

Stone, J. R., and Fritz, S. C. (2006). Multidecadal drought and Holocene climate instability in the Rocky Mountains. *Geology* 34, 409–412. doi: 10.1130/G22225.1

Stone, J. R., Saros, J. E., and Pederson, G. T. (2016). Coherent late-Holocene climate-driven shifts in the structure of three Rocky Mountain lakes. *Holocene* 26, 1103–1111. doi: 10.1177/0959683616632886

Stuiver, M., Reimer, P. J., Bard, E., Beck, J. W., Burr, G. S., Hughen, K. A., et al. (1998). INTCAL98 Radiocarbon age calibration 24,000 - 0 cal BP. *Radiocarbon* 40, 1041–1083. doi: 10.1017/S0033822200019123

Thomaz, S. M., Souza, D. C., and Bini, L. M. (2003). Species richness and beta diversity of aquatic macrophytes in a large subtropical reservoir (Itaipu Reservoir, Brazil): the influence of limnology and morphometry. *Hydrobiologia* 505, 119–128. doi: 10.1023/B:HYDR.0000007300.78143.e1

Verschuren, D. (1999). Influence of depth and mixing regime on sedimentation in a small, fluctuating tropical soda lake. *Limnol. Oceanogr.* 44, 1103–1113. doi: 10.4319/lo.1999.44.4.1103

von Einem, J., and Graneli, W. (2010). Effects of fetch and dissolved organic carbon on epilimnion depth and light climate in small forest lakes in southern Sweden. *Limnol. Oceanogr.* 55, 920–930. doi: 10.4319/lo.2010.55.2.0920

Walker, I. R., and Pellatt, M. (2008). Climate change and ecosystem response in the northern Columbia River basin - A paleoenvironmental perspective. *Environ. Rev.* 16, 113–140. doi: 10.1139/A08-004

Whitlock, C., Dean, W. E., Fritz, S. C., Stevens, L. R., Stone, J. R., Power, M. J., et al. (2012). Holocene seasonal variability inferred from multiple proxy records from Crevice Lake, Yellowstone National Park, USA. *Palaeogeogr. Palaeoclimatol. Palaeoecol.* 33, 90–103. doi: 10.1016/j.palaeo.2012.03.001

Whitmore, T. J., Brenner, M., and Schelske, C. L. (1996). Highly variable sediment distribution in shallow, wind-stressed lakes: a case for sediment-mapping surveys in paleolimnological studies. *J. Paleolimnol.* 15, 207–221. doi: 10.1007/BF00213041

Wigdahl, C. R., Saros, J. E., Fritz, S. C., Stone, J. R., and Engstrom, D. R. (2014). The influence of basin morphometry on the regional coherence of patterns of diatom-inferred salinity in lakes of the northern Great Plains (USA). *Holocene* 24, 603–613. doi: 10.1177/0959683614523154

Williams, J. W., Shuman, B., and Bartlein, P. J. (2009). Rapid responses of the prairie-forest ecotone to early Holocene aridity in mid-continental North America. *Glob. Planet. Change* 66, 195–207. doi: 10.1016/j.gloplacha.2008.10.012

Wolin, J. A., and Stone, J. R. (2010). "Diatoms as indicators of water-level change in freshwater lakes," in *The Diatoms: Applications for Environmental and Earth Sciences*, eds E. F. Stoermer and J. P. Smol (Cambridge: Cambridge University Press), 174–185. doi: 10.1017/CBO9780511763175.010

Wright, H. A., and Bailey, A. W. (1982). *Fire Ecology: United States and Southern Canada*. New York: Wiley.

Conflict of Interest Statement: The authors declare that the research was conducted in the absence of any commercial or financial relationships that could be construed as a potential conflict of interest.

frontiers in Earth Science

ORIGINAL RESEARCH
published: 05 March 2019
doi: 10.3389/feart.2019.00025

An Assessment of Plant Species Differences on Cellulose Oxygen Isotopes From Two Kenai Peninsula, Alaska Peatlands: Implications for Hydroclimatic Reconstructions

Miriam C. Jones[1], Lesleigh Anderson[2], Katherine Keller[3], Bailey Nash[4], Virginia Littell[5], Matthew Wooller[6] and Chelsea A. Jolley[7]*

[1] Florence Bascom Geoscience Center, U.S. Geological Survey, Reston, VA, United States, [2] Geosciences and Environmental Change 'Science Center', U.S. Geological Survey, Denver, CO, United States, [3] Department of Earth and Planetary Sciences, Harvard University, Cambridge, MA, United States, [4] Department of Geological and Atmospheric Sciences, Iowa State University, Ames, IA, United States, [5] Department of Earth and Space Sciences, University of Washington, Seattle, WA, United States, [6] Alaska Stable Isotope Facility, University of Alaska Fairbanks, Fairbanks, AK, United States, [7] Department of Geological Sciences, Brigham Young University, Provo, UT, United States

OPEN ACCESS

Edited by:
Michaël Hermoso, UMR7193 Institut des Sciences de la Terre Paris (ISTEP), France

Reviewed by:
Guillemette Ménot, École Normale Supérieure de Lyon, France
Matthew John Amesbury, University of Helsinki, Finland

***Correspondence:**
Miriam C. Jones
miriamjones@usgs.gov

Specialty section:
This article was submitted to Quaternary Science, Geomorphology and Paleoenvironment, a section of the journal Frontiers in Earth Science

Received: *17 October 2018*
Accepted: *05 February 2019*
Published: *05 March 2019*

Citation:
Jones MC, Anderson L, Keller K, Nash B, Littell V, Wooller M and Jolley CA (2019) An Assessment of Plant Species Differences on Cellulose Oxygen Isotopes From Two Kenai Peninsula, Alaska Peatlands: Implications for Hydroclimatic Reconstructions. Front. Earth Sci. 7:25. doi: 10.3389/feart.2019.00025

Peat cores are valuable archives of past environmental change because they accumulate plant organic matter over millennia. While studies have primarily focused on physical, ecological, and some biogeochemical proxies, cores from peatlands have increasingly been used to interpret hydroclimatic change using stable isotope analyses of cellulose preserved in plant remains. Previous studies indicate that the stable oxygen isotope compositions ($\delta^{18}O$) preserved in alpha cellulose extracted from specific plant macrofossils reflect the $\delta^{18}O$ values of past peatland water and thereby provide information on long-term changes in hydrology in response to climate. Oxygen isotope analyses of peat cellulose ($\delta^{18}O_{cellulose}$) have been successfully developed from peat cores that accumulate the same species for millennia. However, to fully exploit the potential of this proxy in species-diverse fens, studies are needed that account for the isotopic variations caused by changes in dominant species composition. This study assesses variation in $\delta^{18}O$ values among peatland plant species and how they relate to environmental waters in two fens informally named Horse Trail and Goldfin, located on the leeward (dry) and windward (wet) side, respectively, of the climatic gradient across the Kenai Peninsula, Alaska. Environmental water $\delta^{18}O$ values at both fens reflect unmodified $\delta^{18}O$ values of mean annual precipitation, although at Goldfin standing pools were slightly influenced by evaporation. Modern plant [mosses and *Carex* spp. (sedges)] $\delta^{18}O_{cellulose}$ values indicate that all *Carex* spp. are higher (~2.5‰) than those of mosses, likely driven by their vascular structure and ecophysiological difference from non-vascular mosses. Moss $\delta^{18}O_{cellulose}$ values within each peatland are similar among the species, and differences appear related to evaporation effects on environmental waters within hummocks and hollows. The plant taxa-environmental water $\delta^{18}O$ differences are applied to the previously determined Horse Trail Fen untreated bulk $\delta^{18}O$ record. Results include significant changes to inferred millennial-to-centennial scale hydroclimatic trends where dominant taxa shift from moss to *Carex* spp., indicating that modern calibration datasets

are necessary for interpreting stable isotopes from fens, containing a mix of vascular and nonvascular plants. Accounting for isotopic offsets through macrofossil analysis and modern plant-water isotope measurements opens new opportunities for hydroclimatic reconstructions from fen peatlands.

Keywords: hydroclimate, peatland archives, oxygen isotopes (δ18O), cellulose, calibration dataset

INTRODUCTION

Peat core records have long served as geologic archives of paleoenvironmental change, using a range of biological, physical, and biogeochemical proxies. Because peat accumulates under waterlogged conditions, previous studies have related the oxygen isotopic signature preserved in alpha cellulose ($\delta^{18}O_{cellulose}$) extracted from peatland plant macrofossils to the isotopic composition of environmental water, i.e., the source from which the plants are absorbing their water (Vardy, 1997; Wissel et al., 2008; Moschen et al., 2009; Loader et al., 2016). The use of $\delta^{18}O_{cellulose}$ values from peatlands was first explored in *Sphagnum*-dominated bogs using analyses of single species (Brenninkmeijer et al., 1982; Ménot-Combes et al., 2002; Zanazzi and Mora, 2005; Daley et al., 2010, 2016; Kühl and Moschen, 2012; Loader et al., 2016). Single-species cellulose in a core limits variability that could arise from isotopic species effects (Ménot-Combes et al., 2002; Daley et al., 2010; Nichols et al., 2010). Bogs, hydraulically sourced only by precipitation, are generally thought to provide the best record of past precipitation change from peatlands, however, relying only on bogs that accumulate monospecific peat for millennia can considerably limit the utility of this proxy to a small number of sites. For example, many Alaska peatlands are primarily groundwater-sourced fens with high species diversity through space and time. The utility of this proxy was tested in one Alaska fen core by analyzing $\delta^{18}O$ changes relative to the plant macrofossils comprising the peat (Jones et al., 2014), and while isotopic shifts occurred that were consistent with other regional records (Fisher et al., 2004; Anderson et al., 2005), questions remain about how closely tied the shifts were to hydroclimate changes vs. other factors, and most specifically, plant species shifts in response to changes in peatland hydrology.

The primary isotopic fractionation involved in biochemically synthesizing cellulose in environmental water has been relatively well constrained to −27‰ (DeNiro and Epstein, 1979, 1981), and while this process was thought to be insensitive to changes in temperature, Sternberg and Ellsworth (2011) quantified a latitudinal influence associated with differences in mean annual air temperatures (MAT) that is −33‰ for high latitudes such as Alaska. In vascular plants, $\delta^{18}O_{cellulose}$ is determined by kinetic and equilibrium fractionation from its environmental water (Amesbury et al., 2015), because values are influenced by both the $\delta^{18}O$ values of environmental water and water within the leaf, which are generally enriched in heavy isotopes due to transpiration and plant vascular mediation (Nichols et al., 2010; Loader et al., 2016). Therefore, in Alaskan peats, which are largely composed of a variety of bryophytes and sedges, contrasting physiological processes for water uptake between bryophytes (mosses; non-vascular) and graminoids (sedges; vascular) likely result in significant differences in their cellulose isotope signatures. Bryophytes, including all mosses and liverworts, lack vascular structure and absorb water through cell walls (Proctor, 2000). In contrast, sedges have roots that can obtain water from deeper horizons and regulate moisture loss via stomata, leading to evaporative enrichment from transpiration through their stomata (Yakir et al., 1990; Amesbury et al., 2015). This may potentially lead to differences not only in environmental-water isotope compositions compared to mosses, but also in additional fractionations of water within the plant related to stomatal conductance (Ménot and Burns, 2001).

To further examine oxygen isotope variations of plant cellulose within Alaskan fens, the goals of this study are to (a) determine the $\delta^{18}O$ values of modern peatland environmental waters and evaluate their relationship to precipitation and groundwater by comparison with local surface water $\delta^{18}O$ values, including Kenai Peninsula lakes, rivers and streams, and the global meteoric water line (GMWL) (Rozanski et al., 1993; Anderson et al., 2016); (b) compare $\delta^{18}O_{cellulose}$ values of plant species with the $\delta^{18}O$ values of their environmental waters to determine whether species $\delta^{18}O$ values significantly differ; and (c) evaluate the range of $\delta^{18}O_{cellulose}$ values exhibited by different peatland-plant species spatially. Lastly, the results are used to evaluate the influence of varying species dominance on bulk peat $\delta^{18}O$ values determined from a ∼14,000-year old core obtained in Horse Trail Fen (HTF) by Jones et al. (2014) that, in turn, influences the hydroclimatic interpretation.

Study Area

The Kenai Peninsula is located in south-central Alaska on the northern coast of the Gulf of Alaska (**Figure 1**). It is bisected along its eastern edge by the Kenai Mountains, composed of Mesozoic bedrock (Rymer and Sims, 1982), which rise to ∼1,025 meters above sea level (m.a.s.l.). The Harding Icefield spans upper elevations of the range, with glaciers terminating at or near sea level to the east and west. The western side of the peninsula is a low-lying landscape shaped by glacial events (Rymer and Sims, 1982; Reger et al., 2008), and is characterized by peatlands, kettle-hole lakes, and boreal forest overlying moraines and glacial outwash. The eastern side of the Kenai Mountains is the wetter, windward side, and precipitation totals are four times higher than on the leeward, western lowlands, spanning a relatively small (<70 km) area. Consequentially, the vegetation on the eastern side comprises the western-most edge of the temperate rainforest, whereas

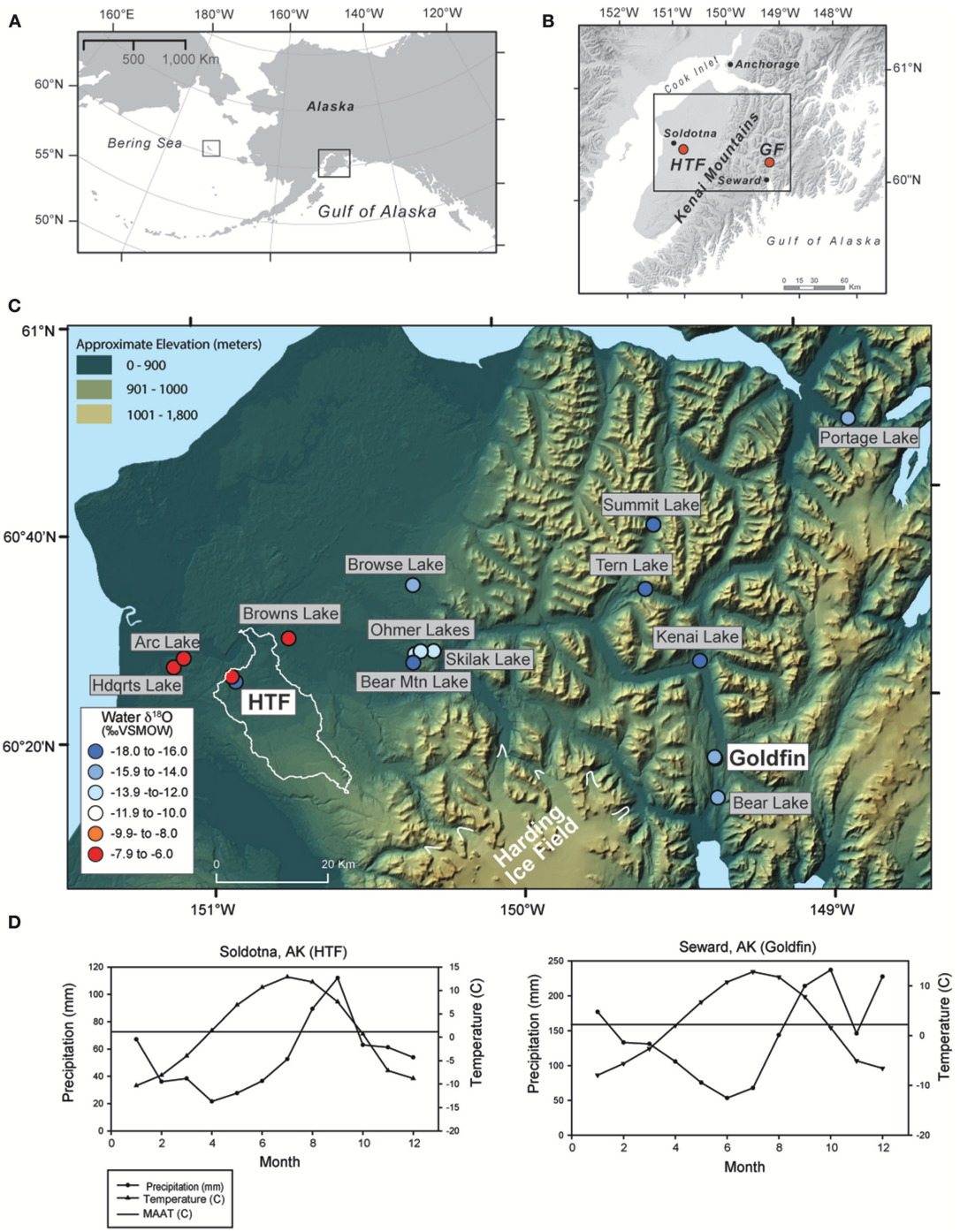

FIGURE 1 | Maps of the Kenai Peninsula **(A)** relative to the North Pacific and Alaska (right black square), also showing the location of St. Matthew Island in the Bering Sea (left black square) **(B)** with Horse Trail fen (HTF) and Golfin (GF) study sites on a gray shaded DEM, **(C)** and lake and peat water sample locations on a color DEM; circle colors indicate water $\delta^{18}O$ values and the light outline around HTF indicates the surface watershed outside the glacial limits of the Kenai icefield, **(D)** precipitation and temperature averages for the closest weather stations to Horse Trail fen and Goldfin (1981–2010 average).

the western lowlands form an ecotone between the boreal and coastal forests.

The climate of the eastern Kenai Mountains is considered maritime, with MAT of 6.5°C with a mean annual precipitation (MAP) of 186.3 cm (Seward, AK), while on the western lowlands, the MAT at Soldotna airport is 6°C and MAP is 46.3 cm (**Figure 1D**; 1981–2010 climate average; Alaska Climate Research Center, http://climate.gi.alaska.edu). On the western

lowlands, the majority of present-day annual precipitation falls during autumn (August, September) and remains relatively high in winter (October-January) and in the eastern Kenai Peninsula, precipitation is highest from September to January (Alaska Climate Research Center, http://climate.gi.alaska.edu), in response to intensification of the Aleutian Low, a semi-permanent low-pressure system that strengthens over the North Pacific and Gulf of Alaska region in late autumn and subsequently wanes in intensity during spring and summer (Overland et al., 1999).

Horse Trail fen (HTF; informal name, 60.264, −149.356, 110 m.a.s.l.), is a large fen complex in the western lowlands near Soldotna, AK. Although located downgradient from the Harding Icefield, watershed analysis using high resolution Digital Elevation Models indicates that the headwater area is isolated from glacial run off (white outline in **Figure 1C**). Goldfin (GF, informal; 60.264, −149.356, 2018 m.a.s.l.), is a small kettle hole peatland located in a narrow north-to-south trending valley ∼30 m above sea level north of Seward, AK. Plant and water isotope samples presented here also include samples obtained from St. Matthew Island (**Figure 1A**), located in the east-central Bering Sea (60.4 °N, −172.7 °W, at sea level elevation).

METHODS

Field collections for this study included modern plants [mosses and sedges (*Carex* spp.)] and associated environmental water. The Horse Trail fen (HTF) site was sampled for water and plants along a 40-m transect from the stream flowing through the peatland to the forest edge at every 10 m in July of 2014. At each point along the transect, surface water associated with plant collections was obtained by submerging 10-mL high-density polyethylene (HDPE) bottles and under the surface of the water table until it filled without bubbles or headspace before sealing under the water. No water was squeezed out of peatland plants. Surface water samples were similarly obtained from near-surface waters of nearby lakes, rivers, and streams (**Figure 1C**).

At each HTF transect position, the dominant plant species were collected, noting whether the plant was submerged, at the water table, or on a hummock. A similar transect was repeated at GF bog in September 2017, starting at the stream flowing at the edge of the bog to 40 m away from the stream. In this bog, an elevation gradient perpendicular to the stream was less apparent and small pools intersected the transect. At the 20-m sampling location, samples were collected from a small pool at the water table and 10 cm above the water table. At the 40-m location, samples were collected from a small pool and an adjacent hummock 10–20-cm high.

Plant species were bagged and labeled with their transect position and subsequently cleaned with deionized water, identified, and separated by species in the laboratory. If enough material was available, species were separated by their stems and leaves. In some cases, whole plants were analyzed, either in addition to separated stems and leaves or in some instances by themselves. Plants and environmental-water samples from St. Matthew Island, Alaska, were collected June 2018, repeating laboratory methods outlined above.

Plant cellulose was extracted by the Cuprammonium (CUAM) method of Wissel et al. (2008) and Moschen et al. (2009). Samples were first bleached using solution of sodium hypchlorite and acetic acid at 70°C to separate the lignin fraction before they were neutralized and freeze dried. The bleached sample was then place in 50-ml centrifuge tubes using a cuprammonium solution ($Cu(NH_3)_4(OH)_2$; "Schweizer solution") for cellulose dissolution, stirred for 6 h, and left to sit at room temperature for an additional 10 h. Once fully dissolved, the copper complex cellulose solution was centrifuged for 25 min at 2,500 rpm and the supernatant was decanted into a clean 50-ml centrifuge tube, leaving the non-cellulosic material behind. This step was repeated to avoid contamination from other plant material. The supernatant was then loaded with ∼3 ml H_2SO_4 (20%) and cold deionized water to induce cellulose precipitation. The tube was shaken and left to sit for 20 min, before it was centrifuged at 2,500 rpm for 25 min. Additional drops of H_2SO_4 (20%) were added until the solution turned from blue to clear, to ensure that cellulose precipitation was complete. The cellulose precipitate was subsequently rinsed with deionized water until it reached a neutral pH by centrifuging at 2,500 rpm for 25 min, before it was freeze dried. A mass of 0.2–0.3 mg of dried cellulose sample was packed in silver capsules and stored in a vacuum drier prior to stable oxygen isotopic analysis.

All oxygen and water hydrogen isotope results for cellulose and water are reported in per mil (‰) as the relative difference of isotope ratios (δ) from the international measurement standard Vienna Standard Mean Ocean Water (VSMOW) defined by

$$\delta^{18}O_{H2O} = [(^{18}O/^{16}O)_{H2O}/(^{18}O/^{16}O)_{SMOW}] - 1 \text{ and}$$
$$\delta^{2}H_{H2O} = [(^{2}H/^{1}H)_{H2O}/(^{2}H/^{1}H)_{SMOW})] - 1. \quad (1)$$

Water samples for isotopic measurements at the University of Illinois at Chicago (UIC) were analyzed on a Picarro l2130-i analyzer by injecting 5 µl of water into a vaporizer at 110°C where they were evaporated and diluted with nitrogen. The vapor stream was then carried into the cavity of the laser absorption spectrometer. All samples were measured six times and the first three injections were rejected due to the influence of between-sample memory. Additional memory corrections were applied to the last three injections, which were then averaged to generate the reported value. Uncertainty is reported as the absolute range of the last three injections and is <0.2‰ and <1.0‰ for oxygen and hydrogen, respectively. Secondary water isotope standards were run intermittently to assess drift and three in-house span standards were analyzed at the end of each run to correct samples to the Vienna Standard Mean Ocean Water (VSMOW) scale ($\delta^{18}O$: −29.9, −15.9, and −0.9‰, and $\delta^{2}H$: −240, −122, and −0.2‰). The methods closely follow those previously described by Gupta et al. (2009), Brand et al. (2009), and Noone et al. (2013). At Idaho State University, water samples for isotope analysis were filtered through 0.45 µm filter and analyzed using a Thermo Scientific, High Temperature Conversion Elemental Analyzer (TC-EA) interfaced to a Delta V Advantage mass spectrometer through the ConFlo IV system. Isotope values of

δ^2H and $\delta^{18}O$ are reported as ‰ values relative to the VSMOW scale. Four in-house standards, which are directly calibrated against VSMOW2, SLAP2, and GISP, were used to create a two-point calibration curve to correct the raw data and to monitor the accuracy of the data. Precisions for both δ^2H and $\delta^{18}O$ values are better than ±2.0‰ and ±0.2‰, respectively.

Plant cellulose samples were measured at the University of Wyoming Stable Isotope Facility and values of $\delta^{18}O_{cellulose}$ were determined by pyrolysis at 1420°C and temperature conversion elemental analysis (TC-EA). Following CO and H_2 gas separation using a gas chromatographic column (GS) at 85°C, isotope ratios were measured by a coupled Thermo Scientific DeltaV Plus isotope ratio mass spectrometer (IRMS). If regularly spaced standard uncertainty was larger than 0.3‰, the samples were all re-analyzed until the 2-sigma expanded standard uncertainty of the result was <1‰. The isotopic composition is reported on the ‰VSMOW scale such that standard reference material IAEA 601 (benzoic acid) and IAEA 602 (benzoic acid), respectively, are +23.3‰ and +71.4‰. At Iowa State University, plant cellulose samples were analyzed on a Finnigan MAT Delta Plus XL mass spectrometer in continuous flow mode connected to a Thermo-Chemical Elemental Analyzer. Reference standards [Sigma-Aldrich alpha cellulose [SAC], benzoic acid [IAEA-601], and sucrose [IAEA-CH-6]] were used for isotopic corrections, and to assign the data to the appropriate isotopic scale. For each isotope value given, two replicates were run for each sample. Analytical precision for the $\delta^{18}O_{cellulose}$ samples are ± <0.3‰. The analytical precision associated with the stable oxygen isotope analyses for the HT Fen core by Jones et al. (2014) was <0.6‰ and is expressed as one standard deviation from the mean based on the results from multiple (n = 10) analyses of a laboratory standard (benzoic acid, Fisher Scientific, Lot No 947459) conducted during the run of samples. Statistical relationships were determined using a t-test in Sigmaplot 13.0.

Horse Trail Fen Core Reanalysis

The Horse Trail fen core (HTF) was previously analyzed on bulk peat ($\delta^{18}O_{bulk}$; Jones et al., 2014), and a select subset of samples, spanning a range of periods of differing species abundances, were analyzed for $\delta^{18}O_{cellulose}$, based on the cellulose extraction method of Wolfe et al. (2001) to determine the relationship between the $\delta^{18}O_{bulk}$ and $\delta^{18}O_{cellulose}$. A statistical regression of the data [$y = 1.0148x-0.0927$ ($R^2 = 0.68856$)] was then used to convert $\delta^{18}O_{bulk}$ to $\delta^{18}O_{cellulose}$ (**Supplemental Tables 1, 2**). This study utilized the plant macrofossil abundances of mosses and sedges identified by Jones et al. (2014; **Figure 6**) to scale respective offsets from their environmental water in the modern environment. Analytical errors were propagated by taking the square root of the squared standard deviation of the bulk peat-cellulose regression plus the squared standard deviation of the modern cellulose isotope to water isotope relationship. In each case, one water value at each location was related to the average of multiple moss or sedge values (**Tables 2**–**4**).

RESULTS

Water

The average modern GF water $\delta^{18}O$ value is −14.1 ± 0.1‰ (n = 5) and ∼2‰ statistically higher than the HTF value of −16.2 ± 0.1‰ (n = 4; P = <0.001) (**Tables 2**, **3**). HTF values from all sampling locations were nearly identical and plot near the intersection between the Local Evaporation Line (LEL), defined by the Kenai lakes measured for this study (**Figure 1**, **Table 1**), which are mostly located in the western lowlands (**Figure 1**), and the GMWL (**Tables 1**–**3**; **Figure 2**). The LEL-GMWL intersection approximates regional mean annual precipitation values (Anderson et al., 2016). The HTF environmental water $\delta^{18}O$ values, which lie on the GMWL, closely approximate the $\delta^{18}O$ values for mean annual precipitation in the western lowlands (**Figure 2**).

TABLE 1 | Kenai lake water isotope data.

Site name	Date	$\delta^{18}O$‰ (vs. VSMOW)	δ^2H‰ (vs. VSMOW)	*dxs*[1]	Lat (°N)	Long (°W)	Elev. (m a.s.l.)	Comments
Horse Trail clearing	7/21/2014	−6.0	−80	−32.14	60.43066	150.91699	122	fen pool
Arc lake	7/24/2014	−7.4	−83	−23.30	60.44990	151.10530	60	
Browns Lake	7/23/2014	−7.1	−80	−22.88	60.48771	150.72458	88	
Headquarters Lake	7/24/2014	−7.8	−82	−19.47	60.46341	151.07106	63	
Lower Ohmer Lake	7/20/2014	−12.7	−108	−6.06	60.45223	150.31454	122	
Bear Mountain Lake	7/20/2014	−13.3	−111	−4.06	60.45512	150.25237	247	
Upper Ohmer Lake	7/20/2014	−13.8	−112	−1.93	60.45599	150.29501	148	
Bear Lake	7/23/2014	−14.4	−109	6.67	60.19139	149.35844	95	
Summit Lake	7/24/2014	−17.8	−134	7.84	60.63585	149.50703	401	
Skilak Lake	7/20/2014	−16.7	−125	8.54	60.43827	150.32146	63	Glacial lake
Tern Lake	7/23/2014	−17.1	−128	8.82	60.53403	149.54771	206	
Kenai Lake	7/23/2014	−17.0	−127	9.33	60.41246	149.38496	140	Glacial lake
Portage Lake	7/24/2014	−15.1	−109	11.59	60.78429	148.84032	27	
Browse Lake	9/5/16	−13.9	−116	−4.46	60.56278	150.30847	131	

[1] *Deuterium excess, dxs* = δ^* $\delta^{18}O$- δ^2H.

TABLE 2 | Goldfin (GF) plant cellulose and environmental water isotopes (sampled 9/1/2017).

Type/location	Species	$\delta^{18}O$‰ (vs. VSMOW)	$\delta^{18}O$‰ water-cellulose*	$\delta^{2}H$‰ (vs. VSMOW)
STREAM				
Plant–submerged	*Sphagnum subnitens* leaves	20.1	−34.1	
Plant–submerged	*Sphagnum subnitens* stems	19.8	−33.8	
Plant–submerged	*Carex* spp.	22.7	−36.7	
Stream water	–	−14.0		−109.5
Stream W of site	–	−14.2		−107.5
1m				
Water table	*Campyllium stellatum* (whole plant)	19.8	−32.4	
Water table	*Sphagnum teres* (whole plant)	19.2	−31.9	
Water table	*Carex* spp.	22.0	−34.6	
Environmental water	–	−12.6		−104.9
20m				
Plant–submerged	*Calliergon stramineum*	21.0	−35.3	
Plant–submerged	*Calypogeia spagnicola*	20.9	−35.2	
Plant–submerged	*Sphagnum rusowii* stems	20.2	−34.5	
Plant–submerged	*Sphagnum russowii* leaves	20.7	−35.0	
Plant–submerged	*Carex* spp.	22.4	−36.7	
Plant– hummock– 30 cm	*Sphagnum rusowii* stems	20.3	−34.6	
Plant– hummock– 30 cm	*Sphagnum russowii* leaves	20.3	−34.6	
Plant– hummock– 30 cm	*Carex* spp.	24.0	−38.3	
Environmental water	–	−14.3		−109.9
40m				
Plant–hummock– 10–20 cm	*Aulacomnium palustre* (whole plant)	21.1	−35.2	
Plant–hummock– 10–20 cm	*Sphagnum capillifolium* leaves	21.3	−35.4	
Plant–hummock– 10–20 cm	*Sphagnum capillifolium* stems	21.2	−35.2	
Plant–hummock– 10–20 cm	*Sphagnum rusowii* stems	19.9	−34.0	
Plant–hummock– 10–20 cm	*Carex* spp.	22.2	−36.3	
Plant–submerged	*Sphagnum teres* leaves	19.6	−33.6	
Plant–submerged	*Sphagnum teres* stems	20.1	−34.1	
Plant–submerged	*Carex* spp.	22.9	−37.0	
Environmental water	–	−14.1		−109.5

**The difference between water isotope values and cellulose isotope values.*

Plant $\delta^{18}O_{cellulose}$ Comparisons by Species and Plant Parts

Within-plant $\delta^{18}O_{cellulose}$ differences were determined from measurements of separated stems and leaves of the same species. On average, HTF *Sphagnum* leaf $\delta^{18}O_{cellulose}$ values were higher than stems by 1.3 ± 0.6‰ ($n = 6$ pairs). GF leaf $\delta^{18}O_{cellulose}$ average was 1.5 ± 0.2‰ higher than stems (n= 5 pairs; analytical error 0.1 ± 0.06‰; **Figure 3**). However, in neither location was the difference between leaf and stem $\delta^{18}O_{cellulose}$ values statistically significant ($P = 0.197$, $P = 0.450$, respectively). The only species for which *Sphagnum* stem values were higher than leaves was *Sphagnum rusowii* at 40 m (−0.4‰) and *Sphagnum teres* at 20 m (−0.3‰). For samples where stems, leaves, and the corresponding whole plant $\delta^{18}O_{cellulose}$ values were measured ($n = 7$), whole plant values were both higher or lower by <2‰ than corresponding stems or leaves (**Table 2**), likely driven by the relative proportion of leaves to stems measured and the potential for debris to have been caught in *Sphagnum* leaves. At GF, brown moss $\delta^{18}O_{cellulose}$ values, which includes all non-*Sphagnum* peat mosses (**Tables 2**, **3**), were consistently higher than *Sphagnum* by 0.5 ±0.1‰ ($n = 3$ transect positions, incorporating 4 brown mosses and 10 *Sphagnum* mosses), but the relationship was not statistically significant ($P = 0.454$). At HTF, the relationship was opposite to that of GF (−0.8 ± 0.1‰, $n = 3$ transect positions, incorporating 18 brown moss and 19 *Sphagnum* samples) and also not statistically significant ($P = 0.908$). In samples where stem and leaf $\delta^{18}O_{cellulose}$ were measured from the same sample (HTF only), brown moss leaves were slightly higher by a mean of 0.4 ± 0.2‰ than stems ($n = 5$ pairs), but the relationship was not statistically significant ($P = 0.373$). *Carex* spp. leaf $\delta^{18}O_{cellulose}$ values at all HTF and GF sampling locations were higher than their bryophytic (*Sphagnum* and brown moss) counterparts, but differences varied. However, the average difference between moss and sedge (*Carex* spp.) values at GF ($n = 16$ mosses, $n = 4$

TABLE 3 | Horse Trail fen (HTF) plant cellulose and environmental water isotopes (sampled 7/21/2014).

Type/location	Species	$\delta^{18}O$‰ (vs. VSMOW)	$\delta^{18}O$‰ water-cellulose	$\delta^{2}H$‰ (vs. VSMOW)
1m				
Plant	*Sphagnum teres* (whole plant)	16.2	−32.5	–
Plant	*Sphagnum teres* stems	16.0	−32.3	–
Plant	*Calliergon stramineum* (whole plant)	15.7	−32.0	–
Plant	*Calliergon stramineum* leaves	16.6	−32.9	–
Plant	*Calliergon stramineum* stems	16.4	−32.7	–
Plant	*Carex* spp.	26.3	−42.6	–
Plant	*Carex* spp.	26.3	−42.5	–
Plant	*Carex* spp.	25.9	−42.2	–
Plant	*Carex* spp.	26.1	−42.4	–
Environmental water	–	−16.3	–	−124
10m				
Plant	*Calliergon giganteum* leaves	18.4	−34.8	–
Plant	*Calliergon giganteum* stems	18.2	−34.6	–
Plant	*Sphagnum teres* (whole plant)	13.9	−30.3	–
Plant	*Calliergon* spp. (whole plant)	16.3	−32.7	–
Plant	*Calliergon stramineum* stems	16.9	−33.3	–
Plant	*Sphagnum teres* stems	16.6	−33.0	–
Plant	*Sphagnum teres* leaves	17.9	−34.3	–
Environmental water	–	−16.4	–	−125
20m	*Sphagnum teres* leaves	16.2	−32.4	
Plant	*Sphagnum teres* stems	16.5	−32.7	
Plant	*Sphagnum teres* (whole plant)	18.0	−34.1	
Plant	Bulk peat	17.4	−33.5	
Environmental water	–	−16.1	–	−123
30m				
Plant	*Sphagnum* spp. leaves	19.5	−35.6	–
Plant	*Aulacomnium palustre* (whole plant)	20.3	−36.4	–
Plant	*Paludella squarrosa* (whole plant)	16.3	−32.4	–
Plant	*Drepanocladus* spp. (whole plant)	16.6	−32.7	–
Plant	*Sphagnum* spp. Stems	18.2	−34.3	–
Plant	*Paludella squarrosa* (leaves)	16.8	−32.9	–
Plant	*Paludella squarrosa* (stems)	16.3	−32.4	–
Plant	*Sphagnum teres* leaves	20.1	−36.2	–
Plant	*Sphagnum teres* stems	18.3	−34.4	–
Plant	*Sphagnum russowii/subfulvum* leaves	19.2	−35.3	–
Plant	*Sphagnum russowii/subfulvum* stems	18.5	−34.6	–
Plant	*Calliergon straminium* leaves	17.4	−33.5	–
Plant	*Calliergon straminium* stems	16.8	−32.9	–
Plant	*Calliergon stramineum* (whole plant)	16.6	−32.7	–
Plant	*Sphagnum teres* (whole plant)	18.5	−34.6	–
Plant	*Drepanocladus revolvens* (leaves)	17.3	−33.4	–
Plant	*Drepanocladus revolvens* (stems)	16.6	−32.7	–
Plant	*Sphagnum* spp. Leaves	19.4	−35.5	–
Plant	*Paludella squarrosa* (whole plant)	16.9	−33.0	–
Plant	*Carex* spp.	23.4	−39.5	–
Plant	*Carex* spp.	23.5	−39.6	–
Plant	*Carex* spp.	22.7	−38.8	–
Plant	Bulk peat	18.7	−34.8	–
Environmental water	–	−16.1	–	−123

(Continued)

TABLE 3 | Continued

Type/location	Species	$\delta^{18}O$‰ (vs. VSMOW)	$\delta^{18}O$‰ water-cellulose	$\delta^{2}H$‰ (vs. VSMOW)
40m*				
Plant	*Sphagnum rusowii* stems	20.2	−36.3	–
Plant	*Sphagnum rusowii* leaves	19.8	−35.9	–
Plant	*Sphagnum rusowii* (whole plant)	18.9	−35.0	–
Plant	Bulk peat	20.8	−36.9	–

**Water–cell calculated with 30 m environmental water value.*

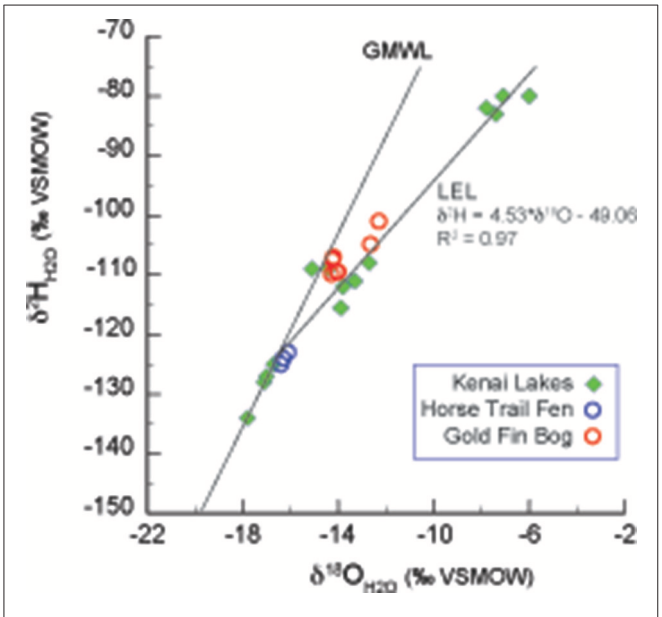

FIGURE 2 | Lake water oxygen and hydrogen isotopes from the Kenai Peninsula, AK (green diamonds; **Figure 1** and **Table 1**) were used to form the Local evaporation line (LEL) which is shown with the global meteoric water line (GMWL; Rozanski et al., 1993), and with surface waters from Horse Trail fen (HTF, **Table 2**, open blue circles), and Goldfin (GF, **Table 3**, open red circles).

sedges) and at HTF ($n = 38$ mosses, $n = 7$ sedges) was statistically significant at both locations ($P < 0.001$ with 7 and 10 degrees of freedom from HTF and GF, respectively).

Plant $\delta^{18}O_{Cellulose}$ Values by Water Table Position

The HTF transect was hypothesized to reflect a hydrologic gradient in terms of water table position that was assumed to be at stream level and progressively deeper below the fen surface with distance from the stream to 40 m, which lies at the upland forest edge. Although water isotope values were nearly identical at all transect locations, the bryophyte samples taken at greater distances from the stream showed progressively higher $\delta^{18}O_{cellulose}$ values, ranging from ∼16 to 19‰ with progressively higher values at each location farther from the stream (**Table 2**). The difference in mean values between the lowest transect position (1 m; 16.165 ± 0.360‰) and 30 and 40 m (19.63 ± 0.630‰) transect are statistically significant ($P = 0.005$ and $P < 0.001$, respectively). Of the more limited *Carex* spp. samples taken at HTF, the sample at 1-m ($n = 4$) distance was 3‰ ±0.6 higher than the sample taken at 30-m distance (n = 3), both of which were higher by variable amounts (**Figure 4**, **Table 3**) than the moss samples from the respective transect positions, but additional samples are needed to verify this trend.

The relatively level surface of GF transect was not thought to provide a hydrologic gradient in terms of water table position, but the two sampling locations (referred to here as 20, 40 m) provided a comparison between submerged and sub-aerially exposed hummock plants (**Table 2**). The mean bryophyte $\delta^{18}O_{cellulose}$ value differences between the 20-m site that was submerged ($n = 4$; 19.8 ± 0.378‰) and exposed ($n = 2$; 20.3 ± 0.044‰) were small (<0.5‰), and the relationship was not statistically significant ($P = 0.204$) (**Figure 4**; **Table 2**). The mean bryophyte $\delta^{18}O_{cellulose}$ value differences between the 40-m site submerged ($n = 2$; 19.8 ± 0.38‰) and hummock ($n = 4$; 20.87 ± 0.655‰) was ∼1.5‰, and the difference was not statistically significant ($P = 0.111$). The differences among sedge $\delta^{18}O_{cellulose}$ value values across all transect positions at GF was low (average = 22.7 ± 0.7‰), although they were on average higher than the difference amongst the bryophytes by 2.5‰ ($P < 0.001$).

Mean $\delta^{18}O_{cellulose}$ values were calculated for dominant plant types to evaluate the range of variability within a peatland and to better understand how to interpret changes in a peat core. The mean bryophyte $\delta^{18}O_{cellulose}$ value at all HTF transect sites was 17.6 ± 1.2‰ ($n = 35$; median 16.9‰), with a range of 15.7–20.3‰ (**Table 3**). The mean bryophyte $\delta^{18}O_{cellulose}$ values at the GF sites was 20.2 ± 0.6‰ (median 20.3‰), with a range of 19.2–21.2‰. The difference in means between HTF and GF $\delta^{18}O_{cellulose}$ values is statistically significant ($P <$ 0.001). In contrast, the mean sedge $\delta^{18}O_{cellulose}$ value at HTF is 24.7 ±2.1‰ ($n = 7$; median: 25.9‰) is higher than the GF values of 22.7 ± 0.7‰ (median: 22.6‰), a difference that is not great enough to reject the null hypothesis ($P = 0.0661$).

Plant-Environmental Water $\delta^{18}O$ Comparisons ($\Delta\delta^{18}O_{cellulose\text{-}water}$)

At HTF, the difference between $\delta^{18}O_{cellulose}$ values of individual moss species and the $\delta^{18}O$ values of environmental waters ($\Delta\delta^{18}O_{cellulose-water}$) ranged from −30 to −37‰ with an average value of −33 ± 3.2‰ (**Tables 2**, **4**). $\Delta\delta^{18}O_{cellulose-water}$ values increased from −31.2 to −35.8‰ with increasing distance from the stream because although environmental water $\delta^{18}O$ values

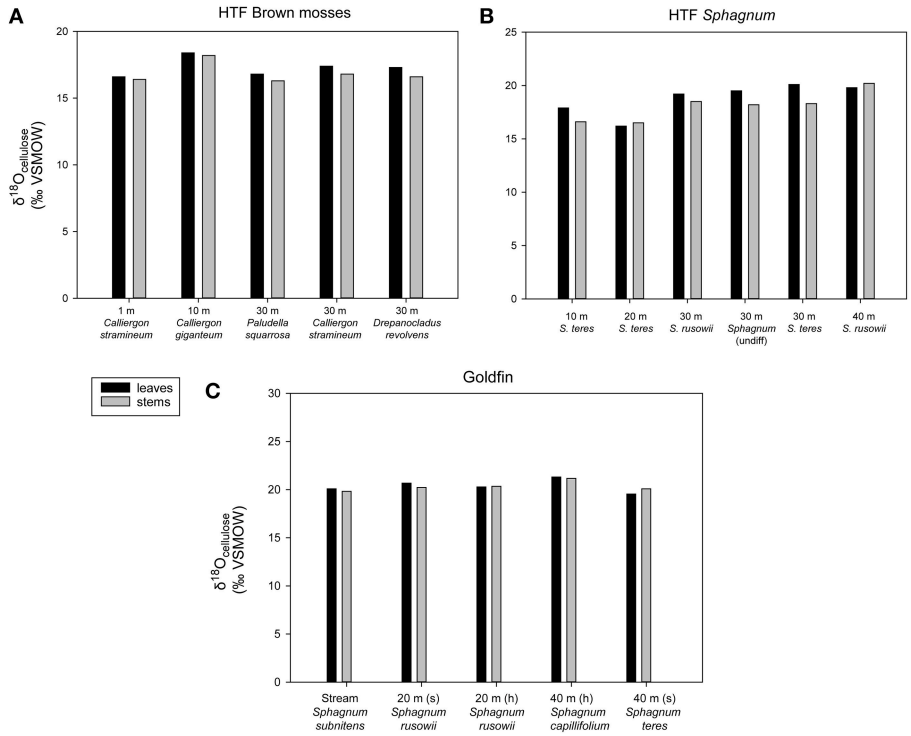

FIGURE 3 | Intra-plant $\delta^{18}O_{cellulose}$ values along the two transects **(A)** HTF brown mosses, **(B)** HTF *Sphagnum* mosses, **(C)** GF *Sphagnum* mosses. Each sample had one replicate with an analytical error of <0.3‰. All brown mosses and *Sphagnum* mosses found in **Tables 2**, **3** are included. "(s)" refers to submerged, "(h)" refers to hummock.

were invariant, plant $\delta^{18}O_{cellulose}$ values increased. The two sedge samples had a larger $\mathbf{\Delta}\delta^{18}O_{cellulose-water}$ value, with an average of −41.1‰. The 1-m site had a larger $\mathbf{\Delta}\delta^{18}O_{cellulose-water}$ value (−42.4‰) than the 40-m site (−39.4‰) (**Table 5**).

At GF, $\mathbf{\Delta}\delta^{18}O_{cellulose-water}$ ranged from −33 to −35‰ with an average value of −33.9‰ ± 1.2 with larger values for sedge of −36.4‰ ± 1.2. $\mathbf{\Delta}\delta^{18}O_{cellulose-water}$ for submerged and hummock samples were similar at the 20-m site (0.1‰), but at the 40-m site, the hummock samples were 1.3‰ larger. In general, the range of $\mathbf{\Delta}\delta^{18}O_{cellulose-water}$ values at GF was lower than at HTF.

To evaluate $\mathbf{\Delta}\delta^{18}O_{cellulose-water}$ across as wide a range of water values as possible, data from St. Matthew Island is included (**Table 4**; **Figure 5**). Considering data from HTF, Goldfin, and St. Matthew Island provided a larger range of water $\delta^{18}O$ values from −16.2 to −9.4‰ and $\delta^{18}O_{cellulose}$ values of 17.5 to 23.9‰, indicating a mean $\mathbf{\Delta}\delta^{18}O_{cellulose-water}$ value for all site of −33.4‰. The linear regression using data from the three locations provides a slope of 0.79 with an R^2 of 0.811 (**Tables 2–5**; **Figure 5**).

Species Effects in the HTF Bulk Peat $\delta^{18}O$ Core Record

While Jones et al. (2014) found no apparent relationship between plant macrofossil assemblage and $\delta^{18}O_{bulk}$ (**Supplemental Figure 1**), the results of the modern plant analysis showed a significant difference between $\delta^{18}O_{cellulose}$ moss and *Carex* spp. (**Figure 4**), which at HTF was 7.06 ± 2.38‰ ($P < 0.001$). To illustrate how these adjustments translate to inferred environmental waters, samples that were primarily bryophytic were adjusted by −33.9 ± 1.88‰ according to the modern calibration, an adjustment supported by the cellulose fractionation factor determined by Sternberg and Ellsworth, (2011). In contrast, samples dominated by *Carex* spp. were adjusted by −41.1 ± 2.4‰, based on the HTF sedge-environmental water differences measured on the modern (**Table 5**; **Figure 6**). Samples whose bryophyte and *Carex* spp. macrofossil sum did not equal 100% were omitted so as to not introduce additional sources of error (**Supplemental Table 2**). Species-weighted $\delta^{18}O$ calculations were made as follows:

$$\text{Inferred water}\delta^{18}O = \delta^{18}O_{moss-water} * (\%\text{moss abundance}) + \delta^{18}O_{carex-water} * (\%Carex \text{ abundance}), \quad (2)$$

Where $\delta^{18}O_{moss-water} = -33.9 \pm 1.88‰$ and $\delta^{18}O_{carex-water} = -41.1 \pm 2.5‰$ (**Figure 6D**). Errors were propagated by taking the square root of the sum of the squared sources of error (cellulose errors for mosses and sedges, error of water $\delta^{18}O$ values).

Although the plant species-adjusted $\delta^{18}O_{cellulose}$ values resulted in a shift toward higher values in the sedge-dominated intervals (**Figure 6C**), the inferred environmental water $\delta^{18}O$ value adjustment resulted in a downward shift to lower values

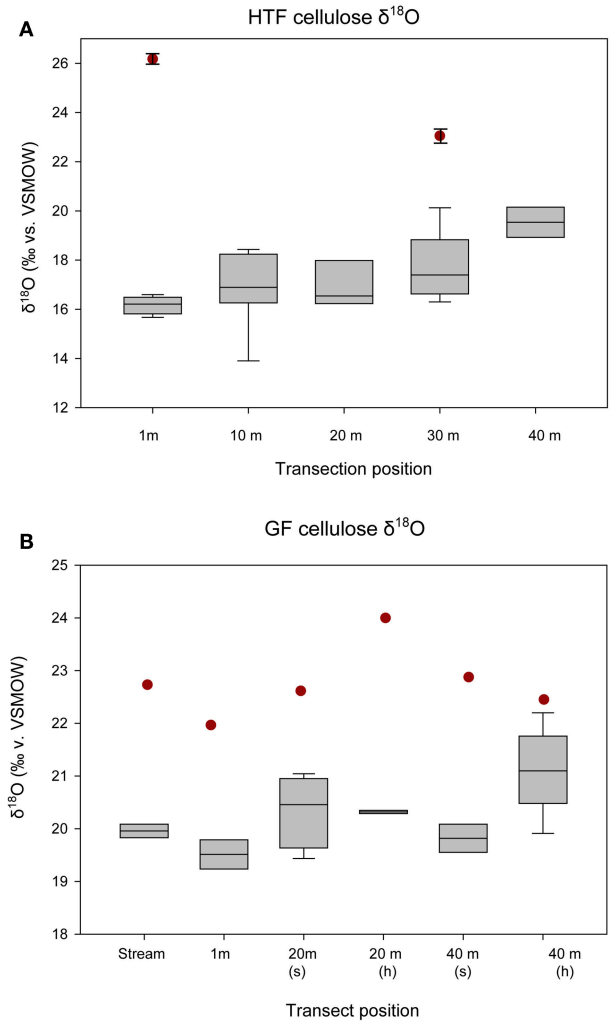

FIGURE 4 | $\delta^{18}O_{cellulose}$ values of bryophytes and *Carex* spp. by location on transect, starting from the stream and increasing out toward the forest edge. "S" refers to submerged, "h" refers to hummock for **(A)** HTF and **(B)** GF. The boxes and whiskers apply to the all measured bryophytes at each transect location. The red circles indicate *Carex* spp. leaf values at each transect location. At HTF, *Carex* spp. was only measured at two positions on the transect (1 m, $n = 4$; 30 m, $n = 3$), and only one *Carex* spp. replicate was analyzed at each position on the transect at GF and analytical errors are not shown.

(**Figure 6D**), amplifying periods of the record that were already indicated decreased $\delta^{18}O_{bulk}$ values in the unadjusted plots. This was particularly the case at ∼4–3 ka and 11.7–10.8 ka (**Figures 6C,D**), resulting in inferred environmental water values of −30 to −35‰ during the most extreme lows.

DISCUSSION

Peatland Isotope Hydrology

The water isotope results indicate that the peatland surface water in both HTF and GF plot on the GMWL, suggesting that the water in these systems reflects the local precipitation signature with evaporative effects limited to pools of standing water

TABLE 4 | St Matthew Island plant cellulose and environmental water isotopes (sampled 6/2016).

Type/ location	Species	$\delta^{18}O$‰ (vs. VSMOW)	$\delta^{18}O$‰ water–cell	$\delta^{2}H$‰ (vs. VSMOW)
Plant	*Calliergon (whole plant)*	22.0	−32.9	–
Environmental water	Stream	−12.6	–	−76.1
Plant	*Carex* spp.	22.8	−33.7	–
Environmental water	Stream	−10.8	–	−72.5
Plant	*Carex* spp.	23.5	−32.9	–
Environmental water	Standing peatland water	−9.4		−65.3
Plant	*Drepanocladus unicatus*	23.6	−33.3	–
Plant	*Carex* spp. *(living)*	22.5	−32.2	–
Water	Standing peatland water	−9.7		−72.1
Water	Standing peatland water	−9.8		−72.4

**Environmental water value of −9.7‰.*

TABLE 5 | Plant and water isotope summary and statistics.

Location	*n* =	Mean $\delta^{18}O$‰ (vs. VSMOW)	SD	Mean $\delta^{18}O$‰ water-plant (vs. VSMOW)	SD
HORSE TRAIL FEN					
Water	4	−16.2	1.0		
Moss	37	17.6	1.5	−33.8	1.8
Carex spp.	7	24.9	1.6	−41.1	1.9
GOLDFIN BOG					
Water	5	−13.9	0.7		
Moss	16	20.4	0.6	−34.2	0.9
Carex spp.	6	22.7	0.7	−36.6	1.0
St. MATTHEW ISLAND					
Water	5	−10.5	1.3		
Moss	2	22.8	1.4	−33.3	1.9
Carex spp.	3	23	0.5	−33.5	1.4

(**Figure 2**). Higher $\delta^{18}O$ and $\delta^{2}H$ values at GF (∼14.1, −109.5‰, respectively), on the windward side of the Kenai Mountains compared to HTF (−16.2, −124‰, respectively), on the leeward side, is consistent with Rayleigh distillation effects (Dansgaard, 1964) across the Kenai Mountain barrier. As moisture is lifted over the Kenai Mountains, heavier isotopes of precipitation are preferentially rained out on the windward side, whereas on the leeward side precipitation values are relatively-isotopically enriched in light isotopes. Consequently, GF waters are 2‰ higher than HTF, and this relationship held for the average range of $\delta^{18}O_{cellulose}$ values for the two peatland sites despite variability

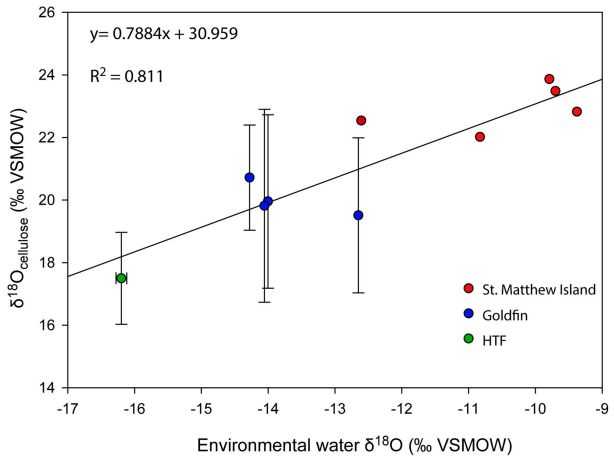

FIGURE 5 | $\delta^{18}O$ relationship between environmental water and cellulose from the Kenai Peninsula samples and St. Matthew Island, Alaska. One average water $\delta^{18}O$ value was used to correspond with multiple cellulose $\delta^{18}O$ values (Y-axis errors). X-axis error bars for HTF do not occur because water values across the site were nearly identical. Red points without errors from St. Matthew Island have only one $\delta^{18}O_{cellulose}$ value associated with one water isotopic value.

in species values (**Tables 2**, **3**; **Figures 3**, **4**). GF water $\delta^{18}O$ values have a wider range; one samples was collected from a standing pool of water at the GF 1m location had isotopic values that plot on the LEL. This indicates the isotopic effects of evaporation that are also reflected by relatively low *dxs* value of −3.67. In contrast, higher GF isotopic values for the stream and peatland surface waters at GF that plot near the GMWL (compared to HTF) are not affected by evaporation and more probably reflect the combined effects of the site's location on the windward side of the Kenai Mountains, in the rain-out zone, at an elevation near sea level.

Although previous studies of $\delta^{18}O_{cellulose}$ peat records have focused on bogs, which are peatlands fed by precipitation and therefore presumptively more reflective of isotopically unmodified precipitation (Daley et al., 2010), the HTF water isotope values indicate that in Alaska fens can also host unmodified precipitation as a source, a conclusion that previous hydrologic studies support (Ford and Bedford, 1987; Reeve and Gracz, 2008). Water uptake in plants may also be more susceptible to evaporation in bogs during dry spells, which can lead to the preferential evaporation of light isotopes in water, complicating their interpretations. Similar to studies in lakes (Anderson et al., 2016), understanding of the hydrology of a system and its relation to isotopes of precipitation serves to constrain the interpretation of the sedimentary record. Both of the HTF and GF peatlands are fens that receive some fraction of their water from groundwater. The proximity of the fen water relative to the GMWL suggests the groundwater residence times (seasonal to annual) do not lead to significant evaporative evolution and thereby supports an interpretation of $\delta^{18}O_{cellulose}$ as a proxy for hydroclimate on decadal, centennial, and millennial timescales.

Intra-Plant Part and Species Effects

Differences in $\delta^{18}O_{cellulose}$ values between *Sphagnum* stems and branches have been reported (Moschen et al., 2009; Kaislahti Tillman et al., 2010). However, because of the difficulty in separating individual stems and branches while omitting leaves, we only evaluated collections of stems and leaves and found that the differences in $\delta^{18}O_{cellulose}$ values were negligible (<1‰) relative to the 5–10‰ range of observed $\delta^{18}O_{cellulose}$ values in peat core records, similar to results reported by Moschen et al. (2009). Also similar to previous findings (Moschen et al., 2009), the $\delta^{18}O_{cellulose}$ values of *Sphagnum* leaves and all brown moss samples were higher than those in stems in most instances, suggesting a difference in the biochemical synthesis of cellulose in stems vs. leaves and branches. In the few cases where the relationship was reversed, the reversal could be explained by detrital organic matter caught in *Sphagnum* leaves, but this is untested. In general, the intra-plant $\delta^{18}O_{cellulose}$ value differences have little effect on interpretation of larger isotopic shifts in a peat core record.

Different moss-species $\delta^{18}O_{cellulose}$ values across the HTF transect varied by ∼5‰ (**Figure 4**) and distinct patterns emerged among species that reflect local hydrologic conditions (drier vs. wetter). Generally, submerged moss species had lower $\delta^{18}O_{cellulose}$ values relative to those species on hummocks, and values increased from wet to the dry locations with increased distance from streams. Other modern calibration studies have found a strong relationship between relative humidity near the moss growth position and the respective isotopic composition of the cellulose (Loader et al., 2016). The Loader et al. (2016) study recorded relative humidity values between 50 and 70% some evaporative enrichment was observed in subaerially exposed peatland mosses. However, a strong relationship between the environmental water and moss-$\delta^{18}O_{cellulose}$ values indicated that the factors influencing isotopic alteration during the growing season remain stable influences on the $\delta^{18}O_{cellulose}$ values of *Sphagnum,* consistent with findings from this study.

Sedge (*Carex* spp.) $\delta^{18}O_{cellulose}$ values measured here were always higher (∼2.5‰) than mosses suggesting that while mosses passively uptake water and are governed by the same biochemical synthesis of oxygen from water into cellulose, the $\delta^{18}O_{cellulose}$ values of vascular plants are enriched in heavy isotopes by stomatal regulation of water loss (**Figure 4**; Ménot-Combes et al., 2002; Zanazzi and Mora, 2005; Amesbury et al., 2015). Further, Amesbury et al. (2015) found a consistent offset of 3‰ between root-associated water and environmental water in a species of rush, indicating that fractionation during uptake of water in vascular plants also can occur, further contributing to a larger offset between sedges and mosses. We observed no clear trend with respect to sedge and water table position (**Figure 4**), although the sample size was small ($n = 6$ transect positions). The lack of a trend could be the result of both stomatal regulation of water loss and to the depth at which sedges obtain their water, which could have a different isotopic signature from surface water.

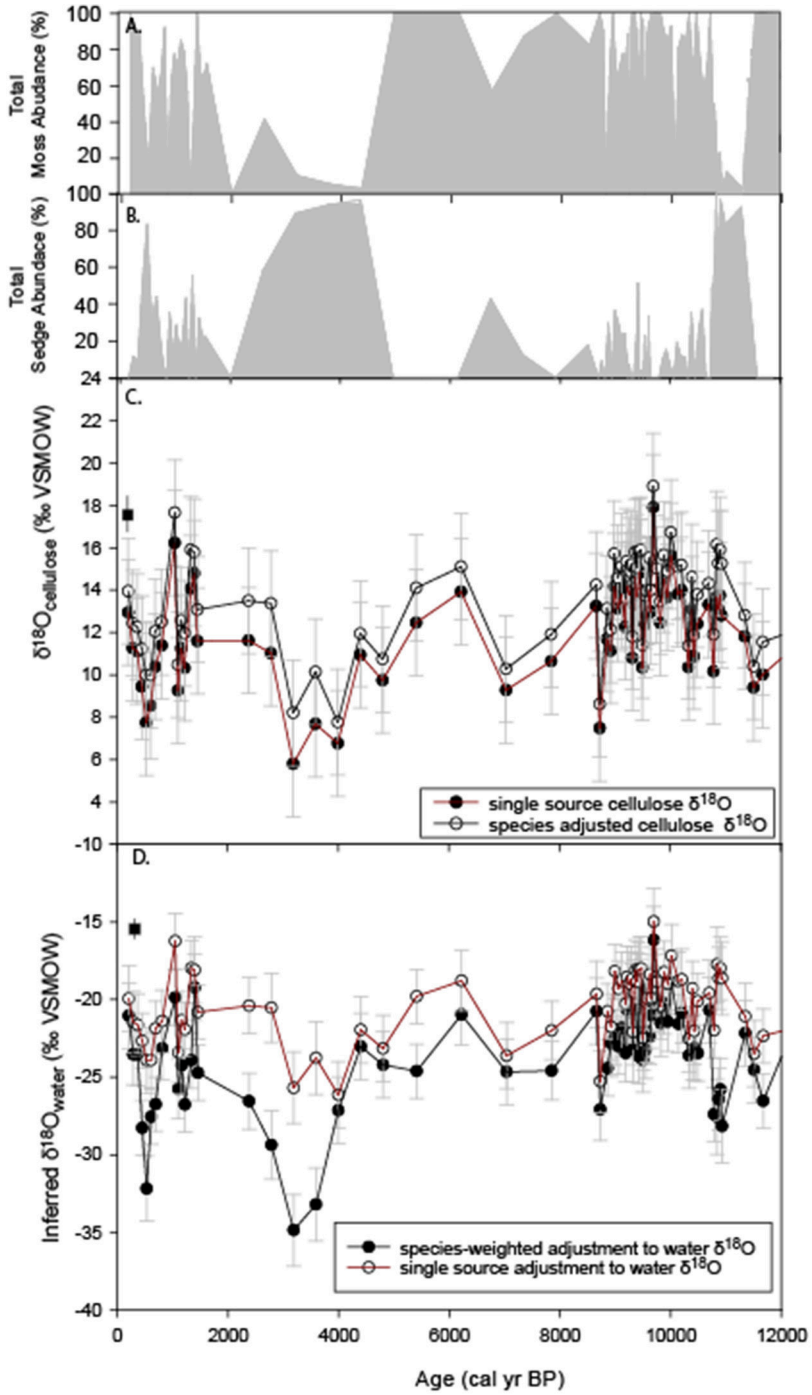

FIGURE 6 | Re-analysis of HTF peat $\delta^{18}O$ record of Jones et al. (2014). **(A)** percent abundance of moss macrofossils (*Sphagnum* + brown mosses), **(B)** percent abundance of *Carex* spp. macrofossils, **(C)** The original bulk $\delta^{18}O_{cellulose}$ values (red) and species adjusted values determined by this study (black square), **(D)** Peat-inferred water $\delta^{18}O$ values using a constant cellulose fractionation offset of −33‰ for bulk peat (red) and variable offsets depending on relative abundance of moss and *Carex* spp. macrofossils (black). The average modern water $\delta^{18}O$ value determined by this study for year 2014 is the black square at 0 cal yr BP.

A linear regression between the $\delta^{18}O_{cellulose}$ values of aquatic moss and its environmental water with a slope of 1:1 suggests $\delta^{18}O_{cellulose}$ values of aquatic moss are governed by the $\delta^{18}O$ values of environmental water (Zhu et al., 2014). In laboratory experiments where aquatic mosses were not subject to evapotranspiration, the environmental water and cellulose $\delta^{18}O$ slopes range between 0.78 and 0.97 with R^2 values between 0.88 and 0.998 (Sauer et al., 2001; Mayr et al., 2013; Zhu et al., 2014). By comparison, the $\delta^{18}O$ regression between our Alaska terrestrial moss and peatland environmental waters in this study

has a slope of 0.79 and R^2 of 0.81 (**Figure 5**). Although the terrestrial moss regression does not overlap with the aquatic moss regression, likely because of different relationships between peat water and plants compared with lake water and aquatic moss (Loader et al., 2016). The relationship between Alaska peatland moss and environmental water documented here supports inferred environmental-water interpretations of peat core records. The offset of moss $\delta^{18}O_{cellulose}$ to the $\delta^{18}O_{water}$ is on average −33‰, which is higher than the previously assumed constant offset of −27‰ identified by DeNiro and Epstein (1981) but is in agreement with a latitudinal-temperature effect identified by Sternberg and Ellsworth (2011), where lower MAAT corresponds to lower $\delta^{18}O_{cellulose}$.

The results of this study suggest that at a given site, mosses do not differ significantly from one another but that significant difference exists between bryophytic (moss) samples and graminoid (sedge: *Carex* spp.) samples, likely owing to the ecophysiological differences between vascular and nonvascular plants. This suggests that $\delta^{18}O$ interpretations of peat cores should have modern site-level information on species differences and that these differences need to be accounted for when peat composition transitions from vascular to nonvascular.

Reanalysis of the HTF $\delta^{18}O$ Record

The results of this study show significant species difference between mosses and *Carex* spp. (**Figure 4**). Although comparisons between specific peat macrofossil abundances and unaltered $\delta^{18}O_{bulk}$ revealed no substantial relationship (**Supplemental Figure 1**), the +2.5‰ difference between sedge and moss $\delta^{18}O_{cellulose}$ values and−8‰ between sedge and moss inferred-water $\delta^{18}O$ values suggests variations in their respective abundance could lead to substantial deviations from the $\delta^{18}O_{bulk}$ record (**Figure 6**). This could have implications for the interpretation of the $\delta^{18}O_{bulk}$ record that assumed no differences in the way in which vascular and non-vascular plants fractionate water (Jones et al., 2014). Adjusting the $\delta^{18}O_{cellulose}$ values for abundance of *Carex* spp. and moss, as outlined above, slightly reduced the overall $\delta^{18}O_{cellulose}$ range of variability of the record compared to the single-source adjusted values (**Figure 6C**), and the change in the absolute value of the isotopic signature falls within the errors of each respective curve. However, a larger opposite effect occurs when the species-adjusted values are further adjusted to infer environmental water $\delta^{18}O$ values. Inferred-water $\delta^{18}O$ values are substantially lower during periods of sedge dominance (**Figure 6D**).

There are additional alternative explanations for the shifts in the HTF $\delta^{18}O_{bulk}$ values. The unaltered $\delta^{18}O_{bulk}$ analysis on the entire peat core and subsequent cellulose extraction applied to selected peat samples (Jones et al., 2014) did not remove clay minerals and chitin impurities (Wolfe et al., 2007), which have been shown to be a source of significant contamination in sediment-cellulose $\delta^{18}O$ measurements (Wissel et al., 2008) and cannot be ruled out as contributing to the unusually low bulk peat and inferred water values. The CUAM method has been shown to produce the purest cellulose and higher $\delta^{18}O_{cellulose}$ values would be expected because they are higher than that of other organic compounds (Zhu et al., 2014). Although Jones et al. (2014) found a compelling relationship between the $\delta^{18}O_{bulk}$ and $\delta^{18}O_{cellulose}$, standard deviations are as large as 2.5‰ and values declines correspond with changes in %LOI and mineral content (**Supplemental Figure 2**), which could suggest influence of the mineral component on the $\delta^{18}O$, but the change in %LOI also implies a changing depositional environment and/or climate change. Additional analyses are required to more precisely determine the effect of cellulose extraction methods on the HTF $\delta^{18}O_{bulk}$ values (**Figures 6C,D**).

A prominent period when shifts to greater *Carex* spp. abundances substantially alter the interpretation of the unaltered $\delta^{18}O_{bulk}$ record occurs between ∼11.7 and 10.8 ka (**Figures 6B,D**). The unadjusted record shows values similar to the rest of the early Holocene (**Figure 6C**), but the species-adjusted inferred $\delta^{18}O$ water values are substantially lower at the beginning of the Holocene (∼-27‰; 11.7–10.8 ka). The resulting lower values, combined with the species assemblage change, suggest that a previously unrecognized hydroclimatic shift occurred between the early Preboreal (11.7–10.8 ka) and the subsequent early Holocene period (10.8–9 ka). Lower environmental water $\delta^{18}O$ values during this period could reflect the influence of rising sea levels and more extensive sea ice conditions (e.g., Gaglioti et al., 2017). Other mechanisms could include altered atmospheric circulation dynamics, including changing seasonality and longer transport over the continent: lower values are consistent with greater winter precipitation influence on the groundwater signature, as winter precipitation $\delta^{18}O$ values are lower than summer values (IAEA/WMO, 2001; Bailey et al., 2015).

Another period of *Carex* spp. dominance occurs between ∼4 and 3 ka, when rising species-adjusted $\delta^{18}O_{cellulose}$ are higher than unadjusted bulk $\delta^{18}O_{cellulose}$ values (**Figure 6C**), leading to inferred water values (**Figure 6D**) that are the lowest of the entire record (−35 to −32‰). In this case, the recorded declines are enhanced by correcting for species, but the overall trend is unchanged. This interval at HTF coincides with a notable decline in organic matter (**Supplemental Figure 2**), due to an increase in silt percentages that was previously interpreted to reflect a combination of climate-induced peat decomposition and silt deposition, but may reflect the influence of more negative clay mineral water isotope values; bulk peat values may to some degree represent changes in clay mineral abundance. Another potential could be that there is a difference in the $\delta^{18}O$ values derived from sedge roots and shoots, which was found to be as large as 10‰ in a specific peat-forming rush in New Zealand (Amesbury et al., 2015), and bulk samples could represent variable amounts of root and shoot material. Although this study focused on shoot material from *Carex* spp., the bulk peat core material was likely a mixture of root and shoot material. Amesbury et al. (2015) suggests the smaller offset in the root $\delta^{18}O_{cellulose}$ could make root $\delta^{18}O_{cellulose}$ the more viable component for proxy development, but further study is required to determine if a similar relationship exists in peat-forming sedges. In general, results indicate that core analyses using consistent cellulose extraction methodologies are ideal.

It is difficult to identify mechanisms that can explain the anomalously low inferred-water $\delta^{18}O$ values of −35 to

−30‰. They are unrealistic when compared to the closest (∼700 km) modern global network of isotopes in precipitation (GNIP) data from Bethel, Alaska, and Whitehorse, Yukon Territory (IAEA/WMO, 2001), and reported values of last glacial maximum (LGM) water in interior Alaska (−28‰; Lachniet et al., 2012). Notwithstanding the unrealistic absolute values of the species-adjusted inferred water values, the declining trends could suggest declining temperatures, a shift toward winter-dominant precipitation, or more northerly derived moisture during this time interval. It is also possible that the large decrease between ∼4 and 3 ka could reflect water from a non-precipitation source, such as an outburst flooding event driven by glacial meltwater, intruded into the peatland, although this hypothesis remains untested. Interestingly, after accounting for age model uncertainty, the timing roughly corresponds (∼3.3–2.5 ka) to a similar isotope excursion (Wooller et al., 2012) and flood deposits along the Tanana River in Interior Alaska (Sattler and Jordan, 1987; Mason and Begét, 1991) and from the central Brooks Range (Hamilton, 1981), suggesting widespread flooding. Assuming that at least some of the decrease is related to the plant's environmental water and a non-cellulose source, another hypothesis for the earlier anomalously low $\delta^{18}O$ values is that lower Pleistocene-aged meltwater could explain the low $\delta^{18}O$ values. Given the proximity of the HTF site to the margin of the ice sheet during the early Holocene, it is conceivable that the low inferred water $\delta^{18}O$ values from 11.7 to 10.8 ka were derived from glacial meltwater, as the ice sheet was rapidly melting under a warming climate (Kaufman et al., 2004).

HTF Paleo-Hydroclimate Relative to Modern Results

The HTF $\delta^{18}O_{cellulose}$ values have a mean of 11.9‰, which falls well below the mean $\delta^{18}O_{cellulose}$ estimates (17.5‰ ± 1.4) at HTF today. Furthermore, the mean $\delta^{18}O$ water value at HTF today (−16‰) falls well above the Holocene and late-glacial average values (−23.6‰, adjusted; −20.4‰, unadjusted; **Figure 6D**). Unless the 6–7‰ discrepancies are caused by differences in extraction methods and sample purity, the disparity between the modern and paleo $\delta^{18}O_{cellulose}$ values suggests that (1) the sampling has not fully encapsulate the range of variables affecting the $\delta^{18}O_{cellulose}$ values through time, such as large changes in temperature (Sternberg and Ellsworth, 2011), and (2) that modern hydrologic conditions on the Kenai are largely unlike the conditions of the past 14 ky, with notable exceptions for two periods at ∼9.6 ka and ∼ 1–1.5 k (**Figure 6D**). Higher water isotope values generally suggest some combination of warmer temperatures, more proximal moisture sources or those originating from primary moisture sources to the south (i.e., the Gulf of Alaska and North Pacific), or a shift in predominance to summer precipitation. Evidence from other studies has shown intensification of the Aleutian Low over the last 150 years (Anderson et al., 2016; Osterberg et al., 2017), which is supported by the increasing values toward present in the HTF record and the higher modern values reported here.

CONCLUSIONS

In this study, we have determined (a) that Kenai fen water reflects modern precipitation, (b) the relationship between $\delta^{18}O$ values of moss and *Carex* spp. cellulose with environmental water, (c) the range of $\delta^{18}O$ values among species of moss and sedge commonly found within Alaskan peatlands, and (d) moss and sedge species separation is necessary for more accurate inferences of variability in environmental water $\delta^{18}O$ values from Alaska peat records.

The use of $\delta^{18}O_{cellulose}$ from peat cores has the potential to dramatically improve the spatio-temporal resolution in paleoclimate studies in regions where peatlands are abundant, such as vast areas of the boreal and Arctic. However, the results of this study show that, similar to lake studies, efforts to better characterized peatland hydrology with modern water isotope sampling serves to improve interpretations of paleoclimate studies. Furthermore, prominent shifts in vegetation assemblages, particularly shifts between moss (nonvascular)- and *Carex* spp. (vascular)-plant dominated intervals common in fens, necessitate modern studies of the relationships between the $\delta^{18}O$ values of plants and environmental waters. Fens are the dominant wetland type in Alaska and circumpolar boreal peatlands, and this study has served to highlight their potential as hydroclimatic archives, particularly spanning periods of substantial deglacial sea level and climate change.

AUTHOR CONTRIBUTIONS

MJ conceived of the study, designed the research, analyzed data, and wrote the manuscript. LA helped design the research, analyze data, and helped write the manuscript. KK, BN, and VL processed samples and created protocol to extract cellulose. MW helped write the manuscript and analyze data. CJ separated moss species and plant parts.

ACKNOWLEDGMENTS

The authors would like to thank the Kenai National Wildlife Refuge and the Alaska Maritime National Wildlife Refuge for access to field sites and Tony Degange and Marc Romano for help with sample collection on St. Matthew Island, Alaska. The authors thank Jessica Rodysill, Laura Gemery, and two reviewers for helpful comments that improved the quality of this manuscript. This study was funded by the USGS Land Change Science Program R&D. Any use of trade, product, or firm names is for descriptive purposes only and does not imply endorsement by the U.S. government.

SUPPLEMENTARY MATERIAL

The Supplementary Material for this article can be found online at: https://www.frontiersin.org/articles/10.3389/feart.2019.00025/full#supplementary-material

REFERENCES

Amesbury, M. J., Charman, D. J., Newnham, R. M., Loader, N. J., Goodrich, J., Royles, J., et al. (2015). Can oxygen stable isotopes be used to track precipitation moisture source in vascular plant-dominated peatlands? *Earth Planet. Sci. Lett.* 430, 149–159. doi: 10.1016/j.epsl.2015.08.015

Anderson, L., Abbott, M., Finney, B., and Burns, S. (2005). Regional atmospheric circulation change in the North Pacific during the Holocene inferred from lacustrine carbonate oxygen isotopes, Yukon Territory, Canada. *Quat. Res.* 64, 21–35. doi: 10.1016/j.yqres.2005.03.005

Anderson, L., Berkelhammer, M., Barron, J. A., Steinman, B. A., Finney, B. P., and Abbott, M. B. (2016). Lake oxygen isotopes as recorders of North American Rocky Mountain hydroclimate: holocene patterns and variability at multi-decadal to millennial time scales. *Glob. Planet. Change* 137, 131–148. doi: 10.1016/j.gloplacha.2015.12.021

Bailey, H. L., Kaufman, D. S., Henderson, A. C. G., and Leng, M. J. (2015). Synoptic scale controls on the δ^{18}O in precipitation across Beringia. *Geophys. Res. Lett.* 42, 4608–4616. doi: 10.1002/2015GL063983

Brand, W. A., Geilmann, H., Crosson, E. R., and Rella, C. W. (2009). Cavity ring-down spec- troscopy versus high-temperature conversion isotope ratio mass spectrometry; a case study on d2H and d18O of pure water samples and alcohol/water mixtures. *Rapid Commun. Mass Spectrom.* 23:1879e1884. doi: 10.1002/rcm.4083

Brenninkmeijer, C. A. M., van Geel, B., and Mook, W. G. (1982). Variations in the D/H and 18O/16O ratios in cellulose extracted from a peat bog core. *Earth Planet. Sci. Lett.* 61, 283–290. doi: 10.1016/0012-821X(82)90059-0

Daley, T. J., Barber, K. E., Hughes, P. D. M., Loader, N. J., Leuenberger, M., and Street-Perrott, F. A. (2016). The 8.2-ka BP event in north-eastern North America: first combined oxygen and hydrogen isotopic data from peat in NewfoundlandJournal of Quaternary. *Science* 31, 416–425. doi: 10.1002/jqs.2870

Daley, T. J., Barber, K. E., Street-Perrott, F. A., Loader, N. J., Marshall, J. D., Crowley, S. F., et al. (2010). Holocene climate variability revealed by oxygen isotope analysis of Sphagnum cellulose from Walton Moss, northern England. *Quat. Sci. Rev.* 29, 1590–1601. doi: 10.1016/j.quascirev.2009.09.017

Dansgaard, W. (1964). Stable isotopes in precipitation. *Tellus* 16, 436–468. doi: 10.3402/tellusa.v16i4.8993

DeNiro, M. J., and Epstein, S. (1979). Relationship between the oxygen isotope ratios of terrestrial plant cellulose, carbon dioxide, and water. *Sci. N. Ser.* 204, 51–53. doi: 10.1126/science.204.4388.51

DeNiro, M. J., and Epstein, S. (1981). Isotopic composition of cellulose from aquatic organisms. *Geochim. Cosmochim. Acta* 45, 1885–1894. doi: 10.1016/0016-7037(81)90018-1

Fisher, D. A., Wake, C., Kreutz, K., Yalcin, K., Steig, E., Mayewski, P., et al. (2004). Stable isotope records from mount logan, eclipse ice cores and nearby jellybean lake. water cycle of the north pacific over 2000 years and over five vertical kilometres: sudden shifts and tropical connections. *Géograp. Physique et Quat.* 58, 337. doi: 10.7202/013147ar

Ford, J., and Bedford, B. L. (1987). The hydrology of Alaskan wetlands, USA: a review. *Arct. Alp. Res.* 19, 209–229. doi: 10.1080/00040851.1987.12002596

Gaglioti, B. V., Mann, D. H., Wooller, M. J., Jones, B. M., Wiles, G. C., Groves, P., et al. (2017). Younger-Dryas cooling and sea-ice feedbacks were prominent features of the Pleistocene-Holocene transition in Arctic Alaska. *Quat. Sci. Rev.* 169, 330–343. doi: 10.1016/j.quascirev.2017.05.012

Gupta, P., Noone, D., Galewsky, J., Sweeney, C., and Vaughn, B. H. (2009). Demonstration of high-precision continuous measurements of water vapor isotopologues in laboratory and remote field deployments using wavelength-scanned cavity ring-down spectroscopy (WS-CRDS) technology. *Rapid Commun. Mass Spectrom.* 23:2534e2542. doi: 10.1002/rcm.4100

Hamilton, T. D. (1981). "Episodic Holocene alluviation in the Brooks Range: chronology, correlations and climatic implications," in *US Geological Survey in Alaska: Accomplishments During 1979*, ed R. Albert (US Geological Survey Circular), 21–24.

IAEA/WMO (2001). "Global network for isotopes in precipitation," in *The GNIP Database*. Available online at: http://isohis.iaea.org

Jones, M. C., Wooller, M., and Peteet, D. M. (2014). A deglacial and Holocene record of climate variability in south-central Alaska from stable oxygen isotopes and plant macrofossils in peat. *Quat. Sci. Rev.* 87, 1–11. doi: 10.1016/j.quascirev.2013.12.025

Kaislahti Tillman, P., Holzkämper, S., Kuhry, P., Sannel, A. B. K., Loader, N. J., and Robertson, I. (2010). Stable carbon and oxygen isotopes in Sphagnum fuscum peat from subarctic Canada: Implications for palaeoclimate studies. *Chem. Geol.* 270, 216–226. doi: 10.1016/j.chemgeo.2009.12.001

Kaufman, D. S., Ager, T. A., Anderson, N. J., Anderson, P. M., Andrews, J. T., Bartlein, P. J., et al. (2004). Holocene thermal maximum in the Western Arctic (0–180 W). *Quat. Sci. Rev.* 23, 529–560. doi: 10.1016/j.quascirev.2003.09.007

Kühl, N., and Moschen, R. (2012). A combined pollen and $\delta^{18}O_{Sphagnum}$ record of mid-Holocene climate variability from Dürres Maar (Eifel, Germany). *Holocene* 22, 1075–1085. doi: 10.1177/0959683612441838

Lachniet, M. S., Lawson, D. E., and Sloat, A. R. (2012). Revised 14 C dating of ice wedge growth in interior Alaska (USA) to MIS 2 reveals cold paleoclimate and carbon recycling in ancient permafrost terrain. *Quat. Res.* 78, 217–225. doi: 10.1016/j.yqres.2012.05.007

Loader, N. J., Street-Perrott, F. A., Mauquoy, D., Roland, T. P., van Bellen, S., Daley, T. J., et al. (2016). Measurements of hydrogen, oxygen and carbon isotope variability in *Sphagnum* moss along a micro-topographical gradient in a southern Patagonian peatland: Stable Isotopic Variability in Patagonian Peat. *J. Quat. Sci.* 31, 426–435. doi: 10.1002/jqs.2871

Mason, O. K., and Begét, J. E. (1991). Late Holocene flood history of the Tanana River, Alaska, USA. *Arct. Alp. Res.* 23, 392–403.

Mayr, C., Lücke, A., Wagner, S., Wissel, H., Ohlendorf, C., Haberzettl, T., et al. (2013). Intensified Southern Hemisphere Westerlies regulated atmospheric CO2 during the last deglaciation. *Geology* 41, 831–834. doi: 10.1130/G34335.1

Ménot, G., and Burns, S. J. (2001). Carbon isotopes in ombrogenic peat bog plants as climatic indicators: calibration from an altitudinal transect in Switzerland. *Org. Geochem.* 32, 233–245. doi: 10.1016/S0146-6380(00)00170-4

Ménot-Combes, G., Burns, S. J., and Leuenberger, M. (2002). Variations of 18O/16O in plants from temperate peat bogs (Switzerland): implications for paleoclimatic studies. *Earth Planet. Sci. Lett.* 202, 419–434. doi: 10.1016/S0012-821X(02)00794-X

Moschen, R., Kühl, N., Rehberger, I., and Lücke, A. (2009). Stable carbon and oxygen isotopes in sub-fossil Sphagnum: assessment of their applicability for palaeoclimatology. *Chem. Geol.* 259, 262–272. doi: 10.1016/j.chemgeo.2008.11.009

Nichols, J., Booth, R. K., Jackson, S. T., Pendall, E. G., and Huang, Y. (2010). Differential hydrogen isotopic ratios of Sphagnum and vascular plant biomarkers in ombrotrophic peatlands as a quantitative proxy for precipitation—evaporation balance. *Geochim. Cosmochim. Acta* 74, 1407–1416. doi: 10.1016/j.gca.2009.11.012

Noone, D., Risi, C., Bailey, C. M., Berkelhammer, M. B., Brown, D. P., Buenning, N. H., et al. (2013). Water sources and turbulent transport from tall tower profiles of water vapor isotope ratios after a snow storm in Colorado. *Atmos. Chem. Phys.* 13:1607e1623. doi: 10.5194/acp-13-1607-2013

Osterberg, E. C., Winski, D. A., Kreutz, K. J., Wake, C. P., Ferris, D. G., Campbell, S., et al. (2017). The 1200 year composite ice core record of Aleutian Low intensification: Aleutian Low Ice Core Record. *Geophys. Res. Lett.* 44, 7447–7454. doi: 10.1002/2017GL073697

Overland, J. E., Adams, J. M., and Bond, N. A. (1999). Decadal Variability of the aleutian low and its relation to high-latitude circulation*. *J. Clim.* 12, 1542–1548. doi: 10.1175/1520-0442(1999)012andlt;1542:DVOTALandgt;2.0.CO;2

Proctor, M. (2000). Mosses and alternative adaptation to life on land. *New Phytol.* 148, 1–6. doi: 10.1111/j.1469-8137.2000.00751.x

Reeve, A. S., and Gracz, M. (2008). Simulating the hydrogeologic setting of peatlands in the Kenai Peninsula Lowlands, Alaska. Wetlands 28:92. doi: 10.1672/07-71.1

Reger, R. D., Sturmann, A. G., Berg, E. E., and Burns, P. A. C. (2008). *A Guide to the Late Quaternary History of Northern and Western Kenai Peninsula*. Guidebook GB 8. Fairbanks, AK: Department of Natural Resources; Division of Geological & Geophysical Surveys.

Rozanski, K., Araguas-Araguas, L., and Gonfiantini, R. (1993). "Isotopic patterns in modern global precipitation" in *Climate Change in Continental Isotopic Records, Geophysical Monograph*, eds Swart, P. K., Lohman, K. C., McKenzie, J., Savin, S (Washington, DC: American Geophysical Union), 1e36. doi: 10.1029/GM078p0001

Rymer, M. J., and Sims, J. D. (1982). Lake-sediment evidence for the date of deglaciation of the Hidden Lake area, Kenai Peninsula, Alaska. *Geology* 10:314. doi: 10.1130/0091-7613(1982)10andlt;314:LEFTDOandgt;2.0.CO;2

Sattler, R. A., and Jordan, J. W. (1987). Late Holocene alluvium of the lower Tanana River, central Alaska. *J. Northern Sci.* 1:8091.

Sauer, P. E., Miller, G. H., and Overpeck, J. T. (2001). Oxygen isotope ratios of organic matter in arctic lakes as a paleoclimate proxy: field and laboratory investigations. *J. Paleolimnol.* 25, 43–64. doi: 10.1023/A:1008133523139

Sternberg, L., and Ellsworth, P. F. V. (2011). Divergent biochemical fractionation, not convergent temperature, explains cellulose oxygen isotope enrichment across latitudes. *PLoS ONE* 6:e28040. doi: 10.1371/journal.pone.0028040

Vardy, S. R. (1997). *Climate Change and Postglacial Environmental History of Permafrost Peatlands in the Mackenzie Delta Area*. NWT Dissertation, University of Waterloo.

Wissel, H., Mayr, C., and Lücke, A. (2008). A new approach for the isolation of cellulose from aquatic plant tissue and freshwater sediments for stable isotope analysis. *Org. Geochem.* 39, 1545–1561. doi: 10.1016/j.orggeochem.2008.07.014

Wolfe, B. B., Edwards, T. W., Elgood, R. J., and Beuning, K. R. (2001). "Carbon and oxygen isotope analysis of lake sediment cellulose: methods and applications," in *Tracking Environmental Change Using Lake Sediments*, eds W. M. Last and J. P. Smol (Dordrecht: Springer), 373–400. doi: 10.1007/0-306-47670-3_14

Wolfe, B. B., Falcone, M. D., Clogg-Wright, K. P., Mongeon, C. L., Yi, Y., Brock, B. E., et al. (2007). Progress in isotope paleohydrology using lake sediment cellulose. *J. Paleolimnol.* 37, 221–231. doi: 10.1007/s10933-006-9015-8

Wooller, M. J., Kurek, J., Gaglioti, B. V., Cwynar, L. C., Bigelow, N., Reuther, J. D., et al. (2012). An ∼11,200 year paleolimnological perspective for emerging archaeological findings at Quartz Lake, Alaska. *J. Paleolimnol.* 48, 83–99. doi: 10.1007/s10933-012-9610-9

Yakir, D., DeNiro, M. J. and Gat, J. R. (1990). Natural deuterium and oxygen-18 enrichment in leaf water of cotton plants grown under wet and dry conditions: evidence for water compartmentation and its dynamics. *Plant. Cell Environ.* 13, 49–56. doi: 10.1111/j.1365-3040.1990.tb01298.x

Zanazzi, A., and Mora, G. (2005). Paleoclimatic implications of the relationship between oxygen isotope ratios of moss cellulose and source water in wetlands of Lake Superior. *Chem. Geol.* 222, 281–291. doi: 10.1016/j.chemgeo.2005.08.006

Zhu, J., Lücke, A., Wissel, H., Mayr, C., Ohlendorf, C., and Zolitschka, B. (2014). Characterizing oxygen isotope variability and host water relation of modern and subfossil aquatic mosses. *Geochim. Cosmochim. Acta* 130, 212–228. doi: 10.1016/j.gca.2014.01.013

Conflict of Interest Statement: The authors declare that the research was conducted in the absence of any commercial or financial relationships that could be construed as a potential conflict of interest.

frontiers in Earth Science

ORIGINAL RESEARCH
published: 12 March 2019
doi: 10.3389/feart.2019.00043

Late-Glacial Paleoecology of the Middle Susitna Valley, Alaska: Environmental Context for Human Dispersal

Nancy H. Bigelow[1], Joshua D. Reuther[2,3], Kristi L. Wallace[4], Émilie Saulnier-Talbot[5], Katherine Mulliken[2,6] and Matthew J. Wooller[5,7]*

[1] Alaska Quaternary Center, University of Alaska, Fairbanks, AK, United States, [2] Department of Anthropology, University of Alaska Fairbanks, Fairbanks, AK, United States, [3] University of Alaska Museum of the North, University of Alaska Fairbanks, Fairbanks, AK, United States, [4] U.S. Geological Survey, Alaska Volcano Observatory, Anchorage, AK, United States, [5] Water and Environmental Research Center, University of Alaska Fairbanks, Fairbanks, AK, United States, [6] Division of Geological and Geophysical Surveys, State of Alaska Department of Natural Resources, Fairbanks, AK, United States, [7] College of Fisheries and Ocean Sciences, Institute of Marine Science, University of Alaska, Fairbanks, AK, United States

OPEN ACCESS

Edited by:
Dorothy M. Peteet, Goddard Institute for Space Studies (NASA), United States

Reviewed by:
Maarten Blaauw, Queen's University Belfast, United Kingdom
Li Wu, Anhui Normal University, China

***Correspondence:**
Nancy H. Bigelow
nhbigelow@alaska.edu

Specialty section:
This article was submitted to Quaternary Science, Geomorphology and Paleoenvironment, a section of the journal Frontiers in Earth Science

Received: *24 October 2018*
Accepted: *22 February 2019*
Published: *12 March 2019*

Citation:
Bigelow NH, Reuther JD, Wallace KL, Saulnier-Talbot É, Mulliken K and Wooller MJ (2019) Late-Glacial Paleoecology of the Middle Susitna Valley, Alaska: Environmental Context for Human Dispersal. Front. Earth Sci. 7:43. doi: 10.3389/feart.2019.00043

We present here the results of multi-proxy analyses (sediment geochemistry, diatoms, and pollen) from sediment cores collected at four lakes in the middle Susitna Valley, Alaska. These lakes form a transect from the tundra to the boreal forest. The retrieved cores span from ∼12,000 cal yr BP to the present, with age control provided by radiometric dates and tephra deposits, some of which are newly identified. Results indicate that deglaciation occurred before 12,000 cal yr BP and that by that time, the lakes were deep, productive, and surrounded by shrub tundra. The lake with the highest sampling resolution indicates a brief climatic reversal ∼11,500 cal yr BP with decreased diatom-inferred lake level and lowered lake productivity, and reduced shrub presence. During the early to middle Holocene, all of the sedimentary records provide evidence of climatic amelioration with tree expansion and productive lakes. A middle to late Holocene climatic deterioration with reduced trees and a shallower, less productive lake is also indicated. In addition, the prominent Watana tephra at ∼4,000 cal yr BP likely reduced lake productivity and affected the vegetation. Even though the region was relatively productive soon after deglaciation, people did not occupy the region until ∼11,000 cal yr BP, about 1000 years later, and then only sparsely. By the middle and late Holocene, the region was more densely populated and this shift in human occupancy presumably reflects changes in resource abundance, especially caribou. Whether the Watana ashfall influenced caribou abundance and thus people, is still under investigation, but given the tephra's effect on vegetation and lake productivity, it seems likely.

Keywords: pollen, isotopes, tephra, diatoms, human paleoenvironments, central Alaska

INTRODUCTION AND BACKGROUND

Hundreds of archeological sites spanning 11,000 years are found in the Susitna River drainage of Alaska. For this reason, it is critically important to reconstruct landscape change from deglaciation (before 12,000 years ago [cal yr BP]) to the late Holocene. We focus here on the middle reaches of the river (**Figure 1**), where the oldest archeological site (Jay Creek Ridge ∼11,100 cal yr BP]) has been found (Dixon et al., 1985; Bowers et al., 2011). We present multi-proxy investigations (sediment geochemistry, tephra, diatoms, and pollen) based on the sedimentary archives of four Susitna lakes located in the tundra, forest-tundra ecotone, and boreal forest, which span from deglaciation through to today. Prior to this study, only one lake record with a problematic chronology existed for the region (Dilley, 1988; Ager, 2018). In contrast, the terrestrial stratigraphy at natural sections and archeological sites are well documented (Dilley, 1988; Mulliken, 2016), but there is a lack of synthetic paleoenvironmental analysis in the context of post-glacial human occupation of the region.

Below, we summarize our current understanding of the landscape, paleoecology, and human prehistory of the middle Susitna and surrounding regions. The Late-Glacial (>∼14,000 cal yr BP) was a period of landscape instability that may have maintained extensive ranges of herbaceous tundra and reduced competition from woody plants, as well as hindering paludification (Guthrie, 1990; Mann et al., 2015). By 14,000 cal yr BP, climate was warming, but still much cooler than modern (Viau et al., 2008) and moisture was increasing as reflected in rising lake levels and rapid shrub expansion (Abbott et al., 2000; Bigelow and Edwards, 2001; Bigelow, 2013). The Younger Dryas chronozone (∼12,900–11,700 cal yr BP [Rasmussen et al., 2014]) occurred at the end of the Late-Glacial. While this episode of climate deterioration is well-documented in southern and coastal Alaska (Engstrom et al., 1990; Peteet and Mann, 1994; Hansen and Engstrom, 1996; Kokorowski et al., 2008), it is less-well expressed elsewhere in the state.

The early Holocene (∼11,700–8,200 cal yr BP) ushered in a period of warming summer temperatures (Berger, 1978). Significant landscape changes included a transient expansion of *Populus* (cottonwood or aspen), the initial expansion of spruce (Anderson et al., 2004; Bigelow, 2013), as well as permafrost degradation and peatland development (Jones and Yu, 2010; Mann et al., 2010; Walter Anthony et al., 2014). Archeological evidence indicates people were using resources in the Susitna Valley as early as ∼11,100 cal yr BP (Dixon, 1999; Wygal and Goebel, 2012; Blong, 2016, 2018), but sites are scarce before 10,000 cal yr BP and somewhat ephemeral, probably reflecting short-term seasonal hunting forays (Wygal and Goebel, 2012; Blong, 2018). These sites are typically found on elevated features and people focused on a broad spectrum of subsistence resources such as bison and elk (Wapiti) (Yesner, 2007; Graf and Bigelow, 2011; Potter, 2011; Blong, 2016). Caribou, sheep, waterfowl and fish were also used, albeit in low quantities (Potter, 2008b).

Later, the middle Holocene (∼8,200–4,200 cal yr BP) may have also been relatively warm, based on pollen (continued spruce expansion) and midge-based temperature reconstructions, while the late Holocene (∼4,200 cal yr BP-present) was generally cooler with neoglacial ice advances (Kaufman et al., 2016). By ∼6,000 cal yr BP, the vegetation in the middle Susitna region was similar to modern, although sites at high elevations show a subsequent retraction of tree line (this study).

Three widespread tephra deposits dating to the middle and late Holocene are widely recognized in terrestrial sections of the Susitna River Valley (Dixon and Smith, 1990): the informally named Oshetna (∼6570–7930 cal yr BP), Watana (∼3,360–4,400 cal yr BP), and Devil (∼1625–1825 cal yr) tephras (Dixon et al., 1985; Dilley, 1988; Dixon and Smith, 1990; Mulliken, 2016). The Watana tephra is the most widespread and thickest of the tephra deposits (up to 20 cm thick in terrestrial sections) and is the only one of the three present in our lake cores. The source volcano for both the Watana and Devil tephra units was Hayes Volcano, where proximal sediments (Units H1, H2, F2, E, and D of Wallace et al., 2014) are highly correlated with these distal units (Mulliken, 2016). In contrast, the Oshetna tephra has a very diverse glass chemistry and is not well documented outside of the Susitna River Valley.

In terms of archeology, a notable shift in resource acquisition, land use strategies, and lithic technologies occurred after 6,000 cal yr BP (Dixon, 1985; Esdale, 2008; Potter, 2008a). These Northern Archaic populations were mobile, highly reliant on seasonally available resources including fish and caribou (Dixon, 1985; Esdale, 2008; Potter, 2008b), and occupied diverse landforms including lakeshores and lower riverbanks (Potter, 2008a). Middle Holocene archeological horizons (components) are relatively abundant, especially in uplands where caribou took on more importance as a subsistence resource. Around 1,500 cal yr BP, the "Athabascan Tradition" reflects a shift from lithic to organic and metal tool technological strategies, with an increase in moose acquisition (Cook, 1975; Workman, 1978; Dixon, 1985; Esdale, 2008; Potter, 2008a). These late Holocene populations expanded the use of seasonally abundant resources, including caribou and fish, with storage pits and subterranean houses becoming common on lakeshores and river and stream terraces (Potter, 2008a).

STUDY SITES

The study sites are located in the mountains, between ∼600 and ∼900 m above sea level (MASL). The nearest weather station is at the Chulitna River in Broad Pass about 90 km to the west, and somewhat lower, at ∼400 MASL (**Figure 1**). The Chulitna River climate normals (1981–2010) indicate a mean annual temperature of ∼0.3°C, a mean July temperature of ∼13°C, a mean January temperature of ∼−11.5°C, and mean annual precipitation of ∼850 mm, with ∼70% falling between July and December (Alaska Climate Research Center, 2014). Climate at the study sites themselves is probably somewhat cooler in the summer and perhaps receive more precipitation than at the Chulitna River. The regional vegetation is a birch and willow shrub tundra with occasional alder, especially above 850 MASL. Occasionally, spruce trees are present in protected localities at 800 MASL, but closed boreal forest is

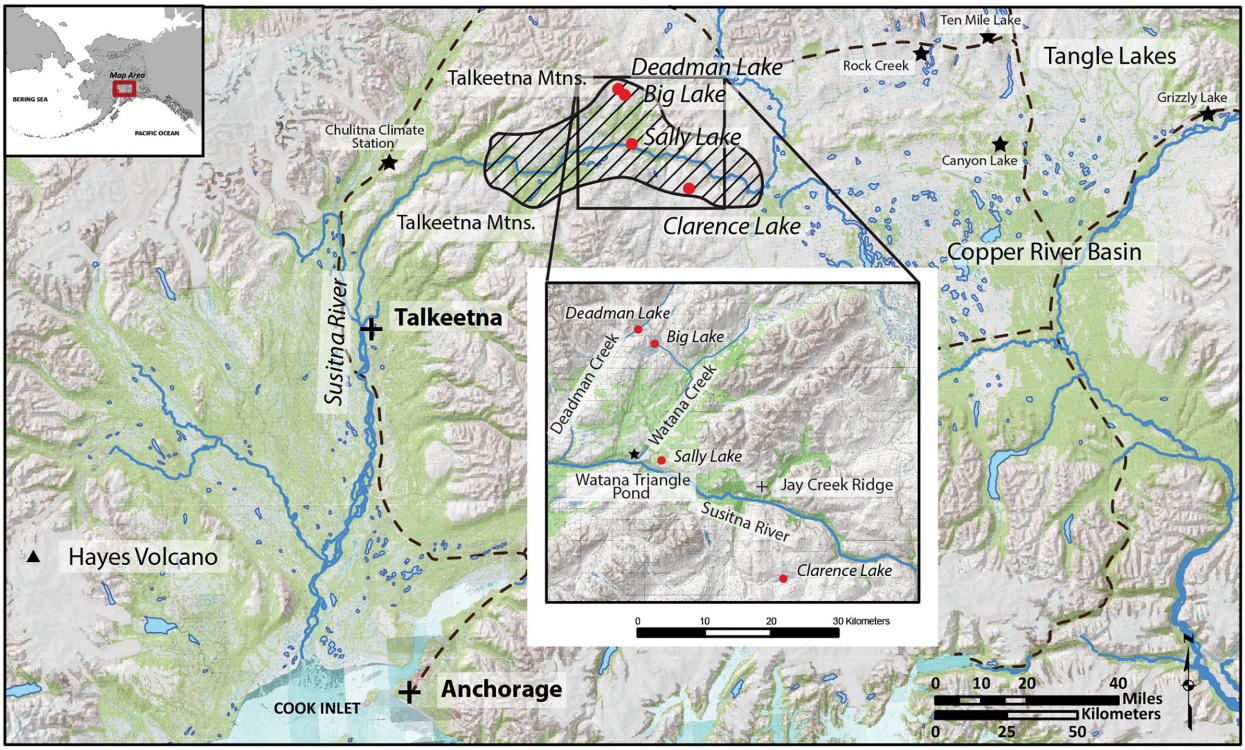

FIGURE 1 | Localities mentioned in the text. Diagonal hatching marks the middle Susitna Valley. Red circles are the study lakes, stars mark other sites and dashed lines are major roads.

found only below 600 MASL, especially along the Susitna River (Boggs et al., 2014).

Much of the study area was heavily glaciated during the Late Wisconsinan (~25,000–14,000 cal yr BP), with ice originating from the Alaska Range as well as the Talkeetna Mountains to the south and northwest (Woodward-Clyde Consultants, 1982; Reger et al., 1990) and the region's topography is heavily influenced by past glaciations and associated outwash (Thorson et al., 1981; Dixon et al., 1985; Reger et al., 1990). Moraines, eskers, kames, and kettle lakes lie adjacent to steep-walled scarps and canyons created by post-glacial down-cutting (Kachadoorian, 1974; Dixon et al., 1985; Reger et al., 1990) and large proglacial lakes once covered vast portions of the study area (Reger et al., 1990).

The regions around Deadman, Big, and Sally lakes (**Figure 1**) were covered by thick ice until deglaciation and the basal radiocarbon dates in those lakes suggest deglaciation was before 12,000 cal yr BP. However, the region around Clarence Lake (**Figure 1**) apparently remained ice-free during the Late-Wisconsinan (Woodward-Clyde Consultants, 1982). After deglaciation, Holocene-aged ice was limited to cirques with little growth into the valleys, and the study lakes would have been affected indirectly (if at all) by these ice advances (Woodward-Clyde Consultants, 1982; Reger et al., 1990).

Clarence Lake

Clarence Lake (N 62.6784°; W 147.8108° [**Supplementary Table 1**]) is located south of the Susitna River at about 870 MASL, ~120 km east northeast of Talkeetna (**Figure 1**). The lake is ~3.2 km long and ~0.5 km wide at its widest point, with the long axis oriented northeast-southwest. The lake has a current maximum water depth of ~11 m, with the surrounding hills rising to ~100 m above the lake's margins (**Figure 2**). The lake has three major inlets at its eastern and northern margins, and an outlet at the western end of the lake that ultimately drains into the Susitna River. The present vegetation around the lake is shrub tundra with widely scattered spruce trees.

Deadman and Big Lakes

Deadman Lake (N 63.0059°; W 148.2650°) and Big Lake (N 62.9979°; W 148.2051°) (**Supplementary Table 1**) are paired lakes located north of the Susitna River ~120 km northeast of Talkeetna (**Figure 1**) and are situated in a basin shaped by late Pleistocene glaciations. The surrounding landscape consists of higher elevation peaks that reach up to 1,500 MASL (nearly 600 m above the lakes), which are at 934 and 936 MASL, respectively. Deadman Lake is ~2 km long and 1 km wide with its long axis oriented roughly east-west (**Figure 2**). At Deadman Lake, the Alaska Department of Fish and Game (2019) bathymetric map indicates the maximum lake depth in 1983 was ~92 feet (~28 m). Big Lake is ~3 km long and 1.3 km wide, with a large, shallow (1–2 m) embayment at its northwest end (**Figure 2**). Spot water depth measurements indicate a basin depth of at least 29 m. Deadman Lake and Big Lake were likely once part

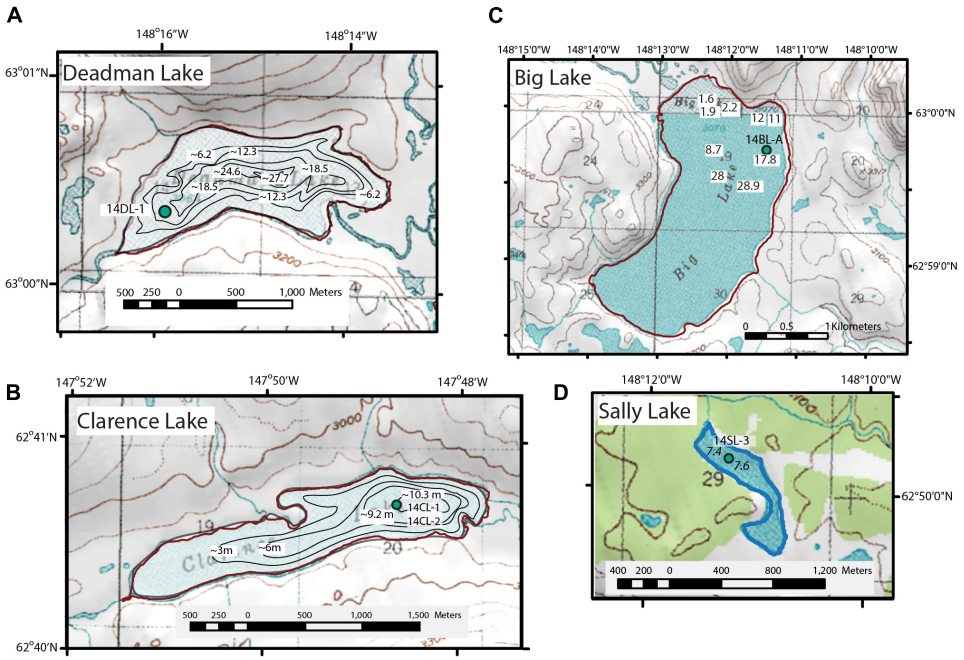

FIGURE 2 | Lakes and coring sites (green circles) in this study. **(A)** Deadman Lake. **(B)** Clarence Lake. **(C)** Big Lake. **(D)** Sally Lake. Clarence Lake (Alaska Department of Fish and Game, 2019) and Deadman Lake (Alaska Department of Fish and Game, 1983) bathymetries were originally in feet. Spot water depths in m are marked in Big and Sally lakes. Topographic maps are USGS 1:63,360 quads and elevations are in feet.

of a larger proglacial lake system in the area (Reger et al., 1990). Deadman Creek serves both as an inlet at the eastern margin and as an outlet at the western margin of Deadman Lake. Watana Creek serves as an outlet for Big Lake at its eastern shore. Inlets into Big Lake are relatively minor, draining seasonal meltwater from the surrounding hills into its basin. Present-day vegetation around the lakes is tundra with low and tall shrubs, including birch, willow, and ericads, along with alder in the creek drainages (Alaska Biological Research, 2014). A few spruce trees were noted on the slopes to the northeast of Big Lake.

Sally Lake

Sally Lake (N62.8356; W148.1878, **Supplementary Table 1**) is located just north of the Susitna River, ∼113 km northeast of Talkeetna (**Figure 1**), at an elevation ∼620 MASL. The lake is likely a kettle lake that formed on a glaciofluvial plain that was eroded by the Susitna River, which created a terrace scarp ∼1 km south of the lake (Woodward-Clyde Consultants, 1982; Dixon et al., 1985; Reger et al., 1990). The hills surrounding Sally Lake rise $\leq$35 m above the lake margins, and are somewhat lower in elevation than those surrounding the other study lakes. The lake is about 1 km long with a width that varies between 250 and 100 m and consists of two basins. Water depth was measured only in the northern basin, where it was ∼7.6 m (**Figure 2**). An outlet at the northwestern margin of Sally Lake drains into Watana Creek. Boreal forest surrounds the lake, although the spruce trees are more widely scattered than at lower elevations.

MATERIALS AND METHODS

Field Methods

We collected a series of lake sediment cores from the ice surface at the study lakes in April, 2014. Coring locations were chosen to avoid potential reworking due to debris flows, focusing on lakes with relatively flat basins and with water depths less than about 20 m, the maximum depth allowed by our equipment. All coring and water-depth measurement sites were located with a GPS (**Supplementary Table 1**). We collected the sediment-water interface with a 7 cm diameter polycarbonate corer (a *Bolivia* corer) and preserved the core by adding a super absorbent polymer that gelled the overlying water and stabilized the sediments. Underlying sediments were collected with a 1 m-long modified square-rod Livingstone corer with a 5 cm diameter steel barrel (Wright et al., 1984). The depths of each Livingstone drive are presented in **Supplementary Table 2** and as a rule, the drives were consecutive, except at Sally Lake, where difficulties extruding the 5 cm-thick Watana tephra lead to multiple attempts to collect and extrude an undisturbed core section. At all lakes, each Livingstone drive was extruded into a split ABS pipe lined with plastic film liner, wrapped, labeled, and packaged for transport to the University of Alaska Fairbanks (UAF). We collected only one long core and one or more surface core from each of the lakes, except at Clarence Lake, where we collected two adjacent long cores (14CL-1 and 14CL-2) in addition to a surface core. The majority of the analyses were conducted on 14CL-2, although tephra analyses were conducted on both cores.

Geochronology

Sediment cores from our study lakes were dated using radioisotopes (^{14}C [**Table 1**], ^{210}Pb, and ^{137}Cs [**Supplementary Table 3**]). Radiocarbon was used for pre-industrial aged samples, while ^{210}Pb dating was employed to produce a sediment chronology over the last 160 years (1855–2014 AD). Samples for radiocarbon analysis (plant macrofossils, pollen, and in one case, *Daphnia* ephippia) were sieved and cleaned with reverse osmosis (RO) water prior to analysis at the Center for Applied Isotope Studies, University of Georgia. In addition to plant macrofossils, pollen extracts (primarily spruce pollen) were radiocarbon dated at the same facility. Details of the pollen extraction methods are in **Supplementary Text**. Only Dead Man Lake was analyzed for ^{210}Pb and ^{137}Cs, where the upper 10 cm of the surface core was subsampled at 0.5 cm intervals. ^{137}Cs and ^{210}Pb activities were measured by gamma spectrometry at the Flett Research Ltd (**Supplementary Table 3**). The 1966 ^{137}Cs peak[1] was recognized in the top 2.5 cm of the core, confirming that physical mixing of the upper sediments was relatively negligible and would not affect the ^{210}Pb chronology. We used Bacon ver. 3.3.5 to build the age models (Blaauw and Christen, 2011), which, using IntCal13 for calibration to cal yr BP, generates mean and median ages for each sample, as well as the 2 standard deviation (2 SD) error range.

Tephra Identification

Tephras and presumed tephras were identified visually and texturally in split sediment core surfaces (**Supplementary Table 4**). Individual tephras were sampled from one side of the split core, reserving the other half for archiving. Single samples were collected for layers $\leq$1 cm thick and multiple samples were collected for thicker layers (>1 cm) to test for possible compositional zonation. All tephra samples were processed and archived at the U.S. Geological Survey (USGS) Alaska Tephra Laboratory & Data Center in Anchorage, Alaska. Splits of the bulk samples were wet sieved using tap water into three size fractions (0.063, 0.125, and 0.250 mm) to remove very fine-grained ash and allow for microscopic analysis. Basic visual descriptions of the tephras including physical characteristics of the juvenile glass component were performed using either a binocular or a petrographic microscope at 100x and 500x magnification. All tephras were confirmed by the presence of glass shards or pumice grains and/or glass coatings on minerals and mineral fragments. For very fine-grained samples (<0.063 mm), confirming volcanic glass was not possible using traditional microscopic techniques and thus, such samples were mounted on pin mounts and imaged using the USGS JEOL JSM-6510LV scanning electron microscope in Anchorage, Alaska. Back-scattered electron images were used to determine if the deposit was volcanic based on presence of glass shards and/or glass-coated crystals.

The 0.250–0.125 mm size fraction was preferentially mounted for electron microprobe microanalysis (EPMA) or the 0.125–0.063 mm material was used for finer-grained samples. Samples finer than 0.063 mm could not be analyzed using the electron microprobe and therefore, there are no geochemical analyses for those samples. Details of the major-element glass analyses are in **Supplementary Text**. Glass compositions were compared among lakes and with a database of major-element compositions of reference tephras found in terrestrial sections in the Susitna River Valley (Mulliken, 2016), reference tephras from Hayes volcano (Wallace et al., 2014) and the Alaska tephra database (Cameron et al., 2019). Geochemical similarity was measured using the weighted similarity coefficient (SC) of Borchardt (1974), as well as binary plots. Similarity Coefficients of $\geq$ 0.95 are often indicative of correlative tephras.

[1]http://www.flettresearch.ca/Radioisotope.html

Magnetic Susceptibility and Geochemistry

Magnetic susceptibility (MS) was measured using a Bartington MS ring on whole cores at 1, 2, or 5 cm intervals. Samples for stable isotopic analyses (∼1cc) were taken at four or five cm intervals from along the length of the cores. For isotope analysis, each sample was acid fumed with HCl to remove any trace amounts of carbonate. Samples were then freeze-dried and weighed for analysis using an isotope ratio mass spectrometer at the Alaska Stable Isotope Facility (ASIF) at UAF. Stable carbon and nitrogen isotope ratios are expressed in typical delta notation (i.e., δ^{13}C and δ^{15}N values), and are also expressed relative to the Vienna Pee Dee Belemnite (VPDB) and air, respectively. Total organic carbon (TOC [%C]) total nitrogen (TN [%N]) and C:N values were also produced from each sample analysis. Analytical precisions for δ^{13}C, δ^{15}N, %C and %N, based on multiple analyses of a reference standard (peptone), were <0.2, <0.3, <0.6, and <0.6, respectively.

Diatoms

For diatom analyses, a measured amount of wet sediment (between 0.11 and 0.15 g) was treated from 25 samples distributed throughout the Clarence Lake core. Diatom preparation followed standard procedures using H_2O_2 outlined in Battarbee et al. (2001). Cover slips were mounted using Meltmount, a plastic resin with the same refractive index as Naphrax. A minimum of 400 diatom valves were enumerated for each sample using a Leica DM microscope (1000x magnification under oil immersion). Identification followed mainly northern and western Canadian floras, including Cumming et al. (1995); Fallu et al. (2000), and Antoniades et al. (2008). A diatom-based inference model developed from a set of Alaska lakes (Gregory-Eaves et al., 1999) was applied to the sedimentary data to reconstruct past variations in relative lake depth, conductivity and total phosphorous (TP). The model was implemented and results plotted using the software C2 (Juggins, 2014).

Pollen

Pollen samples were processed using standard techniques described in Faegri and Iversen (1989). In brief, this includes adding a known quantity of exotic pollen (tablets of *Lycopodium clavatum* spores) and washing the sample in acid and base washes to remove carbonates, organics, and silica. The details of the pollen processing method are in **Supplementary Text**.

TABLE 1 | Radiocarbon dates from the study lakes.

Lab#	Lake	Core	Depth in core (cm)	Material dated	δ13C ‰	14C age ± 1 SD	Cal Median	Calibrated 2 SD range	
								Younger limit	Older limit
UGAMS-18842	Big Lake	14BL-A	1	Bryophytes	−33.8	520 ± 20	533	512	551
UGAMS-18843	Big Lake	14BL-A	24–26	Organics	−27.5	450 ± 35	508	340	540
UGAMS-18844	Big Lake	14BL-A	34–36	Organics	−25.3	1760 ± 55	1674	1559	1817
UGAMS-18845	Big Lake	14BL-A	43–45	Organics	−26.6	2040 ± 40	1998	1899	2116
UGAMS-18846	Big Lake	14BL-A	45–47	Organics	−25.7	2480 ± 40	2576	2379	2724
UGAMS-18847	Big Lake	14BL-A	49–51	Organics	−26.3	2320 ± 25	2343	2313	2358
UGAMS-18848	Big Lake	14BL-A	51–53	Organics	−24.3	2620 ± 30	2752	2725	2778
UGAMS-18849	Big Lake	14BL-A	64–66	Organics	−24	3200 ± 30	3420	3366	3470
UGAMS-18850	Big Lake	14BL-A	109–111	Organics	−28.6	6880 ± 40	7712	7620	7816
UGAMS-18851	Big Lake	14BL-A	180–182	Organics	−27.8	9340 ± 30	10554	10438	10657
UGAMS-18852	Big Lake	14BL-A	190–192	Organics	−26.4	9820 ± 40	11230	11181	11290
UGAMS-19730	Clarence	14CL-2	102–104	Bark	−27.4	3690 ± 25	4035	3929	4141
UGAMS-18753	Clarence	14CL-2	112–116	Organics	−25.9	4870 ± 30	5608	5494	5655
UGAMS-18832	Clarence	14CL-2	116–118	*Picea* needle (charred)	−27.6	4620 ± 30	5412	5297	5461
UGAMS-18755	Clarence	14CL-2	126–128	Organics	−26.8	5700 ± 25	6477	6411	6549
UGAMS-19731	Clarence	14CL-2	162–166	Plant fragments	−24.2	4770 ± 40	5516	5330	5592
UGAMS-18756	Clarence	14CL-2	272–274	Organics	−28.5	9480 ± 35	10726	10588	11065
UGAMS-18757	Clarence	14CL-2	275–279	Organics	−27.1	9990 ± 30	11446	11285	11613
UGAMS-18754	Clarence	14CL-2	309.5–313.5	*Daphnia* ephippia	−34.9	9370 ± 70	10593	10300	10768
UGAMS-19732	Clarence	14CL-2	317–318.5	Plant fragments	−27.2	9950 ± 30	11341	11249	11600
UGAMS-18176	Deadman	14DL-1	1–2	Leaf fragments	−28.3	Modern			
UGAMS-18833	Deadman	14DL-1	35–38	Wood and plant fragments	−28.9	340 ± 30	391	311	480
UGAMS-18834	Deadman	14DL-1	57–59	Wood and plant fragments	−26.7	1010 ± 20	934	913	963
UGAMS-18835	Deadman	14DL-1	85–88	Wood and plant fragments	−26.0	1770 ± 30	1675	1606	1811
UGAMS-18836	Deadman	14DL-1	114–116	Wood and plant fragments	−28.1	2500 ± 30	2587	2485	2736
UGAMS-18837	Deadman	14DL-1	157–158	Wood	−27.4	4450 ± 25	5079	4966	5280
UGAMS-18177	Deadman	14DL-1	182	Charred wood	−26.0	5430 ± 25	6240	6198	6288
UGAMS-18175	Deadman	14DL-1	210	Charred wood	−27.3	9260 ± 30	10446	10296	10553
UGAMS-20052	Sally	14SL-3	35–39	Pollen	−28.4	2180 ± 20	2254	2123	2306
UGAMS-20053	Sally	14SL-3	88–92	Pollen	−28.4	3740 ± 20	4102	3991	4153
UGAMS-19733	Sally	14SL-3	157–161	Wood	−27.2	10200 ± 35	11903	11758	12061

Pollen preparations were mounted on slides with silicon oil and analyzed at 400x and 1,000x. Pollen identifications were made by comparison with the pollen reference collection housed at UAF, as well as comparison with published pollen atlases (McAndrews et al., 1973; Moriya, 1976; Moore et al., 1991). As the pollen grains were counted, the exotic pollen (*Lycopodium clavatum*) was also tallied so that pollen concentration [grains(cm^{-3})] and influx [grains(cm^{-2})(yr^{-1})] could be calculated, in addition to percent calculations. Details of the percent calculations are in **Supplementary Text**. Pollen diagrams were made with Tilia ver. 2.1.1 (Grimm, 2016). At Clarence and Deadman lakes, pollen counting stopped when a sum of at least 300 terrestrial pollen grains was reached. With Sally Lake, counting stopped at a terrestrial pollen sum of ∼120–200 grains.

RESULTS

Chronologies

A suite of thirty-one radiocarbon dates from the cores, plus a suite of nine ^{210} Pb samples from Deadman Lake form the chronologies (**Table 1** and **Supplementary Table 3**).

For Clarence Lake, in the forest-tundra ecotone, nine radiocarbon dates form the age model (**Figure 3**). The median

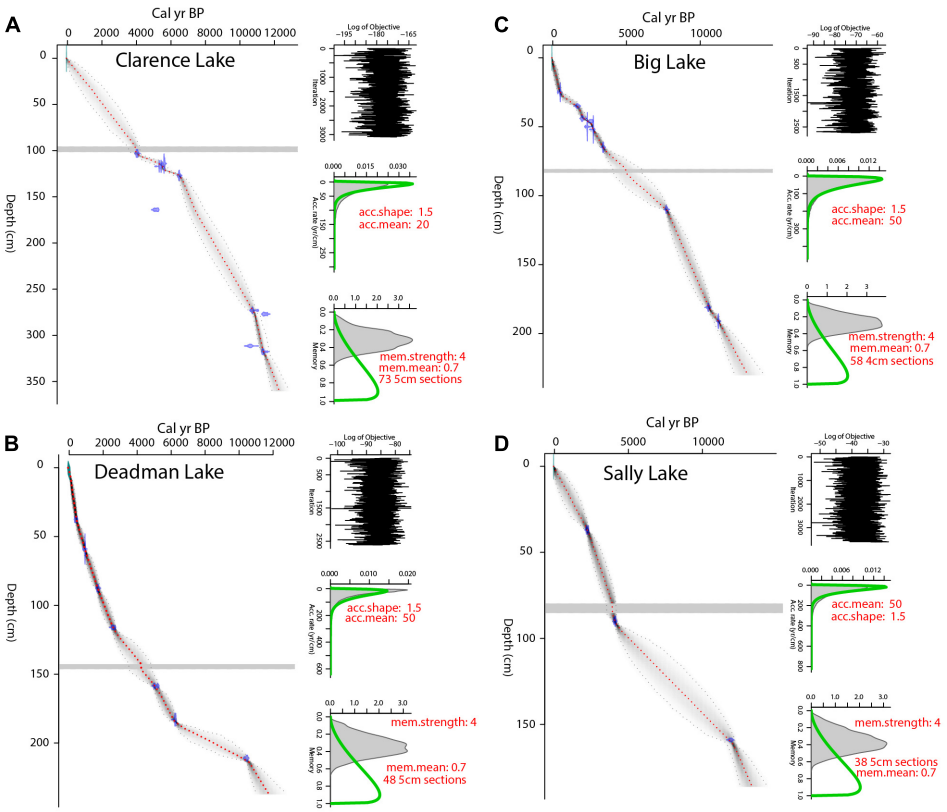

FIGURE 3 | Bacon-generated age models (Blaauw and Christen, 2011) for **(A)** Clarence, **(B)** Deadman, **(C)** Big, and **(D)** Sally lakes. Red, dashed lines mark the mean ages and gray shading marks the 2 SD error range. In each plot, the horizontal bar marks the Watana tephra.

2 SD range is 915 years, with a maximum 2 SD range of about 1589 yr at ∼2060 cal yr BP. The core base, which is nearly 40 cm below the lowest ^{14}C date, has a modeled age of about 12,280 cal yr BP.

The age models for adjacent Deadman and Big lakes are based on eight and 11 radiocarbon dates, respectively. Deadman Lake also has a suite of nine ^{210}Pb ages (linear model) for the top 4.5 cm. The Deadman Lake chronology has a median 2 SD error of 488 years, with a maximum 2 SD range of nearly 2500 years at ∼8600 cal yr BP. The Deadman record dates at least to ∼10,440 cal yr BP, although if one extrapolates, the core base dates at least to ∼12,000 cal yr BP (**Figure 3**). At Big Lake, the median 2SD range is 866 yr, with the maximum 2SD range of 2136 yr at ∼5660 cal yr BP. The Big Lake chronology may be running old, at least in the middle Holocene, as the modeled age for the Watana tephra is ∼900 yr older than published ages of ∼4000 cal yr BP for this deposit (Beget et al., 1991; Wallace et al., 2014; Mulliken, 2016). This chronology indicates that the Big Lake record dates to ∼11,230 cal yr BP, though the core base is substantially older if one extrapolates (**Figure 3**).

Sally Lake, in the boreal forest, has a chronology based on three radiocarbon dates and is the least well-dated of the sites. The median 2 SD range is 1068 years, with a maximum 2 SD range of 3334 years at ∼8590 cal yr BP. The core dates at least to ∼11,800 cal yr BP, but may date to ∼13,000 cal yr BP if one extrapolates (**Figure 3**).

Lithology and Magnetic Susceptibility

At Clarence Lake, the basal 40 cm of sediment is silt and sand, reflecting an ephemeral and shallow lake (**Figure 4**). Above this (starting at about 320 cm, ∼11,450 + 280/−110 cal yr BP [ages and 2 SD errors are rounded to the nearest decade]) and continuing to the core top, gyttja (organic-rich lake mud) dominates. Zones of mm-scale laminae occur at 320–260 cm (∼11,450 to ∼10,350 + 370/−470 cal yr BP) and 178–110 cm (∼7,800 + 620/−520 to 4,820 + 410/−500 cal yr BP). Silt bands are scattered throughout the core, though they dominate in the basal half (below ∼200 cm) and two mm-scale diatom layers were also identified at 211 cm and 238 cm. Six visible tephras are preserved at Clarence Lake. They range from 0.05 to 4 cm thick and are located at 330.5, 289, 226.5, 224.5, 98–102, and 49 cm below the sediment-water interface.

Magnetic susceptibility (MS) peaks in Clarence Lake (**Figure 4**) mark the major tephra units at about 100 and 330 cm. However, the thin, mm-scale tephras were not identified through MS because the analytical resolution was too coarse. The MS data do indicate areas with low mineral influx (when the MS is near zero), such as ∼300–200 cm (∼11,150 + 360/−170 to ∼8,490 + 680/−610 cal yr BP). MS increases higher in the core,

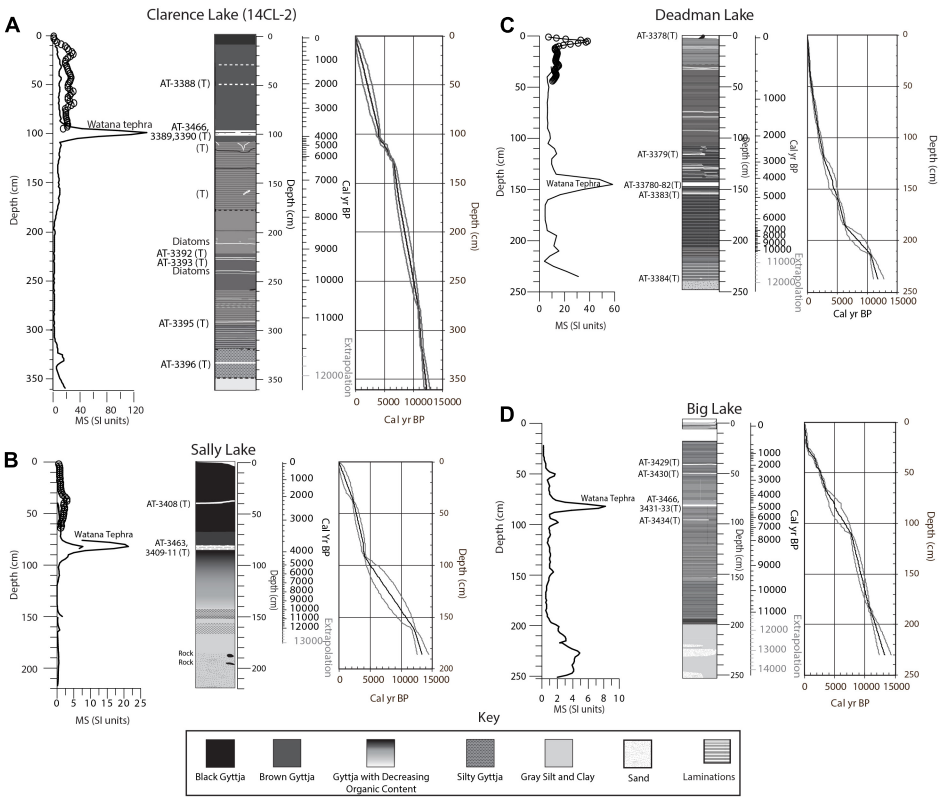

FIGURE 4 | Core stratigraphies, MS measurements and age scales, with 2 SD error envelopes for **(A)** Clarence, **(B)** Sally, **(C)** Deadman, and **(D)** Big lakes. Tephra units are marked with "(T)"and analyzed tephras are indicated by the sample number (AT-#). These sample numbers are keyed to **Figure 5** and **Supplementary Table 4**. Circles on the MS graphs are measurements from the surface core for each lake. In the age scales, gray-shaded ages are extrapolations below the lowest radiocarbon date. In the error envelopes, the thick black line marks the mean sample age and gray lines mark the 2 SD error range.

with the core top having MS values that are only slightly less than the silt and clay at the base.

In Deadman Lake, the basal ∼10 cm of the core is gray silt, sand, granules and probably represent the lake basin prior to filling (**Figure 4**). Above this is about 20 cm of gray and tan silt, to about 210 cm below the sediment-water interface. The presence of *Pediastrum* nets indicate the basin was perennially filled (if shallow) at this time. Starting at ∼220 cm (∼10,900 + 510/−330 cal yr BP), the remainder of the core is gyttja with bands of laminae, fine silt, and tephra. Lenses of fine silt are present after about 4,060 + 650/−700 cal yr BP (∼140 cm) and probably represent episodes of shoreline instability. The MS spikes in Deadman Lake mark tephras ranging in thickness from 0.5 mm to 4 cm at 142–146 cm (Watana), ∼116 cm, and at the core top. However, two additional tephras at 153.5 and 237 cm have low MS values, and aside from the tephras, MS values are low throughout the core, except at the core base where there is increasing silt and sand.

In Big Lake, the basal ∼50 cm (∼250–200 cm) is dominated by gray silt and clay with sand bodies (**Figure 4**). Starting at 200 cm (∼11,710 + 520/−410 cal yr BP [but ages below ∼82 cm may be too old]), laminated silty gyttja (indicating a perennial lake) dominates much of the remainder of the core with occasional zones of massive gyttja. The gyttja is increasingly organic-rich in the upper 50 cm (younger than ∼2,670 + 60/−190 cal yr BP), where the laminations also become less frequent. Tephras, ranging in thickness from 1 mm to 4 cm, are located at 96, 80 (Watana), 49, and 40 cm below the sediment-water interface and are also marked by the MS data. Aside from the tephras, the MS values are highest in the sand and silt at the core base. The lowest values are in the gyttja and near the core top.

In Sally Lake, the basal ca 35 cm of the core (∼219–168 cm) consists of sand, clay, silt, rocks, and ∼15 cm of gray sticky clay (**Figure 4**). Shells were not observed in the core, but the $\delta^{13}C$ data from this level strongly suggests the presence of carbonates, which would be consistent with loess deposition or possibly an ephemeral lake. Above this, starting abruptly at about 168 cm, silty gyttja and then gyttja dominate the core. Extrapolating from the nearest radiocarbon date, about 10 cm higher in the core, the transition to silty gyttja occurred ∼12,440 + 560/−470 cal yr BP and marks the onset of a perennial lake. The gyttja is initially light-colored, but darkens up-core, indicating increased organic input. Two tephras are preserved in the core and are marked by the MS data (**Figure 4**), a ∼4 cm thick continuous tephra at 81–85 cm (Watana) and a 0.5 cm thick layer at 39 cm. MS is lowest about 150–120 cm (∼10,750 + 970/−1,390 to ∼7,320 + 1,680/−1,500

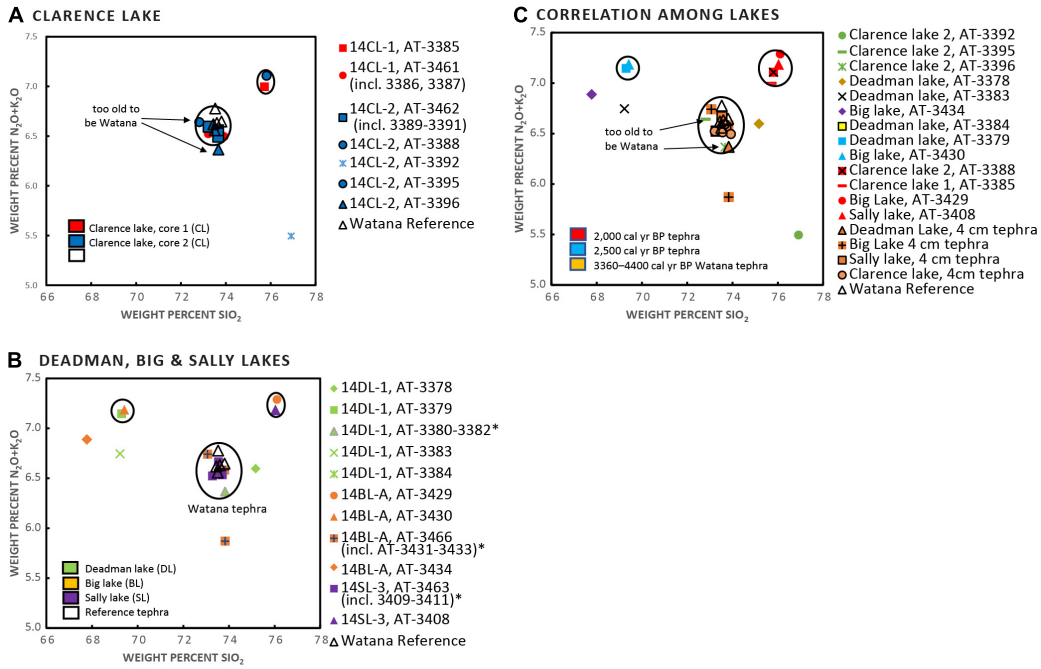

FIGURE 5 | Geochemical scatter plots of tephra units at **(A)** Clarence Lake, **(B)** Deadman, Big, and Sally lakes, and **(C)** Correlations between lakes. In **(A–C)**, each symbol is identified first by the core, then by a unique number (AT-#). Asterisks indicate multiple samples from a single tephra horizon. **Figure 4** shows the stratigraphic placement of the samples (identified by AT-#). In all plots, the open triangle marks the Watana reference material.

cal yr BP) and increases slightly in the non-tephra layers higher in the core.

Tephras

Six distinct tephra deposits were identified among the two Clarence Lake cores, five of which were found in both cores, and one that was only identified in core CL-2 (**Figure 4** shows only CL-2 as it is the more complete core). In core CL-1, five tephras were identified, but only two were coarse-grained enough to be geochemically analyzed. In core CL-2, six tephras were identified, of which five were of adequate grainsize to be geochemically analyzed. Of the six analyzed tephras from the Clarence Lake cores, only one correlates with Susitna River Valley reference tephras (the informally named Watana tephra, a widespread deposit found in terrestrial sections in the Susitna River Valley [Dilley, 1988; Dixon and Smith, 1990; Mulliken, 2016]). This 5 cm-thick tephra at ∼96–101 cm depth was subsampled to check for chemical zonation or the possibility that it may be a composite of multiple tephra layers erupted over time from the same volcano. There is definite geochemical spread within these subsamples (**Supplementary Table 4** and **Figure 5**) although all analyses correlate together with very high similarity coefficients (SC) (0.95–0.99) and also correlate with the Watana tephra. However, tephras at 289 and 330.5 cm, the lowest two tephras in core CL-2, are geochemically identical to the 5-cm thick Watana tephra (96–101 cm depth), which is confusing and suggests that eruptions from the same source volcano occurred more than 11,000 cal yr BP. There is no known evidence of an eruption of Hayes volcano during this time frame, although deposits of this age are rarely preserved due to vast ice cover at this time and this could be a newly discovered eruption of Hayes. These layers are distinct and continuous in the core and therefore considered true layers and not a relic of the coring process. The upper-most tephra at 49 cm depth strongly resembles tephra from Augustine volcano, based on comparison with published glass geochemistry queried from the Alaska Tephra Database (Cameron et al., 2019).

Deadman Lake contains five distinct tephra deposits (**Figure 4**), all of which were geochemically analyzed (**Supplementary Table 4** and **Figure 5**). Of the five tephra layers, only one (at 142–146 cm depth) geochemically correlates to terrestrial reference tephra from the Susitna River Valley (Watana tephra with SCs of 0.98–0.99). The upper-most tephra at 0–2 cm depth strongly resembles tephra from Augustine volcano, based on comparison with published glass geochemistry queried from the Alaska Tephra Database (Cameron et al., 2019). The remaining four tephras are unknown.

Big Lake contains four distinct tephra deposits (**Figure 4**), all of which were geochemically analyzed (**Supplementary Table 4** and **Figure 5**). Of the four tephra layers, only one 4 cm-thick tephra at 80–84 cm depth geochemically correlates to a terrestrial reference tephra from the Susitna River Valley (Watana tephra, with SCs of 0.95–0.96). Subsamples of the prominent 4-cm thick tephra show a high degree of similarity (SCs of 0.95-97). The remaining three tephras are unknown.

Sally Lake contains two distinct tephra deposits (**Figure 4**), both of which were geochemically analyzed

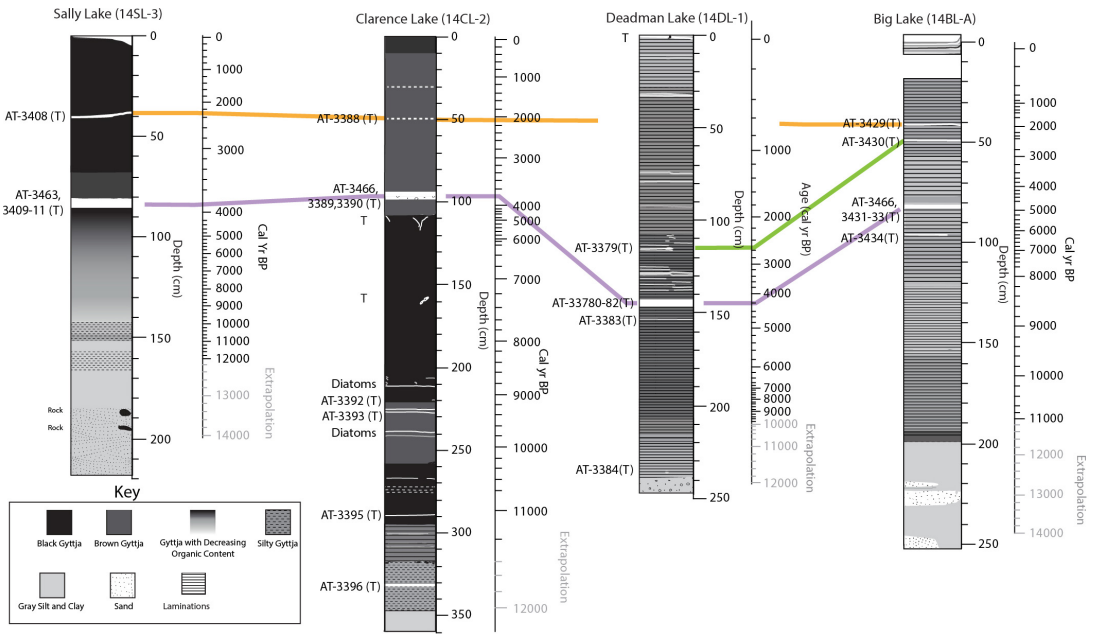

FIGURE 6 | Stratigraphic correlations of the tephra units among the study lakes. The purple line marks the Watana correlates, the orange and green correlates are unknown.

(**Supplementary Table 4** and **Figure 5**). A prominent tephra about 4 cm thick at 81–85 cm is geochemically correlates with Susitna River Valley Watana reference material (SC of 0.96–0.98). Subsamples of this tephra show a high degree of similarity (SC of 0.97–0.99). The upper-most tephra at 39–41 cm depth strongly resembles tephra from Augustine volcano, based on comparison with published glass chemistry queried from the Alaska Tephra Database (Cameron et al., 2019).

Correlation of tephra deposits among the four lakes and with Susitna River Valley reference tephra was assessed using stratigraphic context, radiocarbon age, physical sample characteristics, and geochemical similarity (**Figures 5**, **6**). Correlations of individual samples among lakes are also shown in **Supplementary Table 4**.

The late Holocene Watana tephra is present in all four lakes as a prominent 4–5 cm thick layer (**Figure 6**). With the exception of Big Lake, the lacustrine chronologies are internally consistent, indicating an age of 3900 (Sally and Clarence lakes) to 4,200 cal yr BP (Deadman Lake) for this tephra fall, which is within the range of terrestrial ages for this deposit in the middle Susitna Valley (Mulliken, 2016). In contrast, the Big Lake chronology indicates an age of ∼4,900 cal yr BP. The most parsimonious explanation is a problem with the Big Lake chronology and is unlikely the result of multiple eruptions.

Two additional tephras have been correlated between the lakes, although they are unknown in the regional Susitna River Valley tephra stratigraphy. The older tephra, aged about 2,500 cal yr BP, is present in Deadman and Big Lakes (SC 0.98), but is absent in the lower elevation Clarence and Sally lakes. The youngest tephra, dated ∼2,000 cal yr BP is present in Sally, Clarence, and Big lakes, but is absent in Deadman Lake (**Figure 6**).

Paleoecology

%C, C/N, $\delta^{13}C$, and $\delta^{15}N$

At Clarence Lake (**Figure 7**), %C is < 3% from the core base to 320 cm (∼11,450 + 280/−110 cal yr BP), where it abruptly increases, first to 5% and then to 7%. With some fluctuations, %C remains at about 7% to ∼180 cm (∼7,850 + 620/−530 cal yr BP), when it gradually decreases to modern levels (∼5%), with a very brief and abrupt decrease to 3% immediately above the Watana tephra. C/N ratios vary around 10% in the lower half of the core, rising slightly above the Watana tephra to ∼13%, indicating greater allochthonous material entering the lake (Meyers and Ishiwatari, 1993). $\delta^{13}C$ is elevated (∼-30‰) from the core base to ∼315 cm (∼11,320 + 350/−160 cal yr BP), subsequently decreasing to ∼-33‰ at 290 cm (∼11,030 + 310/−150 cal yr BP) and then gradually rising again so that at 160 cm (∼7,300 + 530/−410 cal yr BP) it is only slightly lower than modern levels of −27‰.

%C at Deadman Lake is ≤2% from the core base to ∼210 cm (∼10,040 + 480/−800 cal yr BP), where it increases to ∼8% (**Figure 7**). %C subsequently decreases to ∼4% at 160 cm (∼5120 ± 190 cal yr BP) and decreases again to <1% immediately above the Watana tephra. %C then increases to near modern levels of 3–4%. C/N ratios fluctuate around 10% for most of the record, though increasing to ∼13% by the core top. $\delta^{13}C$ is high (−23‰) at the extreme base of the core, immediately decreasing to ∼30‰, where it remains until 220 cm (∼10,900 + 510/−330 cal yr BP) where it increases again ∼−25‰. $\delta^{13}C$ values then gradually decrease to ∼−27‰

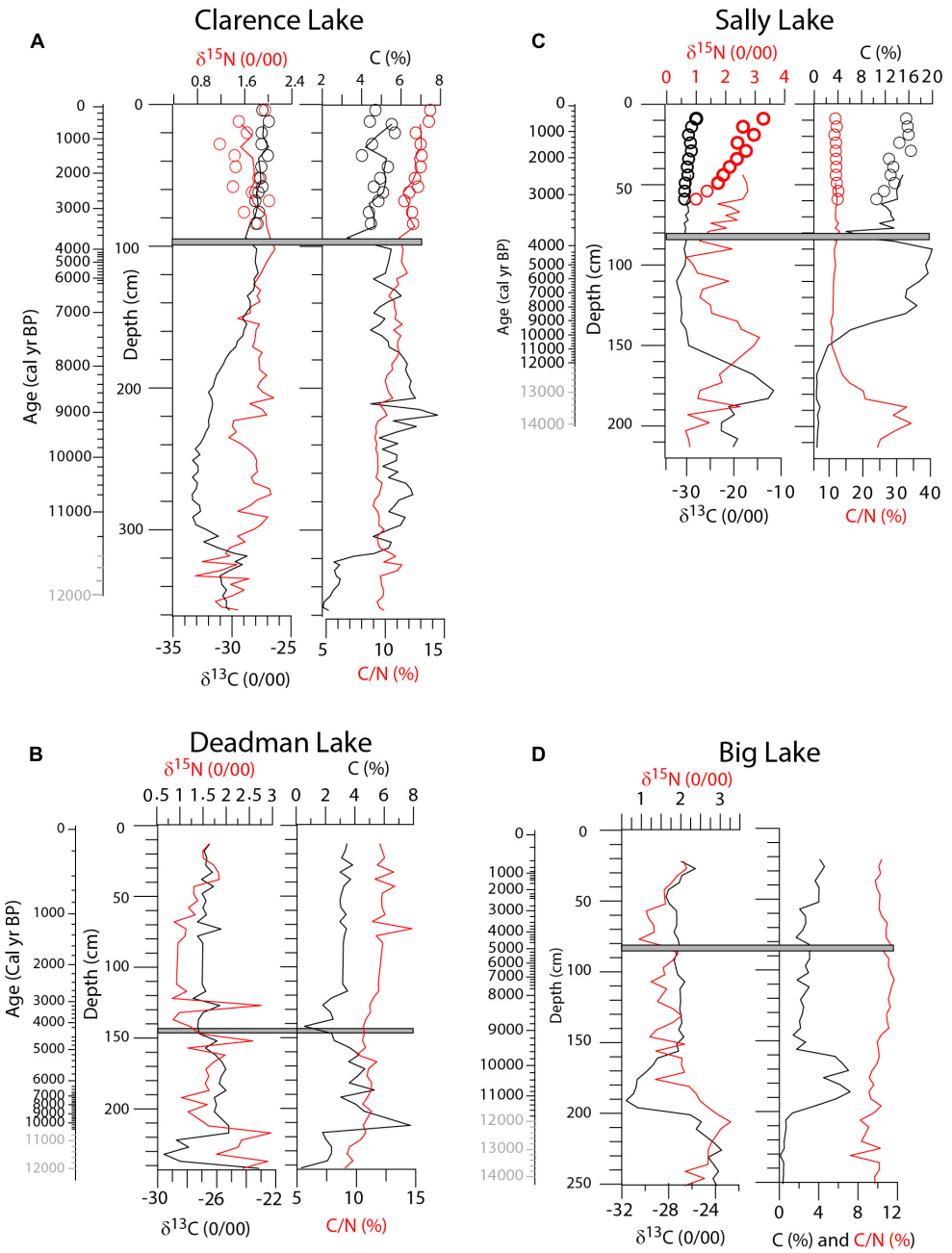

FIGURE 7 | $\delta^{13}C$, $\delta^{15}N$, %C, and C/N for **(A)** Clarence Lake, **(B)** Deadman Lake, **(C)** Sally Lake, and **(D)** Big Lake. The gray bar in all plots marks the Watana tephra. Ages in gray are extrapolations.

at 150 cm (~4,470 + 520/−660 cal yr BP), where it remains until the core top.

The Big Lake chronology is problematic and the ages mentioned here (especially at depths > 80 cm) are probably too old and should be viewed with caution. %C at Big Lake is <1% at the base of the core, rising to ~5% at ~190 cm (~11,150 + 180/−270 cal yr BP), remaining at that level to ~160 cm (~9,750+460/−550 cal yr BP) and subsequently falling to ~2%, where it stays for the remainder of the core (**Figure 7**). C/N ratios fluctuate around 10% for the entire core. $\delta^{13}C$ is high (~-24‰) at the core base, decreasing to ~30‰ at ~200 cm (11,710 + 520/−410 cal yr BP). Subsequently, $\delta^{13}C$ values increase, so that by ~140 cm (8,940 + 520/−500 cal yr BP) it is ~−28‰, where it remains until ~40 cm (~1,920 + 260/−270 cal yr BP), where it then increases to ~−26‰.

Sally Lake, because of carbonates in the core, has a markedly different geochemistry. %C is <1% from the core base to ~150 cm (~10,750+970/−1,390 cal yr BP), where it increases

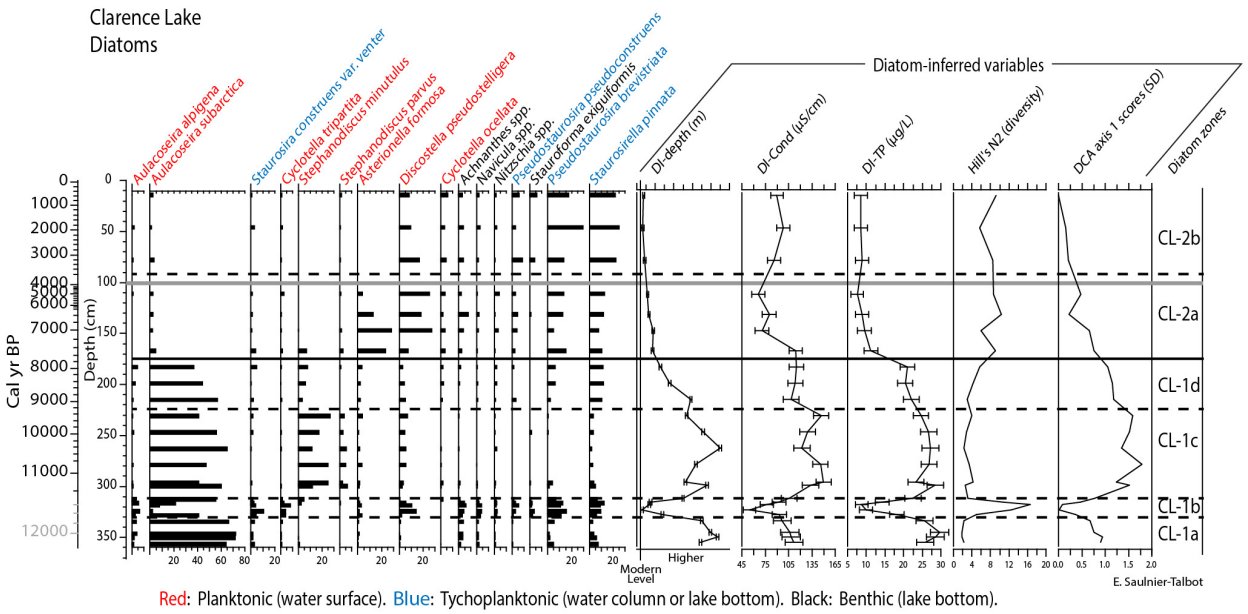

FIGURE 8 | Diatom relative abundances (%) and diatom-inferred variables at Clarence Lake. Diatom taxa are color-coded according to life-form (planktonic, tychoplanktonic, and benthic). The gray bar marks the Watana tephra. Ages in gray are extrapolations. Reconstructed water depth is dimensionless and labeled relative to the modern water level because the maximum reconstructed water depths were unrealistically high, even though the pattern of water level change is probably reliable.

first to 5% and then to 15% at 130 cm (∼8,470 + 1,580/−1,690 cal yr BP) (**Figure 7**). At 90 cm (∼4,090 + 160/−180 cal yr BP) %C is about 20%, subsequently decreasing to 5% immediately above the Watana tephra. Afterward, %C increases to modern levels of 14–15%. C/N ratios are high (>20%) at the base of the core (probably reflecting incomplete removal of carbonates, even after acid-fuming of the samples), decreasing to ∼10% at 150 cm (∼10,750 + 970/−1,390 cal yr BP). $\delta^{13}C$ values are very high (up to −10‰) from the core base to ∼170 cm and reflect carbonate in the core. By 150 cm, $\delta^{13}C$ values decrease to ∼−30‰, where they stay for the remainder of the core.

The $\delta^{15}N$ values at all the lakes fluctuate very little, (∼1–3‰), throughout their records, indicating the source of nitrogen was within the watersheds and not from marine sources, such as from anadromous salmon.

Diatoms

The Clarence Lake diatom record (**Figure 8**) can be divided into two main periods: the first, older, section of the core (diatom zones 1a, 1b, 1c, and 1d; 357–170 cm, >∼11,400 to ∼7,560 + 600/−460 cal yr BP), is largely dominated by the planktonic taxon *Aulacoseira subarctic*a (up to 72% relative abundance). This taxon is associated with deep, productive (high nutrient) subarctic lakes (e.g., Gregory-Eaves et al., 1999; Moos et al., 2009). Its dominance in the older section of the core indicates that Clarence Lake in the past was generally much deeper and more productive than today. Other components of the assemblage in this section include other planktonic species often associated with productive lakes, including *Stephanodiscus minutulus*, *S. parvus*, *Asterionella formosa,* and *Discostella pseudostelligera*.

This older section of the record can be subdivided into four sub-zones. The first sub-zone (zone 1a; 357–330 cm (>∼11,670 + 350/−190 cal yr BP) is strongly dominated by *A. subarctica*. Small *Fragilaria* sensu lato (*Staurosira construens* var. *venter*, *Pseudostaurosira brevistriata*, *Staurosirella pinnata*) are also present in the assemblage. The second sub-zone in this section (zone 1b; 330–313 cm, ∼11,670–11,300 + 350/−160 cal yr BP) is particular in that there is a sudden and significant change in the assemblage, with an important increase in species richness (the most diverse of the entire record) and a switch from a dominance of *A. subarctica* to an assemblage where small tychoplanktonic (water column and bottom-living) *Fragilaria sensu lato* dominate, along with planktonic cyclotelloid species (*Cyclotella tripartita*, *C. ocellata*, *Discostella pseudostellligera*). Achnanthaceae and Navicualceae are also present in the assemblage. Chrysophyte cyst abundances (not shown) drop markedly in this sub-zone relative to the preceding and following sub-zones. The sudden change in assemblage composition in zone 1b indicates a probable short-lived drop in lake-level, presumably reflecting increased aridity. In the third sub-zone (zone 1c; 313–225 cm, ∼11,300 to ∼9,280 + 590/−620 cal yr BP), there is a switch back to high relative abundances of *A. subarctica*, along with high relative abundance of planktonic *S. minutulus*. *S. parvus*, *A. formosa*, *D. pseudostelligera,* and *S. pinnata* are also notable components of the assemblage. The high relative abundance of the genus *Stephanodiscus* in zone 1c indicates a highly productive, nutrient-rich ecosystem. This is not uncommon for Alaskan lakes, as Gregory-Eaves et al.,

1999 note that diatom floras from Alaska differ from other circumpolar regions in that meso-eutrophic to eutrophic taxa such as *Stephanodiscus* are present in greater abundances due to higher concentrations of total phosophorus (TP). The fourth sub-zone (zone 1d; 225–175 cm, ∼9,380 to ∼7,710 + 600/−500 cal yr BP) shows a gradual decrease in abundances of *A. subarctica*, a drop in *S. minutulus* and quasi disappearance of *S. parvus*, along with an increase in *S. pinnata*. *P. brevistriata* also reappears in this zone. There is a notable drop in Chrysophyte cyst abundance (not shown), which remains low for the remainder of the record. Lower abundances of *Stephanodiscus* taxa in zone 1d point to decreased productivity in the lake.

The second, younger, main section of the core (zone 2; 175 cm to the core top, ∼7,710 cal yr BP to present) sees a sudden drastic drop in the abundance of *A. subarctica* to values < 5% and an increase in diatom diversity due to the fact that no one taxa is as dominant in this section of the core. This section of the core is subdivided into two sub-zones with the Watana tephra between them, although we cannot correlate changes in the diatom assemblage with the tephra deposit, as the nearest diatom samples are ∼20 cm above and ∼10 cm below the tephra. In the first sub-zone (zone 2a; 175–100 cm, ∼7,710 to ∼3,960 + 250/−360 cal yr BP), *A. subarctica* is replaced by the planktonic *A. formosa* and *D. pseudostelligera*. Other notable taxa in the assemblage of this zone include small *Fragilaria sensu lato*, namely *Pseudostaurosira pseudoconstruens*, *P. brevistriata* and *Staurosirella pinnata*, and benthic (bottom-living) *Achnanthes*, *Navicula* and *Nitzschia*. *Pseudostaurosira brevistriata* and *Staurosirella pinnata* become the dominant species in the most recent section of the record (zone 2b; 100 cm to the core top), as *Discostella pseudostelligera* abundances progressively decrease and *A. formosa* disappears altogether. The profound change in the structure of the diatom assemblage since the mid-Holocene suggests a gradual decrease in lake depth and a significant change in trophic state. As the lake became shallower, it also became more oligotrophic, as suggested by the dominance of small *Fragilaria sensu lato* in the more recent past. *Pseudostaurosira brevistriata* and *Staurosirella pinnata* are tychoplanktonic taxa, meaning that they can either live on the lake floor or in the water column. They are particularly well-adapted to life in highly turbulent conditions, with short growing seasons and low to highly variable nutrient availability (Saulnier-Talbot, 2007). Their dominance in the younger diatom assemblage indicates a deterioration of the climate with, in all likelihood, drier, colder, and perhaps windier conditions.

The transfer functions developed to infer lake depth, conductivity and total phosphorous (TP) are a simple weighted-averaging model with classical deshrinking, with an r^2_{boot} = 0.52–0.53, a strength comparable to those generated from other northern calibration studies (Gregory-Eaves et al., 1999). The three diatom-inferred variables show similar trends throughout the core, with generally higher values in the older section, with the exception of zone 1b where there is a marked drop in values of the reconstructed variables, and progressive decreases from zone 1d to lower values in the more recent past. Reconstructed lake depth indicates an initially deep lake (zone 1a) with a sudden drop in lake level (zone 1b), followed by an increase back to initial values (zone 1c). Lake depth subsequently decreases (zone 1d) and stabilizes in the more recent section of the core (zones 2a and 2b). Diatom-inferred conductivity values are initially moderately high (zone 1a) and briefly dip to their lowest values (zone 1b) before progressively increasing to their highest values (zone 1c). They then decrease to moderately high levels (zone 1d) before decreasing even further (zone 2a). Conductivity values increase again slightly in the most recent past (zone 2b). Diatom-inferred TP values are highest at the base of the core (zone 1a), followed by a sharp drop to very low values (zone 1b) before returning to very high levels (zone 1c). Concentrations then decrease somewhat (zone 1d) before decreasing to low levels for the remainder of the record (zones 2a and 2b).

The results of the diatom-inferred reconstructions provide information on the magnitude of environmental change throughout the Holocene in the lake and its catchment. The inference models applied to the sedimentary diatom assemblage data were developed for a set of 51 Alaskan lakes distributed along a latitudinal gradient from the South (Gulf of Alaska) to the North (Arctic Ocean) of the state and include lakes from the region of the Alaska Range, where Clarence Lake is located (Gregory-Eaves et al., 1999). It was therefore deemed appropriate to apply the models to the data of this study. The overwhelming dominance of *A. subarctica* in the bottom section of the core is a concern for the fit of the model to the sedimentary data because it is only found at a maximum relative abundance of 43% in the model lake set, whereas it is present in abundances > 40% in all (except one) samples of zones 1a, 1c, and 1d of the Clarence Lake core. Therefore, the inferred values for the older section of the core (i.e., below 170 cm) should be considered with caution, especially for lake depth since they appear greatly overestimated for this variable, at least. The lake levels inferred for this section of the record are in fact much higher than the deepest lakes included in the inference model (33 m), which make them suspect. However, the results for lake depth in the upper section of the core appear to be more reliable and the top-most value for lake depth corresponds exactly to current measured values (11 m), which lends more credibility to the diatom-inferred values in the upper section of the core. While the accuracy of the inferred values appears to be statistically questionable, especially for the lower section of the core, the inferred trends provide a reliable scenario for the magnitude and trajectory of environmental change which occurred over the past ∼ 11,000 years in and around Clarence Lake.

Pollen

The Clarence Lake pollen record (**Figure 9**) is divided into three zones, CL-1, CL-2, and CL-3. CL-1 spans from 355 cm (the base of the pollen record) to 270 cm, (>∼11,400 to ∼10,650 + 230/−340 cal yr BP) and is dominated by birch (*Betula*) pollen with willow (*Salix*) and sedges (Cyperaceae) as secondary components. At the bottom of the core, birch pollen percentages and influx [grains(cm^{-2})(yr^{-1})] increase, this probably marks the expansion of birch in the region. Pollen concentration (grains(cm^{-3}) [not shown]) and influx is relatively high throughout the zone, suggesting a productive landscape. However, a brief period of reduced birch pollen

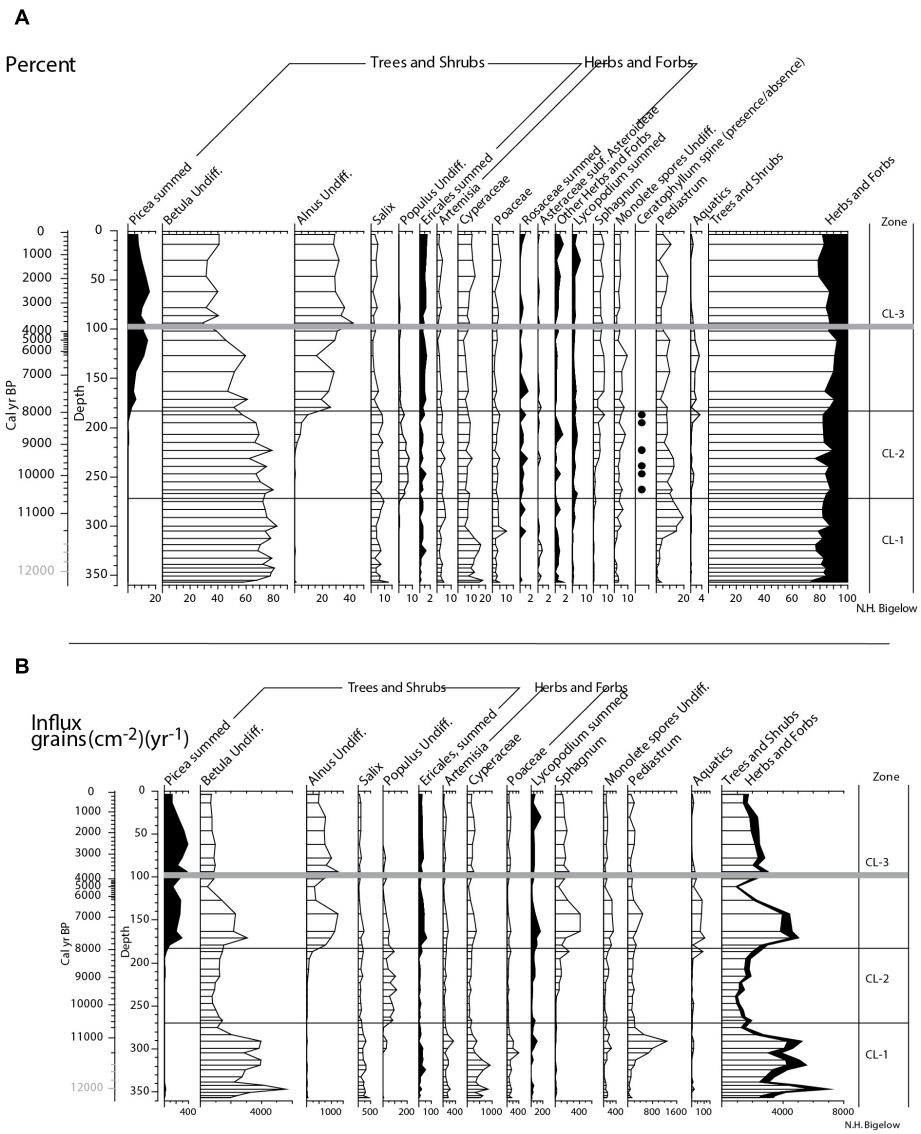

FIGURE 9 | Clarence Lake summary pollen; **(A)** percent and **(B)** influx. To emphasize rare taxa in both plots, some *x*-axes have been enlarged. Gray bar in both plots marks the Watana tephra and ages in gray are extrapolations.

as well as total influx at 340–320 cm (∼11,870 + 440/−280 to ∼11,450 + 280/−110 cal yr BP) suggests a less productive landscape which generally coincides with marked shifts in diatom assemblages. The vegetation in this zone was a birch-dominated shrub tundra, but willows were also a significant component. Sedge, grass, and *Artemisia* dominate the herbs, with monolete spores (mainly ferns) becoming more prominent in the latter half of the zone.

Zone CL-2 spans from ca. 270–180 cm and dates between 10,650 + 230/−340 and 7,860 + 620/−530 cal yr BP. Birch pollen continues to dominate, followed by willow and sedge pollen, and then by *Artemisia* and grass pollen. The key feature of this zone is the presence of *Populus* (cottonwood/aspen) pollen and *Ceratophyllum* spines. Both taxa suggest warm summer temperatures. The vegetation was a birch and willow shrub tundra with scattered cottonwood/aspen stands, possibly around the lake or at its outlet. Pollen influx is low throughout the zone.

Zone CL-3 spans from 180 cm to the core top and dates between 7,860 + 620/−530 cal yr BP and the present. Birch percentages decline in this zone (but influx remains stable, indicating continued importance), while alder (*Alnus*), and then spruce (*Picea*) percentages increase. *Populus* and *Salix* pollen also decline. *Artemisia*, grass, and sedge pollen continue as before. Pollen influx is higher here, due to the addition of alder and spruce pollen. Using the 5% threshold for spruce (Hu et al., 1993) and 20% threshold for alder (Anderson and

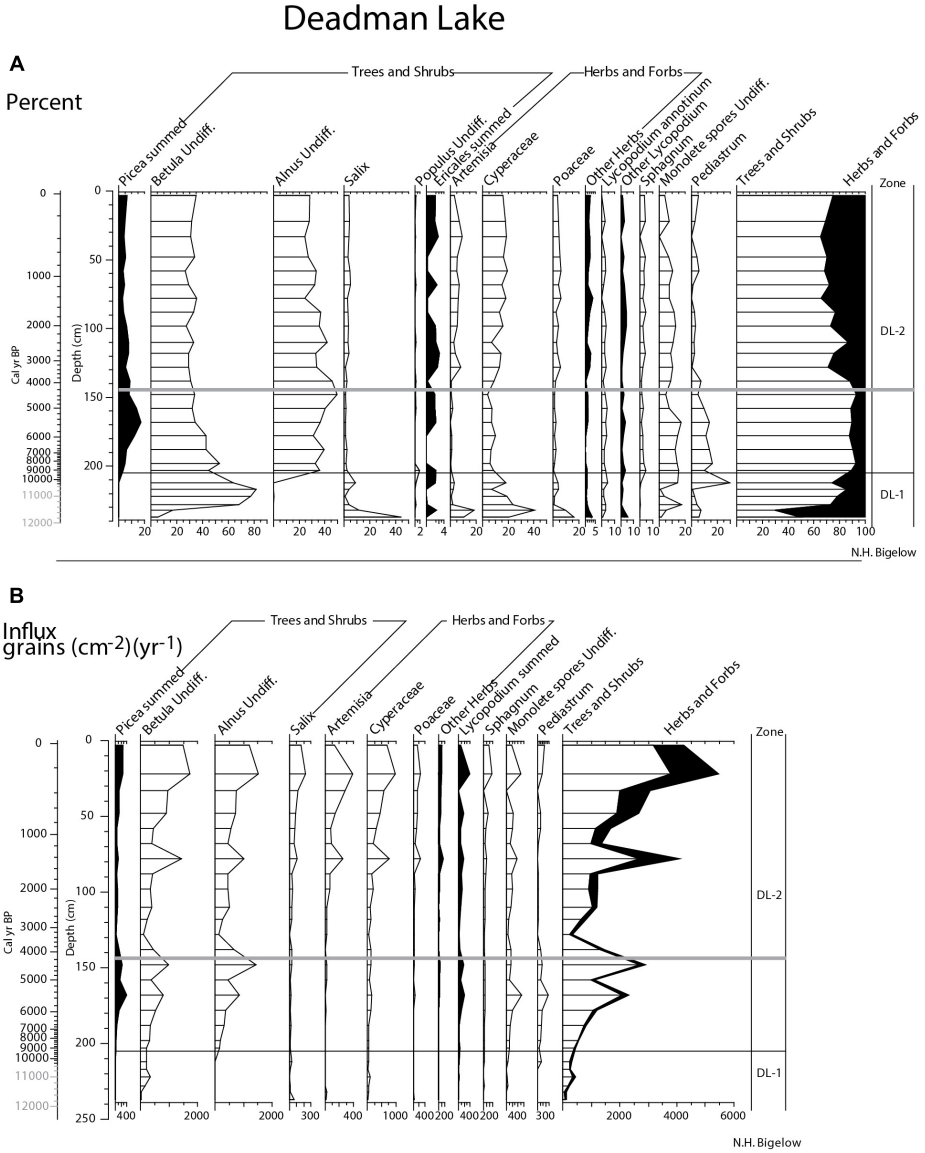

FIGURE 10 | Deadman Lake summary pollen; **(A)** percent and **(B)** influx. To emphasize rare taxa in both plots, some *x*-axes have been enlarged. Gray bar in both plots marks the Watana tephra and ages in gray are extrapolations.

Brubaker, 1986), spruce was probably locally present at ∼170 cm (∼7,560 + 600/−460 cal yr BP), slightly after alder, the pollen of which crosses the 20% threshold at 180 cm (∼7,860 cal yr BP). The vegetation was a birch and alder shrub tundra with widely scattered spruce and possibly birch trees at least in the middle of the zone when spruce pollen is most abundant.

At Deadman Lake, the pollen record is divided into two zones (DL-1 and DL-2) (**Figure 10**). Zone DL-1 spans from the record base (238 cm) to ∼205 cm; >10,400 to ∼9,260 + 880/−1040 cal yr BP. Birch pollen increases from 20 to 80% and then decreases to about 50% at the top of the zone. At the base of the zone, when birch pollen has the lowest frequencies, willow, *Artemisia*, sedge, and grass pollen are at their highest frequencies which then decrease as birch increases. However, influx measurements (**Figure 10**) indicate that all taxa increase in this zone, suggesting greater plant abundance, probably in areas that were unvegetated earlier. The vegetation was a sparse shrub tundra, initially dominated by willow, but later with increasing birch. Understory taxa include very sparse sedge, *Artemisia*, and grass, along with a few mesic taxa such as ferns (monolete spores).

Pollen zone DL-2 (205-0 cm; ∼9,260 + 880/−1040 cal yr BP to the present) is marked by increased spruce and alder frequencies. Birch pollen frequencies decrease, but increase in the influx data, suggesting it continued to be an important feature of the vegetation. Spruce pollen crosses the 5% threshold at 198 cm (∼8,200 + 1160/−1170 cal yr BP) and reaches its maximum frequency of nearly 20% at 168 cm (∼5,510 + 360/−340 cal yr BP), after which it decreases to ∼5%. Alder pollen crosses

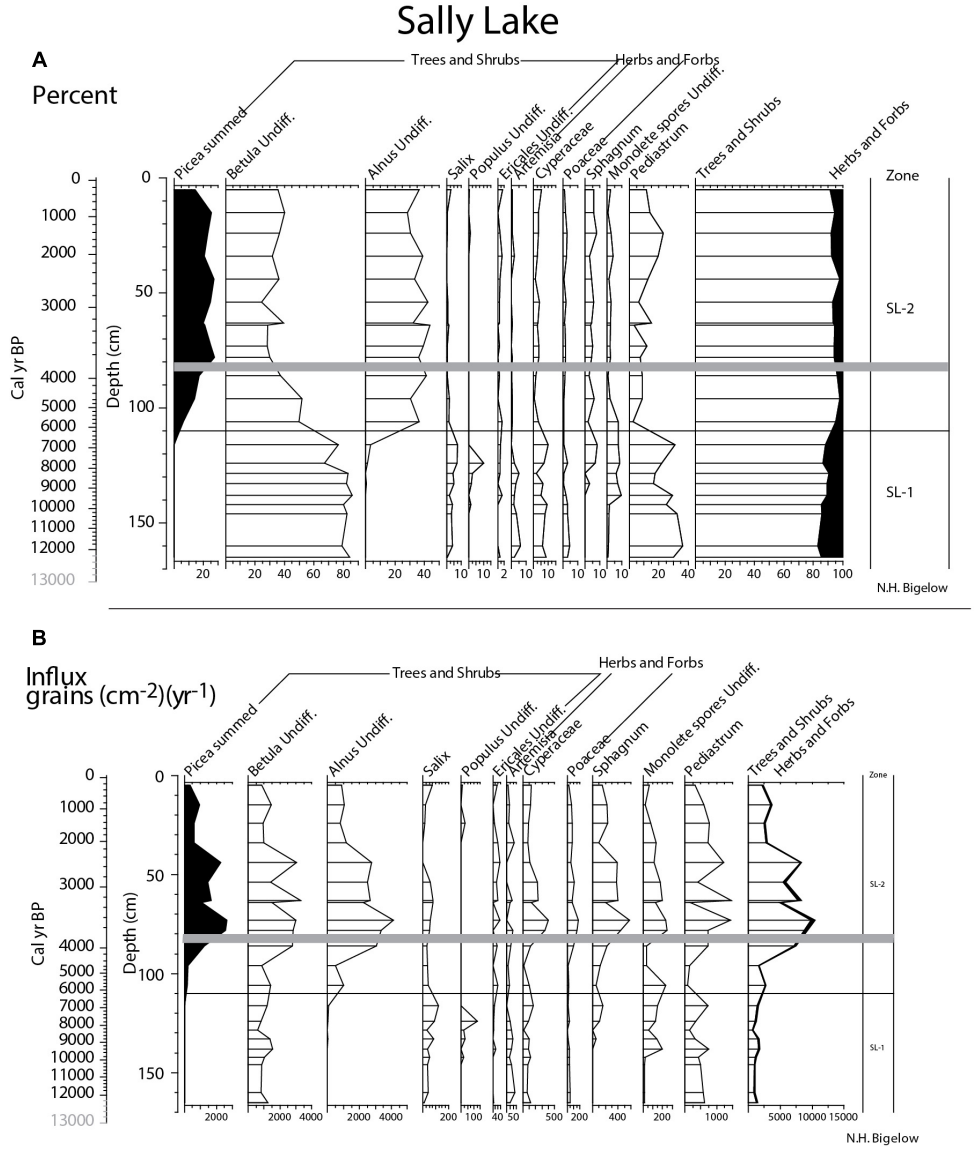

FIGURE 11 | Sally Lake summary pollen; **(A)** percent and **(B)** influx. To emphasize rare taxa in both plots, some *x*-axes have been enlarged. Gray bar in both plots marks the Watana tephra and ages in gray are extrapolations.

the 20% threshold at the beginning of the zone and remains at this level throughout the remainder of the core. Willow, *Artemisia*, and grass pollen are present in low frequencies in the first half of the zone, but increase slightly above 140 cm (∼4,060 + 650/−700 cal yr BP). Ferns and *Sphagnum* are present in moderate frequencies throughout the zone. The vegetation during this zone was a birch, alder, and willow shrub tundra with varying amounts of spruce and possibly a few birch trees. Spruce was probably present (if very rare [as it is today]) by ∼8,200 cal yr BP, but was more common than today ∼6,000 to 5,000 cal yrs BP, after which it decreased, so that by today, only a very few trees are present in the watershed (when spruce pollen frequencies are about 5%). Pollen influx suggests herbaceous taxa become more abundant in the upper half of the zone, possibly expanding into previously unvegetated areas as the shrub influx also increases.

In Sally Lake, pollen zone SL-1, the basal 55 cm of the record (165–110 cm; ∼12,270 + 410/−440 to ∼6,180 + 1,570/−1180 cal yr BP), is dominated by birch pollen (80%), with minor amounts of sedge (Cyperaceae), willow, and *Artemisia* (**Figure 11**). *Populus* pollen frequencies peak to 10% in a single sample at 124 cm, ∼7,780 + 1,620/−1,550 cal yr BP, subsequently falling to near zero. Fern spores (monolete spores) increase at 138 cm (∼9,390 + 1,410/−1,630 cal yr BP) while *Sphagnum* spores increase afterward at 124 cm (∼7,780 + 1,620/−1,550 cal yr BP). The vegetation was initially a birch and willow shrub tundra with grass, sedge, and *Artemisia*. *Populus* trees (cottonwood or aspen) were probably briefly present about 7900 cal yr BP, but were

subsequently much reduced in the watershed. Increases in the spores (ferns and *Sphagnum*) indicate increasing moisture toward the latter half of the zone.

Zone SL-2 (110–0 cm; ~6,180 + 1,570/−1,180 cal yr BP-present) is dominated by birch, alder, and spruce pollen. The decrease in *Betula* pollen frequencies in this zone is an artifact of the percent calculation; influx data indicates it remained an important component of the pollen assemblage (**Figure 11**). Spruce pollen crosses the 5% threshold indicating local presence at about 5,900 cal yr BP. The vegetation throughout this zone was spruce-birch-alder boreal forest. Pollen influx decreases from ~40 cm (~2400 + 250/−180 cal yr BP) to the core top suggesting reduced pollen production and lowered landscape productivity.

DISCUSSION

Our study sheds light on Late-Glacial and Holocene paleoecology and landscape change in the middle Susitna Valley. Below, we discuss our results within a chronological framework, especially in the context of what we know from adjacent regions. In addition, we present our current understanding of the human prehistory of the Susitna Valley uplands and discuss how these landscape changes could have affected people living in the region at various times.

De-glaciation and Late-Glacial (~12,000–11,700 cal yr BP)

Chronologies from Deadman, Big, and Sally lakes indicate deglaciation had occurred by about 12,000 cal yr BP, if one accepts the extrapolated ages at the core bases. The apparent absence of Late Wisconsinan ice around Clarence Lake is intriguing. If this is correct, then the formation of Clarence Lake was not directly related to ice recession and aridity may have limited lake formation. This would be consistent with ice-free areas of interior Alaska to the north, where extensive dunes and loess formation (Hopkins, 1982; Muhs et al., 2003) as well as the general absence of lakes prior to ~14,000 cal yr BP suggest extreme aridity.

Immediately after deglaciation, all lakes were relatively deep and productive. Diatom-inferred variables at Clarence Lake indicate high lake levels, increased conductivity (an indicator for bedrock weathering), and high total phosphorous (a proxy for lake productivity) (**Figure 8**). This is consistent with the isotope results from Clarence, Deadman and Big lakes, where $\delta^{13}C$ and %C values are relatively low (**Figure 7**). At the same time, a birch or willow shrub tundra covered the landscape from low-elevation Sally Lake to the high-elevation Deadman Lake. However, pollen influx varied among the lakes, so that Clarence Lake had relatively high influx at this time, while at Deadman and Sally lakes, the influx was lower (**Figures 9–11**), suggesting that plant productivity may have varied across the region.

In terms of archeology, people ranged into higher elevations (>600 MASL) to the north (Teklanika, Nenana, and Bull river valleys) by ~12,800–12,290 cal yr BP and into the Tangle Lakes region by 11,940 cal yr BP (summarized in Blong, 2018). There is currently no evidence that people occupied the middle and upper reaches of the Susitna River Valley before ~11,140 cal yr BP, over 1,000 years after people began occupying similar elevations in interior Alaska. This suggests that the relatively high productivity around Clarence Lake did not translate into abundant game resources upon which people depended. If the density of herd animals was less than the lowlands and the Tanana Valley upland margins (Yesner, 2007), then hunting forays or explorations into the Susitna uplands before 11,140 cal yr BP would have been very limited, and would account for the very low archeological visibility during this period in the region (Blong, 2018).

A Brief Environmental Excursion at Clarence Lake (~11,800–11,200 cal yr BP)

High-resolution sampling at Clarence Lake revealed a marked shift in climate and environment during ~11,800–11,200 cal yr BP (**Figure 12**). Diatom-inferred lake levels decreased markedly,

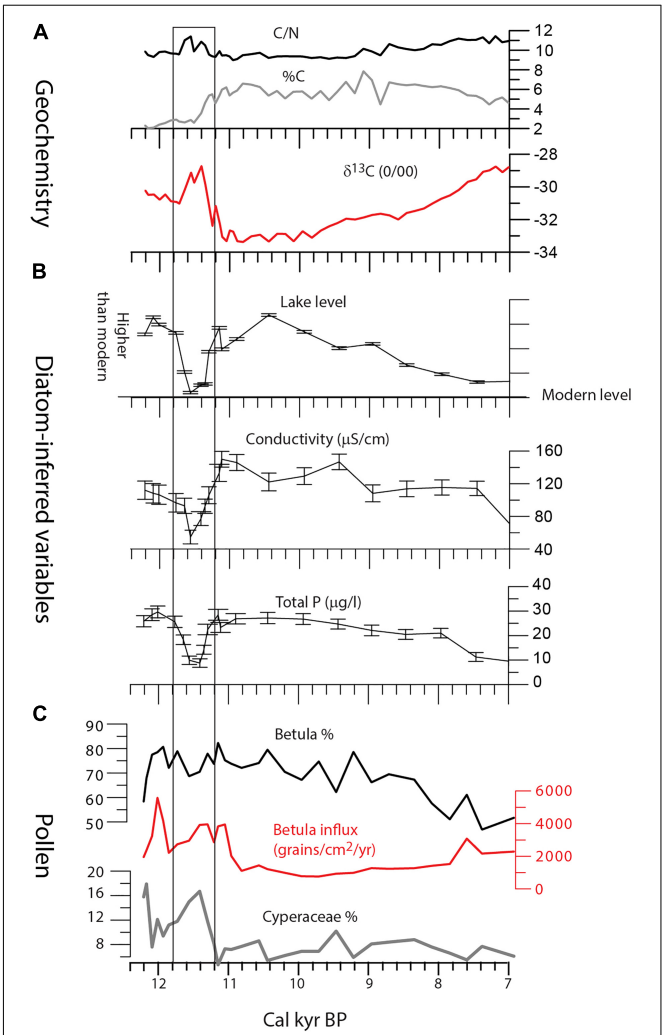

FIGURE 12 | Key variables at Clarence Lake between 12,000 and 7,000 cal yr BP (cal kyr BP). **(A)** $\delta^{13}C$, C/N, and %C. **(B)** Diatom-inferred variables. **(C)** *Betula* (birch) pollen percent and influx and Cyperaceae (mainly sedge) pollen percent. Box marks the zone with significant shifts of diatom-inferred variables at ~11,800–11,200 cal yr BP.

as did diatom-inferred conductivity. Diatom diversity was also very high, suggesting a greater diversity of habitats, which is consistent with lowered lake levels. The $\delta^{13}C$ values increased during this period, which seems consistent with the decreased lake levels and a possible decrease in the available DIC pool for autochthonous primary production, which is consistent with slightly higher %C toward the end of the excursion. C/N ratios increase slightly, indicating greater allochthonous input into the lake, also consistent with lower water level. Shrub abundance decreased while herbs (especially sedge) increased, and overall pollen production was reduced, suggesting a less productive landscape, at least at the onset.

The timing of this event (∼11,800–11,200 cal yr BP) suggests it may be related to the Younger Dryas (YD) climate event. While the age is young for the YD chronozone (which is dated ∼ 12,900 to 11,700 cal yr BP [Rasmussen et al., 2014]), proxy responses at Clarence Lake may be lagged, as has been shown elsewhere (Muschitiello and Wohlfarth, 2015). In addition, the proxies suggest a shift to cooler and/or drier environments, which is consistent with a YD oscillation. This excursion was recognized only at Clarence lake because of the diatom analysis and high-resolution sampling there.

If the Clarence Lake excursion corresponds to the YD, this would be consistent with much of what is already known about the YD in Alaska. The YD has been recognized in numerous sites from southern and southeast Alaska (Kokorowski et al., 2008 and references therein, plus Briner et al., 2002; Jones et al., 2009; Kaufman et al., 2010), the Bering Sea (Wooller et al., 2018), the Alaska Range (Kokorowski et al., 2008 and references therein), on the north slope of the Brooks Range (Gaglioti et al., 2017) and the Arctic Coastal Plain (Meyer et al., 2010). In general, various proxies indicate cooling and/or drying during this interval, except in southwest Alaska and the Kenai Peninsula, where increased moisture is indicated (Jones et al., 2009; Jones and Yu, 2010; Kaufman et al., 2010). Interestingly, peatland initiation frequencies did not decrease during the YD (**Figure 13**), although on the Kenai Peninsula, carbon accumulation rates were low (Jones and Yu, 2010). North Pacific sea surface temperatures decreased (Kallel et al., 1988; Max et al., 2012; Praetorius and Mix, 2014) and winter precipitation in southern Alaska may have been higher, as indicated by various climate models (Mikolajewicj et al., 1997; Peteet et al., 1997) On the North Slope, proxies suggest increased stream incision, eolian deposition, and reduced pollen from woody taxa (Mann et al., 2002), and probably increased summer sea ice (Gaglioti et al., 2017). In Utqiagvik (formerly Barrow), an oxygen and deuterium isotope record from wedge ice also suggests much colder winter temperatures during the YD (Meyer et al., 2010).

Compared to YD records from around the North Atlantic region (Björck, 2007 and references therein), the Clarence Lake excursion was short-lived and relatively subtle. In scale and duration, it is similar to most Alaskan records, consistent with the idea that the YD in Alaska was the result of teleconnections from the North Atlantic region. Reduced North Atlantic sea surface temperatures could have affected westerly flow, which in turn influenced north Pacific sea surface temperatures as well as the strength and location of the Aleutian Low (Kokorowski et al., 2008).

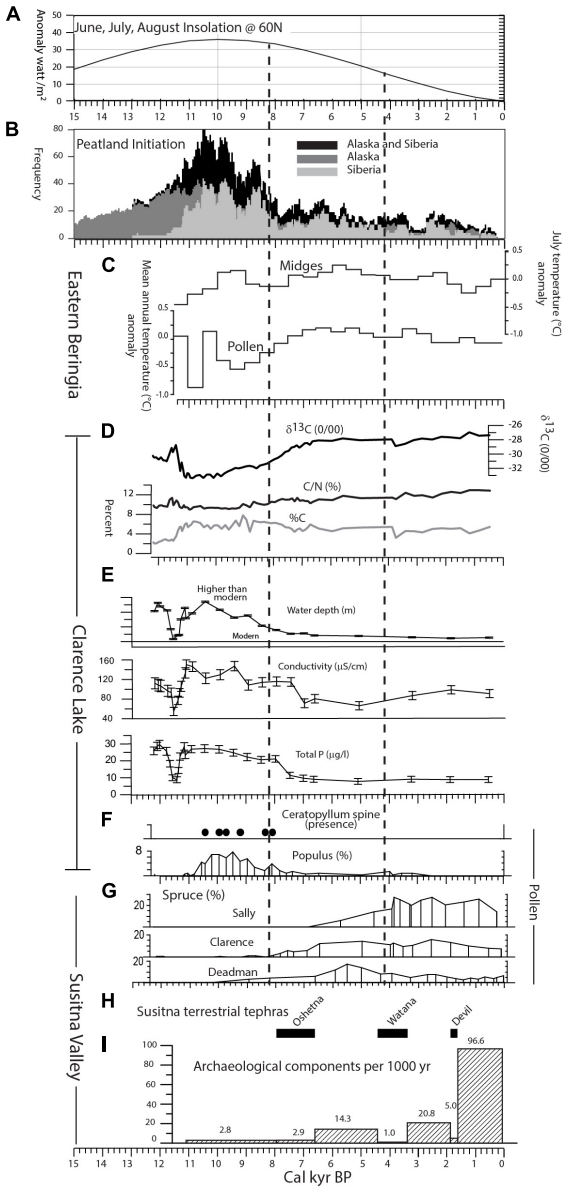

FIGURE 13 | Summary figure of regional studies and key results from this study plotted against age (cal kyr BP). **(A)** June, July, August insolation at 60° N from 15,000 cal yr BP to the present (Berger, 1978). **(B)** Peatland initiation frequency (redrawn from Jones and Yu, 2010). **(C)** Eastern Beringia midge- and pollen-inferred temperatures (redrawn from Kaufman et al., 2016). **(D–F)** Clarence Lake geochemistry, diatom-inferred variables, and pollen/macrofossils, respectively. **(G)** Spruce pollen (%) in the study lakes. **(H)** Terrestrial tephras in the Susitna Valley. **(I)** Archeological components per 1000 year in stratigraphic bins relative to the tephra deposits (see text). Dashed vertical lines mark middle and late Holocene boundaries at 8,200 and 4,200 cal yr BP, from Kaufman et al. (2016).

With the continued lack of vegetative productivity and increased aridity, the middle Susitna Valley likely remained very sparsely inhabited by larger terrestrial mammals (i.e., bison, elk,

and caribou) that were important resources for humans. This potential lack of subsistence resources during this time period would have made the region less attractive for humans use. This is in contrast to sites in Interior Alaska, where *Artemisia* and grasses expanded during the YD (Bigelow and Edwards, 2001), likely creating additional pasture lands for bison, elk and caribou, resulting in those areas having archeological sites dating to the YD (Graf and Bigelow, 2011).

Early Holocene (∼11,200 – ∼ 8200 cal yr BP)

In our study area, lake sediment geochemistry and sedimentary diatoms suggest the lakes were relatively deep and productive, at least at the outset of the period. At Clarence Lake, diatom-inferred variables indicate a rapid lake-level rise beginning ∼11,300 cal yr BP, along with increased bedrock weathering and greater watershed productivity, which is consistent with the higher %C and lowered $\delta^{13}C$ at this time. However, by ∼10,500 cal yr BP, productivity was decreasing (lowered TP) as lake level and conductivity also decreased (**Figure 13**).

Pollen records from Clarence Lake and Sally Lake contain an episode of increased cottonwood/aspen pollen frequencies that span most of the early Holocene (**Figures 9**, **11**). As *Populus* pollen does not travel far from its source and is easily degraded, this indicates that the trees were growing near the lakes (Edwards and Dunwiddie, 1985). However, Deadman Lake does not record a similar cottonwood/aspen blip (although a few pollen grains were encountered), suggesting the *Populus* expansion did not reach as high as Deadman lake, at about 960 m.

At Clarence Lake, *Ceratophyllum* spines (presumably *C. demersum*) were encountered at the same levels as the increased cottonwood/aspen pollen frequencies (**Figures 9**, **13**). *C. demersum* is an aquatic plant that favors still, relatively shallow waters found at the lake margin. Today, it is found mainly within the boreal forest, although it has been found at a few localities at the spruce limit or just beyond it (Holmquist, 1971; Les, 1986). While it is unknown whether *C. demersum* grows in Clarence Lake today, its presence in the lake during the early Holocene is highly suggestive of warmer than modern summer temperatures.

Shifts in solar insolation suggest marked summer warming during the early Holocene (**Figure 13**) (Berger, 1978). However, a recent summary of Beringian early Holocene proxy climatic records noted a surprising amount of incoherence among records, with significant geographical and proxy-based complexity (Kaufman et al., 2016), which is reflected in the somewhat contrasting midge and pollen based temperature reconstructions (**Figure 13**). Complexity at the regional scale is also mirrored in the current study. Here, the early Holocene is characterized by initial warming (pollen), increased moisture (diatoms), and increased lake productivity (sediment geochemistry and diatoms). However, diatoms and sediment geochemistry also suggest lower lake levels and lake productivity especially after ∼10,500 cal yr BP, while the pollen suggests continued summer warmth to ∼8,200 cal yr BP. These somewhat contrasting results probably reflect the relative sensitivity of the proxy and whether the terrestrial (pollen) or lacustrine (diatoms) environments were equally sensitive to climate change. Changes in the diatom-inferred variables after 10,500 cal yr BP mirror reduced summer insolation, as well as reduced peatland initiation (**Figure 13**). This suggests that the lacustrine environments were driven by external factors such as temperature and moisture, but that terrestrial environments may have been mediated by internal factors that are indirectly related to climate, such as soil development, paludification, and plant succession.

The earliest evidence of humans using the upper and middle Susitna Valley date to the early Holocene (∼11,140–10,520 cal yr BP) with the lowest components at Jay Creek Ridge and other sites (Dixon, 1999; Blong, 2016; Reuther et al., 2018) (**Figure 1**). Degradation of organic remains resulting from slow burial and acidic soils have hampered the dating of many archeological sites, and older archeological remains may be present but cannot be reliably dated. However, Wygal and Goebel (2012) suggest that this region and southcentral Alaska were colonized from the northern interior areas, in particular the Nenana and Tanana River Valleys, which have records of human occupation 2,000–3,000 years earlier. Even though the Susitna Valley was deglaciated one or two millennia prior to occupation, as described above, current archeological evidence suggests that the region was apparently unattractive for human habitation.

Because a large number of archeological components currently do not have reliable radiocarbon ages (Mulliken, 2016), it is best to view the chronology of the human occupation of the middle Susitna Valley as a whole, using relative age estimates based on their stratigraphic position relative to tephras with known age ranges (Dixon and Smith, 1990). We present the archeological data in terms of numbers of components per 1000 years within each stratigraphic category (i.e., below Oshetna, within Oshetna, between Oshtena and Watana, etc.) (**Figure 13**). Archeological components below the Oshetna tephra are older than ∼7,900 cal yr BP with some like Jay Creek Ridge Component 1 dating as far back as ∼11,140 cal yr BP (**Figure 13**). There are currently nine components (<4% of the total) that unequivocally lie below the Oshetna tephra, with a frequency of about 2.8 components per 1000 years. The upper and middle Sustina regions appear to be sparsely occupied during the pre-Oshetna time periods, most of the usage of the uplands areas being short hunting forays (Graf and Bigelow, 2011; Potter, 2011; Blong, 2018).

Middle (∼8200–4200 cal yr BP) and Late (∼4200–0 cal yr BP) Holocene

Diatom-inferred lake levels and productivity decreased or remained at lower levels during the middle and late Holocene, while bedrock weathering increased slightly during the late Holocene (**Figure 13**). Using 5% spruce pollen to indicate the local presence of trees (this study and Hu et al., 1993), we found that spruce were growing locally at Deadman Lake by ∼8,200 cal yr BP, at Clarence Lake by ∼7,600 cal yr BP, and at Sally Lake by ∼5,900 cal yr BP (**Figure 13**). Taking into account the 2 SD errors associated with the age models, spruce presence was contemporaneous at Deadman and Clarence lakes (9360–7030 and 8200–7120 cal yr BP, respectively), but was later at Sally (7310–4725 cal yr BP).

The expansion of spruce across interior Alaska started in the early Holocene, but continued through the middle Holocene and marked a radical change in the landscape that was probably driven initially by greater summer warmth. In interior Alaska, especially in the Tanana Valley, spruce was present by ∼11,000 cal yr BP (Bigelow and Powers, 2001), although it was slightly later in the tributary valleys (Bigelow and Edwards, 2001). In contrast, spruce trees were present in the lower Susitna Valley somewhat later, by ∼9,500 cal yr BP (Ager, personal communication), which is prior to its appearance in the middle Susitna Valley. In terms of chronology, the lower valley could be a source area, but spruce was present earliest at the sites furthest from the lower valley (Deadman and Clarence lakes) and latest at the site closest to the lower valley (Sally Lake) (**Figure 13**). This is unexpected, as the obvious route for spruce migration would seem to be up the Susitna Valley. The source of the spruce was likely from sites east of our study area where pollen records from Rock Creek (Schweger, 1981), Ten Mile Lake (Anderson et al., 1994), and Canyon Lake (Shimer, 2009), and sites in the Copper River Basin (Ager, 1989) (**Figure 1**) indicate that spruce trees were present at those sites by ∼10,000 cal yr BP.

Pollen records at two of the lakes (Deadman and Clarence lakes) indicate a reduction in spruce abundance in the late Holocene (after ∼5,000 cal yr BP at Deadman Lake, possibly somewhat later at Clarence Lake). In contrast, the Sally Lake record shows no such decline, except maybe at the very top. This indicates that spruce retracted its range at the higher elevations, but that lower elevations (such as at Sally Lake) were largely unaffected. Spruce distribution is strongly correlated with summer temperature (Thompson et al., 1999), and reduced spruce abundance, especially at tree-line, implies summertime cooling. This cooling is consistent with the midge and pollen-based temperature reconstructions (**Figure 13**), as well as well-documented neoglacial ice advances in numerous Alaskan mountain ranges, although they have not been mapped in our region (Porter, 2007; Kaufman et al., 2016).

While the informally named Oshetna, Watana and Devil tephra deposits have been documented in the middle and upper Susitna Valley (Dilley, 1988; Dixon and Smith, 1990; Mulliken, 2016), only the widespread Watana tephra (∼4000 cal yr BP [Beget et al., 1991; Wallace et al., 2014; Mulliken, 2016]) is preserved in all our lake cores. Clarence and Sally Lakes, because of their high sampling resolution may preserve evidence of a transient landscape change associated with the Watana tephra. At both lakes, lowered %C may indicate a brief reduction in lake productivity and pollen suggests a transient increase in spruce and decrease in birch (**Figures 7**, **9**, **11**). While these data are still preliminary (we need additional high-resolution analyses), they do suggest that the vegetation in the region was sensitive to these tephra falls. However, the impact on people living in the region is still a matter of debate, as discussed below.

In terms of archeology, Northern Archaic components are stratigraphically situated between the Oshetna and Watana ashfalls (∼6,570–4,400 cal yr BP), and between the Watana and Devil ashfalls (∼3,360–1,825 cal yr BP). The numbers of components and the density of refuse left behind at sites significantly increases after the deposition of the Oshetna ashfall (Dixon et al., 1985; Mulliken, 2016). The frequency of components between the Oshetna and Watana tephras (n = 31; 14.3 components/1000 years) and between the Watana and Devil tephras (n = 32; 20.8 components/1000 years) are similar, but increase slightly after the Watana ashfall (**Figure 13**). While the number of components increases after the Watana ashfall, the few sites that are radiocarbon dated do suggest a hiatus in use of the area following the Watana tephra (Mulliken, 2016). In all, these Northern Archaic components account for 26% of the components in the region for all time periods. Populations during the Northern Archaic period likely increased their hunting ranges focusing on more seasonally abundant resources than previous populations and targeting montane and upland landscapes more intensively (Potter, 2008a).

Mason and Bigelow (2008) hypothesized that Northern Archaic populations thrived in cooler periods, specifically pointing to a cold anomaly ∼5,600 to 5,000 cal yr BP in the GISP2 ice core record, when caribou populations may have expanded (*sensu* Mason et al., 2001). In Alaska, radiocarbon dated Northern Archaic components appear to peak between 5,700 and 4,500 cal yr BP (Esdale, 2008), which would roughly correspond to this cooling period and components that are situated between the Oshetna and Watana tephras could date to this period. However, our regional paleoecological data do not show significant landscape responses to cooling in this region between 5,500 and 5,000 cal yr BP. As noted above, it is only after ∼5,000 cal yr BP that we see potential effects of lower summertime temperatures evident in a retraction of spruce from higher elevation sites (i.e., Deadman Lake). Caribou abundance may have risen in the study area after the retraction of spruce, and, in turn, Northern Archaic populations would have increased their usage of the region. However, while components dating to after the Oshetna ashfall may have utilized higher elevations once spruce retracted its range, we cannot directly correlate the two events because of problems in the archeological chronology mentioned above.

Components after the Devil deposition span the earliest part of the Athabascan Tradition period to early historic times when Euroamerican explorers and settlers entered interior Alaska (Dixon et al., 1985). Over 60% of the archeological components for all time periods lie above the Devil tephra (with a frequency of 96.6 components/1000 years), a very notable increase that is likely biased toward an increased archeological visibility, as many of these are near the surface and not deeply buried in sediment. Upland usage and the subsistence resource bases did not change between Northern Archaic and Athabascan Traditions, with the exception of more moose acquired by the latter (Potter, 2008a).

Several studies demonstrate the potential for negative ecological impacts of distal tephras in boreal forest and tundra ecosystems at high latitudes, especially to important subsistence resources (caribou), as well as reduced usable landscape for humans (VanderHoek and Nelson, 2007; Kuhn et al., 2010; Mullen, 2012). While regional landscape use and resource exploitation did not dramatically change over the last 6000 years in the study area, if caribou herds were impacted by changes in vegetation following deposition regional tephras, the Northern Archaic and Athabascan Traditions would likely have also been impacted because of their specialized focus of hunting caribou

in the upland regions (Mulliken, 2016). People would have likely abandoned the middle Susitna Valley to hunt caribou in other areas of interior Alaska not impacted by tephra deposition, only returning once caribou abundance increased sufficiently to support sustained human use in the region. As noted above, paleoecological data from most of our study lakes indicate that vegetation was impacted by at least the Watana deposition. However, because of the inexact archeological chronology in the middle Susitna Valley, we cannot currently calculate a period of abandonment, or if one actually did indeed occur, following deposition of the Watana tephra.

CONCLUSION

This study presents the results of a multidisciplinary research effort in the middle Susitna Valley. Lacustrine cores from lakes in the boreal forest and tundra shed light on tephra deposition and landscape change after ∼12,000 cal yr BP.

The lake cores preserve several tephra deposits, although only one (Watana tephra at ∼4,000 cal yr BP) is also preserved in terrestrial sections in the region. Other terrestrial tephra units (the locally named Oshetna and Devil tephras) are not present in the lake cores. However, in the lake records, tephras dated ∼11,000 and ∼11,600 cal yr BP are new to the region and glass chemistry indicates it may have originated from Hayes Volcano, suggesting a previously unknown eruption from that source. Other tephras are currently unidentified.

Paleoecological analyses indicate the lakes were productive immediately after formation ∼12,000 cal yr BP. The vegetation was a shrub tundra, which was relatively unproductive at some lakes, but not others, suggesting a mosaic across the region. High-resolution analyses at Clarence Lake indicate a brief but dramatic change in the lake with a drop in water level and reduced productivity which coincides with a transient reduction in woody taxa. Taken together, these events indicate climatic cooling and increased aridity. This event could be linked with the YD, although uncertainties in the lake chronology make a formal correlation premature. Subsequently, various proxies at all lakes returned to previous levels, though productivity immediately began to taper off, a trend which continued through the Holocene. In contrast, pollen records indicate the expansion first of cottonwood/aspen, then of spruce beyond their current limits in the early Holocene, both of which point to greater summer warmth. Cottonwood/aspen then retracted by about 8,000 cal yr BP and spruce retracted after about 4,500 cal yr BP.

The extent that people were affected by landscape changes and tephra falls is important for a better understanding of human-environment interactions in the region. The middle Susitna Valley has hundreds of archeological components that span about 11,000 years. However, the region was unoccupied earlier, even though the data presented here suggest this upland landscape may have been somewhat productive. Lower valleys, such as the Tanana and Nenana River Valleys, may have had enough resources, including bison and elk, to support much of the populations before 11,000 cal yr BP, therefore the need to use the sparse upland resources was minimal (Yesner, 2007; Graf and Bigelow, 2011; Potter, 2011). The earliest evidence of humans using the upper and middle Susitna Valleys date to the early Holocene (∼11,140–10,520 cal yr BP), coinciding with a period of greater summer warmth and the expansion of cottonwood/aspen.

Our data suggests that the Watana tephra had an effect on the landscape with reduced lake productivity and minor changes in the vegetation. How these might have affected resource abundance, especially caribou populations, is currently unclear, and will require a more refined archeological chronology to determine if human use of the region was impacted.

DATA AVAILABILITY

Geochemistry, diatom, and pollen data are all available upon request. Tephra data are included in **Supplementary Materials**.

AUTHOR CONTRIBUTIONS

NB, JR, and MW participated in field work. NB, JR, MW, KW, KM, and ÉS-T generated data and wrote and edited the text.

FUNDING

This study was funded by the State of Alaska with a grant to the Susitna-Watana Hydroelectric Project.

ACKNOWLEDGMENTS

We would like to thank the Alaska Energy Authority and the Susitna-Watana Hydroelectric Project for funding this project. We would like to thank Patrick Hall, Justin Hayes, and Gerad Smith of Northern Land Use Alaska for helping in the field, and we would also like to thank Cassidy Phillips for making the stratigraphic diagrams.

SUPPLEMENTARY MATERIAL

The Supplementary Material for this article can be found online at: https://www.frontiersin.org/articles/10.3389/feart.2019.00043/full#supplementary-material

REFERENCES

Abbott, M. B., Finney, B. P., Edwards, M. E., and Kelts, K. R. (2000). Lake-level reconstructions and paleohydrology of Birch Lake, Central Alaska, based on seismic reflection profiles and core transects. *Quat. Res.* 53, 154–166. doi: 10.1006/qres.1999.2112

Ager, T. A. (1989). "History of late Pleistocene and Holocene vegetation in the Copper River Basin, South-Central Alaska," in *Late Cenozoic History of the Interior Basins of Alaska and the Yukon. U.S. Geological Survey Circular 1026*, eds D. L. Carter, T. D. Hamilton, and J. P. Galloway (Washington, DC: U.S. Geological Survey), 89–92.

Ager, T. A. (2018). *Pollen Data from Watana Triangle Pond* [*Online*]. *Data lodged in Neotoma Paleoecology Database*. Available at: https://apps.neotomadb.org/explorer/ [accessed September, 2018].

Alaska Biological Research (2014). *Vegetation and Wildlife Habitat Mapping Study in the Upper and Middle Susitna Basin Study Plan Section 11.5: Initial Study Report Part A: Sections 1-6, 8-10. (Anchorage: Alaska Energy Authority)*. Available at: "http://www.susitna-watanahydro.org/wp-content/uploads/2014/05/11.5_VWHAB_ISR_PartA.pdf ". Data: "http://gis.suhydro.org/isr/11-Botanical/"

Alaska Climate Research Center (2014). *Alaska Climate Normals 1981-2010*. Available at: http://akclimate.org/Climate/Normals [Online] [accessed March 24, 2014].

Alaska Department of Fish and Game (1983). *Deadman Lake Bathymetry*. Available at: http://www.adfg.alaska.gov/index.cfm?adfg=fishingsportstockinghatcheries.lakesdatabase

Alaska Department of Fish and Game (2019). *Clarence Lake Bathymetry. Alaska Departement of Fish and Game*. Available at: http://www.adfg.alaska.gov/index.cfm?adfg=fishingSportLakeData.lakeDetail&LakeID=435

Anderson, P. M., and Brubaker, L. B. (1986). Modern pollen assemblages from northern Alaska. *Rev. Palaeobot. Palynol.* 46, 273–291. doi: 10.1111/j.1365-294X.2010.04881.x

Anderson, P. M., Edwards, M. E., and Brubaker, L. B. (2004). "Results and paleoclimate implications of 35 years of paleoecological research in Alaska," in *The Quaternary Period in the United States*, eds A. R. Gillespie and S. C. Porter (Amsterdam: Elsevier), 427–440.

Anderson, P. M., Lozhkin, A. V., Eisner, W. R., Kozhevnikova, M. V., Hopkins, D. M., Brubaker, L. B., et al. (1994). Two late Quaternary pollen records from south-central Alaska. *Géograph. Phys. Quat.* 48, 131–143. doi: 10.7202/032990ar

Antoniades, D., Hamilton, P. B., Douglas, M. V. S., and Smol, J. P. (2008). "Diatoms of North America: the freshwater floras of Prince Partick, Ellef Ringnes and northern Ellesmere Islands from the Canadian Arctic Archipelago," in *Iconographica Diatomologica 17*, ed. H. Lange-Bertalot (Ruggell: A. R. G. Gantener-Verlag).

Battarbee, R. W., Jones, V. J., Flower, R. J., Cameron, N. G., Bennion, H., Carvalho, L., et al. (2001). "Diatoms," in *Tracking Environmental Change Using Lake Sediments Volume 3 (Terrestrial, Algal and Siliceous Indicators)*, eds J. P. Smol, H. J. B. Birks, and W. M. Last (Dordrecht: Kluwer Academic Publishers), 155–202.

Beget, J. E., Reger, R. D., Pinney, D., Gillispie, T., and Campbell, K. (1991). Correlation of the Holocene Jarvis Creek, Tangle Lakes, Cantwell, and Hayes tephras in south-central and central Alaska. *Quat. Res.* 35, 174–189. doi: 10.1016/0033-5894(91)90065-D

Berger, A. (1978). Long-term variations of daily insolation and Quaternary climatic changes. *J.f Atmosph. Sci.* 35, 2362–2367. doi: 10.1175/1520-0469(1978)035<2362:LTVODI>2.0.CO;2

Bigelow, N. H. (2013). "POLLEN RECORDS, LATE PLEISTOCENE | Northern North America," in *Encyclopedia of Quaternary Science*, 2nd Edn, eds S. A. Elias and C. J. Mock (Amsterdam: Elsevier), 39–51.

Bigelow, N. H., and Edwards, M. E. (2001). A 14,000 yr paleoenvironmental record from Windmill Lake, central Alaska: lateglacial and Holocene vegetation in the Alaska Range. *Quat. Sci. Rev.* 20, 203–215. doi: 10.1016/S0277-3791(00)00122-0

Bigelow, N. H., and Powers, W. R. (2001). Climate, vegetation, and archaeology 14,000-9000 cal yr B.P. in central Alaska. *Arctic Anthropol.* 38, 171–195.

Björck, S. (2007). "Younger Dryas Oscillation, Global Evidence," in *Encyclopedia of Quaternary Science*, ed. S. A. Elias (Amsterdam: Elsevier), 1985–1993.

Blaauw, M., and Christen, J. A. (2011). Flexible paleoclimate age-depth models using and autoregressive gamma process. *Bayesian Anal.* 6, 457–474.

Blong, J. C. (2016). *Prehistoric Landscape use in the central Alaska Range*. Unpublished Ph.D. thesis, Texas A&M University, College Station, TX.

Blong, J. C. (2018). Late-Glacial Hunter-Gatherers in the Central Alaska Range and the Role of Upland Ecosystems in the Peopling of Alaska. *PaleoAmerica* 42, 1–31. doi: 10.1080/20555563.2018.1460156

Boggs, K., Boucher, T. V., Kuo, T. T., Fehringer, D., and Guyer, S. (2014). *Vegetation Map and Classification: Northern, Western and Interior Alaska [Online]*. Anchorage: University of Alaska Anchorage.

Borchardt, G. A. (1974). The SIMAN coeffiecient for similarity analysis. *Classif. Soc. Bull.* 3, 2–8.

Bowers, P. M., Reuther, J., Stern, R. O., Gelvin-Reymiller, C., Slaughter, D., Baxter-McIntosh, J., et al. (2011). *Susitna-Watana Hydrological Project Cultural Resources Data Gap Analysis. Report Prepared for the Alaska Energy Authority by Northern Land Use Research, Inc.". (Fairbanks)*. Available at: http://www.arlis.org/docs/vol1/Susitna2/1/SuWa122.pdf

Briner, J. P., Kaufman, D. S., Werner, A., Caffee, M., Levy, L., Manley, W. F., et al. (2002). Glacier readvance during the late glacial (Younger Dryas?) in the Ahklun Mountains, southwestern Alaska. *Geology* 30, 679–682. doi: 10.1130/0091-7613(2002)030<0679:GRDTLG>2.0.CO;2

Cameron, C. E., Mulliken, K. M., Crass, S. W., Schaefer, J. R., and Wallace, K. L. (2019). *Alaska Volcano Observatory Geochemical Database; Version 2: Alaska Division of Geological & Geophysical Surveys Digital Data Series 8 v. 2* (Fairbanks, AK: Alaska Division of Geological & Geophysical Surveys), 26. doi: 10.14509/30058

Cook, J. P. (1975). Archeology of interior Alaska. *Western Can. J. Anthropol.* 5, 125–133.

Cumming, B. F., Wilson, S. E., Hall, R. I., and Smol, J. P. (1995). Diatoms from British Columbia (Canada) lakes and their relationship to salinity, nutrients and other limnological variables. *Bibl. Diatomol.* 31, 1–207.

Dilley, T. E. (1988). *Holocene Tephra Stratigraphy and Pedogenesis in the Middle Susitna River Valley*. Unpublished M.S. thesis, University of Alaska Fairbanks, Fairbanks, AK.

Dixon, E. J. (1985). Cultural chronology of central interior Alaska. *Arctic Anthropol.* 22, 47–66.

Dixon, E. J. (1999). *Bones, Boats and Bison: Archaeology and the First Colonization of Western North America*. Albuquerque: University of New Mexico Press.

Dixon, E. J., Andrefsky, W., Utermohle, C. J., Smith, G. S., and Saleeby, B. M. (1985). *Susitna Hydroelectric Project: Cultural Resources Investigations 1979-1985*. Fairbanks, AK: University of Alaska.

Dixon, E. J., and Smith, G. S. (1990). "A regional application of tephrochronology in Alaska," in *Archaeological Geology of North America*, eds N. P. Lasca and J. Donahue (Boulder: Geological Society of America), 383–398.

Edwards, M. E., and Dunwiddie, P. W. (1985). Dendrochronological and palynological observations on *Populus balsamifera* in northern Alaska, U. S. A. *Arct. Alp. Res.* 17, 271–278. doi: 10.2307/1551017

Engstrom, D. R., Hansen, B. C. S., and Wright, H. E. (1990). A possible Younger Dryas record in southeastern Alaska. *Science* 250, 1383–1385. doi: 10.1126/science.250.4986.1383

Esdale, J. A. (2008). A current synthesis of the Northern Archaic. *Arct. Anthropol.* 45, 3–38. doi: 10.1353/arc.0.0006

Faegri, K., and Iversen, J. (1989). *Textbook of Pollen Analysis*. Chichester: John Wiley & Sons.

Fallu, M.-A., Allaire, N., and Pienitz, R. (2000). Freshwater diatoms from northern Québec and Labrador. *Bib. Diatomol.* 45, 1–200.

Gaglioti, B. V., Mann, D. H., Wooller, M. J., Jones, B. M., Wiles, G. C., Groves, P., et al. (2017). Younger-Dryas cooling and sea-ice feedbacks were prominent features of the Pleistocene-Holocene transition in Arctic Alaska. *Quat. Sci. Rev.* 169, 330–343. doi: 10.1016/j.quascirev.2017.05.012

Graf, K. E., and Bigelow, N. H. (2011). Human response to climate during the Younger Dryas chronozone in central Alaska. *Quat. Int.* 242, 434–451. doi: 10.1016/j.quaint.2011.04.030

Gregory-Eaves, I., Smol, J. P., Finney, B. P., and Edwards, M. E. (1999). Diatom-based transfer functions for inferring past climatic and environmental changes in Alaska. U.S.A. *Arct. Antarct. Alp. Res.* 4, 353–365. doi: 10.1080/15230430.1999.12003320

Grimm, E. C. (2016). *Tilia [Online]*. Available at: https://www.tiliait.com/

Guthrie, R. D. (1990). *Frozen Fauna of the Mammoth Steppe*. Chicago: University of Chicago Press. doi: 10.7208/chicago/9780226159713.001.0001

Hansen, B. C. S., and Engstrom, D. R. (1996). Vegetation history of Pleasant Island, southeastern Alaska, since 13,000 yr B. P. *Quat. Res.* 46, 161–175. doi: 10.1006/qres.1996.0056

Holmquist, C. (1971). Northerly localities for three aquatic plants, *Lemna trisulca* L., *Ceratophyllum demersum* L., and *Myriophyllum spicatum* L. *Bot. Notiser* 124, 335–342.

Hopkins, D. M. (1982). "Aspects of the paleogeography of Beringia during the late Pleistocene," in *Paleoecology of Beringia*, eds D. M. Hopkins, J. J. V. Matthews, C. E. Schweger, and S. B. Young (New York, NY: Academic Press), 3–28.

Hu, F. S., Brubaker, L. B., and Anderson, P. M. (1993). A 12,000 year record of vegetation change and soil development from Wien Lake, central Alaska. *Can. J. Bot.* 71, 1133–1142. doi: 10.1139/b93-133

Jones, M. C., Peteet, D. M., Kurdyla, D., and Guilderson, T. (2009). Climate and vegetation history from a 14,000-year peatland record, Kenai Peninsula, Alaska. *Quat. Res.* 72, 207–217. doi: 10.1016/j.yqres.2009.04.002

Jones, M. C., and Yu, Z. (2010). Rapid deglacial and early Holocene expansion of peatlands in Alaska. *Proc. Natl. Acad. Sci. U.S.A.* 107, 7347–7352. doi: 10.1073/pnas.0911387107

Juggins, S. (2014). *C2 Version 1.7.6 Software for Ecological and Palaeoecological Data Analysis and Visualisation [Online]*. Newcastle upon Tyne: Newcastle University.

Kachadoorian, R. (1974). *Geology of the Devil Canyon Dam site, Alaska*. Open-file Report, No. 74-40. Reston, VI: United States Geological Survey.

Kallel, H., Labeyrie, L. C., Arnold, M., Okada, H., Dudley, W. C., and Duplessy, J.-C. (1988). Evidence of cooling during the Younger Dryas in the western North Pacific. *Oceanol. Acta* 11, 369–375.

Kaufman, D. S., Axford, Y. L., Henderson, A. C. G., McKay, N. P., Oswald, W. W., Saenger, C., et al. (2016). Holocene climate changes in eastern Beringia (NW North America) – A systematic review of multi-proxy evidence. *Quat. Sci. Rev.* 147, 312–339. doi: 10.1016/j.quascirev.2015.10.021

Kaufman, D. S., Scott Anderson, R., Hu, F. S., Berg, E., and Werner, A. (2010). Evidence for a variable and wet Younger Dryas in southern Alaska. *Quat. Sci. Rev.* 29, 1445–1452. doi: 10.1016/j.quascirev.2010.02.025

Kokorowski, H. D., Anderson, P. M., Mock, C. J., and Lozhkin, A. V. (2008). A re-evaluation and spatial analysis of evidence for a Younger Dryas climatic reversal in Beringia. *Quat. Sci. Reviews* 27, 1710–1722. doi: 10.1016/j.quascirev.2008.06.010

Kuhn, T. S., McFarlane, K. A., Groves, P., Mooers, A. Ø, and Shapiro, B. (2010). Modern and ancient DNA reveal recent partial replacement of caribou in the southwestern Yukon. *Mol. Ecol.* 19, 1312–1323. doi: 10.1111/j.1365-294X.2010.04565.x

Les, D. H. (1986). The phytogeography of *Ceratophyllum demersum* and *C. echinatum* (Ceratophyllaceae) in glaciated North America. *Can. J. Bot.* 64, 498–509. doi: 10.1139/b86-064

Mann, D. H., Groves, P., Reanier, R. E., Gaglioti, B. V., Kunz, M. L., and Shapiro, B. (2015). Life and extinction of megafauna in the ice-age Arctic. *Proc. Natl. Acad. Sci. U.S.A.* 112, 14301–14306. doi: 10.1073/pnas.1516573112

Mann, D. H., Groves, P., Reanier, R. E., and Kunz, M. L. (2010). Floodplains, permafrost, cottonwood trees, and peat: What happened the last time climate warmed suddenly in Arctic Alaska? *Quat. Sci. Rev.* 29, 3812–3830. doi: 10.1016/j.quascirev.2010.09.002

Mann, D. H., Peteet, D. M., Reanier, R. E., and Kunz, M. L. (2002). Responses of an arctic landscape to Lateglacial and early Holocene climatic changes: the importance of moisture. *Quat. Sci. Rev.* 21, 997–1021. doi: 10.1016/S0277-3791(01)00116-0

Mason, O. K., and Bigelow, N. H. (2008). The crucible of early to mid-Holocene climate in northern Alaska; Does Northern Archaic represent the people of the spreading forest? *Arct. Anthropol.* 45, 39–70. doi: 10.1353/arc.0.0008

Mason, O. K., Bowers, P. M., and Hopkins, D. M. (2001). The early Holocene Milankovitch thermal maximum and humans: adverse conditions for the Denali complex of eastern Beringia. *Quat. Sci. Rev.* 20, 525–548. doi: 10.1016/S0277-3791(00)00100-1

Max, L., Riethdorf, J.-R., Tiedemann, R., Smirnova, M., Lembke-Jene, L., Fahl, K., et al. (2012). Sea surface temperature variability and sea-ice extent in the subarctic northwest Pacific during the past 15,000 years. *Paleoceanography* 27:A3213. doi: 10.1029/2012pa002292

McAndrews, J. H., Berti, A. A., and Norris, G. (1973). *Key to the Quaternary Pollen and spores of the Great Lakes Region*. Toronto: Royal Ontario Museum. doi: 10.5962/bhl.title.60762

Meyer, H., Schirrmeister, L., Yoshikawa, K., Opel, T., Wetterich, S., Hubberten, H.-W., et al. (2010). Permafrost evidence for severe winter cooling during the Younger Dryas in northern Alaska. *Geophys. Res. Lett.* 37:L03501. doi: 10.1029/2009GL041013

Meyers, P. A., and Ishiwatari, R. (1993). Lacustrine organic geochemistry—an overview of indicators of organic matter sources and diagenesis in lake sediments. *Organ. Geochem.* 20, 867–900. doi: 10.1016/0146-6380(93)90100-P

Mikolajewicj, U., Crowley, T. J., Schiller, A., and Voss, R. (1997). Modelling teleconnections between the North Atlantic and North Pacific during the Younger Dryas. *Nature* 387, 384–387. doi: 10.1038/387384a0

Moore, P. D., Webb, J. A., and Collinson, M. E. (1991). *Pollen Analysis*. Oxford: Blackwell Scientific Publications.

Moos, M. T., Laird, K. R., and Cumming, B. F. (2009). The Holocene Climate-related eutrophication of a small boreal lake in northwestern Ontario: a palaeolimnological perspective. *Holocene* 19, 359–367. doi: 10.1177/0959683608101387

Moriya, K. (1976). *Flora and Palynomorphs of Alaska*. Tokyo: Kodansha Pub. Co.

Muhs, D. R., Ager, T. A., Bettis, E. A., McGeehin, J., Been, J. M., Begét, J. E., et al. (2003). Stratigraphy and palaeoclimatic significance of Late Quaternary loess-palaeosol sequences of the Last Interglacial-Glacial cycle in central Alaska. *Quat. Sci. Rev.* 22, 1947–1986. doi: 10.1016/S0277-3791(03)00167-7

Mullen, P. O. (2012). An archaeological test of the effects of the White River Ash eruptions. *Arct. Anthropol.* 49, 35–44. doi: 10.1353/arc.2012.0013

Mulliken, K. (2016). *Holocene Volcanism and Human Occupation in the Middle Susitna River Valley,Athe Chulitna River in Broad Pass about laska*. Unpublished MA. thesis, University of Alaska Fairbanks, Fairbanks, AK.

Muschitiello, F., and Wohlfarth, B. (2015). Time-transgressive environmental shifts across Northern Europe at the onset of the Younger Dryas. *Quat. Sci. Rev.* 109, 49–56. doi: 10.1016/j.quascirev.2014.11.015

Peteet, D. M., Del Genio, A., and Lo, K. K.-W. (1997). Sensitivity of northern hemisphere air temperatures and snow expansion to North Pacific sea surface temperatures in the Goddard Institute for Space Studies general circulation model. *J. Geophys. Res.* 102, 23781–23791. doi: 10.1016/j.quascirev.2014.11.015

Peteet, D. M., and Mann, D. H. (1994). Late-glacial vegetational, tephra, and climatic history of southwestern Kodiak Island. Alaska. *Écoscience* 1, 255–267. doi: 10.1029/97JD01573

Porter, S. C. (2007). "GLACIATIONS | Neoglaciation in the American Cordilleras," in *Encyclopedia of Quaternary Science*, ed. S. A. Elias (Oxford: Elsevier), 1133–1142. doi: 10.1080/11956860.1994.11682250

Potter, B. A. (2008a). A first approximation of Holocene inter-assemblage variability in central Alaska. *Arct. Anthropol.* 45, 89–113. doi: 10.1353/arc.0.0013

Potter, B. A. (2008b). Exploratory models of intersite variability in mid to late Holocene central Alaska. *Arctic* 61, 407–425.

Potter, B. A. (2011). "Late Pleistocene and early Holocene assemblage variability in central Alaska," in *From the Yenisei to the Yukon: Interpreting Lithic Assemblage Variability in Late Pleistocene/Early Holocene Beringia*, eds T. Goebel and I. Buvit (College Station, TX: Texas A&M University Press), 215–233.

Praetorius, S. K., and Mix, A. C. (2014). Synchronization of North Pacific and Greenland climates preceded abrupt deglacial warming. *Science* 345, 444–448. doi: 10.1126/science.1252000

Rasmussen, S. O., Bigler, M., Blockley, S. P., Blunier, T., Buchardt, S. L., Clausen, H. B., et al. (2014). A stratigraphic framework for abrupt climatic changes during the Last Glacial period based on three synchronized Greenland ice-core records: refining and extending the INTIMATE event stratigraphy. *Quat. Sci. Rev.* 106, 14–28. doi: 10.1016/j.quascirev.2014.09.007

Reger, R. D., Bundtzen, T. K., and Smith, T. E. (1990). *Geology of the Healy A-3 Quadrangle, Alaska. Public-data File 90-1*. Fairbanks, AK: Alaska Division of Geological and Geophysical Surveys. doi: 10.14509/1433

Reuther, J. D., Dixon, E. J., Mulliken, K., and Potter, B. A. (2018). The early Holocene-Aged component at the Jay Creek Ridge site, middle Susitna River Valley, Alaska. *PaleoAmerica* 1–5. doi: 10.1080/20555563.2018.1554963

Saulnier-Talbot, É. (2007). *Impacts de L'évolution Climatique Postglaciaire sur les lacs de L'extrême nord de l'Ungava*. Unpublished Ph.D. thesis, Université Laval, Québec, QC.

Schweger, C. (1981). Chronology of late glacial events from the Tangle Lakes, Alaska Range, Alaska. *Arct. Anthropol.* 18, 97–101.

Shimer, G. (2009). *Holocene Vegetation and Climate Change at Canyon Lake, Copper River Basin, Alaska*. Unpublished MS. thesis, University of Alaska Fairbanks, Fairbanks, AK.

Thompson, R. S., Anderson, K. H., and Bartlein, P. J. (1999). *Atlas of Relations Between Climatic Parameters and Distribution of Important Trees and Shrubs in North America–Introduction and Conifers", in: U.S. Geological Survey Professional Paper 1650-A*. Washington: U.S. Dept. of the Interior.

Thorson, R. M., Dixon, E. J., Smith, G. S., and Batten, A. R. (1981). Interstadial proboscidean from south-central Alaska: implications for biogeography, geology, and archaeology. *Quat. Res.* 16, 404–417. doi: 10.1016/0033-5894(81)90019-3

VanderHoek, R., and Nelson, R. E. (2007). "Ecological roadblocks on a constrained landscape: the cultural effects of catastrophic Holocene volcanism on the Alaska Peninusla, southwest Alaska," in *Living Under the Shadow: Cultural Impacts of Volcanic Eruptions*, eds J. Grattan and R. Torrence (Walnut Creek, CA: Left Coast Press), 133–152.

Viau, A. E., Gajewski, K., Sawada, M. C., and Bunbury, J. (2008). Low- and high-frequency climate variability in eastern Beringia during the past 25 000 years. *Can. J. Earth Sci.* 45, 1435–1453. doi: 10.1139/E08-036

Wallace, K. L., Coombs, M. L., Hayden, L. A., and Waythomas, C. F. (2014). *Significance of a near-source tephra-stratigraphic sequence to the eruptive history of Hayes Volcano, south-central Alaska:* U.S. Geological Survey Scientific Investigations Report 2014–5133. Reston, VA: U.S. Geological Survey doi: 10.3133/sir20145133

Walter Anthony, K. M., Zimov, S. A., Grosse, G., Jones, M. C., Anthony, P. M., Chapin, F. S., et al. (2014). A shift of thermokarst lakes from carbon sources to sinks during the Holocene epoch. *Nature* 511, 452–456. doi: 10.1038/nature13560

Woodward-Clyde Consultants (1982). *Final Report on Seismic Studies for Susitna Hydroelectric Project: Subtasks 4.09 through 4.15*. Buffalo, NY: Acres American Incorporated.

Wooller, M. J., Saulnier-Talbot, É, Potter, B. A., Belmecheri, S., Bigelow, N., Choy, K., et al. (2018). A new terrestrial palaeoenvironmental record from the Bering Land Bridge and context for human dispersal. *R. Soc. Open Sci.* 2018:180145. doi: 10.1098/rsos.180145

Workman, W. B. (1978). *Prehistory of the Aishihik-Kluane area, southwest Yukon Territory*. Ottowa, ON: National Museum of Man. doi: 10.2307/j.ctv16s1t

Wright, H. E., Mann, D. H., and Glaser, P. H. (1984). Piston corers for peat and lake sediments. *Ecology* 65, 657–659. doi: 10.2307/1941430

Wygal, B. T., and Goebel, T. (2012). Early prehistoric archaeology of the middle Susitna valley. *Arct. Anthropol.* 49, 97–108. doi: 10.1353/arc.2012.0014

Yesner, D. R. (2007). "Faunal extinction, hunter-gatherer foraging strategies, and subsistence diversity among Eastern Beringian Paleoindians," in *Foragers of the Terminal Pleistocene in North America*, eds R. B. Walker and B. N. Driskell (Lincoln: University of Nebraska Press), 15–31.

Conflict of Interest Statement: The authors declare that the research was conducted in the absence of any commercial or financial relationships that could be construed as a potential conflict of interest.

frontiers in Earth Science

ORIGINAL RESEARCH
published: 03 April 2019
doi: 10.3389/feart.2019.00053

Holocene Thermokarst Lake Dynamics in Northern Interior Alaska: The Interplay of Climate, Fire, and Subsurface Hydrology

Lesleigh Anderson[1], Mary Edwards[2], Mark D. Shapley[3], Bruce P. Finney[4,5] and Catherine Langdon[2]*

[1] U.S. Geological Survey, Geosciences and Environmental Change Science Center, Denver, CO, United States, [2] School of Geography and Environment, University of Southampton, Highfield, United Kingdom, [3] Continental Scientific Drilling Coordination Office and National Lacustrine Core Facility (LacCore), University of Minnesota, Minneapolis, MN, United States, [4] Department of Biological Sciences, Idaho State University, Pocatello, ID, United States, [5] Department of Geosciences, Idaho State University, Pocatello, ID, United States

OPEN ACCESS

Edited by:
Daniel Nývlt, Masaryk University, Czechia

Reviewed by:
Sebastian Wetterich, Alfred Wegener Institute Helmholtz Centre for Polar and Marine Research (AWI), Germany
Mingrui Qiang, South China Normal University, China

***Correspondence:**
Lesleigh Anderson
land@usgs.gov

Specialty section:
This article was submitted to Quaternary Science, Geomorphology and Paleoenvironment, a section of the journal Frontiers in Earth Science

Received: *03 October 2018*
Accepted: *06 March 2019*
Published: *03 April 2019*

Citation:
Anderson L, Edwards M, Shapley MD, Finney BP and Langdon C (2019) Holocene Thermokarst Lake Dynamics in Northern Interior Alaska: The Interplay of Climate, Fire, and Subsurface Hydrology. Front. Earth Sci. 7:53. doi: 10.3389/feart.2019.00053

The current state of permafrost in Alaska and meaningful expectations for its future evolution are informed by long-term perspectives on previous permafrost degradation. Thermokarst processes in permafrost landscapes often lead to widespread lake formation and the spatial and temporal evolution of thermokarst lake landscapes reflects the combined effects of climate, ground conditions, vegetation, and fire. This study provides detailed analyses of thermokarst lake sediments of Holocene age from the southern loess uplands of the Yukon Flats, including bathymetry and sediment core analyses across a water depth transect. The sediment core results, dated by radiocarbon and ^{210}Pb, indicate the permanent onset of finely laminated lacustrine sedimentation by ~8,000 cal yr BP, which followed basin development through inferred thermokarst processes. Thermokarst expansion to modern shoreline configurations continued until ~5000 cal yr BP and may have been influenced by increased fire. Between ~5000 and 2000 cal yr BP, the preservation of fine laminations at intermediate and deep-water depths indicate higher lake levels than present. At that time, the lake likely overflowed into an over-deepened gully system that is no longer occupied by perennial streams. By ~2000 cal yr BP, a shift to massive sedimentation at intermediate water depths indicates that lake levels lowered, which is interpreted to reflect a response to drier conditions based on correspondence with Yukon Flats regional fire and local paleoclimate reconstructions. Consideration of additional contributing mechanisms include the possible influence of catastrophic lake drainages on down-gradient base-flow levels that may have enhanced subsurface water loss, although this mechanism is untested. The overall consistency between the millennial lake-level trends documented here with regional paleoclimate trends indicates that after thermokarst lakes formed, their size and depth has been affected by North Pacific atmospheric circulation in

addition to the evolution of permafrost, ground ice, and subsurface hydrology. As the first detailed study of a Holocene thermokarst basin that links expansion, stabilization and subsequent climate-driven lake level variations in a loess upland, these results provide a framework for future investigations of paleoclimatic signals from similar lake systems that characterize large regions of Alaska and Siberia.

Keywords: Alaska, Holocene, permafrost, thermokarst lakes, lake levels, paleoclimate

INTRODUCTION

Lakes of thermokarst origin are hallmark surface features of arctic and sub-arctic permafrost landscapes. Ground-collapse following initial permafrost warming is referred to as thermokarst, whereas water-filled depressions that further deepen and expand by talik formation and thermal/mechanical erosion are thermokarst lakes, or thaw lakes (Grosse et al., 2013). Recognized for their regional and global importance, thermokarst lakes are significant drivers of ecosystem shifts with fundamental implications for biogeochemistry, hydrology, ecosystems, and infrastructure (e.g., Jorgenson and Osterkamp, 2005; Jones et al., 2011; Roach et al., 2011; Kokelj and Jorgenson, 2013; Strauss et al., 2017 and references therein). As an agent of landscape change over millennia (e.g., Wetterich et al., 2009; Biskaborn et al., 2013; Walter Anthony et al., 2014), the study of thermokarst lakes provides opportunities to develop long-term perspectives on the consequences of ongoing and future thermokarst dynamics in response to recent permafrost warming (Romanovsky et al., 2010; Jones and Arp, 2015; Lenz et al., 2016).

Previous studies of thermokarst lakes in northern Alaska are largely focused on tundra environments within continuous permafrost landscapes such as the northern Seward Peninsula (Jones et al., 2011; Farquharson et al., 2016; Lenz et al., 2016) and on the shallow lakes (∼2–10 m deep) of the Arctic Coastal Plain (e.g., Jorgenson and Shur, 2007). In the boreal zone, deep (>10 m) extant thaw lakes in Siberia have been described in relation to carbon fluxes (Zimov et al., 1997; Walter et al., 2006) and two studies in the Old Crow Basin, Yukon, Canada document the evolution of thaw lakes through the Holocene (Lauriol et al., 2002; Burn and Smith, 2006). It has only been with the advent of high-resolution digital elevation detection that additional thermokarst features have been 'uncovered' in the densely forested regions of interior Alaska. Using these techniques, Edwards et al. (2016) broadly outline post-glacial and early Holocene development of deep thaw lakes within the active thermokarst landscape of the Yukon Flats in interior Alaska. Vegetation cover and associated soil development has long been recognized as a major stabilizing influence on permafrost in the interior regions of Alaska (Jorgenson et al., 2010). On the other hand, Holocene forest establishment in interior Alaska enhanced fire (Edwards et al., 2016), which can act to trigger thermokarst initiation (see Brown et al., 2015 for contemporary evidence).

Considerably less attention has focused on thermokarst lake level variations within boreal regions where the interplay between climate, vegetation and fire further complicates a clear understanding of the influence of anticipated climatic change on surface water. In the Yukon Flats, trends in fire dynamics over the Holocene have been shown to closely correspond with vegetation history (Kelly et al., 2013) and are consistent with independent records of late Holocene hydroclimate (Anderson et al., 2018). This background sets the stage for the goals of this study which are to document Holocene thaw lake evolution from detailed multi-proxy sediment analyses of three sediment cores across a water depth transect dated with macrofossils (aquatic and terrestrial) and pollen extracts using AMS radiocarbon techniques. This study provides the basis to explore biophysical interactions and feedbacks among climate, vegetation, and fire, and we propose additional mechanisms related to subsurface hydrology. As with other regions of Interior Alaska, the climate of the Yukon Flats is affected by both Arctic and North Pacific influences and we explore the potential for past thermokarst lake levels to provide insights into past atmospheric circulation patterns and trends.

Sediment cores and stratigraphic studies have long provided information on paleo thaw-lake dynamics. The general framework for identifying thaw lake sediment sequences originally developed by Hopkins and Kidd (1988) largely remains applicable today (e.g., Gaglioti et al., 2014; Farquharson et al., 2016). Although thaw lakes display suites of sediments that vary with the nature of the environment (e.g., tundra, peatland, eolian sand and silt), they also have generally distinctive characteristics that allow clear differentiation from non-thaw lake sediment sequences. Major features include (1) fine-grained, relatively organic-rich, bedded lacustrine sediments overlying (2) a basal detrital unit, commonly known as a 'trash' layer, which includes terrestrial components, which in turn overlies (3) a formerly frozen terrestrial surface that has thawed within the lake's talik (e.g., taberal deposits) that may also include ice-wedge pseudomorphs which extend downward into older sediments (see Wetterich et al., 2009; Farquharson et al., 2016, and references therein). Following these principles, Edwards et al. (2016) interpreted profundal sediment-core sequences for two lakes on the southern loess uplands of the Yukon Flats; Six Loon (6L) and Dune Two (D2) Lakes (**Figure 1A**). Using conventional radiocarbon dates of bulk organics within trash layers, results placed thermokarst initiation between ∼13,000 and 11,000 cal yr BP. Overlying sediments of early to middle Holocene age were interpreted to reflect general lake deepening and expansion followed by stabilization. To further explore the Holocene evolution of thaw lakes on the loess uplands, and the potential of their sediment records as paleoclimatic archives, this study presents a detailed examination of sediment cores from

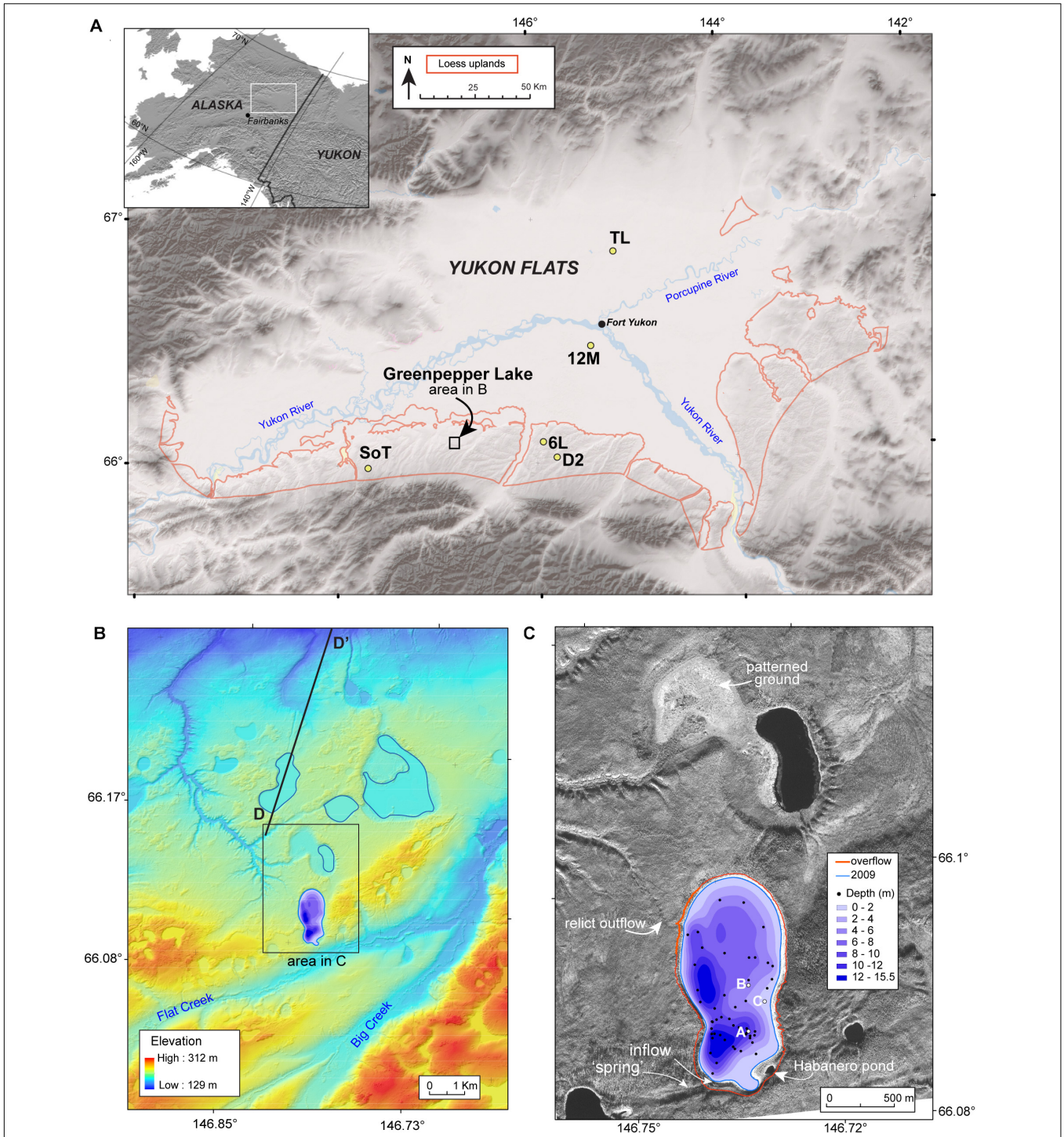

FIGURE 1 | Map of the Yukon Flats, Alaska study area: **(A)**. The southern loess uplands are enclosed by the red line: TL, Track Lake; 12M, Twelvemile Lake; SoT, Sands of Time Lake; 6L, Six Loon Lake; D2, Dune Two Lake. **(B)** Bathymetric contour map of Greenpepper Lake (purple shading) is shown on a 5-m IFSAR digital elevation model of the Flat and Big Creek areas. The electromagnetic survey line D-D' from Minsley et al. (2012) indicates a deep talik underneath the lake to the north of Greenpepper; blue outlines of modern lake levels indicate the two partially filled basins. **(C)** Bathymetry (purple shading) on black imagery (Digital Globe WV02) in June of 2009, prior to the July 2009 fire, showing the locations of the sediment cores **(A–C)**, lake shorelines in 2009 (blue) and at the surface overflow elevation (red), and the 'spring' and inflow water sampling sites. Patterned ground is evident within the partially filled lake basin and the drainage channel intersects the same gully system as the raised relict outflow channel from Greenpepper Lake.

Greenpepper Lake (informal name, 66.089°N, 146.730°W, 207 m a.s.l.; **Figures 1B,C**).

Study Area

Located within the boreal forest near the Arctic Circle, the Yukon Flats is a broad, low lying basin where the westward flowing Porcupine River joins the northward flowing Yukon River as it bends to the west (**Figure 1**). Along the lower slopes of the Yukon-Tanana Upland that borders the southern margins of the Yukon Flats, nearly contiguous and extensive loess overlies late Tertiary or early Quaternary alluvium (Williams, 1962). Stratigraphic analyses of this loess indicate ages from the early to middle Pleistocene (Begét, 2001; McDowell and Edwards, 2001; Matheus et al., 2003 and references therein) and the late Pleistocene (Froese et al., 2005) with geochemical evidence for sources from expanded glaciation in the Brooks Range to the north and the Alaska Range to the south (Muhs et al., 2018).

Williams (1962) reported that the southern marginal loess is perennially frozen 1–2 m below the surface and contains ground-ice as small veins, stringers, polygonal wedges and large irregular, tabular and polygonal masses, which was supported by observations made by Edwards et al. (2016). Airborne electromagnetic surveys reported by Minsley et al. (2012) included an observation line that crossed the southern loess margin and indicated thick permafrost (D-D' on **Figure 1B**). Deep unfrozen zones occur below deep lakes and in creek valleys that could provide groundwater conduits to the flats (Williams, 1970).

The climate of the Yukon Flats supports permanently frozen ground with a mean annual temperature of ∼−6°C (Jepsen et al., 2013). Large seasonal temperature differences range from winter minima near −55°C and summer maxima of 35°C. Mean annual precipitation is ∼250 mm with slightly more than half falling as rain during the summer and early fall. The modern vegetation of the flats is a dynamic mosaic of open meadow, spruce forest (*Picea glauca* and *P. mariana*) and successional birch-aspen forest (*Betula neoalaskana* and *Populus tremuloides*). Tall shrubs include *Salix* and *Alnus*. The southern loess uplands are dominated by spruce and successional hardwoods with tree-line at ∼900 m a.s.l. in the White Mountains to the south.

Greenpepper Lake indents an area of high ground on the north side of Flat Creek, a tributary of Big Creek, mapped as an escarpment within the southern loess uplands by Williams (1962) (**Figure 1A**). The elongate, bell pepper shaped lake is ∼2 km in length and 750 m wide. We observed pervasive permafrost throughout the area near Greenpepper Lake. During July 2010, ground and airborne observations indicated extensive near-surface permafrost thaw along the southern lake margins, which had burned in 2009 (**Supplementary Figure 1**). Thawed silt was readily mobilized in sheet and stream flow down hillslopes across extensively burned areas to the south. At a point of surface discharge along the lake's southern margins, a silt delta formed below slopes that were actively undergoing fracture and slump (seen as corrugated thermokarst slump features in imagery; **Figure 1C**). Airborne observations identified patterned ground in the partially drained lake basin to the north that is also evident in high-resolution imagery (**Figure 1C**).

The surface of Greenpepper Lake currently (2018) lies several meters below the surrounding land surface. A small, round water-filled depression of unknown depth, informally named here as Habanero Pond, lies near the southern lake margin. Along the northern and southern lake margins, steep loess bluffs, 3–5 m high, are fully or partially stabilized by vegetation. Lower terrain lies near the lake margins to the east and west. A dry outlet channel at an elevation of ∼211.5 m a.s.l. was identified on the ground within dense forest; its base is currently ∼4.5 m above the lake surface. The channel is evident in aerial photography and high-resolution imagery (**Figures 1B,C**). It converges with two other channels that emanate from three partially drained lakes to the north, and together these form a deep gully that in many locations appears dry and, in a few places, contains standing water.

Raised shorelines and relict outlet channels indicate the neighboring lakes to the north of Greenpepper were once larger and deeper, with water lost at some time in the past (**Figures 1B,C**). Based on the depth and elevation of the drainage channels and on recent observations of other "catastrophic" lake drainage (i.e., extensive lake drainage over hours to days), they likely lowered to the levels of their outlets by one or more episodes of rapid lake drainage, but they did not drain completely. In a nearby drainage event that occurred in 2013, an outlet channel cut down several meters to massive permafrost and then stopped lowering because the permafrost possibly acted as a physical and thermal barrier to further erosion (Josh Rose, 2016, personal communication; Paul Carling, 2018, personal communication). The presence of massive ice at depth may be a key reason for the abundance of partially full lakes across the southern marginal upland.

The differing histories of Greenpepper and adjacent lakes and their heterogenous surface features leads us to speculate that a locally complex hydrologic system may be operating. Greenpepper currently appears to undergo changes in lake level (**Supplementary Figure 1**) and a full lake to the north has a deep talik as revealed by an electromagnetic survey line (D-D' on **Figure 1B**; Minsley et al., 2012). If a similarly deep unfrozen zone lies beneath Greenpepper, its level may be responding to local changes in subsurface hydrology and groundwater routes, which are linked to surface-water dynamics. Thus, deep taliks may influence individual lake levels via both filling and drawing down and, on occasion, filling of lakes may drive overflow and drainage, possibly through a series of lakes, as it did in 2013.

MATERIALS AND METHODS

Bathymetry was determined at Greenpepper Lake from 60 global positioning system (GPS)-located, sonar-measured water depths that are shown relative to the elevation of the 2009 shoreline in **Figures 1B,C**. The relict shoreline elevation was determined from a 2-m interferometric synthetic aperture radar (IFSAR) Digital Elevation Model (DEM). Lake volumes and surface areas

were calculated at 1.0-m depth increments using a kriging interpolation method within ArcGIS 3D Analyst; hypsometric results are shown in **Table 1**.

In July 2010, surface and water-column measurements of Greenpepper Lake temperature (T), pH, specific conductance (Spc) and dissolved oxygen (DO) were collected with a calibrated HydroLab Quanta^{TM} sonde, which has accuracies of ±0.15°C for T, ±0.2 units for pH, ±0.1% of Spc reading, and ±0.2 mg/L for DO. Greenpepper Lake water chemistry data for samples obtained in 2007 and 2008 are published in Halm and Guldager (2012). Near-surface water samples were collected in 2010 from the lake, Habanero Pond, the 'spring' and inflowing stream for isotope and major ion analyses in 30 ml high-density polyethylene (HDPE) Whatman^{TM} bottles and sealed with no headspace. Major ions for samples from Habanero Pond, 'spring' and inflowing stream (**Table 2**) were determined in 2018 on filtered and acidified (cations) aliquots from refrigerated archived samples at the U.S. Geological Survey Colorado Water Science Center, Denver, CO. Chloride, nitrate, and sulfate were determined using a Dionex ion chromatograph and calcium, magnesium, sodium, potassium, and silica were determined by a PerkinElmer inductively coupled plasma-atomic emission spectrometer (ICP-AES). All analytical runs have an uncertainty better than 5% based on analyses of blanks, replicates, and standard reference materials following U.S. Geological Survey quality assurance protocols (Fishman et al., 1994). Mineral saturation indices for lake water were calculated using PHREEQC (Parkhurst and Appelo, 1999); solute-based residence time estimates use the reactive mass-balance approach of Donovan (1994).

Water samples for isotope analysis were filtered through 0.45-μm filters and analyzed using a Thermo Scientific, High Temperature Conversion Elemental Analyzer (TC-EA) interfaced to a Delta V Advantage mass spectrometer through the ConFlo IV system at Idaho State University Stable Isotope Laboratory, Pocatello, United States, ID. Four in-house standards, which are directly calibrated against Vienna Standard Mean Ocean Water 2 (VSMOW2), Standard Light Antarctic Precipitation 2 (SLAP2), and Greenland Ice Sheet Precipitation (GISP), were used to create a two-point calibration curve to correct the raw data and to monitor accuracy. Precision for δ^2H and $\delta^{18}O$ is better than ±2.0‰ and ±0.2‰ respectively. Random replicates represent ∼15% of analyzed samples and results fell within the range of analytical error. Water oxygen and hydrogen isotope results are reported in per mil (‰) as the relative difference of isotope ratios (δ) from the international measurement standard Vienna Standard Mean Ocean Water (VSMOW) defined by $\delta^{18}O_{H2O} = [(^{18}O/^{16}O)_{H2O}/(^{18}O/^{16}O)_{VSMOW}] - 1$ and $\delta^2H_{H2O} = [(^2H/^1H)_{H2O} / (^2H/^1H)_{VSMOW})] - 1$.

Sediment cores were obtained from a securely anchored floating platform in July 2010 from three locations, A, B, and C, with water depths of 10, 5, and 1.85 m respectively (**Figure 1C**). Core A was located slightly to the east of the deepest water depth of 15.5 m measured in the southernmost basin to avoid any potential slumped sediments from the steep slope along the southwest shoreline. Core B is located on the gently grading slope on the east side of the northern basin and Core C was within 10 m of the eastern shoreline in the littoral zone. Cores with an undisturbed sediment-water interface were obtained at all three locations using a customized polycarbonate tube fit with a piston and extruded in the field at 0.5-cm increments (Glew et al., 2001). Lower sediments were obtained using modified Livingstone and 'Bolivia' coring devices.

Following whole-core magnetic susceptibility measurements at 1-cm increments using a Bartington susceptibility meter, the cores were split, imaged with a digital line-scanner with cross-polarized filters, sampled for petrographic smear slides, and visually logged on the basis of Munsell color, sedimentary composition, structure, and biogenic features at LacCore, at the University of Minnesota, Minneapolis, MN, United States (**Supplementary Figure 2**). Sediment classification of lithostratigraphic units are based on color, composition and structure, and petrographic smear slide mineral identification according to Schnurrenberger et al. (2003). Dry bulk density was determined on contiguous 1-cm^3 samples taken at 0.5- and 1.0-cm increments. Percent organic and inorganic carbon was determined from dry, pulverized subsamples using total carbon (TC) and total inorganic carbon (TIC) measurements by a UIC Inc.^{TM} carbon dioxide coulometer (Engleman et al., 1985) at the U.S. Geological Survey, Lakewood, CO, United States. Accuracy and precision and sample reproducibility for both TC and TIC is 0.1%. Percent organic carbon was calculated as the difference between TC and TIC and converted to percent organic matter by a factor of 2.5, an approximation

TABLE 1 | Greenpepper Lake hypsometric estimates.

Shoreline Elevation (m)	Maximum Water Depth (m)	Lake Area (m^2)	Lake Volume (m^3)	Comments	% of 2009 Area	% of 2009 Volume
211.5	20.0	1042479	8998948	Relict outflow	125	188
211	19.5	1012714	8485397		122	178
210	18.5	966804	7496432		116	157
209	17.5	926123	6550128	1952 shoreline	111	137
208	16.5	886715	5643929		107	118
207	15.5	831673	4776947	2009 shoreline	100	100
206	14.5	740568	3994444		85.4	74.8
205	13.5	672822	3288514		90.8	82.3
204	12.5	610795	2646872		90.8	80.5
203	11.5	543638	2068549		89.0	78.2
202	10.5	468662	1561781		86.2	75.5
201	9.5	388006	1132393		82.8	72.5
200	8.5	249592	810522		64.4	71.6
199	7.5	182138	598515		73.0	73.8
198	6.5	139983	438422		76.9	73.3
197	5.5	113110	312927		80.8	71.4
196	4.5	91397	210851		80.8	67.4
195	3.5	70023	129923		76.6	61.6
194	2.5	51525	69813		73.5	53.7
193	1.5	34264	26772		66.5	38.3
192	0.5	10690	3082		31.2	11.5

TABLE 2 | Aqueous geochemistry of Greenpepper Lake.

Parameter	Greenpepper lake[1]	Habanero pond	'Spring'[2]	YF Lakes Mean[3]	α[4] (lake:inflow)	inferred % to sediment
Surface Field Measurements						
Temperature (°C)	18.1	18.9	6.6–7.6			
pH	9.0	9.3	7.6–7.9	7.8		
Specific conductivity (μS/cm)	900	230	248–219	442		
Dissolved Oxygen (mg/L)	9.5	11.3	11.3–11.4			
Major ions (mg/L)						
Calcium – Ca^{2+}	23.2–21.1	30.5	42–38	27.9	0.57	99
Magnesium – Mg^{2+}	87.2–73.8	15.0	7.9–11.2	20.6	8.25	83
Sodium – Na^{+}	79.4–66.3	3.2	2.2–2.3	45.9	32.24	34
Potassium – K^{+}	14.3–11.9	0.5	1.3–0.6	10.0	13.70	72
Alkalinity	212.5	–	–	253	–	–
Chloride – Cl^{-}	55.3–45.2	1.1	0.95–0.42	3.6	48.78	0
Sulfate – SO_4^{2-}	8.6–5.9	10.5	7.6–4.9	8.2	1.10	98
Mg:Ca (molar)	5.2–5.9	0.8	0.3–0.5	–		
Dissolved carbon and gasses	**March/May 2008**					
DIC (μmol/L)	6389, 8684					
δ^{13}C-DIC (‰VPDB)	−2.21, −2.45					
DOC (mg/L)	43, 33					
δ^{13}C-DOC (‰VPDB)[5]	−26.14[5]					
^{14}C Age -DOC (years BP)[5]	125 ± 25[5]					
δ^{13}C-POC (‰VPDB)[6]	−30.43[6]					
CO_2 (ppm)	741, 973					
CH_4 (ppm)	53, 26					

[1]In Halm and Guldager (2012) range of values between August 2007, March 2008, May 2008. [2] Range from point of 'spring' to surface discharge into lake, sampled September 2010. [3]Yukon Flats summary statistics for shallow lakes (n = 129) from Heglund and Jones (2003). [4]Concentration ratio of Donovan (1994). [5]Courtesy of K. Wickland: sample $\delta^{14}C = -150.4$‰, $F_{modern} = 0.8556 \pm 0.0028$. [6]POC = Particulate Organic Carbon, this study, sampled September 2007.

based on the molar fraction of carbon to hydrocarbons that make up lipids, carbohydrates and proteins (Meyers and Teranes, 2001). Biogenic silica ($bSiO_2$) was determined from a single extraction of silica by 0.1 M Na_2CO_3 and modified molybdate-blue spectrophotometry (Mortlock and Froelich, 1989) at Idaho State University Department of Geosciences, Pocatello, ID, United States. The absorbance is normalized to sediment mass and sedimentary silicon content is converted to biogenic opal by a factor of 2.4, assuming 10% water in biogenic silica by weight. All results have an estimated error of <5%, calculated as a coefficient of variation, based on one blank, one sample replicate, and three standard analyses for every 25 samples.

Subsamples for organic carbon (OC) and organic nitrogen percentages used to calculate organic C/N ratios, and for OC isotope analyses were acidified with 1 N HCl, rinsed to neutral, freeze dried and pulverized for combustion to CO_2 and NO_2 by a Carlo Erba^{TM} CN elemental analyzer coupled with a Finnigan Delta^{TM} Advantage isotope ratio mass spectrometer at the Idaho State University Stable Isotope Laboratory, Pocatello, ID, United States. Analytical precision for both OC and nitrogen percentages, calculated from analysis of standards distributed throughout each run, is <0.5%. OC isotope ratios are reported in per mil (‰) as the relative isotope-ratio difference from the international standard Vienna Pee Dee Belemnite (VPDB), defined by $\delta^{13}C_{Org} = [(^{13}C/^{12}C)_{Org}/(^{13}C/^{12}C)_{VPDB}] - 1$. Analytical precision, calculated from standards distributed throughout each run, is ±0.2‰.

Pollen samples throughout core B were analyzed at ∼20-cm intervals through the upper 120 cm and at ∼10-cm intervals through the basal 60 cm at the University of Southampton, United Kingdom; four samples were scanned for pollen (low counts) from core A basal silts at 194, 197, 202, 204 cm depth. These samples were also analyzed for macrofossils (>150 μm size fractions) at the U.S. Geological Survey, Lakewood, CO, United States. Core B sample volumes were all 1-cm^3 whereas 4-cm^3 was sampled for the organic-poor basal silts of core A. Preparation, identification and counting followed the conventional methods of Faegri and Iverson (1989). Reference material held at the University of Southampton was consulted as required. The pollen sum was >300 terrestrial pollen grains, except in the lowermost two units of core B and for the scan counts at the base of core A, where concentrations were extremely low. The pollen percentage diagram for core B was plotted using TILIA software (Grimm, 1990). Core B macro-charcoal (>125 μm) was counted from 1-cm^3 samples taken at 4-cm intervals at the University of Southampton, United Kingdom. Samples were deflocculated in 10% sodium pyrophosphate for 24 h. A 5% bleach solution cleared the color from organic matter other than charcoal. Samples were then sieved and counted at x20 magnification. All charcoal pieces

in the sample were counted, thereby providing charcoal concentrations (count/cm^3).

The sediment chronologies are based on accelerator mass spectrometry (AMS) radiocarbon measurements on fine charcoal and selected terrestrial and aquatic macrofossils graphitized at the Institute for Arctic, Antarctic and Alpine Research at the University of Colorado, Boulder, CO, United States (CURL lab numbers), the Lawrence Livermore National Laboratory, Livermore, CA, United States (CAMS lab numbers), and the U.S. Geological Survey Radiocarbon Laboratory, Lakewood, CO, United States (USGS lab number); pollen extracts, prepared at LacCore, were dated at a few stratigraphic intervals where no macrofossils were present (Brown et al., 1993). Both measured and calibrated radiocarbon ages (Calib 7.0.1; Stuiver and Reimer, 1993) are reported but only calibrated ages (cal yr BP; 1950) are used for discussion (**Table 3**). ^{210}Pb was measured on 0.5 cm

TABLE 3 | Greenpepper lake chronostratigraphic data.

Core Depth (cm)	Material	^{210}Pb Age[2] (year AD)	^{210}Pb Age Error	AMS ^{14}C Lab #	^{14}C Age (^{14}C yr BP)	Measured δ^{13}C (‰ VPDB)	Calibrated Age[1] (Cal yr BP)	1σ–range (Cal yr BP)	Offset[3]	Corrected Age
A10										
0	Surface	2010	1.75	–	–	–	−60	–	–	−60
0.5	Lead-210	2009.6	1.72	–	–	–	−58.6	–	–	–
1.5	Lead-210	2001.9	1.98	–	–	–	−49.1	–	–	–
2.5	Lead-210	1990.0	1.56	–	–	–	−36.8	–	–	–
3.5	Lead-210	1976.9	1.68	–	–	–	−23.6	–	–	–
4	Lead-210	1970.7	1.81	–	–	–	−17.7	–	–	–
4.5	Lead-210	1964.8	2.03	–	–	–	−11.8	–	–	–
5	Lead-210	1958.5	2.26	–	–	–	−5.2	–	–	–
5.5	Lead-210	1952.4	3.11	–	–	–	0.4	–	–	–
6.5	Lead-210	1938.9	5.45	–	–	–	15.2	–	–	–
7.5	Lead-210	1919.4	8.90	–	–	–	36.5	–	–	–
8.5	Lead-210	1891.9	13.25	–	–	–	66.0	–	–	–
9	Lead-210	1876.9	19.25	–	–	–	80.3	–	–	–
9.5	Lead-210	1862.9	32.43	–	–	–	94.0	–	–	–
10	Lead-210	1837.2	32.43	–	–	–	112.8	–	–	–
42.5	Pollen			CAMS-159532	3055 ± 30	–	3270*	120	−2000	970
62.5	Pollen			CAMS-159533	3820 ± 35	–	4215*	135	−2010	1915
72	Bryophyte			CAMS-179997	2955 ± 35	–	3115*	110	−990	2125
88.5	Charcoal			CAMS-159483	2465 ± 35	–	2565	140	0	2565
113.5	Charcoal			CAMS-159484	3275 ± 50	–	3285	130	0	3285
153.5	Charcoal			CAMS-159485	4845 ± 90	–	5845	200	0	5845
189.5	Pollen			CAMS-159534	9085 ± 45	–	10240*	55	−2755	7480
194.5	*Betula* seed			USGS-1310	7020 ± 110	–	7850	210	0	7850
B10										
0	Surface			–	–	–	−60	–	0	−60
30.5	Bryophyte			CAMS-180052	2590 ± 280		2670	515	−990	1680
157.5	Wood			CURL-14946	5875 ± 20	−25.7	6700	50	0	6700
157.5	Bryophyte			CURL-14963	6680 ± 25	−30.9	7550	65	−850	6700
161.5	Wood			CURL-14947	5635 ± 20	−26.8	6420	40	0	6420
161.5	Bryophyte			CURL-14973	6730 ± 20	−36.2	7590	30	−1170	6420
169.5	Wood			CURL-14982	5845 ± 20	−25.7	6675	75	0	6675
171	Wood			CURL-14962	5820 ± 20	−26.1	6640	100	0	6640
171	Psidium			CURL-15094	6715 ± 20	−4.6	7585	25	−945	6640
172	Charcoal			CURL-14977	6225 ± 20	−23.8	7165	210	0	7165
175	Vascular			CURL-14978	5710 ± 20	−25.4	6490	80	0	6490
C10										
80	Bryophyte			CAMS-179995	2690 ± 50	–	2800	80	−990	1810
100	Bryophyte			CAMS-179995	4610 ± 30	–	5400	75	−990	4410
166	Wood			CURL-16694	4251 ± 25	−29.6	4750	125	0	4750

*[1]Calib 7.0.1, median of 1-sigma range. [2]Constant Rate of Supply (CRS) age model. [3]Difference between pollen and Bacon modeled ages (**Supplementary Figure 3**) or difference between wood and bryophyte at same core depth, or the 990-year wood-bryophyte average. *Excluded from core A Bacon age model.*

intervals for core A from the surface to 26 cm depth at the St. Croix Research Station of the Science Museum of Minnesota (**Table 3**). Although maximum values of 10 pCi/g are considered low, they are typical of high-latitude values and similar to those measured from recent sediments at nearby Track and Twelvemile Lakes (**Figure 1**; Anderson et al., 2018). There is a well-defined break between sediment containing unsupported ^{210}Pb below the relatively smooth down-core declines in supported ^{210}Pb. ^{210}Pb-ages were determined by a Constant Rate of Supply (CRS) age model (Appleby, 2001). An age model for core A was generated with ^{210}Pb and radiocarbon measurements of terrestrial macrofossils using the Bayesian software Bacon (v2.3; Blaauw and Christen, 2011, 2013; **Supplementary Figure 3**) which uses the most recent calibration curve (Reimer et al., 2013) and default prior assumptions.

RESULTS

Bathymetry and Limnology

Water column measurements indicate that Greenpepper Lake is dimictic with summer thermal stratification indicated by declines in temperature, DO, Spc and pH between 4 and 6 m water depth (**Figure 2A**). The hypolimnion below the thermocline is anoxic with a temperature of 6°C, pH of 8.75, and Spc values near 1000 µS/L. The surface pH value of 9 is higher than most Yukon Flats (YF) lakes and surface Spc values of 900 µS/L are two times higher than average (**Table 2**). Calcium and alkalinity concentrations are slightly lower than average whereas sodium, magnesium and chloride are elevated. The lake is supersaturated in carbon dioxide and methane and has high concentrations of dissolved organic (DOC) and inorganic carbon (DIC); a DOC age of ∼125 years was determined by the National Ocean Sciences Accelerator Mass Spectrometer at the Woods Hole Oceanographic Institution (Wickland, 2018 personal communication).

The bathymetric study identified two steep-sided basins ∼15.5 m deep immediately below the lake's western margins separated by a narrow sill between 5 and 6 m water depth (**Figure 1C**). Most other areas have water depths of ∼5 m and low-gradient slopes dip toward the depocenters to the west. Littoral shorelines are lined with horsetail (*Equisetum* sp.) and sedge (*Scirpus* sp.) and water depths between 3 and 1 m host abundant pond weeds (*Potamogetonaceae*). Cloud-free historic air photos and remotely sensed imagery (air photography, LandSat, SPOT, and Digital Globe) for ice-free months are available for Greenpepper for the years 1952, 1977, 1978, 1990, 2008, 2009, 2012, and 2017 (**Supplementary Figure 1**). They indicate higher lake levels during the early 1950s, while since ∼1990 the shoreline has been near the 2009 elevation.

Surface inflow to the lake in the form of a permanent stream has not been observed between 2007 and 2018, either in the field or from historic imagery, with the exception of the small point of surface discharge observed in 2010; this represented converging silt-rich sheet-flow originating from a thawed slump-block area within the burn along the southern lake margins

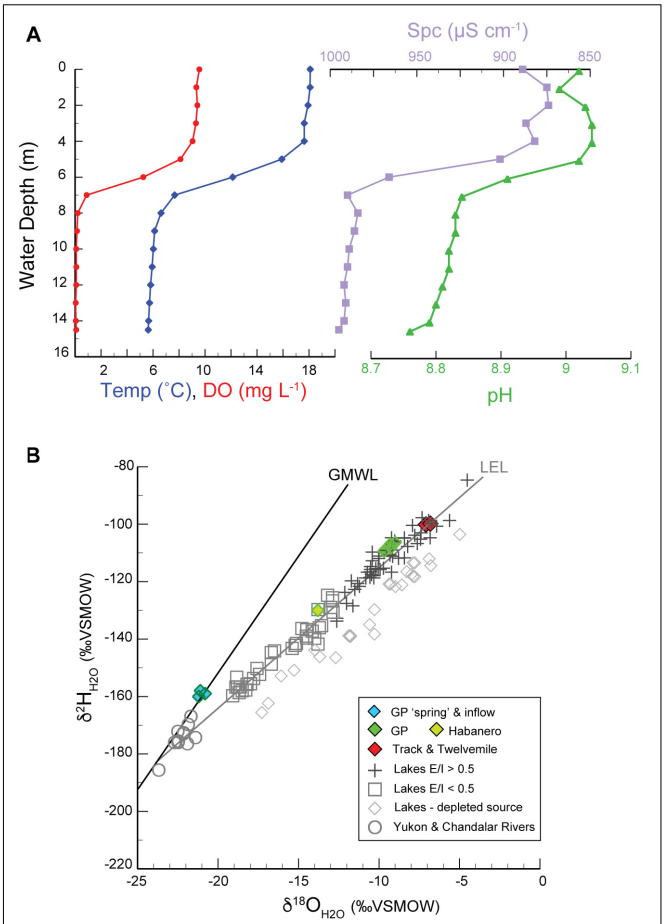

FIGURE 2 | (A) Greenpepper Lake water column physical properties measured within the core A basin in July 2010; temperature [Temp (°C)], dissolved oxygen [DO (mg L^{-1})], specific conductivity [Spc (µS cm^{-1})], and pH. **(B)** Oxygen and hydrogen isotope values for Greenpepper Lake (dark green diamonds), Habanero Pond (light green diamond), the 'spring' and inflow (blue diamonds), Track and Twelvemile Lakes (red diamonds), with reference Yukon Flats lake and river samples from Anderson et al. (2013; open symbols) and the Global Meteoric Water Line (GMWL). Reference lakes are characterized by evaporation to inflow ratios (E/I) as either open (E/I < 0.5 = open squares) or closed (E/I > 0.5 = crosses). Regression for open and closed lakes form a Local Evaporation Line (LEL) with a slope of 4.88. Reference lakes with more isotopically depleted sources such as snow and/or permafrost thaw form a third group (open diamonds) and are not included in the LEL regression.

(**Figure 3A**). The source of the surface stream was an active point of subsurface discharge within the banks of a thaw-collapse channel, found ∼100 m upslope to the southwest from this location and is referred to here as a 'spring' (**Figure 1C**). It is unknown if this area has been a perennial source of inflow into the lake prior to the 2009 fire or if it has continued to supply water since.

The lake has no surface outflow and lake-water isotope compositions are highly enriched in heavy isotopes relative to lakes in the region, indicating significant water loss by evaporation (**Figure 2B**). The Yukon Flats local evaporation line (LEL) has a slope of 4.89 (R^2 = 0.88) for lakes sourced

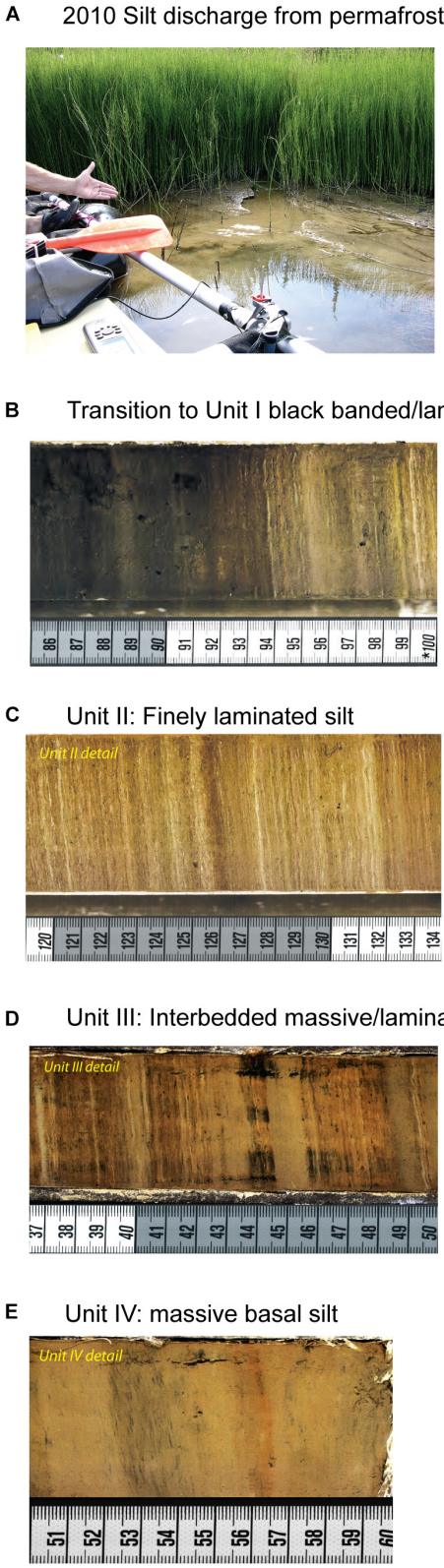

FIGURE 3 | (A) Point of surface discharge into Greenpepper Lake observed in 2010 with high silt loads originating from southern lake margins undergoing *(Continued)*

FIGURE 3 | Continued
active permafrost thaw following a July 2009 forest fire (**Figure 1C** and **Supplementary Figure 1**). High-resolution image details from the four major lithologic facies identified in core A with scale units in cm. **(B)** Uppermost Unit I black banded/faintly laminated silt and the transition to upper Unit II; **(C)** Unit II finely laminated brown silt; **(D)** Transition Unit III with interbedded massive silt with finely laminated silt intervals; **(E)** Massive, brown basal silt Unit IV. Image brightness and contrast was adjusted to enhance sediment features.

by precipitation (from Anderson et al., 2013) and the intercept with the Global Meteoric Water Line (GMWL) has a $\delta^{18}O$ value of −23‰. Greenpepper 'spring' and inflow water isotope values are positioned slightly higher on the GMWL, with a $\delta^{18}O$ value of −21‰, and their linear regression with lake water has a slightly lower slope than the LEL (4.37, R^2 = 0.99). The extent of water loss by evaporation at Greenpepper Lake is further illustrated by applying the isotope mass balance methods discussed in Gibson et al. (2016) used to estimate the ratio of lake evaporation to inflow (E/I). The Greenpepper E/I value of 0.96 (from Anderson et al., 2013) indicates that water loss by evaporation during the ice-free season is nearly two times the amount of inflow gain.

Comparison of major-ion concentrations of Greenpepper Lake and inflow (**Table 2**) when converted to molar compositions indicate a notable shift in molar Mg:Ca from near 0.5 (inflow) to between 5 and 6 (lake). This is among the highest known regionally and largely reflects precipitation of calcium carbonate within the lake water column, promoted by evaporative concentration and dissolved carbon equilibration, and its burial in sediments. There is also a nearly four-fold increase in specific conductance, a proxy for total dissolved solids (TDS). Chloride ion, considered approximately conservative in its behavior in dilute lakes, is elevated 50 to 100-fold relative to inflow, reflecting the balance of conservative solutes. If chloride is delivered solely by inflow and previous net evaporation estimates are correct (23 cm in Anderson et al., 2018), then lake hydraulic residence times are ∼25 years. Shorter residence times only arise if there are large, unrecognized chloride influxes from atmospheric or geologic sources. This result is consistent with the residence times implied by the isotopic enrichment and the relatively old radiocarbon age of DIC; old DIC may be accounted for through the combined effect of long hydraulic lake residence times and contribution of dissolved carbon from respiration of ancient remnant organic matter in the watershed and from thawed permafrost sources.

Lake Sediments

Sediment cores were obtained on a transect from deep to shallow water at depths of 10, 5, and 1.85 m below modern levels (BML). At each core location, overlapping stratigraphic intervals were visually matched and confirmed or adjusted by bulk sedimentary data to form composite core sections (**Supplementary Figure 2**). Core A is 205 cm in length (**Figures 4**, **5**), core B is 188 cm (**Figures 5**–**7**) and core C is 195 cm (**Figures 5**, **8**). Below are detailed lithologic unit descriptions, including smear slide mineralogy, and their timing

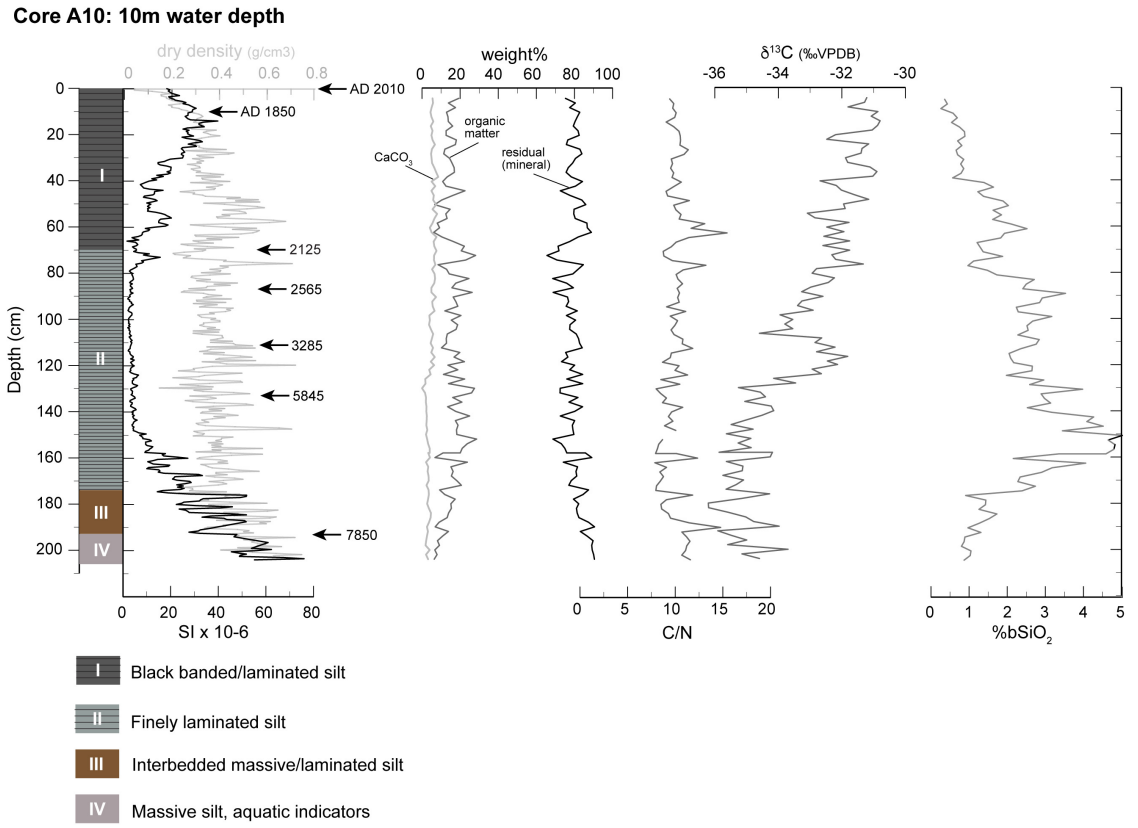

FIGURE 4 | Sediment core A lithology, physical and geochemical properties, and radiocarbon ages in cal yr BP (arrows): magnetic susceptibility (SI × 10^{-6}), dry bulk density (g/cm^3), weight percentages (weight%) calcium carbonate ($CaCO_3$), organic matter, and residual mineral matter, organic C/N ratio, organic matter $\delta^{13}C$ values (‰VPDB), and weight percentages of biogenic silica (%$bSiO_2$).

and environmental interpretation which are briefly summarized in **Table 4**.

Core A (10 m BML)

Basal unit IV (205-195 cm depth; **Figures 3E**, **4**; >8,500 cal yr BP based on pollen stratigraphy – see below) is composed of near-massive, clayey and slightly calcareous dark gray-brown medium silt. Bulk sediments are high in magnetic susceptibility (40–60 SI), and dry bulk density (∼0.6 g/cm^3), and low in $bSiO_2$ (1%) and calcium carbonate (<5%). Organic matter is present in trace quantities as very fine fragmentary material; C/N ratios are ∼11 and $\delta^{13}C$ values vary between −33 and −34‰. In smear slides, mafic minerals are relatively abundant (est. 15–20% in silt size range) and erosionally resistant accessory minerals (zircon, rutile) are observed in addition to diagenetic sulfide minerals, including both highly reactive monosulfides and abundant pyrite framboids up to 20 μm in diameter. Other diagenetic indicators, such as opaque coatings on quartz and feldspar grains, are common. The silt grains are dominantly sub-angular with modal size near 30 μm. The presence of microzooplanktonic *Daphnia* ephippia (water flea egg cases) indicates standing water (permanent or seasonal). Pollen at 204 cm is dominated by *Betula*; *Alnus* is absent and there are abundant fungal hyphae. Fluctuating *Picea* percentages from 204 cm (<10%) to 202 cm (29%) and 197 cm (<10%) may partly reflect reworked sediments as many grains in all samples are poorly preserved (**Supplementary Table 1**). Alternatively, the fluctuations could reflect a pond edge environment, where large amounts of floating *Picea* grains are blown shoreward. Despite these uncertainties, the high *Betula* count and lack of *Alnus* indicates the sediments are older than ∼8,500 cal yr BP, according to ages that bracket similar assemblages at 6L and Sands of Time (SoT) lakes (Edwards et al., 2016).

Unit III (195-173 cm depth; **Figures 3D**, **4**; ∼8,000 to 7,000 cal yr BP) is a transitional sequence, characterized by alternating cm-scale bands of finely laminated reddish-brown silt and massive gray brown silt. High magnetic susceptibility and dry bulk density and low $bSiO_2$ and calcium carbonate are similar to Unit IV. Organic matter was present in trace quantities as very fine fragmentary material; C/N ratios fluctuate near ∼10 and $\delta^{13}C$ values vary between −34 and −36‰. The prominent gray bands, composed of well-sorted medium silt, lack much of the obvious reactive Fe apparent in other components. Elsewhere, evidence is widespread for diagenesis involving Fe phases (oxide coatings on sand grains, co-occurring ferric oxides and sulfides; vivianite occurrences) and carbonates (resorption textures). The earliest (lowermost) laminated sequence at 194 cm has abundant *Daphnia* sp. in addition to rare insect parts and a birch seed

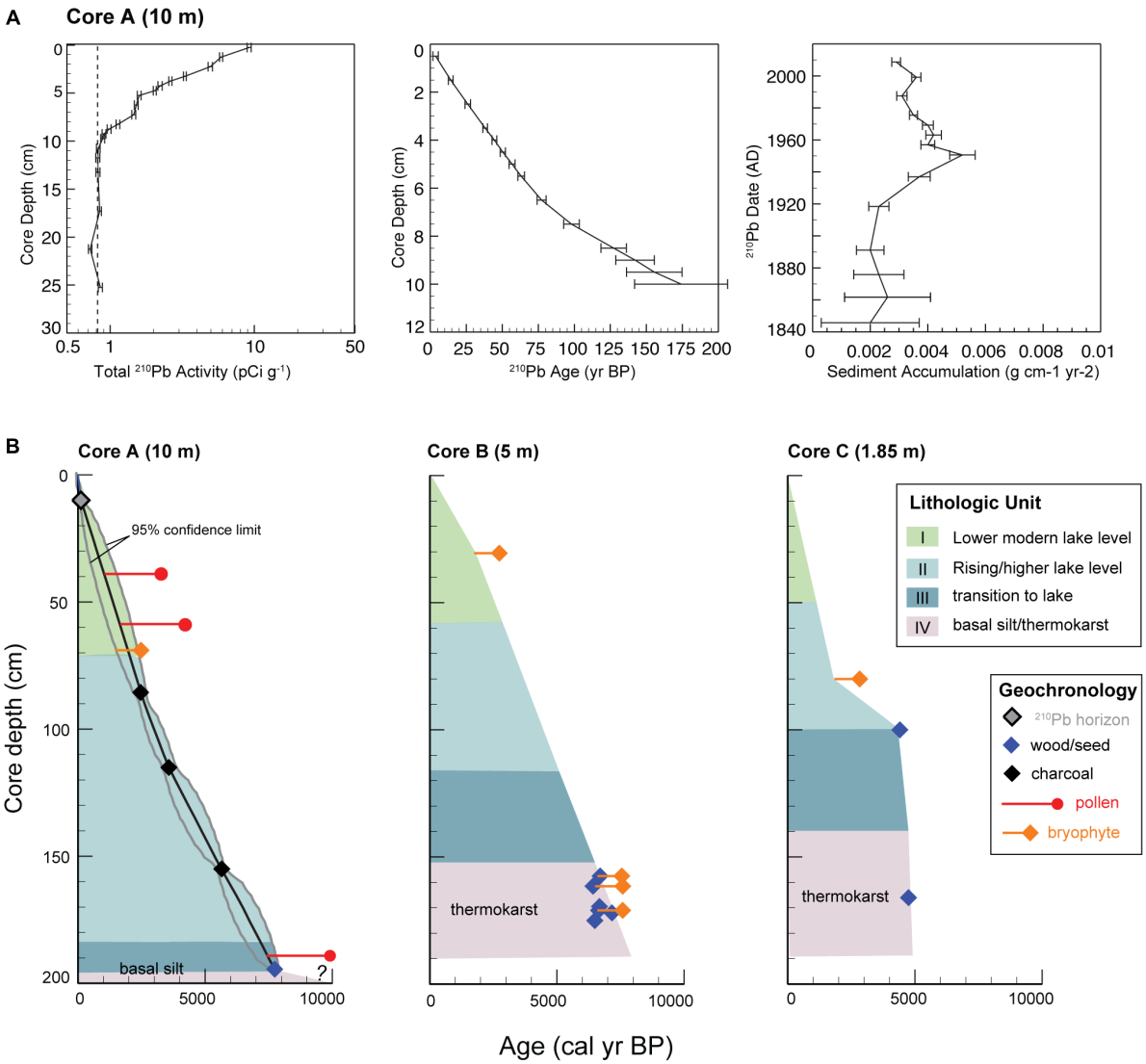

FIGURE 5 | (A) Sediment core A ^{210}Pb activity, CRS ages, and sediment accumulation rates with error ranges. **(B)** Core A (10-m water depth) Bacon age model (mean is black line and gray lines indicated 95% confidence limits; **Supplementary Figure 3**) shown with lithologic units and all calibrated radiocarbon ages (cal yr BP) for core B (5-m water depth) and core C (1.85 m water depth); charcoal (black), pollen (red) and aquatic bryophytes (orange). The radiocarbon age symbols are larger than calibrated 1-sigma age errors and tails on the pollen and bryophyte symbols reflect age offsets (**Table 3**).

(*Betula*. sp.) that provided an age of 7850 cal yr BP. The pollen is dominated by *Betula* (74%) and *Picea* (22%), and one grain of the aquatic macrophyte *Myriophyllum* was counted.

Unit II (173-70 cm depth; **Figures 3C**, **4**; ∼7,000 to 2000 cal yr BP) is a deep lacustrine facies of continuous finely laminated (<1 mm) very dark gray-brown, moderately calcareous and medium grained silt. The laminae are distinct but frequently irregular and often appear knotted or crumpled as well as bundled into 1–5 cm bands by oxidized Fe phases. The contact with lower Unit III is reflected by lower magnetic susceptibility (<10 SI) and dry bulk density (∼0.35 g/cm^3), and higher $bSiO_2$ (5%), organic matter (10–20%) and calcium carbonate (∼5%). Notwithstanding the higher $bSiO_2$ percentages, diatoms rarely occur in smear slides. Organic matter is amorphous and the only identifiable fragmentary material is bryophytic; organic C/N ratios of ∼10 are stable throughout the unit as $\delta^{13}C$ values increase up core to >−33‰. Purified pollen provided an age of 10,240 cal yr BP at 189 cm, but comparison with the *Betula* seed age indicates that the pollen age is at least ∼2700 years too old (**Table 3** and **Figure 5**). The age model indicates that the top of the unit dates to ∼2080 cal yr BP, which is supported by a corrected bryophyte age of 2125 cal yr BP. Occasional laminae and nodules are dominated by fine (<10 μm) endogenic carbonate, typically twinned. Occasional gray laminae are dominated by angular to sub-angular siliciclastic medium silt with minor carbonate. Peaks in magnetic susceptibility correspond to concentrations in reactive Fe textures with abundant

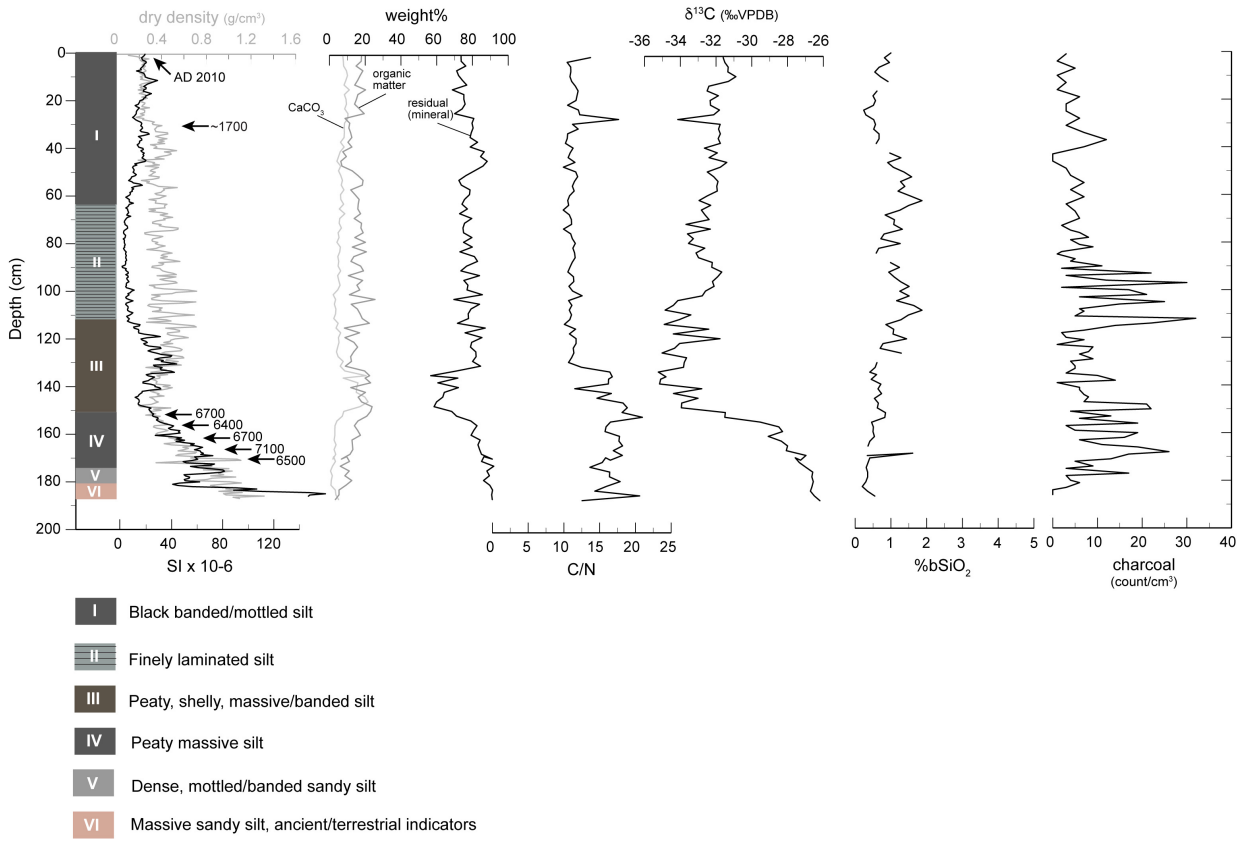

FIGURE 6 | Sediment core B lithology, physical and geochemical properties, and radiocarbon ages in cal yr BP (arrows): magnetic susceptibility (SI × 10^{-6}), dry bulk density (g/cm^3), weight percentages (weight%) calcium carbonate ($CaCO_3$), organic matter, and residual mineral matter, organic C/N ratio, organic matter $\delta^{13}C$ values (‰ VPDB), weight percentages of biogenic silica (%$bSiO_2$), and charcoal abundance (count/cm^3).

opaque framboids (sulfides) and Fe oxides as crystallites and grain coatings. The initial near-black core face color oxidized within 72 h as further indication of readily oxidized Fe-monosulfide minerals.

Unit I (70-0 cm depth; **Figure 3B**; ∼2000 to −60 cal yr BP) is a lacustrine lithology that reflects a shift to near-black silt with diffuse to discontinuous lamination. There is an increase in magnetic susceptibility (∼40 SI) and decline in $bSiO_2$ as percentages of carbonate and OC remain unchanged. Occasional pulses of medium to coarse-grained sub-angular silt occurring as 1-mm gray clastic laminae with mafic minerals and detrital zircons correspond to a rise in magnetic susceptibility at 75-70 cm (20 SI) as the laminations become less distinct, and at 60-58 cm, where they are prominent. Carbonates include diverse endogenic forms, apparent detrital grains and occasional diagenetic nodules. Recognizable diatoms are absent and organic matter is amorphous. Organic C/N ratios decline slightly (∼9.5 to 9) as $\delta^{13}C$ values increase to −31‰. The near surface Unit I sediments (<20 cm depth) are dark black watery silt that produced a distinctly pungent odor, although free of H_2S. The sediments contained dispersed mineral grains of pyrite, visible in bright sunlight and subsequently confirmed by x-ray diffraction (xrd) and petrographic observations of smear slides. The presence of highly reactive Fe-monosulfides prominently influence sediment color and its stability.

The ^{210}Pb age model confirmed the presence of an intact sediment-water interface (**Figure 5**) and indicates that the upper 10 cm of sediment accumulation occurred during the past ∼175 years (0.06 cm/yr), including a doubling of mass accumulation (g cm^{-1} yr^{-2}) between AD 1920 and 1950. The average core A sedimentation rates based on the depths of the ^{210}Pb horizon and the charcoal ages used in the Bacon model is ∼0.03 cm/yr. Purified pollen from Unit I at 42.5 and 62.5 cm depth produced stratigraphically ordered ages of 3270 and 4215 cal yr BP, respectively, with reasonably consistent sedimentation rates of ∼0.02 cm/yr (**Figure 5**). However, comparison with modeled ages of 1050 and 1710 cal yr BP (**Supplementary Figure 3**) indicates that they are likely ∼2000 and 2110 years too old, respectively. Although it is not certain, the old pollen extract ages obtained in this study likely reflect the inclusion of ancient remnant organic matter fragments from the watershed and thawed permafrost sources.

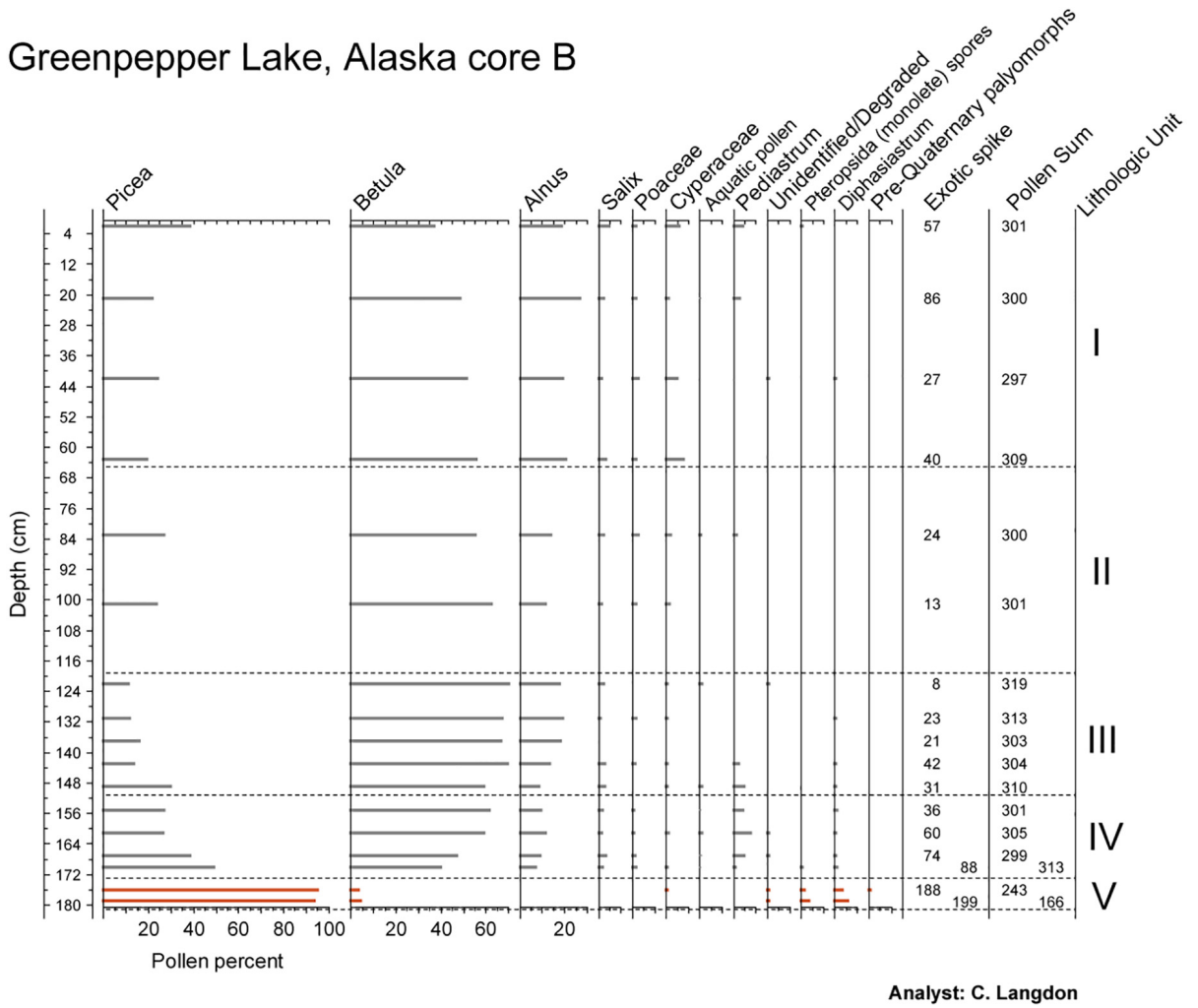

FIGURE 7 | Core B pollen type percentages by core depth with pollen sum amounts. Basal unit *V* values are highlighted in orange.

Core B (5 m BML)

Basal Unit VI (187 to 180 cm depth; **Figures 5–7**; 6700 to 6400 cal yr BP) is massive dark-gray slightly sandy silt, and the overlying Unit V (180 to 175 cm depth) consists of slightly sandy, crudely banded silt (50–60 μm modal grain size range). Both units are compact and micaceous, with angular to sub-angular coarse silt, and minor carbonate and fragmentary organic matter. Abundant biotite (chlorite?) grains have opaque and hematitic coatings. Other mafic minerals are common and trace amounts of weathering resistant heavy minerals, such as rutile, occur. Magnetic susceptibility and dry bulk density values are high (140 to 60 SI, and 1.1 to 0.8 g/cm^3) and percentages of $bSiO_2$, organic matter and carbonate are low (<1%, <5%, <10%, respectively). Charcoal concentrations are low (<5 count/cm^3), and low pollen/spore counts (150–250 grains) are dominated by *Picea*, plus monolete spores, *Diphasiastrum* spores, and pre-Quaternary palynomorphs (**Figure 7**). Wood pieces, aquatic bryophytes, and *Pisidium* shells from the same depths (157.5, 161.5, 169, and 171 cm) had ages between 7600 and 6700 cal yr BP (**Table 3**). The wood ages of 6700, 6420, 6675, and 6640 cal yr BP with increasing depth are consistently younger than the paired aquatic macrofossils by ∼850 to 1170 years (average 990 years) and most accurately date the timing of this 'trash' layer formation to ∼6400–6700 cal yr BP.

Unit IV (175 to 150 cm depth; **Figures 5–7**; ∼6400 to ∼6000 cal yr BP) transition is marked by a distinct contact with near-black, massive, moderately calcareous, very silty fibrous peat with abundant macrofossils of bryophyte, wood, charcoal, and *Pisidium* shells. Bryophyte fragments increase in abundance and preservation upward. Magnetic susceptibility and dry bulk density abruptly decline (<20 SI, 0.35 g/cm^3) as percentages of organic matter and carbonate begin to increase, with high C/N ratios (15–20) and declines in $\delta^{13}C$ values from −27 to −34‰. Diverse carbonate forms include fine (<10 μm) twinned endogenic laths and blocky detrital grains. Charcoal counts rise (10–20 count/cm^3), as do pollen percentages with an assemblage

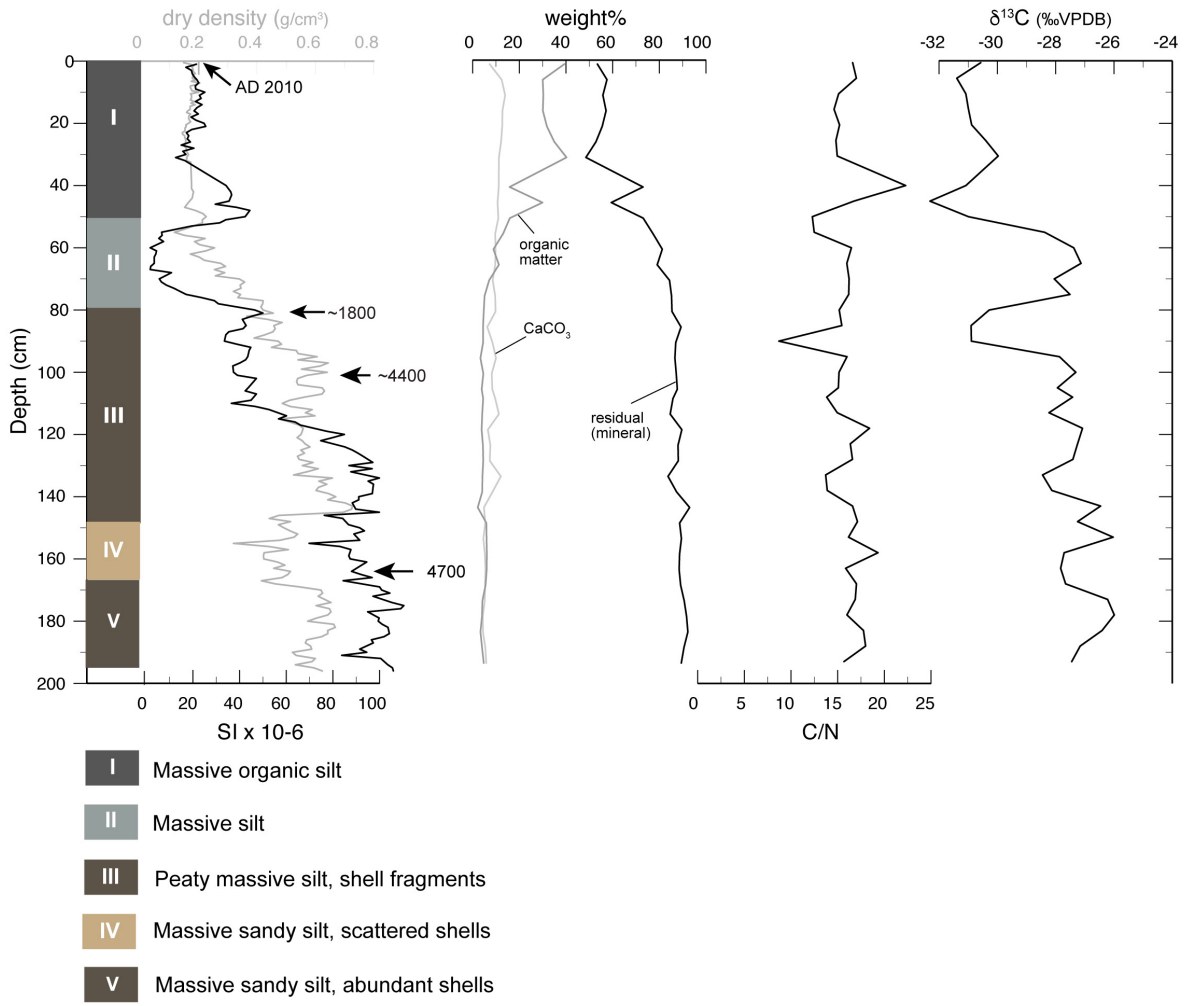

FIGURE 8 | Sediment core C lithology, physical and geochemical properties, and corrected radiocarbon ages in cal yr BP (arrows): magnetic susceptibility (SI × 10^{-6}), dry bulk density (g/cm^3), weight percentages (weight%) calcium carbonate ($CaCO_3$), organic matter, and residual mineral matter, organic C/N ratio, organic matter $\delta^{13}C$ values (‰ VPDB).

dominated by *Beluta*, *Picea*, and rising *Alnus*. The first aquatic indicators (*Pediastrum* cell nets) in the core B pollen record appear in unit IV.

Unit III (150 to 112 cm depth; **Figures 5–7**; ∼6000 to ∼5000 cal yr BP) is a transition lithology with a distinct contact to dark gray-brown crudely banded calcareous silt with abundant gastropod shells. Transition into this unit is reflected by a rise in magnetic susceptibility (30–40 SI), dry bulk density (0.4 g/cm^3), and organic matter and carbonate percentages (20%) with high C/N ratios (15–20) and low $\delta^{13}C$ values (−35‰). Carbonate occurs in diverse forms including fine, irregular silt, complex micritic aggregates, and subordinate but prominent large (>30 μm) ellipsoidal scales. Charcoal counts decline (5–10 count/cm^3) and the pollen assemblage is dominated by *Beluta* (60%), with *Picea* and *Alnus* both 10–15%. *Pediastrum* values decline.

Unit II (112 to 65 cm depth; **Figures 5–7**; ∼5000 to ∼2000 cal yr BP) is a lacustrine lithology with a gradational contact characterized by upward development of finely laminated and banded dark gray-brown, moderately calcareous, silt. Prominent gray laminae are well-sorted angular to sub angular silt with prominent mafic minerals, and trace occurrences of zircon and rutile. Very thin, clotted laminae dominated by twinned endogenic carbonate occur episodically throughout. Magnetic susceptibility declines (<10 SI) and dry bulk density values stabilize (0.3 and 0.5 g/cm^3) as $bSiO_2$ percentages rise slightly (1–2%), and percentages of carbonate decline (<10%) and percentages of organic matter, evident as fine fragmentary material and occasional coarser plant material, stabilize (10–20%). C/N ratios stabilize at a lower value of 10 and $\delta^{13}C$ values rise slightly before stabilizing near −32‰. Charcoal concentrations in the lower half of the unit are significantly

TABLE 4 | Greenpepper Lake sediment core lithology, interpretation, and estimated ages.

Core	Unit	Lithologic Description	Environmental Interpretation	Age (cal yr BP)
A	I	Near black silt: banded to faintly laminated, sulfidic and carbonate bearing	Modern depth, 10 m	Present – ∼2000
	II	Gray-brown silt: finely laminated	>10 m water depth, suboxic hypolimnion	∼2000 – 7000
	III	Reddish brown silt: interbedded laminated and massive gray intervals	Transition to lake >5 m water depth	∼7000 – 8000
	IV	Dark gray-brown silt: massive	Shallow thaw pond	>8,000
B	I	Near black silt: faintly banded or mottled, sulfidic and carbonate bearing	Modern depth, 5 m	Present – ∼2000
	II	Very dark gray-brown silt: finely laminated	>10 m water depth, suboxic hypolimnion	∼2000 – 5000
	III	Gray to dark gray-brown peaty silt: massive, fibrous, shelly	Littoral zone <2 m water depth	∼5000 – 6000
	IV	Near-black fibrous peaty silt: massive, bryophyte rich with abundant macropores	Reworked shoreline	∼6400 – 6000
	V	Near-black sandy silt: dense, mottled, or crudely color banded	Active thermokarst	∼6400 – 6700
	VI	Dark-gray sandy silt: dense, massive	Active thermokarst	>6700
C	I	Dark brown organic silt: massive	Modern depth, 1.85 m, Littoral zone	Present – ∼2000
	II	Near black silt: massive, scattered bryophyte and shell fragments	Nearshore, reworked	∼2000 – 4000
	III	Peaty silt grading upward to dark gray-brown silt: massive with shell fragments throughout	Nearshore, reworked	∼4000 – 5000
	IV	Gray-brown sandy silt: massive with scattered shells and abundant macropores	Active thermokarst	∼5000
	V	Gray to dark gray-brown very sandy silt: massive, abundant shell fragments throughout	Active thermokarst	∼5000

higher (up to 30 count/cm^3) and then decline to low values (<15 count/cm^3). Pollen is dominated by *Betula*, *Picea,* and *Alnus*.

Unit I (65 to 0 cm depth; **Figures 5–7**; ∼2000 to −60 cal yr BP) is a lacustrine lithology of near-black medium silt where gradational loss of laminae to a mottled texture is accompanied by a rise in magnetic susceptibility (30–40 SI), declining dry bulk density (0.3 g/cm^3), and a slight rise in organic matter percentages (15–20%). Mineralogy is sulfidic and moderately calcareous while the silt is dominated by angular to sub-angular quartz and feldspar with subordinate pyroxene and other mafic minerals. Opaque phases include framboidal pyrite (20 μm in diameter) and reactive Fe-monosulfides. Charcoal counts remain generally low, and the pollen continues to be dominated by *Betula*, *Picea* and *Alnus*. *Cyperaceae* pollen is present at 5–10% and *Pediastrum* increases in the uppermost levels.

Core C (1.85 m BML)

Core C was taken within the littoral zone in an area of abundant submerged vegetation, and the five recognized lithostratigraphic units all belong to near-shore or littoral facies.

Basal units V (195 to 168 cm depth) and IV (168 to 143 cm depth; **Figures 5**, **8**; ∼5000 cal yr BP) are gray-brown massive to crudely banded, locally mottled, slightly calcareous, sandy silt with abundant shell fragments. Both units are characterized by high magnetic susceptibility (80–100 SI) and high dry bulk density (0.4–0.6 g/cm^3). Percentages of OC and carbonate are low (<10%), C/N ratios are high (15–20) and δ^{13}C values are high (−28 to −26‰). A radiocarbon age from wood at 166 cm depth of 4750 cal yr BP dates the reworked deposition (**Table 3**).

Unit III (143 to 80 cm depth; **Figures 5**, **8**; ∼5000 cal yr BP) is reflected by a distinct contact to moderately calcareous peaty silt which grades upward to dominantly silt, as reflected by step declines in magnetic susceptibility, and dry bulk density, but little change in percentages of carbonate and organic matter. A date of 5400 cal yr BP from a bryophyte overlaps with the age of wood at 166 cm depth in Unit IV, indicating significant reworking (**Table 3**). Diverse carbonate forms include fine irregular scraps, large tabular or ellipsoidal grains, and ostracode shell fragments. A prominent negative excursion in δ^{13}C from values of −27 to −30‰ occurs near the top of the unit.

Unit II (80 to 50 cm depth; **Figures 5**, **8**; ∼4000 to 2000 cal yr BP) is marked by a gradational change to near black silt with scattered bryophyte and shell fragments which are reflected by an abrupt rise in δ^{13}C values, declines in magnetic susceptibility and dry bulk density, and are dated by a bryophyte radiocarbon age of 2800 cal yr BP at 80 cm (**Table 3**).

Unit I (50 to 0 cm depth; **Figures 5**, **8**; ∼2000 to −64 cal yr BP) is marked by a subsequent rise in magnetic susceptibility (from 10 to 40 SI) between 55 and 45 cm depth that is followed by an increase in the percentages of organic matter and an abrupt decline in δ^{13}C values (from −28 to −32‰). Near-surface sediments (<20 cm depth) are watery dark brown organic silts with abundant egg cases, shells, and living macrophyte fragments and roots.

DISCUSSION

Evolution of Greenpepper Lake

Whereas the loess uplands represent a permafrost-affected landscape, not all lakes owe their origin primarily to thermokarst. For example, at Sands of Time Lake (SoT; **Figure 1**) silt accumulated during deglaciation between ∼22 and 13 ka in a small pond lying in a swale. However, many owe their origin, at least in part, to thaw of ground ice. Lakes that occupy basins within deep valleys rich in ground ice have proven to be deep where measured (>20 m), suggesting that for these lakes, valley ground ice is likely to have influenced their formation. In other lakes, such as Six Loon (6L) and Dune Two (D2), basal sediments strongly indicate thermokarst origins. Their central

water depths are >10 m (similar to Greenpepper) and their basal silt is overlain by, and/or chaotically interbedded with, terrestrial organic shallow-water sediments or peat, which contains detrital plant material, aquatic molluscs, and charcoal. Chaotic sediment textures and structure are consistent with cryoturbation during the growth of shallow initial ponds that erode and promote collapse of older, underlying sediments. It should also be noted that while trash layers can be prominent, in other cases the boundary between underlying thawed silt (talik) and overlying lake sediments can be subtle. Furthermore, the dilution of aquatic indicators can occur due to the high mobility of thawed silt, its potentially rapid deposition, and/or winnowing by bottom currents or wind disturbance (Hopkins and Kidd, 1988), thus making the onset of lacustrine deposition difficult to determine via biotic proxies.

Our Greenpepper sediment record begins with a basal silt (core A Unit IV), which does not resemble a classic 'trash' layer. However, although silt represents the primary sediment component (∼80%) at all of the core sites throughout the lake's history, the core A basal silts are unique because the gray color and massive texture are in contrast to the dark brown finely laminated facies above this unit (**Figure 3**). Trace macrofossils indicate that basal silt deposition occurred within an aquatic environment that was probably a shallow thaw pond, or even a seasonal pool. Thus, it is likely that additional basal sediments with a 'trash' layer were not retrieved due to equipment limitations. A thaw-pond or seasonal pool environment is consistent with relatively low C/N (10) and low $\delta^{13}C$ values (−33 to −34‰) that reflect organic matter originating as aquatic phytoplankton (**Figure 9**). Low $\delta^{13}C$ values could also reflect depleted carbon sources derived from methane-producing bacteria during early thaw phases (Wooller et al., 2012; Walter Anthony et al., 2014; Davies et al., 2016). The *Betula* seed age of 7850 cal yr BP provides an age for the transition from proto-Greenpepper thaw ponds to a deepening lake and the underlying pollen stratigraphy (dominated by *Betula*, some *Picea*, but virtually no *Alnus*) is similar to that of 6L and SoT lakes for the time period ca 9500 to 8500 cal yr BP. The modern bathymetry suggests two isolated thermokarst basins developed into deeper ponds with sufficiently suboxic hypolimnia for fine laminae preservation at the sediment water interface. Following this reasoning, the 10-m bathymetric contour is used in **Figure 10A** to draw a schematic of the early thaw pond shorelines by ∼9,000 cal yr BP that followed thermokarst initiation.

At the core B location, active thermokarst is clearly evident by the lowermost 25 cm of sediment, which resembles a 'trash' layer composed of massive peaty silt, rich in woody material and charcoal of detrital origin and with high C/N and $\delta^{13}C$ values (**Figure 9**). This material overlies stiff, inorganic silt with a pollen assemblage that includes damaged pre-Quaternary palynomorphs and damaged *Picea* grains. This is not a typical Holocene lake assemblage, and it suggests the presence of older sediment underlying the initial shallow lake; the lake is indicated by relatively high values of cell nets of the aquatic alga *Pediastrum* above ∼170 cm depth. Ages from terrestrial and aquatic material show that reversals and overlaps occur during the period between ∼6700 to 6400 cal yr BP and indicate that detrital material was deposited rapidly and chaotically at this time. The core B location on the 5-m bathymetric contour is used to estimate the expanding shoreline location of the lake by ∼7000 cal yr BP (**Figure 10A**).

The basal sequence at the core C location is composed of detrital 'trash' layers (Units V and IV), with 80 cm of dense, massive to crudely banded, poorly sorted silt, rich in peat, bryophytes and shells indicating some mass transport into the lake but negligible resuspension or mobilization of detrital sediment. Overlapping radiocarbon ages reflect rapid and chaotic deposition over the period ∼5400 to 4750 cal yr BP before a transition to re-worked shoreline facies took place. Comparison with ages of the 'trash' layers in core B indicates that shoreline expansion to the core C location occurred over a 1000 to 2000 year period between ∼7000 and 5000 cal yr BP (**Figures 5**, **10A**).

Between ∼5000 and 2000 cal yr BP, the preservation of fine laminae in Units II of both core A and B (**Figure 5**) indicates a deeper water column where suboxic conditions led to fine laminae preservation at the sediment-water interface. The limnological measurements of the modern water column indicate that declines in temperature, conductivity, and dissolved oxygen between ∼4 and 6 m water depths resulted in some laminae preservation at 10 m (core A) and massive, mottled textures at 5 m (Core B). If oxyclines/thermoclines formed at depths similar to today following the stabilization of Greenpepper Lake's shorelines by ∼5000 cal yr BP, then contrasting sedimentation above and below the boundary provides a means to estimate former lake levels from the sediment cores. Following this model, the fine laminae at core A (unit II) indicate water depths > 5m by ∼9 ka. Subsequent expansion and deepening is indicated by the charcoal age of 5845 cal yr BP within core A laminae (Unit II), which corresponds with core B laminae (Unit II) and the lake transition facies at core C (Unit III), and reflects the establishment of the near-modern Greenpepper bathymetry and shoreline by that time (**Figure 5**). Soon after rising lake levels by ∼5000 cal yr BP, surface overflow could have formed the stranded outflow channel. With an elevation of 211.5 m, the outflow channel requires lake levels ∼4 m higher than modern and water depths of ∼14, 9, and 6 m at the core A, B, and C, locations respectively (**Figure 10A**). It is also possible that earlier thaw-basin configurations could have led to surface overflow, although prominent downward thaw mechanisms for areas rich in ground ice (i.e., where lakes rapidly deepen) would suggest that this is not likely.

By ∼2000 cal yr BP, there was transition to massive or faintly banded sedimentation at the sediment-water interfaces at locations A and B and detrital re-working within Unit II at core C. These changes are consistent with lake-level declines that led to more frequent oxygenation of the hypolimnion and which have persisted to the present day. The lake-level lowering led to continuous littoral sedimentation at core C (Unit I), suggesting shoreline stability. A basin-wide change in Fe-sulfide redox balance and carbonate preservation at the sediment-water interface may also reflect increased hydraulic residence times. Lower lake levels are also supported by

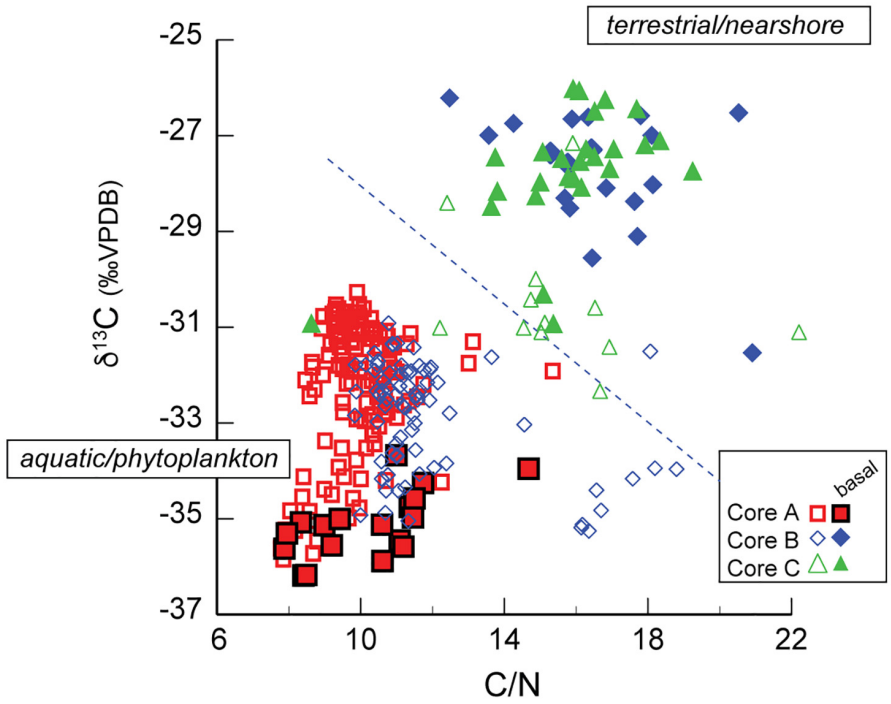

FIGURE 9 | Sediment core organic matter C/N ratios and $\delta^{13}C$ values with a delineation between aquatic/phytoplankton and terrestrial/nearshore organic carbon sources. Symbols for core A are red squares, core B are blue diamonds, and core C are green triangles, with solid symbols for basal sediments and open symbols for lacustrine muds.

higher percentages of *Cyperaceae*, which dominate the shoreline of the lake today.

Holocene Thermokarst and Paleoclimate in the Yukon Flats

The reconstruction of Greenpepper Lake's evolution suggests a thermokarst origin, likely as two adjacent small thaw ponds by ∼9000 cal yr BP that eventually coalesced and developed water depths > 5 m by ∼8000 cal yr BP. Lake-basin expansion and deepening through ∼5000 cal yr BP eventually led to bathymetric stabilization and the likelihood of full talik development (West and Plug, 2008). By this time, lake levels were also ∼4 m above the modern shoreline and the lake was either permanently or intermittently hydrologically open, with surface overflow occurring through the now-abandoned outflow channel. Beginning ∼2000 cal yr BP, there was further water loss and lake levels declined with water losses to near-modern levels; this led to the surficially closed hydrology of the lake today, the longer hydraulic residence times and significant water losses by evaporation.

Clear sedimentary evidence for Greenpepper Lake's thermokarst initiation was not obtained but expansion by thermokarst is clearly shown by the basal parts of cores B and C. Basin formation at 6L and D2 lakes dates to the late glacial/early Holocene transition (∼13,000 to 9,000 cal yr BP), a period of widespread thermokarst across northern Siberia and Alaska attributed to post-glacial warming and effective moisture increases on a landscape vulnerable to thaw (**Figure 10B**; Walter Anthony et al., 2014; Edwards et al., 2016). With the expansion of *Picea* ∼9,500 cal yr BP (Kelly et al., 2013), permafrost would have been increasingly insulated by the development of moss-heath ground cover and thicker organic-rich soils (e.g., Gaglioti et al., 2014; Edwards et al., 2016). Thermokarst initiation at Greenpepper was probably in place by ∼10,000 cal yr BP, just before the expansion of *Picea* forest, although a definitive conclusion is not possible from our data. Currently, heterogeneous ground ice conditions in the loess uplands are observed to exert strong controls on the evolution of thermokarst. For instance, during deglaciation, ground ice may have been closer to the surface and thermokarst relatively quick to initiate. Now, particularly in areas with deeper depths to the tops of syngenetic wedges, thermokarst development may require more extreme disturbance to initiate. High charcoal concentration in the core B trash layer that dates to ∼ 7000 to 6000 cal yr BP may indicate fire-enhanced expansion of Greenpepper Lake. At this time, *P. mariana*, the most flammable species in Alaskan boreal forests, expanded regionally, and is reported to have driven late-Holocene increase in fire frequency (**Figure 10B**; Kelly et al., 2013).

Holocene reconstructions of interior Alaska's water balance indicate increasing lake levels from the early to mid-Holocene, and positive Holocene maxima between ∼5000 and 3000 cal yr BP (Abbott et al., 2000; Barber and Finney, 2000). This wet period also broadly corresponds

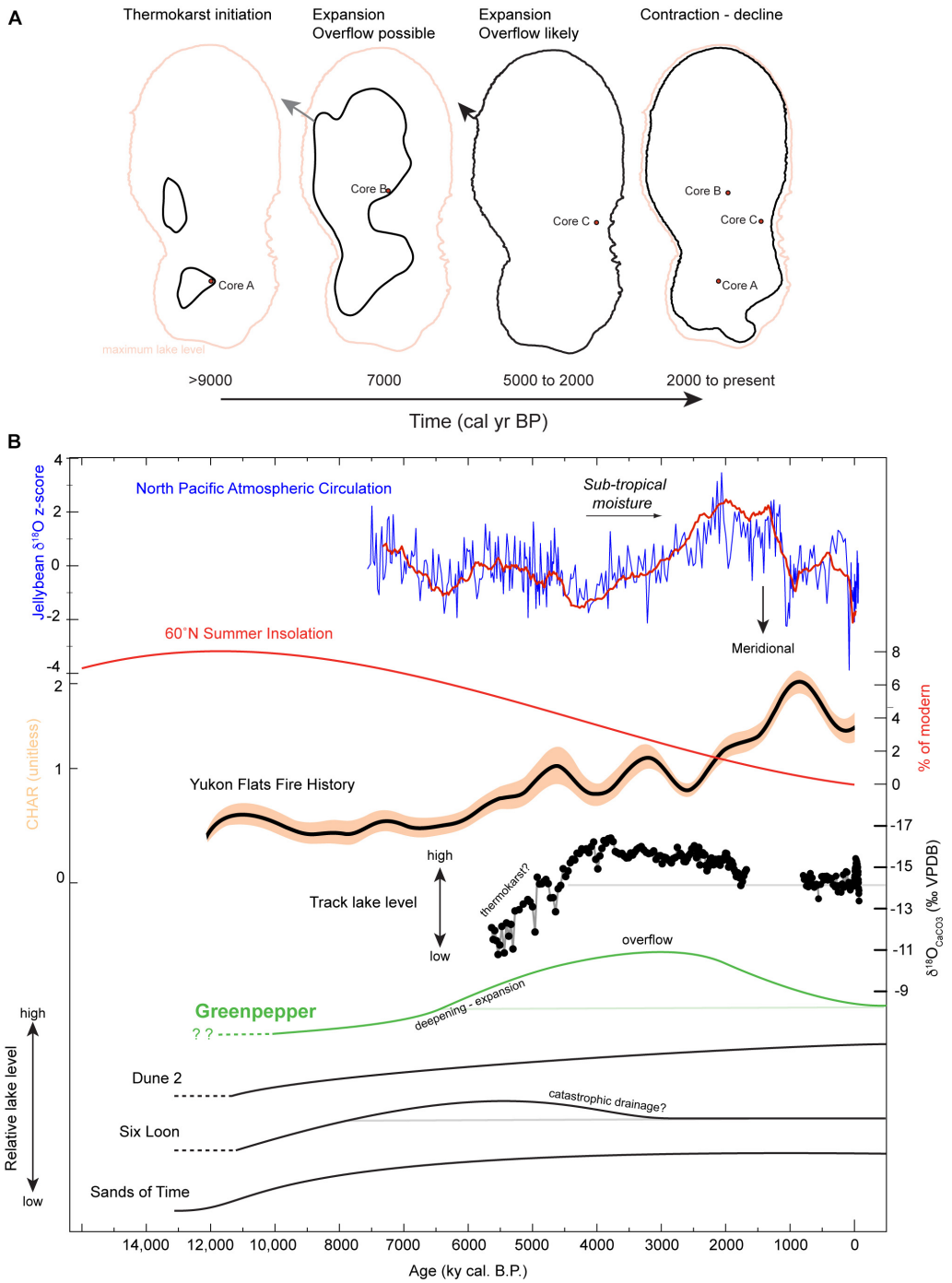

FIGURE 10 | (A) Schematic of Greenpepper Lake shoreline evolution from ~9000 cal yr BP to present. Faint orange outline of outlet elevation shoreline at 211.5 m is shown on each panel for context. **(B)** The evolution of loess plateau lakes on a relative lake level scale including Greenpepper (this study), and SoT, 6L, and D2 Lakes adapted from Edwards et al. (2016). Dashed lines represent periods of 'trash' layer development indicating thermokarst initiation and solid lines indicate periods of lacustrine sedimentation. The loess plateau lake levels are shown with the Jellybean Lake oxygen isotope record of North Pacific atmospheric circulation (*z*-score; Anderson et al., 2016), 60°N summer solar insolation (percent of modern), Yukon Flats fire history (normalized scale, Kelly et al., 2013), and Track Lake levels based on carbonate oxygen isotopes (Anderson et al., 2018).

with our higher inferred lake levels at Greenpepper and at nearby Track Lake, a lower elevation site on the Yukon Flats (**Figures 1A**, **10B**; Anderson et al., 2018). A similar pattern to Greenpepper – of high lake levels followed by partial drainage – may also have occurred ~5000 to 4000 cal yr BP at 6L lake (Edwards et al., 2016). Other proxy records

indicate that this was a period of high effective moisture throughout the northern interior region (Anderson et al., 2018 and references therein). High Greenpepper lake levels could reflect some combination of local declines in evaporative losses and increase in precipitation and, with establishment of deep groundwater-surface water connectivity following talik development, an increase in groundwater influx; all would contribute to an increase in regional-to-local water balance. Similar lake level declines at Greenpepper and Track lakes after ∼2000 cal yr BP strongly implicate regional climate mechanisms for reduced effective moisture. Water-balance declines are also apparent in proxy data from low elevations in the northern interior (Anderson et al., 2007; Bird et al., 2009; Clegg et al., 2011; Rodysill et al., 2018); these declines correspond with cooling temperatures reflected by alpine glacier advances (Barclay et al., 2009; Anderson et al., 2011), which coincide with changes in North Pacific atmospheric circulation (**Figure 10B**; Anderson et al., 2016).

The raised shorelines around the two partially filled lake basins north of Greenpepper also indicate previously higher lake levels (**Figure 1B**). Although not sampled or dated, these two basins share the same relict drainage that intersects Greenpepper, allowing the reasonable assumption that all three lakes overflowed concurrently. Analyses of the digital elevation model indicate an elevation of the overflow channels for the smaller northern lakes that resulted in their catastrophic drainage, whereas the raised relict outflow from Greenpepper did not. However, a subsurface hydrologic connection between Greenpepper and the down-gradient lakes could have facilitated sub-surface water loss if base levels lowered following their catastrophic drainage, although this hypothesis is not tested.

Wetter conditions in low-elevation regions of interior Alaska, such as those after ∼5000 and before 2000 cal yr BP, were most likely to have occured with patterns where North Pacific ocean-atmosphere dynamics, such as the position of the Aleutian Low, enabled moisture to reach interior Alaska from primary moisture sources to the southwest, without encountering major topographic barriers (described in detail in Anderson et al., 2005, 2007, 2011). These patterns also generally delivered warmer air to the region and reflect a late-Holocene shift in dominance to sub-tropical influences on Alaskan climate (Barron and Anderson, 2011; Anderson et al., 2016). Reversal of moisture patterns by ∼2000 cal yr BP may have been restricted to lower elevations in the interior, since the Gulf of Alaska region experienced increasing coastal moisture and high-elevation glacial advance at this time. The Jellybean Lake record of North Pacific circulation regimes indicates that after ∼2000 cal yr BP, intensified Aleutian Low activity led to enhanced meridional flow variability, which is supported by subsequent ice core studies in the Alaska Range and by regional lake synthesis (Steinman et al., 2014; Osterberg et al., 2017; Winski et al., 2017). By amplifying topographic rain-out, intensified meridional flow restricts moisture delivery to the interior, and, with alternating northerly Arctic flow, could result in more frequent colder and drier air masses.

CONCLUSION

This study provides further insight on the evolution of thermokarst and the direction of large-scale changes in effective moisture during the Holocene in the Yukon Flats of Interior Alaska. We have provided detailed documentation of early Holocene thermokarst, basin expansions and stabilization, and subsequent climate-driven lake level variations. Similarities between the late-Holocene moisture records from Greenpepper and Track Lakes lend additional support to previously proposed hypotheses for North Pacific circulation adjustments as a major control on effective moisture changes within interior Alaska during the late Quaternary (Edwards et al., 2001; Anderson et al., 2005; Fisher et al., 2008).

Widespread permafrost instability and thermokarst development in the loess uplands of the Yukon Flats was enhanced during the warm, moist post-glacial period (as compared with earlier cool/cold and dry periods). While thermokarst development slowed with the establishment of boreal forest, it did not cease. After lakes formed, their size and depth has likely been affected directly by atmospheric circulation pattern changes and fire disturbance and indirectly through changes of permafrost, ground ice and sub-surface hydrology. Thus, in a loess landscape characterized by discontinuous permafrost, changes in lakes and drainages are likely to be complex. Changes in lake level and water chemistry may be (but are not always) strongly linked to prevailing precipitation. Loess-upland lake systems characterize several regions of Alaska (Arp and Jones, 2008) and Siberia (Walter et al., 2007). This study provides a framework for future investigation of the high-frequency paleoclimatic and paleolimnological signals embedded in their lithology and sediment chemistry, such as the finely laminated sediments in Greenpepper Lake.

AUTHOR CONTRIBUTIONS

LA conceived the project, collected samples and measurements, developed and interpreted the data, and wrote the manuscript. ME interpreted the pollen and charcoal data, provided background, and reviewed and edited the manuscript. MS collected the core samples, produced lithological descriptions, interpreted the aqueous geochemistry, and reviewed and edited the manuscript. BF collected the core samples, produced the carbon isotope data, and reviewed the manuscript. CL produced the pollen data.

FUNDING

This research is supported by the U.S. Geological Survey Land Change Science Program.

ACKNOWLEDGMENTS

The USGS ScienceBase data release reference for this publication is https://doi.org/10.5066/P9O7255D. We would like to thank

Nikki Guldager, the U.S. Fish and Wildlife Service Yukon Flats National Wildlife Refuge, and Jim Webster, who provided the air transportation and logistical support that made this research possible. LacCore at the University of Minnesota provided core scanning; Tom Guilderson at the Lawrence Livermore National Laboratory and Chad Wolack at the Institute for Arctic, Antarctic and Alpine Research (INSTAAR) at the University of Colorado Boulder, provided AMS radiocarbon ages; Dan Engstrom at the Science Museum of Minnesota provided ^{210}Pb analyses; Alisa Mast at the U.S. Geological Survey Colorado Water Science Center, provided water chemistry data; Million Hailemichael at the Idaho State University Stable Isotope Laboratory provided stable isotope data. We also would like to thank Paco VanSistine for assistance with imagery and GIS, Colin Penn for coulometric measurements, Jeff Honke for pollen slide preparation, Laura Strickland for macrofossil identification, Will Wenban for analyzing charcoal, and Jeremy Haven's for assistance with figures. We appreciate assistance by Jessica Rodysill and the two journal reviewers for constructive criticisms and suggestions that served to significantly improve the manuscript. Any use of trade, firm, or product names is for descriptive purposes only and does not imply endorsement by the U.S. Government.

SUPPLEMENTARY MATERIAL

The Supplementary Material for this article can be found online at: https://www.frontiersin.org/articles/10.3389/feart.2019.00053/full#supplementary-material

REFERENCES

Abbott, M. B., Finney, B. P., Edwards, M. E., and Kelts, K. R. (2000). Lake-level reconstructions and paleohydrology of Birch Lake, Central Alaska, based on seismic reflection profiles and core transects. *Quat. Res.* 53, 154–166. doi: 10.1006/qres.1999.2112

Anderson, L., Abbott, M. B., Finney, B. P., and Burns, S. J. (2005). Regional atmospheric circulation change in the North Pacific during the Holocene inferred from lacustrine carbonate oxygen isotopes, Yukon Territory, Canada. *Quat. Res.* 64, 21–35. doi: 10.1016/j.yqres.2005.03.005

Anderson, L., Abbott, M. B., Finney, B. P., and Burns, S. J. (2007). Late Holocene moisture balance variability in the southwest Yukon Territory, Canada. *Quat. Sci. Rev.* 26, 130–141. doi: 10.1016/j.quascirev.2006.04.011

Anderson, L., Berkelhammer, M., Barron, J. A., Steinman, B. A., Finney, B. P., and Abbott, M. B. (2016). Lake oxygen isotopes as recorders of North American Rocky Mountain hydroclimate: holocene patterns and variability at multi-decadal to millennial time scales. *Glob. Planet. Change* 137, 131–148. doi: 10.1016/j.gloplacha.2015.12.021

Anderson, L., Birks, S. J., Rover, J., and Guldager, N. (2013). Controls on recent Alaskan lake changes identified from water isotopes and remote sensing. *Geophys. Res. Lett.* 40, 3413–3418. doi: 10.1002/grl.50672

Anderson, L., Finney, B. P., and Shapley, M. D. (2011). Lake carbonate-δ18O records from the Yukon Territory, Canada: little Ice Age moisture variability and patterns. *Quat. Sci. Rev.* 30, 887–898. doi: 10.1016/j.quascirev.2011.01.005

Anderson, L., Finney, B. P., and Shapley, M. D. (2018). Lake levels in a discontinuous permafrost landscape: late Holocene variations inferred from sediment oxygen isotopes, Yukon Flats, Alaska. *Arct. Antarct. Alp. Res.* 50:e1496565. doi: 10.1080/15230430.2018.1496565

Appleby, P. G. (2001). "Chronostratigraphic techniques in recent sediments," in *Tracking Environmental Change Using Lake Sediments: Basin Analysis, Coring, and Chronological Techniques*, eds W. M. Last and J. P. Smol (Dordrecht: Kluwer Academic Publishers), 171–203.

Arp, C. D., and Jones, B. M. (2008). *Geography of Alaska Lake Districts: Identification, Description, and Analysis of Lake-Rich Regions of a Diverse and Dynamic State*. U.S. Geological Survey Scientific Investigations Report 2008–5215.

Barber, V., and Finney, B. P. (2000). Late Quaternary paleoclimatic reconstructions for interior Alaska based on paleolake-level data and hydrologic models. *J. Paleolimnol.* 24, 29–41. doi: 10.1023/A:1008113715703

Barclay, D. J., Wiles, G. C., and Calkin, P. E. (2009). Holocene glacier fluctuations in Alaska. *Quat. Sci. Rev.* 28, 2034–2048. doi: 10.1016/j.quascirev.2009.01.016

Barron, J., and Anderson, L. (2011). Enhanced Late Holocene ENSO/PDO Expression along the margins of the Eastern North Pacific. *Quat. Int.* 235, 3–12. doi: 10.1016/j.quaint.2010.02.026

Begét, J. (2001). Continuous Late Quaternary proxy climate records from loess in Beringia. *Quat. Sci. Rev.* 20, 499–507. doi: 10.1016/S0277-3791(00)00102-5

Bird, B. W., Abbott, M. B., Finney, B. P., and Kutchko, B. (2009). A 2000 year varve-based climate record from the central Brooks Range, Alaska. *J. Paleolimnol.* 41, 25–41. doi: 10.1007/s10933-008-9262-y

Biskaborn, B. K., Herzschuh, U., Bolshiyanov, D., Savelieva, L., Zibulski, R., Diekmann, B., et al. (2013). Late Holocene thermokarst variability inferred from diatoms in a lake sediment record from the Lena Delta, Siberian Arctic. *J. Paleolimnol.* 49, 155–170. doi: 10.1007/s10933-012-9650-1

Blaauw, M., and Christen, J. A. (2011). Flexible paleoclimate age-depth models using an autoregressive gamma process. *Bayesian Anal.* 6, 457–474.

Blaauw, M., and Christen, J. A. (2013). *Bacon Manual v2.3.3*. Available at: http://www.chrono.qub.ac.uk/blaauw/bacon.html [accessed November 20, 2018].

Brown, D. R. N., Jorgenson, M. T., Douglas, T. A., Romanovsky, V. E., Kielland, K., Hiemstra, C., et al. (2015). Interactive effects of wildfire and climate on permafrost degradation in Alaskan lowland forests. *J. Geophys. Res. Biogeosci.* 120, 1619–1637. doi: 10.1002/2015JG003033

Brown, T. A., Farwell, G. W., Grootes, P. M., and Schmidt, F. H. (1993). Radiocarbon AMS dating of pollen extracted from peat samples. *Radiocarbon* 34, 550–556. doi: 10.1017/S0033822200063815

Burn, C. R., and Smith, M. W. (2006). Development of thermokarst lakes during the holocene at sites near Mayo, Yukon territory. *Permafrost Periglacial Process.* 1, 161–175. doi: 10.1002/ppp.3430010207

Clegg, B. F., Kelly, R., Clarke, G. H., Walker, I. R., and Hu, F. S. (2011). Nonlinear response of summer temperature to Holocene insolation forcing in Alaska. *Proc. Natl. Acad. Sci. U.S.A.* 108, 19299–19304. doi: 10.1073/pnas.1110913108

Davies, K. L., Pancost, R. D., Edwards, M. E., Walter Anthony, K. M., Langdon, P. G., and Chaves Torres, L. (2016). Diploptene d13C values from contemporary thermokarst lake sediments show complex spatial variation. *Biogeosciences* 13, 2611–2621. doi: 10.5194/bg-13-2611-2016

Donovan, J. J. (1994). On the measurement of reactive mass fluxes in evaporative groundwater-source lakes, sedimentology and geochemistry of modern and ancient saline lakes. *Soc. Sediment. Geol.* 50, 33–50.

Edwards, M. E., Grosse, G., Jones, B. M., and McDowell, P. (2016). The evolution of a thermokarst-lake landscape: late Quaternary permafrost degradation and stabilization in interior Alaska. *Sediment. Geol.* 340, 3–14. doi: 10.1016/j.sedgeo.2016.01.018

Edwards, M. E., Mock, C. J., Finney, B. P., Barber, V. A., and Bartlein, P. J. (2001). Potential analogues for paleoclimatic variations in eastern interior Alaska during the past 14,000 yr: atmospheric circulation controls or regional temperature and moisture responses. *Quat. Sci. Rev.* 20, 189–202. doi: 10.1016/S0277-3791(00)00123-2

Engleman, E. E., Jackson, L. L., and Norton, D. R. (1985). Determination of carbonate carbon in geological materials by coulometric titration. *Chem. Geol.* 53, 125–128. doi: 10.1016/0009-2541(85)90025-7

Faegri, K., and Iverson, J. (1989). *Textbook of Pollen Analysis*, 4th Edn. London: Wiley, 328.

Farquharson, L., Anthony, K. W., Bigelow, N., Edwards, M., and Grosse, G. (2016). Facies analysis of yedoma thermokarst lakes on the northern Seward Peninsula, Alaska. *Sediment. Geol.* 340, 25–37. doi: 10.1016/j.sedgeo.2016.01.002

Fisher, D., Osterberg, E., Dyke, A., Dahl-Jensen, D., Demuth, M., Zdanowicz, C., et al. (2008). The Mt Logan Holocene-late Wisconsinan isotope record: tropical Pacific-Yukon Connections. *Holocene* 18, 667–677. doi: 10.1177/0959683608092236

Fishman, M. J., Raese, J. W., Gerlitz, C. N., and Husband, R. A. (1994). *U.S. Geological Survey Approved Inorganic and Organic Methods for the Analysis of Water and Fluvial Sediment*. U.S. Geological Survey Open-File Report 94–351, 55.

Froese, D. G., Smith, D. G., and Clement, D. T. (2005). Characterizing large river history with shallow geophysics: middle Yukon River, Yukon Territory and Alaska. *Geomorphology* 67, 391–406. doi: 10.1016/j.geomorph.2004.11.011

Gaglioti, B. V., Mann, D. H., Jones, B. M., Pohlman, J. W., Kunz, M. L., and Wooller, M. J. (2014). Radiocarbon age-offsets in an arctic lake reveal the long-term response of permafrost carbon to climate change: radiocarbon age-offsets. *J. Geophys. Res. Biogeosci.* 119, 1630–1651. doi: 10.1002/2014JG002688

Gibson, J. J., Birks, S. J., and Yi, Y. (2016). Stable isotope mass balance of lakes: a contemporary perspective. *Quat. Sci. Rev.* 131, 316–328. doi: 10.1016/j.quascirev.2015.04.013

Glew, J. R., Smol, J. P., and Last, W. M. (2001). "Sediment core collection and extrusion," in *Tracking Environmental Change Using Lake Sediments?: Basin Coring, and Chronological Techniques*, eds W. Last and J. P. Smol (Dordrecht: Kluwer Academic Press), 77–105.

Grimm, E. C. (1990). TILIA and TILIA*GRAPH. PC spreadsheet graphics software for pollen data. *INQUA Work. Group Data Handl. Methods Newsl.* 4, 5–7.

Grosse, G., Jones, B., and Arp, C. (2013). "8.21 thermokarst lakes, drainage, and drained basins," in *Treatise on Geomorphology*, ed. J. F. Shroder (Amsterdam: Elsevier), 325–353.

Halm, D. R., and Guldager, N. (2012). *Water-Quality Data of Lakes and Wetlands in the Yukon Flats, Alaska, 2007-2009*. U.S. Geological Survey Open-File Report 2012–1208.

Heglund, P. J., and Jones, J. R. (2003). Limnology of shallow lakes in the Yukon Flats National Wildlife Refuge, interior Alaska. *Lake Reserv. Manag.* 19, 133–140. doi: 10.1080/07438140309354079

Hopkins, D. M., and Kidd, J. G. (1988). "Thaw lake sediments and sedimentary environments. Thaw lake sediments and sedimentary environments," in *Proceedings of the Fifth International Permafrost Conference*, Vol. 1, Trondheim, 790–795.

Jepsen, S. M., Voss, C. I., Walvoord, M. A., Minsley, B. J., and Rover, J. (2013). Linkages between lake shrinkage/expansion and sublacustrine permafrost distribution determined from remote sensing of interior Alaska, USA. *Geophys. Res. Lett.* 40, 1–6. doi: 10.1002/grl.50187

Jones, B. M., and Arp, C. D. (2015). Observing a catastrophic thermokarst lake drainage in northern Alaska: catastrophic thermokarst lake drainage. *Permafrost Periglacial Process.* 26, 119–128. doi: 10.1002/ppp.1842

Jones, B. M., Grosse, G., Arp, C. D., Jones, M. C., Walter Anthony, K. M., and Romanovsky, V. E. (2011). Modern thermokarst lake dynamics in the continuous permafrost zone, northern Seward Peninsula, Alaska. *J. Geophys. Res.* 116:G00M03. doi: 10.1029/2011JG001666

Jorgenson, M. T., and Osterkamp, T. E. (2005). Response of boreal ecosystems to varying modes of permafrost degradation. *Can. J. For. Res.* 35, 2100–2111. doi: 10.1139/x05-153

Jorgenson, M. T., Romanovsky, V., Harden, J., Shur, Y., O'Donnell, J., Schuur, E. A. G., et al. (2010). Resilience and vulnerability of permafrost to climate change. *Can. J. For. Res.* 40, 1219–1236. doi: 10.1139/X10-060

Jorgenson, M. T., and Shur, Y. (2007). Evolution of lakes and basins in northern Alaska and discussion of the thaw lake cycle. *J. Geophys. Res.* 112:F02S17. doi: 10.1029/2006JF000531

Kelly, R., Chipman, M. L., Higuera, P. E., Stefanova, I., Brubaker, L. B., and Hu, F. S. (2013). Recent burning of boreal forests exceeds fire regime limits of the past 10,000 years. *Proc. Natl. Acad. Sci.* 110, 13055–13060. doi: 10.1073/pnas.1305069110

Kokelj, S. V., and Jorgenson, M. T. (2013). Advances in thermokarst research: recent advances in research investigating thermokarst processes. *Permafrost Periglacial Process.* 24, 108–119. doi: 10.1002/ppp.1779

Lauriol, B., Duguay, C. R., and Riel, A. (2002). Response of the Porcupine and Old Crow rivers in northern Yukon, Canada to Holocene climatic change. *Holocene* 12, 27–34. doi: 10.1191/0959683602hl517rp

Lenz, J., Grosse, G., Jones, B. M., Walter Anthony, K. M., Bobrov, A., Wulf, S., et al. (2016). Mid-Wisconsin to holocene permafrost and landscape dynamics based on a drained lake basin core from the Northern Seward Peninsula, Northwest Alaska: mid-Wisconsin to holocene landscape dynamics, NW Alaska. *Permafrost Periglacial Process.* 27, 56–75. doi: 10.1002/ppp.1848

Matheus, P., Begét, J., Mason, O., and Gelvin-Reymiller, C. (2003). Late Pliocene to late Pleistocene environments preserved at the Palisades Site, central Yukon River, Alaska. *Quat. Res.* 60, 33–43. doi: 10.1016/S0033-5894(03)00091-7

McDowell, P. F., and Edwards, M. E. (2001). Evidence of Quaternary climatic variations in a sequence of loess and related deposits at Birch Creek, Alaska: implications for the Stage 5 climatic chronology. *Quat. Sci. Rev.* 20, 63–76. doi: 10.1016/S0277-3791(00)00131-1

Meyers, P. A., and Teranes, J. L. (2001). "Sediment organic matter," in *Tracking Environmental Change Using Lake Sediments: Basin Coring, and Chronological Techniques*, eds W. Last and J. P. Smol (Dordrecht: Kluwer Academic Press), 239–269.

Minsley, B. J., Abraham, J. D., Smith, B. D., Cannia, J. C., Voss, C. I., Jorgenson, T., et al. (2012). Airborne electromagnetic imaging of discontinuous permafrost. *Geophys. Res. Lett.* 39:L02503. doi: 10.1029/2011GL050079

Mortlock, R. A., and Froelich, P. N. (1989). A simple method for the rapid determination of biogenic opal in pelagic marine sediments. *Deep Sea Res.* 36, 1415–1426. doi: 10.1016/0198-0149(89)90092-7

Muhs, D. R., Pigati, J. S., Budahn, J. R., Skipp, G. L., Bettis, E. A., and Jensen, B. (2018). Origin of last-glacial loess in the western Yukon-Tanana Upland, central Alaska, USA. *Quat. Res.* 89, 797–819. doi: 10.1017/qua.2018.11

Osterberg, E. C., Winski, D. A., Kreutz, K. J., Wake, C. P., Ferris, D. G., Campbell, S., et al. (2017). The 1200 year composite ice core record of Aleutian Low intensification. *Geophys. Res. Lett.* 44, 7447–7454. doi: 10.1002/2017GL073697

Parkhurst, D. L., and Appelo, C. A. J. (1999). *Users Guide to PHREEQC (version 2) - A Computer Program for Speciation, Batch-Reaction, One-Dimensional Transport, and Inverse Geochemical Calculations*. U.S. Geological Survey Water Resources Investigations Report 99–4295.

Reimer, P. J., Bard, E., Bayliss, A., Beck, J. W., Blackwell, P. J., Bronk Ramsey, C., et al. (2013). IntCal 13 and Marine13 radiocarbon age calibration curves 0-50,000 years cal BP. *Radiocarbon* 55, 1869–1887. doi: 10.1016/j.dib.2018.10.040

Roach, J., Griffith, B., Verbyla, D., and Jones, J. (2011). Mechanisms influencing changes in lake area in Alaskan boreal forest. *Glob. Change Biol.* 17, 2567–2583. doi: 10.1111/j.1365-2486.2011.02446.x

Rodysill, J. R., Anderson, L., Cronin, T. M., Jones, M. C., Thompson, R. S., Wahl, D. B., et al. (2018). A North American Hydroclimate Synthesis (NAHS) of the common era. *Glob. Planet. Change* 162, 175–198. doi: 10.1016/j.gloplacha.2017.12.025

Romanovsky, V. E., Smith, S. L., and Christiansen, H. H. (2010). Permafrost thermal state in the polar Northern Hemisphere during the international polar year 2007-2009: a synthesis. *Permafrost Periglacial Process.* 21, 106–116. doi: 10.1002/ppp.689

Schnurrenberger, D., Russell, J., and Kelts, K. (2003). Classification of lacustrine sediments based on sedimentary components. *J. Paleolimnol.* 29, 141–154. doi: 10.1023/A:1023270324800

Steinman, B. A., Abbott, M. B., Mann, M. E., Ortiz, J. D., Feng, S., Pompeani, D. P., et al. (2014). Ocean-atmosphere forcing of centennial hydroclimate variability in the Pacific Northwest. *Geophys. Res. Lett.* 41, 2553–2560. doi: 10.1002/2014GL059499

Strauss, J., Schirrmeister, L., Grosse, G., Fortier, D., Hugelius, G., Knoblauch, C., et al. (2017). Deep Yedoma permafrost: a synthesis of depositional characteristics and carbon vulnerability. *Earth Sci. Rev.* 172, 75–86. doi: 10.1016/j.earscirev.2017.07.007

Stuiver, M., and Reimer, P. J. (1993). Extended 14C data base and revised Calib 3.0 14C age calibration program. *Radiocarbon* 35, 215–230. doi: 10.1017/S0033822200013904

Walter, K. M., Edwards, M. E., Grosse, G., Zimov, S. A., and Chapin, F. S. III (2007). Thermokarst lakes as a source of atmospheric CH4 during the last deglaciation. *Science* 318, 633–636. doi: 10.1126/science.1142924

Walter, K. M., Zimov, S. A., Chanton, J. P., Verbyla, D., and Chapin, F. S. III (2006). Methane bubbling from Siberian thaw lakes as a positive feedback to climate warming. *Nature* 443, 71–75. doi: 10.1038/nature 05040

Walter Anthony, K. M., Zimov, S. A., Grosse, G., Jones, M. C., Anthony, P. M., Chapin, F. S. C. III, et al. (2014). A shift of thermokarst lakes from carbon sources to sinks during the Holocene epoch. *Nature* 511, 452–456. doi: 10.1038/nature13560

West, J. J., and Plug, L. J. (2008). Time-dependent morphology of thaw lakes and taliks in deep and shallow ground ice. *J. Geophys. Res.* 113:F01009. doi: 10.1029/2006JF000696

Wetterich, S., Schirrmeister, L., Andreev, A. A., Pudenz, M., Plessen, B., Meyer, H., et al. (2009). Eemian and late glacial/Holocene palaeoenvironmental records from permafrost sequences at the Dmitry Laptev Strait (NE Siberia, Russia). *Palaeogeogr. Palaeoclimatol. Palaeoecol.* 279, 73–95. doi: 10.1016/j.palaeo.2009.05.002

Williams, J. R. (1962). Geologic reconnaissance of the Yukon flats district, Alaska. *U.S. Geol. Surv. Bull.* 1111-H, 289–306.

Williams, J. R. (1970). *Ground Water in the Permafrost Regions of Alaska*. U.S. Geological Survey Professional Paper 696. doi: 10.3133/pp696

Winski, D., Osterberg, E., Ferris, D., Kreutz, K., Wake, C., Campbell, S., et al. (2017). Industrial-age doubling of snow accumulation in the Alaska Range linked to tropical warming. *Sci. Rep.* 7:17869. doi: 10.1038/s41598-017-18022-5

Wooller, M. J., Pohlman, J. W., Gaglioti, B. V., Langdon, P., Jones, M., Walter Anthony, K. M., et al. (2012). Reconstruction of past methane availability in an Arctic Alaska wetland indicates climate influenced methane release during the past ∼12,000 years. *J. Paleolimnol.* 48, 27–42. doi: 10.1007/s10933-012-9591-8

Zimov, S. A., Voropaev, V., Semiletov, S. P., Davidov, S. F., Prosiannikov, F. S., Chapin, M. C. III, et al. (1997). North Siberian lakes: a methan source fueled by Pleistocene carbon. *Science* 277, 800–802. doi: 10.1126/science.277.5327.800

Conflict of Interest Statement: The authors declare that the research was conducted in the absence of any commercial or financial relationships that could be construed as a potential conflict of interest.

frontiers in Earth Science

ORIGINAL RESEARCH
published: 09 April 2019
doi: 10.3389/feart.2019.00061

Holocene Vegetation, Climate, and Carbon History on Western Kodiak Island, Alaska

Dorothy M. Peteet[1,2], Jonathan E. Nichols[2] and Daniel H. Mann[3]*

[1] NASA Goddard Institute for Space Studies, New York, NY, United States, [2] Lamont-Doherty Earth Observatory, Columbia University, Palisades, NY, United States, [3] Department of Geosciences, University of Alaska Fairbanks, Fairbanks, AK, United States

At Phalarope Pond, western Kodiak Island, a multidisciplinary study using pollen and spores, macrofossils, stable isotopes, and carbon accumulation provides the Holocene vegetation and climate history following the deglaciation that began over 16,000 cal years ago (yr BP). Following a cold and dry Younger Dryas, a warm and wet early Holocene was characterized by abundant ferns in a sedge tundra environment with maximum carbon accumulation, similar to high latitude peatlands globally. About 8,700 cal yr BP sedge and ferns declined and climate remained warm as drier conditions prevailed, limiting carbon sequestration. The abrupt shift in D/H isotopes of about 60% indicates a shift to cooler conditions or a more distal moisture source. Neoglaciation beginning about 3,700 cal yr BP is evident from increases in *Artemisia*, *Empetrum* and *Betula*, signifying cooler conditions, while *Alnus* declines, paralleling regional trends.

Keywords: Kodiak Island, Holocene, pollen, macrofossils, isotopes, carbon sequestration, Alaska

OPEN ACCESS

Edited by:
Randel Tom Cox, The University of Memphis, United States

Reviewed by:
Daniel Larsen, The University of Memphis, United States
Chengyu Weng, Tongji University, China

****Correspondence:***
Dorothy M. Peteet
peteet@ldeo.columbia.edu

Specialty section:
This article was submitted to Quaternary Science, Geomorphology and Paleoenvironment, a section of the journal Frontiers in Earth Science

Received: *30 November 2018*
Accepted: *13 March 2019*
Published: *09 April 2019*

Citation:
Peteet DM, Nichols JE and Mann DH (2019) Holocene Vegetation, Climate, and Carbon History on Western Kodiak Island, Alaska. Front. Earth Sci. 7:61. doi: 10.3389/feart.2019.00061

INTRODUCTION

Peatlands in subarctic Alaska provide a window into the history of a high latitude area that today is warming almost twice as fast as the rest of the globe (Cohen et al., 2014). Describing the Holocene history of this region and its impact on carbon sequestration becomes increasingly important as we experience this warming. While warmer temperatures foster both increased primary production and decomposition, the net carbon stored often depends on the type of vegetation (Kuiper et al., 2014) and its moisture content. While we previously identified Kodiak Island as an area that experienced a marked Younger Dryas cooling during the late-glacial (Peteet and Mann, 1994; Hadjas et al., 1998) using pollen and macrofossils, we now use these same vegetational indicators along with stable isotope to explore the vegetational, climatic, and carbon accumulation history throughout the Holocene from the same site.

Study Site

Phalarope Pond (57°N, 154°26 W) is a kettle pond located in a recessional moraine of a glacier that flowed seaward out of Olga Bay on southwestern Kodiak Island (**Figure 1**). Deglaciation occurred ca. 14,700 ^{14}C years BP (Mann and Peteet, 1994; Peteet and Mann, 1994).

The mountainous interior of Kodiak Island results in a climatic gradient between the warmer, maritime, eastern side of the island where the town of Kodiak is located to the colder, drier, Shelikof Strait side. The town of Kodiak has an average January temperature of 0°C and a July

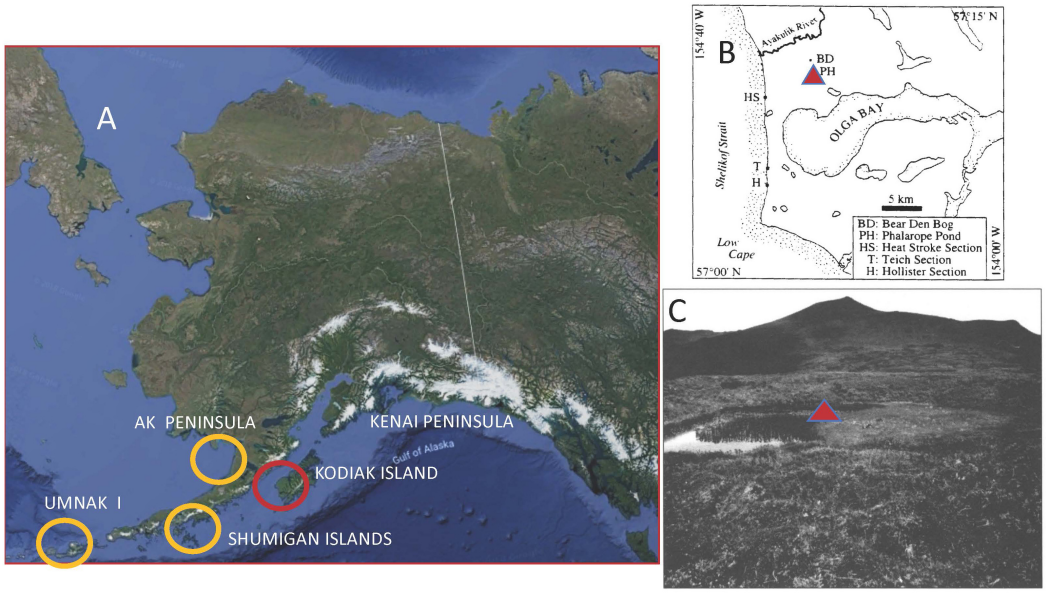

FIGURE 1 | Location of Phalarope Pond, western Kodiak Island, Alaska, with regional sites and photo of the coring site. **(A)** Core site location on western Kodiak and neighboring comparative sites. **(B)** Phalarope Pond (PH) core site north of Olga Bay, western Kodiak Island. **(C)** Photo of Phalarope Pond, Kodiak Island with core site (triangle).

temperature of 12.1°C (National Oceanic and Atmospheric Administration [NOAA], 1985). Karlstrom (1969) noted that January temperatures over 30 cal yr BP are 3°C colder on the Shelikof Strait side of the archipelago. While Kodiak town receives 170–185 cm of precipitation a year (National Oceanic and Atmospheric Administration [NOAA], 1985, 2018), the Shelikof Strait side receives less than half that amount (Karlstrom, 1969). To the west, the Shumigan Islands receive a similar amount of precipitation at about 87 cm (Heusser, 1983), and Cold Bay on the western Alaskan Peninsula[1] about 91 cm.

Landscapes on the western side of Kodiak Island are primarily treeless, with occasional trees appearing where *Picea sitchensis* seeds find mineral soil, sometimes atop mountains. Moist peatlands are typical of the valley bottoms, with a dominance of sedge and moss tundra, but with shrubs of *Salix*, *Betula*, and *Alnus* throughout. Drier lowland hummocks are blanketed with heaths such as *Empetrum nigrum*, *Arctostaphylos uva-ursi*, *Vaccinium vitis-idaea*, *V. uliginosum*, as well as *Betula nana*. Wetland habitats such as border Phalarope Pond contain abundant *Sphagnum* and *Carex together with Ledum palustre*, *V. vitis-idaea*, *Rubus chamaemorus*, and *Drosera rotundifolia*. *Emergent/quatic plants* include *Menyanthes trifoliata*, *Hippuris vulgaris*, and *Nuphar polysepalum*. Blanketing moist slopes above the peatlands are meadows of abundant herbs such as *Veratrum viride*, *Sanguisorba stipulata*, *Polemonium acutiflorum*, and *Epilobium angustifolium*, while drier slopes include *Calamagrostis canadensis* subsp. *Langsdorffii* and *Heracleum lanatum* and ferns such as *Dryopteris dilatata* and *Athyrium filix-femina*. At the boundary of meadows and alpine heath, *Alnus* shrubs and *Rubus spectabilis* occur.

MATERIALS AND METHODS

Phalarope Pond (**Figure 1**), at 30 m elevation, is a small circular kettle from which we retrieved an 8.2-m core at the center of the pond, along the edge of an encroaching bog mat which extends halfway across the pond. A modified Livingstone piston corer (Wright et al., 1984) was used for sediment extraction. Cores were extruded in the field, wrapped in plastic film and aluminum foil, and stored in the refrigerated repository at LDEO. The lowest 4 m of sediment are comprised of silty organics, ending in gravel at the base. The core was sampled for pollen and spores at 5- or 10-cm intervals. Samples were processed using 2 ml of sediment, following the procedures of Heusser and Stock (1984). *Lycopodium clavatum* tablets were added to calculate pollen concentrations, and processing included use of KOH, HCL and HF, 150 and 7 micron screening, as well as acetolysis, alcohol dehydration, and silicone oil mounts. At least 300 pollen grains were counted for each sample, and spores tallied in addition. Pollen slides were examined at 400×, and identified with a coastal Alaskan reference collection (i.e., Heusser and Peteet, 1987). Percentage of spores is based upon the sum of pollen and spores. Nomenclature follows Hulten (1968), and data were plotted using Tiliagraph (Grimm, 1992).

Soluble lipids were extracted from freeze-dried peat samples by three successive rounds of ultrasonic agitation in hexane. The three rinses were combined for the total lipid extract (TLE). TLE was separated by silica gel flash column chromatography into three fractions: hydrocarbons are eluted with hexane; ketones,

[1]http://www.cold-bay.climatemps.com/

esters, and aromatic compounds with dichloromethane; and polar compounds with methanol. Hydrocarbons were quantified prior to hydrogen isotope analysis by gas chromatography-flame ionization detection (GC-FID). Hydrogen isotope ratios of individual *n*-alkanes were determined by continuous flow isotope ratio mass spectrometry. Eluent from a gas chromatograph (Thermo Trace GC) passes through a pyrolysis reactor (Thermo GC IsoLink) where organic compounds are converted to H_2 gas, which then is passed to the IRMS (Thermo Delta V) via a continuous flow device (Nichols et al., 2014a).

Hydrogen isotope ratios of peatland water is calculated from the δD of C_{29} *n*-alkane (*n*-nonacosane) using an empirical apparent enrichment factor. For each sample an elw is chosen based on the macrofossil stratigraphy. In parts of the stratigraphy where vascular vegetation is dominated by sedges, a median elw for monocots is used, and where vascular vegetation of the peatland is dominated by ericads, a median elw for dicots is used. Enrichments for these vegetation types are from published literature (Sachse et al., 2012). Uncertainty around these enrichment factors (about ±30‰) as well as analytical uncertainty (±2‰ are propagated through calculations of peatland water δD). We only interpret changes in δD of peatland water that exceed 75% confidence based on this propagated uncertainty (Nichols et al., 2014a,b).

Percent weight loss on ignition (LOI) followed Dean (1974), and after drying, samples were burned at 550 C for 2 h. LOI and bulk density measurements were multiplied to calculate ash-free bulk density. Carbon content was calculated from the ash-free bulk density by multiplying by.423 in Sphagnum peat and 0.511 in sedge peat (Loisel et al., 2014).

Samples were screened for macrofossils at 5 cm intervals using screens of 0.5 and 0.1 mm, picked in water at a magnification of 20–60×, and identified using the macrofossil collection at LDEO. All samples are stored in the LDEO refrigerated repository in water. Identified samples for AMS dating were sent to the National Ocean Science AMS Facility (NOSAMS, Woods Hole).

Radiocarbon ages on identified plant macrofossils are presented in **Table 1**. The ^{14}C ages were calibrated using CALIB 7.1 html (Stuiver et al., 2019). We used the "Bacon" Bayesian age-depth modeling tool to estimate the ages of sediment samples (Blaauw and Christen, 2011). All radiocarbon dates fell within the 95% confidence intervals around the resulting age model. Input and "priors" files are available here as a supplement. Ages are presented in calibrated years, years BP (Before Present,; 0 year BP = 1950 AD), and uncertainties are shown at the 95% (2- sigma) confidence level. Pollen and spore percentage diagrams as well as the macrofossil diagram were drafted using Tilia (Grimm, 1992). Pollen and macrofossil data are stored in the Neotoma database.

RESULTS

The three tephras that define the earliest late-glacial- (purple), the mid- Younger Dryas white tephra, and the early Holocene gray tephra (10,200 cal yr BP) are described along with the chronology, pollen and spores, and macrofossils in Peteet and Mann (1994). We refer to that discussion for the late-glacial, but will here begin descriptions of the core with the earliest Holocene, which includes many cryptic tephras. As Heusser (1990) noted, tephra can play a role in shaping vegetational communities if edaphic conditions are changed due to drainage shifts or additional nutrients. Because the tephras are not clearly visible in the Holocene peat, we cannot attribute any vegetational shifts to tephra, but they may have played a role.

TABLE 1 | AMS radiocarbon depths, macrofossil identification, and ^{14}C ages.

Lab number	Depth (cm)	Macrofossil	C-14 age (year BP)	Age error
OS-83647	76.5	2 *Nuphar* seeds	1,390	20
OS-83648	76.5	*Vaccinium* stem, *Empetrum* seed	1,280	15
OS-83921	106.5	3 *Empetrum* lvs	2,630	55
OS-83927	121.5	*Empetrum* leaf, *Polytrichum* moss	3,560	45
OS-87759	152	Woody fragments	2,800	45
OS-87494	154.5	Woody fragments	2,700	45
OS-87459	202.5	*Isoetes* spores	5,700	40
OS-83646	236.5	*Empetrum* seed and woody frag	2,500	30
OS-87762	277.5	*Carex* seed	7,470	100
OS-84809	322.5	1 *Carex* seed, 3 *Eriophorum* seeds	8,120	410
OS-84810	412.5	Wood	8,830	470
OS-87753	432.5	Purified leaf-wax n-alkanes	9,760	50
	500	Gray tephra		

Chronology, Figure 2 and Table 1

Identified macrofossils from 12 samples were pre-treated with an acid-alkali-acid chemical digestion prior to combustion, graphitization, and measurement by accelerator mass spectrometry. The age-depth model based on AMS dates (**Table 1**) is presented in **Figure 2**, which shows highest sedimentation rates in the lower part of the core and a shift to lower rates at about 2 m from the surface, followed by higher rates again about 1.5 m when the site shifts from a shallow pond to a peatland as indicated in the lithology and LOI results.

LOI, Sedimentation Rate, and Carbon Accumulation Rate, g/m^2/Year (CAR), Figures 3–5

Loss on ignition (<10%) and sedimentation rates were low during the late glacial (0.3 mm/year, **Figure 3**), while CAR was relatively high (**Figure 5**), linked to the relatively warm, moist Bölling–Alleröd period prior to the cold and dry Younger Dryas (Peteet and Mann, 1994). Above the gray tephra, pond sediment is comprised of low organic content, increasing from around 2% at the level of the gray tephra at 5 m, to close to 10% between 5 and 4 m depth, between 10 ka and 8,500 cal yr BP. Highest sedimentation rates occurred during the earliest Holocene when they reached 1 mm/year. The carbon accumulation rate averaged about 10 g/m^2/a until about 10 cal kyr when it increased to

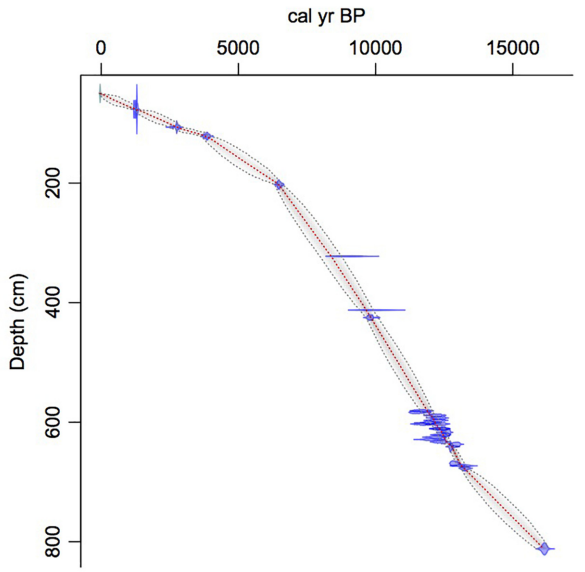

FIGURE 2 | Age-depth model. Red line indicates median age. Dotted lines indicate 95% confidence interval around the median age. Blue areas indicate calibration ranges for individual radiocarbon dates.

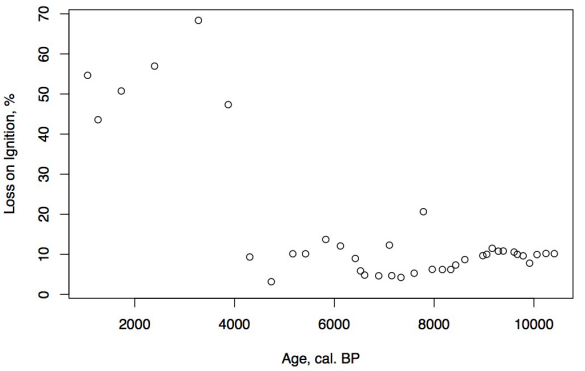

FIGURE 3 | Holocene age-depth plot and LOI for the Phalarope Pond core.

20 g/m^2/a, a maximum for the entire core. Above a depth of 350 cm (8,700 cal yr BP) the LOI, sedimentation rate, and CAR decline, with the LOI averaging less than 10%, the sedimentation rate declining from 0.6 to 0.2 mm/year, and the CAR fluctuating at <10 g/m^2/yr. Above 150 cm (4,775 cal yr BP), LOI increases and averages close to 50%, sedimentation rate rises to between 0.2 and 0.6 mm/year, and CAR increase again to almost 15 g/m^2/year in the uppermost peat near the surface of the floating mat of peat.

Pollen, Spores, and Macrofossil Analysis Groupings and Zonation (Figures 6, 7)

Modern pollen-vegetational relationships were described by Peteet and Mann (1994) for this area of western Kodiak Island. We can use these relationships to interpret the vegetational history of the Holocene, just as we did for the late-glacial.

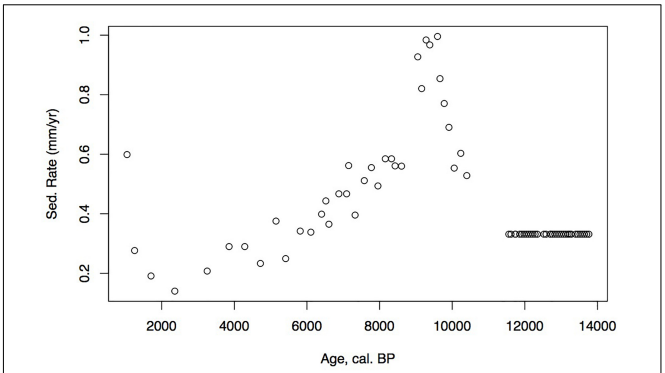

FIGURE 4 | Holocene age-depth plot and sedimentation rates (mm/year) for Phalarope Pond, Kodiak, AK.

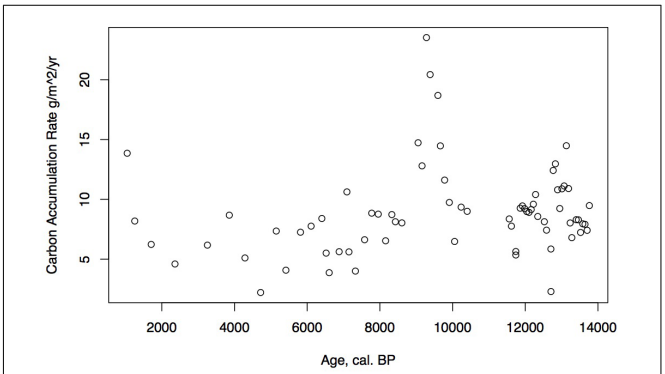

FIGURE 5 | Holocene carbon accumulation rate (CAR) in g/m^2/year for Phalarope Pond, AK.

Zone P-4, (11,500–8,700 ka, 550–350 cm Depth)

Zone P-4 encompasses the earliest Holocene zone, and the peat brackets the 70 cm of thick gray tephra. Polypodiaceae reach maximum values in this zone (80%), and Cyperaceae and Poaceae reach 40%, while Ericales remain at 10%, *Empetrum* leaves are sometimes present, and Apiaceae, *Sanguisorba*, and Asteraceae are quite visible in the record. *Sanguisorba* and *Fritillaria* are consistently present, while *Betula* and *Alnus* appear in very low percentages. *Isoetes* microspores and macrospores gradually increases upward, indicative of a wet environment, along with the fluctuating presence of other aquatic indicators such as *Nuphar* and *Naias*, bryozoan statoblasts, and cladoceran ephippia. Lenticular *Carex* achenes appear along with some *Empetrum* leaves, *Viola* seeds, and *Vaccinium uliginosum* and *Rubus arcticus* seeds. *Sphagnum* leaves are present throughout this zone, along with three other bryophytes.

Zone P-5, (8,700–7,600 ka, 300–275 cm Depth)

Ericales remain at about 10%, while Cyperaceae decline to as low as 25%, and then increase again at the top of the zone. Poaceae

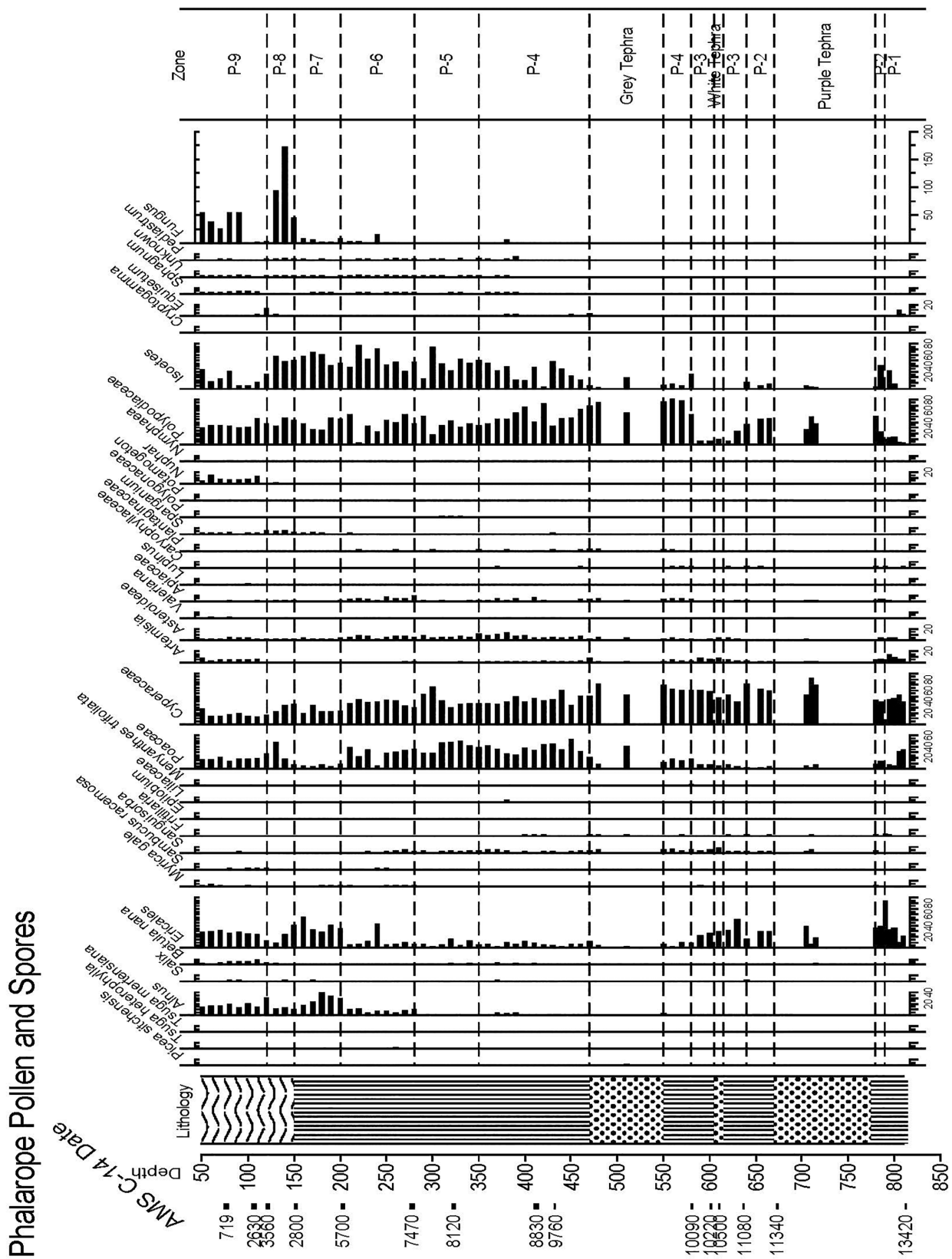

FIGURE 6 | Pollen and spore percentage data from Phalarope Pond, Kodiak Island.

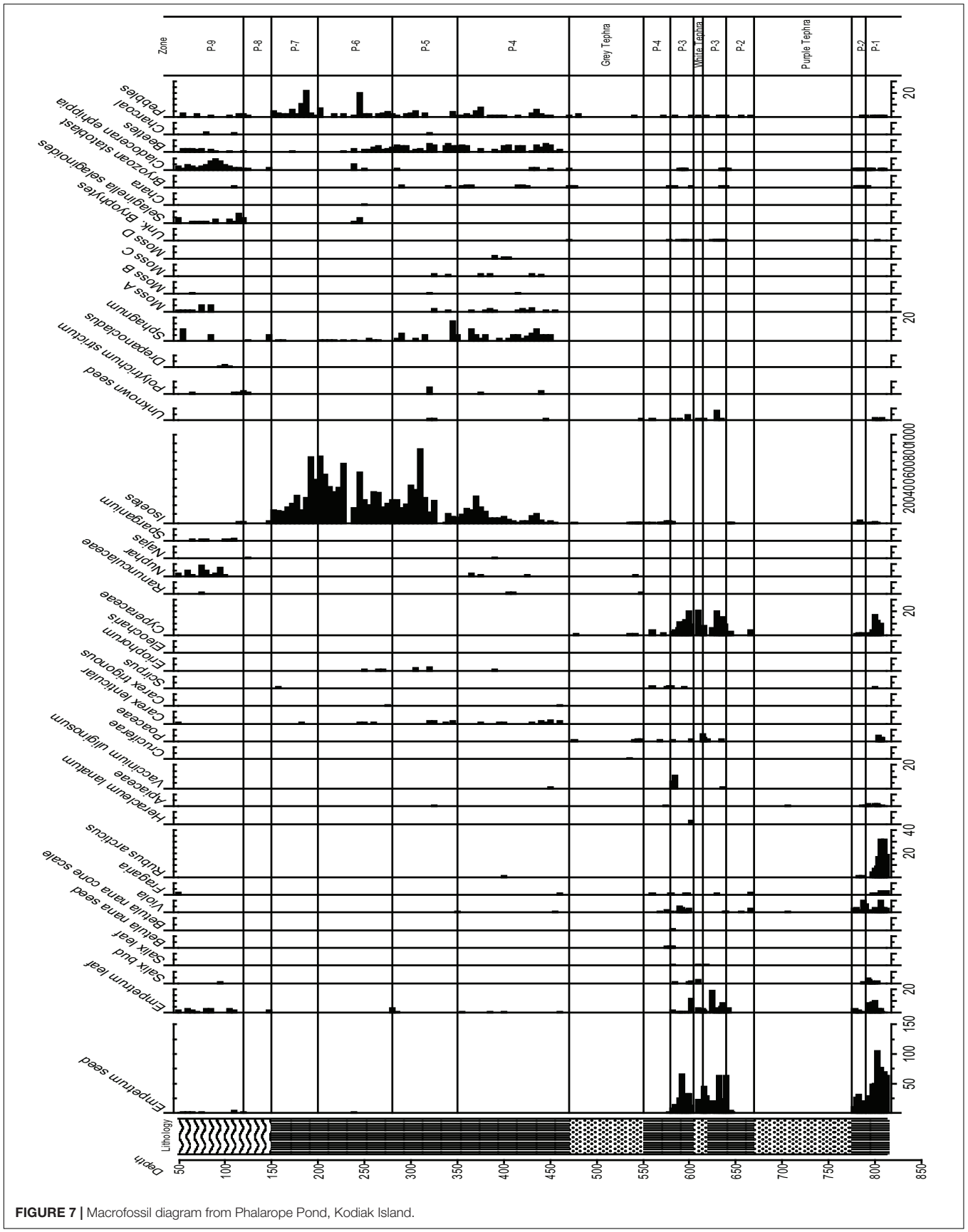

FIGURE 7 | Macrofossil diagram from Phalarope Pond, Kodiak Island.

remain close to 40%, while ferns decline to below 40%, and *Isoetes* spores continue to increase. A decline in the Apiaceae, disappearance of *Alnus*, *Nuphar* and cladoceran ephippia, as well as bryozoan statoblasts is notable. *Sanguisorba* is present, and *Eriophorum* seeds appear in this zone. A marked decline in *Sphagnum* is visible, and an increase in *Polytrichum* in one sample is paralleled by charcoal.

Zone P-6, (7,600–6,500 ka, 275–200 cm Depth)

Alnus consistently reaches 10%, *Myrica gale* is present, Ericales remain at the same value generally, and Poaceae and Cyperaceae decline to between 30 and 40%. Apiaceae reach maximum values, *Sanguisorba* remains throughout, Asteroideae are still abundant, Polypodiaceae again increase, and *Isoetes* microspores reach maximum values while *Sphagnum* declines but is still present throughout. *Selaginella selaginoides* macrospores make a first appearance, and cladoceran ephippia are present.

Zone P-7, (6,500–4,800 ka, 200–150 cm Depth)

While Poaceae decline markedly in this zone to 10%, Ericales increase from 10 to greater than 40%. Alnus rises from 10–30%. Cyperaceae decline, while Polypodiaceae fluctuate between 20 and 40%, and *Isoetes* microspores remain abundant while *Isoetes* macrospores decline to 0. The zone is almost devoid of macrofossils, and more pebbles are present in this zone than previous zones. *Salix* increases while Apiaceae disappear.

Zone P-8, (4,800–3,700 ka, 150–120 cm Depth)

Betula increase, Ericales decline while Poaceae, Cyperaceae, and *Sparganium* increase, and fungal spores become abundant. The zone is almost devoid of macrofossils, with the exception of minimal cladoceran ephippia, 1 *Empetrum* leaf, 1 *Naias* seed, and minimal *Sphagnum*, and *Polytrichum strictum* at the top of the zone, along with many fungal spores.

Zone P-9, (3,700- Present, 120 – Core Surface, With 50 cm Water Depth)

Especially distinctive in this zone are *Betula* and *Artemisia*, which reach their maximum values here, along with *S. selaginoides* macrospores. *Empetrum* seeds and leaves are consistently present along with *Nuphar* pollen and seeds, while *Alnus* declines and both Poaceae and Cyperaceae decline. Fungal spores are also prominent, and *Sphagnum* leaves appear.

DISCUSSION

Early Holocene (11,500–8,700 ka)

The low organic matter but presence of shallow aquatic indicators such as *Nuphar polysepalum*, *Naias*, bryozoan statoblasts, and cladoceran ephippia, along with the increasing presence of *Isoetes*, indicate a shallow pond environment. The extremely high percentages of fern spores along with high percentages of sedge and grass, *Sphagnum*, and a diversity of moss species indicate this period was relatively warm and moist. Supporting this inference is the presence of *Fritillaria*, along with Apiaceae, *Sanguisorba*, and Asteroideae. CAR reaches its highest rates for the entire core (20 g/m^2/year, **Figure 5**), a rate similar or greater than at coastal Alaskan sits such as the Kenai Peninsula (Jones and Yu, 2010) where this interval is recognized as the Holocene thermal maximum (HTM). Similarly, the highest CAR from Corser Bog, near Cordova Alaska, occurs during this same early Holocene interval (Peteet et al., 2016), although rates there are significantly higher. The D/H ratios of peatland water are enriched relative to the rest of the record, (**Figure 8**) suggesting precipitation is derived from local air masses originating in the North Pacific. Alternatively, enriched isotopes of precipitation could indicate increased warm season precipitation. Either interpretation would support moist growing season conditions during this interval, favorable for more rapid carbon accumulation. West of Kodiak, a well-dated site on Adak Island in the Aleutians shows a very high accumulation rate during the early Holocene, similar to Phalarope (Noguchi et al., 2018). Rapid peatland expansion and highest C accumulation during this interval is linked to early Holocene peatland carbon storage throughout the Subarctic (Loisel et al., 2014).

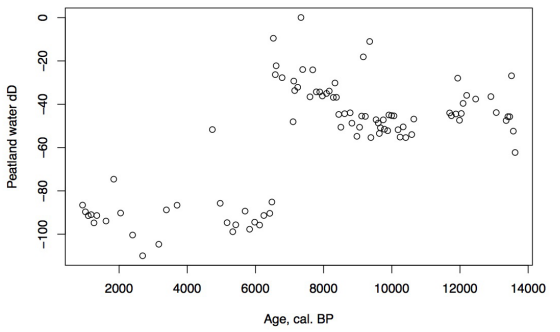

FIGURE 8 | *D/H* ratios of peatland water for Phalarope Pond, Kodiak Island.

Interestingly, the very low percentage of *Alnus* in this interval, less than 5%, is in contrast to sites on eastern Kodiak during the early Holocene where it reaches up to 50% of the pollen sum (Heusser, 1960). At the village site of Karluk, north of our site on the western edge of Kodiak Island, both Heusser (1960) and Nelson and Jordon (1988) retrieved cores dating back to the mid-Holocene, and both show a large decline in *Alnus* from the mid-Holocene toward the present, similar to this pollen record.

Early Mid-Holocene (8,700–7,600 ka)

The decline in fern spores as well as *Sphagnum* and Cyperaceae, with the increase in grasses suggests a slightly warm, drier environment, but one that is still very moist. As the sedimentation rate declines, so does the CAR, to an average less than 10 g/m^2/a. The shallow lake sediment with *Isoetes* includes the first evidence of fire on the landscape.

Mid-Holocene (7,600–6,500 ka)

Alnus appears to expand its range into southwestern Kodiak Island in response to early Holocene warmth. The vegetation suggests a climate that was warm and moist until the close of the zone. Specifically, Apiaceae pollen reach maximal values, fern spores remain abundant, and *Sanguisorba* and *S. selaginoides* – both moist peatland indicators – are present. At the close of this zone ca. 6,500 cal yr BP, D/H ratios of peatland water show a large shift of about 60‰ toward more depleted values (**Figure 8**), Several climatic factors could contribute to this dramatic depletion. Precipitation source could have shifted away from the warm, nearby North Pacific to higher-latitude, colder, or more distal moisture sources, such as from the Bering Sea (Lachniet et al., 2016), which would have less precipitable moisture. Also, a shift in seasonality of precipitation resulting in more cold season precipitation and less warm season could produce a similar shift (Nichols et al., 2009). Any of these influences, however, would result in less available moisture for peatland vegetation, resulting in the lowered rates of carbon accumulation we observe in the subsequent interval.

Late Mid-Holocene (6,500–3,700 ka)

The continued decline of Apiaceae, Cyperaceae, fern spores, and *Sphagnum* spores, with some fluctuation along with a declining sedimentation rate and CAR all suggest further drying of the landscape. *Alnus*, which was rare earlier in the Holocene, is consistently present, suggesting migration into the area from the eastern part of the island (Heusser, 1960). Alnus pollen reached 50% at Karluk to the north at around 4,500 cal yr BP. Further west, *Alnus* is present in the Shumigan Islands in the mid-Holocene (Heusser, 1983). *Sanguisorba*, a moist peatland herb, disappears. The presence of *Artemisia* and Ericales (probably *Empetrum* expansion) suggests a drier climate. Fungal spores reach their peak, also suggestive of drier conditions. The D/H ratio of peatland water (**Figure 8**) remains very depleted generally during this interval relative to the Early Holocene, suggesting the prevalence of air masses coming from colder and/or more distal regions or decreased growing season precipitation in favor of winter. Carbon accumulation continues to decline to less than 10 g/m^2/year (**Figure 5**).

Late Holocene (3,700 to Present)

The shallow pond begins to be covered by a mat of peat as indicated by the increase in *Sphagnum* spores and the decline in *Isoetes*. LOI, sedimentation rate, and carbon accumulation rate increase. At the same time, *Nuphar* pollen and seeds, *Sparganium* pollen, and cladoceran ephippia indicate the presence of shallow pools of water in the peatland. However, the sustained presence of *Artemisia* and *Betula* along with the decline of *Alnus* suggest colder and possibly drier conditions, as does the fungal presence. Carbon accumulation begins to increase as *Sphagnum* increases, until it ranges between 10 and 15 g/m^2/year. The *Alnus* decline in the late Holocene is paralleled in Heusser's (1960) records from both sides of Kodiak Island, as is the general increase in Ericales and *Sphagnum*. Nelson and Jordon's (1988) Karluk site similarly shows an increase in *Artemisia* in the late Holocene, with a decline in fern spores. The D/H ratios of peatland water continue to show very depleted values (**Figure 8**). As the North Pacific high presumably moves eastward, drier, isotopically depleted air masses derived from the Bering Sea region may have been brought to the site. In contrast to locations bordering the eastern Gulf of Alaska (Heusser, 1960; Heusser et al., 1985; Peteet, 1986; Ager et al., 2010; Peteet et al., 2016) where colder, wetter climate occurred during the late Holocene, at Phalarope Pond climate seems to have been cooler, but the available moisture is difficult to discern.

Ages ka	**E.Aleutian Islands** Umnak[1]	**Alaska Peninsula** Kinzarof Marsh[2]	**Alaska Peninsula** Cape Aliaksin[2]	**Shumagin Islands** Unga[3]	**W.Kodiak Island** (this paper)	**Climate**
0						
3700	Poa-Cyp	Cyp-Emp-Al-Cyp-Poa	Cyp-Bet-Emp	Bet-Al-Cyp	Emp-Cyp-Poa-Bet-Art	Cooler
6500	Sal-Poa-Cyp	Poa-Poly-Emp Emp-Art-Poa	Bet-Emp Cyp-Bet-Emp Cyp-Poa-Sal	Cyp Cyp-Bet	Cyp-Poa Aster	Drier
11,500	Cyp-Api-Poa-Poly		Cyp-Poa-Emp	Bet-Emp-Poa Poa-Sal-Art	Poly-Cyp-Poa	Warm, wet
					Cyp-Emp	Cold

FIGURE 9 | Regional chart of pollen and spore dominance on Kodiak Island compared with sites in the Aleutians, the Shumigan Islands, and the western Alaskan Peninsula, along with inferred climate. Al, Alnus; Ap, Apiaceae; Art, Artemisia; Aster, Asteraceae; Bet, Betula; Cyp, Cyperaceae; Emp, Empetrum; Poa, Poaceae; Poly, Polypodiaceae; Sal, Salicaceae. Heusser, 1973; Heusser, 1983; Jordan and Krumhardt, 2003.

CONCLUSIONS IN A REGIONAL CONTEXT

Early Holocene (11.5–8,700 cal yr BP) warmth and moisture characterize western Kodiak Island, with maximum carbon sequestration reaching (20 g/m^2/year) (**Figures 5**, **9**). This pattern of increased early Holocene CAR is similar to peatlands in the central and eastern Gulf of Alaska (Jones and Yu, 2010; Peteet et al., 2016) which have much higher rates of C accumulation (up to 50 g/m^2/year) as well as high latitude peatlands globally (Loisel et al., 2014). Yet while western Kodiak Island has a dry and cool climate compared with peatlands surrounding the Gulf of Alaska to the east, carbon storage does fluctuate in response to climate forcing throughout the Holocene. A drier, more evaporative climate is present in the mid-Holocene (8,700–3,700 cal yr BP) when low LOI, low sedimentation rates, and increases in the abundances of fungal spore are concurrent with low rates of carbon accumulation. An abrupt depletion in D/H ratio of peatland water at ca. 6,500 cal yr BP suggests a commensurately abrupt shift to a cooler or more distal moisture source. Westward on Umnak Island and in the Shumigans (**Figures 1**, **9**), warmer conditions also prevailed (Heusser, 1973; Heusser, 1983). On the western Alaskan Peninsula, Jordan and Krumhardt (2003) find warmer conditions with active dunes. Neoglaciation (3,500 cal yr BP – present) followed, as seen in many other pollen records (Heusser, 1960, 1983; Heusser et al., 1985; Peteet, 1986, 1991; Jones et al., 2009; Ager et al., 2010; Peteet et al., 2016) along with glacial advances (Barclay et al., 2009, 2013) resulting in a cooler climate with increasing *Artemisia* and *Betula*, declines in *Alnus*, increased *Sphagnum* and *S. selaginoides* and a rise in carbon accumulation to between 10 and 15 g/m^2/year. A late-Holocene shift in sea surface temperatures indicative of cooling is also noted by Sabin and Pisias (1996) with intensification of the Aleutian Low. As a warming climate continues, it is clear that the availability of moisture will determine whether peatlands on western Kodiak Island and throughout the northern high latitudes will store more carbon or less.

AUTHOR CONTRIBUTIONS

DP and DM participated in field work, while all authors generated data, conducted analyses, and produced figures. DP, JN, and DM wrote and edited the text.

FUNDING

This study was funded by NASA/GISS, NSF ARC #1022979 and the Climate Center of the Lamont-Doherty Earth Observatory.

ACKNOWLEDGMENTS

Many thanks again to Jill Bubier, Brett Engstrom, Fred Haering, Lawrence Plug, Michael Shephard, and George Stone III for robust field assistance. Personnel of the Kodiak Wildlife Refuge donated advice and support, and R. Ruoss provided logistical aid in air support.

REFERENCES

Ager, T. A, Carrara, P. E., McGeehin, J. P. (2010). Ecosystem development in the Girdwood area, south-central Alaska, following late Wisconsin glaciation. *Can. J. Earth Sci.* 47, 971–985. doi: 10.1139/E10-020

Barclay, D. J., Wiles, G. C., and Calkin, P. E. (2009). Holocene glacier fluctuations in alaska. *Quat. Sci. Rev.* 28, 2034–2048. doi: 10.1016/j.quascirev.2009.01.016

Barclay, D. J., Yager, E. M., Graves, J., Klozko, M., and Calkin, P. (2013). Late holocene glacial history of the copper river delta, coastal south-central alaska, and controls on valley glacier fluctuations. *Quat. Sci. Rev.* 81, 74–89. doi: 10.1016/j.quascirev.2013.10.001

Blaauw, M., and Christen, J. A. (2011). Flexible paleoclimate age-depth models using an autoregressive gamma process. *Bayesian Anal.* 6, 457–474.

Cohen, J., Screen, J. A., Furtado, J. C., Barlow, M., Whittleston, D., Coumou, D., et al. (2014). Recent arctic amplification and extreme mid-latitude weather. *Nat. Geosci.* 7, 627–637. doi: 10.1038/ngeo2234

Dean, W. Jr. (1974). Determination of carbonate and organic matter in calcareous sediments and sedimentary rocks by loss on ignition: comparison with other methods. *J. Sediment. Petrol.* 44, 242–248.

Grimm, E. (1992). *Tilia and Tilia-graph Software. Version* 2.0. Springfield: Illinois State University.

Hadjas, I., Bonani, G., Boden, P., Peteet, D., and Mann, D. (1998). Cold reversal on kodiak island correlated with european YD using variations of the atmospheric 14C/12C. *Geology* 26, 1047–1050. doi: 10.1130/0091-7613(1998)026<1047:CROKIA>2.3.CO;2

Heusser, C. J. (1960). *Late Pleistocene Environments of North Pacific North America*. New York, NY: American Geographical Society.

Heusser, C. J. (1973). Postglacial vegetation on Umnak Island, Aleutian Islands, Alaska. *Rev. Palaeobot. Palynol.* 15, 277–285. doi: 10.1016/0034-6667(73)90033-X

Heusser, C. J. (1983). Pollen diagrams from the Shumagin Islands and adjacent Alaska Peninsula, southwestern Alaska. *Boreas* 12, 279–295. doi: 10.1111/j.1502-3885.1983.tb00322.x

Heusser, C. J. (1990). Late Quaternary vegetation of the Aleutian Islands, southwestern Alaska. *Can. J. Bot.* 68, 1320–1326. doi: 10.1139/b90-168

Heusser, C. J., Heusser, L., and Peteet, D. (1985). Late Quaternary climate changes on the American North Pacific coast. *Nature* 315, 485–487. doi: 10.1038/315485a0

Heusser, C. J., and Peteet, D. M. (1987). Spores of *Lycopodium* and *Selaginella* of the American North Pacific Region. *Can. J. Bot.* 66, 508–525. doi: 10.1139/b88-074

Heusser, L. E., and Stock, C. E. (1984). Preparation techniques for concentrating pollen from marine sediments and other sediments with low pollen density. *Palynology* 8, 225–227. doi: 10.1080/01916122.1984.9989279

Hulten, E. (1968). *Flora of Alaska, and the Yukon*. Lund: Gleerup.

Jones, M., Peteet, D., Kurdya, D., and Guilderson, T. (2009). A 14,000-year peatland record from the Kenai, Alaska: vegetation history and implications for atmospheric circulation patterns. *Quatern. Res.* 72, 207–217. doi: 10.1016/j.yqres.2009.04.002

Jones, M. and Yu, Z. (2010). Rapid deglacial and early Holocene expansion of peatlands in Alaska. *Proc. Natl. Acad. Sci.* 107, 7347–7352. doi: 10.1073/pnas.0911387107

Jordan, J. W., and Krumhardt, A. (2003). Postglacial climate and vegetation of the western Alaskan Peninsula. *Alaska J. Anthropol.* 1, 16–33.

Karlstrom, T. N. V. (1969). "Geological investigation of the Kodiak Island Refugium," in *The Kodiak Island Refugium: Its Geology, Flora, Fauna, and History*, eds T. N. V. Karlstrom and G. E. Ball (Whitby: Ryerson Press), 20–54.

Kuiper, J. J., Mooij, W. M., Bragazza, L., and Robroek, B. (2014). Plant functional types define magnitude of drought response in peatland CO2 exchange. *Ecology* 95, 123–131. doi: 10.1890/13-0270.1

Lachniet, M. S., Lawson, D. E., Stephen, H., Sloat, A. R., and Patterson, W. P. (2016). Isoscapes of δ 18O and δ 2H reveal climatic forcings on Alaska and Yukon precipitation. *Water Res. Res.* 52, 6575–6586. doi: 10.2193/2007-2115

Loisel, J., Yu, Z., Beilman, D. W., Camill, B., Alm, J., Amesbury, M. J., et al. (2014). Northern peatland database and synthesis. *Holocene* 24:1028. doi: 10.1177/0959683614538073

Mann, D. H., and Peteet, D. M. (1994). Extent and timing of the last glacial maximum in southwestern Alaska. *Quatern. Res.* 42, 136–148. doi: 10.1006/qres.1994.1063

National Oceanic and Atmospheric Administration [NOAA] (1985). *Climates of the States,* Vol. 1. Detroit: Gale Research Company.

National Oceanic and Atmospheric Administration [NOAA] (2018). *Data Tools: 1981-2010 Normals*. Available at https://www.ncdc.noaa.gov/cdo-web/datatools/normals

Nelson, R. E., and Jordon, R. H. (1988). A postglacial pollen record from western Kodiak Island, Alaska. *Arctic* 41, 59–63. doi: 10.14430/arctic1693

Nichols, J., Isles, P. D. F., and Peteet, D. M. (2014a). A novel framework for quantifying past methane recycling by Sphagnum-methanotroph symbiosis using carbon and hydrogen isotope ratios of leaf wax biomarkers. *Geochem. Geophys. Geosyst* 15, 1827–1836. doi: 10.1002/2014GC005242

Nichols, J., Peteet, D. M., Moy, C. M., Castaneda, I. S., McGeachy, A., and Perez, M. (2014b). Impacts of climate and vegetation change on carbon accumulation in a south-central Alaskan peatland assessed with novel organic geochemical techniques. *Holocene* 24, 1146–1155. doi: 10.1177/0959683614540729

Nichols, J., Walcott, M., Bradley, R., Pilcher, J., and Huang, Y. (2009). Quantitative assessment of precipitation seasonality and summer surface wetness using ombrotrophic sediments from an Arctic Norwegian peatland. *Quatern. Res.* 72, 443–451. doi: 10.1016/j.yqres.2009.07.007

Noguchi, M., Fujiki, T., Okuno, M., Gualtieri, L., Hatfield, V., Sarata, B., et al. (2018). Vegetation changes around Haven Lake, Adak Island, Aleutians, Alaska, determined from pollen analysis. *Radiocarbon* 60, 1483–1492. doi: 10.1017/RDC.2018.103

Peteet, D. M. (1986). Vegetational history of the malaspina glacier district, alaska. *Quatern. Res.* 25, 100–120. doi: 10.1016/0033-5894(86)90047-5

Peteet, D. M. (1991). Postglacial history of lodgepole pine near Yakutat, Alaska. *Can. J. Bot.* 69, 786–796. doi: 10.1139/b91-102

Peteet, D. M., and Mann, D. H. (1994). Late-glacial vegetational, tephra, and climatic history of southwestern Kodiak Island, Alaska. *Ecoscience* 1, 255–267. doi: 10.1080/11956860.1994.11682250

Peteet, D. M., Nichols, J., Moy, C., McGeachy, A., and Perez, M. (2016). Recent and Holocene climate change controls on vegetation and carbon accumulation in Alaskan coastal muskegs. *Quatern. Sci. Rev.* 131, 168–178. doi: 10.1016/j.quascirev.2015.10.032

Sabin, A. L., and Pisias, N. G. (1996). Sea surface temperature changes in the northeastern Pacific Ocean during the last 20,000 years and their relationship to climate change in northwestern North America. *Quatern. Res.* 46, 48–61. doi: 10.1006/qres.1996.0043

Sachse, D., Sachse, D., Billault, I., Bowen, G. J., Chikaraishi, Y., Dawson, T. E., et al. (2012). Molecular paleohydrology: interpreting the hydrogen-isotopic composition of lipid biomarkers from photosynthesizing organisms. *Annu. Rev. Earth Planet. Sci.* 40, 221–249. doi: 10.1146/annurev-earth-042711-105535

Stuiver, M., Reimer, P. J., and Reimer, R. W. (2019). *CALIB 7.1* [WWW Program]. Available at: http://calib.org

Wright, H. E. Jr., Mann, D. H., and Glaser, P. H. (1984). Piston corers for peat and lake sediments. *Ecology* 65, 657–659. doi: 10.2307/1941430

Conflict of Interest Statement: The authors declare that the research was conducted in the absence of any commercial or financial relationships that could be construed as a potential conflict of interest.

frontiers in Earth Science

ORIGINAL RESEARCH
published: 11 April 2019
doi: 10.3389/feart.2019.00074

Pacific Southwest United States Holocene Droughts and Pluvials Inferred From Sediment $\delta^{18}O_{(calcite)}$ and Grain Size Data (Lake Elsinore, California)

Matthew Edward Christopher Kirby[1], William Paul Patterson[2], Matthew Lachniet[3], James A. Noblet[4], Michael A. Anderson[5], Kevin Nichols[6] and Judith Avila[1]*

[1] Department of Geological Sciences, California State University, Fullerton, Fullerton, CA, United States, [2] Department of Geological Sciences, University of Saskatchewan, Saskatoon, SK, Canada, [3] Department of Geoscience, University of Nevada, Las Vegas, Las Vegas, NV, United States, [4] Department of Chemistry and Biochemistry, California State University, San Bernardino, San Bernardino, CA, United States, [5] Department of Environmental Sciences, University of California, Riverside, Riverside, CA, United States, [6] Department of Mathematics, California State University, Fullerton, Fullerton, CA, United States

OPEN ACCESS

Edited by:
Lesleigh Anderson, United States Geological Survey, United States

Reviewed by:
Maarten Blaauw, Queen's University Belfast, United Kingdom
Olga Nikolaevna Solomina, Institute of Geography (RAS), Russia
Matthew Jones, University of Nottingham, United Kingdom

***Correspondence:**
Matthew Edward Christopher Kirby
mkirby@fullerton.edu

Specialty section:
This article was submitted to Quaternary Science, Geomorphology and Paleoenvironment, a section of the journal Frontiers in Earth Science

Received: *24 September 2018*
Accepted: *22 March 2019*
Published: *11 April 2019*

Citation:
Kirby MEC, Patterson WP, Lachniet M, Noblet JA, Anderson MA, Nichols K and Avila J (2019) Pacific Southwest United States Holocene Droughts and Pluvials Inferred From Sediment $\delta^{18}O_{(calcite)}$ and Grain Size Data (Lake Elsinore, California). Front. Earth Sci. 7:74. doi: 10.3389/feart.2019.00074

Records of past climate can inform us on the natural range and mechanisms of climate change. In the arid Pacific southwestern United States (PSW), which includes southern California, there exist a variety of Holocene records that can be used to infer past winter conditions (moisture and/or temperature). Holocene records of summer climate, however, are rare from the PSW. In the future, climate changes due to anthropogenic forcing are expected to increase the severity of drought in the already water stressed PSW. Hot droughts are of considerable concern as summer temperatures rise. As a result, understanding how summer conditions changed in the past is critical to understanding future predictions under varied climate forcings. Here, we present a c. 10.9 kcal BP $\delta^{18}O_{(calcite)}$ record from Lake Elsinore, California, interpreted to reflect $\delta^{18}O_{(lake\,water)}$ values as controlled by over-water evaporation from summer-to-early fall. Our results reveal three millennial scale intervals: (1) the highly evaporative Early Holocene (10.55–6.65 kcal BP), (2) the less evaporative Mid-Holocene (6.65–2.65 kcal BP); and (3) the evaporative Late Holocene (2.65–0.55 kcal BP). These results are coupled with an inferred winter precipitation runoff (sand content) record from Kirby et al. (2010). Using these data together, we estimate the duration and severity of centennial-scale Holocene droughts and pluvials (e.g., high $\delta^{18}O_{(calcite)}$ values plus low sand content = drought and vice versa). Furthermore, the coupled $\delta^{18}O_{(calcite)}$ and sand data provide a generalized Holocene lake level history. The most severe, long-lasting droughts (i.e., maximum summer-to-early fall evaporation and minimum winter precipitation runoff) occur in the Early Holocene. Fewer, less severe, and shorter duration droughts occurred during the Mid-Holocene as pluvials became more common. Droughts return with less severity and duration in the Late Holocene. Notably, the Little Ice Age is characterized as the wettest period during the Late Holocene.

Keywords: Lake Elsinore, isotopes, holocene, evaporation, drought

INTRODUCTION

Extracting seasonality from climatic archives is a major challenge in the field of paleoclimatology (Anderson et al., 1987; Leavitt and Long, 1991; Wurster and Patterson, 2001; Miller et al., 2010; Labotka et al., 2016). For success, the archive must, in some way, capture varying seasonal signals through time. Moreover, the seasonal signal must be strong enough for subsequent preservation, extraction, and interpretation. This is easier said than done. In the winter precipitation dominated, Pacific southwestern United States (PSW), for example, most previous Holocene-length work infers some component of past winter hydroclimates, without any significant insight to summer conditions (Enzel and Wells, 1997; McDonald et al., 2003; Wells et al., 2003; Bird and Kirby, 2006; Bird et al., 2010; Kirby et al., 2010, 2012, 2014, 2015; Pigati et al., 2011). This insight includes the highly resolved tree ring records for the PSW, which record predominantly winter precipitation surpluses and deficits (Graumlich, 1993; Hughes and Graumlich, 1996; Meko et al., 2001; Cook et al., 2007, 2014, 2015; Wise, 2010, 2016; Ault et al., 2013; Griffin and Anchukaitis, 2014; St George and Ault, 2014). Nonetheless, the characterization and explanation of Holocene summer climate is important, particularly for the PSW where summer conditions rapidly amplify, or reduce, winter-generated water deficiencies (i.e., drought) (Griffin and Anchukaitis, 2014; Cook et al., 2015; Diffenbaugh et al., 2015; Shukla et al., 2015; Luo et al., 2017). For example, the most recent Californian drought (2012–2015 AD) is attributed generally to changes in temperature rather than simple reductions precipitation; this is sometimes referred to as a "hot drought" (Griffin and Anchukaitis, 2014; Diffenbaugh et al., 2015; Shukla et al., 2015; Luo et al., 2017).

Fortunately, there are a handful of Holocene PSW summer reconstructions from which we can begin to build a story (cf. Metcalfe et al., 2015). For example, paleo-runoff records from a Mojave Desert alluvial fan (Miller et al., 2010) suggest periods of increased summer precipitation (i.e., North American monsoon) in the Mojave region between 14–9 and 6–3 kcal BP (1000s or years before the present, where the present is AD 1950). However, McDonald et al. (2003) attribute these periods to more frequent warm season tropical cyclones rather than monsoonal moisture. Holmgren et al. (2010) use packrat middens from Joshua Tree National Park to infer the post-glacial onset of monsoonal moisture into southeastern CA by 11 kcal BP. There is, however, only one Holocene summer paleotemperature reconstruction from the study region – a July temperature pollen-reconstruction for the San Jacinto Mountains (headwaters to Lake Elsinore) (Wahl, 2002; Ohlwein and Wahl, 2012). In general, this pollen reconstruction shows above-average to average July temperatures for most of the Holocene, excepting a cooling at 2.4 and 0.3–0.2 kcal BP. A closer look reveals a more nuanced signal described in the discussion. In the adjacent San Bernardino Mountains, Bird and Kirby (2006), Bird et al. (2010), and Kirby et al. (2012) argue that enhanced Early Holocene runoff and associated higher lake levels at Dry Lake may reflect an expanded monsoon in response to higher-than-today, summer insolation. Kirby et al. (2005, 2007) proposed a similar mechanism for enhanced runoff into Lake Elsinore during the Early Holocene. However, neither of these lake studies can provide unequivocal evidence for summer climate, only inferred evidence based on suspected climatic forcings (i.e., summer insolation effect).

Combined with an existing reconstruction of historical winter precipitation and runoff from Lake Elsinore, here we re-examine the site's Holocene record using a particularly sensitive lake sediment proxy for arid and semi-arid environment lakes – the oxygen isotopes of endogenic calcite (Leng and Marshall, 2004; Steinman and Abbott, 2013; Dean et al., 2015; Anderson et al., 2016; Horton et al., 2016). The stable oxygen isotopes values ($\delta^{18}O$) of lacustrine endogenic calcite reflect a combination of water temperature and the $\delta^{18}O_{(lake\ water)}$ values during mineral precipitation (e.g., Stuiver, 1970). Lakes located in arid regions, such as Lake Elsinore, often display variations in $\delta^{18}O_{(lake\ water)}$ associated with changing P:E ratios (precipitation : evaporation) more so than lake water temperature changes (Kelts and Talbot, 1990; Li and Ku, 1997; Li et al., 2000; Kirby et al., 2004; Leng and Marshall, 2004; Dean et al., 2015). Rather, the $\delta^{18}O_{(lake\ water)}$ values are primarily controlled by the rate of evaporation and lake source water $\delta^{18}O$ values, including lake water residence time (Kelts and Talbot, 1990; Li and Ku, 1997; Li et al., 2000; Benson et al., 2002; Leng and Marshall, 2004; Dean et al., 2015). Using modern isotopic and hydrologic observations from a lake helps to unravel these complexities (Steinman and Abbott, 2013; Dean et al., 2015). With the supporting modern lake water, the dominant hydroclimatic signal preserved in the $\delta^{18}O_{(calcite)}$ values can be inferred back through time.

In this paper, we use a lacustrine sediment $\delta^{18}O_{(calcite)}$ archive from Lake Elsinore, California to infer centennial to multi-centennial scale changes in Holocene summer-to-early fall $\delta^{18}O_{(lake\ water)}$ values (i.e., period of maximum $CaCO_3$ precipitation). In turn, these changes are interpreted to reflect summer-to-early fall over-water evaporation. Combined with a winter precipitation and runoff history based on sand content (Kirby et al., 2010), we consider the severity and duration of past Holocene droughts and pluvials that also provides a generalized Holocene lake level history. Finally, we compare our results to a pollen-based, July temperature anomaly reconstruction from the San Jacinto Mountains – the headwater catchment area for Lake Elsinore (Wahl, 2002; Ohlwein and Wahl, 2012).

BACKGROUND

Study Site and Limnology

Lake Elsinore is the largest natural lake in the PSW (**Figure 1**). This pull-apart basin contains a sediment package of up to 1000 m based on gravimetric studies (Hull, 1990). The lake is polymictic, experiences occasional hypolimnic anoxia, and precipitates epilimnic $CaCO_3$. The highest rates of $CaCO_3$ precipitation occur in the warm summer months, based on sediment trap studies (Anderson, 2001). At Elsinore, $CaCO_3$ precipitation is likely the result of late-spring/summer/early fall algae blooms, their photosynthetic uptake of CO_2, and the subsequent change in epilimnic pH, which favors the precipitation of $CaCO_3$ (Anderson, 2001). Warm season, biomediated $CaCO_3$ precipitation in lacustrine environments

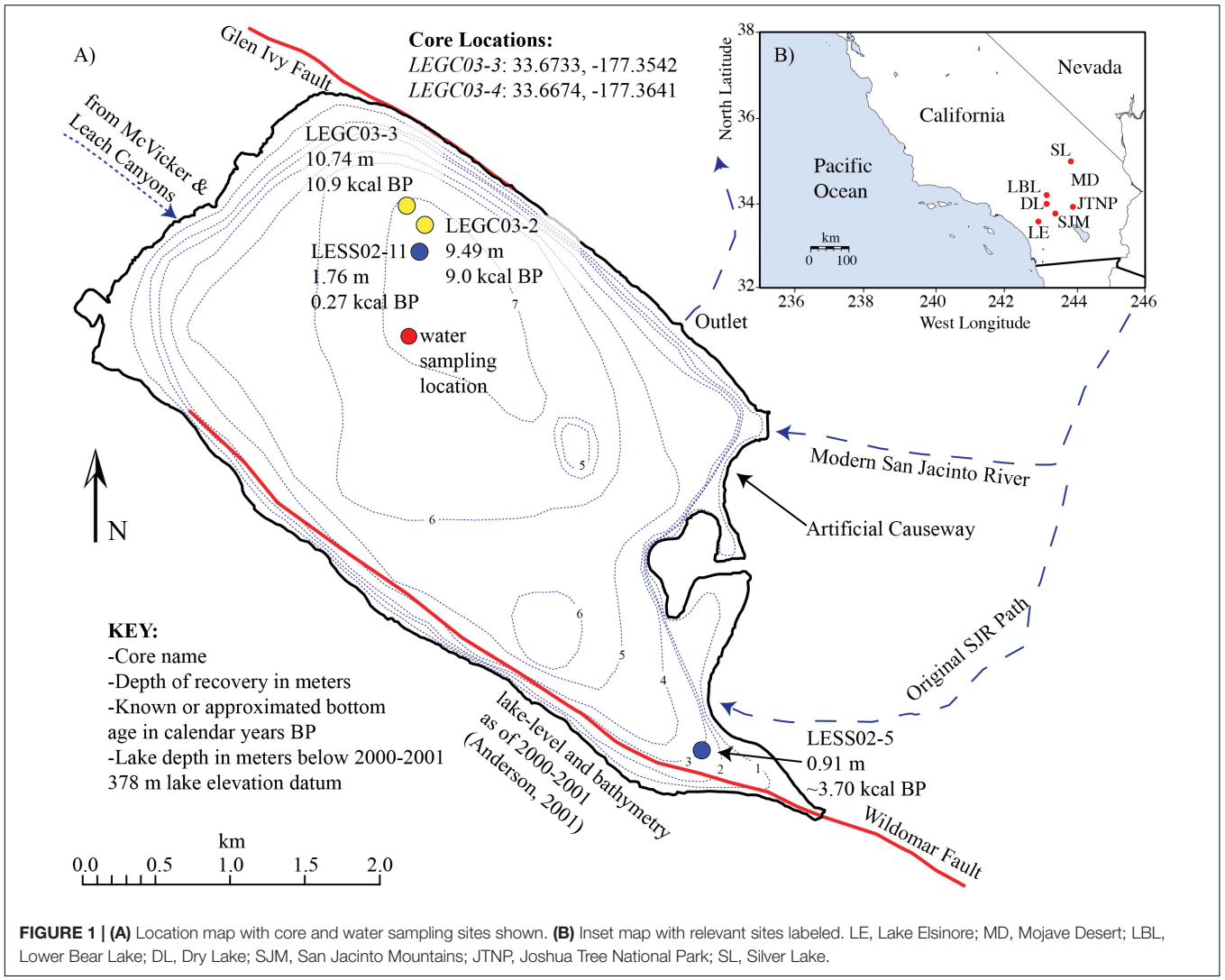

FIGURE 1 | (A) Location map with core and water sampling sites shown. **(B)** Inset map with relevant sites labeled. LE, Lake Elsinore; MD, Mojave Desert; LBL, Lower Bear Lake; DL, Dry Lake; SJM, San Jacinto Mountains; JTNP, Joshua Tree National Park; SL, Silver Lake.

is a well-documented phenomenon with proven value for interpreting past lake conditions (Lebo et al., 1994; Anderson et al., 1997; Thompson et al., 1997; Hodell et al., 1998; Mullins, 1998, 2011; Kirby et al., 2002, 2004; Lajewski et al., 2003; Leng and Marshall, 2004). The preservation of warm season precipitated $CaCO_3$ is also favored by a warmer water column and the associated decrease in $CaCO_3$ solubility at higher water temperatures. The latter relationship is apparent in Lake Elsinore via the presence and near absence of $CaCO_3$ during the warmer Holocene versus the colder Glacial, respectively (Kirby et al., 2007, 2013, 2018).

Hydrologically, Lake Elsinore is considered a closed basin lake with only occasional, short-lived overflow (Kirby et al., 2004). Lake level responds directly to the amount of winter precipitation runoff and subsequent summer-to-early fall evaporation (Kirby et al., 2004, 2010). This direct response is not unexpected for arid environment sites, especially those dominated by a winter precipitation climatology such as the PSW (Kirby et al., 2006). Although summer precipitation is a negligible contributor to the lake's annual hydrologic budget, net over-water evaporation peaks in the hot summer-to-early fall months, totaling ~1.4 m evaporation $year^{-1}$ (Anderson, 2001). Simplified, Lake Elsinore's net annual hydrologic budget is a combination of two seasonal end members – winter precipitation (P) and summer-to-early fall evaporation (E), hereafter referred to as the P:E ratio. The winter end member is documented in several papers using changes in grain size and other physical or chemical parameters to infer precipitation-related runoff dynamics (Kirby et al., 2007, 2010, 2013, 2018). However, a direct summer-to-early fall evaporation indicator was not available for Lake Elsinore, thereby limiting our knowledge of Holocene precipitation seasonality trends in the PSW.

Climatology

The climate of the PSW is Mediterranean – cool, wet winters and hot, dry summers (Bailey, 1966). In general, the coastal plain and low-lying inland regions (i.e., Lake Elsinore) receive less precipitation than the adjacent mountain ranges (Masi, 2005). Year-to year winter precipitation variability is related predominantly to tropical and north Pacific ocean-atmosphere

dynamics and their modulation of the winter storm track over the PSW (Cayan and Peterson, 1989; Brito-Castillo et al., 2003; Hanson et al., 2006). For example, both El Niño-Southern Oscillation (ENSO) and the Pacific Decadal Oscillation (PDO) modulate the mean winter position of the eastern Pacific subtropical high and thus the average latitude of the Pacific winter storm track (Cayan and Peterson, 1989; Brito-Castillo et al., 2003; Hanson et al., 2006). When storms track south, they cause higher than average precipitation and greater river discharge at Lake Elsinore, whereas a more northerly position results in lower than average precipitation and less river discharge (Cayan et al., 1999; Hanson et al., 2006; Gray et al., 2015).

Winter precipitation in the PSW is frequent and characterized by lower precipitation stable oxygen isotope values ($\delta^{18}O_{(precipitation)}$), whereas summer precipitation is infrequent and characterized by higher $\delta^{18}O_{(precipitation)}$ values (Friedman et al., 1992). For example, the average 6-month winter $\delta^{18}O_{(precipitation)}$ value between 1985 and 1986 A.D. for Mt. San Jacinto (the headwaters of Lake Elsinore) was −12.2 and −14.0‰, respectively. Summer $\delta^{18}O_{(precipitation)}$ for the same years averaged −9.2 and −6.9‰. 50 km NNW of Mt. San Jacinto, $\delta^{18}O_{(precipitation)}$ at Big Bear for winter and summer over the same period of time were −11.8, −14.9 and −5.8, −7.1‰, respectively. The contribution of summer precipitation, however, plays no significant role in the annual hydrological budget at Lake Elsinore. Importantly, the Friedman et al. (1992) study confirms that winter precipitation in the PSW is sourced solely from Pacific Ocean-origin storm tracks and that the associated isotopic signature of winter precipitation is significantly lower than summer sourced precipitation.

A study by Williams and Rodoni (1997) focused specifically on the coastal PSW provides a variety of river, groundwater, and lake water $\delta^{18}O$ data. For example, four data points from Lake Elsinore between 1992 and 1994 provide $\delta^{18}O_{(lake\ water)}$ values of +4.00‰ (01/18/92), −5.78‰ (05/28/93), −4.84‰ (09/03/93), and −3.86‰ (01/04/94), respectively. The initial value of +4.00‰ occurred during a period of extreme low lake levels (the second lowest in the 20th century) and its subsequent reflection of a highly evaporative hydrologic system. Following this lowstand is an abrupt increase in lake level caused by several exceptionally wet winters. This period of extreme runoff produced $\delta^{18}O_{(lake\ water)}$ values much lower than anything measured in our study, recording the rapid influx of low $\delta^{18}O$, winter precipitation (Friedman et al., 1992). These studies are important because they reveal the range of $\delta^{18}O_{(lake\ water)}$ values that can occur in arid environment lakes such as Lake Elsinore. As a result, they provide a baseline understanding for the range of potential and measured $\delta^{18}O_{(calcite)}$ values we observe through the Holocene (discussed below).

MATERIALS AND METHODS

Core Retrieval and Sedimentology

Details on sediment core LESS02-11 and LEGC03-3 acquisition and sediment methods (i.e., environmental magnetic susceptibility, LOI 550°C, LOI 950°C, and grain size) are detailed in Kirby et al. (2007, 2010). Magnetic susceptibility, LOI 550°C, and LOI 950°C data are included on **Supplementary Table S1**. Grain size data are available on the NOAA Paleoclimatology Data website[1]. New to this paper are x-ray diffraction (XRD) data. Fifty bulk (<2000 μm) sediment samples were analyzed in 2008 using x-ray diffraction at the Institute of Arctic and Alpine Research (University of Colorado, Boulder, CO, United States) to determine their respective mineralogies. The program RockJock (Eberl, 2004) was used to convert the XRD data into mineral type by weight% (e.g., Andrews and Eberl, 2012).

Age Control

In the absence of salvageable macro- or micro-organic matter, bulk organic matter (i.e., carbon) was used for age control. Eight dates were measured on core LEGC03-2 and 18 dates were measured on LEGC03-3. All radiocarbon samples were measured at the University of California, Irvine W. M. Keck Carbon Cycle Accelerator Mass Spectrometry Laboratory. Each sample was pre-treated with a standard acid-base-acid method. Five ages from LESS02-11 were determined previously by Kirby et al. (2007, 2010), including the surface age (2003 AD, −0.053 kcal BP), Elemental Pb (1975 AD, −0.025 kcal BP), Cs^{137} (1963 AD, −0.013 kcal BP), and exotic pollen markers (*Eucalyptus*, 1910 AD, 0.040 kcal BP; *Erodium*, 1800 AD, 0.15 kcal BP). A new age model was created using the Bacon v.2.2 age-modeling software (Blaauw and Christen, 2011).

Sediment Isotope Data

Samples were extracted from LEGC03-3 for bulk sediment $\delta^{18}O_{(calcite)}$ and $\delta^{13}C_{(calcite)}$ at approximately 1–3 cm intervals between 10 and 1073 cm (n = 491). Bulk sediment samples were dried at room temperature and gently ground into a powder. Mean (0.5) grain size for the core is 8.4 μm (mode: 10.8 μm), thus suggesting that the $CaCO_3$ component is likely found in the very fine silt size fraction. SEM analyses of lake sediment show distinct micron size $CaCO_3$ grains dispersed throughout the sediment, thus confirming the occurrence of fine grain carbonate (Anderson, 2001). The lack of carbonate bedrock in the lake's drainage basin eliminates the likelihood that the isotopic values record a detrital carbonate source (Engel, 1959). Bulk sediment samples were roasted *in vacuo* at 200°C to remove water and volatile organic contaminants that may confound stable isotope values of carbonate. Stable oxygen and carbon isotope values were obtained using a Finnigan Kiel-IV carbonate preparation device directly coupled to the inlet of a Finnigan MAT 253 ratio mass spectrometer in the stable isotope laboratories at the University of Saskatchewan. Twenty to forty micrograms of carbonate were reacted at 70°C with three drops of anhydrous phosphoric acid for 90 s. Isotope ratios were corrected for acid fractionation and ^{17}O contribution and reported in per mil notation (‰) relative to VPDB standards. Precision and calibration of data were monitored through daily analysis of NBS-18 and NBS-19 carbonate standards. $\delta^{18}O$ values of the samples are bracketed by those of the standards. Precision is better than ± 0.1‰ for both carbon and oxygen isotope values.

[1]https://www.ncdc.noaa.gov/data-access/paleoclimatology-data

Lake Water Data and Oxygen Isotopic Calculations

Lake water isotope samples ($\delta^{18}O$ and δD) were collected at 0.5 m water depth in the center of the lake throughout the year between January 1, 2006 and April 4, 2010 (n = 72) (**Figure 1**). Each sample was collected using a lake-water rinsed (3x), high density Nalgene 100 mL bottle. Water was filled to the top, immediately covered by parafilm, and the cap tightened firmly. Samples were placed in the cooler and transported to the CSUF Lab where they were stored in a refrigerator (4°C). Water isotope values were measured at either the University of Saskatchewan or the University of Nevada, Las Vegas. At UNLV, waters were analyzed on a ThermoElectron high temperature thermal conversion elemental analyzer (TC/EA) with a ConFlo III interfaced in continuous flow mode to a Delta V Plus mass spectrometer. Samples were injected into a reactor at 1450°C to produce CO and H2 in a stream of ultra-high purity helium, and gasses were separated on a gas chromatograph column. Regular analysis of internal standards was done in each run with unknowns, with standards calibrated to VSMOW and VSLAP, with the latter values defined as −55.5 and −428‰ for $\delta^{18}O$ and $\delta^{2}H$, respectively (Coplen, 1996). At the University of Saskatchewan, water samples were analyzed using a Picarro L1102-i Isotopic Liquid Water Analyzer based on wavelength-scanned cavity ring down spectroscopy (WS-CRDS). Each sample was analyzed six consecutive times. The first three injections were discarded to eliminate memory effects and the averages of the last three injections were used to calculate $\delta^{18}O_{(H2O)}$ and $\delta D_{(H2O)}$ values. No drift calibration was necessary. Long-term sample precision was determined to be ± 0.1‰ for $\delta^{18}O$ and ± 1‰ for δD based upon the two internal standards (n = 80). Precision was significantly higher based upon 150 deionized water samples run consecutively (± 0.04‰ for $\delta^{18}O$ and ± 0.2‰ for δD), because the memory effect between the samples was insignificant. δ values ($\delta^{18}O$ and δD) presented here are in ‰ relative to VSMOW, after calibration to VSMOW-VSLAP. Water temperature was also measured at each water isotope sampling site at 0.5 m water depth throughout the year. Lake level data are from the Elsinore Valley Municipal Water District. We use the Kim and O'Neil (1997) equation to calculate $\delta^{18}O_{(calcite)}$ from the 2006–2010 AD water temperature (°C) and $\delta^{18}O_{(lake\ water)}$ and $\delta D_{(lake\ water)}$ data set.

RESULTS AND ISOTOPIC INTERPRETATIONS

Core Sedimentology

LEGC03-3 core description and results for environmental magnetic susceptibility, LOI 550°C, LOI 950°C, and grain size are detailed in Kirby et al. (2007, 2010). Core LEGC03-3 is dominantly a gray, homogenous clayey silt with occasional very-fine-to-fine sand units – most sand units are <1–2 cm thickness and they are often disseminated within matrix. Here, we focus on the calcite, Mg-calcite, and aragonite XRD results, as they are relevant to the isotopic data. Calcite is the dominant carbonate mineral, averaging 6.7 ± 2.9% with a maximum of 15.5% and a minimum of 0.4%. Mg-calcite average 3.0 ± 1.4% with a maximum of 6.2% and a minimum of 0.6%. Aragonite average 0.08 ± 0.13% with a maximum of 0.45% and a minimum of 0.0%. Calcite and Mg-calcite show a positive, but weak correlation (n = 50, r = 0.38, p < 0.006). Aragonite is not correlated to either calcite or Mg-calcite.

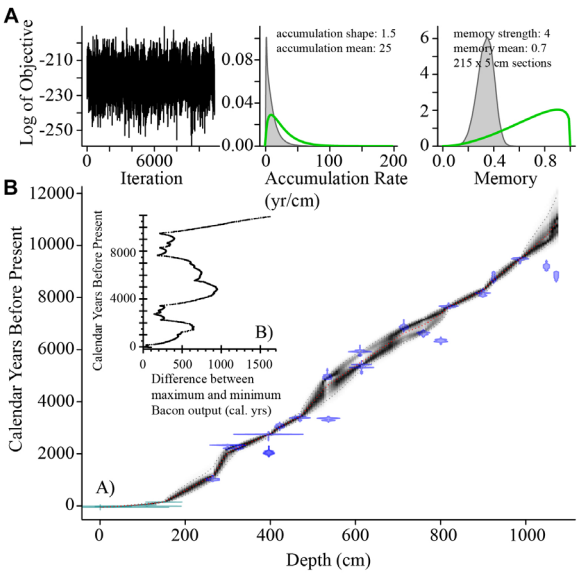

FIGURE 2 | (A) Bacon v.2.2 age model for combined LEGC03-3 and LESS02-11 ages. **(B)** Difference between maximum and minimum Bacon v.2.2 age model output. Maximum and minimum based on 2.5 and 97.5% quantiles (95% confidence ranges).

Age Control

A new age model, building on that from Kirby et al. (2007, 2010), was developed using 26 dates entered into the Bacon v.2.2 (IntCal13) age-modeling software (**Figure 2A** and **Table 1**) (Blaauw and Christen, 2011). Ages from core LESS02-11 and LEGC03-2 were transferred to LEGC03-3 using centimeter-scale sedimentological data to create a single age model for LEGC03-3 spanning −0.053 kcal BP to ∼10.9 kcal BP (Kirby et al., 2010). Five radiocarbon dates were not used in the age model due to suspected reworking (**Table 1**). The date at 105–106 cm is stratigraphically above the *Eucalyptus* pollen age (AD 1910) at 110 cm, and it is therefore considered too old. The dates at 162–163 and 195–196 cm are significantly older than the pollen age at 150 cm. As a result, they require a significant decrease in sedimentation or a hiatus to explain their age-depth relationship. Based on the core description and sedimentological data, we conclude that a sudden decrease in sedimentation and/or a hiatus is unrealistic and requires substantial age model adjustment that is not supported by the sediment data. Finally, the ages at 635–636 and 683–684 cm are from thin, sharply bounded units with higher-than-average magnetic susceptibility and C:N ratios (data not shown), which indicate potential reworking of terrestrial organic matter, thus questioning the accuracy of the bulk organic carbon ages.

TABLE 1 | LEGC03-2 and 3 and LESS02-11 age control data.

Core ID	Depth interval	Core LEGC03-3 equivalent	UCIAMS ID	$\delta^{13}C$ (‰)	^{14}C AGE (BP)	±	Material dated
LESS 02-11ab	0	0	NA	NA	NA	0	Intact Surface (2003 AD)
LESS 02-11ab	31	31	NA	NA	NA	5	Elemental Pb (1970 AD)
LESS 02-11ab	46	46	NA	NA	NA	0	^{137}Cs (1963 AD)
LEGC03-3*	105–106	105.5	8263	−20.7	860	25	Bulk organics
LESS 02-11ab	110	110	NA	NA	NA	10	Exotic Pollen (*Eucalyptus*) (1910 AD)
LESS 02-11ab	150	150	NA	NA	NA	20	Exotic Pollen (*Erodium*) (1800 AD)
LEGC03-3*	162–163	162.5	8264	−20.4	650	20	Bulk organics
LEGC03-3*	195–196	195.5	8265	−17.9	1,180	20	Bulk organics
LEGC03-3	264–265	264.5	8266	−17.5	1,115	25	Bulk organics
LEGC03-2	298–299	299.5	8260	−17.8	2,290	20	Bulk organics
LEGC03-3	324–325	324.5	8267	−18.4	2,270	30	Bulk organics
LEGC03-3	395–396	395.5	8268	−20.3	2,610	20	Bulk organics
LEGC03-2	405–406	396.5	6832	−21.0	2,075	25	Bulk organics
LEGC03-2	405–406	396.5	6695	−14.2	2,060	35	Bulk organics
LEGC03-2	432–433	421.93	8261	−16.2	2,915	25	Bulk organics
LEGC03-3	469–470	469.5	8270	−17.6	3,160	25	Bulk organics
LEGC03-2	556–557	533.79	8262	−15.2	4,385	30	Bulk organics
LEGC03-3	536–537	536.5	8271	−19.2	3,125	20	Bulk organics
LEGC03-3	610–611	610.5	8272	−16.1	5,160	30	Bulk organics
LEGC03-2	624–625	614.17	6833	−15.8	4,605	25	Bulk organics
LEGC03-3*	635–636	635.5	8274	−18.4	4,955	30	Bulk organics
LEGC03-3*	683–684	683.5	8275	−18.1	4,945	30	Bulk organics
LEGC03-3	713–714	713.5	8277	−17.6	6,025	35	Bulk organics
LEGC03-3	759–760	759.5	8278	−17.3	5,820	30	Bulk organics
LEGC03-3	800–801	800.5	8279	−18.1	5,540	40	Bulk organics
LEGC03-2	850–851	818.69	6834	−14.4	6,825	30	Bulk organics
LEGC03-2	947–948	899	6835	−17.7	7,350	30	Bulk organics
LEGC03-3	924–925	924.5	8280	−19.4	7,910	50	Bulk organics
LEGC03-3	986–987	986.5	8283	−14.9	8,465	40	Bulk organics
LEGC03-3	1048–1049	1048.5	8284	−17.0	8,225	40	Bulk organics
LEGC03-3	1071–1072	1071.5	8286	−18.0	7,965	40	Bulk organics

* = *not used in the age model.*

Figure 3 illustrates the differences between the Kirby et al. (2007, 2010) age model and that determined for this paper. In general, the difference between the age models increases with depth such that the new Bacon age model is up to 1200 years older at the base of the core than the Kirby et al. (2007, 2010) age model (**Figure 3**). Importantly, this updated age model does not invalidate interpretations in Kirby et al. (2007, 2010). However, the absolute timing of the Kirby et al. (2010) sand-inferred pluvials and droughts have changed (see section "Discussion").

To assess the range of ages associated with the new Bacon age model, we have plotted the difference between the maximum and minimum Bacon age output on **Figure 2B**. The maximum and minimum ages represent the 95% confidence ranges, based on 2.5 and 97.5% quantiles (Blaauw and Christen, 2011). This assessment shows that the age range is greatest between 0.5 and 2.0 kcal BP (up to 680 years), 4.0–7.0 kcal BP (up to a 1000 years), and 9.8 kcal BP through to the core bottom (up to 1600 years). Knowing this range of ages provides some constraint of the accuracy of the assigned pluvial and drought intervals. Considering this range of potential ages, we limit our temporal interpretation to centennial-to-multi-centennial timescales to account for age model uncertainty. Future use of these sand and isotope data should consider this inherent age variability when interpreting apparent site-to-site correlations.

Modern Lake Water and Sediment Isotope Comparisons

Recent lake level and lake water isotopic data are shown in **Figure 4**. For the period of overlapping data, lake level ranges from a minimum of 377.6 m to a maximum of 381.2 m. Over the same period, $\delta^{18}O_{(lake\ water)}$ ranges from a minimum of −1.0‰ to a maximum of 5.3‰ (n = 72) with a mean of 2.4‰ (**Supplementary Table S2**). $\delta D_{(lake\ water)}$ ranges from a minimum of −19.2‰ to a maximum of 12.1‰ (n = 72) with a mean value of −2.3‰ (**Supplementary Table S2**). Notably, there is a negative relationship between lake level and $\delta^{18}O_{(lake\ water)}$ between 1/3/2006 and 4/2/2010. As lake level drops, the $\delta^{18}O_{(lake\ water)}$ values increase (**Figure 4**). This coupling is expected in an arid environment where

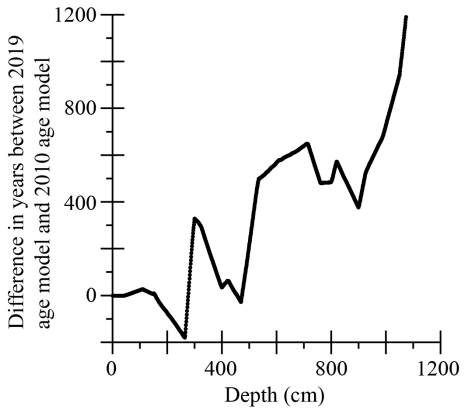

FIGURE 3 | Difference in years (cal BP) between the 2019 Elsinore Bacon v.2.2 age model and the Kirby et al. (2010) age model.

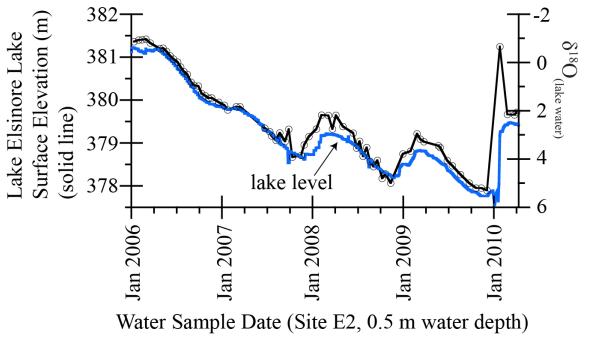

FIGURE 4 | Lake Elsinore lake level (m) and measured lake water (0.5 m water depth) $\delta^{18}O$ values.

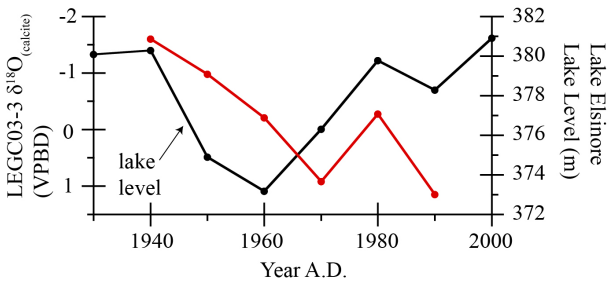

FIGURE 5 | 20th century 10-year binned $\delta^{18}O_{(calcite)}$ values and lake level data.

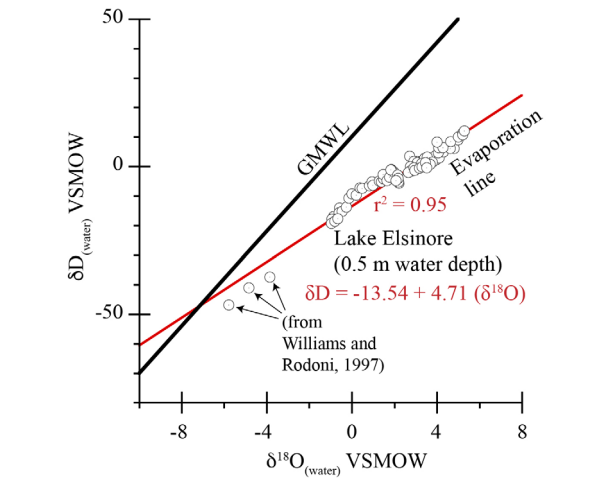

FIGURE 6 | Lake Elsinore water (0.5 m water depth) oxygen and hydrogen isotopic values plotted versus the GMWL. Note the strong departure from the GMWL by the Lake Elsinore $\delta^{18}O_{(lake\ water)}$ values in response to evaporation.

annual net evaporation strongly influences lake hydrology (Leng and Marshall, 2004; Dean et al., 2015; Anderson et al., 2016). As an additional test of this modern relationship, we compare 20th century 10-year binned Lake Elsinore lake level to core LEGC03-3 $\delta^{18}O_{(calcite)}$ data (**Figure 5**). A similar negative relationship is observed; although, the 20th century comparison is based on only six data points. Other factors that may have influenced the 20th century relationship include: (1) human modification of the influent during and following the 1950s drought (Hudson, 1978), which likely altered natural $\delta^{18}O_{(lake\ water)}$ values; and (2) high uncertainty associated with the 20th century age model (**Figure 2** and **Table 1**). Nonetheless, both the modern and 20th century data suggest that changes in $\delta^{18}O_{(lake\ water)}$ values reflect the relative strength of over-water evaporation and its modulation of the lake's hydrologic and isotopic budget. Finally, a strong departure from the Global Meteoric Water Line (GMWL) further supports the interpretation that evaporation plays a dominant role in governing the lake's isotopic composition (**Figure 6**) (Williams and Rodoni, 1997).

Lake water temperatures measured at the same location and depth (0.5 m below the lake surface) as the water isotope samples, range from a minimum of 9.4°C to a maximum of 28.9°C with a mean of 20.3°C (n = 77) (**Figure 7** and **Supplementary Table S2**). These temperature data are combined with the measured $\delta^{18}O_{(lake\ water)}$ values to calculate the $\delta^{18}O_{(calc\ sed\ calcite)}$ values using the Kim and O'Neil (1997) equation. These calculations were made to examine how well the modern system captures the range of $\delta^{18}O_{(calcite)}$ values observed in the Holocene (**Figure 8**), and to evaluate if the modern system a reasonable benchmark for interpreting the paleo $\delta^{18}O_{(calcite)}$ values. The similarity between calculated modern (range = −3 to 5‰) and Holocene (range = −7.9 to 5.1‰) values suggests that our modern $\delta^{18}O_{(calc\ sed\ calcite)}$ values capture a large part of the natural isotopic variability in the Lake Elsinore system and are congruent with values measured in the paleo-record (**Figures 7**, **8**). This indicates that fractionation between $\delta^{18}O_{(lake\ water)}$ and subsequent epilimnic $\delta^{18}O_{(calcite)}$ values is likely conservative and reflects similar drivers through time. Time-averaging the Holocene $\delta^{18}O_{(calcite)}$ values into 100-year bins dampens higher frequency isotopic variability and their effect on our interpretations, such as that caused by potential non-equilibrium processes, changes in over-water

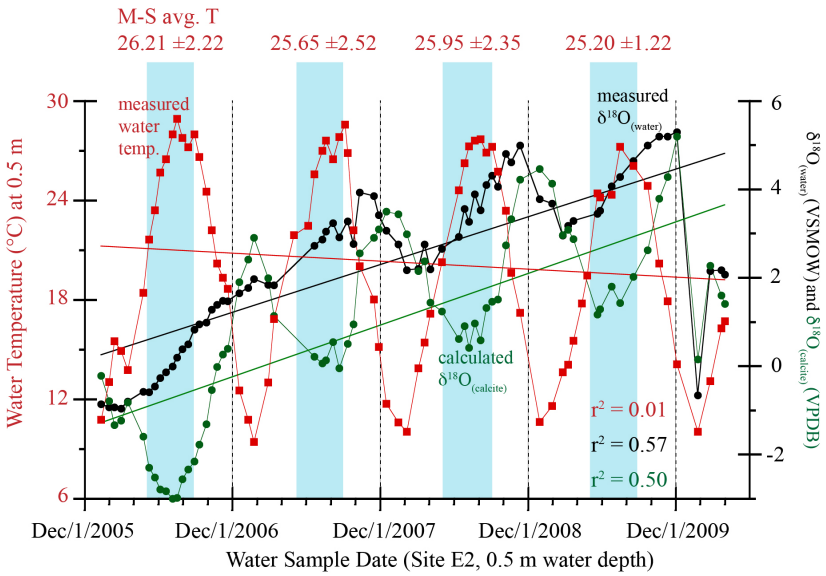

FIGURE 7 | Lake Elsinore measured $\delta^{18}O_{(lake\ water)}$ values, measured water temperature (0.5 m water depth), and $\delta^{18}O_{(calc.sed.calcite)}$. Shaded areas represent months of peak calcite precipitation. Average May (M) – September (S) lake water temperatures are shown at the top of the figure with standard deviation values.

relative humidity, and/or other unforeseen isotopic imbalances (Gat, 1996; Leng and Marshall, 2004).

Calculated $\delta^{18}O_{(calc\ sed\ calcite)}$ values range from a minimum of −3.0‰ to a maximum of 5.2‰ with a mean of 1.0‰ ($n = 72$) (**Figure 7**). Whilst lake temperatures show no significant trend over the period of study, the $\delta^{18}O_{(lake\ water)}$ and the $\delta^{18}O_{(calc\ sed\ calcite)}$ data show a very similar 4+ year trend. Over the 4+ years of measured data, lake level dropped consistently with only nominal winter recovery (**Figure 4**). Lake water isotopic values capture this evaporative trend as do the calculated $\delta^{18}O_{(calc\ sed\ calcite)}$ values. The combination of, and relationship between, measured lake level data, measured $\delta^{18}O_{(lake\ water)}$ values, and $\delta^{18}O_{(calc\ sed\ calcite)}$ values provides the basis for our interpretation that the predominant control on Lake Elsinore sediment $\delta^{18}O_{(calcite)}$ values over time is the isotopic value of the lake water, not water temperature. As additional support for this interpretation, we note that predominant interval of epilimnic calcite precipitation is likely during the late spring through early fall, when lake productivity re-emerges from its winter dormancy (or suppression) (**Figure 7**). During this period of peak calcite precipitation, lake water temperatures – averaged from May through September – are relatively stable and uniformly warm from year-to-year, thus contributing nominally to the resultant $\delta^{18}O_{(calcite)}$ values (Anderson, 2001) (**Figure 7**).

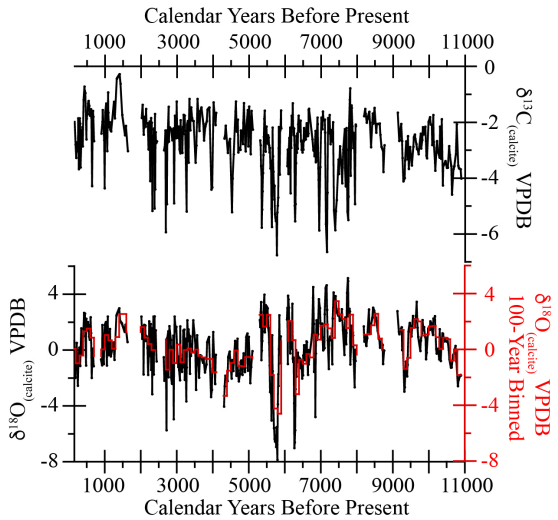

FIGURE 8 | Raw bulk sediment $\delta^{18}O_{(calcite)}$ and $\delta^{13}C_{(calcite)}$ values. The solid red line represent the 100-year binned $\delta^{18}O_{(calcite)}$ data.

Holocene Sediment Oxygen Isotope Data

The raw and 100-year binned sediment isotope data are shown by **Figure 8**. Although the raw data are shown, the discussion is based on $\delta^{18}O_{(calcite)}$ 100-year binned averages to account for age model uncertainty (e.g., 0.2 kcal BP BIN = 0.15–0.25 kcal BP average value, etc.) (**Figure 8** and **Supplementary Table S3**). Centuries not included in the binned data due to either missing core or disturbed sections include: 0.8, 1.7–1.9, 2.5, 4.2, 5.2, 6.0, 8.1, and 8.8–9.1 kcal BP. Intervals not included due to too few data points for an accurate 100-year bin include: 0–1.0, 1.5, 2.6, 3.9, and 4.1–4.3 kcal BP. The raw $\delta^{18}O_{(calcite)}$ range from a minimum of −7.9‰ to a maximum of 5.1‰ VPDB with a mean 0.2‰ and a standard deviation of 2.1‰ ($n = 491$) (**Figure 8**). Notably, the Holocene range of $\delta^{18}O_{(calcite)}$ values as well as the mean are not too dissimilar to the $\delta^{18}O_{(calc\ sed\ calcite)}$ values (**Figure 7**), excepting the anomalously low $\delta^{18}O_{(calcite)}$ values ca. 5.7–5.8 kcal BP. We interpret this similarity to indicate that our 4+ year modern study captured a fair amount of the natural variation – in terms of averages and max/min – that

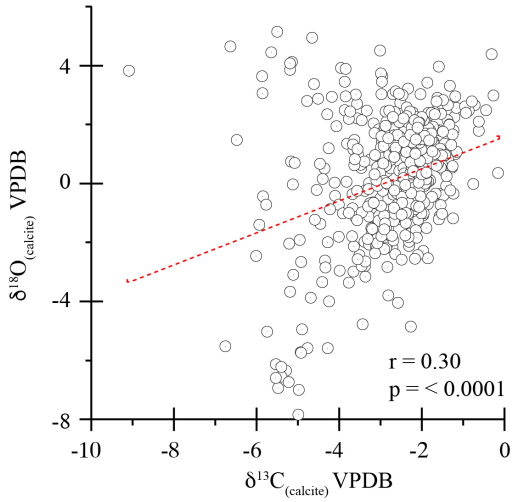

FIGURE 9 | Scatter plot comparing Holocene sediment $\delta^{18}O_{(calcite)}$ and $\delta^{13}C_{(calcite)}$ values.

occur at Lake Elsinore. $\delta^{18}O_{(calcite)}$ show a weak, but positive correlation to both LOI 550°C ($r = 0.23$, $p < 0.0001$, $n = 491$) and LOI 950°C ($r = 0.21$, $p < 0.0001$, $n = 491$). $\delta^{13}C_{(calcite)}$ range from a minimum of −9.1‰ to a maximum of −0.2‰ with a mean of −2.7‰ and a standard deviation of 1.2‰ ($n = 491$) (**Figure 5** and **Supplementary Table S4**). $\delta^{18}O_{(calcite)}$ to $\delta^{13}C_{(calcite)}$ covariance over the length of the record is poor ($r = 0.30$) but statistically significant ($p = < 0.001$), possibly indicating sustained periods of lake closure, $\delta^{13}C_{(DIC)}$ evaporative enrichment, and/or a productivity link related to seasonal evapoconcentration of nutrients, or a transition in terrestrial supply of DIC, DOC, and POC associated with decreased precipitation (**Figure 9**) (Talbot, 1990; Drummond et al., 1995; Li and Ku, 1997; Kirby et al., 2002; Leng and Marshall, 2004; Horton et al., 2016). A more detailed look at $\delta^{18}O_{(calcite)}$ to $\delta^{13}C_{(calcite)}$ covariance reveals six intervals of positive and statistically significant covariance, and one interval of negative and statistically significant covariance (**Supplementary Table S5**). This detailed examination of $\delta^{18}O_{(calcite)}$ to $\delta^{13}C_{(calcite)}$ covariance suggests a predominantly closed basin through time, as suspected based on 20th century lake level data (**Figures 4**, **5**) (Kirby et al., 2004). The $\delta^{13}C_{(calcite)}$ Holocene data are not discussed further here.

The relationship between the 100-year binned $\delta^{18}O_{(calcite)}$ values and the 100-year binned sand data is not statistically significant ($n = 90$, $r = -0.02$, $p < 0.84$), indicting that there is no *consistent* relationship between $\delta^{18}O_{(calcite)}$ values (i.e., E in the P:E relationship) and the sand data (i.e., P in the P:E relationship) over the Holocene. In the discussion we explore the relationship between the $\delta^{18}O_{(calcite)}$ values and the sand data on a century-to-century basis to identify intervals of similar or dissimilar responses. Based on this comparison, we infer the duration and severity of Holocene droughts and pluvials as well as speculate on a generalized Holocene lake level interpretation for Lake Elsinore.

DISCUSSION

Holocene Pluvials, Droughts, and Lake Level

Using the similarity between the Holocene and 20th century average $\delta^{18}O_{(calcite)}$ values (0.2 and −0.3‰, respectively), we select 0.0‰ as the break point to define above-average and below-average, Holocene summer-to-early fall over-water evaporation (**Figure 10**). These 100-year binned data are then bracketed by color (orange = above-average evaporation; blue = below-average evaporation), when there are two or more adjacent 100-year bins.

At first look, the $\delta^{18}O_{(calcite)}$ data can be divided into three millennial scale intervals characterizing changes in summer-to-early fall, over-water evaporation: (1) the highly evaporative Early Holocene (10.45–6.65 kcal BP), (2) the less evaporative Mid-Holocene (6.65–2.65 kcal BP); and (3) the evaporative Late Holocene (2.65–0.55 kcal BP) (**Figure 7**). As an independent assessment of the $\delta^{18}O_{(calcite)}$ data from core LEGC03-3, we compare to $\delta^{18}O_{(calcite)}$ values from a separately dated sediment core extracted from the lake's modern littoral zone (LESS02-5; Kirby et al., 2004) (**Figures 1**, **10**). Although not perfect, the comparison exhibits similar changes across the interval of shared time (3.5–1.8 kcal BP), suggesting that our profundal core reliably records the lake's integrated isotopic signal.

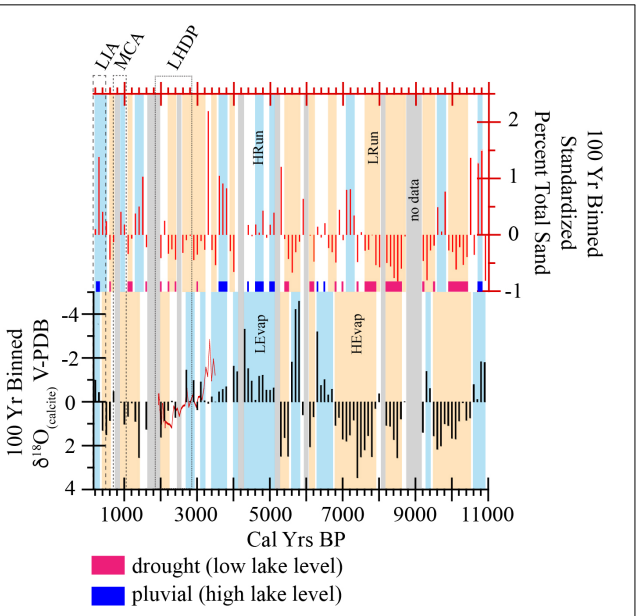

FIGURE 10 | 100-year binned $\delta^{18}O_{(calcite)}$ and sand values. Inset line on the bottom graph shows the $\delta^{18}O_{(calcite)}$ data from LESS02-5 (Kirby et al., 2004) on its own age model. The light blue and light orange boxes unique to each data set reflect intervals of two or more centuries of above/below-average $\delta^{18}O_{(calcite)}$ or sand. Intervals of shared $\delta^{18}O_{(calcite)}$ values and sand drought are shown by dark red boxes and vice versa for pluvials (dark blue boxes) at the intersection of the upper and lower graphs. HRun, high runoff; LRun, low runoff; LEvap, low evaporation; HEvap, high evaporation; LIA, Little Ice Age (Masson-Delmotte et al., 2013); MCA, Medieval Climatic Anomaly (Masson-Delmotte et al., 2013); Late Holocene Dry Period (Mensing et al., 2013).

Changes in lake water $\delta^{18}O$ values from which the calcite precipitates reflect both evaporation during the peak season of calcitic mineralization as well as changes in the relative influx of low $\delta^{18}O$, winter precipitation runoff. As a result, the final interpretation of the $\delta^{18}O_{(calcite)}$ values must consider the latter. To assess the role played by winter season precipitation (P) and its relative input of low $\delta^{18}O$ runoff, the $\delta^{18}O_{(calcite)}$ data were compared to the Kirby et al. (2010) sand-inferred winter precipitation runoff data; these data are similarly binned by 100-years and colored coded. Despite the poor statistical relationship between the two variables (n = 90, r = −0.02, p < 0.84), comparison between the individual 100-year bins provides insight to centuries sharing a similar signal (e.g., low sand [less winter precipitation runoff] plus high $\delta^{18}O_{(calcite)}$ [evaporative summers] = drought [low lake level] and vice versa for pluvials). Drought are colored coded as red and pluvials as dark blue (**Figure 10**). **Supplementary Table S3** provides a list of inferred drought (low lake level) and pluvial (high lake level) centuries, based on this visual comparison.

Taken together, this comparison reveals a dynamic Holocene hydroclimate characterized by centennial to multi-centennial scale intervals of both above-average and below-average winter precipitation (pluvials) and summer-to-early fall over-water evaporation (drought) (**Figure 10** and **Supplementary Table S3**). In general, the same three-part millennial scale Holocene divisions are observed as described above. However, our P:E comparison (i.e., sand vs. $\delta^{18}O_{(calcite)}$) informs on the duration and severity of centennial to multi-centennial scale wet-dry periods that are not apparent when examining only the $\delta^{18}O_{(calcite)}$ or sand data. Long-lasting droughts, indicated by low lake levels, occurred in the Early Holocene (10.45–5.35 kcal BP). There is only one sustained pluvial during this time (10.85–10.65 kcal BP). By 5.15 kcal BP, there is shift to more frequent pluvials (n = 9 centuries [periods of high lake level]) until 3.55 kcal BP, with the longest between 4.85 and 4.55 kcal BP. From 3.05 to 0.55 kcal BP, there are eight centennial droughts (periods of low lake level) with no apparent pluvials. The most recent, pre-historical (>0.15 kcal BP) pluvial occurs during the Little Ice Age (0.35–0.15 kcal BP). We note that there are several intervals that lack data (unrecovered core sections or disturbed sediment or too few data points for an accurate 100-year bin; **Supplementary Table S3**).

To assess the $\delta^{18}O_{(calcite)}$ evaporation interpretation, we use the only existing, quantitative reconstruction of Holocene summer temperature from the PSW (Wahl, 2003; Ohlwein and Wahl, 2012). This pollen-based, July temperature anomaly reconstruction was derived using a 253 cm sediment core from a wet meadow (Taquitz Meadow, 33°46′8″ N, 116°39′44″ W, 2399 m elevation) in the San Jacinto Mountains (**Figure 11**) (Wahl, 2003; Ohlwein and Wahl, 2012). Temperature anomalies were reconstructed using a "Bayesian generalized linear model based on pollen ratios of (all conifers)/(all conifers + oak + important shrubs)" (Ohlwein and Wahl, 2012). Limitations of this temperature reconstruction are likely associated with a "systematic underestimation of model uncertainties due to a spatial correlation of unaccounted explanatory variables" (Ohlwein and Wahl, 2012). The reconstruction is temporally-constrained using an age-to-age linear sedimentation rate age model based on eight radiocarbon dates between 30 and 243 cm (Wahl, 2002). The surface age is assumed the year the core was recovered. Each sample represents about 20–50 years integrated time. Notably, there is a thick event layer between 124 and 151 cm depth, which is interpreted to reflect a single storm event in the catchment (Wahl, 2002). The reconstruction uses only one sample from this event layer. Using the Bacon v.2.2 age-modeling software (Blaauw and Christen, 2011), we explored how different and up-dated age models – without removing the event layer – influenced the timing of the reconstruction. Our analyses revealed no significant difference between Wahl's (2002) age-to-age linear sedimentation rate age model and our Bacon v.2.2 derived age model. As a result, we use Wahl's (2002) age model for comparison to our isotope data (**Figure 11**).

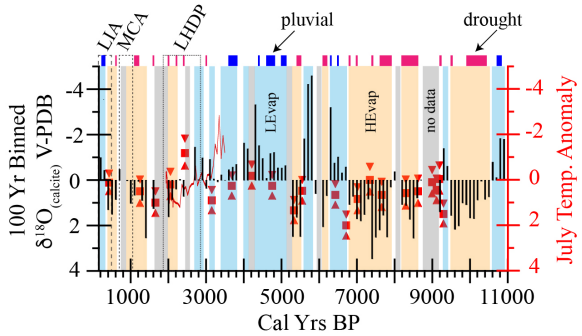

FIGURE 11 | 100-year binned $\delta^{18}O_{(calcite)}$ values versus the pollen July temperature anomaly reconstruction (July temperature axis is inverted) from the San Jacinto Mountains (Wahl, 2003; Ohlwein and Wahl, 2012). Inverted triangles represent the one-sigma range associated with the temperature reconstruction (Wahl, 2003; Ohlwein and Wahl, 2012). Intervals of shared $\delta^{18}O_{(calcite)}$ values and sand drought are shown by dark red boxes and vice versa for pluvials (dark blue boxes) at the graph. LEvap, low evaporation; HEvap, high evaporation; LIA, Little Ice Age (Masson-Delmotte et al., 2013); MCA, Medieval Climatic Anomaly (Masson-Delmotte et al., 2013); Late Holocene Dry Period (Mensing et al., 2013).

In general, the pollen-based, July temperature anomaly reconstruction shows average-to-above-average July temperatures for most of Holocene, with approximately 4°C one-sigma total temperature range. A closer look at longer trends reveals a more nuanced signal (**Figure 11**; July temperature axis is inverted). However, to avoid over-interpretation, and with consideration for the differences in sample-to-sample resolution between the Elsinore and the Taquitz Meadow records, we limit our comparison to the three Elsinore $\delta^{18}O_{(calcite)}$-derived Holocene intervals: (1) the highly evaporative Early Holocene (10.55–6.65 kcal BP), (2) the less evaporative Mid-Holocene (6.65–2.65 kcal BP); and (3) the evaporative Late Holocene (2.65–0.55 kcal BP) (**Figure 7**). Early Holocene July temperature anomalies are characterized by average-to-above average temperatures with limited variability (Ohlwein and Wahl, 2012). The Mid-Holocene, however, reveals a general trend toward lower July temperatures, reaching a low at 4.2 kcal BP, before rising slightly until 3.1 kcal BP. This Mid Holocene

interval is also characterized by the largest amplitude, Holocene temperature changes reconstructed. Finally, the Late Holocene begins with the largest negative July temperature anomaly on record at 2.4 kcal BP. Following this negative excursion, temperatures rise and stabilize at or slightly below average.

The millennial scale trends are broadly similar but it is important to recognize the limitations of the comparison. For example, the $\delta^{18}O_{(calcite)}$ data are scale independent such that any given isotopic value cannot be assigned an absolute value for evaporation rate. Furthermore, ecological inertia limits the functional response of the vegetation to environmental stresses. The hydrology of Lake Elsinore, however, experiences change on a variety of timescales (**Figures 4**, **5**, **8**), that are unlikely recorded in the San Jacinto pollen-temperature record (Kirby et al., 2018).

CONCLUSION

Although the PSW's hydroclimate is dominated by winter precipitation, summer evaporation (i.e., temperature) plays an important role in lake and reservoir hydrology. This input–output dynamic is often referred to the as the P:E ratio for lakes in arid and semi-arid environments. Lake Elsinore is a good site for evaluating the interplay between winter precipitation, summer evaporation, and lake hydrology. Until now, the story told using Lake Elsinore sediments has been winter focused. Kirby et al. (2010) inferred wet-dry intervals over the past 9.7 kcal BP, using changes in sand content to interpret winter-related, paleo-runoff.

In the PSW, drought is often contributed to deficits in winter precipitation only. However, the most recent Californian drought (2012–2015 AD) highlighted the importance of temperature as an amplifier of drought conditions (Griffin and Anchukaitis, 2014; Diffenbaugh et al., 2015; Shukla et al., 2015; Luo et al., 2017). This temperature-related drought is now referred to as a "hot drought" (Griffin and Anchukaitis, 2014; Diffenbaugh et al., 2015; Shukla et al., 2015; Luo et al., 2017). In the PSW, summer-to-early fall temperatures coincide with maximum evaporation and subsequent lake level regressions (**Figure 4**). Coupled with less winter precipitation, a hot drought can produce large changes in a lake's hydrologic budget – larger perhaps than winter precipitation deficits alone. To examine the relative roles of winter precipitation and summer-to-early fall evaporation (i.e., temperature) in the geological record requires seasonally-sensitive indicators. Knowing this, we coupled the Kirby et al. (2010) winter precipitation, runoff indicator (i.e., sand) with $\delta^{18}O_{(calcite)}$ values – a well-known recorder of evaporation in arid and semi-arid lacustrine environments. We also updated the age model using a more sophisticated Bayesian methodology.

Together, these data reveal periods of sustained drought (i.e., lower lake levels) based on 100-year bins of shared high $\delta^{18}O_{(calcite)}$ values (i.e., greater summer-to-early fall over-water evaporation) and low sand content (lower winter precipitation runoff). The opposite relationship is used to infer pluvials. In general, the Early Holocene is characterized by the driest summers (high $\delta^{18}O_{(calcite)}$ values) and the lowest winter precipitation runoff (low sand content). The Mid-Holocene sees a return to more mild conditions with lower over-water evaporation and several pluvial episodes. Evaporative conditions and associated drought return in the Late Holocene with the exception of the wet LIA.

Finally, from a broader North Pacific point of view, Lake Elsinore is located far south of the average latitude (∼40°N latitude) of the western United States winter precipitation dipole (Dettinger et al., 1998; Wise, 2010, 2016). As a result, the lake represents a key location for comparison to sites located within, and north of, the dipole. Future work will examine the spatial expression, strength, and persistence of the precipitation dipole during the Holocene. However, our results suggest that – when possible – researchers should locate and study sediment records that capture some component of seasonality, to view a more nuanced view of past climate. This nuanced view is required if we are to understand the relative roles played by changes in seasonality as well as to examine/evaluate the forcings that modulate Holocene drought and pluvials.

AUTHOR CONTRIBUTIONS

MK conceived the project, interpreted the data, and wrote the manuscript. WP produced the sediment isotope data and some of the water isotope data, reviewed and edited the manuscript. ML produced some of the water isotope data, reviewed and edited the manuscript. JN collected the water samples, reviewed and edited the manuscript. MA collected some of the water samples, reviewed and edited the manuscript. KN helped with the Bacon age model. JA reviewed and edited the manuscript.

FUNDING

This research was funded by the National Science Foundation (EAR-0602269-01) to MK. Additional funds were provided by a Lake Elsinore-San Jacinto Water Authority (LESJWA) contract to MK and MA and the American Chemical Society-Petroleum Research Fund (ACS-PRF: Grant #41789-GB8) to MK. Funds from Cal-State Fullerton Faculty-Student Creative Research Grants provided summer stipends for several students.

ACKNOWLEDGMENTS

Special thanks to the City of Lake Elsinore, particularly Mr. Patrick Kilroy (former Lake Manager) for access to the lake; Mr. David Ruhl (LESJWA) for contract management; Gregg Drilling and Testing, Inc. for exceptional quality service. Thanks to Dr. Sandra Timsic whom analyzed water and calcite samples in the Saskatchewan Isotope Lab. We thank three reviewers as well as LA for thorough, insightful, and helpful comments.

SUPPLEMENTARY MATERIAL

The Supplementary Material for this article can be found online at: https://www.frontiersin.org/articles/10.3389/feart.2019.00074/full#supplementary-material

REFERENCES

Anderson, L., Berkelhammer, M., Barron, J. A., Steinman, B. A., Finney, B. P., Abbott, M. B., et al. (2016). Lake oxygen isotopes as recorders of North American Rocky mountain hydroclimate: holocene patterns and variability at multi-decadal to millennial time scales. *Global Planet. Change* 137, 131–148. doi: 10.1016/j.gloplacha.2015.12.021

Anderson, M. A. (2001). *Internal Loading and Nutrient Cycling in Lake Elsinore*. Lake Elsinore: Santa Ana Regional Water Quality Control Board, 52.

Anderson, R. Y., Hemphill-Haley, E., and Gardner, J. V. (1987). Persistent late pleistocene-holocene seasonal upwelling and varves off the coast of California. *Quat. Res.* 28, 307–313. doi: 10.1016/0033-5894(87)90069-X

Anderson, W. T., Mullins, H. T., and Ito, E. (1997). Stable isotope record from Seneca Lake, New York: evidence for a cold paleoclimate following the Younger Dryas. *Geology* 25, 135–138. doi: 10.1130/0091-7613(1997)025<0135:SIRFSL>2.3.CO;2

Andrews, J. T., and Eberl, D. D. (2012). Determination of sediment provenance by unmixing the mineralogy of source-area sediments: the "SedUnMix" program. *Mar. Geol.* 29, 24–33. doi: 10.1016/j.margeo.2011.10.007

Ault, T. R., Cole, J. E., Overpeck, J. T., Pederson, G. T., St George, S., Otto-Bliesner, B., et al. (2013). The continuum of hydroclimate variability in western north america during the last millennium. *J. Clim.* 26, 5863–5878. doi: 10.1175/JCLI-D-11-00732.1

Bailey, H. P. (1966). *The Climate of Southern*. Berkeley, CA: University of California Press.

Benson, L., Kashgarian, M., Rye, R., Lund, S., Paillet, F., Smoot, J., et al. (2002). Holocene multidecadal and multicentennial droughts affecting Northern California and Nevada. *Quat. Sci. Rev.* 21, 659–682. doi: 10.1016/S0277-3791(01)00048-8

Bird, B. W., and Kirby, M. E. (2006). An alpine lacustrine record of early Holocene North American Monsoon dynamics from Dry Lake, southern California (USA). *J. Paleolimnol.* 35, 179–192. doi: 10.1007/s10933-005-8514-3

Bird, B. W., Kirby, M. E., Howat, I. M., and Tulaczyk, S. (2010). Geophysical evidence for Holocene lake-level change in southern California (Dry Lake). *Boreas* 39, 131–144. doi: 10.1111/j.1502-3885.2009.00114.x

Blaauw, M., and Christen, J. A. (2011). Flexible paleoclimate age-depth models using an autoregressive gamma process. *Bayesian Anal.* 6, 457–474.

Brito-Castillo, L., Douglas, A. V., Leyva-Contreras, A., and Lluch-Belda, D. (2003). The effect of large-scale circulation on precipitation and streamflow in the Gulf of California continental watershed. *Int. J. Climatol.* 23, 751–768. doi: 10.1002/joc.913

Cayan, D. R., and Peterson, D. H. (1989). "The influence of North Pacific atmospheric circulation on streamflow in the west," in *Aspects of Climate Variability in the Pacific and the Western Americas*, Vol. 55, ed. D. H. Peterson (Washington, DC: American Geophysical Union), 375–397.

Cayan, D. R., Redmond, K. T., and Riddle, R. G. (1999). ENSO and hydrologic extremes in the western United States. *J. Climate* 12, 2881–2893. doi: 10.1175/1520-0442(1999)012<2881:EAHEIT>2.0.CO;2

Cook, B. I., Ault, T. R., and Smerdon, J. E. (2015). Unprecedented 21st century drought risk in the American Southwest and Central Plains. *Sci. Adv.* 1:e1400082. doi: 10.1126/sciadv.1400082

Cook, B. I., Smerdon, J. E., Seager, R., and Cook, E. R. (2014). Pan-continental droughts in North America over the Last Millennium. *J. Clim.* 27, 383–397. doi: 10.1175/JCLI-D-13-00100.1

Cook, E. R., Seager, R., Cane, M. A., and Stahle, D. W. (2007). North American drought: reconstructions, causes, and consequences. *Earth-Sci. Rev.* 81, 93–134. doi: 10.1016/j.earscirev.2006.12.002

Coplen, T. B. (1996). New guidelines for reporting stable hydrogen, carbon, and oxygen isotope-ratio data. *Geochim. Cosmochim. Acta* 60, 3359–3360. doi: 10.1016/0016-7037(96)00263-3

Dean, J. R., Eastwood, W. J., Roberts, N., Jones, M. D., Yiğitbaşıoğlu, H., Allcock, S. L., et al. (2015). Tracking the hydro-climatic signal from lake to sediment: a field study from central Turkey. *J. Hydrol.* 529, 608–621. doi: 10.1016/j.jhydrol.2014.11.004

Dettinger, M. D., Cayan, D. R., Diaz, H. F., and Meko, D. M. (1998). North-south precipitation patterns in western North America on interannual-to-decadal timescales. *J. Clim.* 11, 3095–3111. doi: 10.1175/1520-0442(1998)011<3095:NSPPIW>2.0.CO;2

Diffenbaugh, N. S., Swain, D. L., and Touma, D. (2015). Anthropogenic warming has increased drought risk in California. *Proc. Natl. Acad. Sci. U.S.A.* 112, 3931–3936. doi: 10.1073/pnas.1422385112

Drummond, C. N., Patterson, W. P., and Walker, J. C. (1995). Climatic forcing of carbon-oxygen isotopic covariance in temperate-region marl lakes. *Geology* 23, 1031–1034. doi: 10.1130/0091-7613(1995)023<1031:CFOCOI>2.3.CO;2

Eberl, D. (2004). Quantitative mineralogy of the Yukon River system: changes with reach and season, and determining sediment provenance. *Am. Mineral.* 89, 1784–1794. doi: 10.2138/am-2004-11-1225

Engel, R. (1959). *Geology of the Lake Elsinore Quadrangle, California*. San Francisco, CA: California Division of Mines, 52.

Enzel, Y., and Wells, S. G. (1997). Extracting Holocene paleohydrology and paleoclimatology information from modern extreme flood events: an example from southern California. *Geomorphology* 19, 203–226. doi: 10.1016/S0169-555X(97)00015-9

Friedman, I., Smith, G. I., Gleason, J. D., Warden, A., and Harris, J. M. (1992). Stable isotope composition of waters in Southeastern California.1. Modern Precipitation. *J. Geophys. Res. Atmos.* 97, 5795–5812. doi: 10.1029/92JD00184

Gat, J. R. (1996). Oxygen and hydrogen isotopes in the hydrologic cycle. *Anu. Rev. Earth Planet. Sci.* 24, 225–262. doi: 10.1146/annurev.earth.24.1.225

Graumlich, L. J. (1993). A 1000-year record of temperature and precipitation in the sierra-nevada. *Quat. Res.* 39, 249–255. doi: 10.1006/qres.1993.1029

Gray, A. B., Pasternack, G. B., Watson, E. B., Warrick, J. A., and Goñi, M. A. (2015). The effect of El Niño Southern Oscillation cycles on the decadal scale suspended sediment behavior of a coastal dry-summer subtropical catchment. *Earth Surf. Process. Landforms* 40, 272–284. doi: 10.1002/esp.3627

Griffin, D., and Anchukaitis, K. J. (2014). How unusual is the 2012-2014 California drought? *Geophys. Res. Lett.* 41, 9017–9023. doi: 10.1002/2014GL062433

Hanson, R. T., Dettinger, M. D., and Newhouse, M. W. (2006). Relations between climatic variability and hydrologic time series from four alluvial basins across the southwestern United States. *Hydrogeol. J.* 14, 1122–1146. doi: 10.1007/s10040-006-0067-7

Hodell, D. A., Schelske, C. L., Fahnenstiel, G. L., and Robbins, L. L. (1998). Biologically induced calcite and its isotopic composition in Lake Ontario. *Limnol. Oceanogr.* 43, 187–199. doi: 10.4319/lo.1998.43.2.0187

Holmgren, C. A., Betancourt, J. L., and Rylander, K. A. (2010). A long-term vegetation history of the Mojave-Colorado desert ecotone at Joshua Tree National Park. *J. Quat. Sci.* 25, 222–236. doi: 10.1002/jqs.1313

Horton, T. W., Defliese, W. F., Tripati, A. K., and Oze, C. (2016). Evaporation induced 18 O and 13 C enrichment in lake systems: a global perspective on hydrologic balance effects. *Quat. Sci. Rev.* 131, 365–379. doi: 10.1016/j.quascirev.2015.06.030

Hudson, T. (1978). *Lake Elsinore Valley: Its Story*, 3rd Edn. Lake Elsinore, CA: Mayhall Print Shop.

Hughes, M. K., and Graumlich, L. J. (1996). "Climatic variations and forcing mechanisms of the last 2000 years," in *Multi-Millennial Dendroclimatic Studies from the Western United States*, eds P. D. Jones, R. S. Bradley, J. Jouzel (Berlin: Springer), 109–124. doi: 10.1007/978-3-642-61113-1_6

Hull, A. G. (1990). Seismotectonics of the Northern Elsinore fault zone, southern California. *Bull. Seismol. Soc. Am.* 82, 800–818.

Kelts, K., and Talbot, M. R. (1990). "Lacustrine carbonates as geochemical archives of environmental change and biotic/abiotic interactions," in *Large Lakes: Ecological Structure and Function*, Chap. 15, eds M. M. Tilzer and C. Serruya. (Berlin: Springer-Verlag), 288–315.

Kim, S.-T., and O'Neil, J. R. (1997). Equilibrium and nonequilibrium oxygen isotope effects in synthetic carbonates. *Geochim. Cosmochim. Acta* 61, 3461–3475. doi: 10.1016/S0016-7037(97)00169-5

Kirby, M. E., Feakins, S. J., Bonuso, N., Fantozzi, J. M., and Hiner, C. A. (2013). Latest pleistocene to Holocene hydroclimates from Lake Elsinore, California. *Quat. Sci. Rev.* 76, 1–15. doi: 10.1016/j.quascirev.2013.05.023

Kirby, M. E., Feakins, S. J., Hiner, C. A., Fantozzi, J., Zimmerman, S. R. H., Dingemans, T., et al. (2014). Tropical pacific forcing of Late-Holocene hydrologic variability in the coastal southwest United States. *Quat. Sci. Rev.* 102, 27–38. doi: 10.1016/j.quascirev.2014.08.005

Kirby, M. E., Heusser, L., Scholz, C., Ramezan, R., Anderson, M. A., Markle, B., et al. (2018). A late Wisconsin (32-10k cal a BP) history of pluvials, droughts and

vegetation in the pacific south-west United States (Lake Elsinore, CA). *J. Quat. Sci.* 33, 238–254. doi: 10.1002/jqs.3018

Kirby, M. E., Knell, E. J., Anderson, W. T., Lachniet, M. S., Palermo, J., Eeg, H., et al. (2015). Evidence for insolation and Pacific forcing of late glacial through Holocene climate in the Central Mojave Desert (Silver Lake, CA). *Quat. Res.* 84, 174–186. doi: 10.1016/j.yqres.2015.07.003

Kirby, M. E., Lund, S. P., Anderson, M. A., and Bird, B. W. (2007). Insolation forcing of Holocene climate change in Southern California: a sediment study from Lake Elsinore. *J. Paleolimnol.* 38, 395–417. doi: 10.1007/s10933-006-9085-7

Kirby, M. E., Lund, S. P., and Bird, B. W. (2006). Mid-Wisconsin sediment record from Baldwin Lake reveals hemispheric climate dynamics (Southern CA, USA). *Palaeogeogr. Palaeoclimatol. Palaeoecol.* 241, 267–283. doi: 10.1016/j.palaeo.2006.03.043

Kirby, M. E., Lund, S. P., Patterson, W. P., Anderson, M. A., Bird, B. W., Ivanovici, L., et al. (2010). A Holocene record of pacific decadal oscillation (PDO)-related hydrologic variability in Southern California (Lake Elsinore, CA). *J. Paleolimnol.* 44, 819–839. doi: 10.1007/s10933-010-9454-0

Kirby, M. E., Lund, S. P., and Poulsen, C. J. (2005). Hydrologic variability and the onset of modern El Nino Southern Oscillation: a 19,250-year record from Lake Elsinore, southern California. *J. Quat. Sci.* 20, 239–254. doi: 10.1002/jqs.906

Kirby, M. E., Mullins, H. T., Patterson, W. P., and Burnett, A. W. (2002). Late glacial-Holocene atmospheric circulation and precipitation in the northeast United States inferred from modern calibrated stable oxygen and carbon isotopes. *Geol. Soc. Am. Bull.* 114, 1326–1340. doi: 10.1130/0016-7606(2002)114<1326:LGHACA>2.0.CO;2

Kirby, M. E., Poulsen, C. J., Lund, S. P., Patterson, W. P., Reidy, L., Hammond, D. E., et al. (2004). Late Holocene lake level dynamics inferred from magnetic susceptibility and stable oxygen isotope data: Lake Elsinore, southern California (USA). *J. Paleolimnol.* 31, 275–293. doi: 10.1023/B:JOPL.0000021710.39800.f6

Kirby, M. E., Zimmerman, S. R. H., Patterson, W. P., and Rivera, J. J. (2012). A 9170-year record of decadal-to-multi-centennial scale pluvial episodes from the coastal Southwest United States: a role for atmospheric rivers? *Quat. Sci. Rev.* 46, 57–65. doi: 10.1016/j.quascirev.2012.05.008

Labotka, D., Grissino-Mayer, H., Mora, C., and Johnson, E. (2016). Patterns of moisture source and climate variability in the southeastern United States: a four-century seasonally resolved tree-ring oxygen-isotope record. *Clim. Dynam.* 46, 2145–2154. doi: 10.1007/s00382-015-2694-y

Lajewski, C., Mullins, H., Patterson, W., and Callinan, C. (2003). Historic calcite record from the Finger Lakes, New York: impact of acid rain on a buffered terrane. *Geol. Soc. Am. Bull.* 115, 373–384. doi: 10.1130/0016-7606(2003)115<0373:HCRFTF>2.0.CO;2

Leavitt, S. W., and Long, A. (1991). Seasonal stable-carbon isotope variability in tree rings: possible paleoenvironmental signals. *Chem. Geol. Isotope Geosci. Sect.* 87, 59–70. doi: 10.1016/0168-9622(91)90033-S

Lebo, M. E., Reuter, J. E., and Meyers, P. A. (1994). Historical changes in sediments of Pyramid Lake, Nevada, USA: consequences of changes in the water balance of a terminal desert lake. *J. Paleolimnol.* 12, 87–101. doi: 10.1007/BF00678089

Leng, M. J., and Marshall, J. D. (2004). Palaeoclimate interpretation of stable isotope data from lake sediment archives. *Quat. Sci. Rev.* 23, 811–831. doi: 10.1016/j.quascirev.2003.06.012

Li, H. C., Bischoff, J. L., Ku, T. L., Lund, S. P., and Stott, L. D. (2000). Climate variability in east-central California during the past 1000 years reflected by high-resolution geochemical and isotopic records from Owens Lake sediments. *Quat. Res.* 54, 189–197. doi: 10.1006/qres.2000.2163

Li, H.-C., and Ku, T.-L. (1997). delta13C-delta18O covariance as a paleohydrological indicator for closed-basin lakes. *Palaeogeogr. Palaeoclimatol. Palaeoecol.* 133, 69–80. doi: 10.1016/S0031-0182(96)00153-8

Luo, L., Apps, D., Arcand, S., Xu, H., Pan, M., Hoerling, M., et al. (2017). Contribution of temperature and precipitation anomalies to the California drought during 2012–2015. *Geophys. Res. Lett.* 44, 3184–3192. doi: 10.1002/2016GL072027

Masi, G. J. (2005). "Orographic and large-scale influence on Southern California precipitation patterns," in *Proceedings of the Sixth Conference on Coastal Atmospheric and Oceanic Prediction and Processes*, San Diego, CA.

Masson-Delmotte, V., Schulz, M., Abe-Ouchi, A., Beer, J., Ganopolski, A., Gonzaìlez Rouco, J. F., et al. (2013). "Information from paleoclimate archives," in *Climate Change 2013: The Physical Science Basis. Contribution of Working Group I to the Fifth Assessment Report of the Intergovernmental Panel on Climate Change*, eds T. F. Stocker, D. Qin, G.-K. Plattner, M. Tignor, S. K. Allen, J. Boschung, et al. (Cambridge: Cambridge University Press), 383–464.

McDonald, E. V., McFadden, L. D., Wells, S. G., Enzel, Y., and Lancaster, N. (2003). "Regional response of alluvial fans to the pleistocene-holocene climatic transition, Mojave Desert, California," in *Paleoenvironments and Paleohydrology of the Mojave and Southern Great Basin Deserts*, eds Y. Enzel, S. G. Wells, and N. Lancaster (Boulder, CO: Geological Society of America Special Paper) 368, 189–205. doi: 10.1130/0-8137-2368-X.189

Meko, D. M., Therrell, M. D., Baisan, C. H., and Hughes, M. K. (2001). Sacramento river flow reconstructed to A.D. 869 from tree Rings1. *JAWRA J. Am. Water Resour. Assoc.* 37, 1029–1039. doi: 10.1111/j.1752-1688.2001.tb05530.x

Mensing, S. A., Sharpe, S. E., Tunno, I., Sada, D. W., Thomas, J. M., Starratt, S., et al. (2013). The late holocene dry period: multiproxy evidence for an extended drought between 2800 and 1850 cal yr BP across the central Great Basin, USA. *Quat. Sci. Rev.* 78, 266–282. doi: 10.1016/j.quascirev.2013.08.010

Metcalfe, S. E., Barron, J. A., and Davies, S. J. (2015). The Holocene history of the North American Monsoon: 'known knowns' and 'known unknowns' in understanding its spatial and temporal complexity. *Quat. Sci. Rev.* 120, 1–27. doi: 10.1016/j.quascirev.2015.04.004

Miller, D. M., Schmidt, K. M., Mahan, S. A., McGeehin, J. P., Owen, L. A., Barron, J. A., et al. (2010). Holocene landscape response to seasonality of storms in the Mojave Desert. *Quat. Int.* 215, 45–61. doi: 10.1016/j.quaint.2009.10.001

Mullins, H. T. (1998). Environmental change controls of lacustrine carbonate, Cayuga Lake, New York. *Geology* 26, 443–446. doi: 10.1130/0091-7613(1998)026<0443:ECCOLC>2.3.CO;2

Mullins, H. T., Patterson, W. P., Teece, M. A., and Burnett, A. W. (2011). Holocene climate and environmental change in central New York (USA). *J. Paleolimnol.* 45, 243–256. doi: 10.1007/s10933-011-9495-z

Ohlwein, C., and Wahl, E. R. (2012). Review of probabilistic pollen-climate transfer methods. *Quat. Sci. Rev.* 31, 17–29. doi: 10.1016/j.quascirev.2011.11.002

Pigati, J. S., Miller, D. M., Bright, J. E., Mahan, S. A., Nekola, J. C., Paces, J. B., et al. (2011). Chronology, sedimentology, and microfauna of groundwater discharge deposits in the central Mojave Desert, Valley Wells, California. *Geol. Soc. Am. Bull.* 123, 2224–2239. doi: 10.1130/B30357.1

Shukla, S., Safeeq, M., AghaKouchak, A., Guan, K., and Funk, C. (2015). Temperature impacts on the water year 2014 drought in California. *Geophys. Res. Lett.* 42, 4384–4393. doi: 10.1002/2015GL063666

St George, S., and Ault, T. R. (2014). The imprint of climate within Northern Hemisphere trees. *Quat. Sci. Rev.* 89, 1–4. doi: 10.1016/j.quascirev.2014.01.007

Steinman, B. A., and Abbott, M. B. (2013). Isotopic and hydrologic responses of small, closed lakes to climate variability: hydroclimate reconstructions from lake sediment oxygen isotope records and mass balance models. *Geochim. Cosmochim. Acta* 105, 342–359. doi: 10.1016/j.gca.2012.11.027

Stuiver, M. (1970). Oxygen and carbon isotope ratios of fresh-water carbonates as climatic indicator. *J. Geophys. Res.* 75, 5247–5257. doi: 10.1029/JC075i027p05247

Talbot, M. R. (1990). A review of the palaeohydrological interpretation of carbon and oxygen isotopic ratios in primary lacustrine carbonates. *Chem. Geol. (Isotope Geosci. Sect.)* 80, 261–279. doi: 10.1016/0168-9622(90)90009-2

Thompson, J. B., SchultzeLam, S., Beveridge, T. J., and DesMarais, D. J. (1997). Whiting events: biogenic origin due to the photosynthetic activity of cyanobacterial picoplankton. *Limnol. Oceanogr.* 42, 133–141. doi: 10.4319/lo.1997.42.1.0133

Wahl, E. R. (2002). *Paleoecology and Testing of Paleoclimate Hypotheses in Southern California During the Holocene*. PhD Dissertation, University of Minnesota, Minneapolis, MN, 248.

Wahl, E. R. (2003). Assigning climate values to modern pollen surface sample sites and validating modern analog climate reconstructions in the southern California region. *Madroño* 50, 271–285.

Wells, S. G., Brown, J. B., Enzel, Y., Anderson, R. Y., and McFadden, L. D. (2003). "Late quaternary geology and paleohydrology of pluvial Lake Mojave, southern California," in *Paleoenvironments and Paleohydrology of the Mojave and Southern Great Basin Deserts*, eds Y. Enzel, S. G. Wells, and N. Lancaster

(Boulder, CO: Geological Society of America), 79–115. doi: 10.1130/0-8137-2368-X.79

Williams, A. E., and Rodoni, D. P. (1997). Regional isotope effects and application to hydrologic investigations in southwestern California. *Water Resour. Res.* 33, 1721–1729. doi: 10.1029/97WR01035

Wise, E. K. (2010). Spatiotemporal variability of the precipitation dipole transition zone in the western United States. *Geophys. Res. Lett.* 37, L07706. doi: 10.1029/2009GL042193

Wise, E. K. (2016). Five centuries of US West Coast drought: occurrence, spatial distribution, and associated atmospheric circulation patterns. *Geophys. Res. Lett.* 43, 4539–4546. doi: 10.1002/2016GL068487

Wurster, C. M., and Patterson, W. P. (2001). Seasonal variation in stable oxygen and carbon isotope values recovered from modern lacustrine freshwater mollusks: paleoclimatological implications for sub-weekly temperature records. *J. Paleolimnol.* 26, 205–218. doi: 10.1023/A:1011194011250

Conflict of Interest Statement: The authors declare that the research was conducted in the absence of any commercial or financial relationships that could be construed as a potential conflict of interest.

frontiers in Earth Science

ORIGINAL RESEARCH
published: 16 April 2019
doi: 10.3389/feart.2019.00073

Synchronous Modes of Terrestrial and Marine Productivity in the North Pacific

*Max Berkelhammer**

Department of Earth and Environmental Sciences, University of Illinois at Chicago, Chicago, IL, United States

The primary productivity of adjacent terrestrial and marine ecosystems can display synchronous responses to climate variability. Previous work has shown that this behavior emerges along the California coast where internal modes of climate variability, such as El Niño Southern Oscillation (ENSO) and the Pacific Decadal Oscillation (PDO), alter jet stream dynamics that influence marine ecosystems through changes in upwelling and terrestrial ecosystems through changes in precipitation. This study assesses whether marine-terrestrial synchrony is a widespread phenomenon across the North Pacific by utilizing satellite-derived Solar-Induced Fluorescence (SIF) and chlorophyll-α as proxies for land and sea productivity, respectively. The results show that terrestrial and marine ecosystems are consistently synchronized across 1000's of kms of the North Pacific coastline. This synchrony emerges because both marine and terrestrial ecosystems respond to climate modes with a similar north-south dipole pattern that is mirrored across the coastal interface. The strength of synchrony is modulated by the relative states of the PDO and ENSO because the terrestrial north-south dipole is strongly controlled by the PDO while the marine pattern follows ENSO. The consequence is marine and terrestrial productivity anomalies that are opposite one another along adjacent regions of the coastline. If ENSO and the PDO have shared low-frequency variance, then synchrony would be the dominant state despite local topographic and trophic diversity along the coastlines. This result suggests that climate proxy stacks that include biologically sensitive marine and terrestrial proxies would have a selective sensitivity to modes such as PDO that drive synchrony. Lastly, the coupling of land and sea productivity may have the effect of generating amplified regional responses of the carbon budget to climate variability by simultaneously enhancing the terrestrial and marine carbon sinks.

Keywords: climate, ecohydrology, carbon cycle, remote sensing, fluorescence

OPEN ACCESS

Edited by:
Miriam Jones,
United States Geological Survey,
United States

Reviewed by:
Milad Janalipour,
K. N. Toosi University of Technology,
Iran
Andrew C. Thomas,
University of Maine, United States

***Correspondence:**
Max Berkelhammer
berkelha@uic.edu

Specialty section:
This article was submitted to Quaternary Science, Geomorphology and Paleoenvironment, a section of the journal Frontiers in Earth Science

Received: *06 November 2018*
Accepted: *22 March 2019*
Published: *16 April 2019*

Citation:
Berkelhammer M (2019) Synchronous Modes of Terrestrial and Marine Productivity in the North Pacific. Front. Earth Sci. 7:73. doi: 10.3389/feart.2019.00073

1. INTRODUCTION

Climate variability drives synchronous responses in ecosystems over large spatial domains. This effect has been well-illustrated through the tree ring network from the western US that shows spatially coherent interannual and decadal variations in tree growth (Cook et al., 2007; Fang et al., 2018). The ecological response to climate variability may also "straddle" both terrestrial and aquatic systems and generate synchronous responses across the coastal interface. This is, in fact, an assumption embedded in multi-proxy climate reconstructions that incorporate

biologically-sensitive proxies from land, lake and marine systems (e.g., Abram et al., 2016). It is difficult to assess the strength and/or persistence of the terrestrial-aquatic synchrony because records such as tree rings or sediment cores are not continuous across the land-sea interface and because both age uncertainty and/or differences in the timescale of proxy response functions may obscure the presence or absence of coupled behavior. An explicit assessment of this phenomenon was done by Guyette and Rabeni (1995), who found significant correlation between the annual growth rings of trees and stream fish in the Ozark region of the US. The species share a common response to summer rainfall, which affected water availability for the trees and nutrient availability for the fish. Ong et al. (2016) extended this type of analysis to the regional scale by analyzing the common responses of corals, trees and fish across NW Australia using overlapping growth chronologies from this collection of both marine and terrestrial taxa. The authors found a common response of all species to El Niño (ENSO) through its effect on regional rainfall and SSTs. In another example from this region, Ruthrof et al. (2018) found that in response to a significant 2011 heat wave in western Australia, there was ecological collapse that straddled the coastal land and sea ecosystems leading to both widespread tree morality and coral bleaching. As illustrated by these studies in western Australia, the increase in the frequency of heat waves and potential for increased variance in ENSO with global warming has the capacity to drive greater degrees of synchrony (Rosenzweig et al., 2008; Hoegh-Guldberg and Bruno, 2010).

The North Pacific serves as an interesting domain to consider the mechanisms and pervasiveness of aquatic and terrestrial synchrony. It is a region that experiences high amplitude climate variability at a variety of timescales associated with ENSO, the Pacific Decadal Oscillation (PDO) and the Arctic Oscillation (AO) (Cayan et al., 1999; Smith and Sardeshmukh, 2000; Mantua and Hare, 2002; Newman et al., 2003; Wise, 2016), all of which have documented effects on both marine (Karl et al., 1995; Mantua et al., 1997; Fisher et al., 2015; Lindegren et al., 2018) and terrestrial ecosystems (Biondi et al., 2001; Trouet and Taylor, 2010; McCabe et al., 2012). Black et al. (2014) and Black et al. (2018) undertook a series of studies that focused on common responses between the terrestrial ecosystems in California and the marine systems in the adjacent coastal upwelling zone. Marine primary productivity along the coast is strongly tied to wind-driven upwelling (Jacox et al., 2015; García-Reyes et al., 2018), which is affected by the wintertime high pressure patterns in the North Pacific. It is these same pressure patterns that influence winter precipitation and growing season soil moisture, which limit terrestrial primary productivity and tree growth. Consequently, coherence between terrestrial and aquatic ecosystems arises through the ubiquitous effects of these atmospheric circulation patterns on regional climate (e.g., rainfall, snowpack, wind fields and temperature). By utilizing a combination of blue oak tree ring chronologies, otolith growth-increment chronologies, records of sea-bird egg laying dates and breeding success, the studies by Black et al. were able to identify synchronous behavior tied to a common wintertime atmospheric blocking pattern (Wise, 2016). As in the case of northwestern Australia (Ong et al., 2016), the periods of strongest synchrony were correlated with large ENSO events.

The aforementioned work on this topic has primarily considered synchrony in terms of coincident changes in individual aquatic and terrestrial species (e.g., blue oak or rock fish). The results have thus emphasized this phenomenon in terms of its ecological impacts, namely that changes in breeding success or mortality events could produce cascading trophic changes (Black et al., 2018). The work presented here builds from the concepts of these previous studies but seeks to assess the generality of terrestrial-marine synchrony by utilizing satellite-derived indicators of primary productivity or changes in biomass. Through the use of satellite indices, the analysis is able to consider the spatial extent of synchrony over an area of 1000's of km and test whether synchrony manifests at the scale of grid-averaged primary productivity as opposed to the response of individual species. The work is intended to expand upon the known ecological implications of terrestrial and aquatic synchrony by considering whether coherence between terrestrial and aquatic productivity might also influence interannual or decadal variability in the global carbon budget (Le Quéré et al., 2012). The motivation for this analysis is that there is significant interannual and decadal variability in the global carbon budget associated with climatic-driven variations in the terrestrial (Poulter et al., 2014; Ahlström et al., 2015) and oceanic (Eddebbar et al., 2017) carbon sinks, which can influence the rate that CO_2 accumulates in the atmosphere in spite of the dominant trend associated with anthropogenic emissions (Ballantyne et al., 2012). Understanding the temporal variability of these surface carbon sink terms is critical for the development of robust carbon cycle models (Landschuetzer et al., 2016; Li et al., 2016). If terrestrial and aquatic carbon cycles are tightly coupled, this could exacerbate the effects of climate modes on variability of the global carbon budget. On the other hand, if productivity between land and sea is decoupled or asynchronous, it could have the effect of buffering the role of ocean-atmosphere climate modes (such as ENSO) on the carbon budget.

Besides potential impacts of land-ocean coupling on the global carbon budget, synchrony is also a critical aspect of the climate signal stored in multi-proxy climate reconstructions that incorporate biotic proxies from terrestrial, lacustrine and marine systems (e.g., Ahmed et al., 2013). If certain modes of climate variability have synchronous effects across the aquatic and terrestrial interface, then these modes would be strongly represented in the proxy record. For example, the aforementioned study by Guyette and Rabeni (1995) from the Ozarks showed that summer rainfall influenced both fish and tree growth whereas the trees were influenced by summer temperatures and the fish by winter temperatures. From this example, it is possible to envision how a simple proxy stack using these two records would accentuate the rainfall signal while losing the specific information on temperature seasonality within the individual records. Aspects of this problem have been discussed in the context of comparisons between lake and tree ring records by Steinman et al. (2014) who noted

discrepancies between these proxies may be the result of the tree rings' sensitivity to summer moisture and the lakes' sensitivity to winter moisture. There has already been significant work on the issue of proxy seasonality and how it can be addressed within multi-proxy syntheses (e.g., Abram et al., 2016) and the analyses presented here takes a general look at this issue by quantifying the response of regional land and marine productivity to North Pacific climate modes.

The study utilizes three types of analyses applied to satellite retrievals of solar-induced fluorescence and chlorophyll-α to illustrate synchrony between marine and terrestrial ecosystems in the North Pacific. In the first part of the paper, an EOF analysis is applied to both the terrestrial, marine and a joint terrestrial and marine matrix to identify the dominant spatiotemporal modes of variability and their respective drivers (i.e., section Spatio-Temporal Patterns of Productivity and **Figures 1**, **3**–**6**). In the second part of the paper, specific years are discussed (2015, 2012 and 2009), which highlight the signature and potential climate mechanisms that drive synchronous behavior (i.e., Section Case Studies of 2009, 2012, and 2015 and **Figures 6**, **7**) and the paper concludes with a regression analysis between adjacent coastal and marine indices of productivity to specifically assess the spatial signature of terrestrial-aquatic synchrony (Section Spatial Analysis of Synchrony from Regression Analysis and **Figure 8**).

2. MATERIALS AND METHODS

2.1. Spatial Domain

This study focuses on a domain bounded between 30° and 65°N latitude and −180° to −110 °W longitude. This area was chosen to encompass the eastern half of the North Pacific Basin and western North America. As opposed to previous work done in this region and elsewhere (Guyette and Rabeni, 1995; Black et al., 2014; Ruthrof et al., 2018), the intent was to select a large region associated with diverse marine and terrestrial ecoregions to assess the maximum scale at which synchronous behavior might be expected. The northern boundary of the domain was defined by the interface between the Pacific and Arctic oceans. While the western boundary is somewhat arbitrary, the vast majority of the chlorophyll variance occurs along the coastal margin and thus the results were not sensitive to the western boundary choice (Messié and Chavez, 2011). The terrestrial domain includes xeric regions in the southwestern US, hydric sites along the coastal ranges and arctic sites in Alaska. The consequence of including such a large terrestrial domain is that a single dominant limiting factor for productivity such as summer rainfall or radiation was not present.

2.2. Satellite and Reanalysis Datasets

2.2.1. Solar-Induced Fluorescence

Solar-Induced Fluorescence (SIF) is emitted as a byproduct of photosynthesis with two predominant peaks centered near 685 and 740 nm. A number of satellite platforms are now capable of retrieving SIF and this study uses data from the Global Ozone Monitoring Experiment 2 (GOME-2), which is flown on the MetOp-A satellite (Joiner et al., 2013). The native spatial resolution of the data was 40 × 80 km until 2013 when the resolution was improved to 40 × 40 km. The SIF retrievals used in this study are from the 734 to 758 nm window (i.e., the 740 nm peak). In this study, the Version 27 Level 3 data is used, which is a gridded product (0.5° × 0.5° grid) that has undergone some cloud filtering and bias correction (Joiner et al., 2014). We use data that covers January 2007 to December 2017, yielding 11 complete annual cycles. Further details of this dataset and how it was processed can be found in the following publications: Yang et al. (2015) and Joiner et al. (2013, 2014). This satellite product has already been applied toward analysis of spatial and temporal variability in terrestrial primary productivity in the western US forests (Berkelhammer et al., 2017), northern high latitude tundra (Luus et al., 2017) and high-latitude boreal forests (Jeong et al., 2017) and is therefore suitable for analysis of productivity within the domain of this study. No additional corrections or changes in projection/resolution were done to the data which is available from the Goddard Aura Validation Center (https://avdc.gsfc.nasa.gov/pub/data/satellite/MetOp/GOME_F/). We note that as opposed to other satellite indices of vegetation (such as NDVI), SIF is a retrieval of a rate-process (fluorescence emission) and is therefore a more direct proxy for primary productivity.

2.2.2. Chlorophyll-α

The analysis of marine productivity was undertaken using satellite retrievals of ocean chlorophyll from the MODerate-resolution Imaging Spectroradiometer (MODIS), which flies on the National Aeronautics and Space Administration (NASA) Earth Observing System (EOS). Data from the Aqua platform were used that has an early afternoon overpass. MODIS retrieves bandwidths from the following 7 channels: 620–670 (red), 841–876 (near infrared 1), 459–479 (blue), 545–565 (green), 1,230–1,250 (near infrared 2), 1,628–1,652 (short-wave infrared 1) and 2,105–2,155 nm (short-wave infrared 2). Surface chlorophyll-α concentrations in the units of mg m^{-3} are derived from an algorithm utilizing the green, blue and red bands that has been optimized through comparison with direct observations of chlorophyll (Hu et al., 2012). The analysis presented here is based on the Level 3 monthly product that is gridded onto a 4 km global grid over the period 2003–2017. This product and its predecessors have a long legacy for studies on analysis and modeling of marine ecosystem productivity. The satellite chlorophyll retrievals provide a robust proxy for phytoplankton biomass (e.g., Dore et al., 2008), which, in turn, has made them useful as inputs to models for marine primary productivity (Platt et al., 1991; Behrenfeld et al., 2006). We note that, unlike SIF, the chlorophyll data is an indicator of biomass concentration as opposed to primary productivity, which is a flux. Because of differences in photoefficiency, the chlorophyll retrievals cannot be taken as a linear and quantitative indicator of primary productivity. Nonetheless, we treat chlorophyll as a proxy for primary productivity (and refer to it as "marine productivity" hereafter), which is an assumption that is not always valid and one that limits the direct applicability of these results toward understanding the spatial structure of marine productivity and its influence on the strength of the carbon sink.

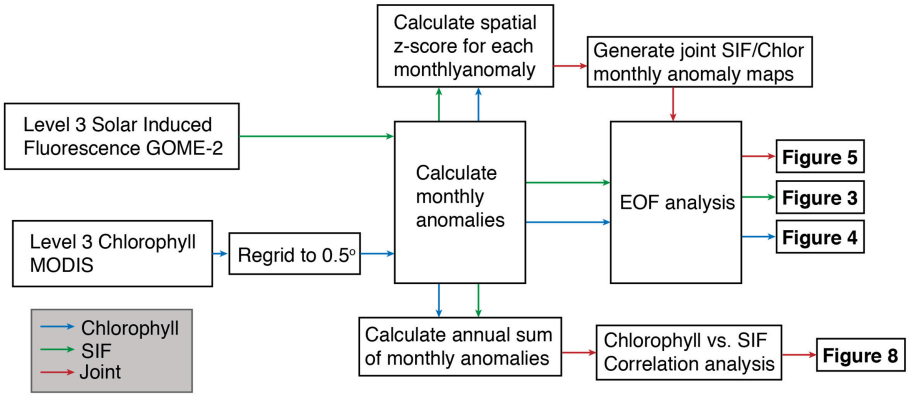

FIGURE 1 | Diagram showing workflow of analyses and the respective figures produced through these analyses.

2.2.3. Supporting Climate Data

For analysis of climate conditions during specific years, data from NASA's modern-era retrospective analysis for research and applications (MERRA) was used (Rienecker et al., 2011). This is a reanalysis product that assimilates meteorological data and satellite retrievals to yield a global gridded estimate of the climate state on a global 0.5° latitude × 0.66° longitude grid. Comparisons of this reanalysis product and others (e.g., NCEP and ERA Interim) can be found in Rienecker et al. (2011). For this study, we utilize monthly resolved sea level pressure (Pa), 10 m U and V wind speeds (m s^{-1}) and 2 m surface temperatures (K). In addition to the Reanalysis data, the spatiotemporal patterns in productivity were compared against the following climate modes: the Pacific Decadal Oscillation (PDO) (Mantua et al., 1997; Mantua and Hare, 2002), ENSO (specifically, the Oceanic Niño Index index) (Ropelewski and Halpert, 1986; Cayan et al., 1999; McCabe et al., 2004) and the Pacific North American pattern (PNA) (Trouet and Taylor, 2010). While this is not an exhaustive list of climate modes, these were the modes that produced the strongest correlation with the leading principal components of the different satellite products. Monthly timeseries for each of these datasets were accessed from National Ocean and Atmospheric Administration and all data were reported in normalized units. It is important to note that for PDO and ENSO, the strongest expression of the modes appears during the winter months. However, we found the strongest correlation between the climate modes and the satellite ecosystem indicators to emerge using the annual averages of the climate modes. We thus report and discuss the climate modes in terms of their annual averages, which has the effect of buffering their interannual variability by occasionally averaging periods that may include transitions from positive to negative states. There are multiple reasons why the correlations with productivity are stronger using the annual averages including that peak productivity occurs during spring and summer but may inherent legacy of the previous winter's conditions. In other words, spring wind fields might influence real time upwelling whereas wintertime anomalies in tropical Pacific SST might influence higher latitude thermocline conditions months later. Thus, there is ecological sensitivity to conditions over a longer seasonal window. While future work could benefit from exploring seasonal dynamics in the drivers of synchrony, for simplicity we hereafter discuss variability based on annual averaging.

2.3. Empirical Orthogonal Function Analysis

An Empirical Orthogonal Function (EOF) analysis was performed on monthly SIF and chlorophyll data from the domain bounded by 30° and 65°N latitude and −180° to −110 °W longitude. Both data were treated by subtracting the monthly climatological value at each grid cell to generate timeseries of monthly anomalies for each grid cell (Björnsson and Venegas, 1997) (**Figure 1**). For the individual analysis of the SIF and chlorophyll data, the data were not normalized by variance, which resulted in highly productive coastal regions having a larger weight on the analysis (Messié and Chavez, 2011). In order to generate a composite SIF/chlorophyll map, each of these datasets were normalized (as a spatial z-score) to produce a continuous land-sea productivity map. EOFs were then computed for the region, yielding a spatial pattern (i.e., an EOF) and a principal component (PC) time series that captured the temporal variability of each EOF mode. We consider only the first two EOFs for each analysis, which in all cases explained >50% of the variance. A calendar-year average for each of the PCs was then computed for comparison with the climate mode data. We note that the direction of the loading patterns is arbitrary, which becomes important when comparing the patterns that emerge from the individual EOF analyses (**Figures 3**, **4**) with the joint EOF analysis (**Figure 5**).

2.4. Terrestrial-Aquatic Regression Analysis

To consider the spatial signature of terrestrial-aquatic synchrony, a linear regression analysis was performed between adjacent chlorophyll and SIF timeseries along each 0.5° region of the coastline. This was done by selecting all chlorophyll and SIF grid cells within 300 km of each coastal grid cell and computing an

interannual average timeseries for the land and sea (**Figure 1**). The choice of 300 km is arbitrary but the analysis was largely insensitive to thresholds ranging from 200 to 500 km. The respective 300 km averaged land and sea timeseries were regressed against one another and a Pearson's correlation coefficient calculated. Synchrony was defined by coastal grid cells where the correlation coefficient was positive and the $p < 0.1$.

3. RESULTS

3.1. Regional Patterns of Productivity and Seasonality

To provide context for the subsequent analyses, the regional patterns of chlorophyll and SIF seasonality and amplitude were assessed over the entire domain (**Figure 2**). **Figure 2A** shows the presence of high chlorophyll concentrations across the coastal regions and throughout the Arctic. At this scale, the complex pattern in the timing of peak productivity can be clearly observed (**Figure 2B**). The boundary between the southern and northern part of the Northeastern Pacific Basin is delineated by the North Pacific Current and observable by differences in chlorophyll seasonality such that the southern region has a peak in January and the northern region has a peak in September (Hurlburt et al., 1996). This current partially isolates the northern part of the basin affected by the Alaska and Kamchatka Currents (**Figure 2**). The chlorophyll peak in the intermediate zone between the north and south parts of the basin is poorly defined and is quite dynamic between years. The coastal regions of Alaska and the Pacific Northwest display a consistent chlorophyll maximum in May (Di Lorenzo et al., 2008; García-Reyes et al., 2018) while the timing of peak chlorophyll for the southern coastal regions are not spatially coherent. In terms of terrestrial productivity, SIF is maximum along the coastal mountains of the west coast of the US and across a region of high productivity in the plains of Canada that is an extension of the highly productive agricultural regions of the midwestern US (Hilton et al., 2017). Unlike chlorophyll, the terrestrial ecosystems are dominated by a wide homogenous region where peak productivity occurs in June and July. The exceptions can be found in the domain influenced by the North American Monsoon, that experiences its peak in productivity in August, and in parts of the *Basin and Range* region where peak productivity occurs in March (St. George et al., 2010; McCabe et al., 2012). These results are summarized by the histogram shown in **Figure 2C**, which illustrates the narrow and distinct distributions between the timing of peak productivity for terrestrial and coastal marine systems. In the North Pacific, the offset between the peak in terrestrial (July) and coastal marine (May) productivity is, on average, 2 months.

3.2. Spatio-Temporal Patterns of Productivity

The EOF analysis of SIF identifies two dominant modes of variability that explain 34% and 24% of the variance (**Figures 3A,C**). The first of these modes is characterized by a strong dipole with a negative loading that runs along most of the west coast of the US and positive loadings along the coast of British Columbia and southern Alaska. The dipole is centered around a latitude of ∼50° N. The PC of this EOF shows limited interannual variability and is highly correlated ($r = 0.90$) with annually-averaged PDO (**Figure 3B**). The effect of the PDO in generating a north-south dipole in tree ring widths in the western US has been identified elsewhere (e.g., MacDonald and Case, 2005) and the analysis presented here provides a spatially continuous depiction of this pattern of variability. The second EOF is also characterized by a north-south dipole with an opposite sign that has a positive loading isolated in California and into Baja and a negative loading that is diffuse across latitudes north of ∼40° N (**Figure 3C**). The PC of this EOF is associated with higher frequency variability and most strongly correlates with the PNA (r=0.52) (Leathers et al., 1991) (**Figure 3D**). When taken together, these two EOFs illustrate how terrestrial productivity along the west coast is predominated by a dipole that displays both low frequency variability associated with the oceanic mode of the PDO (EOF 1) and higher frequency variability associated with the atmospheric mode of the PNA (EOF 2). The dipole largely reflects modulations between a more meridional or zonal wintertime westerly storm track such that storms can retain a zonal trajectory and strike the California coast or follow a meridional pattern due to high pressure blocking cells that results in precipitation delivered preferentially to British Columbia and Alaska (Salathé, 2006).

The EOF analysis of chlorophyll is also characterized by two dominant modes of variability that similarly explain 33 and 25% of the variance. With both modes, the dominant loading centers occur along the coastlines where the majority of variance occurs. The first of the EOF patterns is characterized by a strong dipole with negative loadings along the central and southern California coastline and south of the Aleutian Islands. This mode is associated with positive anomalies that span the coast of northern California, Oregon, British Columbia and through to southern Alaska (**Figure 4A**). The PC of this EOF strongly correlates with ENSO ($r = 0.85$) (**Figure 4B**). The influence of ENSO on coastal chlorophyll is through the combined effects of changes in the tropical Pacific thermocline that migrate poleward and changes in coastal winds associated with the establishment and strength of atmospheric blocking cells in the North Pacific (Jacox et al., 2015). The second EOF of chlorophyll is associated with a widespread but diffuse negative loading along the entire coastline with isolated positive loading anomalies along the Northern California and Oregon coastlines and Vancouver Island (**Figure 4C**). This mode is associated with more low frequency variance and correlates most strongly with the PDO ($r = 0.69$) (**Figure 4D**) (Chhak and Di Lorenzo, 2007).

By combining the normalized maps of SIF and chlorophyll, a third EOF analysis was done to specifically assess whether the basin-wide mode of productivity generates coherent loading between adjacent coastal and terrestrial regions. The first EOF of this field explains 33% of the variance (**Figure 5A**) and is associated with a strong dipole pattern centered at ∼40°N. While the EOFs of individual SIF and chlorophyll fields implied there would be shared spatial variance associated with the PDO, this analysis provides explicit evidence of variability that is seamless across the marine and terrestrial interface over

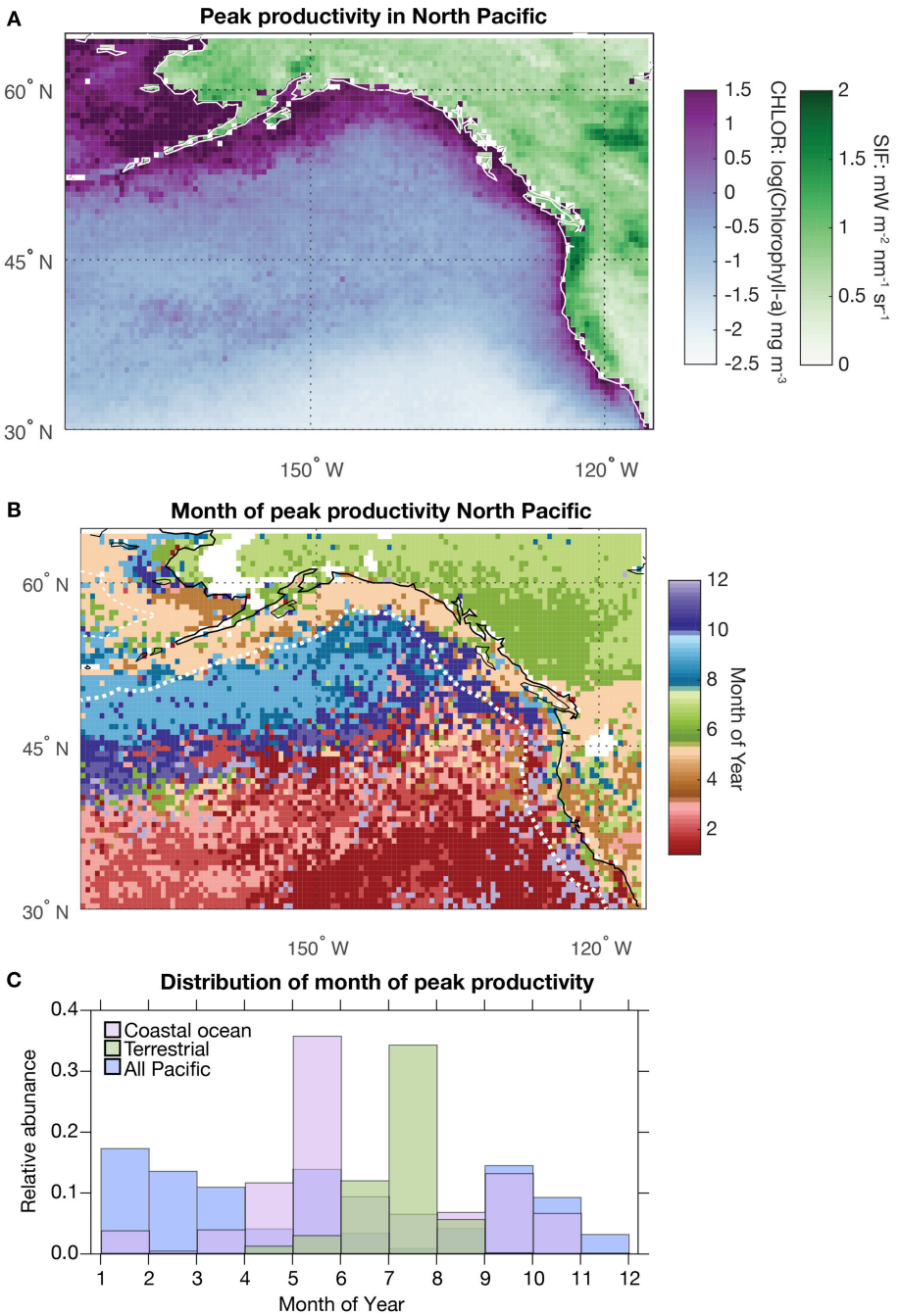

FIGURE 2 | (A) Map showing the average of each year's maximum value for Solar-Induced Fluorescence (SIF) (greens) and chlorophyll-α (purples). **(B)** Map showing the average month that each grid cell reaches its peak in SIF and chlorophyll-α (as in **A**). The SIF data spans 2007–2017 and the chlorophyll-α data spans 2003–2017. Each dataset was gridded to a common 0.5° spatial resolution (**Figure 1**). **(C)** Distribution of the month of peak SIF and chlorophyll based on the data in **(B)**. The coastal chlorophyll data includes all grid cells contained within the dotted white line shown in **(B)** (as in **Figure 8**).

broad regions of the coastline from California to southern Alaska. The aquatic-terrestrial synchrony exists because of the presence of a "mirrored dipole" such that both the marine and terrestrial systems display dipoles with similar spatial extents and loadings in the same direction. The PC associated with the mirrored dipole EOF is strongly correlated with the PDO (r = 0.89) (**Figure 5B**). The evidence for strong synchrony in California is consistent with previous results from Black et al. (2018) but has been expanded here across a larger domain. Only a single EOF is shown for the joint

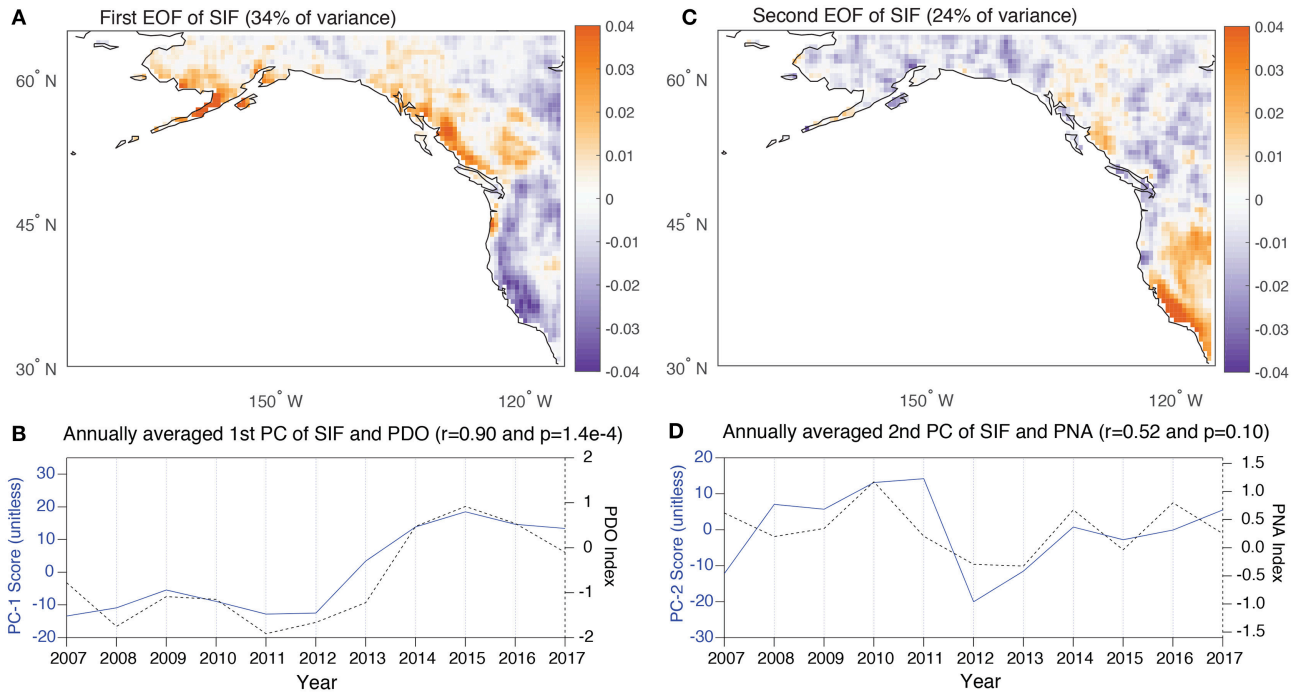

FIGURE 3 | (A,C) The first and second EOF of SIF for the region of interest. The units are dimensionless loadings with explained variances of 34 and 24%, respectively. **(B,D)** The first and second annually averaged vectors of the PCs associated with the EOFs shown in above panels. The first PC vector is plotted alongside the annually-averaged PDO index (r = 0.90) and the second PC is plotted alongside PNA (r = 0.52).

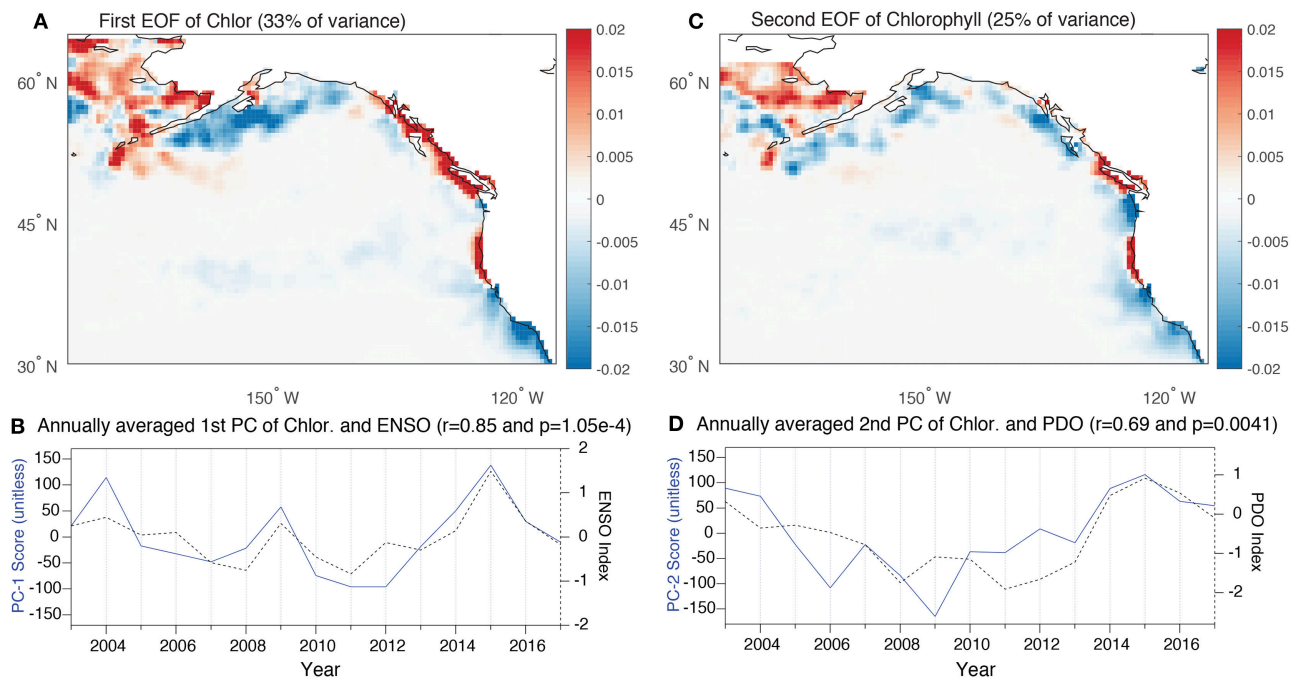

FIGURE 4 | (A,C) The first and second EOF of chlorophyll for the region of interest. The units are dimensionless loadings with explained variances of 33 and 25%, respectively. **(B,D)** The first and second annually averaged vectors of the PCs associated with the EOFs shown in above panels. The first PC is plotted alongside the annually-averaged ENSO index (r = 0.89) and the second PC is plotted alongside PDO as in **Figure 2** (r = 0.69).

marine/terrestrial field because all subsequent modes had limited explanatory power.

3.3. Case Studies of 2009, 2012 and 2015

To complement the EOF analyses, a specific assessment of the absolute chlorophyll and SIF anomalies during selected years was conducted. The first of these years, 2015, was chosen as one where SIF (**Figure 3**), chlorophyll (**Figure 4**) and the joint SIF/chlorophyll (**Figure 5**) EOF analyses all indicated a strong north-south dipole pattern. The pattern of SIF and chlorophyll anomalies during 2015 (**Figure 6A**), were characterized by significant negative anomalies in productivity along the California coastline and positive anomalies across much of coastal British Columbia and southern Alaska. The dipole pattern in both terrestrial and marine productivity thus produce widespread synchrony. It is noted, however, that further north into Alaska the synchrony breaks down such that the terrestrial ecosystems were associated with positive anomalies and the ocean with negative anomalies. In contrast to 2015, 2012 was a year that was associated with a negative loading in the PC score of the joint SIF/Chlorophyll EOF (**Figure 5**). Indeed, unlike 2015, 2012 was not associated with a chlorophyll dipole but rather a widespread negative loading across the coastline from California through to southern Alaska. This pattern was largely mirrored on land with relatively low SIF values across the region. Like 2015, 2012 was thus also associated with synchronous behavior but with a pattern distinct from the familiar dipole. The last year considered was 2009, which was chosen as a contrasting example, where the first PC of chlorophyll indicated a strongly positive anomaly whereas the first PC of SIF indicated a weak or inverted anomaly pattern. Indeed, 2009 was associated with strongly opposing anomalies between productivity in the land and sea across much of the California coastline and northward to southern Alaska (**Figure 6B**). The conditions during 2009 represent the only year in the timeseries with significantly asynchronous behavior.

To explain the distinct pattern between years, we begin with an analysis of the annually averaged climate modes for these years. 2015 was associated with both strong ENSO and PDO anomalies, with the former driving the dipole pattern in chlorophyll and the latter the dipole pattern in SIF (Fisher et al., 2015; Lindegren et al., 2018) (**Figures 3**, **4**). In contrast, 2009 was associated with a negative PDO and positive ENSO, such that the terrestrial dipole was inverted relative to 2015 and the chlorophyll dipole remained the same. The effect was strong terrestrial-marine asynchrony during this year. The comparison between these years suggests that when ENSO and PDO are in phase, synchrony emerges and when the two are out of phase asynchrony emerges. However, the year of 2012 challenges this simple depiction as this year had similar annual averages for both ENSO and the PDO as 2009 yet also exhibited synchrony. It is likely that the difference between 2009 and 2012 emerged because of subseasonal variations in ENSO and the PDO. Specifically, in 2009 ENSO began negative but transitioned to a positive state.

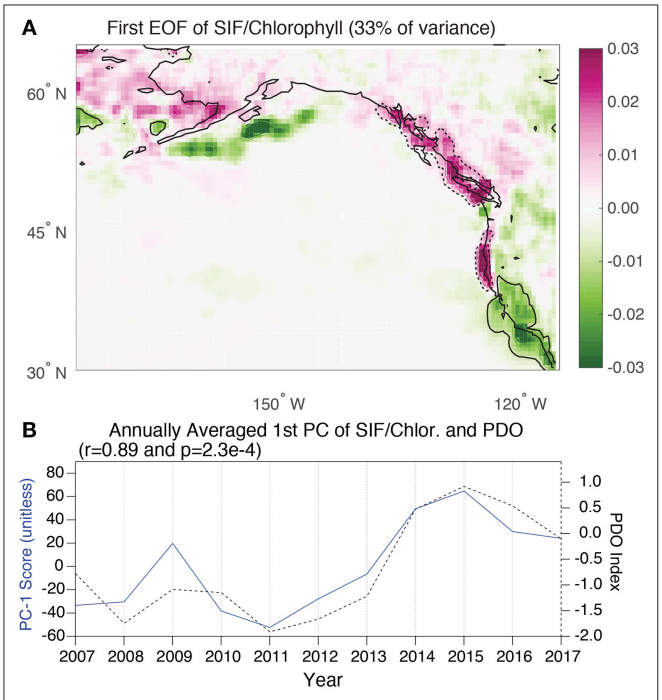

FIGURE 5 | (A) The first EOF of the merged normalized SIF and chlorophyll maps for the region of interest. The units are dimensionless loadings with an explained variance of 33%. The dark contour (dotted and continuous) are used to highlight particular areas of synchrony and asynchrony, respectively. **(B)** The first annually-averaged PC vector associated with the EOF shown in above panel. The PC timeseries is plotted alongside the annually-averaged PDO index (r = 0.89).

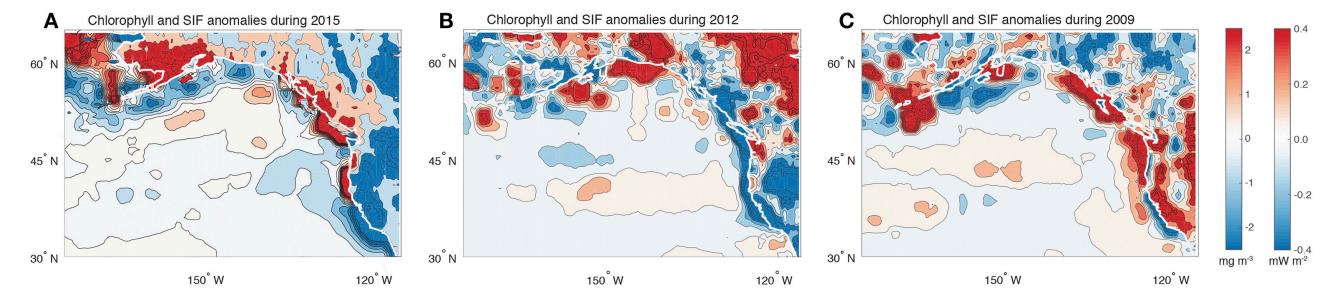

FIGURE 6 | Maps showing the annually-averaged anomalies in SIF and chlorophyll during the 2015 **(A)**, 2012 **(B)**, and 2009 **(C)** calendar years.

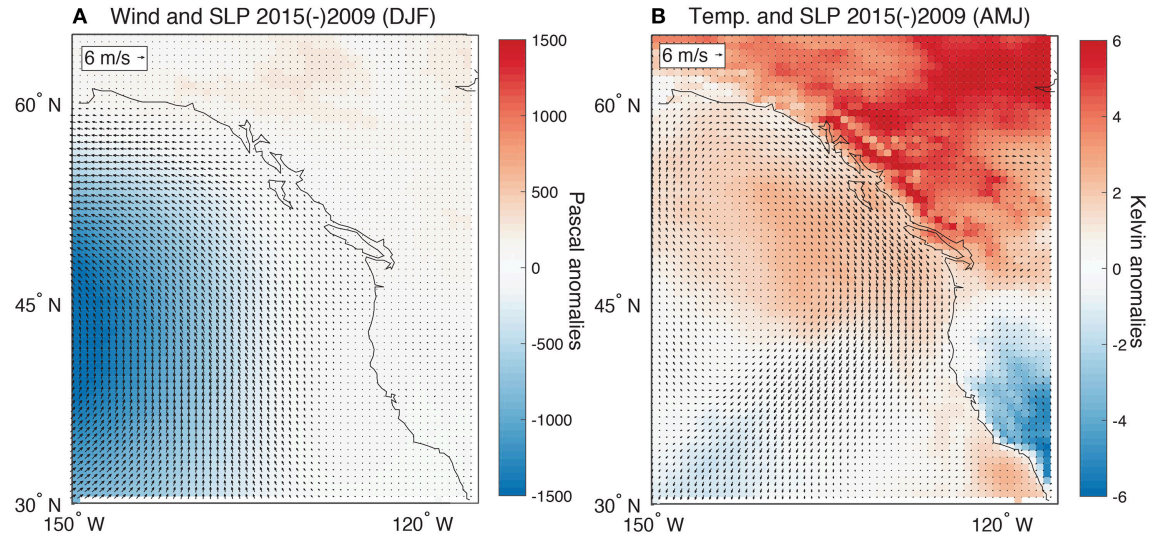

FIGURE 7 | (A) The difference in SLP and 10 m wind fields for DJF between 2015 and 2009. Units for SLP are Pa and the wind vectors are plotted with reference to 6 m s^{-1} vector shown in the top left. **(B)** The 2 m air temperature and 10 m wind fields for AMJ between 2015 and 2009. Units for temperature are K and the wind vectors are plotted with reference to 6 m s^{-1} vector shown in the top left. All data were extracted from the MERRA reanalysis database (Rienecker et al., 2011).

In contrast, 2012 ENSO and PDO were persistently out of phase throughout the year.

To further explore the mechanisms associated with synchrony (2015) or asynchrony (2009), a comparison between the climate conditions of these two contrasting years was conducted. During the winter, 2015 had a significantly stronger and southerly displaced Aleutian Low relative to 2009. This led to enhanced southerly winds during the winter months (Wise, 2016) (**Figure 7A**). The wintertime atmospheric conditions may have preconditioned growing season productivity anomalies through changes in snowpack and soil moisture. Specifically, this atmospheric pattern would have lead to storm tracks focused along the British Columbian coastline and southern Alaska (Ropelewski and Halpert, 1986; McCabe et al., 2004). It is also notable that 2015 was associated with anomalously warm (cool) conditions in the spring and early summer in the northern (southern) regions of the domain along with anomalous northerly winds across the coastlines north of California (Smith and Sardeshmukh, 2000) (**Figure 7B**). These patterns would have contributed to an earlier onset of spring in the north and the positive anomalies in SIF (McCabe et al., 2012). The coastal wind field anomalies along the British Columbian and southern Alaskan coastlines would also have lead to increased upwelling or reduced downwelling and contributed to the observed positive chlorophyll anomalies. The comparison between 2009 and 2015 reveals effects during both winter and summer months and highlights why the use of annual averages for the climate modes produced the strongest correlations with the EOF patterns.

3.4. Spatial Analysis of Synchrony From Regression Analysis

Figure 8 shows the correlation coefficient between adjacent marine and terrestrial domains along the entire coastline. The results show that along ∼40% of the coastline there is a statistically significant interannual correlation between SIF and chlorophyll. The correlation is strongest at the Southern California Bight, along the Oregon and Vancouver Island coastlines and along the southern Alaskan coast (**Figure 8A**). While there are a few regions of the coast where the correlation is negative (i.e., asynchrony), the principal pattern is one of synchrony. This shows that in spite of the complexities of the spatiotemporal aspects of synchrony, as described in the previous analyses, coastal regions broadly exhibit terrestrial-marine synchrony. Alongside the correlation map, is a separate analysis showing the lag between when terrestrial and aquatic ecosystems experience their respective peaks in productivity (**Figure 8B**). A comparison between these maps shows that synchrony, or lack thereof, is not tied in any systematic way to local differences between terrestrial and marine seasonality. This can be explained by the fact that the processes driving annual variations in productivity, whether it be marine or terrestrial, persist for multiple months.

4. DISCUSSION

The analyses presented here were designed to test whether synchrony between terrestrial and marine ecosystems is a fundamental characteristic of the North Pacific. Previous work along the California coastline established the presence of regional-scale coherence that manifested at the scale of species (Black et al., 2018). This previous work hypothesized that the mechanism linking ecosystems across the coastal interface was atmospheric circulation anomalies that simultaneously influenced upwelling through altered wind fields and rainfall through variations in the storm track. However, across 1000's of km of coastline the large scale coupling associated with

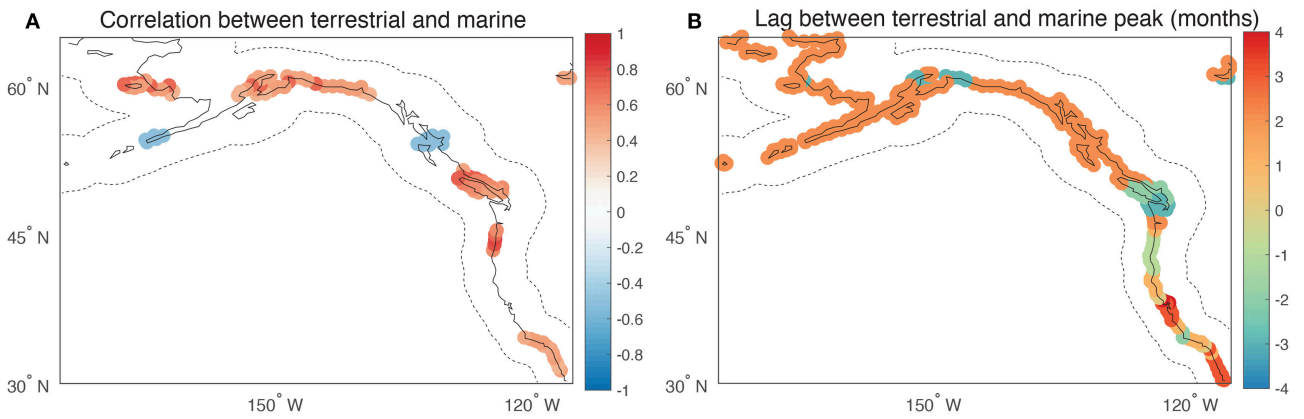

FIGURE 8 | (A) Map showing the correlation coefficient between adjacent (± 300 km as contained by the dotted lines) swaths of land (SIF) and sea (chlorophyll). Points are only plotted where the p-value of the correlation is <0.1. **(B)** The lag between when adjacent land and sea regions reach their peak in productivity with units of month. The scale of regions used in the calculation are identical to those used in **(A)**. The calculation of when the peak in productivity occurred is as shown in **Figure 2**.

atmospheric modes could be strengthened or weakened through myriad secondary mechanisms operating at the local scale. These could include the influence of SSTs on the development of marine fog, the effect of SSTs on convective storm development and atmospheric humidity and changes in runoff that influence marine productivity through nutrient availability (Persson et al., 2005; Warrick et al., 2005; Johnstone and Dawson, 2010). In considering the diverse ways that marine and terrestrial ecosystems could become coupled through climate variability, it is feasible that the synchrony previously observed at the regional scale may only emerge under a specific set of conditions.

As illustrated by the EOF analyses of SIF and chlorophyll (**Figures 3**, **4**), productivity is characterized in both the marine and terrestrial ecosystems by north-south dipole modes that correlate strongly with known ocean-atmosphere indices (Hare and Mantua, 2000; Di Lorenzo et al., 2008). ENSO is the dominant driver for the chlorophyll variability with strong localized and opposing loading centers that reflect the response of upwelling to wind and thermocline anomalies (Karl et al., 1995; Jacox et al., 2015; García-Reyes et al., 2018). Surprisingly, the EOF analysis of SIF did not indicate any strong impact of ENSO on the dominant spatiotemporal patterns in terrestrial ecosystems (Cayan et al., 1999; McCabe et al., 2012). It may be that because the effects of ENSO are strongest in the semi-arid water-limited regions in the southwestern US, the apparent effect of ENSO was minimized by including northern latitudes in the analysis. Instead, the results showed that terrestrial productivity was predominately driven by lower frequency (multi-annual) variability, which is in phase with the PDO (MacDonald and Case, 2005; Fang et al., 2018). The dominant influence of PDO on the spatiotemporal pattern reflects not only precipitation changes associated with this oceanic mode of variability but also through its effects on surface temperatures in coastal British Columbia and southern Alaska (Steinman et al., 2014).

Despite the fact that the leading terrestrial and marine EOFs were correlated with different ocean-atmospheric modes, the combined EOF analysis showed strong evidence that the PDO can generate a mirrored dipole pattern with coherent terrestrial and marine anomalies that span 1000's of km of the North Pacific coastline (**Figure 5**). That said, regions of isolated asynchrony associated with this dominant mode of variability were present along the Washington coastline and off the Aleutian Islands. The isolated areas of asynchrony highlight where local processes acting on either the marine or terrestrial systems may disrupt the joint sensitivity of terrestrial and marine ecosystems to ocean-atmosphere variability. When considering this result along with the regression analysis presented in **Figure 8**, it can be concluded that synchrony is a widespread phenomenon along the eastern margin of the North Pacific. This is apparently the case even when distinct ENSO and PDO states prevail as illustrated by synchrony during 2012 and 2015 despite differences in ENSO and PDO states. One potential factor considered here to explain the spatial pattern of synchrony was the seasonal phasing between adjacent terrestrial and marine systems. It was presumed *a priori* that in areas where the seasonal cycles of land and sea productivity were in phase, there would be greater synchrony. However, there was limited evidence to suggest this was the case (**Figure 8**), implying that synchrony does not generally emerge in this region from the immediate responses to specific synoptic events such as a heatwave or flood states (Ruthrof et al., 2018). Instead, the results suggest that synchrony reflects more slowly evolving responses to preceding wintertime atmospheric circulation patterns and springtime temperatures. The consequence is that even in areas where the terrestrial and aquatic ecosystems lag one another by 3–4 months, there may still be interannual coherence.

The examples of 2009 and 2015 highlight how ENSO and PDO modes can modulate the strength of synchrony. Although the analysis is based on only a short timeseries, the results suggest that simultaneously positive ENSO and PDO modes drive synchrony (2015) while positive ENSO and negative PDO lead to asynchrony (2009). The analysis relied on annual averages of these two modes, which is in contrast to previous

studies that tended to focus on wintertime values when these patterns manifest most strongly. Future studies would benefit from exploring in more detail how specific seasonal patterns might strengthen or disrupt synchrony. Nonetheless, to the extent that PDO and ENSO can become phase locked for multiple years (or longer) (Newman et al., 2003), synchrony would be the dominant pattern over longer time periods. This is relevant in considering proxy records where it can be expected that the correlation between proxies for land and sea productivity (such as tree growth and $\delta^{13}C$ of foraminifera) would predominantly reflect variations in the PDO or a similar mode of variability. The exact physical mechanism that drives synchrony during positive PDO and ENSO cannot be ascertained without further modeling but the analysis of climate conditions during opposing years suggests it emerges from a combination of: (1) a strong Aleutian Low that drives anomalous wintertime southerly winds, (2) a dipole in spring temperature anomalies over land that impact growing season length and (3) anomalous northerly coastal wind fields that influence coastal upwelling or downwelling. A longer timeseries that includes additional examples of joint ENSO and PDO anomalies, including ones with specific seasonal manifestations, would help to further shed light on the dynamics that underlie the synchrony.

The broader motivation in quantifying synchrony was to assess whether coupling between terrestrial and marine productivity would amplify the sensitivity of the global carbon cycle to interannual climate variability. Existing data suggest that the strength of the ocean and terrestrial carbon sinks are important sources of interannual variability of the carbon budget (Ballantyne et al., 2012). Despite the extensive work done on this topic, few studies have addressed whether the terrestrial and marine carbon sinks become synchronized in response to ocean-atmosphere climate modes. The results from this study show that the terrestrial and marine carbon sinks in the western US are highly responsive to climate variability, which is consistent with previous assessments on the role of semi-arid and mid-latitude ecosystems on interannual variability of the global carbon cycle (Poulter et al., 2014; Ahlström et al., 2015; Berkelhammer et al., 2017). However, both terrestrial and aquatic systems respond to interannual modes with a north-south dipole such that the total regional carbon sink (i.e., integrated anomalies across the domain) is not likely to show significant interannual changes. However, there will be latitudinal shifts in where primary productivity is highest and also locations such as the California and British Columbian coasts that are associated with locally enhanced (or diminished) carbon sinks that result from the mirrored terrestrial and marine dipole.

An important caveat to this study is that while chlorophyll and SIF provide indicators of changes in productivity, they do not provide constraints on the net ecosystem exchange of carbon (i.e., respiration-photosynthesis). This is specifically an issue with chlorophyll, which is an indicator of biomass concentration but not directly for primary productivity. Further, the marine flux of carbon is tightly controlled by physical processes, which may be more important to air-sea exchange of carbon than primary productivity (Eddebbar et al., 2017). To fully assess whether terrestrial and marine synchrony influences regional carbon budgets, a more holistic approach is needed that considers both the physical aspects of air-sea exchange of carbon and how terrestrial respiration is also responding to climate variability (Li et al., 2016; Liu et al., 2017). Ultimately, whether terrestrial and marine synchrony play an important role in interannual carbon budgets will depend on whether the behavior observed here in the North Pacific is common elsewhere. Future studies on this topic might find additionally strong examples of synchrony in regions such as southern South America and the high Arctic where the seasonality of terrestrial and aquatic productivity are in phase with one another (not shown). The data are available to test this and as new satellite platforms generate data with higher spatial resolution and accuracy, a better understanding of the importance of these linkages will be possible.

5. CONCLUSIONS

This study set out to test whether the productivity of terrestrial and marine ecosystems in the North Pacific display synchronous responses to climate variability. Previous work had addressed this topic in the context of trophic dynamics but we consider here whether this synchrony may enhance the response of regional carbon cycle dynamics to climate variability. The results show that over 1,000's of km of the North Pacific coastline, there is a common temporal response between the productivity of adjacent terrestrial and marine ecosystems. While there are exceptions to this behavior, the results suggest that the effects of ocean-atmosphere variability on wind fields, rainfall and temperature have a tendency to produce common or synchronous responses across the coastal interface. The synchrony appears most pronounced in response to the Pacific Decadal Oscillation (PDO) though this is apparently modulated by the state of ENSO, such that if ENSO and the PDO oppose one another so too does the strength of coupling between terrestrial and marine productivity. The results ultimately suggest there is not likely to be a significant region-wide response of the carbon cycle to this synchrony because the modes of variability are predominated by opposing north-south anomalies such that there are rarely examples of basin-scale productivity anomalies as in 2012. However, there may be local regions such as the California coastline where the synchrony is strong enough to influence the regional carbon sink. Future studies using Earth System Models that include both the terrestrial and marine carbon cycles could be used to explore the dynamics that give rise to the regions of highly synchronous behavior particularly in the context of canonical ENSO and PDO climate variability.

AUTHOR CONTRIBUTIONS

MB designed the research, performed all the analyses and wrote the paper.

FUNDING

Funding for this research was provided by NSF grant #1502776 to MB.

ACKNOWLEDGMENTS

The author would like to thank J. Joiner and the rest of the MetOp team for making the fluorescence data available.

REFERENCES

Abram, N. J., McGregor, H. V., Tierney, J. E., Evans, M. N., McKay, N. P., Kaufman, D. S., et al. (2016). Early onset of industrial-era warming across the oceans and continents. *Nature* 536, 411. doi: 10.1038/nature19082

Ahlström, A., Raupach, M. R., Schurgers, G., Smith, B., Arneth, A., Jung, M., et al. (2015). The dominant role of semi-arid ecosystems in the trend and variability of the land CO_2 sink. *Science* 348, 895–899. doi: 10.1126/science.aaa1668

Ahmed, M., Anchukaitis, K. J., Asrat, A., Borgaonkar, H. P., Braida, M., Buckley, B. M., et al. (2013). Continental-scale temperature variability during the past two millennia. *Nat. Geosci.* 6, 339. doi: 10.1038/ngeo1797

Ballantyne, A., Alden, C., Miller, J., Tans, P., and White, J. (2012). Increase in observed net carbon dioxide uptake by land and oceans during the past 50 years. *Nature* 487, 70. doi: 10.1038/nature11299

Behrenfeld, M. J., O'Malley, R. T., Siegel, D. A., McClain, C. R., Sarmiento, J. L., Feldman, G. C., et al. (2006). Climate-driven trends in contemporary ocean productivity. *Nature* 444, 752. doi: 10.1038/nature05317

Berkelhammer, M., Stefanescu, I., Joiner, J., and Anderson, L. (2017). High sensitivity of gross primary production in the Rocky Mountains to summer rain. *Geophys. Res. Lett.* 44, 3643–3652. doi: 10.1002/2016GL072495

Biondi, F., Gershunov, A., and Cayan, D. R. (2001). North pacific decadal climate variability since 1661. *J. Clim.* 14, 5–10. doi: 10.1175/1520-0442(2001)014<0005:NPDCVS>2.0.CO;2

Björnsson, H., and Venegas, S. (1997). A manual for eof and svd analyses of climatic data. *CCGCR Rep.* 97, 112–134.

Black, B. A., Sydeman, W. J., Frank, D. C., Griffin, D., Stahle, D. W., García-Reyes, M., et al. (2014). Six centuries of variability and extremes in a coupled marine-terrestrial ecosystem. *Science* 345, 1498–1502. doi: 10.1126/science.1253209

Black, B. A., van der Sleen, P., Di Lorenzo, E., Griffin, D., Sydeman, W. J., Dunham, J. B., et al. (2018). Rising synchrony controls western North American ecosystems. *Glob. Change Biol.* 24, 2305–2314. doi: 10.1111/gcb.14128

Cayan, D. R., Redmond, K. T., and Riddle, L. G. (1999). ENSO and hydrologic extremes in the western United States. *J. Clim.* 12, 2881–2893. doi: 10.1175/1520-0442(1999)012<2881:EAHEIT>2.0.CO;2

Chhak, K., and Di Lorenzo, E. (2007). Decadal variations in the California Current upwelling cells. *Geophys. Res. Lett.* 34:L14604. doi: 10.1029/2007GL030203

Cook, E. R., Seager, R., Cane, M. A., and Stahle, D. W. (2007). North American drought: Reconstructions, causes, and consequences. *Earth Sci. Rev.* 81, 93–134. doi: 10.1016/j.earscirev.2006.12.002

Di Lorenzo, E., Schneider, N., Cobb, K. M., Franks, P., Chhak, K., Miller, A. J., et al. (2008). North Pacific Gyre Oscillation links ocean climate and ecosystem change. *Geophys. Res. Lett.* 35. doi: 10.1029/2007GL032838

Dore, J. E., Letelier, R. M., Church, M. J., Lukas, R., and Karl, D. M. (2008). Summer phytoplankton blooms in the oligotrophic North Pacific Subtropical Gyre: historical perspective and recent observations. *Progr. Oceanogr.* 76, 2–38. doi: 10.1016/j.pocean.2007.10.002

Eddebbar, Y. A., Long, M. C., Resplandy, L., Rödenbeck, C., Rodgers, K. B., Manizza, M., et al. (2017). Impacts of ENSO on air-sea oxygen exchange: observations and mechanisms. *Glob. Biogeochem. Cycles* 31, 901–921. doi: 10.1002/2017GB005630

Fang, K., Cook, E., Guo, Z., Chen, D., Ou, T., and Zhao, Y. (2018). Synchronous multi-decadal climate variability of the whole Pacific areas revealed in tree rings since 1567. *Environ. Res. Lett.* 13, 024016. doi: 10.1088/1748-9326/aa9f74

Fisher, J. L., Peterson, W. T., and Rykaczewski, R. R. (2015). The impact of E l N iño events on the pelagic food chain in the northern California Current. *Glob. Change Biol.* 21, 4401–4414. doi: 10.1111/gcb.13054

García-Reyes, M., Lamont, T., Sydeman, W. J., Black, B. A., Rykaczewski, R. R., Thompson, S. A., et al. (2018). A comparison of modes of upwelling-favorable wind variability in the Benguela and California current ecosystems. *J. Mar. Syst.* 188, 17–26. doi: 10.1016/j.jmarsys.2017.06.002

Guyette, R. P., and Rabeni, C. F. (1995). Climate response among growth increments of fish and trees. *Oecologia* 104, 272–279. doi: 10.1007/BF00328361

Hare, S. R., and Mantua, N. J. (2000). Empirical evidence for North Pacific regime shifts in 1977 and 1989. *Progr. Oceanogr.* 47, 103–145. doi: 10.1016/S0079-6611(00)00033-1

Hilton, T. W., Whelan, M. E., Zumkehr, A., Kulkarni, S., Berry, J. A., Baker, I. T., et al. (2017). Peak growing season gross uptake of carbon in north america is largest in the midwest usa. *Nat. Clim. Change* 7, 450–454. doi: 10.1038/nclimate3272

Hoegh-Guldberg, O., and Bruno, J. F. (2010). The impact of climate change on the world's marine ecosystems. *Science* 328, 1523–1528. doi: 10.1126/science.1189930

Hu, C., Lee, Z., and Franz, B. (2012). Chlorophyll aalgorithms for oligotrophic oceans: a novel approach based on three-band reflectance difference. *J. Geophys. Res.* 117. doi: 10.1029/2011JC007395

Hurlburt, H. E., Wallcraft, A. J., Schmitz, W. J., Hogan, P. J., and Metzger, E. J. (1996). Dynamics of the Kuroshio/Oyashio current system using eddy-resolving models of the North Pacific Ocean. *J. Geophys. Res.* 101, 941–976. doi: 10.1029/95JC01674

Jacox, M. G., Fiechter, J., Moore, A. M., and Edwards, C. A. (2015). ENSO and the california current coastal upwelling response. *J. Geophys. Res.* 120, 1691–1702. doi: 10.1002/2014JC010650

Jeong, S.-J., Schimel, D., Frankenberg, C., Drewry, D. T., Fisher, J. B., Verma, M., et al. (2017). Application of satellite solar-induced chlorophyll fluorescence to understanding large-scale variations in vegetation phenology and function over northern high latitude forests. *Remote Sens. Environ.* 190, 178–187. doi: 10.1016/j.rse.2016.11.021

Johnstone, J. A., and Dawson, T. E. (2010). Climatic context and ecological implications of summer fog decline in the coast redwood region. *Proc. Natl. Acad. Sci. U.S.A.* 107, 4533–4538. doi: 10.1073/pnas.0915062107

Joiner, J., Guanter, L., Lindstrot, R., Voigt, M., Vasilkov, A., Middleton, E., et al. (2013). Global monitoring of terrestrial chlorophyll fluorescence from moderate spectral resolution near-infrared satellite measurements: methodology, simulations, and application to gome-2. *Atmos. Meas. Techn.* 6, 2803–2823. doi: 10.5194/amt-6-2803-2013

Joiner, J., Yoshida, Y., Vasilkov, A., Schaefer, K., Jung, M., Guanter, L., et al. (2014). The seasonal cycle of satellite chlorophyll fluorescence observations and its relationship to vegetation phenology and ecosystem atmosphere carbon exchange. *Remote Sens. Environ.* 152, 375–391. doi: 10.1016/j.rse.2014.06.022

Karl, D., Letelier, R., Hebel, D., Tupas, L., Dore, J., Christian, J., et al. (1995). Ecosystem changes in the North Pacific subtropical gyre attributed to the 1991–92 El Nino. *Nature* 373, 230. doi: 10.1038/373230a0

Landschuetzer, P., Gruber, N., and Bakker, D. C. (2016). Decadal variations and trends of the global ocean carbon sink. *Glob. Biogeochem. Cycles* 30, 1396–1417. doi: 10.1002/2015GB005359

Le Quéré, C., Andres, R. J., Boden, T., Conway, T., Houghton, R. A., House, J. I., et al. (2012). The global carbon budget 1959–2011. *Earth Syst. Sci. Data Discuss.* 5, 1107–1157. doi: 10.5194/essdd-5-1107-2012

Leathers, D. J., Yarnal, B., and Palecki, M. A. (1991). The Pacific/North American teleconnection pattern and United States climate. Part I: regional temperature and precipitation associations. *J. Clim.* 4, 517–528. doi: 10.1175/1520-0442(1991)004<0517:TPATPA>2.0.CO;2

Li, W., Ciais, P., Wang, Y., Peng, S., Broquet, G., Ballantyne, A. P., et al. (2016). Reducing uncertainties in decadal variability of the global carbon budget with multiple datasets. *Proc. Natl. Acad. Sci. U.S.A.* 13, 13104–13108. doi: 10.1073/pnas.1603956113

Lindegren, M., Checkley, D. M. Jr., Koslow, J. A., Goericke, R., and Ohman, M. D. (2018). Climate-mediated changes in marine ecosystem regulation during El Niño. *Glob. Change Biol.* 24, 796–809. doi: 10.1111/gcb.13993

Liu, J., Bowman, K. W., Schimel, D. S., Parazoo, N. C., Jiang, Z., Lee, M., et al. (2017). Contrasting carbon cycle responses of the tropical continents to the 2015–2016 El Niño. *Science* 358:eaam5690. doi: 10.1126/science.aam5690

Luus, K., Commane, R., Parazoo, N., Benmergui, J., Euskirchen, E., Frankenberg, C., et al. (2017). Tundra photosynthesis captured by satellite-observed solar-induced chlorophyll fluorescence. *Geophys. Res. Lett.* 44, 1564–1573. doi: 10.1002/2016GL070842

MacDonald, G. M., and Case, R. A. (2005). Variations in the Pacific Decadal Oscillation over the past millennium. *Geophys. Res. Lett.* 32. doi: 10.1029/2005GL022478

Mantua, N. J., and Hare, S. R. (2002). The Pacific Decadal Oscillation. *J. Oceanogr.* 58, 35–44. doi: 10.1023/A:1015820616384

Mantua, N. J., Hare, S. R., Zhang, Y., Wallace, J. M., and Francis, R. C. (1997). A Pacific interdecadal climate oscillation with impacts on salmon production. *Bull. Am. Meteorol. Soc.* 78, 1069–1080. doi: 10.1175/1520-0477(1997)078<1069:APICOW>2.0.CO;2

McCabe, G. J., Ault, T. R., Cook, B. I., Betancourt, J. L., and Schwartz, M. D. (2012). Influences of the El Niño Southern Oscillation and the Pacific Decadal Oscillation on the timing of the North American spring. *Int. J. Climatol.* 32, 2301–2310. doi: 10.1002/joc.3400

McCabe, G. J., Palecki, M. A., and Betancourt, J. L. (2004). Pacific and Atlantic Ocean influences on multidecadal drought frequency in the United States. *Proc. Natl. Acad. Sci. U.S.A.* 101, 4136–4141. doi: 10.1073/pnas.0306738101

Messié, M., and Chavez, F. (2011). Global modes of sea surface temperature variability in relation to regional climate indices. *J. Clim.* 24, 4314–4331. doi: 10.1175/2011JCLI3941.1

Newman, M., Compo, G. P., and Alexander, M. A. (2003). ENSO-forced variability of the Pacific decadal oscillation. *J. Clim.* 16, 3853–3857. doi: 10.1175/1520-0442(2003)016<3853:EVOTPD>2.0.CO;2

Ong, J. J., Rountrey, A. N., Zinke, J., Meeuwig, J. J., Grierson, P. F., O'donnell, A. J., et al. (2016). Evidence for climate-driven synchrony of marine and terrestrial ecosystems in northwest Australia. *Glob. Change Biol.* 22, 2776–2786. doi: 10.1111/gcb.13239

Persson, P. O. G., Neiman, P., Walter, B., Bao, J., and Ralph, F. (2005). Contributions from California coastal-zone surface fluxes to heavy coastal precipitation: a CALJET case study during the strong El Niño of 1998. *Mon. Weather Rev.* 133, 1175–1198. doi: 10.1175/MWR2910.1

Platt, T., Caverhill, C., and Sathyendranath, S. (1991). Basin-scale estimates of oceanic primary production by remote sensing: the North Atlantic. *J. Geophys. Res.* 96, 15147–15159. doi: 10.1029/91JC01118

Poulter, B., Frank, D., Ciais, P., Myneni, R. B., Andela, N., Bi, J., et al. (2014). Contribution of semi-arid ecosystems to interannual variability of the global carbon cycle. *Nature* 509, 600. doi: 10.1038/nature13376

Rienecker, M. M., Suarez, M. J., Gelaro, R., Todling, R., Bacmeister, J., Liu, E., et al. (2011). MERRA: NASA's modern-era retrospective analysis for research and applications. *J. Clim.* 24, 3624–3648. doi: 10.1175/JCLI-D-11-00015.1

Ropelewski, C. F., and Halpert, M. S. (1986). North American precipitation and temperature patterns associated with the El Niño/Southern Oscillation (ENSO). *Mon. Weather Rev.* 114, 2352–2362. doi: 10.1175/1520-0493(1986)114<2352:NAPATP>2.0.CO;2

Rosenzweig, C., Karoly, D., Vicarelli, M., Neofotis, P., Wu, Q., Casassa, G., et al. (2008). Attributing physical and biological impacts to anthropogenic climate change. *Nature* 453, 353. doi: 10.1038/nature06937

Ruthrof, K. X., Breshears, D. D., Fontaine, J. B., Froend, R. H., Matusick, G., Kala, J., et al. (2018). Subcontinental heat wave triggers terrestrial and marine, multi-taxa responses. *Sci. Rep.* 8, 13094. doi: 10.1038/s41598-018-31236-5

Salathé, E. P. Jr. (2006). Influences of a shift in North Pacific storm tracks on western North American precipitation under global warming. *Geophys. Res. Lett.* 33:L19820. doi: 10.1029/2006GL026882

Smith, C. A., and Sardeshmukh, P. D. (2000). The effect of ENSO on the intraseasonal variance of surface temperatures in winter. *Int. J. Climatol.* 20, 1543–1557. doi: 10.1002/1097-0088(20001115)20:13<1543::AID-JOC579>3.0.CO;2-A

Steinman, B. A., Abbott, M. B., Mann, M. E., Ortiz, J. D., Feng, S., Pompeani, D. P., et al. (2014). Ocean-atmosphere forcing of centennial hydroclimate variability in the Pacific Northwest. *Geophys. Res. Lett.* 41, 2553–2560. doi: 10.1002/2014GL059499

St. George, S., Meko, D. M., and Cook, E. R. (2010). The seasonality of precipitation signals embedded within the North American Drought Atlas. *Holocene* 20, 983–988. doi: 10.1177/0959683610365937

Trouet, V., and Taylor, A. H. (2010). Multi-century variability in the Pacific North American circulation pattern reconstructed from tree rings. *Clim. Dyn.* 35, 953–963. doi: 10.1007/s00382-009-0605-9

Warrick, J. A., Washburn, L., Brzezinski, M. A., and Siegel, D. A. (2005). Nutrient contributions to the Santa Barbara Channel, California, from the ephemeral Santa Clara River. *Estuarine Coastal Shelf Sci.* 62, 559–574. doi: 10.1016/j.ecss.2004.09.033

Wise, E. K. (2016). Five centuries of US West Coast drought: Occurrence, spatial distribution, and associated atmospheric circulation patterns. *Geophys. Res. Lett.* 43, 4539–4546. doi: 10.1002/2016GL068487

Yang, X., Tang, J., Mustard, J. F., Lee, J.-E., Rossini, M., Joiner, J., et al. (2015). Solar-induced chlorophyll fluorescence that correlates with canopy photosynthesis on diurnal and seasonal scales in a temperate deciduous forest. *Geophys. Res. Lett.* 42, 2977–2987. doi: 10.1002/2015GL063201

Conflict of Interest Statement: The author declares that the research was conducted in the absence of any commercial or financial relationships that could be construed as a potential conflict of interest.

frontiers in Earth Science

ORIGINAL RESEARCH
published: 03 May 2019
doi: 10.3389/feart.2019.00082

Timing and Potential Causes of 19th-Century Glacier Advances in Coastal Alaska Based on Tree-Ring Dating and Historical Accounts

Benjamin V. Gaglioti[1,2], Daniel H. Mann[2], Gregory C. Wiles[3], Benjamin M. Jones[4], Josh Charlton[3], Nicholas Wiesenberg[3] and Laia Andreu-Hayles[1]*

[1] Lamont-Doherty Earth Observatory of Columbia University, Palisades, NY, United States, [2] Department of Geosciences, University of Alaska Fairbanks, Fairbanks, AK, United States, [3] Department of Earth Sciences, The College of Wooster, Wooster, OH, United States, [4] Water and Environmental Research Center, University of Alaska Fairbanks, Fairbanks, AK, United States

The Little Ice Age (LIA), ca. CE 1250–1850, was a cold period of global extent, with the nature and timing of reduced temperatures varying by region. The Gulf of Alaska (GOA) is a key location to study the climatic drivers of glacier fluctuations during the LIA because dendrochronological techniques can provide precise ages of ice advances and retreats. Here, we use dendrochronology to date the most recent advance of La Perouse Glacier in the Fairweather Range of Southeast Alaska. After maintaining a relatively contracted state since at least CE 1200, La Perouse advanced to its maximum LIA position between CE 1850 and 1895. Like many other glaciers bordering the GOA, the La Perouse Glacier reached this maximum position relatively late in the LIA compared with glaciers in other regions. This is curious because reconstructions of paleoclimate in the GOA region indicate the 19th century was not the coldest period of the LIA. Using newly available paleoclimate data, we hypothesize that a combination of moderately cool summers accompanying the Dalton Solar Minimum and exceptionally snowy winters associated with a strengthened Aleutian Low could have caused these relatively late LIA advances. Such a scenario implies that winter climate processes, which are heavily influenced by ocean-atmospheric variability in the North Pacific region, have modulated these coastal glaciers' sensitivity to shifts in summer temperatures.

Keywords: glaciers, dendrochronology, Little Ice Age, Southeastern Alaska, St. Elias Mountains, climate change

OPEN ACCESS

Edited by:
Lesleigh Anderson, United States Geological Survey, United States

Reviewed by:
Johannes Koch, Brandon University, Canada
Olga Nikolaevna Solomina, Institute of Geography (RAS), Russia

****Correspondence:***
Benjamin V. Gaglioti
bengaglioti@gmail.com

Specialty section:
This article was submitted to Quaternary Science, Geomorphology and Paleoenvironment, a section of the journal Frontiers in Earth Science

Received: *21 December 2018*
Accepted: *04 April 2019*
Published: *03 May 2019*

Citation:
Gaglioti BV, Mann DH, Wiles GC, Jones BM, Charlton J, Wiesenberg N and Andreu-Hayles L (2019) Timing and Potential Causes of 19th-Century Glacier Advances in Coastal Alaska Based on Tree-Ring Dating and Historical Accounts. Front. Earth Sci. 7:82. doi: 10.3389/feart.2019.00082

INTRODUCTION

The Little Ice Age

The Little Ice Age (LIA) saw episodes of lowered temperatures from approximately CE 1250 to 1850, or, in some cases, to 1900 (Wiles et al., 2004; Barclay et al., 2009; Ahmed et al., 2013; Solomina et al., 2015; Anchukaitis et al., 2017). During the LIA, many Northern Hemisphere alpine glaciers advanced to their greatest Holocene extents (Solomina et al., 2015, 2016). These advances were partly a response to declining summer insolation over the last 8 ka of the Holocene (Berger and Loutre, 1991; Solomina et al., 2015). Contrary to what this millennial trend in orbital forcing

would predict, the Holocene glacier record is more complicated than a progressive buildup of glacial ice. Numerous glacier advances and retreats occurred during the Holocene (Solomina et al., 2015), and, within these millennial-scale events, there were also century- and decade-scale glacier fluctuations (Luckman, 1993; Grove, 2001; Wiles et al., 2004; Bräuning, 2006; Miller et al., 2012; Solomina et al., 2016). The cyclic and nested nature of the Holocene glacier record indicates that a complex of non-orbital climate forcing agents affected how glaciers responded to the overall long-term cooling imposed by Milankovitch forcing (i.e., Miller et al., 2012). A similar complex of interacting climate processes is expected to continue operating in the future and determine how glaciers respond to ongoing anthropogenic warming (Oerlemans and Fortuin, 1992; Bitz and Battisti, 1999; Marzeion et al., 2014). Analysis of paleo-records can identify processes that may be of key importance to glaciers both in the past and in our warmer future.

The Little Ice Age in the Gulf of Alaska Region

The Gulf of Alaska (GOA; **Figure 1**) serves as an interesting region in which to examine the relationships between LIA climate and glaciers. This is partly because its mild maritime climate allows forests to repeatedly regrow in the wake of retreating glaciers. When glaciers then readvance, it is possible to use dendrochronology to precisely date glacier-affected trees (Luckman, 1993; Wiles et al., 2008; Barclay et al., 2009; Coulthard et al., 2013). Overriding glaciers, aggrading outwash, proglacial lake-level changes, and moraine building can kill, tilt, and injure trees. These annually-dated archives can provide a precise record of glacial history (Coulthard and Smith, 2013).

Glacier history in the GOA region also provides a useful LIA case study because the climate there is known to be sensitive to volcanic events, solar variability, and North Pacific Decadal Variability (NPDV) (see Study Area section) (Mock et al., 1998; Anderson et al., 2005; Hartmann and Wendler, 2005; Luckman and Wilson, 2005; Wiles et al., 2014; Osterberg et al., 2017; Bailey et al., 2018; Gaglioti et al., in press). Previous studies involving a survey of 143 glaciers in Alaska (Wiles et al., 2004, 2008; Barclay et al., 2009) indicate that LIA advances occurred in three phases that were associated with minima of the De Vries Cycle of solar irradiance, with the most recent and in some cases most extensive advance associated with the Dalton Minimum (CE 1790–1830) (Bard et al., 1997; Wiles et al., 2004). Glacial chronologies in the GOA region constructed using dendrochronology offer a means for disentangling the interactions and relative strengths of these climate drivers.

Here we use dendrochronology to crossdate tree-ring samples collected from standing dead trees in an exceptionally well-preserved "ghost" forest buried by the outwash and ice of the advancing La Perouse Glacier in the Fairweather Range of the St. Elias Mountains in northern Southeast Alaska (**Figures 1**, **2**). We compare this new record with what is known about the timing of the LIA chronologies of nearby coastal glaciers (**Figure 1**), and then use newly available paleoclimate proxy data from other studies to infer which climate variables and forcing agents may have controlled LIA glacier fluctuations in this region.

STUDY AREA

Geography and Climate

The St. Elias Mountains of Southeast Alaska are the most heavily glaciated coastal mountains outside of Greenland and Antarctica. Peaks higher than 4000 m above sea level (asl) rise directly from tidewater, and these ranges intercept extra-tropical cyclonic storms, which are fueled by moisture evaporated from the Subtropical and mid-latitude Pacific Ocean (Rodionov et al., 2007). As a result, the climate along this coast is hyper-maritime, with a mean annual precipitation of 3.9 m at sea level in Yakutat, Alaska (**Figure 1a**), where mean July and January temperatures are 12.4 and −2.1°C, respectively (Arguez et al., 2012). Strong orographic effects cause even greater precipitation in the mountains and a pronounced rain shadow on the inland side of the range (Arguez et al., 2012).

Decadal variability in air and ocean temperatures and precipitation in the GOA region is largely controlled by shifting modes of NPDV (Wendler et al., 2016). Together, variations in the wintertime strength of the Aleutian Low pressure system (AL) and sea surface temperature anomalies (SSTAs) related to the Pacific Decadal Oscillation (PDO) comprise the dominant ocean-atmospheric modes of NPDV, and both are influenced by the El Niño Southern Oscillation (ENSO) (Newman et al., 2016). A strong AL/positive PDO regime is accompanied by winters with relatively low sea-level pressure and increased meridional flow in the atmosphere over the North Pacific, as well as enhanced storm intensity, increased precipitation, and warm SSTAs along the GOA coastline (Newman et al., 2016). Weak AL/negative PDO regimes are associated with the opposite wintertime patterns. The combination of decadal ENSO variations, seasonal changes in ocean-mixing depths (i.e., "re-emergence" of SSTAs), and poorly understood ocean to atmosphere feedbacks are thought to endow NPDV with its inter-annual autocorrelation (winter-to-winter memory) (Alexander and Deser, 1995; Newman et al., 2016). As a result, multi-decadal ocean-atmospheric regimes separated by abrupt state changes are salient features of the AL, PDO, and therefore the climate of coastal Alaska (Trenberth and Hurrell, 1994; Mantua and Hare, 2002; Hartmann and Wendler, 2005; Wendler et al., 2016).

Glaciers

The geo-climatic setting of the GOA coastal mountains nourishes ice caps and valley glaciers that extend down to sea level and cover about 18% of the GOA watershed (Neal et al., 2010). Mean equilibrium line altitudes on these glaciers are ∼900 m asl nearest the coast, rising to ∼2000 m asl 175 km inland (McGrath et al., 2017). Many coastal range glaciers terminate and calve icebergs into either tidewater bays or freshwater lakes (**Figure 1b**).

The La Perouse Glacier arises from the southern slopes of Mount Crillon (3200 m asl) and extends down to sea level (**Figure 1**). The La Perouse Glacier has been the only

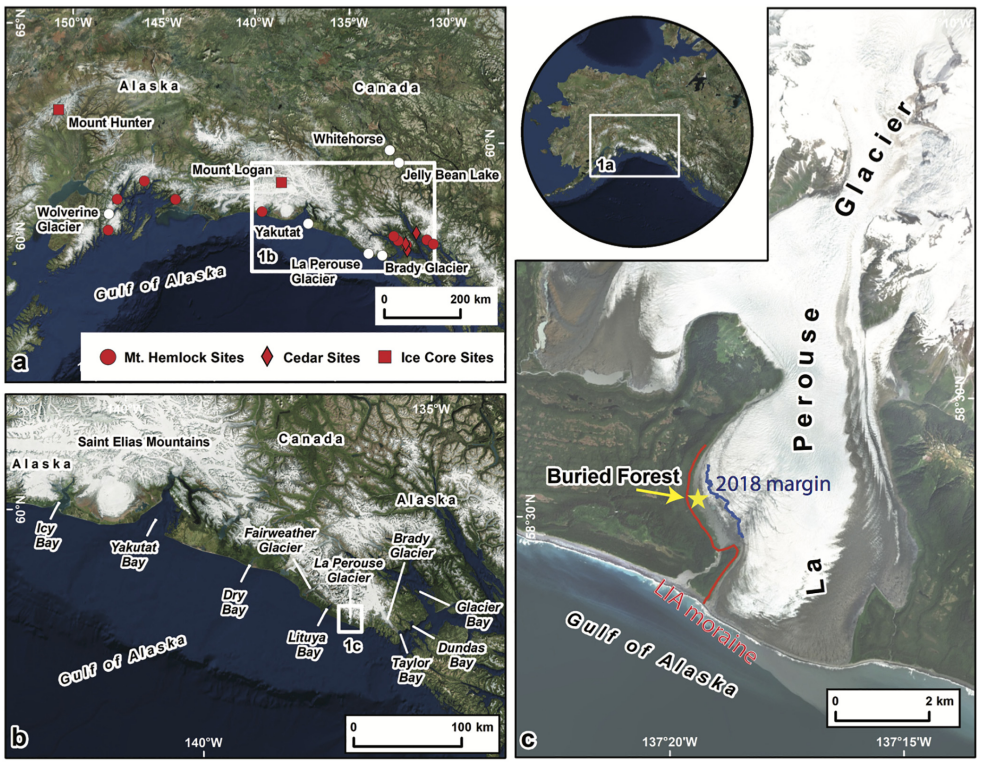

FIGURE 1 | Maps and aerial images of the study area. **(a)** Locations described in the text including sources of paleoclimate and tree-ring data. **(b)** Locations of glaciers described in the text. **(c)** Extent of La Perouse Glacier in 2010 (satellite imagery) with the location of the exhumed forest we crossdated (**Figure 2**), the Little Ice Age moraine, and field-surveyed ice margin in July of 2018.

glacier in the North Pacific region that in recent times has calved directly into the surf of the open ocean. When the La Perouse Glacier was in a retracted state, the valley morphometry indicates that it probably calved into a saltwater bay or a deep freshwater lake.

Of particular importance for the maritime glaciers in the GOA are shifts in the amount of winter precipitation they receive, which may modulate their sensitivity to variations in summer temperature. The Northeast Pacific experiences high-magnitude, decadal-scale shifts in winter precipitation patterns related to changes in the strength of the AL and phase of the PDO. For example, interannual variability in snowfall determined changes in the annual mass balance of the land-terminating Wolverine Glacier between 1967 and 1990 (**Figure 1**; Bitz and Battisti, 1999). Beginning in 1976, a shift toward a positive PDO and stronger AL – a synoptic pattern associated with increased winter precipitation in the GOA – caused an increased annual mass balance in Wolverine Glacier. Although this positive PDO and strong AL phase lasted until ca. 1998, its effects on glacier mass balance via increased winter snowfall were trumped in the early 1990s by warmer air temperatures that forced the Wolverine Glacier, and many other glaciers in the region, to retreat (Arendt et al., 2002). This mass balance deficit has accelerated in the last decade with the continued warming trends in the region (Van Beusekom et al., 2010), and lowered albedo from the eruption of Mount Redoubt in 2009 (Arendt et al., 2013). In the absence of this exceptional warming trend, the Wolverine Glacier may have continued to have a positive mass balance and possibly even advance in response to the increased snowfall associated with the 1976 regime shift. Shifts in winter snowfall may have been a key factor in controlling glacier fluctuations in the GOA region throughout the Holocene.

Vegetation

The coastlines bordering the GOA support temperate rainforest vegetation up to ∼1000 m asl. The species composition and age of these conifer-dominated, old-growth forests can provide insights into glacial and landscape history. Sitka spruce [*Picea sitchensis* (Bong.) Carr] and western hemlock [*Tsuga heterophylla* (Raf.) Sarg] are dominant at lower and middle elevations, while Alaska yellow cedar (*Callitropsis nootkatensis* D. Don) and shore pine (*Pinus contorta* subsp. *contorta* Douglas) typically grow at mid-elevation sites often in or bordering muskegs. Mountain hemlock [*Tsuga mertensiana* (Bong.) Carr] and Sitka spruce typically form the alpine treeline (Harris et al., 1974; Thompson et al., 2006).

In addition to altitude, the time-since-deglaciation or time-since-other disturbances (i.e., flooding, landslides, abrupt coastal uplift due to seismic events, or windthrow) affect the age and species composition of these forests. On recently disturbed terrain, forest succession proceeds from alder (*Alnus* spp.), to balsam poplar (*Populus trichocarpa* Torr. & A.Gray

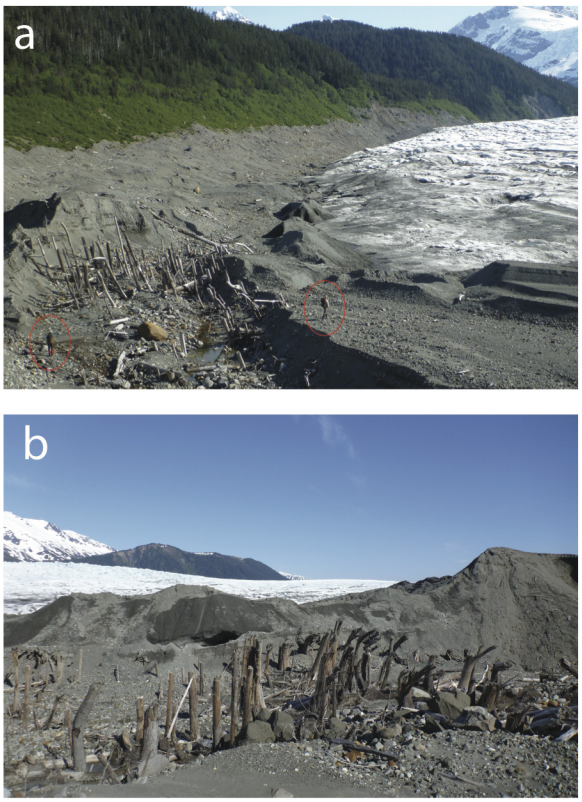

FIGURE 2 | (a) The La Perouse Glacier in retreat in 2016 exposing an *in situ* interstadial forest. Humans (circled) for scale. **(b)** These trees were covered by glacial outwash deposited as the glacier advanced. Tree trunks were sheared off by the glacier where they protruded above the protective outwash gravel. Note the flagged logs pointing in the direction of glacier flow.

ex. Hook.), to Sitka spruce, and eventually to western hemlock; a sequence that can take ∼300 years or more to complete (Chapin et al., 1994; Fastie, 1995). At lower elevation forests with moist soil conditions, large Alaska yellow cedar trees can co-dominate with hemlock and spruce beginning a few centuries after disturbance (Harris et al., 1974). The ring widths of long-lived yellow cedar, spruce, and hemlock trees can be sensitive to interannual variations in air temperatures, which facilitates the cross-dating of sub-fossil logs (Barclay et al., 1999; Beier et al., 2008; Wiles et al., 2012, 2014).

Historical Accounts

Following Vitus Bering's brief visit in 1741, a series of European expeditions explored the coast of the northeastern GOA in the 18th and 19th centuries. Of particular relevance are the observations and maps made by the scientific expeditions led by Jean-François de Galaup, Comte de Lapérouse in 1786, Allessandro Malaspina in 1791, and George Vancouver in 1794 (Fisher and Johnston, 1993; La Pérouse, 1994; Olson, 2002; Malaspina and David, 2003). La Perouse described and mapped the glaciers in the coastal St. Elias Mountains and Lituya Bay, the Malaspina expedition mapped and observed the coastline and glaciers in the ice-choked Yakutat Bay while searching in vain for the Northwest Passage, and Vancouver charted Cross Sound (**Figure 1**). Approximately a century after these first European explorers, the Harriman expedition (Gilbert, 1910; Burroughs and Muir, 1986), and the Boundary Commission of the United States and Canada provided observations and maps of glacier extent during the late 19th and earliest 20th century[1], including detailed observations of La Perouse Glacier. These early observations are summarized by Tebenkov (1850); Davidson (1904), and Tarr and Martin (1914) and allow us to compare the extents of glaciers in the late 18th century with their extents 100 and 200 years later.

MATERIALS AND METHODS

Field Sampling

While exploring the La Perouse forefield in May of 2016, we discovered an ancient forest recently exposed by the retreating margin of the glacier (**Figure 2**). We collected tree cores to determine when these trees began growing and when they died in order to infer the limiting ages of glacier retreat and advance. We identified the different tree genera based on bark characteristics, stem and branch habit, and wood aroma. Two tree cores (0.5 mm diameter) offset by 90° were collected from 50 of the recently exhumed trees within an area of 0.5 km^2. Radiocarbon (^{14}C) samples were collected from the bark of one tree to constrain the timing of tree death, and two other ^{14}C samples were collected from the base of buried soil organic horizons located 50 m from one another in order to provide minimum dates on the initiation of soil development following the penultimate glacier retreat. Radiocarbon samples were analyzed by accelerator mass spectrometry at Beta Analytic in Miami, Florida, and then calibrated to calendar years using the IntCal13 curve (Reimer et al., 2013).

Tree-Ring Measuring and Cross-Dating

Tree cores were sanded with progressively finer sand paper from 100 to 600 grit to reveal ring boundaries. Ring widths were measured either manually to 0.001 mm using a Velmex stage Quick Check counter and the program MeasureJ2X, or digitally using high-resolution scans uploaded to the computer program CooRecorder 8.1. Ring-width series were visually and statistically cross-dated using standard dendrochronological techniques (Holmes, 1983; Stokes and Smiley, 1996).

We developed two ring-width chronologies from the exhumed forest at the La Perouse Glacier. One is based entirely on Alaska yellow cedar, and the other on western hemlock and Sitka spruce (hereafter "hemlock–spruce"). The individual tree-ring series from the buried forest were cross-dated with previously measured, calendar-dated chronologies from the GOA region (**Figure 1**; Wiles et al., 2012, 2014) and visually checked for shared marker years using skeleton plots generated by the dplr package in Rstudio (Bunn, 2008).

[1] internationalboundarycommission.org/en/about.php

TABLE 1 | Radiocarbon dates reported in the text.

Lab number	Sample name	Dated material	$\delta^{13}C$ (‰)	$\delta^{13}C$ normalized age and error	2σ calibrated age range (AD)	
					Lower 95% limit	Lower 95% limit
Beta-439170	14-May 2016 C	Basal peat of soil	-26.4	1740 ± 30	235	385
Beta-498378	2-June 2018 A	Basal peat of soil	-25.5	550 ± 30	1310	1435
Beta-439171	14-May 2016 G	Bark of hemlock	-22.1	310 ± 30	1485	1650

Cross-dated individual series were combined to develop master, calendar-dated chronologies based on the mean, standardized ring-width of all tree-ring series following detrending using a 32 year high-pass spline filter (Holmes, 1983). Correlations between the newly dated La Perouse cedar and hemlock–spruce chronologies and master chronologies from elsewhere in the GOA region (Wiles et al., 2012, 2014) were calculated using the COFECHA program (Holmes, 1983). We also compared the La Perouse chronologies with a ring-width chronology derived from trees killed by the rising waters of an ice-dammed lake along the margin of the Brady Glacier, 36 km to southeast of the La Perouse exhumed forest (**Figure 1**; Capps et al., 2011).

RESULTS AND INTERPRETATION

Field Observations and ^{14}C Ages

Hundreds of *in situ* dead trees have been exhumed from kame-terrace gravels over the last decade by an ice-marginal stream adjacent to the retreating margin of the La Perouse Glacier (**Figures 1**, **2**). This exhumed forest is devoid of living plant tissue but exquisitely well-preserved, probably due to its rapid burial by sand and gravel, which then shielded it from the overriding glacial ice. The exhumed forest contains trees that retained bark and delicate branches, tree saplings, and shrubs, many of which are still rooted in moss-covered soils (**Figure 2**). Forest composition (and basal area percentage) of a 30 × 30 m, representative plot is 53% (60%) Alaska yellow cedar, 46% (39%) western hemlock (cf.), and 1% (1%) Sitka spruce.

The exhumed trees are uniformly bent and sheared off 5–10 m above their root crowns, leaving flags of shattered wood oriented westward in the direction of glacier flow (**Figure 2**). No adventitious roots were found on hemlock or spruce stems, which can occur in these taxa when they are rooted in a gradually aggrading surface (Zobel and Antos, 1982). This suggests that none of these exhumed trees survived initial burial.

The ^{14}C age on the outermost bark of a western hemlock tree had a 95% calibrated age range of CE 1485–1650 (**Table 1**). The two ^{14}C ages from the lowermost peat in two different profiles of organic soil horizons had 95% calibrated age ranges of CE 235–385 and CE 1310–1435 (**Table 1**). The younger date is likely the minimum-limiting age for the penultimate retreat of the La Perouse Glacier, after which the exhumed forest began growth. The older date probably represents an older, inter-stadial soil that was covered in till and is now exposed below the forest soil.

Tree-Ring Analyses

The floating ring-width chronologies from the exhumed forest consist of 49 individual ring-width time series from 30 trees (31 series from 20 hemlock–spruce trees and 18 series from 10 cedar trees) (**Figure 3**). The inter-series correlations within the cedar and hemlock–spruce chronologies are 0.43 and 0.39, respectively (**Figure 3**). After shifting the floating cedar chronology in order to obtain peak correlations with the calendar-dated cedar chronologies based on living trees (Wiles et al., 2012, 2014), correlation values are 0.41 for both the 200- and 300-year windows over which the two chronologies overlap. Peak hemlock–spruce correlations between the calendar-dated, living-tree chronology and the floating, exhumed-forest chronology are 0.49 and 0.44 for 200- and 300-year time windows, respectively (**Figure 3**). After anchoring the floating chronologies to calendar years, the cross-dated chronologies from exhumed trees span the calendar years CE 1451–1866 and CE 1206–1864 for cedar and hemlock–spruce, respectively (**Figure 4**). The oldest cross-dated hemlock and cedar rings are CE 1206 and CE 1451, respectively, and at least several centuries of post-glacial forest succession is typically required in Southeast Alaska for this forest type to assemble itself (Harris et al., 1974).

In summary, the earliest calendar-dated ring (CE 1206) represents the earliest date of forest establishment at this site, and indicates the minimum-limiting age for the penultimate retreat of the La Perouse Glacier, after which the exhumed forest began growth. As indicated by the assigned calendar age on the outermost rings, 20 of the 30 cross-dated trees died when glacial outwash buried them between CE 1850 and 1866 (**Figure 4**). Earlier outer-ring ages are probably the result of abraded outer rings and/or tree death prior to burial.

Recent History of the La Perouse Glacier

"A landing was made near the west end of the La Perouse ice-wall to examine a forest, part of which had been overwhelmed by an advance of the glacier. . ." –excerpt of John Muir's journal from the Harriman Expedition, 1899 (Burroughs and Muir, 1986; Gilbert, 1910).

Accounts by the Harriman expedition in CE 1899 (Gilbert, 1910; Burroughs and Muir, 1986) indicate that the La Perouse Glacier stood at its LIA moraine in 1895 (as relayed to Gilbert by members of the US Fish Commission that visited the site that summer), and had retreated about 100 m by 1899 (Gilbert, 1910). The scientists who visited the La Perouse Glacier terminus in 1899 observed trees near this moraine that had been overrun by the advancing ice about a kilometer

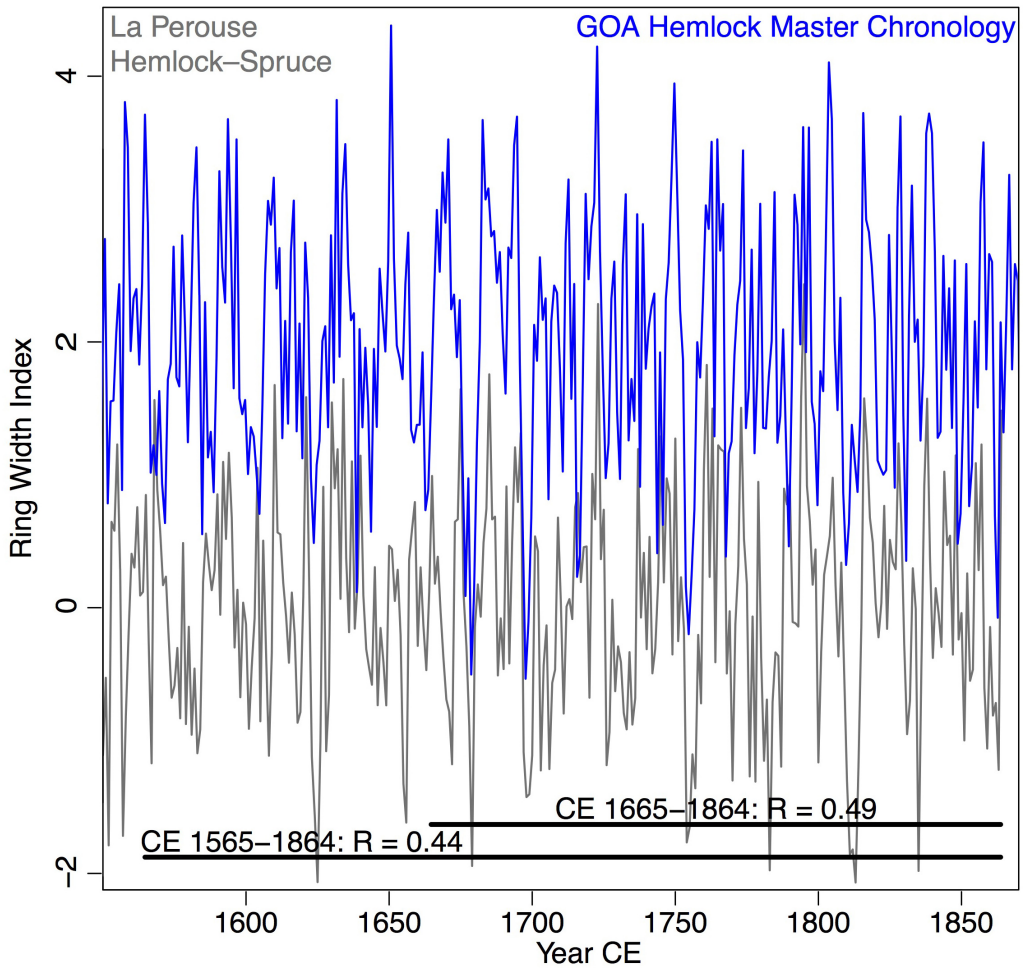

FIGURE 3 | Master ring-width chronology of the La Perouse western hemlock and Sitka spruce trees (gray; bottom) compared with the master chronology of living hemlock and spruce (blue; top) from the Gulf of Alaska region (Wiles et al., 2014; see locations in **Figure 1**).

south of our sampling location (see John Muir's quote above). The oldest pith ages we obtained from ten Sitka spruce trees growing on the crest of this LIA moraine date to CE 1922 (**Figure 4**) (n = 10, pith ages range from CE 1922 to 1937). Establishment of spruce in this recently deglaciated location (i.e., the ecesis age) was likely to take only a few years because spruce seed sources were located adjacent to the moraine. In support of this inference, we have observed spruce seedlings colonizing the La Perouse foreland gravels in areas that were glaciated 5–10 years prior. Several, rapid glacier fluctuations have occurred since 1899, including short-lived re-advances around CE 1910 (Tarr and Martin, 1914) and CE 1949 (Seitz, 1953), but the glacier has mostly been in retreat for the last several decades.

In summary, after being in a retracted state (relative to its 2016 position) since at least CE 1206, based on the cross-dated tree-ring chronology, the La Perouse Glacier was advancing to near its 2016 position between 1850 and 1866 (based on the outer rings of most trees sampled from the buried forest). The glacier reached its LIA maximum position ca. CE 1895, had retreated by 1899, and then had re-advanced to near its LIA moraine in CE 1910. Sometime between CE 1910 and 1922 (based on pith ages of spruce colonizing the LIA moraine), the glacier began a major retreat, and subsequent fluctuations never caused the ice margin to reach the LIA moraine again (**Table 1** and **Figure 4**).

A Brief Review of the Chronology of LIA Glaciation Along the GOA Coastline Between Icy Bay and Icy Strait

Paleoclimate Relevance of La Perouse Glacier

Our dendrochronology-based limiting ages on the advances and retreats of the La Perouse Glacier add new data to the regional LIA glacier record from the northeastern GOA (Wiles et al., 2008). But what do these glacier fluctuations signify in terms of paleoclimate? It is possible that these recent fluctuations of the La Perouse Glacier were driven by internal glacier dynamics rather than climate (Van der Veen, 2013). For example, if the glacier had retreated up its fjord to a point where it terminated on land, a subsequent advance could have occurred regardless of climate.

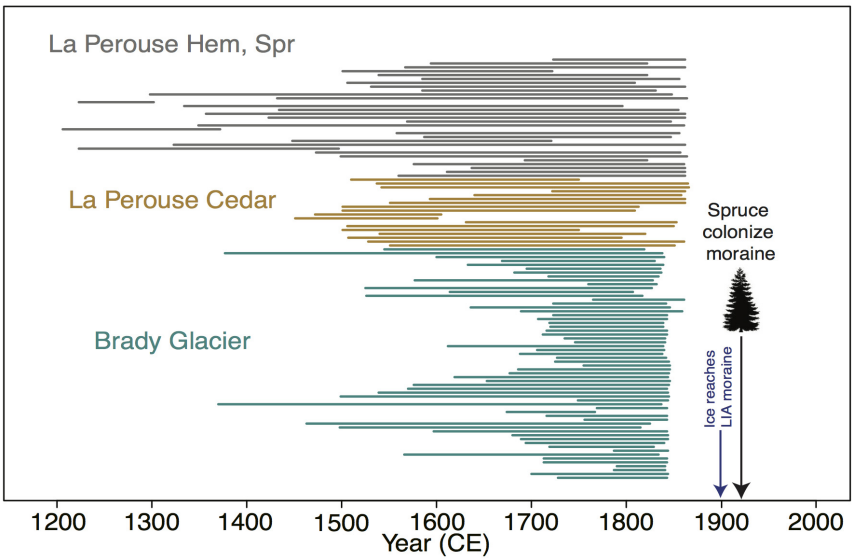

FIGURE 4 | Segment plot of crossdated tree-ring series from the exhumed forest at the La Perouse Glacier and from the nearby Brady Glacier (**Figure 1**; Capps et al., 2011). The calendar ages of the outer rings correspond to the approach of the La Perouse Glacier and its ice-marginal outwash stream. The trees died after being buried by outwash gravel. Also noted are when the La Perouse Glacier reached its LIA moraine in 1895 as related to the Harriman Expedition by the US Fish Commission (Burroughs and Muir, 1986), and the earliest age of spruce that colonized that moraine indicating glacier retreat.

Such "compensatory re-advances" occur when calving ablation ceases after a fjord glacier retreats onto land (Mann, 1986). In the aftermath of a catastrophic calving retreat, this situation can result in extremely positive mass balance, which can then cause the terminus to advance, provided a terminal moraine shoal is accumulating in front of the glacier to protect it from iceberg calving (Mann, 1986; Post et al., 2011). A non-climatically driven scenario like this is the null hypothesis when seeking linkages between climate and the fluctuations of glaciers like La Perouse that at times had calving fronts.

One way to test for climate's role in controlling the LIA fluctuations of the La Perouse Glacier is to compare its history to that of nearby glaciers, including some that began the 1800s at different stages in their calving-glacier cycles, and also to nearby land-terminating glaciers. Finding synchronized glacier advances throughout the GOA region in the 1800s would indicate these changes were indeed climatically driven. Because we are surveying the behavior of different glaciers on the century scale (1790–1900), the variability of glacier response times on shorter time scales should have relatively minor effects for these high-throughput and relatively small glaciers whose response times to climate are on the order of several decades (Oerlemans and Fortuin, 1992). Below we review historical observations and tree-ring dating that constrain the fluctuations of other glaciers draining the St. Elias Mountains during the time when the La Perouse Glacier was advancing to its LIA maximum position.

Icy Bay

The most recent and extensive LIA advance in Icy Bay was underway in the CE 1640s, and had filled most of the inner bay up to Kichyatt Point by the time Vancouver and Malaspina arrived in the CE 1790s ("KP" in **Figure 5a**; Barclay et al., 2006). By CE 1837 when Edward Belcher visited the area (Belcher, 1843; Davidson, 1904), the outer portion of Icy Bay was largely filled by glacier ice. Corroborating the oral tradition of local Native people (Topham, 1889), Barclay et al. (2006) suggest this ∼50 years advance was one of the fastest ice expansions ever recorded for a tidewater glacier, and that it was probably assisted by shallow shoals in outer Icy Bay that reduced ablation from the glacier's iceberg-calving terminus. Belcher (1843) describes the Icy Bay glacier terminus in CE 1837 as a 9-m-high ice cliff located near the present mouth of the bay. Between CE 1837 and 1886, the glacier advanced even further seaward, covering Point Riou ("PR" in **Figure 5a**) and forming a piedmont lobe that calved into the open sea (Barclay et al., 2006). Several minor retreats occurred within this period, and the glacier filling Icy Bay probably reached its maximum extent sometime between CE 1886 and 1904 (Post and Plfaker, unpublished). Recession from the late LIA maximum began between CE 1904 and 1910 (Tarr and Martin, 1914) and has continued with great rapidity up to the present day (**Figure 5a**).

Malaspina Glacier

This glacier is now near its maximum Holocene extent, which means that most evidences of its former fluctuations are concealed beneath it (Though see next section). In general, the Malaspina Glacier (**Figures 5a,b**) has maintained this extended position since at least CE 1786 when first seen by the La Perouse expedition (La Pérouse, 1994). Minor advances and retreats have occurred within the historical period (Topham, 1889; Russell, 1893; Tarr and Martin, 1914). For example, Tebenkov (1850) compiled maps of the coastline bordering the Malaspina Glacier based on the reports and charts of Russian explorers who visited the area between 1788 and 1807. Even though the Malaspina ice front was generally described as being near where it is today,

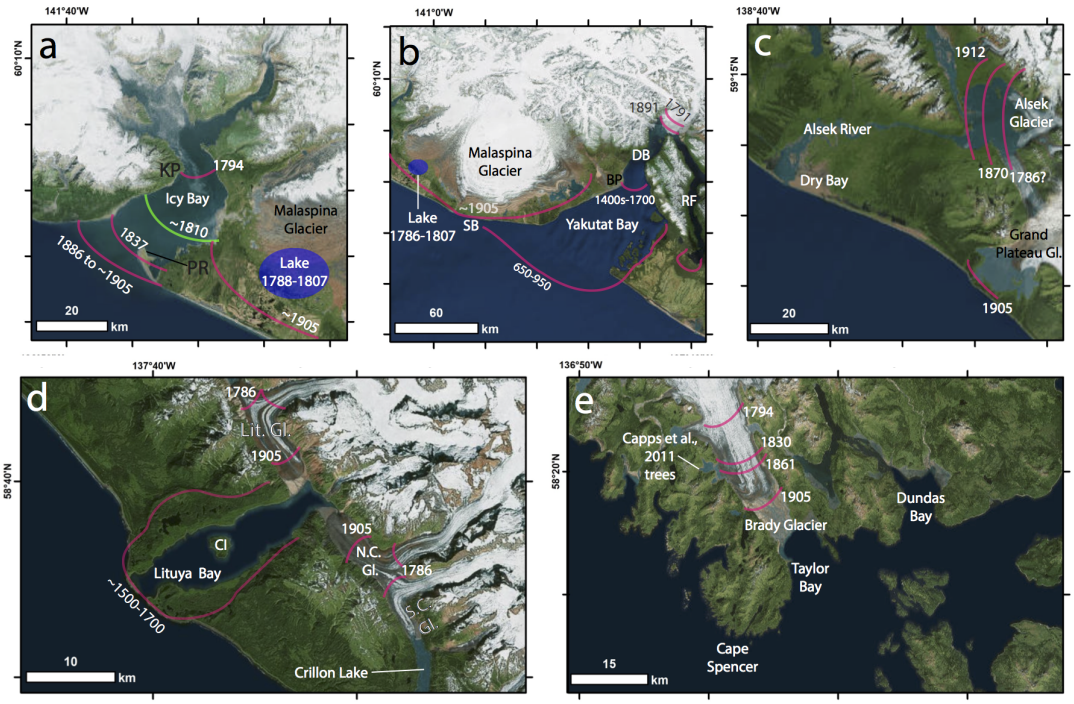

FIGURE 5 | Maps of individual bays and glaciers discussed in the text showing LIA termini positions). **(a)** Icy Bay: Kichyatt Point (KP), Point Riou (PR). **(b)** Malaspina Glacier: Yakutat Bay, Disenchantment Bay (DB), Russel Fjord (RF), Blizhni Point (BP). **(c)** Dry Bay, Alsek River mouth, and Grand Plateau Glacier. **(d)** Lituya Bay: Cenotaph Island (CI), Lituya Glacier (Lit. Gl.), North Crillon Glacier (N.C. Gl.), and South Crillon Glacier (S.C. Gl.), Crillon Lake. **(e)** Cape Spencer region: Brady Glacier, Dundas Bay. Glacier Bay is located immediately to the east of this map.

these early maps show a forested foreland and a ~60 km^2 lake on the southwest side of the glacier terminus just east of Icy Bay (**Figures 5a,b**). Maps drawn by the Boundary Commission in 1905 indicate the Malaspina's ice margin advanced over the site of this lake sometime between 1807 and 1912. Consistent with this is the suggestion by Post and Plafker (unpublished) that an advance of 5–10 km occurred in the vicinity of Sitkagi Bluffs ("SB" in **Figure 5b**) sometime between 1794 and the present. In summary, after reaching its current extended position sometime prior to 1786, the Malaspina Glacier has experienced a series of minor advances and retreats with a significant advance at least along a portion of its wide perimeter during the 1800s.

Glacier Systems in Yakutat Bay, Disenchantment Bay, and Russell Fjord

Conifer trees buried by outwash and till near the mouth of Disenchantment Bay ("DB" in **Figure 5b**) suggest the most recent advance of the Hubbard Glacier was underway prior to ca. CE 250 (Barclay et al., 2001). This advance – probably representing coeval advances by both the Malaspina and Hubbard Glaciers – reached its maximum extent at the mouth of Yakutat Bay (**Figure 5b**), where its calving terminus deposited an arcuate shoal across the fjord mouth. Though fluctuations in position undoubtedly occurred over the intervening time span, the Hubbard/Malaspina Glacier terminated near the mouth of Yakutat Bay between CE 650 and 950 based on a ^{14}C date of 830 ± 160 years before present on detrital wood from the terminal moraine (Plafker and Miller, 1957).

Retreat from this most recent LIA maximum was underway by CE 1300, based on the age of a tree growing in outer Yakutat Bay and the ^{14}C ages of basal organics in kettle ponds there (Barclay et al., 2001), as well as the ca. 700 years old spruce trees growing on outwash trains associated with the LIA moraine near the village of Yakutat (Post and Plafker, unpublished; Barclay et al., 2001). Tree ages further up Yakutat Bay indicate that by CE 1460 the Hubbard Glacier had retreated some 40 km (Barclay et al., 2001). Archeological sites in outer Yakutat Bay date between CE 1040 and 1640 and are consistent with this area being deglaciated during this period (Crowell, 2018, written communication). A prominent but un-dated submarine moraine off Blizhni Point 40 km up-fjord from the mouth of Yakutat Bay may record a readvance of the Hubbard Glacier occurring sometime between CE 1400 and the early 1700s ("BP" in **Figure 5b**). By CE 1791 when it was observed by Malaspina, the Hubbard Glacier had retreated into inner Disenchantment Bay (Tarr and Martin, 1914) and was probably less extensive than it was when Russell charted the Bay in 1891 (**Figure 5b**; Barclay et al., 2001). Since at least CE 1891 (Russell, 1893), the Hubbard Glacier has been engaged in a fluctuating advance, which given this glacier's highly positive mass balance, probably represents the compensatory readvance of a calving-glacier cycle (Post and Motyka, 1995). Both Post and Plafker (unpublished) and Barclay et al. (2001) recognized that the Hubbard Glacier has been caught up in a

calving-glacier cycle and that its recent fluctuations are largely decoupled from climate.

In contrast to Yakutat Bay, the glacier occupying Russell Fjord ("RF" **Figure 5b**) began a slow advance perhaps as early as 3000 calibrated ^{14}C years before present (cal yr BP), reached its late-LIA maximum in the early CE 1600s, and remained in an advanced position until beginning to retreat sometime before CE 1752, which is several centuries after the calving retreat of the Hubbard Glacier into upper Disenchantment Bay (Barclay et al., 2001). The Russell Fjord Glacier was more protected from iceberg calving than the Hubbard Glacier, so its fluctuations have probably been driven mainly by climate (Barclay et al., 2001).

Dry Bay – Alsek Glacier

La Perouse sailed past Dry Bay (**Figures 1**, **5c**) in the summer of CE 1786 (La Pérouse, 1994), but the currents at the mouth of Dry Bay were too swift to allow entry. No glaciers were sighted by his expedition in the upper reaches of Dry Bay (the lower Alsek River valley), even though his cartographers were acutely observant about noting glacier positions. They did record the presence of a large lake in Dry Bay that has since filled with alluvium (US Boundary Commission, 1905). Edward Glace, the first known European to descend the Alsek River in CE 1870, observed the terminus of the Alsek glacier advancing from a side valley 20 km upstream from the coast (Davidson, 1904). This glacier was probably missed by La Perouse because it was in a retracted position when he was there a century earlier. It seems likely that the Alsek Glacier made a significant, land-terminating advance between La Perouse's visit in CE 1786 and 1870, when it was sighted by Glace.

Grand Plateau Glacier and Fairweather Glacier

Located 30 km southeast of Dry Bay, the Grand Plateau Glacier is partly confluent with glaciers flowing into the head of Dry Bay (**Figure 5c**). In maps made by the Boundary Commission Survey in CE 1905 (US Boundary Commission, 1905), this glacier terminates along a prominent moraine bordering the present coastline, and today a large lake occupies the former lower reaches of the glacier. It is likely that the Grand Plateau Glacier was advancing during the 19th century. This is because it was not noted by 18th century explorers, but was mapped as being near the coast at its LIA max position by the Boundary Commission in CE 1905.

Like the Grand Plateau Glacier, the Fairweather Glacier (not shown) is now separated from the open sea by a massive terminal moraine probably constructed during multiple Holocene advances that repeatedly halted at the coast because of rapidly increasing ablation in the open sea. Both Vancouver's map made in CE 1794 (Vancouver, 1799) and the Geodetic Survey's map made in CE 1900 (Davidson, 1904) show a large lake within the terminal moraine of Fairweather Glacier. The presence of this lake in CE 1794 suggests the LIA maximum extent of this glacier was reached sometime before that date. This lake has increased slightly in size over the past several decades. This trend, along with an accumulation area ratio indicating it is roughly in equilibrium with present climate (Mann, 1986), suggest that the Fairweather Glacier is currently retreating in response to recent climate warming.

The Lituya Bay Glacier System

During the LIA, Lituya Bay was filled by a glacier that terminated along a massive, composite moraine bordering the open GOA (**Figure 5d**). This most recent advance began ca. CE 500 and culminated sometime between CE 1500 and 1700 (Mann and Ugolini, 1985). La Perouse's cartographers made a detailed survey of the glaciers draining into Lituya Bay during the expedition's ill-fated visit in July of CE 1786 when 12 men drowned after a dory capsized in rough seas in the outer portion of the Bay (La Pérouse, 1994; an event later commemorated with the naming of Cenotaph Island; "CI" in **Figure 5d**). The La Perouse map shows that the two glaciers now flowing into the head of the bay had retracted far enough to separate into four separate termini, all of which terminated on land. Between CE 1786 and ca. 1905 (**Figure 5d**), these four glaciers re-advanced ∼5 km and coalesced. Their advances continue today at slow rates seemingly dependent on construction of moraine shoals in deep water at the fjord head. The accumulation-area ratios of the present glaciers suggest they are now far out of equilibrium with climate and are engaged in the compensatory re-advance limbs of calving glacier cycles (Mann, 1986). Because the North Crillon Glacier ("N.C. Gl." In **Figure 5d**) in the south arm of Lituya Bay was advancing during the 19th century, it is likely that its southern lobe (South Crillon Glacier; "S.C. Gl." in **Figure 5d**) was advancing into Crillon Lake at the same time (**Figure 5d**).

La Perouse Glacier and Finger Glacier

In support of our tree-ring dates from La Perouse Glacier, Tebenkov's charts do not show the termini of either the La Perouse (**Figure 1**) or Finger Glacier (just southeast of La Perouse Glacier; not shown) near the coast in the late 18th and early 19th centuries (Tebenkov, 1850; Davidson, 1904). However, this assumes that every visible glacier was recorded on these charts. We now know the La Perouse Glacier, which advanced over the exhumed forest between 1850 and 1866, was encountered by the US Fish Commission group in 1895 at its LIA max position, and then observed by John Muir and John Burroughs within ∼100 m of its 1895 terminus in 1899. Similarly, Finger Glacier was not noticed by any 18th century explorers, but was observed by the US Boundary Commission at its LIA max moraine near the present coastline in 1905. Like the La Perouse Glacier, the Finger Glacier probably reached its LIA maximum in the late 1800s.

Brady Glacier and Taylor Bay

"Some of the Taylor Bay and Prince William Sound forests have been destroyed in the same way [as those at the La Perouse Glacier]. Whether simultaneously or not, I am unable to say." –John Muir in 1899, describing the forests being overtaken by the La Perouse Glacier (Burroughs and Muir, 1986).

Vancouver visited Cross Sound in CE 1794, and his cartographers recorded the position of the Brady Glacier's terminus, which they estimated was ∼24 km north of Cape Spencer, putting its terminus ∼8 km further up Taylor Bay than it is today (Davidson, 1904). On the Boundary Commission

maps drawn ca. 1905, the Brady Glacier is estimated to have been ∼17 km north of Cape Spencer, which indicates that the glacier advanced ∼7 km during the 19th century. These historical observations are consistent with the tree-ring dating of lake-level rise in an ice-marginal lake basin that is adjacent to the Brady Glacier (**Figures 1**, **4**, **5e**) where Capps et al. (2011) estimate the Brady Glacier advanced several kilometers between 1830 and 1860. To answer John Muir's question above, the advance at Brady Glacier probably occurred at the same time the La Perouse Glacier was advancing in the mid- to late-19th century (**Figure 4**).

Glacier Bay

The LIA chronology of Glacier Bay is the best known of any glacier system in the region (Mann and Streveler, 2008; Connor et al., 2009). The maximum LIA advance of the Glacier Bay Glacier began ca. CE 300 (Goodwin, 1988). The glacier's rate of advance down the bay was probably constrained by the slow accumulation of the massive moraine shoal required to anchor its terminus in the face of tidewater calving. By CE 1500, the terminus lay in the middle reaches of Glacier Bay, and by CE 1750 it had reached its maximum extent protruding into Icy Strait. In this position, the terminus and its moraine shoal were exposed to strong tidal currents and heavy wave attack, which may have triggered a retreat off the terminal moraine shoal shortly before Vancouver's expedition observed the terminus in CE 1794 (Lamb, 2017). By that year, the terminus had retreated some 15 km behind its LIA limit, and a rapid retreat ensued by ca. 1800 that caused a catastrophic calving retreat of 120 km in less than 160 years (McKenzie and Goldthwait, 1971; Larsen et al., 2005).

Synthesis

Widespread advances of coastal glaciers occurred along the northeastern coastline of the GOA during the 19th century. Between CE 1790 and 1900, eight of the 12 glacier systems discussed here were either expanding toward their LIA maximum positions or were already there and maintaining those positions (Icy Bay glacier system, Malaspina, Dry Bay–Alsek glacier system, Grand Plateau Glacier, Lituya Bay glacier system, La Perouse Glacier, Finger Glacier, and Brady Glacier). Since CE 1900, the Icy Bay glacier system and the La Perouse Glacier have retreated – radically in the case of the calving Icy Bay glacier system, and modestly in the case of the land-terminating La Perouse Glacier. Three glaciers experienced rapid calving retreats back to their fjord heads prior to CE 1780 (Hubbard Glacier after CE 1300; the Lituya Bay glacier system after CE 1500; and the Glacier Bay system after CE 1760). The geometry and bathymetry of these three fjords, their exposure to tidewater, and their present strongly positive mass balances suggest their recent dynamics have been dominated by calving glacier cycles, which has reduced the influence of climate on their advances and retreats. Overall, the 19th century seems to have been a time of widespread positive mass balance for those coastal glaciers not caught within calving glacier cycles.

Glacier advances during the 19th century were also widespread among non-tidewater glaciers in the GOA region (**Figure 6**). In a survey of 75 of the most recent LIA moraines in the mountains of coastal Alaska, around 60% were being built between CE 1775 and 1900, many of which represent their maximum positions for the LIA and Holocene (Wiles et al., 2004, 2008). This broad synchronicity between land-terminating and tidewater glaciers suggests that climate, rather than idiosyncratic glaciological factors relating to the calving glacier cycle, was the probably the main driver of 19th-century glacier advances along the northeastern GOA.

DISCUSSION

The Timing of the Little Ice Age in Coastal Alaska Compared to Other Regions

The 19th-century maximum LIA advance of the La Perouse Glacier is similar to that of other glaciers in the northeastern Pacific region (Wiles et al., 2004, 2008), but differs markedly from LIA glacier records from the Alps, Scandanavia, Iceland, and Greenland (Solomina et al., 2016). In these North Atlantic regions, most glaciers reached maximum LIA extents earlier during the LIA and either re-advanced or remained in advanced positions until ca. CE 1850 (Grove, 2001). More similar to the GOA record are those from the western interior region of Canada and from the Pacific Northwest, where most glaciers reached their LIA maxima in the early 18th century, and several others reached their LIA maxima in the mid-19th century (Burbank, 1981; Heikkinen, 1984; Luckman, 1993; Luckman, 2000; Larocque and Smith, 2003; Lewis and Smith, 2004; Allen and Smith, 2007; Jackson et al., 2008; Menounos et al., 2009; Koch et al., 2011; Koehler and Smith, 2011; Coulthard et al., 2013). These differing geographic patterns suggest that the global causes of the LIA were strongly modified by idiosyncrasies involving glaciological responses to regional climate processes.

Possible Climatic Causes of 19th-Century Glacier Advances in the GOA Region

Although the GOA glacier record involves both calving and non-calving glaciers, the fact they are relatively small, warm-based glaciers with large mass balances suggests their lag times in response to climate are on the time scale of several decades (Bahr et al., 1998). Thus we can use regional climate records from the period CE 1790 to 1900 to infer the identity of climate drivers of glacier fluctuations during this same period. Summer cooling caused by the combination of Milankovitch forcing and solar minima associated with the De Vries Cycle have been important drivers of the LIA glacier record in Alaska (Wiles et al., 2004, 2008). Thus three periods of increased glacier activity in Alaska followed the Spörer, Maunder, and Dalton Minima (**Figure 6**). Glaciers in the hypermaritime region of coastal Alaska may be particularly sensitive to solar-affected air temperatures because of the effects that temperature has on both the length and the warmth of the ablation season within the relatively mild climate in this maritime setting (Oerlemans and Fortuin, 1992; Oerlemans, 2005).

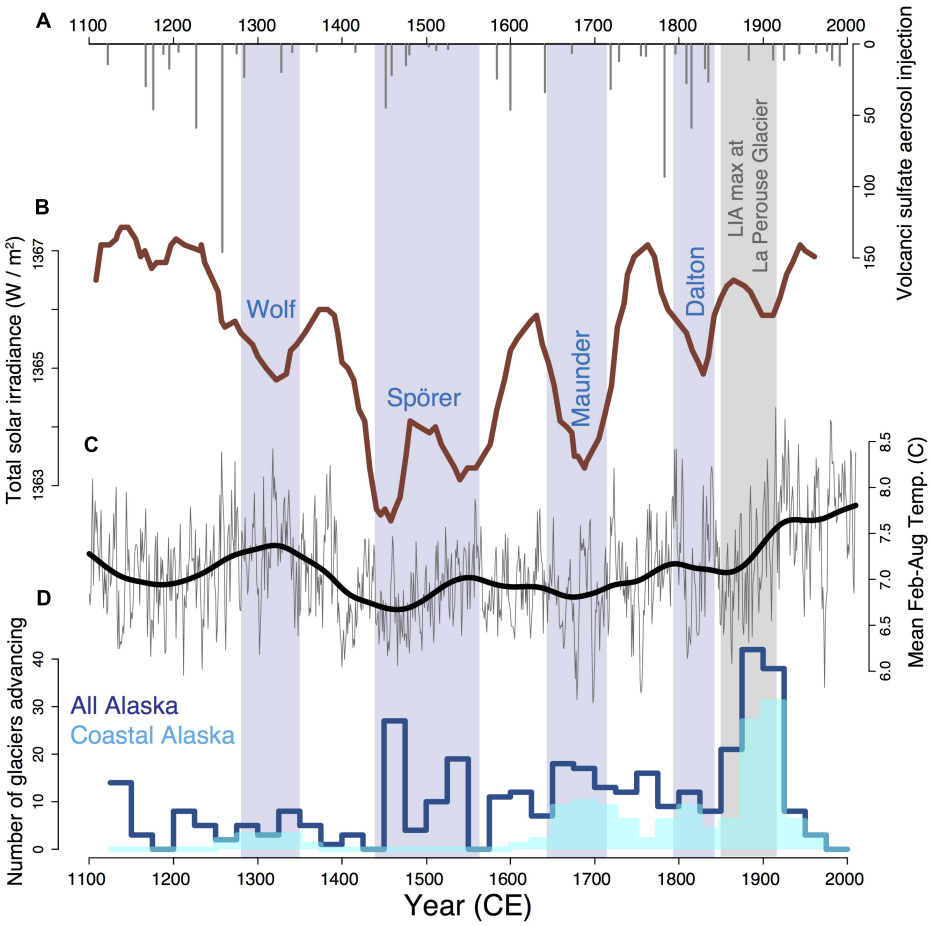

FIGURE 6 | Climate forcing agents, and regional paleoclimate records in the Gulf of Alaska region during the Little Ice Age (LIA). **(A)** Volcanic forcing (Gao et al., 2008). **(B)** Solar activity with solar minima labeled (Bard et al., 2000). **(C)** Reconstructed mean February to August temperature (Wiles et al., 2014). **(D)** LIA glacier moraine record for all of Alaska (dark blue) and south-coastal Alaska (turquoise) (Wiles et al., 2004) including the La Perouse Glacier's maximum advance highlighted in gray. Note that most of the Coastal Alaska glaciers advanced shortly after the Dalton Minimum, which was relatively minor in terms of solar forcing and summertime cooling.

Despite the general pattern of glaciers advancing in response to the cooling caused by orbital forcing and solar minima, it remains unresolved why the frequency and extent of LIA glacier advances along the GOA coastline do not correspond with the length and intensity of solar minima. For example, the most prominent, and, in many cases, the most extensive LIA glacier advances occurred during the 19th century (Wiles et al., 2008), even though these advances were preceded by the shortest and least intense solar minima of the entire LIA (the Dalton Minimum, CE 1790–1840) (**Figure 6**). Although the Dalton Minimum was relatively cool based on the tree-ring-based reconstruction of February-August air temperatures (**Figure 6**; Wiles et al., 2014), it seems unlikely that the climate during this 50-year period alone could have caused widespread glacier advances that surpassed previous LIA advances and, in many cases, persisted into the 1920s (**Figure 6**; Wiles et al., 2004). Overall, the period from CE 1790 to 1900 in the GOA did not see exceptionally cold Feb-Aug temperatures compared to the rest of the LIA (**Figure 7**). Furthermore, the 19th century advances of the La Perouse Glacier and other glaciers in the region followed a slight multi-century warming trend in mean Feb-Aug temperatures that began ca. CE 1750 (**Figure 6**). It therefore seems unlikely that cooler summer temperatures alone account for the relatively late LIA advances that dominate the glacier record along the northeastern GOA coastline.

If the 19th century was *not* the coldest part of the LIA in the GOA region, why did so many glaciers reach their LIA maxima then? One possibility is that increased winter precipitation was a key factor, and that these anomalously late LIA maxima owe their occurrence to the combination of Milankovitch forcing, the Dalton Minimum, enhanced volcanic activity, and increased snow accumulation. This same climatic scenario was first considered and rejected by Tarr and Martin (1914), and proposed again by Miller (1958) and Wiles and Calkin (1994). New paleoclimate data from several sources now allows us to evaluate this hypothesis.

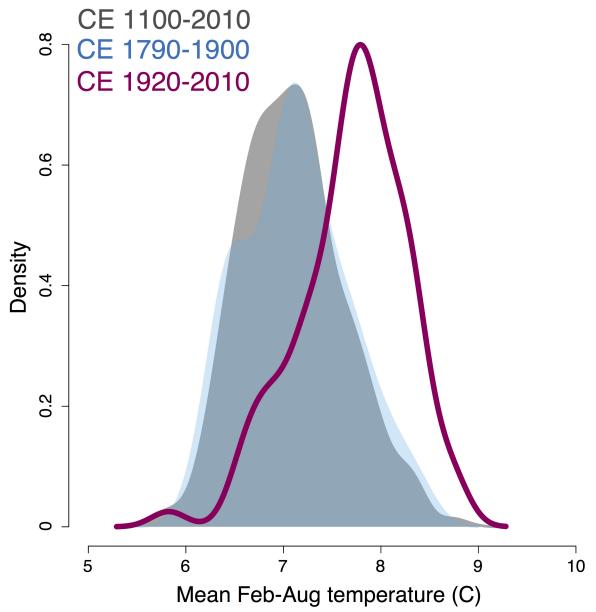

FIGURE 7 | Distribution of mean February to August temperatures based on tree-ring-width reconstructions (Wiles et al., 2014) for all years from CE 1100 to 2010, years when most coastal glaciers were advancing (CE 1790–1900), and years when most coastal glaciers were retreating (1920–2010). These data suggest that warm summers caused widespread glacier retreat after 1920, however, February to August temperatures are not exceptionally cold during the widespread advance observed during the 19th century.

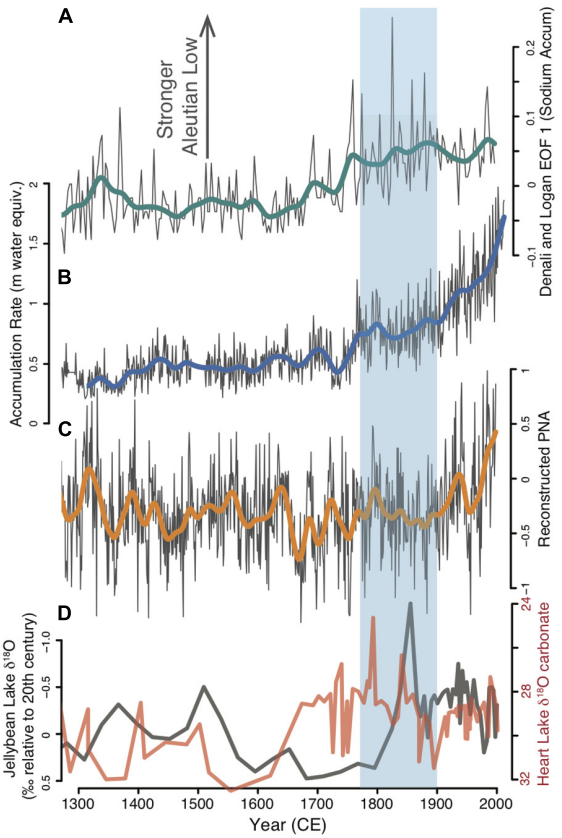

FIGURE 8 | Shifts or trends toward a stronger Aleutian Low pressure system preceded the 19th century glacier advance in Coastal Alaska (blue box). **(A)** Composite sodium record in ice cores from Mt. Logan (Yukon Territory) and Denali (Alaska) (Osterberg et al., 2017). **(B)** Accumulation rate of snow on Mount Hunter in the Alaska Range (Winski et al., 2017). **(C)** Reconstructed Pacific North American atmospheric circulation pattern based on tree rings and varved lake sediments from downwind North America, where more positive values coincide with a stronger Aleutian Low (Liu et al., 2017). **(D)** Oxygen isotopes of carbonate deposited in Jellybean Lake in the Yukon Territory (Anderson et al., 2005). Up in these graphs reflect a stronger Aleutian Low.

Paleo-Records Show the Importance of Winter Precipitation for GOA Glaciers in the 19th Century

Several paleoclimate reconstructions of NPDV along with wintertime conditions in southern Alaska and southwest Yukon Territory indicate that the GOA coastline experienced relatively high snowfall during the 19th century (**Figure 8**). A trend of increasing snow-accumulation rates in the Mount Hunter and Mount Logan ice cores began in the early 1700s (**Figure 8B**; Winski et al., 2017). In addition, variations in sodium fallout in these same ice cores suggests long-term strengthening of the AL that drove more winter storms into the northern GOA after ∼1700, a trend that has continued up to the present (**Figure 8A**; Osterberg et al., 2017). Together, these regional data suggest that increased winter snow accumulation may have contributed to positive mass balances on glaciers throughout southern coastal Alaska. This conclusion is supported by proxy records in downwind North America, where reconstructions of the wintertime PNA exhibit shifts toward more positive PNA patterns in the early CE 1800s, a teleconnection pattern that also implies a strengthening AL and hence increased winter precipitation in the GOA (**Figure 8C**; Liu et al., 2017). Additionally, oxygen-isotope proxies of paleoclimate from carbonates in lake sediment and from the Mount Logan ice core suggest that an abrupt shift to a stronger AL occurred between the mid-18th and early-19th centuries (**Figure 8D**; Fisher et al., 2004; Anderson et al., 2005; Bailey et al., 2018). In summary, recently published paleo-data support the idea that, starting in the 1700s, the combination of increased winter precipitation and moderately cool summers caused positive mass balances in glaciers bordering the northeastern GOA that resulted in the relatively late timing of their LIA maxima during the closing decades of the 19th century (**Figures 6**, **8**).

CONCLUSION

The cross-dated outer rings of 30 *in situ* conifer trees killed by aggrading outwash in front of advancing glacial ice indicate that the La Perouse Glacier in Southeast Alaska advanced to its maximum LIA extent between CE 1850 and 1895, and then began to retreat prior to CE 1922. Prior to this LIA maximum, the glacier had been in a retracted state since at

least CE 1206 based on tree-ring dating, radiocarbon-dated soils, and the lags associated with forest succession. Historical accounts and dendro-glaciological records show that many glaciers surrounding the GOA were also advancing to their LIA-max extents during the 1800s. In contrast, the advances and retreats of a minority of glaciers in the region were partially disconnected from climate by being involved in calving-glacier cycles. Cooler summers caused by the Dalton Solar Minimum were probably not the sole cause of these 1800s advances because the Dalton Solar Minimum was relatively mild, and previous, stronger solar minima were not associated with comparably widespread and extensive glacial advances. Instead, paleoclimate data from ice cores and lake sediments support the interpretation that increased winter precipitation caused by a strengthening of the AL combined with cool summers to cause late-LIA glacial maxima in the GOA region. These results highlight the changing climatic sensitivities of glaciers over relatively short time periods and emphasize the collaborative roles of ocean-atmospheric variability and solar cycles in controlling the fluctuations of mountain glaciers.

AUTHOR CONTRIBUTIONS

BG designed the research, and conducted the fieldwork, part of the analysis, and wrote the manuscript. DM helped designed the research, and conducted the fieldwork, and helped write the manuscript. GW helped to design the research and conducted interpretation on analysis, and provided comparison data and comments on writing. BJ, JC, and NW helped with analysis, and provided comments on writing. LA-H helped with interpretation and provided comments on writing.

FUNDING

The US National Park Service provided financial and logistical support. Fieldwork and support for BG was provided by the Lamont-Doherty Earth Observatory Climate Center Postdoctoral Fellowship, National Geographic Project CP4-151R-18, and US National Science Foundation grant OISE-1743738. Additional support came from the US National Science Foundation's grants OPP-1203271 and PLR-15-04134. LA-H was partially supported by PLR-16-03473 and AGS-15-02150 and GW by AGS – 15-02186.

ACKNOWLEDGMENTS

We thank Gary Thompson and Hans Munich for providing flight service. Carson Baughman, Philip Wilson, and Rowan Sharman helped with fieldwork, and Lewis Sharman provided administrative assistance in Glacier Bay National Park. Earlier drafts of this manuscript benefited from reviews and conversations with Greg Streveler, Nicolas Young, and Michael Kaplan. Constructive comments from Johannes Koch and Olga Solomina improved this manuscript. This is LDEO contribution number 8301.

REFERENCES

Ahmed, M., Anchukaitis, K. J., Asrat, A., Borgaonkar, H., Braida, M., Buckley's, B. M., et al. (2013). Continental-scale temperature variability during the past two millennia. *Nat. Geosci.* 6:339. doi: 10.1038/ngeo1797

Alexander, M. A., and Deser, C. (1995). A mechanism for the recurrence of wintertime midlatitude SST anomalies. *J. Phys. Oceanogr.* 25, 122–137. doi: 10.1175/1520-0485(1995)025<0122:AMFTRO>2.0.CO;2

Allen, S. M., and Smith, D. J. (2007). Late holocene glacial activity of bridge glacier, British Columbia Coast Mountains. *Can. J. Earth Sci.* 44, 1753–1773. doi: 10.1139/e07-059

Anchukaitis, K. J., Wilson, R., Briffa, K. R., Büntgen, U., Cook, E. R., D'Arrigo, R., et al. (2017). Last millennium Northern Hemisphere summer temperatures from tree rings: part II, spatially resolved reconstructions. *Quat. Sci. Rev.* 163, 1–22. doi: 10.1016/j.quascirev.2017.02.020

Anderson, L., Abbott, M. B., Finney, B. P., and Burns, S. J. (2005). Regional atmospheric circulation change in the North Pacific during the Holocene inferred from lacustrine carbonate oxygen isotopes, Yukon Territory, Canada. *Quat. Res.* 64, 21–35. doi: 10.1016/j.yqres.2005.03.005

Arendt, A., Luthcke, S., Gardner, A., O'Neel, S., Hill, D., Moholdt, G., et al. (2013). Analysis of a GRACE global mascon solution for Gulf of Alaska glaciers. *J. Glaciol.* 59, 913–924. doi: 10.3189/2013JoG12J197

Arendt, A. A., Echelmeyer, K. A., Harrison, W. D., Lingle, C. S., and Valentine, V. B. (2002). Rapid wastage of Alaska glaciers and their contribution to rising sea level. *Science* 297, 382–386. doi: 10.1126/science.1072497

Arguez, A., Durre, I., Applequist, S., Squires, M. F., Vose, R. S., Yin, X., et al. (2012). NOAA's 1981–2010 US climate normals: an overview. *Bull. Am. Meteorol. Soc.* 93, 1687–1697. doi: 10.1175/BAMS-D-11-00197.1

Bahr, D. B., Pfeffer, W. T., Sassolas, C., and Meier, M. F. (1998). Response time of glaciers as a function of size and mass balance: 1. Theory. *J. Geophys. Res.* 103, 9777–9782. doi: 10.1029/98JB00507

Bailey, H. L., Kaufman, D. S., Sloane, H. J., Hubbard, A. L., Henderson, A. C. G., Leng, M. J., et al. (2018). Holocene atmospheric circulation in the central North Pacific: a new terrestrial diatom and δ18O dataset from the Aleutian Islands. *Quat. Sci. Rev.* 194, 27–38. doi: 10.1016/j.quascirev.2018.06.027

Barclay, D. J., Barclay, J. L., Calkin, P. E., and Wiles, G. C. (2006). A revised and extended Holocene glacial history of Icy Bay, southern Alaska, USA. *Arct. Antarct. Alp. Res.* 38, 153–162. doi: 10.1657/1523-0430(2006)38[153:ARAEHG]2.0.CO;2

Barclay, D. J., Calkin, P. E., and Wiles, G. C. (2001). Holocene history of Hubbard Glacier in Yakutat Bay and Russell Fiord, southern Alaska. *Geol. Soc. Am. Bull.* 113, 388–402. doi: 10.1130/0016-7606(2001)113<0388:HHOHGI>2.0.CO;2

Barclay, D. J., Wiles, G. C., and Calkin, P. E. (1999). A 1119-year tree-ring-width chronology from western Prince William Sound, southern Alaska. *Holocene* 9, 79–84. doi: 10.1191/095968399672825976

Barclay, D. J., Wiles, G. C., and Calkin, P. E. (2009). Tree-ring crossdates for a first millennium CE advance of Tebenkof Glacier, southern Alaska. *Quat. Res.* 71, 22–26. doi: 10.1016/j.yqres.2008.09.005

Bard, E., Raisbeck, G., Yiou, F., and Jouzel, J. (2000). Solar irradiance during the last 1200 years based on cosmogenic nuclides. *Tellus B,* 52, 985–992. doi: 10.1034/j.1600-0889.2000.d01-7.x

Bard, E., Raisbeck, G. M., Yiou, F., and Jouzel, J. (1997). Solar modulation of cosmogenic nuclide production over the last millennium: comparison between 14C and 10Be records. *Earth Planet. Sci. Lett.* 150, 453–462. doi: 10.1016/S0012-821X(97)00082-4

Beier, C. M., Sink, S. E., Hennon, P. E., D'Amore, D. V., and Juday, G. P. (2008). Twentieth-century warming and the dendroclimatology of declining yellow-cedar forests in southeastern Alaska. *Can. J. Forest Res.* 38, 1319–1334. doi: 10.1139/X07-240

Belcher, S. E. (1843). *Narrative of a Voyage Around the World*, Vol. 2. London: H Colburn.

Berger, A., and Loutre, M.-F. (1991). Insolation values for the climate of the last 10 million years. *Quat. Sci. Rev.* 10, 297–317. doi: 10.1016/0277-3791(91)90033-Q

Bitz, C. M., and Battisti, D. S. (1999). Interannual to decadal variability in climate and the glacier mass balance in Washington, western Canada, and Alaska. *J. Clim.* 12, 3181–3196. doi: 10.1175/1520-0442(1999)012<3181:ITDVIC>2.0.CO;2

Bräuning, A. (2006). Tree-ring evidence of "Little Ice Age"glacier advances in southern Tibet. *Holocene* 16, 369–380. doi: 10.1191/0959683606hl922rp

Bunn, A. G. (2008). A dendrochronology program library in R (dplR). *Dendrochronologia* 26, 115–124. doi: 10.1016/j.dendro.2008.01.002

Burbank, D. W. (1981). A chronology of late Holocene glacier fluctuations on Mount Rainier, Washington. *Arct. Alp. Res.* 13, 369–386. doi: 10.2307/1551049

Burroughs, J., and Muir, J. (1986). *Alaska: The Harriman Expedition, 1899*. Mineola, NY: Dover Publications.

Capps, D. M., Wiles, G. C., Clague, J. J., and Luckman, B. H. (2011). Tree-ring dating of the nineteenth-century advance of Brady Glacier and the evolution of two ice-marginal lakes, Alaska. *Holocene* 21, 641–649. doi: 10.1177/0959683610391315

Chapin, F. S., Walker, L. R., Fastie, C. L., and Sharman, L. C. (1994). Mechanisms of primary succession following deglaciation at Glacier Bay, Alaska. *Ecol. Monogr.* 64, 149–175. doi: 10.1007/BF00396734

Connor, C., Streveler, G., Post, A., Daniel, M., and Wanye, H. (2009). The Neoglacial landscape and human history of Glacier Bay, Glacier Bay National Park and Preserve, southeast Alaska, USA. *Holocene* 19, 381–393. doi: 10.1177/0959683608101389

Coulthard, B., and Smith, D. J. (2013). "Dendroglaciology," in *The Encyclopedia of Quaternary Science*, Vol. 2, ed. S. A. Elias (Amsterdam: Elsevier), 104–111.

Coulthard, B., Smith, D. J., and Lacourse, T. (2013). Dendroglaciological investigations of mid-to late-Holocene glacial activity in the Mt. Waddington area, British Columbia Coast Mountains, Canada. *Holocene* 23, 93–103. doi: 10.1177/0959683612455537

Davidson, G. (1904). The glaciers of Alaska that are shown on Russian charts or mentioned in older narratives. *Trans. Proc. Geog. Soc. Pacific* 3, 1–98.

Fastie, C. L. (1995). Causes and ecosystem consequences of multiple pathways of primary succession at Glacier Bay, Alaska. *Ecology* 76, 1899–1916. doi: 10.2307/1940722

Fisher, D., Wake, C., Kreutz, K., Yalcin, E., Steig, P., Mayewski, L., et al. (2004). Stable isotope records from Mount Logan, Eclipse ice cores and nearby Jellybean Lake. Water cycle of the North Pacific over 2000 years and over five vertical kilometres: sudden shifts and tropical connections. *Géographie Physique et Quaternaire* 58, 337–352. doi: 10.7202/013147ar

Fisher, R., and Johnston, H. J. (1993). *From Maps to Metaphors: The Pacific World of George Vancouver*. Vancouver, BC: UBC Press.

Gaglioti, B. V., Mann, D. H., Williams, A. P., Wiles, G. C., Stoffel, M., Oelkers, R., et al. (in press). Traumatic resin ducts in subalpine mountain hemlock trees provide a new proxy for past winter storminess. *J. Geophys. Res.*

Gao, C., Robock, A., and Ammann, C. (2008). Volcanic forcing of climate over the past 1500 years: an improved ice core-based index for climate models. *J. Geophys. Res. Atmos.* 113. doi: 10.1029/2008JD010239

Gilbert, G. K. (1910). *Harriman Expedition: Alaska Glaciers and Glaciation*, Vol. 3. Boreland: Macritchie Press.

Goodwin, R. G. (1988). Holocene glaciolacustrine sedimentation in muir inlet and ice advance in Glacier Bay, Alaska, U.S.A. *Arct. Alp. Res.* 20, 55–69.

Grove, J. M. (2001). The initiation of the "Little Ice Age" in regions round the North Atlantic. *Climate Change* 48, 53–82. doi: 10.1023/A:1005662822136

Harris, A. S., Hutchison, O. K., Meehan, W. R., Swanston, D. N., Helmers, A. E., Hendee, J. C., et al. (1974). *The Forest Ecosystem of Southeast Alaska: 1. The Setting. Gen Tech Rep PNW-GTR-012*. Portland, OR: US Department of Agriculture.

Hartmann, B., and Wendler, G. (2005). The significance of the 1976 Pacific climate shift in the climatology of Alaska. *J. Clim.* 18, 4824–4839. doi: 10.1175/JCLI3532.1

Heikkinen, O. (1984). Dendrochronological evidence of variations of Coleman Glacier, Mount Baker, Washington, USA. *Arct. Alp. Res.* 16, 53–64. doi: 10.2307/1551172

Holmes, R. L. (1983). Computer-assisted quality control in tree-ring dating and measurement. *Tree Ring Bull.* 43, 69–78. doi: 10.1016/j.dib.2018.08.019

Jackson, S. I., Laxton, S. C., and Smith, D. J. (2008). Dendroglaciological evidence for Holocene glacial advances in the Todd Icefield area, northern British Columbia Coast Mountains. *Can. J. Earth Sci.* 45, 83–98. doi: 10.1139/e07-071

Koch, J., Clague, J. J., and Osborn, G. D. (2011). Glacier fluctuations during the past millennium in Garibaldi Provincial Park, southern coast Mountains, British Columbia. *Can. J. Earth Sci.* 44, 1215–1233. doi: 10.1139/e07-019

Koehler, L., and Smith, D. J., (2011). Late holocene glacial activity in Manatee Valley, southern Coast Mountains, British Columbia, Canada. *Can. J. Earth Sci.* 48, 603–618. doi: 10.1139/E10-087

La Pérouse, J. F. G. (1994). *Comte de. 1994–1995. The Journal of Jean-François de Galaup de la Pérouse, 1785–1788*. London: Hakluyt Society. Available at: https://trove.nla.gov.au/work/5766697?q&sort=holdings+desc&_=1555351663330&versionId=210812644

Lamb, W. K. (2017). *The Voyage of George Vancouver, 1791–1795*. London: Routledge.

Larocque, S. J., and Smith, D. J. (2003). Little ice age glacial activity in the Mt. Waddington area, British Columbia Coast Mountains, Canada. *Can. J. Earth Sci.* 40, 1413–1436. doi: 10.1139/e03-053

Larsen, C. F., Motyka, R. J., Freymueller, J. T., Echelmeyer, K. A., and Ivins, E. R. (2005). Rapid viscoelastic uplift in southeast Alaska caused by post-little ice age glacial retreat. *Earth Planet. Sci. Lett.* 237, 548–560. doi: 10.1016/j.epsl.2005.06.032

Lewis, D. H., and Smith, D. J. (2004). Little ice age glacial activity in strathcona provincial park, Vancouver Island, British Columbia, Canada. *Can. J. Earth Sci.* 41, 285–297. doi: 10.1139/e03-102

Liu, Z., Tang, Y., Jian, Z., Poulsen, C. J., Welker, J. M., and Bowen, G. J. (2017). Pacific North American circulation pattern links external forcing and North American hydroclimatic change over the past millennium. *Proc. Natl. Acad. Sci.* 114, 3340–3345. doi: 10.1073/pnas.1618201114

Luckman, B. H. (1993). Glacier fluctuation and tree-ring records for the last millennium in the Canadian Rockies. *Quat. Sci. Rev.* 12, 441–450. doi: 10.1016/S0277-3791(05)80008-3

Luckman, B. H. (2000). The little ice age in the Canadian Rockies. *Geomorphology* 32, 357–384. doi: 10.1016/S0169-555X(99)00104-X

Luckman, B. H., and Wilson, R. (2005). Summer temperatures in the Canadian Rockies during the last millennium: a revised record. *Clim. Dynam.* 24, 131–144. doi: 10.1007/s00382-004-0511-0

Malaspina, A., and David, A. (2003). *The Malaspina expedition, 1789-1794: journal of the voyage by Alejandro Malaspina*, Vol. 2. London: Hakluyt Society.

Mann, D. H. (1986). Reliability of a fjord glacier's fluctuations for paleoclimatic reconstructions. *Quat. Res.* 25, 10–24. doi: 10.1016/0033-5894(86)90040-2

Mann, D. H., and Streveler, G. P. (2008). Relative sea level history, isostasy, and glacial history in Icy Strait, Southeast Alaska. *Quat. Res.* 69, 201–216. doi: 10.1016/j.yqres.2007.12.005

Mann, D. H., and Ugolini, F. C. (1985). Holocene glacial history of the Lituya District, southeast Alaska. *Can. J. Earth Sci.* 22, 913–928. doi: 10.1139/e85-095

Mantua, N. J., and Hare, S. R. (2002). The Pacific decadal oscillation. *J. Oceanogr.* 58, 35–44. doi: 10.1023/A:1015820616384

Marzeion, B., Cogley, J. G., Richter, K., and Parkes, D. (2014). Attribution of global glacier mass loss to anthropogenic and natural causes. *Science* 345, 919–921. doi: 10.1126/science.1254702

McGrath, D., Sass, L., O'Neel, S., Arendt, A., and Kienholz, C. (2017). Hypsometric control on glacier mass balance sensitivity in Alaska and northwest Canada. *Earth Fut.* 5, 324–336. doi: 10.1002/2016EF000479

McKenzie, G. D., and Goldthwait, R. P. (1971). Glacial history of the last eleven thousand years in Adams Inlet, southeastern Alaska. *Geol. Soc. Am. Bull.* 82, 1767–1782. doi: 10.1130/0016-7606(1971)82[1767:GHOTLE]2.0.CO;2

Menounos, B., Osborn, G., Clague, J. J., and Luckman, B. H. (2009). Latest pleistocene and holocene glacier fluctuations in western Canada. *Quat. Sci. Rev.* 28, 2049–2074. doi: 10.1016/j.quascirev.2008.10.018

Miller, G. H., Geirsdóttir, Á, Zhong, Y., Larsen, D. J., Otto, B. L., Holland, M. M., et al. (2012). Abrupt onset of the Little Ice Age triggered by volcanism and sustained by sea-ice/ocean feedbacks. *Geophys. Res. Lett.* 39:L02708. doi: 10.1073/pnas.1304912110

Miller, M. M. (1958). The role of diastrophism in the regimen of glaciers in the st. Elias District, Alaska. *J. Glaciol.* 3, 293–297. doi: 10.1017/S0022143000023959

Mock, C. J., Bartlein, P. J., and Anderson, P. M. (1998). Atmospheric circulation patterns and spatial climatic variations in Beringia. *Int. J. Climatol.* 18, 1085–1104. doi: 10.1002/(SICI)1097-0088(199808)18:10<1085::AID-JOC305>3.0.CO;2-K

Neal, E. G., Hood, E., and Smikrud, K. (2010). Contribution of glacier runoff to freshwater discharge into the Gulf of Alaska. *Geophys. Res. Lett.* 37:L06404. doi: 10.1111/gcb.13875

Newman, M., Alexander, M. A., Ault, T. R., Cobbd, K. M., Desere, C., Di Lorenzo, E., et al. (2016). The Pacific decadal oscillation, revisited. *J. Clim.* 29, 4399–4427. doi: 10.1175/JCLI-D-15-0508.1

Oerlemans, J. (2005). Extracting a climate signal from 169 glacier records. *Science* 308, 675–677. doi: 10.1126/science.1107046

Oerlemans, J., and Fortuin, J. (1992). Sensitivity of glaciers and small ice caps to greenhouse warming. *Science* 258, 115–117. doi: 10.1126/science.258.5079.115

Olson, W. M. (2002). *Through Spanish Eyes: The Spanish Voyages to Alaska, 1774–1792*. North Branch, MI: Heritage Research.

Osterberg, E. C., Winski, D. A., Kreutz, K. J., Wake, C. P., Ferris, D. G., Campbell, S., et al. (2017). The 1200 year composite ice core record of Aleutian Low intensification. *Geophys. Res. Lett.* 44, 7447–7454. doi: 10.1002/2017GL073697

Plafker, G., and Miller, D. J. (1957). *Glacial Features and Surficial Deposits of the Malaspina District, Alaska US Geological Survey* Report No. 57-91. Washington, DC: US Department of the Interior.

Post, A., and Motyka, R. J. (1995). Taku and Le Conte glaciers, Alaska: calving-speed control of late-Holocene asynchronous advances and retreats. *Phys. Geogr.* 16, 59–82. doi: 10.1080/02723646.1995.10642543

Post, A., O'Neel, S., Motyka, R. J., and Streveler, G. (2011). A complex relationship between calving glaciers and climate. *EOS Trans. Am. Geophys. Union* 92, 305–306. doi: 10.1029/2011EO370001

Reimer, P. J., Bard, E., Bayliss, A., Beck, J. E., Blackwell, P. G., Ramsey, C. B., et al. (2013). IntCal13 and Marine13 radiocarbon age calibration curves 0–50,000 years cal BP. *Radiocarbon* 55, 1869–1887. doi: 10.1016/j.dib.2018.10.040

Rodionov, S. N., Bond, N. A., and Overland, J. E. (2007). The Aleutian Low, storm tracks, and winter climate variability in the Bering Sea. *Deep Sea Res. Part II Top. Stud. Oceanogr.* 54, 2560–2577. doi: 10.1016/j.dsr2.2007.08.002

Russell, I. C. (1893). Malaspina glacier. *J. Geol.* 1, 219–245. doi: 10.1086/606179

Seitz, J. F. (1953). *Ascent at La Perouse*. Seattle, WA: The Mountaineers.

Solomina, O. N., Bradley, R. S., Hodgson, D. A., Ivy-Ochs, S., Jomelli, V., Mackintosh's, A. V., et al. (2015). Holocene glacier fluctuations. *Quat. Sci. Rev.* 111, 9–34. doi: 10.1016/j.quascirev.2014.11.018

Solomina, O. N., Bradley, R. S., Jomelli, V., Geirsdottir, A., Kaufman, D. S., Koch, J., et al. (2016). Glacier fluctuations during the past 2000 years. *Quat. Sci. Rev.* 149, 61–90. doi: 10.1016/j.quascirev.2016.04.008

Stokes, M. A., and Smiley, T. L. (1996). *Introduction to Tree Ring Dating*. Tucson: The University of Arizona Press, 73.

Tarr, R. S., and Martin, L. (1914). *Alaskan Glacier Studies of the National Geographic Society in the Yakutat Bay, Prince William Sound and Lower Copper River Regions*. Washington, DC: National Geographic Society.

Tebenkov, M. D. (1850). *Atlas of the Northwest Coasts of America*. Kingston, ON: Limestone Press.

Thompson, R. S., Anderson, K. H., Strickland, L. E., Shafer, S. L., and Pelltier, R. T. (2006). Atlas of relations between climatic parameters and distributions of important trees and shrubs in North America: Alaska species and ecoregions. *Paper Presented 1650-D, US Dept. of the Interior, US Geological Survey*, Reston, VA. doi: 10.3133/pp1650D

Topham, H. W. (1889). An expedition to Mount St Elias. *Alp. J.* 14, 345–371.

Trenberth, K. E., and Hurrell, J. W. (1994). Decadal atmosphere-ocean variations in the Pacific. *Clim. Dynam.* 9, 303–319. doi: 10.1007/BF00204745

Van Beusekom, A. E., O'Neel, S. R., March, R. S., Sass, L. C., and Cox, L. H. (2010). Re-Analysis of Alaskan Benchmark Glacier Mass-Balance Data Using the Index Method. *US Geological Survey Scientific Investigations* Report No: 5247. Washington, DC: US Department of Interior.

Van der Veen, C. J. (2013). *Fundamentals of Glacier Dynamics*, 2nd Edn. Boca Raton, FL: CRC Press. doi: 10.1201/b14059

Vancouver, G. (1799). *Atlas du Voyage de Vancouver*. Paris: Imprimerie de la République.

Wendler, G., Galloway, K., and Stuefer, M. (2016). On the climate and climate change of Sitka, Southeast Alaska. *Theor. Appl. Climatol.* 126, 27–34. doi: 10.1007/s00704-015-1542-7

Wiles, G. C., Barclay, D. J., Calkin, P. E., and Lowell, T. V. (2008). Century to millennial-scale temperature variations for the last two thousand years indicated from glacial geologic records of Southern Alaska. *Global Planet. Change* 60, 115–125. doi: 10.1016/j.gloplacha.2006.07.036

Wiles, G. C., and Calkin, P. E. (1994). Late Holocene, high-resolution glacial chronologies and climate, Kenai Mountains, Alaska. *Geol. Soc. Am. Bull.* 106, 281–303. doi: 10.1130/0016-7606(1994)106<0281:LHHRGC>2.3.CO;2

Wiles, G. C., D'Arrigo, R. D., Barclay, D., Wilson, R. S., Jarvis, S. K., and Lauren, V. (2014). Surface air temperature variability reconstructed with tree rings for the Gulf of Alaska over the past 1200 years. *Holocene* 24, 198–208. doi: 10.1177/0959683613516815

Wiles, G. C., D'Arrigo, R. D., Villalba, R., Calkin, P. E., and Barclay, D. J. (2004). Century-scale solar variability and Alaskan temperature change over the past millennium. *Geophys. Res. Lett.* 31:L15203. doi: 10.1029/2004GL020050

Wiles, G. C., Mennett, C. R., Jarvis, S. K., Wiesenberg, N., Lawson, D. E., D'Arrigo's, R., et al. (2012). Tree-ring investigations into changing climatic responses of yellow-cedar, Glacier Bay, Alaska. *Can. J. Forest Res.* 42, 814–819. doi: 10.1139/x2012-028

Winski, D., Osterberg, E., Ferris, D., Kreutz, K., Wake, C., Campbell, S., et al. (2017). Industrial-age doubling of snow accumulation in the Alaska Range linked to tropical ocean warming. *Sci. Rep.* 7:17869. doi: 10.1038/s41598-017-18022-5

Zobel, D. B., and Antos, J. A. (1982). Adventitious rooting of eight conifers into a volcanic tephra deposit. *Can. J. Forest Res.* 12, 717–719. doi: 10.1139/x82-108

Conflict of Interest Statement: The authors declare that the research was conducted in the absence of any commercial or financial relationships that could be construed as a potential conflict of interest.

frontiers in Earth Science

ORIGINAL RESEARCH
published: 15 May 2019
doi: 10.3389/feart.2019.00106

Holocene Ecohydrological Variability on the East Coast of Kamchatka

Jonathan Nichols[1], Dorothy Peteet[1,2], Andrei Andreev[3,4], Fabian Stute[5] and Tiara Ogus[6]*

[1] Lamont-Doherty Earth Observatory, Palisades, NY, United States, [2] NASA Goddard Institute for Space Studies, New York, NY, United States, [3] Alfred-Wegener-Institut Helmholtz-Zentrum für Polar- und Meeresforschung, Potsdam, Germany, [4] Institute of Geology and Petroleum Technologies, Kazan Federal University, Kazan, Russia, [5] Fu Foundation School of Engineering, Columbia University, New York, NY, United States, [6] Department of Chemistry, SUNY College of Environmental Science and Forestry, Syracuse, NY, United States

The Late Glacial and Holocene climate of the western North Pacific is less studied than that of the eastern North Pacific. While it is well known that strong east-west gradients in the tropical Pacific Ocean influence terrestrial climate, we seek to better understand how these gradients are expressed in the northern extratropics. Toward this aim, we present an organic and stable isotope geochemical and macrofossil record from a peatland on the east coast of the Kamchatka peninsula. We find that both the early and late Holocene were wetter, with a different assemblage of plants from the middle Holocene, which was drier, with more episodic precipitation. The large ecohydrological changes at several points during the Holocene are contemporaneous with and of the same sense as those we find at places to the east, such as south-central Alaska and to the south, in northern Japan. We also find that the middle Holocene period of warmth, dryness and low carbon accumulation occur contemporaneously with an enhanced east-west gradient in tropical Pacific sea surface temperature. This suggests that that hydroclimatic conditions in the subarctic can be influenced by tropical dynamics.

Keywords: ecohydorology, carbon cycle, peatlands, holocene, Kamchatka

OPEN ACCESS

Edited by:
Randel Tom Cox,
The University of Memphis,
United States

Reviewed by:
Li Wu,
Anhui Normal University, China
Nadia Solovieva,
University College London,
United Kingdom

****Correspondence:***
Jonathan Nichols
jnichols@ldeo.columbia.edu

Specialty section:
This article was submitted to Quaternary Science, Geomorphology and Paleoenvironment, a section of the journal Frontiers in Earth Science

Received: *22 December 2018*
Accepted: *25 April 2019*
Published: *15 May 2019*

Citation:
Nichols J, Peteet D, Andreev A, Stute F and Ogus T (2019) Holocene Ecohydrological Variability on the East Coast of Kamchatka. Front. Earth Sci. 7:106. doi: 10.3389/feart.2019.00106

INTRODUCTION

Peatlands are an important part of the global carbon cycle, storing, at a minimum, 550 Gt of carbon in the form of partially decayed organic matter (Turetsky et al., 2015). Study of northern peatlands has focused mainly on sphagnum-dominated, ombrotrophic bogs. However, sedge-dominated fens are also important carbon-storing environments (Jones et al., 2009; Loisel et al., 2017). Climate and vegetation type are well-known influences on the rate of carbon accumulation in ombrotrophic peatlands, but less is known about the role of nutrient cycling. Here we investigate influence of climate on vegetation, carbon accumulation, and nutrient cycling in a typical fen environment.

The general trends of Holocene climate on Kamchatka have been established by fossil pollen, lacustrine diatoms, chironomids, and other paleoecological indicators. In brief, the early Holocene, from about 10 ka to 7 ka, was moist and cool, transitioning to a warm, dry, and windy climate during the middle Holocene from about 6.5 to at least 5 ka (Andrén et al., 2015; Solovieva et al., 2015). After about 4.5 ka, commonly termed the Neoglacial, conditions return to a cool moist climate (Hammarlund et al., 2015; Meyer et al., 2015). Carbon accumulation rates, too have been measured in various locations throughout the peninsula, and during periods of cool and/or moist climate, as in both the early Holocene and the Neoglacial, peat carbon accumulation is higher than during the dry and/or warm period of the middle Holocene (Zakharikhina, 2014; Turetsky et al., 2015).

While the general association between changes in climate and changes in carbon accumulation in peatlands have been established for Kamchatka, what is less clear in this region, and indeed, globally, are the specific mechanisms by which climate influences carbon accumulation in sedge dominated fens, as opposed to *Sphagnum*-dominated bogs (Jones et al., 2009; Treat et al., 2016; Loisel et al., 2017). In this study we endeavor to link changes in climate with specific changes in plant communities, hydrology, and nutrient cycling in the fen itself in order to establish causal relationships.

Newmarket Fen, a sedge-dominated peatland (**Figure 1**), is located on the eastern coast of Kamchatka, far east Russia, at 53.0°N, 158.5°E, 150 m elevation, which is within the city limits of Petropavlovsk-Kamchatsky. The site has subsequently been covered over by urban development. At least 30 active volcanoes and 300 extinct volcanoes and several mountain ranges add to the complexity of the vegetation history. A wet, windy climate is characteristic of the Pacific coast, with *Betula ermanii* (stone birch) occurring up to 500 m elevation, and *Alnus fruticosa* (shrub alder) above on seaward slopes and snowfields, and alpine tundra at highest elevations (Hultén, 1971).

MATERIALS AND METHODS

In the summer of 1990, a 145 cm core was recovered from the Newmarket Fen and subsampled and described in the field at approximately 5 cm intervals. Subsequently, samples were stored in polyethylene bags with coated metal tie-tops at 4°C in the Lamont-Doherty Earth Observatory (LDEO) Core Repository until analysis. Organic matter content was measured by loss-on-ignition (LOI). Volumetric samples were oven dried to measure dry bulk density, and were then heated in a muffle furnace at 550°C for 3 h. The mass lost divided by dry weight is equal to the fraction organic matter. The weight percent and stable isotope ratios of carbon (expressed as $\delta^{13}C$, per mille vs. VPDB) and nitrogen (expressed as $\delta^{15}N$ per mille vs. air) were measured by elemental analysis/isotope ratio mass spectrometry (EA-IRMS) in the LDEO Stable Isotope Laboratory. CO_2 and N_2 generated from whole, dried sediment samples in a Costech Elemental Analyzer are routed to a Thermo Delta V IRMS through a Thermo ConFlow IV continuous flow device.

Soluble lipids were extracted from 5 cubic centimeter subsamples of peat by ultrasonic agitation in hexane. The total lipid extract (TLE) was decanted and reserved. The solvent-insoluble portion was used for macrofossil analysis. Macrofossil samples were sieved in water at 150 μm and plant parts were identified under low-power microscopy. Plant macrofossil identifications were confirmed by comparison with the LDEO Macrofossil Reference Collection. The TLE was separated by polarity on a silica gel flash column into four fractions. Hydrocarbons are eluted with hexane; ketones, esters, and compounds with aromatic rings elute with dichloromethane; alcohols elute with a 3:1 mixture of hexane and ethyl acetate, and all remaining polar compounds, including fatty acids, elute with methanol. The hydrogen isotope ratios of n-alkanes are measured by continuous flow gas chromatography isotope ratio mass spectrometry at the LDEO Stable Isotope Laboratory. Eluent from a Thermo Trace GC is routed through a pyrolysis reactor in a Thermo GC-IsoLink device and then to a ConFlow IV continuous flow device and then to a Thermo Delta V isotope ratio mass spectrometer. Typical precision for these measurements is ±2%.

Selected stratigraphic levels were subsampled a second time to collect macrofossils for AMS radiocarbon dating. Macrofossils used for paleovegetational analysis were exposed to organic solvents derived from petroleum products and were therefore unsuitable for radiocarbon measurements. As above, subsamples were sieved at 150 μm and macrofossils were identified under low-power microscopy and confirmed against the LDEO reference collection. Macrofossils from these subsamples were analyzed in the AMS radiocarbon lab at the University of California, Irvine (UCIAMS).

RESULTS AND DISCUSSION

Core Stratigraphy and Age Control

Macrofossil analysis and visual inspection reveal that the sediments at Newmarket Fen are dominated by sedge peat from the top of the core all the way down to 132 cm core depth (**Figure 2**). Below the sedge peat are 2 cm of lacustrine sediment underlain by an additional 3 cm of sedge peat, 2 cm of sapropel, and finally, at the basis of the core, sandy clay. The 132 cm of sedge peat are occasionally interrupted by thin layers of tephra.

Five tephra layers with published ages (Bazanova et al., 2005; Zakharikhina, 2014; Andrén et al., 2015; Solovieva et al., 2015) were identified in the field (**Table 1** and **Figure 2**). Samples of individual macrofossils from five additional levels were dated by AMS radiocarbon analysis. Three of the five radiocarbon dates were rejected as too young. It is likely that these were root material that had infiltrated stratigraphically lower levels than contemporaneous material. Four additional tephra layers were identified by correlation with similar nearby sections using the field-identified tephra and radiocarbon ages as a guide (**Supplementary Figure S1**). An age-depth model was constructed using the "Bacon" Bayesian age modeling algorithm with the five field-identified tephra, two acceptable radiocarbon measurements, and four correlated tephra as input (**Figure 1C**).

Vegetation—Macrofossils and Leaf Waxes

Macrofossil counts at Newmarket Fen are dominated by sedges (Cyperaceae) at nearly all horizons above the basal mineral sediments. Four different achene morphotypes belonging to genus *Carex* are identified, three with trigonous morphology (arbitrarily termed *Carices* A, B, and C) and one lenticular (*Carex* D). Achenes could not be identified to species as they lacked perigynia. Seeds of various dicotyledonous taxa were also identified. These taxa include *Betula*, *Rubus*, *Labiatae*, *Triglochin*, and *Ericaceae*. Also abundant throughout the core are insect remains, likely Coleoptera (**Figure 2**).

Concentration of *n*-alkanes were measured for each of the 38 samples. Statistical analyses were performed on the fractional

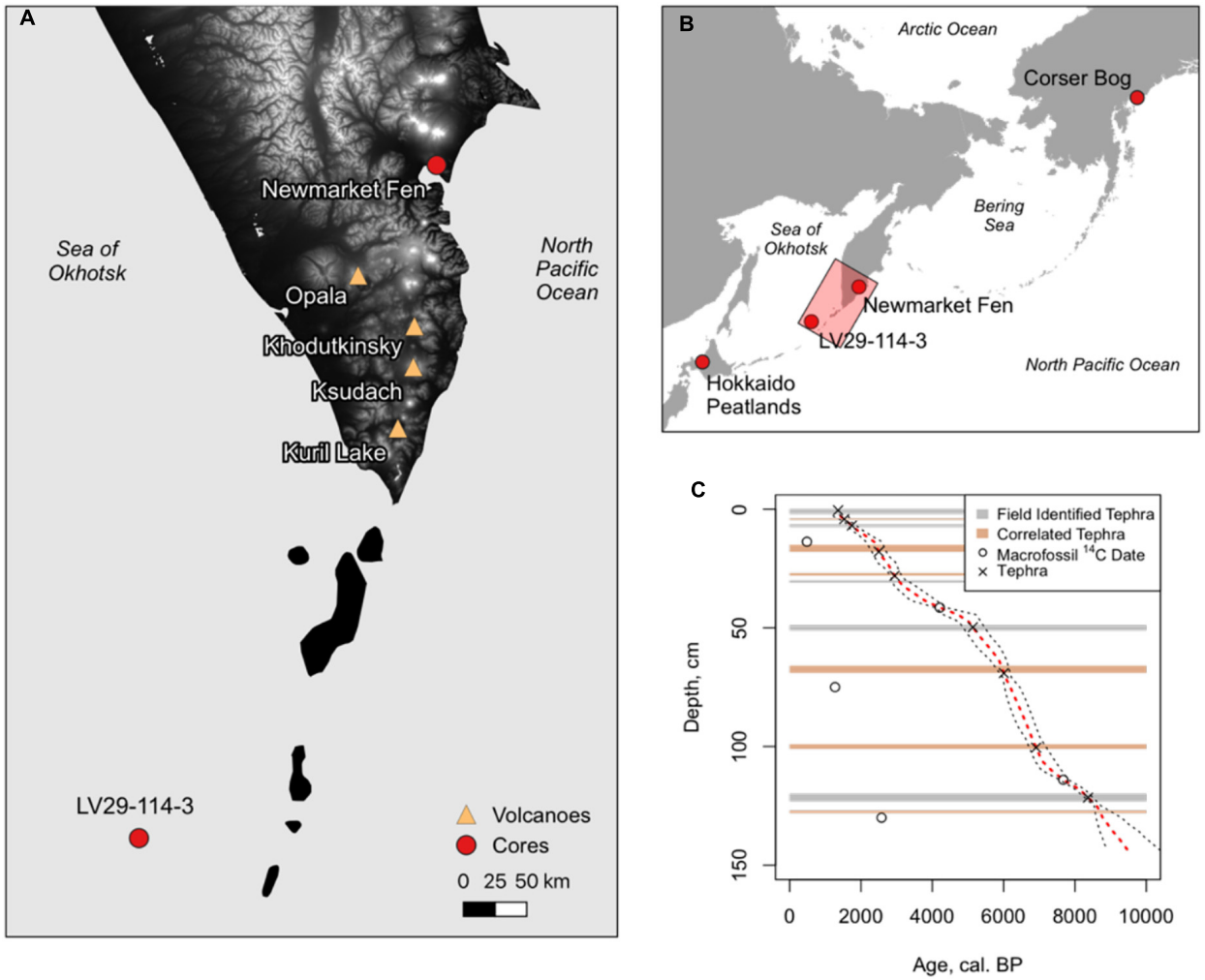

FIGURE 1 | (A) Map of southern Kamchatka Peninsula indicating the locations of Newmarket Fen, marine sediment core LV29-114-3, and volcanoes that are the source of tephras found in Newmarket Fen sediments. **(B)** Overview map showing the locations of other sites mentioned in the text. The inset **(A)** is indicated by the pink rectangle. **(C)** Age-depth model constructed using Bacon (Blaauw, 2011). Locations of age control points, median modeled age, and 95% confidence intervals are shown.

abundance of each n-alkane relative to total n-alkanes. Principal component analysis (**Figure 3**) revealed that the primary mode of variability in the dataset is chain length of odd-carbon-numbered alkanes.

Both macrofossil counts and *n*-alkane concentrations were used to divide the stratigraphy into 5 zones (**Figures 2–4**). Depth-constrained sum-of-squares cluster analysis [CONISS, (Grimm, 1987)] of a Euclidean distance matrix of macrofossil counts revealed three zones, while the same analysis of *n*-alkane relative abundance further divided two of the macrofossil zones, resulting in five total vegetational zones, hereafter labeled with Roman numerals increasing from oldest to youngest (**Table 2**).

In addition to constrained cluster analysis, we also performed an unconstrained hierarchical cluster analysis of the Euclidean distance matrix of *n*-alkane relative abundance. This analysis resulted in three distinct *n*-alkane distribution types, each with different alkane of maximum abundance (**Figure 3**). Zones II and V are dominated by Type 1, for which C_{29} is the most abundant *n*-alkane. Zone III is dominated by Type 3, for which C_{33} is most abundant. Type 2 is a wider distribution with a less distinct mode. This type dominates Zone I and IV along with the transition between II and III. Because individual plants are more likely to have a single alkane as a mode of its distribution (Bush and McInerney, 2013), we interpret Types 1 and 3 to represent more monospecific environments, while Type 2 represents a more diverse assemblage of plants. This interpretation is somewhat supported by the macrofossil data, however, Type 2 could also represent a transitional environment that is a mixture of plants occurring in both Types 1 and 3.

Carbon and Nitrogen

The concentration and isotope ratios of carbon did not change significantly throughout the sedge-dominated portion of the stratigraphy. Unsurprisingly, the concentration of carbon is low

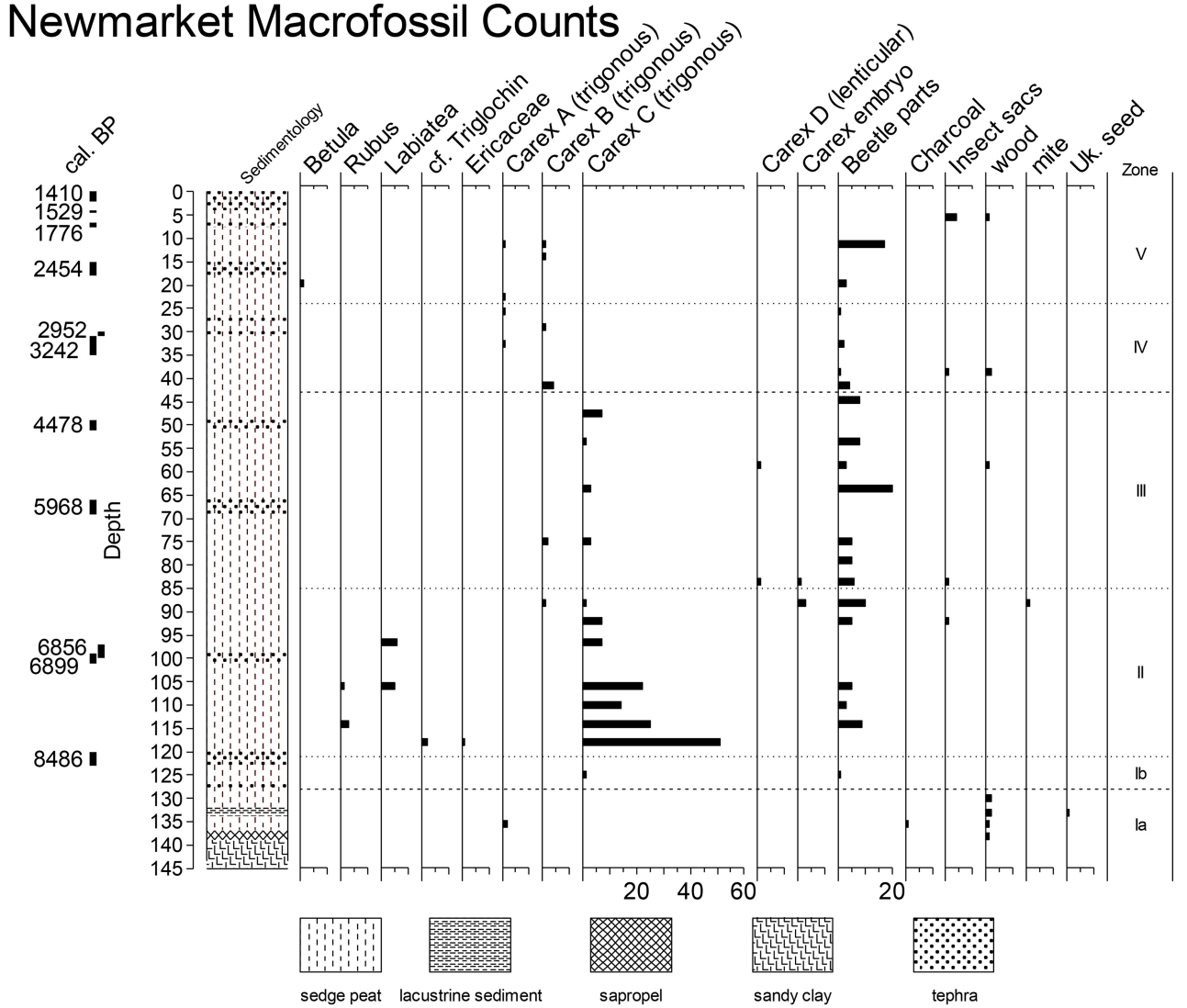

FIGURE 2 | Macrofossil counts at Newmarket Fen along with core stratigraphy. Zonation based on macrofossil analysis is indicated with heavy dashed lines and zonation based on *n*-alkane abundances is indicated with light dotted lines.

in the basal lacustrine sediments as compared with the peat above. Carbon isotope ratios had a median value of −27.6% and ranged from −28.9 to −26.7% with no discernible downcore trend—typical of organic matter originating from plants using the C3 photosynthetic pathway (Meyers, 1994).

The rate of carbon accumulation was calculated by multiplying the dry bulk density (as measured during LOI analysis) by the percent carbon (as determined by EA-IRMS and LOI) and by the sedimentation rate (as determined by the age model). We find that throughout the stratigraphy at Newmarket Fen (**Figure 4**), carbon accumulation rates are, in general, low, with a median at 13 g $m^{-2}yr^{-1}$, compared with that of *Sphagnum* bogs, with a median near 23 g $m^{-2}yr^{-1}$ (Loisel et al., 2014). Carbon accumulation is lowest during the lacustrine phase of the stratigraphy, but during the peat phase, the minimum carbon accumulation rate is about 11 g m^{-2} yr^{-1} and occurs at the top Zone III. Two local maxima occur near the top of Zones II and IV, at about 35 and 25 g m^{-2} yr^{-1}, respectively. Carbon accumulation decreases during phases of the stratigraphy dominated by Type 3 *n*-alkane distributions. Type 2 is also associated with low carbon accumulation, while Type 1 *n*-alkane distributions are associated with increasing carbon accumulation rate.

The concentration and stable isotope ratios of nitrogen changed systematically throughout the stratigraphy. We found that the concentration of nitrogen [N] was anticorrelated to its isotope ratio ($\delta^{15}N$) (**Supplementary Figure S2**), which indicates that denitrification is a control on [N]. We interpret this variability in [N] and $\delta^{15}N$ to be related to peatland hydrology. Under saturated conditions, oxygen is quickly consumed by

TABLE 1 | Age control data for Newmarket Fen.

Eruptive center	*Tephra code*		*Identification*	*Radiocarbon age (BP)*	*Age uncertainty*	*Age ref.*	*Core depth (cm)*
Opala	OP	(Оп)	Field	1478	18	Z, B	1
Avachinsky	AV_{1600}	(AB_{1600})	Correlation	1622	45	B	4.25
Ksudach	KS_1	(KC_1)	Field	1806	16	Z, B	7
Avachinsky	AV_{2500}	(AB_{2500})	Correlation	2524	68	B	16.5
Khodutkinsky	KhD	(ХД)	Field	2805	40	Z, B	30.5
Opala	OP_{tr}	(Оп)	Field	4628	90	Z, B	50
Avachinsky	AV_{5300}	(AB_{5300})	Correlation	5257	23	B	67.5
Ksudach	KS_2	(KC_2)	Correlation	6007	38	Z, B	100
Kuril Lake	KO	(KC)	Field	7666	19	Z, B	121.5
AMS lab code		*Material dated*				*Rejected?*	
UCIAMS-213840		Undiff. sedge parts		410	20	x	13.75
UCIAMS-213841		Above ground plant parts		3830	20		33
UCIAMS-213842		Undiff. sedge parts		1325	15	x	75
UCIAMS-213843		*Carex* seeds		6860	25		98.5
UCIAMS-213844		Undiff. sedge parts		2495	40	x	130

*Z = (Zakharikhina, 2014; Hammarlund et al., 2015; Meyer et al., 2015); B = (Bazanova et al., 2005); field = identified in the field; correlation = identified by correlation with nearby sections with similar stratigraphy (**Supplementary Figure S1**).*

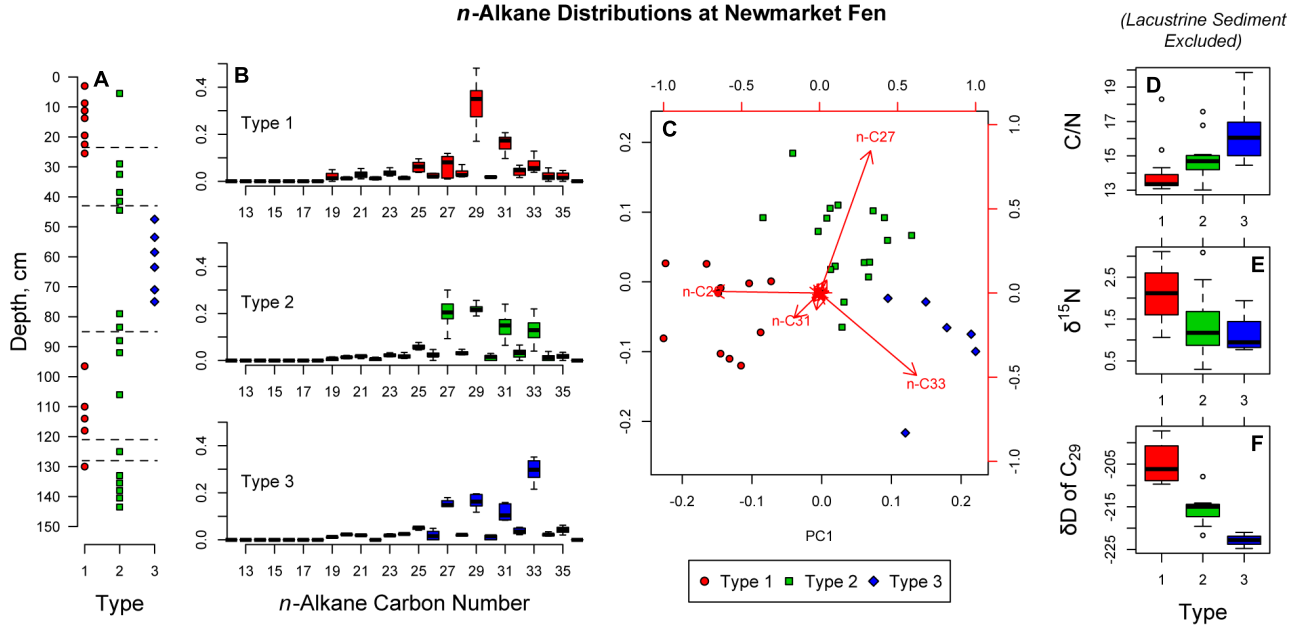

FIGURE 3 | Results of hierarchical cluster analysis and principal components analysis on the relative abundances of leaf wax *n*-alkanes. **(A)** Type assignments by core depth; **(B)** Box-and-whisker plots of *n*-alkane relative abundance for each type; **(C)** Principal components analysis biplot. Point color and shape are determined by hierarchical cluster analysis; **(D–F)** Box-and-whisker plots of C/N ratio, $\delta^{15}N$, and hydrogen isotope ratios of C_{29} *n*-alkane. For all box-and-whisker plots, the heavy line in the center is at the median, the shoulders of the box indicate the interquartile range, the whiskers extend to the most extreme data not more than 1.5 times the interquartile range, and the points beyond 1.5 times the interquartile range from the box are indicated with points.

heterotrophic microorganisms, and nitrate becomes the favored terminal electron acceptor. As denitrifiers remove N from the peat by converting it to N_2 gas, the concentration of nitrogen decreases, and the remaining pool of nitrogen becomes isotopically enriched, as the lighter isotope is more energetically favorable. Under dry conditions, however, the water table in the peatland drops, and is oxygenated. Nitrogen is no longer lost to denitrification as oxygen is favored as a terminal electron acceptor, therefore the concentration of nitrogen is allowed to rebound, and the $\delta^{15}N$ returns to values near that of atmospheric N_2. Such conditions are also associated with low carbon accumulation, suggesting that reduced accumulation could be due to high carbon loss, rather than low primary productivity. By this interpretation,

TABLE 2 | Depths, ages, and paleoenvironmental summaries for each zone.

Zone	Top	Bottom	End	Start	Vegetation	Hydrology	Carbon	Redox
	(cm)	(cm)	(yr)	(yr)				
V	0	24	1424	2530	Carex A and B Type 1 n-Alkanes	Moist	Increasing	Denitrifiers active
IV	24	43	2530	4358	Carex A and B Type 2 n-Alkanes	Dry	Low	Oxic
III	43	85	4358	6498	Carex C and B Type 3 n-Alkanes	Dry	Decreasing	Oxic
II	85	121	6498	8311	Carex C, various dicots Type 1 n-Alkanes	Moist	Increasing	Denitrifiers active
I	121	145	8311	9473	Wood fragments Type 2 n-Alkanes	Open water	Low	Denitrifiers most active

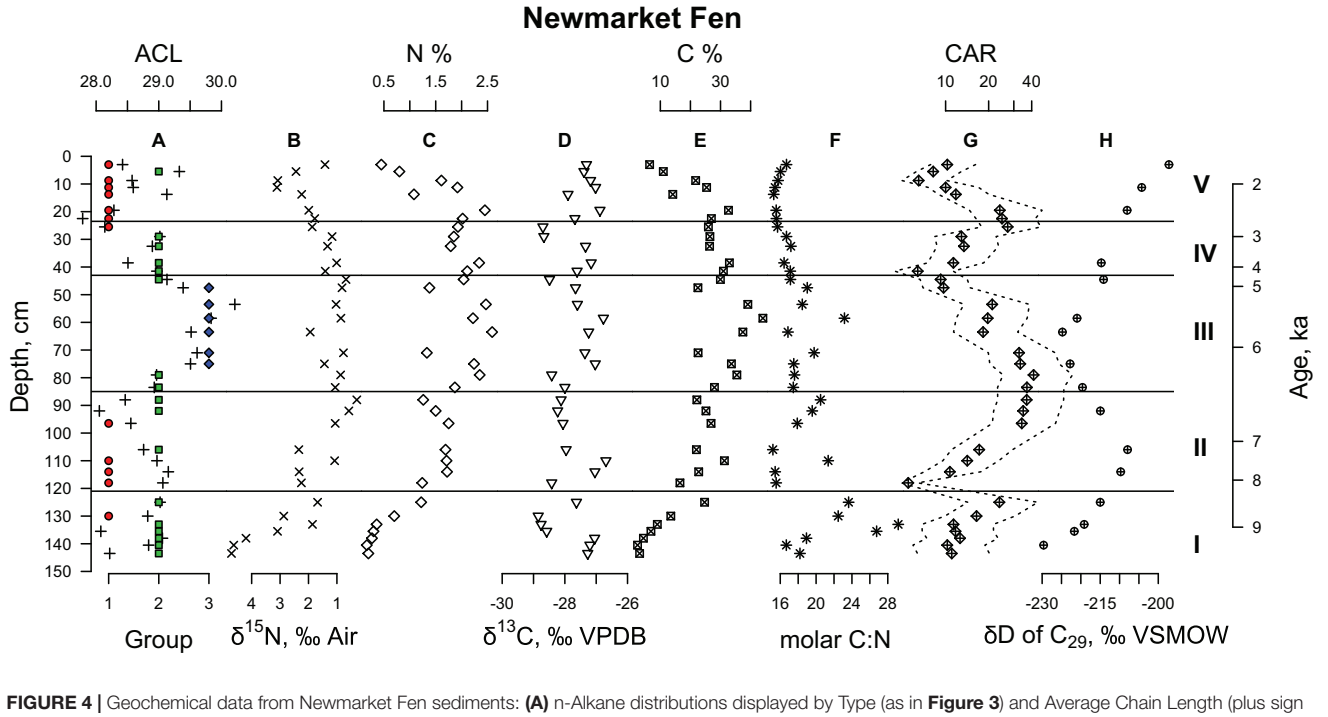

FIGURE 4 | Geochemical data from Newmarket Fen sediments: **(A)** n-Alkane distributions displayed by Type (as in **Figure 3**) and Average Chain Length (plus sign symbols); **(B)** Nitrogen Isotope ratios in per mille vs. air; **(C)** Percent nitrogen by weight; **(D)** Carbon isotope ratios in per mille vs. VPDB; **(E)** Percent carbon by weight; **(F)** Molar carbon to nitrogen ratio; **(G)** Carbon accumulation rate in grams carbon per meter squared per year, with 75% confidence intervals propagated from the Bacon age-depth model; **(H)** Hydrogen isotope ratios of C_{29} *n*-alkane in per mille VSMOW. Horizontal lines indicate macrofossil zones (as in **Figure 2**).

Newmarket Fen experienced wettest conditions during Zone I, relatively wet conditions during Zones II and V, and driest conditions during Zones III and IV.

Each of the three types of *n*-alkane abundance distributions are associated with distinct carbon to nitrogen (C/N) ratios, stable nitrogen isotope ratios and carbon accumulation rates. Types 1 and 3 represent the extrema of these values while Type 2 is intermediate. We find that periods dominated by Type 1 vegetation are characterized by low C/N, high $\delta^{15}N$ and high carbon accumulation. Lower C/N ratios can indicate more herbaceous material and less woody or structural plant material. Higher $\delta^{15}N$ indicates lower oxygen and increased denitrification. When vegetation Type 1 dominates, low oxygen and less woody material results in more carbon stored. Samples dominated by vegetation Type 3 have the highest C/N ratios. Because high C/N is typically associated with woody vegetation, but macrofossil analysis indicates dominance of sedges, our interpretation is that Type 3 vegetation is most likely sedges that are more cespitose—producing dense tussocks—while Type 1 vegetation is more likely to be sedges which produce shoots that are more spread apart with longer rhizomes and fewer dense tussocks. Denser tussocks with more frequent shoots may have a higher transpiration demand on the peatland, drawing down the water table, oxygenating the peat below. This is supported by the low $\delta^{15}N$ in Type 3 samples—low $\delta^{15}N$ indicates little denitrification

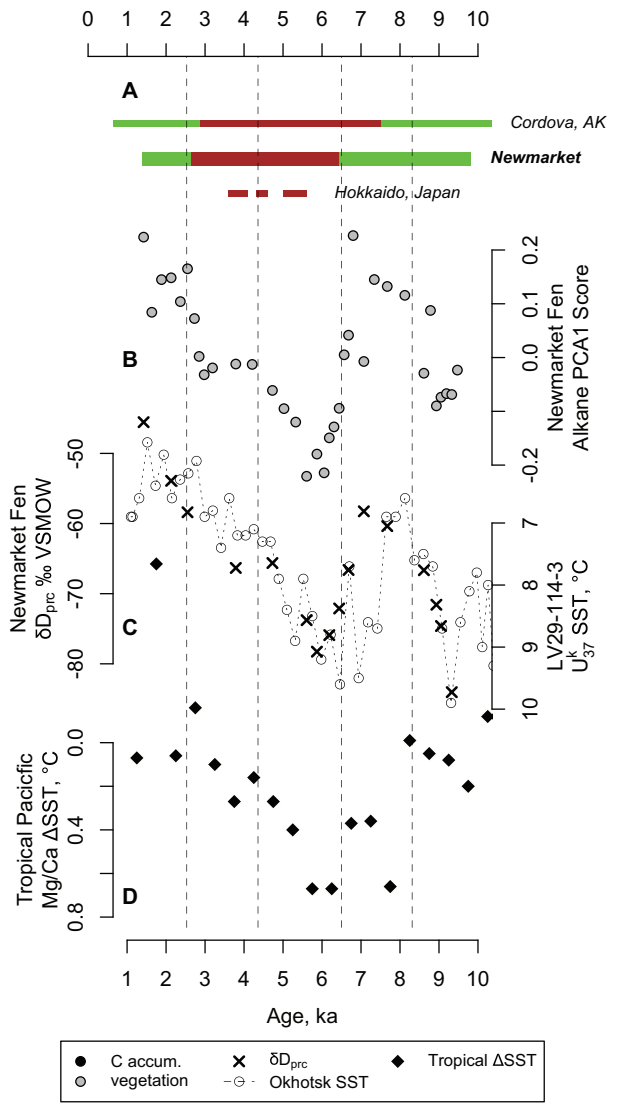

FIGURE 5 | (A): Summary of wet (green) and dry (brown) periods at Newmarket Fen, Alaska (Jones et al., 2009; Nichols et al., 2014; Peteet et al., 2016) and Hokkaido (Ishii et al., 2016, 2017); **(B)** Vegetation change as indicated by the first principal component of leaf wax n-alkane abundances; **(C)** δD of peatland water at Newmarket and alkenone-based SST in the sea of Okhotsk (Max et al., 2012); and **(D)** the tropical SST gradient across the tropical Pacific Ocean based on Mg/Ca SST estimates in the west and east (Koutavas and Joanides, 2012).

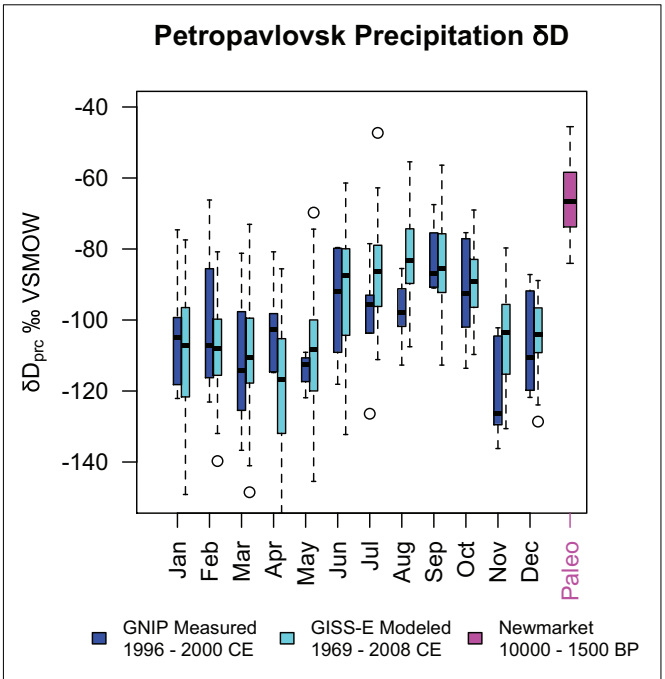

FIGURE 6 | Monthly hydrogen isotopes of precipitation measured at Petropavlovsk-Kamchatsky, modeled by GISS-E and compared with observations (Risi et al., 2012). All reconstructed hydrogen isotope values from Newmarket Fen are shown for comparison.

and dominance of oxic conditions. These oxic conditions likely result in the lower carbon accumulation rates for Type 3 vegetation.

Hydrogen Isotope Ratios of Peatland Water

We used the hydrogen isotope ratios of C_{29} *n*-alkane to estimate the hydrogen isotope ratios of peatland water. Because the vegetation of Newmarket Fen is dominated by sedges (monocotyledons) throughout the stratigraphy, we use a constant lipid-water enrichment factor of 189‰ (Sachse et al., 2012) to estimate peatland water from C_{29} *n*-alkane, which we interpret to be dominated by local precipitation (Sachse et al., 2006; Hou et al., 2008; Nichols et al., 2009, 2014), particularly that which falls during the growing season. Values of precipitation hydrogen isotopes (δD_{prc}) vary between −84.0 and −45.5‰ (**Figure 5**). We find depleted values of δD_{prc} within stratigraphic zones associated with dry, low carbon accumulation conditions in the middle Holocene and vice versa (**Figure 4**). We also find that δD_{prc} corresponds closely with sea surface temperature (SST) in the southeastern Sea of Okhotsk (Max et al., 2012; **Figure 5**).

It is counterintuitive for depleted values of δD_{prc} to correspond with warmer conditions. However, higher SST and overall warmer conditions in the region can increase the length of the growing season, which can allow plants at Newmarket Fen to record δD of peatland water over more of the spring and fall, resulting in a more depleted growing season average δD_{prc} (Nichols et al., 2009). Alternatively, or perhaps in addition, higher SST can also mean reduced sea ice extent in the Sea of Okhotsk. In this case, more Okhotsk moisture could be transported to Newmarket Fen. As this moisture must travel over the central mountain range which runs along the Kamchatka peninsula, Okhotsk-sourced moisture would be more depleted by rainout distillation. There is evidence for reduced sea ice in the Okhotsk during the period of depleted δD_{prc} at Newmarket Fen (Max et al., 2012; Harada et al., 2014).

After about 5 ka, δD_{prc} becomes continuously more enriched, indicating, by our previous interpretation, that climate cooled from 5 to 1.5 ka along with an increase in moisture. Records from elsewhere in Kamchatka support this trend. For example, in central Kamchatka, lake water $\delta^{18}O$ reconstructed from diatom silica was found to decrease from 5 ka to the present along with a decrease in chironomid-inferred temperatures (Meyer et al., 2015). Oxygen isotopes of cellulose in a lake in northern Kamchatka are also depleted beginning at about 5 ka, along with vegetational indicators of cooler climate (Hammarlund et al., 2015).

Variability in sea ice cover in the Okhotsk is also associated with semi-permanent atmospheric pressure systems over the North Pacific. Cooler conditions with increased sea ice cover in the sea of Okhotsk is associated with a weakened or split Aleutian Low (in winter) and strong North Pacific High (in summer) (Rodionov et al., 2007). This weak Aleutian Low can result in reduced storm tracks over the Sea of Okhotsk (Mesquita et al., 2016) and increased southerly flow over eastern Kamchatka (Honda et al., 1999; Rodionov et al., 2007). These atmospheric anomalies would bring more local moisture from Avacha Bay, directly to the south, and the North Pacific in general, resulting in the enriched δD_{prc} we observe in the later Holocene (**Figure 5**).

We also find that the current precipitation δD at the Petropavlovsk-Kamchatsky Global Network for Isotopes in Precipitation (GNIP) monitoring station is depleted relative to the Holocene values that we reconstruct (**Figure 6**) and modeled values (Risi et al., 2012). This can indicate that peatlands in this region are experiencing similar warm, dry conditions today as were associated with carbon loss by increased oxidation in the past.

In addition to the Aleutian Low and North Pacific High, the major control on modern climate in the Pacific is the El Niño-Southern Oscillation (ENSO). The conditions in the tropical Pacific can influence storm tracks and other climatological parameters at higher latitudes (Park et al., 2018). To understand this connection, we compare our records of climate, vegetation and carbon accumulation from Newmarket Fen with the Holocene record of the SST gradient across the tropical Pacific (**Figure 5**). During the middle Holocene, centering on about 6 ka, when conditions at Newmarket are driest and δD_{prc} is most depleted, the SST gradient across the tropical Pacific is steepest, with the warmest west Pacific and coolest eastern Pacific (Koutavas and Joanides, 2012). Such conditions today are associated with an expanded tropical wind belt and contracted northern hemisphere jets (Park et al., 2018). Shifted storm tracks can reduce the amount of moisture received at Newmarket Fen, as flow can become more zonal (Honda et al., 1999; Rodionov et al., 2007; Mesquita et al., 2016). Similar millennial-scale patterns of changing moisture are commonly found in peatlands throughout southern Alaska (**Figure 5**; Jones et al., 2009; Nichols et al., 2014; Peteet et al., 2016), as well as northern Japan (Ishii et al., 2016, 2017), suggesting that a North-Pacific-basin-wide mechanism of hydrological change is plausible. The relationship between precipitation isotopes and tropical SSTs support this hypothesis.

CONCLUSION

Vegetation, hydrology, climate, and carbon accumulation rate are closely linked at Newmarket Fen. We find that under drier, more oxic conditions, the assemblage of sedges growing in the fen favor those more likely to produce C_{33} *n*-alkane and carbon accumulation is reduced, while wetter, less oxic conditions favor a different assemblage of sedges—those more likely to produce C_{29} *n*-alkane—and carbon accumulation is increased. Drier conditions at the site are accompanied by relatively depleted δD of precipitation and warmer SSTs in the Sea of Okhotsk, which we interpret as an increase in moisture originating from the Okhotsk, a more distal air mass, and/or reduced precipitation in the height of the growing season in favor of early and/or late season precipitation. Further, we find that when hydrological conditions are drier and carbon accumulation rate is reduced, the peat becomes more oxygenated, evidenced by a reduction in denitrification. Therefore, we conclude that the low carbon accumulation during the drier interval is primarily due to increased oxidation of organic matter rather than slowed primary production. Several dry millennia within a relatively wet Holocene is similar not only to other sites throughout the Kamchatka peninsula, but also to that found in Alaska and Japan, suggesting that the climate and carbon accumulation around the rim of the North Pacific is linked by a common ocean-atmosphere mechanism, such as the movement of large-scale zonal wind belts.

AUTHOR CONTRIBUTIONS

AA collected and described the sediment core and performed chronostratigraphic analysis. JN, FS, and TO performed the geochemical analyses. DP performed the paleobotanical analyses. JN and DP prepared the manuscript.

FUNDING

The authors would like to acknowledge funding from the United States National Science Foundation (DEB-1557078) in support of JN, the Vetleson Foundation, the Columbia University Center for Climate and Life High School Internship Program which supported JN, and the Lamont-Doherty Earth Observatory Internship Program, which supported FS and TO. The work of AA was partly sponsored by the Russian Government Program of Competitive Growth of Kazan Federal University.

SUPPLEMENTARY MATERIAL

The Supplementary Material for this article can be found online at: https://www.frontiersin.org/articles/10.3389/feart.2019.00106/full#supplementary-material

REFERENCES

Andrén, E., Klimaschewski, A., Self, A. E., Amour, N. S., Andreev, A. A., Bennett, K. D., et al. (2015). Holocene climate and environmental change in north-eastern Kamchatka (Russian Far East), inferred from a multi-proxy study of lake sediments. *Global Planet. Change* 134, 41–54. doi: 10.1016/j.gloplacha.2015.02.013

Bazanova, L. I., Braitseva, O. A., Dirksen, O., Sulerzhitsky, L. D., and Danhara, T. (2005). Ashfalls of the largest holocene eruptions on the Ust Bol'sheretsk–Petropavlovsk Kamchatskii traverse: sources, chronology, and frequency. *Volcanol. Seismol.* 6, 30–46.

Blaauw, M. (2011). Flexible paleoclimate age-depth models using an autoregressive gamma process. *Bayesian Anal.* 6, 457–474. doi: 10.1214/ba/1339616472

Bush, R. T., and McInerney, F. A. (2013). Leaf wax n-alkane distributions in and across modern plants: implications for paleoecology and chemotaxonomy. *Geochim. Cosmochim. Acta* 117, 161–179. doi: 10.1016/j.gca.2013.04.016

Grimm, E. C. (1987). Coniss - a fortran-77 program for stratigraphically constrained cluster-analysis by the method of incremental sum of squares. *Comput. Geosci.* 13, 13–35. doi: 10.1016/0098-3004(87)90022-7

Hammarlund, D., Klimaschewski, A., Amour, N. A. S., Andrén, E., Self, A. E., Solovieva, N., et al. (2015). Global and planetary change. *Global Planet. Change* 134, 91–100. doi: 10.1016/j.gloplacha.2015.04.004

Harada, N., Katsuki, K., Nakagawa, M., Matsumoto, A., Seki, O., Addison, J. A., et al. (2014). Progress in oceanography. *Prog. Oceanogr.* 126, 242–253. doi: 10.1016/j.pocean.2014.04.017

Honda, M., Yamazaki, K., Nakamura, H., and Takeuchi, K. (1999). Dynamic and thermodynamic characteristics of atmospheric response to anomalous sea-ice extent in the sea of Okhotsk. *J. Clim.* 12, 3347–3358. doi: 10.1175/1520-0442(1999)012<3347:datcoa>2.0.co;2

Hou, J., D'Andrea, W., and Huang, Y. (2008). Can sedimentary leaf waxes record D/H ratios of continental precipitation? Field, model, and experimental assessments. *Geochim. Cosmochim. Acta* 72, 3503–3517. doi: 10.1016/j.gca.2008.04.030

Hultén, E. (1971). The plant cover of southern Kamchatka. *Ark. Bot.* 7, 181–257.

Ishii, Y., Hori, K., and Momohara, A. (2017). Global and planetary change. *Global Planet. Change* 153, 1–15. doi: 10.1016/j.gloplacha.2017.04.004

Ishii, Y., Hori, K., Momohara, A., Nakanishi, T., and Hong, W. (2016). Middle to late-Holocene decreased fluvial aggradation and widespread peat initiation in the Ishikari lowland (northern Japan). *Holocene* 26, 1924–1938. doi: 10.1029/2012GL051983

Jones, M. C., Peteet, D. M., Kurdyla, D., and Guilderson, T. (2009). Climate and vegetation history from a 14,000-year peatland record, Kenai Peninsula, Alaska. *Quat. Res.* 72, 207–217. doi: 10.1016/j.yqres.2009.04.002

Koutavas, A., and Joanides, S. (2012). El Niño-southern oscillation extrema in the holocene and last glacial maximum. *Paleoceanography* 27, 1–15. doi: 10.1029/2012PA002378

Loisel, J., van Bellen, S., Pelletier, L., Talbot, J., Hugelius, G., Karran, D., et al. (2017). Earth-science reviews. *Earth Sci. Rev.* 165, 59–80. doi: 10.1016/j.earscirev.2016.12.001

Loisel, J., Yu, Z., Beilman, D. W., Camill, P., Alm, J., Amesbury, M. J., et al. (2014). A database and synthesis of northern peatland soil properties and holocene carbon and nitrogen accumulation. *Holocene* 9, 1028–1042. doi: 10.1177/0959683614538073

Max, L., Riethdorf, J.-R., Tiedemann, R., Smirnova, M., Lembke-Jene, L., Fahl, K., et al. (2012). Sea surface temperature variability and sea-ice extent in the subarctic northwest Pacific during the past 15,000 years. *Paleoceanography* 27:A3213. doi: 10.1029/2012PA002292

Mesquita, M. D. S., Hodges, K. I., Atkinson, D. E., and Bader, J. R. (2016). Sea-ice anomalies in the Sea of Okhotsk and the relationship with storm tracks in the Northern hemisphere during winter. *Tellus A: Dyn. Meteorol. Oceanogr.* 63, 312–323. doi: 10.1029/2006GL026286

Meyer, H., Chapligin, B., Hoff, U., Nazarova, L., and Diekmann, B. (2015). Oxygen isotope composition of diatoms as late holocene climate proxy at two-yurts lake, Central Kamchatka, Russia. *Global Planet. Change* 134, 118–128. doi: 10.1016/j.gloplacha.2014.04.008

Meyers, P. (1994). Preservation of elemental and isotopic source identification of sedimentary organic-matter. *Chem. Geol.* 114, 289–302. doi: 10.1016/0009-2541(94)90059-0

Nichols, J., Peteet, D. M., Moy, C. M., Castaneda, I. S., McGeachy, A., and Perez, M. (2014). Impacts of climate and vegetation change on carbon accumulation in a south-central Alaskan peatland assessed with novel organic geochemical techniques. *Holocene* 24, 1146–1155. doi: 10.1177/0959683614540729

Nichols, J., Walcott, M., Bradley, R., Pilcher, J., and Huang, Y. (2009). Quantitative assessment of precipitation seasonality and summer surface wetness using ombrotrophic sediments from an Arctic Norwegian peatland. *Quat. Res.* 72, 443–451. doi: 10.1016/j.yqres.2009.07.007

Park, Y.-H., Kim, B.-M., Pak, G., Yamamoto, M., Vivier, F., and Durand, I. (2018). A key process of the nonstationary relationship between ENSO and the Western Pacific teleconnection pattern. *Sci. Rep.* 8, 1–13. doi: 10.1038/s41598-018-27906-z

Peteet, D. M., Nichols, J., Moy, C. M., McGeachy, A., and Perez, M. (2016). Recent and holocene climate change controls on vegetation and carbon accumulation in Alaskan coastal muskegs. *Quat. Sci. Rev.* 131, 168–178. doi: 10.1016/j.quascirev.2015.10.032

Risi, C., Noone, D., Worden, J., Frankenberg, C., Stiller, G., Kiefer, M., et al. (2012). Process-evaluation of tropospheric humidity simulated by general circulation models using water vapor isotopologues: 1. Comparison between models and observations. *J. Geophys. Res.* 117:D05303. doi: 10.1029/2011JD016621

Rodionov, S. N., Bond, N. A., and Overland, J. E. (2007). The Aleutian Low, storm tracks, and winter climate variability in the Bering Sea. *Deep Sea Res. Part II Top. Stud. Oceanogr.* 54, 2560–2577. doi: 10.1016/j.dsr2.2007.08.002

Sachse, D., Billault, I., Bowen, G. J., Chikaraishi, Y., Dawson, T. E., Feakins, S. J., et al. (2012). Molecular paleohydrology: interpreting the hydrogen-isotopic composition of lipid biomarkers from photosynthesizing organisms. *Annu. Rev. Earth Planet. Sci.* 40, 221–249. doi: 10.1146/annurev-earth-042711-105535

Sachse, D., Radke, J., and Gleixner, G. (2006). δD values of individual n-alkanes from terrestrial plants along a climatic gradient – Implications for the sedimentary biomarker record. *Org. Geochem.* 37, 469–483. doi: 10.1016/j.orggeochem.2005.12.003

Solovieva, N., Klimaschewski, A., Self, A. E., Jones, V. J., Andrén, E., Andreev, A. A., et al. (2015). The Holocene environmental history of a small coastal lake on the north-eastern Kamchatka Peninsula. *Global Planet. Change* 134, 55–66. doi: 10.1016/j.gloplacha.2015.06.010

Treat, C. C., Jones, M. C., Camill, P., Gallego-Sala, A., Garneau, M., Harden, J. W., et al. (2016). Effects of permafrost aggradation on peat properties as determined from a pan-Arctic synthesis of plant macrofossils. *J. Geophys. Res. Biogeosci.* 121, 78–94. doi: 10.1002/2015JG003061

Turetsky, M. R., Benscoter, B., Page, S., Rein, G., van der Werf, G. R., and Watts, A. (2015). Global vulnerability of peatlands to fire andcarbon loss. *Nat. Geosci.* 8, 11–14. doi: 10.1038/ngeo2325

Zakharikhina, L. V. (2014). The rate of peat accumulation in the Holocene in Kamchatka. *Eurasian Soil Sci.* 47, 556–561. doi: 10.1134/S106422931406012X

Conflict of Interest Statement: The authors declare that the research was conducted in the absence of any commercial or financial relationships that could be construed as a potential conflict of interest.

frontiers in Earth Science

ORIGINAL RESEARCH
published: 29 May 2019
doi: 10.3389/feart.2019.00113

Variability in Shelf Sedimentation in Response to Fluvial Sediment Supply and Coastal Erosion Over the Past 1,000 Years in Monterey Bay, CA, United States

Joseph Carlin[1], Jason Addison[2], Amy Wagner[3], Valerie Schwartz[2], Jamie Hayward[1] and Victoria Severin[1]*

[1] Department of Geological Sciences, California State University, Fullerton, Fullerton, CA, United States, [2] U.S. Geological Survey, Geology, Minerals, Energy, and Geophysics Science Center, Menlo Park, CA, United States, [3] Department of Geological Science, California State University, Sacramento, Sacramento, CA, United States

OPEN ACCESS

Edited by:
Dorothy M. Peteet, Goddard Institute for Space Studies (NASA), United States

Reviewed by:
Fabio Matano, Italian National Research Council (CNR), Italy
Michel Michaelovitch Mahiques, University of São Paulo, Brazil

****Correspondence:***
Joseph Carlin
jcarlin@fullerton.edu

Specialty section:
This article was submitted to Quaternary Science, Geomorphology and Paleoenvironment, a section of the journal Frontiers in Earth Science

Received: *01 October 2018*
Accepted: *30 April 2019*
Published: *29 May 2019*

Citation:
Carlin J, Addison J, Wagner A, Schwartz V, Hayward J and Severin V (2019) Variability in Shelf Sedimentation in Response to Fluvial Sediment Supply and Coastal Erosion Over the Past 1,000 Years in Monterey Bay, CA, United States. Front. Earth Sci. 7:113. doi: 10.3389/feart.2019.00113

Continental shelf environments are uniquely situated to capture some of the most dynamic processes on Earth including climatic variability and anthropogenic modifications to coastal systems. Understanding how these processes have affected sediment delivery and accumulation on the shelf in the past may provide insight into potential changes in the future. To address this, we investigated shelf sedimentation within Monterey Bay, California. Sediment cores were collected from four locations throughout the bay to capture both the modern and late Holocene sedimentological record using grain size analysis, and sediment chronologies determined from ^{210}Pb, ^{137}Cs, and ^{14}C. From the grain size results we focused on the total percent sand, and established a Littoral Sand Fraction (LSF) index to assess sediment contribution from the littoral zone as a result coastal erosion. Grain size results from the multicores consistently showed an increase in sand over the past several decades (post 1970s). For the cores located within the bay proximal to three major rivers, the increase in sand corresponded to a general increase in the LSF over the same period. We attributed these trends to increased sediment contributions to the shelf due to accelerated coastal erosion in the region. This accelerated coastal erosion was likely the combined result of dam construction in the mid-twentieth century that limited fluvial supply to the coast, and a shift in climate toward wetter, stormier period. Applying these sediment characteristics back over the past ∼1,000 years we found that dry climatic periods resulted in deposits that were limited in total sand but enriched in littoral material suggesting elevated coastal erosion. During wet periods deposits were enriched in total sand but limited in littoral sand suggesting elevated fluvial supply and low erosion. Compared to the late Holocene record, the previous several decades represent a shift to a new regime, uncharacteristic of deposits over the past millennia, highlighting the impact humans have had on shelf sedimentation.

Keywords: shelf sedimentation, littoral sand, coastal erosion, dams,climate, grain size, Monterey Bay, California

INTRODUCTION

Continental shelf stratigraphy integrates both terrestrial and marine process (Nittrouer, 1999). Typically, terrestrial sediment is supplied to the shelf by rivers, and often progresses through subsequent stages of deposition, remobilization from waves and currents, and redeposition before ultimate burial (Wright and Nittrouer, 1995). Mid-shelf areas specifically, are uniquely situated to be the ultimate sink for this terrestrially derived sediment that is subsequently modified by marine processes (e.g., Traykovski et al., 2000; Puig et al., 2001). Thus, once buried, these deposits maintain evidence of both the terrestrial processes that influenced sediment delivery, and marine processes that controlled secondary transport and deposition.

This combined terrestrial and marine influence is common across a variety of shelf settings. For example, along the Mississippi River margin in the northern Gulf of Mexico, fluvial flood deposits are initially constrained within the innershelf until increased wave energy during winter months remobilizes that sediment across the shelf (Corbett et al., 2004). Therefore, these mid-shelf deposits are dependent on both the fluvial supply from land and subsequent wave conditions (Corbett et al., 2007). This process is not always so stepwise (e.g., initial flood deposit followed later by wave remobilization), rather along some shelves the supply from flood and wave remobilization can occur almost simultaneously. For example, in the Adriatic Sea, floods within the small mountainous rivers draining the Apennine Mountains often correspond to energetic ocean conditions resulting in terrestrial sediment dispersal over greater distances, and the formation of a shelf clinoform with major depocenters disconnected from fluvial sources (Palinkas and Nittrouer, 2006; Palinkas, 2009). Thus, while shelf deposits are influenced by both terrestrial (flood) and marine (wave) processes, for shelves fed by small mountainous rivers these processes are often driven by the same storm event.

In the northeastern Pacific Ocean many continental shelves share similarities with the Apennine margin. Small mountainous rivers debouch into the ocean with high sediment loads during floods that correspond to energetic ocean conditions (Kniskern et al., 2011; Odigie and Warrick, 2017). The Eel River margin in northern California in particular has been extensively studied, highlighting the processes and the depositional characteristics that result from flood and energetic ocean coherence (e.g., Wheatcroft et al., 1997; Traykovski et al., 2000; Wheatcroft and Borgeld, 2000; Harris et al., 2005).

In central and southern California, the coastal ocean and watersheds can be subjected to more extreme conditions than the Eel River watershed and margin, as prolonged dry conditions are interrupted by extremely wet periods as a result of atmospheric rivers (Dettinger et al., 2011; Dettinger and Ingram, 2013) or El Niño events (Inman and Jenkins, 1999; Farnsworth and Milliman, 2003; Warrick and Farnsworth, 2009). For both atmospheric river and El Niño events, coherence between floods and energetic ocean conditions are common, such that the resulting damage from these extreme events is not just flooding, but coastal erosional as well (e.g., Storlazzi and Griggs, 2000; Sallenger et al., 2002; Barnard et al., 2011; Reynolds et al., 2018). In the case of El Niño events specifically, high precipitation and fluvial floods do not always accompany the elevated wave conditions driving coastal erosion, as was the case in southern California during the 2015–2016 El Niño (Barnard et al., 2017).

For regions like central and southern California where the climate is dynamic and extreme, sediment delivery to the shelf is a function of both the runoff on land and the remobilization from waves along the coast and innershelf areas. It is important therefore, to determine how sedimentation changes during stormy periods when runoff and wave activity are high. Further, it is important to know how shelf sedimentation changes when runoff is low, but wave activity might still be high, like during the 2015–2016 El Niño. Moreover, to better understand the potential future variability in the system with respect to climate change, we must determine what impact human modifications of drainage systems (e.g., dams) have on shelf sedimentation. These modifications have essentially limited runoff but left wave activity (and other coastal processes) largely unaffected. Given these knowledge gaps, the goal of this study was to characterize variability in shelf sedimentation over decadal to centennial time scales. In particular, we were interested in changes in sediment sources and delivery as related to climatic cycles over the late Holocene, and more recent human activity.

To accomplish this goal, we focused on the Monterey Bay continental shelf along the central California coast. Monterey Bay experiences dynamic ocean conditions including wave heights that can exceed 8 m during the winter from the North Pacific, very long period (>20 s) waves from the Southern Ocean during summer, and local wind waves from storms (Storlazzi and Field, 2000). Additionally, the region is subjected to both the net southward flowing California Current, and northward flowing Davidson Current (Griggs, 1974; Huyer et al., 1998), the latter of which dominantly drives fine-grain sediment transport along the mid-shelf (Eittreim et al., 2002; Xu et al., 2002). Terrestrial sediment is supplied to the system predominantly from three rivers, and to a lesser extend from smaller creeks and cliff erosion (Eittreim et al., 2002; Xu et al., 2002). The largest sediment supply is from the Salinas River, which like the Eel River in northern California, can deliver extreme sediment discharges to the ocean during flood events (Farnsworth and Milliman, 2003). These extreme fluvial discharges and dynamic ocean conditions are influenced by larger Pacific Ocean cycles such as El Niño Southern Oscillation (ENSO), Pacific Decadal Oscillation (PDO), and North Pacific Gyre Oscillation (NPGO) (Storlazzi and Griggs, 2000; Schwing et al., 2002; Di Lorenzo et al., 2008; Storlazzi and Reid, 2010; Chenillat et al., 2012; Jacox et al., 2014). From this study we hope to demonstrate the usefulness of physical sediment characteristics on the shelf in distinguishing past changes in terrestrial sediment fluxes to the ocean, and the impact humans have had on the system.

MATERIALS AND METHODS

Sediment Core Collection and Ancillary Analyses

Five sediment cores from 4 locations were collected from throughout Monterey Bay in 2014 on the R/V Point Sur and 2017 on the R/V Shana Rae (**Figure 1**). Cores PS1410-04MC (37.046530°N, 122.404000°W, 100 m water depth) and PS1410-11MC (36.837017°N, 121.882150°W, 63 m water depth) are multicores (∼30 cm long) collected in 2014 using the R/V *Point Sur*. The site of PS1410-04MC is located north of Monterey Bay proper, seaward of Point Ano Nuevo, near the head of Ascension Canyon. The site of PS1410-11MC is located in central Monterey Bay, north of the Monterey Submarine Canyon, proximal to the present-day mouth of the Pajaro River. During this same cruise we also collected an ∼86 cm long gravity core, PS1410-08GC (36.701600°N, 121.905040°W, 85 m water depth) from southern Monterey Bay. In 2017 two additional multicores were collected using the R/V *Shana Rae*. The site of SR1707-07MC (36.873000°N, 122.034840°W, 69 m water depth) is located along the northern Monterey Bay shelf, approximately seaward of the city of Santa Cruz, CA. SR1707-02MC was collected from the same location (within 10 m) as PS1410-08GC from 2014. This core was specifically collected to overlap with the gravity core PS1410-08GC, providing intact surface intervals that may have been disturbed in the gravity corer during retrieval.

For all the multicore sites, four sub-cores were simultaneously collected. The analysis assignment to each of the collected cores were as follows; one was reserved for non-destructive analyses such as multi-sensor core logging, and 3D computed tomography (CT) imaging (the results of these analyses will not be discussed in detail), one was designated for ^{210}Pb and ^{137}Cs analyses, one was utilized for grain size analysis, and one was designated as an archive, or used for analyses not associated with this study.

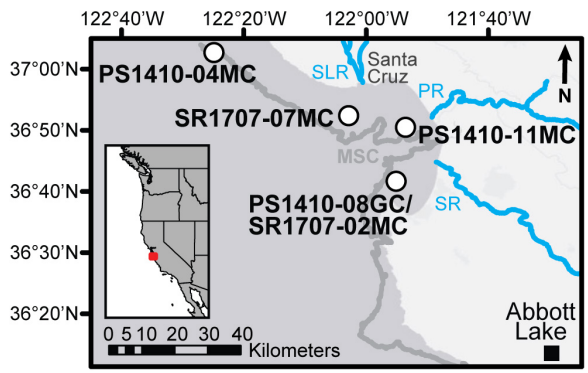

FIGURE 1 | Map of the Monterey Bay study area. Core locations are shown as white dots, note that PS1410-08GC and SR1707-02MC were collected from the same location. The three major rivers draining into Monterey Bay (SLR – San Lorenzo River, PR – Pajaro River, and SR – Salinas River) are shown in blue. The 100 m isobath offshore is shown with the gray line, along with the location of the Monterey Submarine Canyon (MSC). The black square shows the location of Abbott Lake within the Salinas River watershed from which a regional hydroclimate record was utilized (Hiner et al., 2016).

For the gravity core, all logging, imaging, and analyses were performed on the same core. Multi-sensor core logging was performed on intact, full-round cores for the entire length of the core, at a 1 cm sampling interval using a GeoTek Multi-Sensor Core Logger (MSCL-S). For this study, only the gamma-ray wet bulk density data was used for PS1410-08GC to relate to the CT imagery. The CT imaging was performed on split, half-rounds for cores PS1410-04MC, PS1410-11MC, and PS1410-08GC, and on intact, full-round cores for SR1707-07MC, and SR1707-02MC using a GE LightSpeed Ultra medical CT scanner with a source radiation of 140 kV and 120 mA; the analysis was conducted in the SUPRI-A Lab at Stanford University. For PS1410-11MC, CT slices were taken every 1.25 mm for the length of the core, while for all other cores the slices were taken every 2.5 mm for the length of the core. All CT measurements are expressed as Hounsfield units, which is a measure of a material's bulk radiodensity relative to that of water. CT image processing was performed using ImageJ software (Abràmoff et al., 2004). The CT images were used to assess sedimentary fabric throughout the cores.

Grain Size Analysis

Particle size distributions were measured on 1 cm contiguous intervals for the full length of all cores. Approximately 0.5 g of wet sediment was used for analysis. Each sample was pretreated with 30–90 ml of 30% H_2O_2 to remove organic matter, 10 ml of 1 M HCl to remove carbonates, and 10 ml of 1 M NaOH to remove biogenic silica. These pretreatments ensured that the subsequent grain size measurement reflects the particle size distribution of the lithogenic fraction only. Each sample was measured via laser diffraction using a Malvern Mastersizer 2000. Quality control for the instrument was routinely assessed by measuring a 1–16 μm tuff or silica carbide standard at the start of each daily measurement batch, after every 10th sample analyzed, and at the end of each measurement day.

Geochronology

Modern sediment ages were determined from ^{210}Pb and ^{137}Cs geochronologies. Core PS1410-11MC was subsampled into 0.5 cm intervals for the upper 20 cm of the core, and 1 cm intervals below 20 cm. PS1410-04MC was subsampled in 1 cm intervals throughout the whole length of the core, and cores SR1707-07MC and SR1707-02MC were both subsampled in 1 cm intervals for the upper 10 cm of the core and 2 cm intervals below 10 cm. The variability in subsampling was due to instrument demand over the study period, where times of low demand allowed for higher resolution subsampling. Each subsample was dried overnight in an 80°C oven, ground into a fine powder, and packed into petri dishes. Each dish was sealed and incubated for at least 20 days to ensure secular equilibrium ^{226}Ra (supported ^{210}Pb) and the measured daughter isotopes (^{214}Pb and ^{214}Bi) (Goodbred and Kuehl, 1998).

All subsamples were counted for at least 24 h on a High-Purity Broad Energy Germanium Gamma Detector (BE3825, Canberra Industries Inc.) with a multi-channel analyzer (DSA-LX, Canberra Industries Inc.). The activity of total ^{210}Pb was determined from the energy peak at 46.5 keV, with supported

^{210}Pb determine by averaging the activities of the ^{214}Pb peaks (295 keV and 351.9 keV) and the ^{214}Bi peak (609 keV). Excess ^{210}Pb ($^{210}Pb_{xs}$) was calculated for each sample by subtracting the measured supported ^{210}Pb from the measured total ^{210}Pb. All $^{210}Pb_{xs}$ activities were corrected for self-absorption following the methods of Cutshall et al. (1983). The activity of ^{137}Cs was also determined for all samples from the energy peak at 661 keV. All radioisotope activities were decay-corrected to the date when the core was collected, and all errors were propagated from counting statistics.

Sediment cores SR1707-02MC and PS1410-08GC were located within 10 m of one another and were spliced together to create a composite record using the co-occurrence of a low-density bed identified in the CT scan results for the two cores (**Figure 2A**). An age-depth model for the composite depth scale was determined by combining the core-top ages of collection for both cores, the excess ^{210}Pb geochronology results from SR1707-02MC (see section "SR1707-02MC"), and four AMS ^{14}C benthic foraminifera dates from PS1410-08GC (**Table 1**). For this study, since both cores were collected from the shallow continental shelf (85 m water depth) region of Monterey Bay, we explicitly assume benthic foram dates are equivalent to planktic foram dates. The AMS ^{14}C samples were manually calibrated using CALIB (v.7.0.4; Reimer et al., 2013) with the MARINE13 curve (Stuiver and Reimer, 1993) using a marine reservoir correction of $\Delta R = 280 \pm 50$ years. Age-depth modeling was performed using CLAM (v.2.2; Blaauw, 2010), and was programmed to use the 2σ calibration range of each date with weighting by calibrated probabilities, 100,000 Monte Carlo-style iterations, and calendar age-point estimates for depths were based on the weighted average of all non-reversing age-depth curves.

RESULTS

PS1410-04MC

PS1410-04MC was the only core located outside of Monterey Bay proper along the open coast north of the bay near Pt. Ano Nuevo

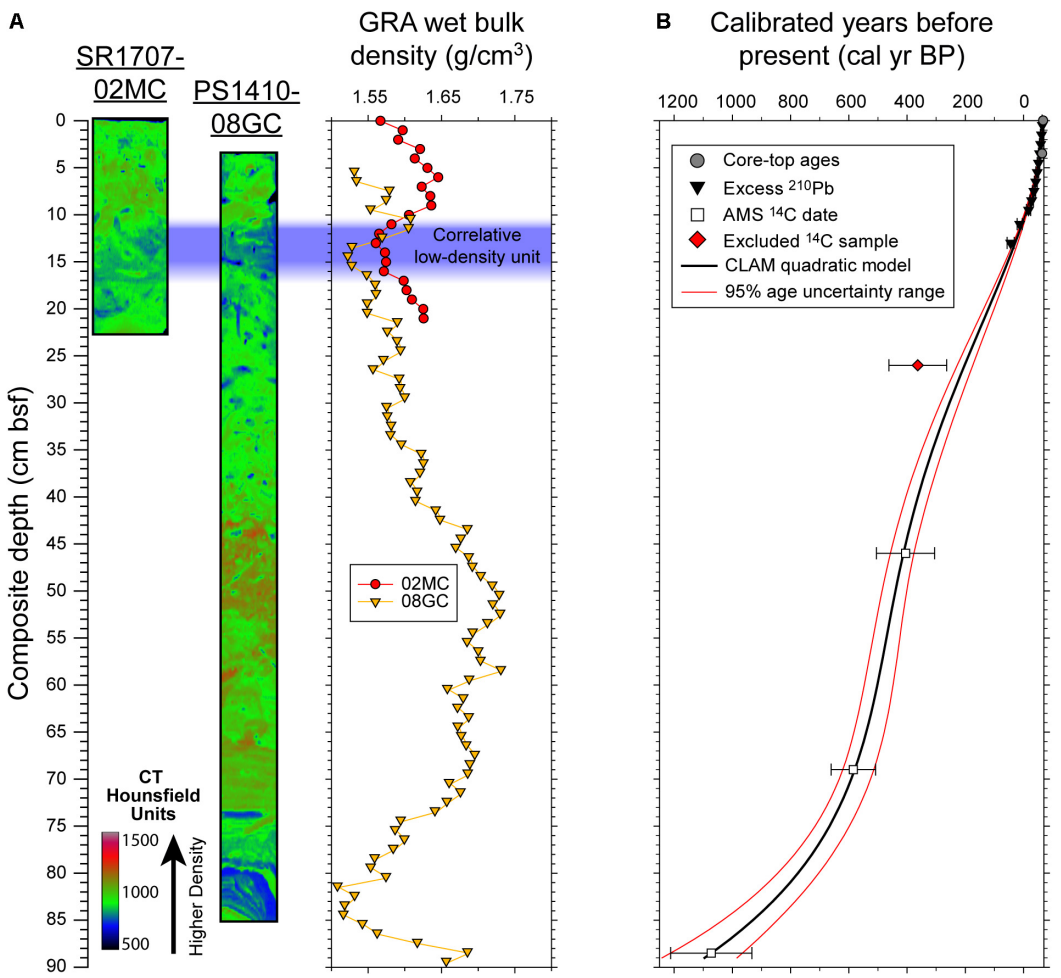

FIGURE 2 | (A) Stratigraphic correlation of SR1707-02MC and PS1410-08GC using CT imaging and GRA wet bulk density. The presence of a low-density horizon allows for the alignment of 08GC to the 02MC datum. **(B)** CLAM quadratic regression age model and 95% uncertainty range. Ages are expressed as years Before Present (BP) where "present" is referenced to 1950 CE.

TABLE 1 | Radiocarbon samples for PS1410-08GC.

AMS sample ID	Depth interval	Composite depth (midpoint; cm bsf)*	Sample type	14C age (yrs BP)	Error	Calibrated age (cal yrs BP)	2-sigma uncertainty	AMS laboratory
203022	34–37 cm	26	Benthic foram (mixed)	990	20	363	99	UCI
203023	54–57 cm	46	Benthic foram (mixed)	1070	20	405	100	UCI
203024	77–80 cm	69	Benthic foram (mixed)	1285	15	584.5	76.5	UCI
175483	96.5–99.5 cm	88.5	Benthic foram (mixed)	1795	35	1072.5	139.5	LLNL-CAMS

**Minus 13 cm to account for foam at the top of PS1410-08GC, plus a 3.5 cm offset to align PS1410-08GC with SR1707-02MC datum horizon (see text for details). UCI, W. M. Keck Carbon Cycle AMS Laboratory at the Univ. of California – Irvine. LLNL-CAMS, Lawrence– Livermore National Laboratory Center for Accelerator Mass Spectrometry.*

(**Figure 1**). The results for PS1410-04MC are shown in **Figure 3**. PS1410-04MC is 35 cm long and the CT image (**Figure 3A**) shows the core is generally well-mixed, with an indistinct mottled texture and few discernable sedimentary structures. There is one large, low-density, distinct mottle spanning depths from ∼20–33 cm. Results from the grain size analyses are shown in **Figures 3B–I**. **Figure 3B** shows the full particle size distributions for all samples down core. From this data we see that most of the

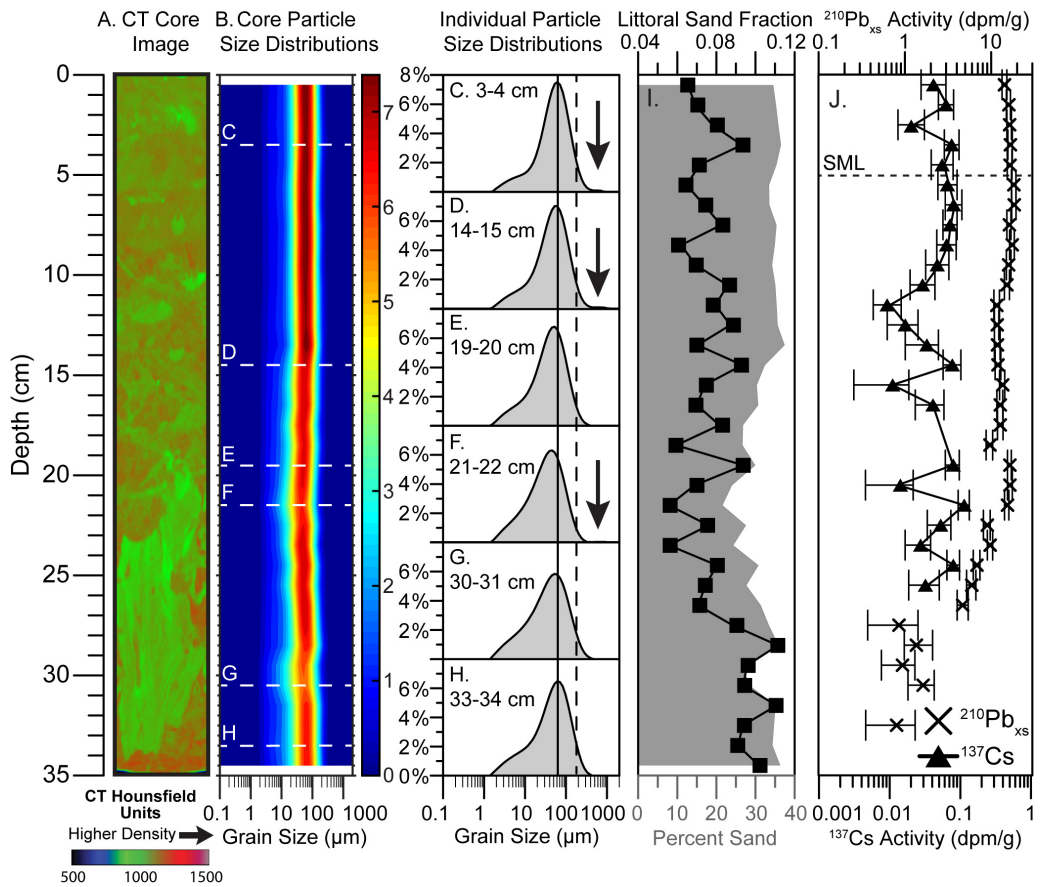

FIGURE 3 | Results from PS1410-04MC (see **Figure 1** for location). **(A)** CT image of the core where cooler colors (blues and greens) are relatively lower density deposits, and warmer colors (reds) are higher density. **(B)** Down core total grain size distribution for all samples. In this plot the y-axis is depth down the core, x-axis is particle size, and the colors represent the volume present of the sample that fall within those size classifications, where warmer colors are higher percentages and cooler colors are lower percentages. The warmest color region across any depth horizon represents the mode for the sample. Representative individual sample particle size distributions (PSD) are shown in **(C–H)**, where the depths of these PSD are highlighted in **(B)** as white dashed lines. The solid black vertical line in **(C–H)** notes the silt/sand boundary at 63 μm and the dashed black vertical line notes the Monterey Bay littoral cutoff diameter at 180 μm (see text for explanation). Black arrows in the plot point to samples with increases in material coarser than the littoral cutoff diameter. The raw measurement size bins for the instrument were used to create the distributions in **(B–H)**. **(I)** Down core results from the grain size analysis with total percent sand (gray area) and the littoral sand fraction (black squares – see text for explanation). **(J)** Down core results for the $^{210}Pb_{xs}$ (black Xs) and ^{137}Cs (black triangles). The dashed horizontal line is the inferred depth of the Surface Mixed Layer (SML) based on the $^{210}Pb_{xs}$ results.

sediment falls between ∼20–200 μm, and the distributions are generally consistent up core. There are two noticeably finer layers around 30 cm and 20 cm, while above 14 cm there are tighter distributions centered around ∼60 μm marked by values >7% (darker red colors) in **Figure 3B**.

Figures 3C–H pull out representative samples from the overall core data to show individual sample particle size distributions (PSD). From these individual PSD we can see that the samples in the upper 14 cm (**Figures 3C,D**) with the observed tighter distributions have high, narrow peaks with the primary mode near the 63 μm silt/sand boundary, and a relatively smaller contribution in the fine silt and clay portion of the distribution below ∼20 μm. By contrast the finer layers (**Figures 3F,G**), show relative increases in the below ∼20 μm region. While the 30–31 cm sample (**Figure 3G**) has a mode that is still near the silt/sand boundary, the mode for the 21–22 cm sample (**Figure 3F**) by contrast is shifted to the left and clearly finer than the silt/sand boundary. Interestingly, in **Figures 3C,D,F** the PSD show a very coarse tail (noted by the black arrows, it may be difficult to see in 3F given the way that this figure laid out) where there is a small sub-population of grains coarser than ∼300 μm.

In **Figure 3I** we have plotted the total sand content (gray shaded) and the Littoral Sand Fraction (discussed in detail below). The total sand ranges between 20–40% throughout the core, and typically ∼35%. For the identified finer layer around 30 cm the total sand content dips to <30%, down from 35%. Around 20 cm is the lowest sand content at ∼20%, part of a broader decrease of sand up core beginning around 25 cm. Above 20 cm the sand then increases back up to ∼35% at a depth of 15 cm.

The $^{210}Pb_{xs}$ and ^{137}Cs results are shown in **Figure 3J**. Overall, the $^{210}Pb_{xs}$ profile exhibits characteristics of both steady-state accumulation and non-steady-state accumulation. From the $^{210}Pb_{xs}$ data we estimate that the surface mixed layer (SML) extends down to ∼5 cm based on the near uniform activity with depth. Below the SML down to ∼10 cm the activity decreases with depth at relatively steep slope. From 10 cm down to ∼20 cm the activity is generally uniform to slightly increasing with depth. Below this section, activities again decrease with depth, although at a noticeably lower slope than above. From ∼25 cm to 32 cm in the core the activities are low (∼1 dpm/g), and generally decrease with depth with some fluctuations. No $^{210}Pb_{xs}$ was detected below 33 cm.

For ^{137}Cs, activities vary between ∼0.01–0.1 dpm/g. There is no clear peak, the highest activities (0.11 ± 0.02 dpm/g) were measured at 22 cm, with comparable values at 15 cm and 25 cm (0.08 ± 0.02 dpm/g for both). The maximum penetration of ^{137}Cs was 26 cm, which after adjusting for the SML thickness, would place the 1954 CE first-occurrence horizon at a depth of 21 cm.

SR1707-07MC

The results from SR1707-07MC are shown in **Figure 4**. This core serves as our northern Monterey Bay representative sample, and the sample closest to the mouth of the San Lorenzo River, which has the 3rd largest sediment input to the bay (Eittreim et al., 2002). Core SR1707-07MC is 17 cm long and lacks any bedding or layers. Rather, the core consists of indistinct mottling throughout (**Figure 4A**). Grain size results show the core is comprised of sandy-mud, with an overall relatively consistent PSD throughout the core (**Figure 4B**). In this core most particles fall between ∼30–150 μm. In the upper ∼6 cm of the core there is tighter distribution (values >8%, marked by dark red colors in **Figure 4B**) similar to what was observed in PS1410-04MC.

From the individual PSD (**Figures 4C–H**) the shapes are comparable between all samples with modes proximal to the silt/sand boundary. The sample from 2–3 cm (**Figure 4C**) has a high, narrow peak with smaller contributions from the fine silt and clay sub-populations. This translates into the tight distribution and dark red colors noted in **Figure 4B**. For the other PSD shown there is a relative increase in the finer fractions (slightly less so at 10–12 cm in **Figure 4F**), but the mode for all samples remains relatively consistent. In **Figures 4D,F,G** we also observed the coarser sub-populations in the core (noted by the black arrow). As with PS1410-04MC, these sub-populations are coarser than ∼300 μm, but in this core these coarse tails are more clearly visible in the plots, and for the sample at 8–9 cm (**Figure 4D**) actually appear detached from full distribution curve.

For the total sand content (**Figure 4I**), the values are consistently ∼30% throughout the core. Total sand is slightly higher between 10–16 cm, closer to ∼35%. The total sand content is lowest between 7–9 cm, although this decrease is only slightly noticeable.

Both $^{210}Pb_{xs}$ and ^{137}Cs were detected through the base of this short core (**Figure 4J**), suggesting that all deposits are at least younger than 1954 CE. Uniform activity with depth in the $^{210}Pb_{xs}$ profile places the base of the SML at a depth of 6 cm. Below the SML the $^{210}Pb_{xs}$ decreases with depth suggesting relatively steady-state accumulation.

PS1410-11MC

PS1410-11MC was collected from central Monterey Bay, proximal to the mouth of the Pajaro River, which is the second largest sediment input to the bay (Eittreim et al., 2002). The core is 32 cm long and contains variable sedimentary fabric throughout. From the CT image in **Figure 5A**, the upper ∼7 cm are indistinctly mottled, dominated by low-density mottles. From ∼7–17 cm higher-density mottles are more common. Core depths between ∼17–20 cm contain thin (sub-centimeter), regular, tabular, and lenticular layers. At a depth of 21 cm, there are three large (centimeter-scale) layers that extend down to ∼25 cm. The uppermost layer is relatively low-density, ∼3 cm thick, with a sharp upper contact, and slightly modified to diffuse lower contact. Below is a ∼1 cm thick relatively high-density layer with a sharp lower contact into a ∼2 cm low-density layer. This lowermost layer has an irregular lower contact that appears as if a large mottle has intruded from below into this distinct layer. Below 25 cm the core again is indistinctly mottled, dominated by lower-density sediment.

This variability in sedimentary fabric corresponds to variability in sediment texture as well. From **Figure 5B** the base of the core is characterized by a fining upward sequence between 23–32 cm, although in a more stairstep-like fashion, as the dominant size class fine from ∼20–100 to ∼10–60 μm. In this

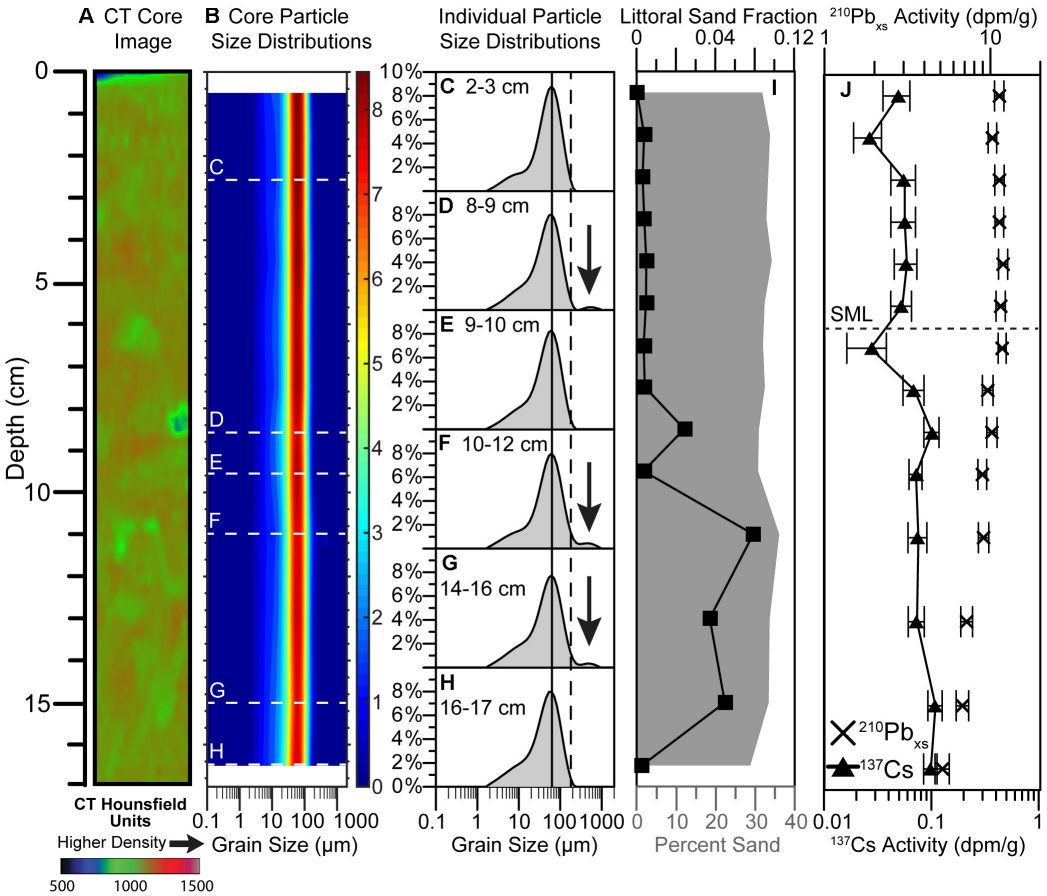

FIGURE 4 | Results from SR1707-07MC (see **Figure 1** for location). **(A)** CT image of the core where cooler colors (blues and greens) are relatively lower density deposits, and warmer colors (reds) are higher density. **(B)** Down core total grain size distribution for all samples. In this plot the y-axis is depth down the core, x-axis is particle size, and the colors represent the volume present of the sample that fall within those size classifications, where warmer colors are higher percentages and cooler colors are lower percentages. The warmest color region across any depth horizon represents the mode for the sample. Representative individual sample particle size distributions (PSD) are shown in **(C–H)**, where the depths of these PSD are highlighted in **(B)** as white dashed lines. The solid black vertical line in **(C–H)** notes the silt/sand boundary at 63 μm and the dashed black vertical line notes the Monterey Bay littoral cutoff diameter at 180 μm (see text for explanation). Black arrows in the plot point to samples with increases in material coarser than the littoral cutoff diameter. The raw measurement size bins for the instrument were used to create the distributions in **(B–H)**. **(I)** Down core results from the grain size analysis with total percent sand (gray area) and the littoral sand fraction (black squares – see text for explanation). **(J)** Down core results for the $^{210}Pb_{xs}$ (black Xs) and ^{137}Cs (black triangles). The dashed horizontal line is the inferred depth of the Surface Mixed Layer (SML) based on the $^{210}Pb_{xs}$ results. Both $^{210}Pb_{xs}$ and ^{137}Cs were detected at the base of this core.

section of the core we do not observe any values >7% (red colors in **Figure 5B**), suggesting wider distributions of grain sizes. Above this section, from ∼13 to 23 cm, the sediment coarsens, marked by a relatively abrupt shift at ∼22 cm, and there is a tighter distribution generally spanning from ∼30 to 100 μm, with values >9% indicating more prominent peaks in the PSD. Above 13 cm to the top of the core, there is an overall gradual coarsening, although with a slightly finer layer ∼9 cm. The uppermost 4 cm show values >7–8% (orange and red-orange colors) suggesting increases in the mode within the distributions.

Unlike the previously discussed cores, the individual PSD for PS1410-11MC are characterized by a variety of shapes (**Figures 5C–H**). In the lowermost section that was described as fining upward, the PSD show relatively broad distributions with modes clearly finer than the silt/sand boundary (**Figures 5G,H**). For these two representative PSD the modes fall between ∼10 and 30 μm. The overlying section is illustrated by the sample from 14 to 15 cm (**Figure 5F**) that shows a shift in mode to the right, closer to but still finer than the silt/sand boundary. This distribution has a high, narrow peak with a small secondary broad peak within the clay to fine silt portion. For the samples above 14 cm (**Figures 5C–E**) the PSD show the coarsening upward sequence as the modes shift to the silt/sand boundary, although the relatively finer layer at 9 cm is shown in **Figure 5D** with the mode shifted back slightly to the left. As with the other cores, the coarse tail is present in **Figures 5C,E,H**, where for these uppermost samples this very coarse sub-population (>300 μm) appears detached from the larger distributions.

The total sand content also fluctuates throughout the core (**Figure 5I**). From the base of the core up to ∼23 cm, total sand content decreases from ∼35 to ∼5%. There is a sandier section above this from ∼15 to 23 cm where the total sand is between ∼20

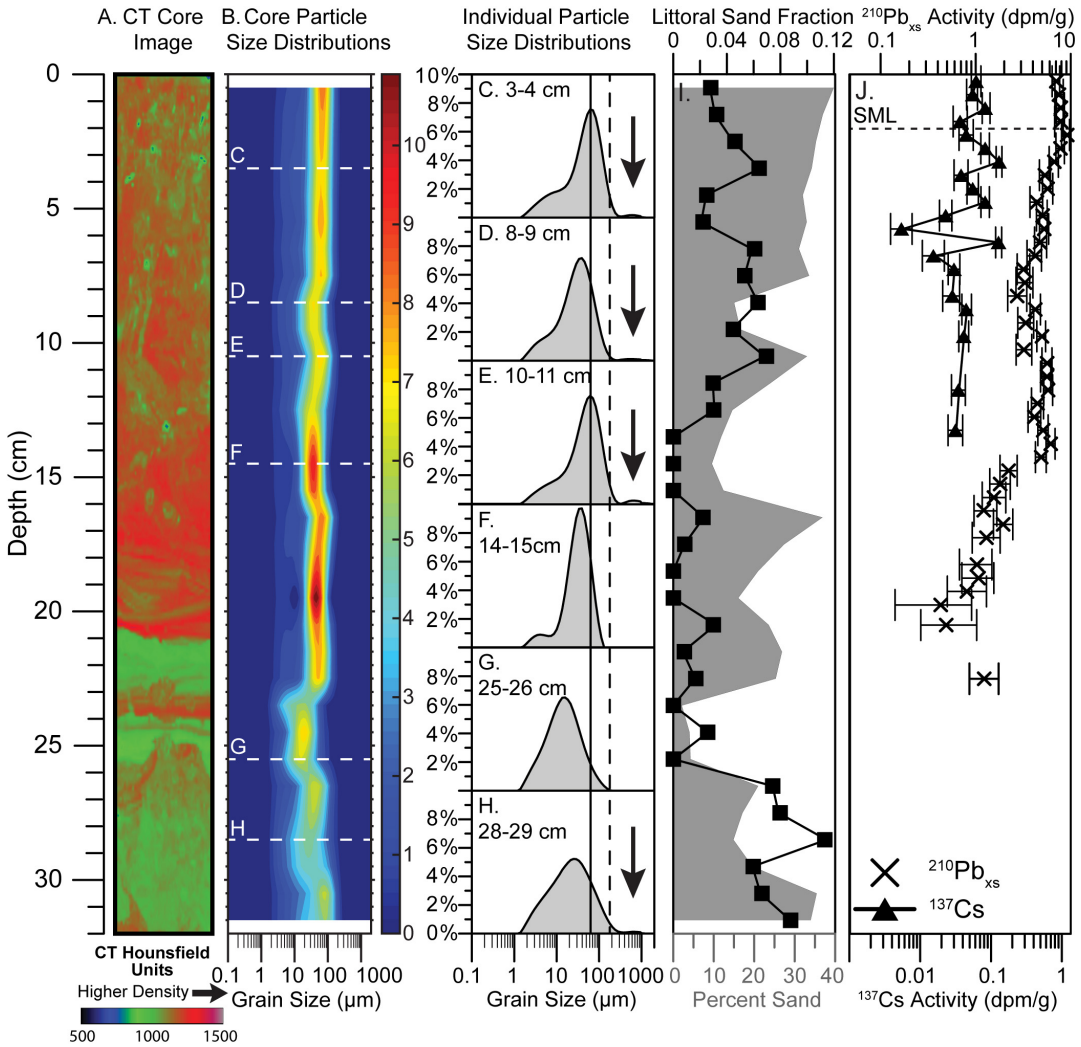

FIGURE 5 | Results from PS1410-11MC (see **Figure 1** for location). **(A)** CT image of the core where cooler colors (blues and greens) are relatively lower density deposits, and warmer colors (reds) are higher density. **(B)** Down core total grain size distribution for all samples. In this plot the y-axis is depth down the core, x-axis is particle size, and the colors represent the volume present of the sample that fall within those size classifications, where warmer colors are higher percentages and cooler colors are lower percentages. The warmest color region across any depth horizon represents the mode for the sample. Representative individual sample particle size distributions (PSD) are shown in **(C–H)**, where the depths of these PSD are highlighted in **(B)** as white dashed lines. The solid black vertical line in **(C–H)** notes the silt/sand boundary at 63 μm and the dashed black vertical line notes the Monterey Bay littoral cutoff diameter at 180 μm (see text for explanation). Black arrows in the plot point to samples with increases in material coarser than the littoral cutoff diameter. The raw measurement size bins for the instrument were used to create the distributions in **(B–H)**. **(I)** Down core results from the grain size analysis with total percent sand (gray area) and the littoral sand fraction (black squares – see text for explanation). **(J)** Down core results for the $^{210}Pb_{xs}$ (black Xs) and ^{137}Cs (black triangles). The dashed horizontal line is the inferred depth of the Surface Mixed Layer (SML) based on the $^{210}Pb_{xs}$ results.

and 40%. This sandier section is overlain by a gradual coarsening upward sequence from ∼15 and 40% total sand, with the finer layer at ∼9 cm being comprised of ∼20% sand.

The $^{210}Pb_{xs}$ profile (**Figure 5J**) consists of sections with uniform activity, and steady-state accumulation similar to PS1410-04MC. The SML extends to a depth 2 cm, below which activities decrease with depth down to ∼9 cm. Similar to PS1410-04MC, between 9 and 14 cm the activity is uniform to slightly increasing with depth. Below 14 cm activities again approximate steady-state accumulation, and no $^{210}Pb_{xs}$ was detected below 23 cm.

The ^{137}Cs results are also similar to PS1410-04MC, with no distinct peak, maximum activity (0.13 ± 0.01 dpm/g) was at a depth of 3.5 cm with similar activity (0.13 ± 0.01 dpm/g) at a depth of 6.5 cm. Maximum penetration was to a depth of 15 cm, which places the 1954 CE time horizon at a depth of 13 cm after adjusting for the SML.

SR1707-02MC

The results for SR1707-02MC are shown in **Figure 6**. This core was retrieved from southern Monterey Bay, ∼10 km west-southwest of the Salinas River mouth. The core is 15 cm

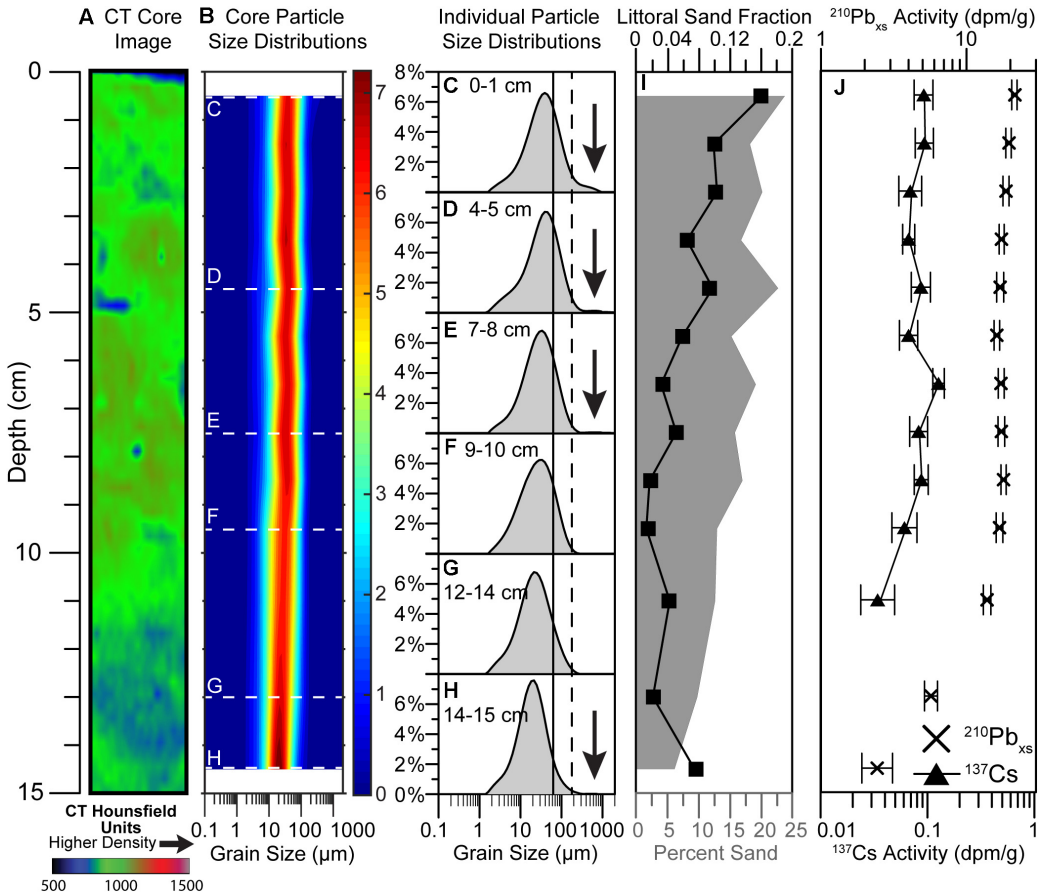

FIGURE 6 | Results from SR1707-02MC (see **Figure 1** for location). **(A)** CT image of the core where cooler colors (blues and greens) are relatively lower density deposits, and warmer colors (reds) are higher density. **(B)** Down core total grain size distribution for all samples. In this plot the y-axis is depth down the core, x-axis is particle size, and the colors represent the volume present of the sample that fall within those size classifications, where warmer colors are higher percentages and cooler colors are lower percentages. The warmest color region across any depth horizon represents the mode for the sample. Representative individual sample particle size distributions (PSD) are shown in **(C–H)**, where the depths of these PSD are highlighted in **(B)** as white dashed lines. The solid black vertical line in **(C–H)** notes the silt/sand boundary at 63 μm and the dashed black vertical line notes the Monterey Bay littoral cutoff diameter at 180 μm (see text for explanation). Black arrows in the plot point to samples with increases in material coarser than the littoral cutoff diameter. The raw measurement size bins for the instrument were used to create the distributions in **(B–H)**. **(I)** Down core results from the grain size analysis with total percent sand (gray area) and the littoral sand fraction (black squares – see text for explanation). **(J)** Down core results for the $^{210}Pb_{xs}$ (black Xs) and ^{137}Cs (black triangles). No Surface Mixed Layer was observed within this core, and $^{210}Pb_{xs}$ was detected at the base.

long, well-mixed, homogeneously low-density with a few smaller distinct mottles dispersed throughout (**Figure 6A**). The grain size results from this core (**Figure 6B**) show a gradual coarsening upward trend, with grain sizes concentrated between ∼10 and 70 μm at the base of the core and ∼20–200 μm at the top. Unlike most of the other cores discussed above, the highest values for a size class (i.e., darkest red colors) were observed at the base of the core (∼13–15 cm) rather than near the top.

From the representative PSD in **Figures 6C–H** these highest values at the base of the core correspond to a high, narrow peak in the sample at 14–15 cm (**Figure 6H**). In the individual PSD we also see the gradual coarsening upward through the core, as each sample distribution has a relatively comparable shape, but the curve is gradually shifted to the right moving up the core. For example, at the base (**Figure 6H**, 14–15 cm) the mode is ∼20 μm, but closer to ∼40–50 μm at the surface (**Figure 6C**, 0–1 cm). Unique to this core, is that all of the samples have a mode that is clearly finer than the silt/sand boundary. Even though this core overall is generally finer than the other cores, there are still sample PSD that contain the very coarse tail (noted by the black arrows in **Figures 6C,E,H**). The very coarse sub-populations were observed in the samples in the upper portion of the core (e.g., 0–1 cm, 4–5 cm, and 7–8 cm), and at the base of the core (14–15 cm).

The total sand content also gradually increases up core (**Figure 6I**). At the base, the total sand content is ∼5%, while at the surface the total sand content is just below 25%. Below ∼9 cm in the core the sand increases from ∼5 to 12%, while above 9 cm the sand generally fluctuates (with a net increasing trend) between ∼17 and 25%.

From the $^{210}Pb_{xs}$ profile (**Figure 6J**), the upper 6 cm exhibits steady-state accumulation with a relatively steep slope. This core did not exhibit a SML based on the $^{210}Pb_{xs}$ profile, and

this was confirmed through measuring excess ^{234}Th (Alexander and Venherm, 2003) as it was only detected at the surface. Note, excess ^{234}Th was not measured on any of the other cores due to instrument availability. From 6 to 9 cm activities are uniform to slightly increasing with depth, while below 9 cm activities decrease with depth, but with a much lower slope as compared to the upper section. Excess ^{210}Pb was detected at the base of this core.

For the ^{137}Cs there is no clearly distinct peak in activity. The maximum activity (0.12 ± 0.02 dpm/g) was detected at 7 cm, but comparable activities (0.09 ± 0.02 dpm/g) were detected at the surface and at a depth of 9 cm. Maximum penetration occurred at a depth of 12 cm, with no mixed layer that would place the 1954 CE time horizon at this depth. Although it should be noted that this measurement spanned a 2 cm sample interval from 10 to 12 cm.

PS1410-08GC

The sediment fabric and grain size results for PS1410-08GC are shown in **Figure 7**. This longer core was from the same location as SR1707-02MC above in southern Monterey Bay. Most of the core has a mottled appearance (**Figure 7A**), where mottled sections vary from dominantly low-density (∼8–12 cm), to high-density (∼40–50 cm), and moderate-density (0–8 cm, 12–40 cm, and 50–63 cm). From 63 cm down to 75 cm the appearance is less mottled, resembling more irregular layering, although without any distinct horizontal contacts. Below 75 cm the layering becomes more distinct, and appears to dip within the core. It is likely that this apparent dipping may be an artifact of the coring process. Note the CT scan does not extend to the base of the core to avoid imaging the core-catcher.

As with the variable sediment fabric, there is variable sediment texture in this core. From **Figure 7B** we see distinct, often stepwise changes throughout the core, with coarser sections (0–7 cm, 38–55 cm, 63–68 cm, and 82–86 cm) separated by finer sections. At the base from 82–86 cm, the core is relatively coarse, but shows a broad distribution with most of the particles falling between ∼3–100 μm. Overlying this section from ∼68–82 cm the sediment is finer, but with a tighter distribution as most particles range from ∼3–40 μm. The core generally coarsens upward above this within two distinct coarser units, the lowermost from 63–68 cm and 38–55 cm above that. In both of these coarser units, the particles fall between ∼20–200 μm, with a more restricted distribution in the 38–55 cm. In this unit most particles are between ∼40–100 μm and individual size classes are greater than 7% (dark red colors in **Figure 7B**). Between these two coarser units is a small finer unit (55–63 cm) where the distributions shift back to the left. Above 38 cm is a thick finer unit (∼9–31 cm) characterized by a broader distribution of sizes evident by the wider color swath in **Figure 7B**, and lack of many depths with values above 6%. At 7 cm there is a shift back to the right indicating a coarser unit, with a narrowing of the distribution as maximum values are between 6 and 7%.

The individual representative PSD in **Figures 7C–H** show a variety of shapes for the distribution curves. For the lowermost coarse unit the sample at 84–85 cm (**Figure 7H**), the curve has a relatively broad distribution, but with a mode close to the silt/sand boundary. Contrast that with the overlying finer unit where the PSD from 76 to 77 cm has a narrow peak centered near 10 μm (**Figure 7G**). **Figures 7E,F** are PSD from the two coarser units between 38 and 68 cm that have generally similar shapes with a mode near the silt/sand boundary. The sample at 44–45 cm (**Figure 7E**) has a more prominent peak, with less material in the clay to fine silt portion of the size spectrum compared to the lower sample from 63 to 64 cm (**Figure 7F**). **Figure 7D** from 27 to 28 cm within the thick finer unit is characterized by a broad distribution with a mode closer to ∼20 μm, while near the surface of the core at 5–6 cm (**Figure 7C**) the distribution is more similar to that at 63–64 cm (**Figure 7F**). As with the other cores, there are discrete samples that also contain the very coarse sub-population (black arrows in **Figures 7D,G**). In these representative samples the coarse tail again appears somewhat detached from larger distribution curve.

Overall, the sediment texture in this core fluctuates between sandy-mud and mud with relatively high total sand content (∼30%) sections at depths of 0–7 cm, 38–55 cm, and 63–68 cm (**Figure 7I**). There is a low total sand (<10%) section from 70–81 cm, while for much of the rest of the core the total sand fluctuates around 20%. See **Table 1** for the geochronological results for this core.

DISCUSSION

Age Models

We developed age-depth models for all the multicores based off of the ^{210}Pb data (**Figure 8**) using the Constant Rate of Supply (CRS) model (Appleby and Oldfield, 1978), and starting below the SML. In cores SR1707-02MC and SR1707-07MC $^{210}Pb_{xs}$ was detected throughout the entire length of the core. To account for an incomplete inventory, the remaining/missing radioisotope inventory was estimated following the methods described by Sanchez-Cabeza and Ruiz-Fernández (2012), where the remaining inventory was estimated from the average mass accumulation rate in the lowermost section of the core.

For core PS1410-04MC the $^{210}Pb_{xs}$ inventory was complete, and the model extends back to the mid-1800s at a depth of ∼30 cm (**Figure 8A**). Of all the multicores, this core gave us the longest record. The SML-adjusted ^{137}Cs 1954 CE horizon at a depth of 21 cm agrees reasonably well with the model, where at 21 cm in the core the model gives a date of 1955 ± 2.4 CE. The overall average sedimentation rate for this core based on the age model was 0.17 cm/yr. Interestingly, the age model shows an inflection point in the curve around 1970 where the slope steepens suggesting that sedimentation rates were faster over the past several decades than earlier in the 20th century. Estimating a sedimentation rate over the past several decades gives us a rate of 0.41 cm/yr since the 1970s for this core.

By contrast SR1707-07MC had the weakest age model, and also the encompassed the shortest time span. Both $^{210}Pb_{xs}$ inventory and ^{137}Cs were detected throughout the core. From the model, ages were only determined from 7 to 16 cm (below the 6 cm SML), spanning the years from 2005 to 1983 CE (**Figure 8B**).

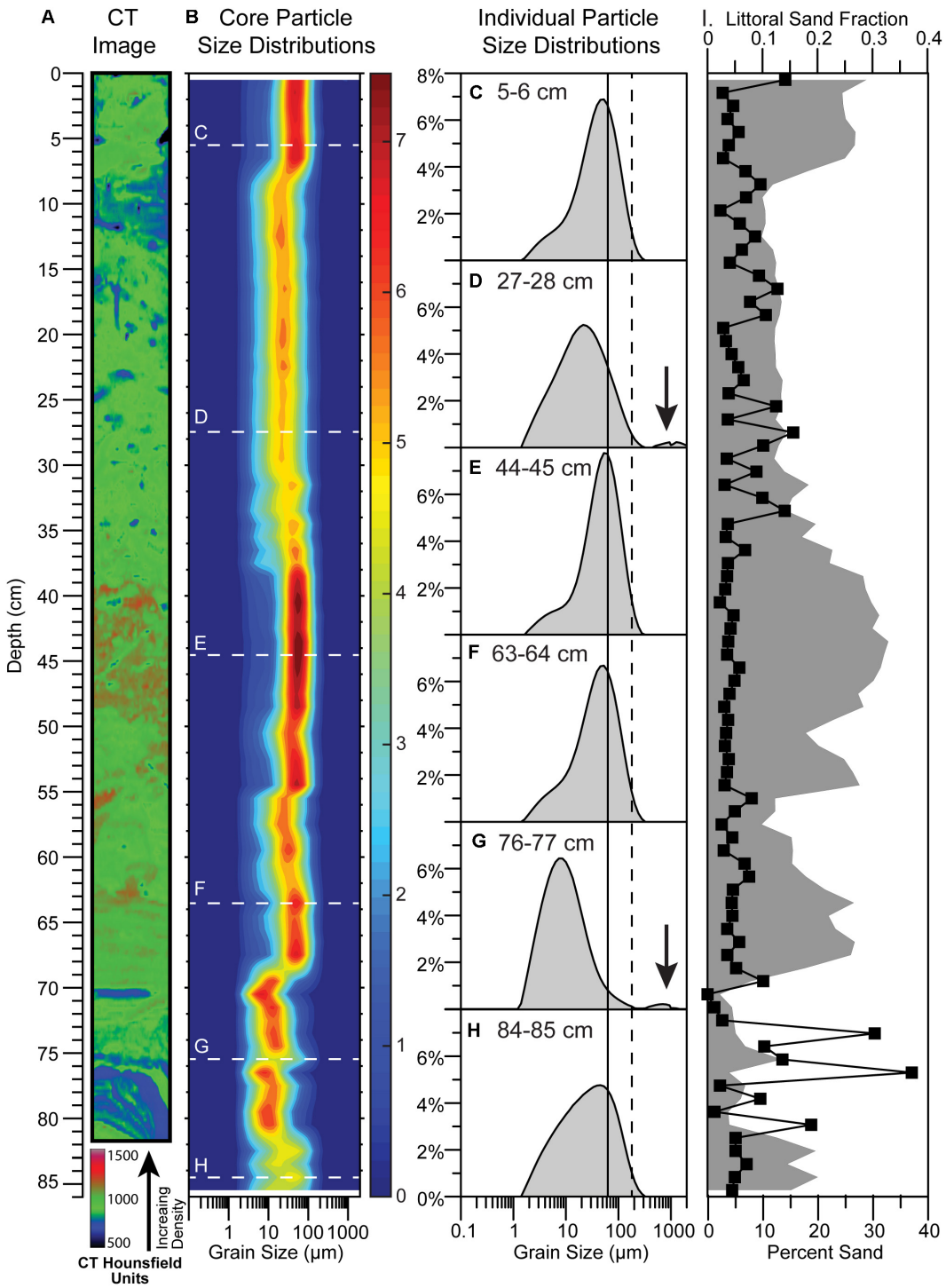

FIGURE 7 | Results from PS1410-08GC (see **Figure 1** for location). **(A)** CT image of the core where cooler colors (blues and greens) are relatively lower density deposits, and warmer colors (reds) are higher density. **(B)** Down core total grain size distribution for all samples. In this plot the y-axis is depth down the core, x-axis is particle size, and the colors represent the volume present of the sample that fall within those size classifications, where warmer colors are higher percentages and cooler colors are lower percentages. The warmest color region across any depth horizon represents the mode for the sample. Representative individual sample particle size distributions (PSD) are shown in **(C–H)**, where the depths of these PSD are highlighted in **(B)** as white dashed lines. The solid black vertical line in **(C–H)** notes the silt/sand boundary at 63 µm and the dashed black vertical line notes the Monterey Bay littoral cutoff diameter at 180 µm (see text for explanation). Black arrows in the plot point to samples with increases in material coarser than the littoral cutoff diameter. The raw measurement size bins for the instrument were used to create the distributions in **(B–H)**. **(I)** Down core results from the grain size analysis with total percent sand (gray area) and the littoral sand fraction (black squares – see text for explanation). For geochronological results from this core, see **Figure 2** or **Table 1**.

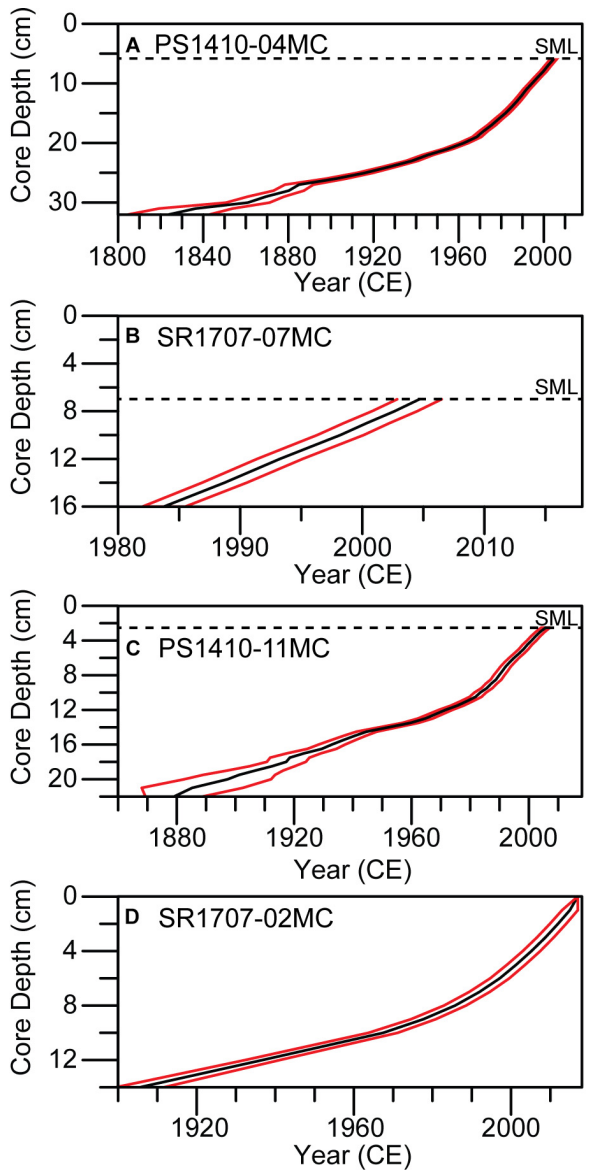

FIGURE 8 | Age-depth models for all the multicores: **(A)** PS1410-04MC, **(B)** SR1707-07MC, **(C)** PS1410-11MC, and **(D)** SR1707-02MC. The ages were determined from the $^{210}Pb_{xs}$ data using the Constant Rate of Supply model. The black line represents the modeled age with the red lines constraining the age uncertainty determined by propagating errors from the counting statistics. Ages were plotted below the Surface Mixed Layer (SML – dashed horizontal line) where present.

While this model cannot be validated with the ^{137}Cs horizons, calculating a sedimentation rate by plotting the natural log of the $^{210}Pb_{xs}$ versus core depth (Kolker et al., 2009) gives a rate of 0.44 cm/yr, thus we should expect only ~3 decades of time within 16 cm of core. Therefore, we feel confident, that at a minimum, this core reflects only the past several decades.

Core PS1410-11MC had the full $^{210}Pb_{xs}$ inventory and extends back to the late 1800s (**Figure 8C**). The ^{137}Cs 1954 CE horizon in this core is at a depth of 13 cm after adjusting for the SML. In the model, 13 cm is 1965 ± 2.6 CE. While there is a discrepancy between the model and the ^{137}Cs data, we remain confident in the ^{210}Pb age model as the dates are within a decade, and there is no 1963 peak to compare to. Further, there are generally low overall ^{137}Cs activities (>0.1 dpm/g), so there is a possibility of deeper penetration but these activities are below the instrument detection limit. The overall average sedimentation rate for this core based on the age model was 0.16 cm/yr. Similar to PS1410-04MC, there is a steepening of the slope over the past several decades, where the most recent sedimentation rate was 0.29 cm/yr since the 1970s.

Similarly, for SR1707-02MC the age model (**Figure 8D**) agrees reasonably well with the ^{137}Cs data. In this core the 1954 CE time horizon is at a depth of 12 cm, which the modeled age for that depth is 1937 ± 4.4 CE. This sample, however, is a 2 cm interval (10–12 cm in the core), and the modeled age of the interval above it at 10 cm is 1968 ± 3.7 CE, thus the actual 1954 CE horizon could be between 10 and 12 cm as modeled and measured. This core also did not capture the full $^{210}Pb_{xs}$ inventory, and the remaining inventory was estimated. Although the remaining inventory was minimal (estimated at ~2% of the total) as the core spans >100 years, near the limit of ^{210}Pb chronological capabilities. The overall average sedimentation rate for this core based on the age model was 0.13 cm/yr. This curve also shows a change in sedimentation rate over the past several decades, where the rate has increased to 0.24 cm/yr since the late 1970s.

The geochronology results for the composite SR1707-02MC and PS1410-08GC spliced record are best modeled using a quadratic regression in CLAM (**Figure 2B**). However, to avoid age reversals, the CLAM model required the exclusion of the AMS ^{14}C date at 26 cm, which has a nearly identical date as that at 46 cm (e.g., 363 ± 99 and 405 ± 100 cal years BP, respectively). Inclusion of the sample at 26 cm would imply a nearly instantaneous deposition of at least 20 cm of sediment, and no such sedimentary unit is observed in the CT scan (**Figures 2A**, **7A**). If this is true, then this suggests that this AMS sample may represent reworked material from a previously lower horizon. This interpretation is supported with the grain size results, which show that those depths likely contain elevated levels of remobilized material (see section "Sedimentation Over the Past 1,000 Years"). The CLAM quadratic regression model yields a 95% confidence range for age uncertainty that spans from 4 years at the beginning of the record (at 2 cm depth, which corresponds to −63 cal years BP [2013 CE]), to a maximum of 257 years at the base (at 89 cm depth, which corresponds to 1095 cal years BP). The overall average sedimentation rate for this core based on the age model was 0.08 cm/year.

Collectively we feel confident in all of these age models. For the multicores that span the past several decades to 100+ years, the overall average sedimentation rates ranged from 0.13 to 0.44 cm/year. These rates are comparable to rates similarly determined by ^{210}Pb and ^{137}Cs in Monterey Bay by Lewis et al. (2002) that ranged from 0.15 to 3.9 cm/year. Moreover, these average rates are also in line with 20th century sea level rise for Monterey Bay (0.15 cm/yr) as determined from tide gage records corrected for local uplift (Reynolds and Simms, 2015), whereby sedimentation rates approximate the accommodation

space created by local sea level rise. Similarly, our overall average rate for the longer core PS1410-08GC at 0.08 cm/yr is also in line with the late Holocene sea level rise estimate for Monterey Bay of 0.13 cm/yr (Reynolds and Simms, 2015).

From the CT images, however, it is clear that bioturbation is present throughout all of the cores. We recognize that such mixing can have a significant impact on how we utilize our age models to interpret the timing of past events identified within the sediment record. To address this issue in terms of the shorter multicores, we only determined ages for sediment below the SML. The thickness of the SML can be thought of as being fixed through time for a given location, whereby sediment "moves" out of the SML at a rate equal the rate at which sediment is added to the surface (i.e., the sedimentation rate) (Wheatcroft, 1990). Therefore, the ages determined from the CRS model below the SML are valid as changes in isotope activity with depth are still a function of the decay rate (known) and the sedimentation rate (the rate that sediment "moves" out of the SML). The CRS model is also a better suited model to use in the presence of mixed sediments, because if the mixing zone spans 10 years of accumulation the maximum age error is still less than 2 years (Appleby, 1998). For the multicores, SML thicknesses ranged from 0 cm in SR1707-02MC (although the sediment does appear mixed) to 6 cm in SR1707-07MC. These SML thicknesses are also comparable to values reported in the region (1–4 cm) by Lewis et al. (2002). Taking the SML thickness per core, and the most recent (post 1970s) sedimentation rates, the mixing zone for PS1410-11MC spans 7 years, while for PS1410-04MC and SR1707-07MC it spans 12 and 13 years, respectively. For SR1707-02MC no SML was detected, but given the mixed appearance in the sediment we can assume mixing might still have occurred. Cores from comparable settings in southern Monterey Bay analyzed by Lewis et al. (2002) had SML thicknesses that ranged from 1 to 3 cm. Using the 3 cm SML thickness for SR1707-02MC the mixed zone would span 12.5 years. Therefore, for all of these cores the maximum age error using the CRS model due to the mixing is still likely only a couple of years as the mixing zones approximate 1 decade of accumulation.

Although the age estimate errors may only be a couple of years, the sedimentary deposits are essentially homogenized over the mixed zone. The sedimentary signal from a specific event will therefore be mixed over a 7–13 year period, where with more time in the mixed zone the likelihood of preserving a distinct sedimentary signal decreases. Recognizing this, we realize that any interpretations of deposits resulting from events (e.g., specific flood or wetter-than-average years) or even inter-annual variations (e.g., ENSO cyclicity) will be difficult to confidently resolve. Multi-decadal processes (e.g., PDO) however, we feel we should be able to confidently resolve given our age determinations even with the presence of sediment mixing.

Similarly, for the longer core PS1410-08GC the mixing will make it unreasonable to resolve event to yearly scales, and arguably even decadal scales further back in the record. Assuming the 3 cm mixing zone (same as was assumed for SR1707-02MC) and conservatively utilizing the overall average sedimentation rate of 0.08 cm/yr, the mixing zone would span 37.5 years. The mixing in this core therefore, could essentially homogenize the sediment over a 1 to 4 decade time period (using the faster recent sedimentation rate estimate from SR1707-02MC above to provide the minimum time boundary) making resolving decadal processes difficult, but multi-decadal to centennial processes reasonable. Ultimately, for either the longer core PS1410-08GC or the short multi cores we will look to focus only on time periods that exceed these depth/time scales of bioturbation in making interpretations of the sediment record.

Modern Sedimentation

With these age models, we can now look at changes in sedimentation over the past several decades, in particular, changes in sediment delivery to Monterey Bay. Sediment delivery to the bay is overwhelmingly by the three largest rivers (Salinas, Pajaro, and San Lorenzo = 97% of sediment), with the Salinas accounting for 77% of the total supply (Eittreim et al., 2002). The Salinas River is one of the largest rivers in California in terms of sediment supply to the ocean, and the sediment loads can be extreme and episodic. For example, from ∼1930 to 2000 CE the mean annual sediment load in the Salinas River exceeded the overall mean value during only 18 of the 70 years (Farnsworth and Milliman, 2003). For the San Lorenzo River, 63% of all suspended sediment transport occurred over only 62 total days within the time period from 1936 to 1998 CE, the result of multiple short-lived and infrequent extreme flooding events that occurred once every decade or two (Willis and Griggs, 2003). This demonstrates that much of the sediment delivery to Monterey Bay occurs in pulses during extreme events. While short-lived and sporadic, these extreme events are significant. The Salinas, along with other California coastal rivers the Eel and Santa Clara, are the only 3 rivers in the United States (from 1950 to 1990) to have a daily sediment load exceed 5×10^6 t/day (Farnsworth and Milliman, 2003).

Elevated discharges within the Salinas, and other California rivers, can transport increased amounts of sand to the ocean, and these extreme events often occur during positive ENSO and PDO climatic periods (Inman and Jenkins, 1999; Farnsworth and Milliman, 2003; Gray et al., 2015a,b). Therefore, variability in the total sand content within shelf sediment should reflect these forcings, and we can look to this sand content as a proxy for climatic variability. Although focusing on the sand fraction alone is admittedly only a fraction of the complete grain size data we presented above, given the relationship outlined above we feel this is the most relevant and concise proxy to assess sedimentation changes driven by climatic variability. As stated above, while we may not be able to distinguish individual events given the amount of sediment mixing we observed within all the cores, we should be able to distinguish the longer-term, multi-decadal cycles (e.g., PDO) within these sediment records.

In **Figure 9A** we have combined the sand content from the four multicores, and plotted this data versus time from each core's individual age models. The sand percentages have been standardized after Kirby et al. (2010), and show the data in standard deviations above or below the mean value for each core. In this way, we can present all the cores on the same scale regardless of the absolute sand content in any core. The data are only presented back to the 1870s, so that there are data from at

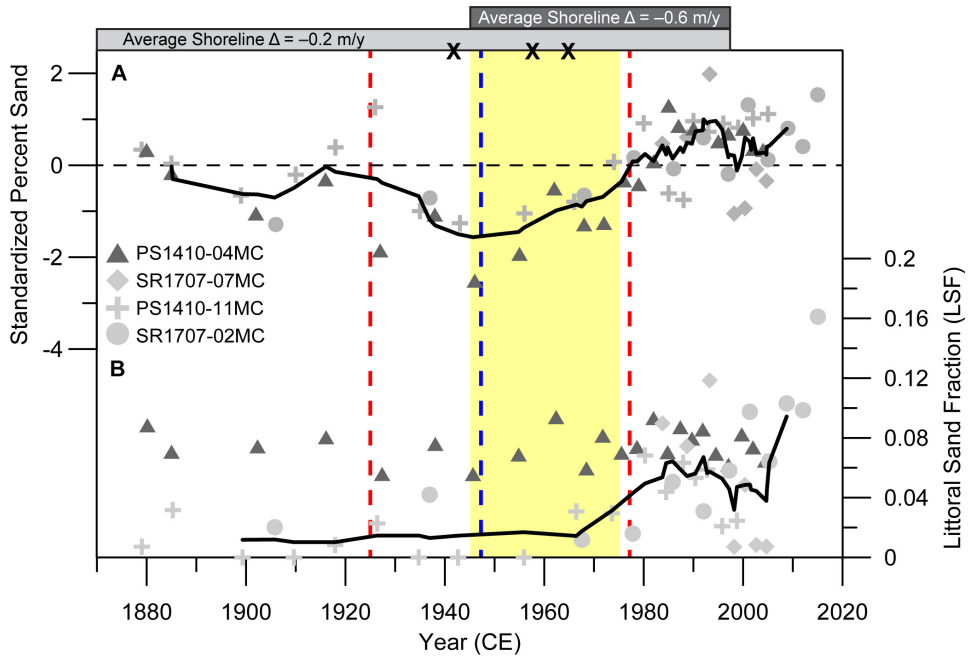

FIGURE 9 | Plot of grain size parameters versus time for the modern time period. **(A)** The standardized percent sand for all cores (see text for explanation) with a 5-point moving average (black line) computed from all core data combined. **(B)** The littoral sand fraction for all cores with a 5-point moving average (black line) that excludes PS1410-04MC (dark gray triangles). For both plots the transitions between major PDO shifts (Mantua et al., 1997) are shown by the vertical dashed lines, where a red line indicates a transition into a positive PDO phase, and a blue line is a transition into a negative PDO phase. The yellow vertical bar indicates the period of maximum dam construction in California (Willis and Griggs, 2003), and the black Xs at the top denote the implementation of the 3 largest dams on the Salinas River (Farnsworth and Milliman, 2003). The gray horizontal bars at the top of the plot show shoreline change results where the width of the bar approximates the period with which the data was averaged, and negative values indicate net erosion (Hapke et al., 2006).

least two cores for every approximate time period. From the plot, we see that prior to the ∼1920s much of the data cluster around the mean (value of 0 on the standardized scale), and generally below the mean (less than average sand in the deposits). From the 1920s through the 1970s the data is substantially below the mean, but after the 1970s sand values are generally above the mean (more sand than average). A five-point running average (black line - all data combined) highlights these overall inter-decadal trends for much of the record.

The sand trends generally follow the broader climate and runoff trends for the area during this time period. The three major PDO shifts in the 20th century are shown in **Figure 9**, where red dashed lines indicate a shift to a positive PDO (1925 and 1977 CE), and the blue dashed line is the shift to a negative PDO in 1947 CE (Mantua et al., 1997). Monterey Bay in central California is aligned with southern California where positive PDO periods tend to bring increased precipitation, runoff, and river discharge (Inman and Jenkins, 1999; Farnsworth and Milliman, 2003; Warrick and Farnsworth, 2009). Specifically, fluvial discharge data from the Salinas show the period preceding 1943 CE as being wet, followed by a low-runoff dry period on the Salinas River from 1944 to 1977 CE (Inman and Jenkins, 1999). After the shift back to a positive PDO in 1977 there was a return to a wet climate with elevated-discharge on the Salinas River (Inman and Jenkins, 1999). The shelf sand data agrees reasonably well with these shifts, where relatively more sand was deposited on the shelf during the wet/high-discharge periods (1920s–1940s and post-1970s), with lower sand during the dry/low-runoff period (1940s–1970s) (**Figure 9**).

We recognize that there are some discrepancies within these general trends (sand is decreasing following shift to a positive PDO in 1925 CE and increasing following a shift to a negative PDO in 1947 CE), but such discrepancies might be the result of limited samples during these times coupled with age uncertainties due to sediment mixing. For example, for all cores collectively there are only 2 samples in each of the following decades: 1920s, 1940s, and 1950s. There are 3 samples for the 1930s, 4 in the 1960s, and finally 5 in the 1970s. Given this limited temporal coverage decade to decade throughout this period and slower sedimentation rates that increase the inherent age uncertainty from mixing, it is not unreasonable that the variability in the data do not precisely correspond with the exact year for the PDO shift. As mentioned above, we recognize our data limitations in being able to resolve annual and inter-annual events. Such a limitation may be demonstrated by the data not corresponding exactly the specific year that marks the shift in PDO. Yet, at decadal scales the data do reasonably well. From the 1920 CE to 1940 CE the data show higher sand content than from 1940 CE to 1970 CE, periods that approximate the changes in the PDO. Where we do have more data and higher sedimentation rates post-1970 that would reduce age uncertainty due to mixing, the trends are much more consistent following the positive PDO shift in 1977 CE.

Taken overall therefore, the shelf sand data does appear to correspond to climate fluctuations, and this is most apparent when comparing the most recent prolonged dry period (negative PDO, 1940s–1970s) to the recent wet period (positive PDO, 1970s–2000s). This difference in sand between these two most recent climate periods is significant (p = 0.008). As shown in **Table 2**, based on all cores, the average sand content during the last positive PDO period (wet climate) was 29.67 ± 7.34 % as compared to 22.41 ± 7.03% during the preceding cool phase. Therefore, the total sand content in shelf deposits may be a good climate indicator.

Interestingly, the standardized sand values were consistently the highest after the 1970s. This is the only section of the plot where the 5-point moving average is positive, and positive throughout. Given that there were other positive PDO periods throughout the record where the sand was not as high, this might point to a larger environmental shift in later-half of the twentieth century resulting from anthropogenic influences that are seen across a variety of social and environmental metrics (see Steffen et al., 2011 and references therein). For example, anthropogenic modification to sediment dispersal systems, which have been shown to have had a significant impact on sediment delivery to the coast (Syvitski et al., 2005).

Dams on coastal rivers for example, can reduce the sediment flux to the ocean. Particularly the coarse sediment (sand and gravel) flux. Dams along coastal rivers in California have reduced sand and gravel discharges to the ocean on average by 25% (Willis and Griggs, 2003). For the Salinas River specifically, the reduction was 33%, and for the Pajaro and San Lorenzo Rivers the reductions were 6% and 2%, respectively (Willis and Griggs, 2003). The majority of dams/dam storage capacity was built between 1945 and 1977 CE (Willis and Griggs, 2003) with major dams on the Salinas constructed in 1941, 1956, and 1965 CE (Farnsworth and Milliman, 2003). These time periods are shown on **Figure 9** (maximum dam construction = yellow vertical bar, Salinas River dams = black Xs). From this figure we see that following the dam construction the sand content on the shelf increases. In other words, dams are built, the fluvial sand and gravel supply to the ocean is reduced, yet sand increases in deposits along the shelf. The implication of this scenario is that the additional sand supplied to the shelf must be coming from a non-fluvial source.

A possible non-fluvial source for the excess sand is supply from coastal erosion and remobilization of littoral zone sediment. Sea level rise can drive coastal erosion, and according to the Bruun rule (Bruun, 1962) as the shoreline migrates landward the eroded material is transported and deposited offshore. While sea level rise has accelerated over the 20th century (Kemp et al., 2011), it is not clear that sea level rise alone could explain the observed increase in sand deposited on the shelf. First, there is some debate as to the validity of the Bruun rule in natural settings (e.g., Cooper and Pilkey, 2004). It has also been noted that this model neglects landward transport of material with shoreline retreat (Rosati et al., 2013) In some cases landward

TABLE 2 | Comparison of sediment characteristics between different time periods.

	Positive PDO[1] (wet) all cores	Negative PDO[2] (dry) all cores	Positive PDO (wet) PS1410-04MC excluded	Negative PDO (dry) PS1410-04MC excluded
Climate – total percent sand				
Number of samples	34	10	23	4
Mean value	29.67	22.41	27.27	15.82
Standard deviation	7.34	7.03	7.79	5.55
P-value	**0.008**		**0.010**	
Climate – littoral sand fraction (LSF)				
Number of samples	34	10	23	4
Mean value	0.058	0.050	0.049	0.018
Standard deviation	0.029	0.031	0.031	0.015
P-value	0.480		0.064	
	Lower erosion pre-1945 all cores	**Higher erosion post-1945 all cores**	**Lower erosion pre-1945 PS1410-04MC excluded**	**Higher erosion post-1945 PS1410-04MC excluded**
Erosion – total percent sand				
Number of samples	19	33	11	19
Mean value	23.25	27.08	18.36	29.93
Standard deviation	9.54	8.23	9.52	8.85
P-value	0.134		0.117	
Erosion – littoral sand fraction (LSF)				
Number of samples	19	33	11	19
Mean value	0.045	0.057	0.019	0.044
Standard deviation	0.038	0.029	0.023	0.031
P-value	0.215		**0.030**	

[1]*Positive PDO period = 1977–2006 CE.*
[2]*Negative PDO period = 1947–1976 CE, Bold values indicate a significant difference.*

transport has been shown to actually dominate lower in the shoreface profile at the boundary between the upper and lower shoreface, and that offshore transport only dominates higher up in the surf zone (Aagaard and Sørensen, 2012). Further, with sea level rise accelerating throughout the century, we would expect the increase in sand to be persistent throughout the century and not just over the past several decades as observed. While global sea level rise has accelerated since the 1990s, this acceleration is actually lower along the Pacific coast of North America due to atmospheric wind patterns (Bromirski et al., 2011).

While sea level rise is likely contributing to coastal erosion, we feel other processes have a greater impact and over the shorter time periods consistent with the observed changes in sedimentation. Both the climatic shifts and dam construction mentioned above can have a dramatic impact on shorelines, particularly in California. California's coastal rivers are dominantly small mountainous rivers which can experience coherence between river floods and energetic ocean conditions (Wheatcroft et al., 1997; Kniskern et al., 2011; Odigie and Warrick, 2017). In this case, the same storms that bring excess precipitation also bring elevated wave heights and strong currents to the coastal ocean. For example, the atmospheric river storms responsible for the historic flooding in the 1861–1862 winter also breached the sandy barrier fronting Carpinteria marsh leaving behind overwash deposits comparable to deposits resulting from hurricanes and tsunamis (Reynolds et al., 2018). Additionally, strong El Niño winters that often drive the extreme fluvial discharges can also result in extreme beach and coastal erosion, such as the 1982–1983, 1997–1998, and 2009–2010 El Niño winters (Storlazzi and Griggs, 2000; Sallenger et al., 2002; Allan and Komar, 2006; Barnard et al., 2011; Barnard et al., 2015).

More recently, the 2015–2016 El Niño winter resulted in unprecedented levels of shoreline retreat due in part to a multi-year drought that preceded this winter that reduced sediment supply to the coast, and the corresponding low precipitation during the event (Barnard et al., 2017). In this case, the sediment supply to the coast had been previously suppressed, and this El Niño did not bring increased precipitation but rather energetic ocean conditions that resulted in extreme coastal erosion. As dams on coastal rivers also suppresses sediment supply to the coast, a similar set-up may have occurred following the dam construction period from the 1940s–1970s and subsequent climate shift to the positive PDO. The more frequent and intense storms during the positive PDO may have overwhelmed a coastal system that had a sand deficit due dam construction, resulting in accelerated coastal erosion.

This combined dams-climate effect is consistent with our shelf sand observations (**Figure 9A**). Sand increases steadily from the 1940s through much of the 1970s as dams are being constructed, but in the late 1970s the sand increases rapidly following the shift to the positive PDO. Not only is the positive PDO period in the 1980s and 1990s the only time in the record that sand content is consistently greater than the mean, but at times it is 1 standard deviation or more. With dams preventing sediment from reaching the coast during this time, we feel the increased influx of sand must be coming from coastal erosion and littoral sources. Dams prevented sediment from reaching the coast, and when the climate changed to one where storms were more intense and frequent, the result was increased coastal erosion similar to what was observed in a smaller scale during the 2015–2106 El Niño. As the coast eroded, a new supply of sand was transported seaward and deposited along the mid-shelf.

Increased erosion during this period has been documented for Monterey Bay. After the mid 1940s, shorelines throughout the bay eroded at an average rate of −0.6 m/year, 3-times the long-term average shoreline change rate of −0.2 m/year from the mid 1850s to late 1990s (Hapke et al., 2006). Clearly coastal erosion increased in Monterey Bay in the latter half of the 20th century, although from the shoreline data we cannot specifically discern the effect of combined dams and climate. Yet as coastal erosion is increasing, the mid-shelf deposits are being enriched in sand at the same time. Simultaneously as more sand is being trapped behind dams, it seems likely that the additional shelf sand is coming from coastal sources.

In order to test whether the increase in sand is from coastal erosion, we looked for coastal indicators within the sediment data. We decided to look at the how much littoral-sized sand was within the shelf deposits. With increased coastal erosion, we expect there will be increased littoral sand within the system, and while much of this sand may ultimately end up in the more prominent littoral sinks (e.g., canyons, estuaries, etc.), offshore transport in also a sink for littoral sand (Komar, 1996). Therefore, we should also see relative increases in the amount of littoral sand escaping the littoral system and being transported across the shelf.

For many locations along the California coast, including Monterey Bay, there is a well-established littoral cutoff diameter. The littoral cutoff diameter is the minimum size threshold for significant quantities of sand to remain within the beach or littoral zone, particles finer than this threshold will be resuspended and transported offshore under relatively normal conditions (Hicks, 1985; Hicks and Inman, 1987; Limber et al., 2008). For Monterey Bay, the littoral cutoff diameter is 180 μm (Best and Griggs, 1991), so material coarser than 180 μm is more likely to be retained within beaches throughout Monterey Bay, primarily moving along the coast within the littoral cell.

Using this local littoral cutoff diameter, we developed the littoral sand fraction (LSF), an index that represents the fraction of the total sand component that is larger than the littoral cutoff diameter. To determine the LSF, we took the percentage of sand greater than 180 μm (local littoral cutoff diameter) and divided that by the total sand percentage for the sample. A LSF value of 1 therefore, would represent a sample that is entirely littoral sand, while a value of 0 would have no littoral sand, and either of these values is independent of the total sand content for a given sample. Increases in the LSF throughout the core therefore, would represent an increased contribution from the littoral zone that is likely created through increased erosion/remobilization.

The LSF results are plotted down core for all the cores in **Figures 3–7**. For PS1410-04MC (**Figure 3I**), the LSF is highest at the base, but is generally consistent through the upper ∼25 cm of the core, fluctuating between ∼0.06 and 0.10. For SR1707-07MC (**Figure 4I**), the LSF low throughout, typically near 0, except for a section between 10 and 15 cm where values are high (∼0.10). For

PS1410-11MC there are 3 distinct LSF sections within the core (**Figure 5I**). A lower section from the base to ∼26 cm where the LSF is high (>0.06), a middle section from ∼12 to 26 cm where the LSF is low (<0.04), and the upper section above 12 cm where the LSF increases and fluctuates between ∼0.02 and ∼0.06. For SR1707-02MC (**Figure 6I**) the LSF decreases in the lowermost section of the core, but increases from ∼9 cm to the surface. The individual PSD in **Figures 3–7** highlight those samples with higher LSF values, where the black arrows denote where the littoral sand section of the distribution is elevated. In many of these representative PSD the littoral sand portion of the plot is often detached from the larger distribution (e.g., **Figures 3G**, **4G**, **5E**) suggesting a completely unique population of grains separate from the larger population within the sample.

These LSF data are plotted versus time in **Figure 9B**. What stands out is that for PS1410-04MC (dark gray triangles) the LSF is steady through time (∼0.08), but for the other cores (light gray symbols) the LSF increases in the latter half of the 20th century. This trend is clearly demonstrated by the 5-point moving average trendline in **Figure 9B** (this trendline excludes PS1410-04MC) that shows average values of <0.02 from the early 1900s to the late 1960s, followed by an increase to >0.06 through the 1990s. Similar to the total sand data, the inflection point for the LSF occurs near the end of the elevated dam construction period and near the PDO shift in the late 1970s.

From **Table 2**, we see that for the LSF, the high erosion period (mid 1940s to late 1990s) is statistically different (p = 0.030) than the earlier data, only when PS1410-04MC is excluded. Interestingly the LSF is not significantly different between climate periods, and the total sand content is not significantly different between the high and low erosion periods whether PS1410-04MC is excluded or not. Therefore, total sand may be a good climate indicator, the LSF may be a good coastal erosion indicator, and these two metrics are seemingly independent.

For this data, however, the LSF is only an erosion indicator when PS1410-04MC is excluded, but this discrepancy may be explained by the location of this core. PS1410-04MC was the only core located outside of Monterey Bay proper along the open coast. This stretch of the coast consists mostly of rocky headlands separated by pocket beaches formed from uplifted marine terraces. By contrast, the coastline within Monterey Bay has a much higher percentage of linear beach and dune systems. These rocky coasts, like where PS1410-04MC was located, are more resistant to erosion than the sandy beaches throughout Monterey Bay. The shoreline change study by Hapke et al. (2006) only focused on sandy beach areas, so there is minimal shoreline change data from the open coast section. Where data are available along this section of the coast south of Point Ano Nuevo, the sediment transport vector for PS1410-04MC (Eittreim et al., 2002), the recent shoreline change data show a mix of slightly accreting to slightly eroding beaches (Hapke et al., 2006). Whereas within Monterey Bay most of the areas are experiencing shoreline erosion over this most recent period (Hapke et al., 2006). Additionally, the open coast area proximal to PS1410-04MC is removed from the major rivers in the region. All of these rivers directly empty into Monterey Bay (**Figure 1**). Rather, this section of the coast is fed by small creeks, and these creeks are undammed. Therefore, we can think of PS1410-04MC as our control site for watershed modification. Where there have been little to no modifications, coastal erosion is minimal, and the LSF stays consistent through time. Within the bay, in the areas fed by modified rivers, we see a significant change in the period following dam construction that corresponds to increased coastal erosion.

Overall, from these data we conclude that sand delivery to the shelf generally follows climatic cycles, where more sand is delivered during wet periods that correspond to a positive PDO. Following dam construction on the Monterey Bay rivers, the shift to the positive PDO resulted in increased coastal erosion, and more sand supplied from littoral sources likely during the large wave events associated with storms. This new littoral source replaced some of the fluvial sand that was being trapped behind dams. For PS1410-04MC which was less impacted with dams, the total sand still responded to the climate shifts, but the lack of a prominent shift the LSF showed that the relative fluvial versus coastal sand supply remained constant.

Sedimentation Over the Past 1,000 Years

From the modern sedimentation within Monterey Bay, the big takeaway is that we can use the combination of total sand and the LSF to investigate variability in fluvial and coastal (erosional) sediment sources. Subsequently, we can apply these metrics to PS1410-08GC, which spans >1,000 years encompassing the climatic variability of the late Holocene including the Medieval Climate Anomaly (MCA) and the Little Ice Age (LIA), to determine if the patterns we observed within the modern record are consistent over a longer time period. For the MCA and LIA we used the age ranges from Masson-Delmotte et al. (2013) of 1050-650 cal years BP and 500–100 cal years BP, respectively.

In **Figure 7I** the LSF is plotted along with the total sand content for PS1410-08GC. From the plot, there are sections of relatively constant and low LSF (∼0.05) from ∼81–86 cm, ∼37–68 cm, and ∼1–6 cm. There are also sections where the LSF fluctuates and contains relatively high values (∼0.1–0.4), for example ∼70–81 cm, ∼23–35 cm, and ∼7–19 cm. Based on what we observed within the modern record, we interpret these periods of relatively high and fluctuating LSF values to represent periods of increased sediment supply from coastal erosion, while the periods of relatively constant and low LSF values represent periods of high fluvial supply. In discussing the age model above, we decided to exclude our date from 21 to 24 cm because we felt the age was too old, and likely incorporated older reworked material. From the plot in **Figure 7I**, we see that this section of the core overlaps with an elevated erosion section based on the LSF data. The near-similar age of the sample from 41 to 44 cm was from a section with low LSF, we would interpret as having limited supply of eroded material. These lithologic characteristics are further support for why we excluded the date at 21–24 cm in favor of the date at 41–44 cm.

Interestingly, the highest LSF values (located ∼70–81 cm in the core) coincided with the lowest total sand, while the highest total sand corresponded to relatively low LSF (∼37–47 cm). This trend is generally consistent throughout the core, where higher total sand corresponds to low LSF, and low total sand corresponds

to elevated LSF (with the exception of the surface of the core). These observations are also consistent with our interpretations from the modern period. The high sand/low LSF periods suggest high fluvial supply with limited erosion, i.e., excess sand being delivered primarily from a fluvial sources offsetting erosion. This would suggest a wet climate. By contrast low sand/high LSF suggest that the overall sand supply is low, i.e., the rivers are not providing significant quantities of sand, this likely results in beaches being sand-starved and susceptible to erosion. As a result, what sand is being supplied to the shelf is increasingly being sourced from this erosion. These low sand/high LSF periods therefore suggests a relatively dry climate.

In **Figure 10** the sand and LSF data for 08GC are plotted versus time with the MCA and LIA climate periods indicated. From this we see that the generally warmer and drier MCA encompasses the period of low sand/high LSF consistent with low runoff and high coastal erosion. Also, the high sand/low LSF peaks fall within the beginning of the cool and wet LIA period suggesting high fluvial runoff during this time.

While these trends are generally consistent to these larger climate periods, we have also plotted the regional climate fluctuation from nearby Abbott Lake (see location in **Figure 1**) identified by Hiner et al. (2016). Abbott lake is located within the Salinas River watershed, specifically within the Arroyo Seco watershed, which has the highest runoff rates of all of the Salinas River tributaries (Farnsworth and Milliman, 2003). The lake is located ∼60 km to the southeast of the PS1410-08GC coring location, and therefore represents an excellent indicator of regional climate fluctuations that would have directly contributed to sedimentation along the southern Monterey Bay continental shelf.

From the Abbott Lake record, we see that the earliest low runoff period from 920 to 680 cal years BP correlates well with the low sand/high LSF period in PS1410-08GC. A transitional climate period followed where sand increases and the LSF decreases. This is followed by a subsequent dry period from 590 to 510 cal years BP where sand decreases and the LSF increases slightly. The transition to the cooler and wetter LIA is consistent at both Abbott Lake and on the shelf as sand peaks and the LSF is low from 510 to 380 cal years BP. However, the LIA is not consistently wet as Hiner et al. (2016) note from the Abbott Lake record. These similar fluctuations manifest in the shelf record as low sand/high LSF sections are observed during the dry and transitional period from 380 to 240 cal years BP. The LSF decreases during the wet period from 240 to 175 cal years BP, and increases again during the dry period from 175 to 130 cal years BP. Following the LIA sand decreases and the LSF remains relatively high until the dam construction begins in the mid-twentieth century.

In general, we feel these shelf sedimentation characteristics compare well with the regional climate variability. Low runoff, dry periods result in a limited total supply of sand, and

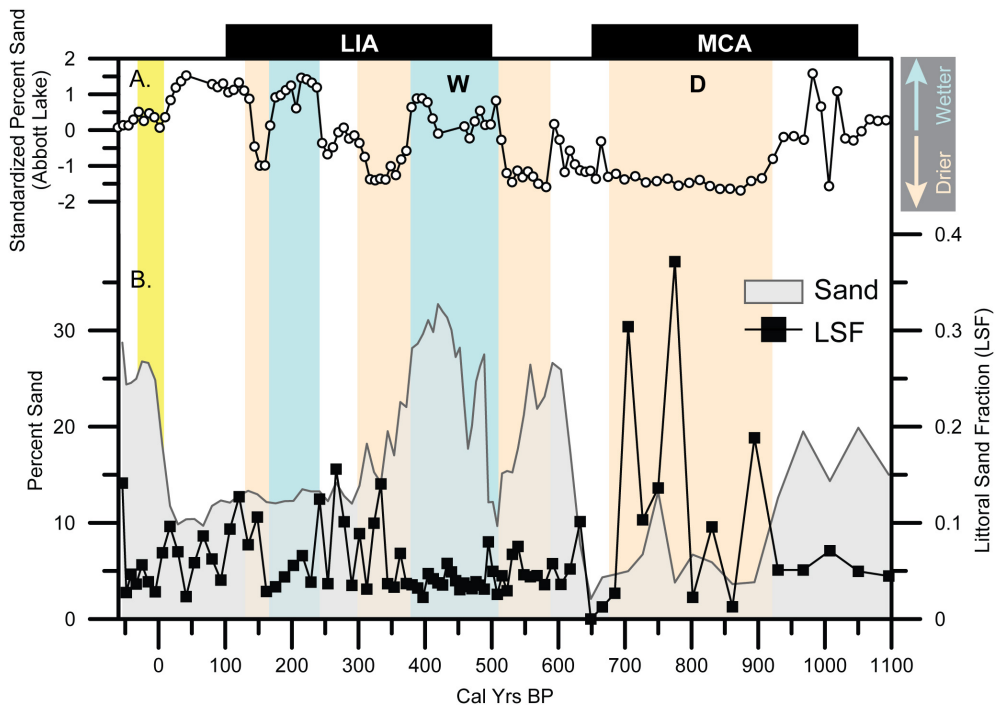

FIGURE 10 | Plot of Holocene changes in grain size characteristics versus climate variability. The time periods for the Medieval Climate Anomaly (MCA) and Little Ice Age (LIA) are shown at the top as black bars (Masson-Delmotte et al., 2013). **(A)** The regional climate climate periods from nearby Abbott Lake by Hiner et al. (2016) are shown as the standardized sand content (white circles) and the correponding blue and orange vertical bars. Blue bars ("W") indicate wetter periods, while orange bars ("D") indicate drier periods. **(B)** The total sand (gray area) and littoral sand fraction (black squares) for PS1410-08GC are plotted vs. time based on the composite age model. The yellow vertical bar depicts the period of maximum dam construction (Willis and Griggs, 2003).

an elevated contribution from coastal erosion. Again, this is likely because a limited sand supply to the coast due to the limited runoff accelerates erosion during large wave events. It is interesting to note that during these dry periods the LSF is not consistently high, but rather fluctuates between high and low values. Perhaps this reflects a dominantly quiescent period punctuated by periodic large storm events, while the wet periods might be more consistent over time. It is also important to note that the climate characteristics over the past ∼1,000 years (dry = low sand/high LSF, wet = high sand/low LSF) are different from what we have observed over the past several decades. During the most recent positive PDO (wet period), we have *high* sand and *high* LSF. Throughout the full >1,000-year record, this was the only instance where both of these metrics were high at the same time. This demonstrates that humans have modified system beyond the natural cyclicity of the past. Further, it might also reflect unprecedented coastal erosion in the region from the combined effect of modified drainage systems, accelerated sea level rise, and more frequent and intense storms due to climate change. The result of all of this is more sand transport offshore from significant erosion of beaches and sandy shorelines.

Broader Perspective and Future Implications

The results from this study demonstrate that Monterey Bay shelf sediments can preserve evidence of environmental variability driven by climate, humans, and the combined effect of climate and humans. It should be noted, however, that this study just focused on one specific location, and thus extrapolating these results to other regions may be difficult. That being said, this study supports the general idea that continental shelf stratigraphy can be a viable paleo-environmental archive similar to other studies that have tied changes in the amount and characteristics of shelf deposits to regional climatic variability (e.g., Hanebuth and Henrich, 2009; Nizou et al., 2010, Weight et al., 2011).

This study also demonstrates that coastal erosion can serve as a sediment source for shelf regions, a process that has been recognized in other areas globally. For example, erosion from the Old Huanghe delta in China over the last 100 years has supplied sediment to mid shelf regions in the Yellow Sea and East China Sea at an order of magnitude greater than the supply from the modern Huanghe River (Zhou et al., 2014). Similarly, an investigation of the Brazos River delta in the Gulf of Mexico showed 20th century abandonment and activation of deltaic lobes (Carlin and Dellapenna, 2015). Abandonment led to both shoreline erosion and erosion within the subaqueous delta with some of the eroded material being incorporated into the newly activated lobe and a new shelf depocenter (Carlin and Dellapenna, 2015).

For the Brazos River delta the most recent shift in the depocenter was attributed to the combined effect of drought and watershed modifications (Carlin and Dellapenna, 2015). This morphologic/stratigraphic change resulting from the combined effect of climate and human modifications is similar to what we observed in Monterey Bay, where the shift in PDO following the dam construction period accentuated the changes in shelf sedimentation. The combination of climate and human activities resulting in stratigraphic change has been observed in other locations along the United States Pacific margin. On the Umpqua River margin off the coast of Oregon, sedimentation increased and fined during the mid-twentieth century interpreted to be due to the combination of intensive timber harvesting and shift in the PDO to a wet hydroclimate phase for the region (Wheatcroft et al., 2013). Therefore, for both the Umpqua River margin and the Monterey Bay shelf there are detectable stratigraphic changes that resulted from the combined effect of humans and natural processes.

Looking toward the future, we expect this sedimentation regime to persist provided that dams remain in place along coastal rivers and coastal erosion remains elevated as a result. As fluvial sediment supplies remain trapped behind dams, storms will likely continue to erode shoreline with more frequent/intense storms during wet periods, and less frequent/intense storms during dry periods (but storms still capable of causing erosion). Yet, there is an increasing push to remove dams along rivers recently, as dam removals have increased exponentially since the 1970s (O'Connor et al., 2015). Studies on the impacts of dam removal have shown that major responses of the fluvial system following dam removal were relatively short-lived, as the system returned to a more natural state within a couple of years (e.g., East et al., 2018). Therefore, with dam removal there is the potential for a relatively rapid shift back to sedimentation that resembles what we have observed over the past ∼1,000 years rather than the past several decades.

CONCLUSION

In this study, we investigated shelf sedimentation within Monterey Bay over decadal and centennial time scales, distinguishing sediment sources from both rivers and coastal erosion. The results demonstrated that during dry periods, relatively little sand was transported to the shelf from rivers, and more was sourced from coastal erosion. Conversely, during wet periods more sand was transported to the shelf overall, primarily from rivers, rather than coastal erosion.

These characteristics throughout the past 1,000 years reflect how coastal erosion can increase when fluvial sediment supply is limited during a dry climate period. The data also showed that dam construction on coastal rivers also increased coastal erosion, and the transport of littoral sediment offshore. The combined effect of dams and a shift to a wetter climate, however, resulted in both increases in littoral and total sand transport to the shelf. These most recent deposits represent an unprecedented shift in shelf sedimentation that is unlike any sedimentary characteristics observed over the past >1,000 years. This change is likely the result of accelerated coastal erosion in region from a combination of human modifications, sea level rise, and climate change. While this study only focused on one location, these results are aligned with other studies that show coastal erosion providing sediment to other shelf depocenters, and studies that observed stratigraphic change resulting from the combination of human

activities and natural processes. Therefore, this study adds to our understanding that shelf sediment records can reflect climatic variability over centennial time scales, and that over the past several decades shelf sedimentation has changed in response to human activities in the watershed and the coastal zone.

AUTHOR CONTRIBUTIONS

JC, JA, and AW carried out the cruise and project planning for the PS1410 cruise with AW acting as Chief Scientist. JC conducted the cruise and project planning for the SR1707 cruise in consultation with JA and AW. JC served as Chief Scientist for the SR1707 cruise. JC, JA, VaS, JH, and ViS performed the sample and data analyses and interpretations. JC and JA conducted the primary writing and figure drafting for this manuscript. AW, VaS, JH, and ViS contributed the feedback that greatly improved this manuscript.

ACKNOWLEDGMENTS

We would like to thank the crew of the R/V *Point Sur* and the scientific party of cruise PS1410 for sample collection in 2014, with special thanks to Kenneth Coale, Mike Prince, Stian Andrini and the NSF/ONR/UNOLS Chief Scientist Training Program. We would like to thank Jim Christmann of the R/V *Shana Rae* and the scientific party of cruise SR1707 for sample collection in 2017, with special thanks to Jennifer White and Dan Powers. We would like to thank Sophie De Beukelaer from the Monterey Bay National Marine Sanctuary for assistance in securing permits to collect samples within the marine sanctuary. Acknowledgment is made to the Donors of the American Chemical Society Petroleum Research Fund, for partial support of this research (PRF #57363-UNI8). Additional support for field work was provided by the California State University Council on Ocean Affairs, Science, and Technology (COAST) Program. Analytical funding was provided by the USGS Climate Research and Development Program, COAST, and California State University, Fullerton Office of Research and Sponsored Projects. Anthony Kovscek and Elliot Kim (Stanford Univ.) performed the CT analyses, and Tom Guilderson (LLNL) and John Southon (UC-Irvine) assisted with ^{14}C measurements. We would also like to thank Matthew Kirby for use of his instrumentation, assistance with the Abbott Lake data, and feedback on figures. Finally, we would like to thank John Barron, the editor DP, and the two reviewers who provided valuable comments to improve this manuscript. Any use of trade, firm, or product names is for descriptive purposes only and does not imply endorsement by the U.S. Government.

REFERENCES

Aagaard, T., and Sørensen, P. (2012). Coastal profile response to sea level rise: a process-based approach. *Earth Surf. Process. Landf.* 37, 354–362. doi: 10.1002/esp.2271

Abràmoff, M. D., Magalhães, P. J., and Ram, S. J. (2004). Image processing with ImageJ. *Biophotonics Int.* 11, 36–42.

Alexander, C. R., and Venherm, C. (2003). Modern sedimentary processes in the Santa Monica, California continental margin: sediment accumulation, mixing and budget. *Mar. Environ. Res.* 56, 177–204. doi: 10.1016/s0141-1136(02)00330-6

Allan, J. C., and Komar, P. D. (2006). Climate controls on US West Coast erosion processes. *J. Coast. Res.* 22, 511–529. doi: 10.2112/03-0108.1

Appleby, P. (1998). "Dating recent sediments by 210-Pb: problems and solutions," in *Proc. 2nd NKS/EKO-1 Seminar*, Helsinki, 7–24.

Appleby, P., and Oldfield, F. (1978). The calculation of 210 Pb dates assuming a constant rate of supply of unsupported 210Pb to the sediments. *Catena* 5, 1–8. doi: 10.1016/s0341-8162(78)80002-2

Barnard, P. L., Allan, J., Hansen, J. E., Kaminsky, G. M., Ruggiero, P., and Doria, A. (2011). The impact of the 2009–10 El Niño Modoki on U.S. West Coast beaches. *Geophys. Res. Lett.* 38:L13604. doi: 10.1029/2011GL047707

Barnard, P. L., Hoover, D., Hubbard, D. M., Snyder, A., Ludka, B. C., Allan, J., et al. (2017). Extreme oceanographic forcing and coastal response due to the 2015–2016 El Niño. *Nat. Commun.* 8:14365. doi: 10.1038/ncomms14365

Barnard, P. L., Short, A. D., Harley, M. D., Splinter, K. D., Vitousek, S., Turner, I. L., et al. (2015). Coastal vulnerability across the Pacific dominated by El Nino/Southern oscillation. *Nat. Geosci.* 8, 801–807. doi: 10.1038/ngeo2539

Best, T. C., and Griggs, G. B. (1991). "A Sediment Budget for the Santacruz Littoral Cell, California," in *From Shoreline to Abyss*, ed. R. H. Osborne (Tulsa, OK: SEPM Society for Sedimentary Geologists), 35–50.

Blaauw, M. (2010). Methods and code for 'classical'age-modelling of radiocarbon sequences. *Quat. Geochronol.* 5, 512–518. doi: 10.1016/j.quageo.2010.01.002

Bromirski, P. D., Miller, A. J., Flick, R. E., and Auad, G. (2011). Dynamical suppression of sea level rise along the Pacific coast of North America: indications for imminent acceleration. *J. Geophys. Res. Oceans* 116:C07005.

Bruun, P. (1962). Sea-level rise as a cause of shore erosion. *J. Waterways Harbors* 88, 117–132.

Carlin, J. A., and Dellapenna, T. M. (2015). The evolution of a subaqueous delta in the anthropocene: a stratigraphic investigation of the Brazos River delta, TX USA. *Cont. Shelf Res.* 111, 139–149. doi: 10.1016/j.csr.2015.08.008

Chenillat, F., Riviere, P., Capet, X., Di Lorenzo, E., and Blanke, B. (2012). North pacific gyre oscillation modulates seasonal timing and ecosystem functioning in the california current upwelling system. *Geophys. Res. Lett.* 39:L01606.

Cooper, J. A. G., and Pilkey, O. H. (2004). Sea-level rise and shoreline retreat: time to abandon the Bruun Rule. *Glob. Planet. Change* 43, 157–171. doi: 10.1016/j.gloplacha.2004.07.001

Corbett, D. R., Dail, M., and McKee, B. (2007). High-frequency time-series of the dynamic sedimentation processes on the western shelf of the Mississippi River Delta. *Cont. Shelf Res.* 27, 1600–1615. doi: 10.1016/j.csr.2007.01.025

Corbett, D. R., McKee, B., and Duncan, D. (2004). An evaluation of mobile mud dynamics in the Mississippi River deltaic region. *Mar. Geol.* 209, 91–112. doi: 10.1016/j.margeo.2004.05.028

Cutshall, N. H., Larsen, I. L., and Olsen, C. R. (1983). Direct analysis of 210 Pb in sediment samples: self-absorption corrections. *Nucl. Instrum. Methods Phys. Res.* 206, 309–312. doi: 10.1016/0167-5087(83)91273-5

Dettinger, M. D., and Ingram, B. L. (2013). The coming megafloods. *Sci. Am.* 308, 64–71. doi: 10.1038/scientificamerican0113-64

Dettinger, M. D., Ralph, F. M., Das, T., Neiman, P. J., and Cayan, D. R. (2011). Atmospheric rivers, floods and the water resources of California. *Water* 3, 445–478. doi: 10.3390/w3020445

Di Lorenzo, E., Schneider, N., Cobb, K., Franks, P., Chhak, K., Miller, A., et al. (2008). North pacific gyre oscillation links ocean climate and ecosystem change. *Geophys. Res. Lett.* 35:L08607. doi: 10.1111/gcb.13171

East, A. E., Logan, J. B., Mastin, M. C., Ritchie, A. C., Bountry, J. A., Magirl, C. S., et al. (2018). Geomorphic evolution of a gravel-bed river under sediment-starved versus sediment-rich conditions: river response to the world's largest dam removal. *J. Geophys. Res. Earth Surf.* 123, 3338–3369.

Eittreim, S. L., Xu, J., Noble, M., and Edwards, B. D. (2002). Towards a sediment budget for the Santa Cruz shelf. *Mar. Geol.* 181, 235–248. doi: 10.1016/s0025-3227(01)00269-9

Farnsworth, K. L., and Milliman, J. D. (2003). Effects of climatic and anthropogenic change on small mountainous rivers: the Salinas River example. *Glob. Planet. Change* 39, 53–64. doi: 10.1016/s0921-8181(03)00017-1

Goodbred, S. L., and Kuehl, S. A. (1998). Floodplain processes in the Bengal Basin and the storage of Ganges-Brahmaputra river sediment: an accretion study using Cs-137 and Pb-210 geochronology. *Sediment. Geol.* 121, 239–258. doi: 10.1016/s0037-0738(98)00082-7

Gray, A. B., Pasternack, G. B., Watson, E. B., Warrick, J. A., and Goñi, M. A. (2015a). Effects of antecedent hydrologic conditions, time dependence, and climate cycles on the suspended sediment load of the Salinas River, California. *J. Hydrol.* 525, 632–649. doi: 10.1016/j.jhydrol.2015.04.025

Gray, A. B., Pasternack, G. B., Watson, E. B., Warrick, J. A., and Goñi, M. A. (2015b). The effect of El Niño southern oscillation cycles on the decadal scale suspended sediment behavior of a coastal dry-summer subtropical catchment. *Earth Surf. Process. Landf.* 40, 272–284.

Griggs, G. (1974). Nearshore current patterns along the central California coast. *Estuar. Coast. Mar. Sci.* 2, 395–405. doi: 10.1016/0302-3524(74)90007-3

Hanebuth, T. J. J., and Henrich, R. (2009). Recurrent decadal-scale dust events over holocene western Africa and their control on canyon turbidite activity (Mauritania). *Quat. Sci. Rev.* 28, 261–270. doi: 10.1016/j.quascirev.2008.09.024

Hapke, C. J., Reid, D., Richmond, B. M., Ruggiero, P., and List, J. (2006). National assessment of shoreline change Part 3: historical shoreline change and associated coastal land loss along sandy shorelines of the California Coast. *US Geol. Survey Open File Rep.* 1219:27.

Harris, C. K., Traykovski, P. A., and Geyer, W. R. (2005). Flood dispersal and deposition by near-bed gravitational sediment flows and oceanographic transport: a numerical modeling study of the Eel River shelf, northern California. *J. Geophys. Res.Oceans* 110:C09025. doi: 10.1029/2004jc002727

Hicks, D. M. (1985). *Sand Dispersion from an Ephemeral Delta on a Wave Dominated Coast*. Ph.D. thesis, University of California, Santa Cruz.

Hicks, D. M., and Inman, D. L. (1987). Sand dispersion from an ephemeral river delta on the central California coast. *Mar. Geol.* 77, 305–318. doi: 10.1016/0025-3227(87)90119-8

Hiner, C. A., Kirby, M. E., Bonuso, N., Patterson, W. P., Palermo, J., and Silveira, E. (2016). Late holocene hydroclimatic variability linked to pacific forcing: evidence from abbott lake, coastal central California. *J. Paleolimnol.* 56, 299–313. doi: 10.1007/s10933-016-9912-4

Huyer, A., Barth, J., Kosro, P., Shearman, R., and Smith, R. (1998). Upper-ocean water mass characteristics of the California Current, summer 1993. *Deep Sea Res. Part II Top. Stud. Oceanogr.* 45, 1411–1442. doi: 10.1016/s0967-0645(98)80002-7

Inman, D. L., and Jenkins, S. A. (1999). Climate change and the episodicity of sediment flux of small California rivers. *J. Geol.* 107, 251–270. doi: 10.1086/314346

Jacox, M., Moore, A., Edwards, C., and Fiechter, J. (2014). Spatially resolved upwelling in the California current system and its connections to climate variability. *Geophys. Res. Lett.* 41, 3189–3196. doi: 10.1002/2014gl059589

Kemp, A. C., Horton, B. P., Donnelly, J. P., Mann, M. E., Vermeer, M., and Rahmstorf, S. (2011). Climate related sea-level variations over the past two millennia. *Proc. Natl. Acad. Sci. U.S.A.* 108, 11017–11022. doi: 10.1073/pnas.1015619108

Kirby, M., Lund, S., Patterson, W., Anderson, M., Bird, B., Ivanovici, L., et al. (2010). A Holocene record of Pacific decadal oscillation (PDO)-related hydrologic variability in southern California (Lake Elsinore, CA). *J. Paleolimnol.* 44, 819–839. doi: 10.1007/s10933-010-9454-0

Kniskern, T. A., Warrick, J. A., Farnsworth, K. L., Wheatcroft, R. A., and Goni, M. A. (2011). Coherence of river and ocean conditions along the US West Coast during storms. *Cont. Shelf Res.* 31, 789–805. doi: 10.1016/j.csr.2011.01.012

Kolker, A. S., Goodbred, S. L., Hameed, S., and Cochran, J. K. (2009). High-resolution records of the response of coastal wetland systems to long-term and short-term sea-level variability. *Estuar. Coast. Shelf Sci.* 84, 493–508. doi: 10.1016/j.ecss.2009.06.030

Komar, P. (1996). The budget of littoral sediment: concepts and applications. *Shore Beach* 64, 18–26.

Lewis, R. C., Coale, K. H., Edwards, B. D., Marot, M., Douglas, J. N., and Burton, E. J. (2002). Accumulation rate and mixing of shelf sediments in the Monterey Bay National Marine Sanctuary. *Mar. Geol.* 181, 157–169. doi: 10.1016/s0025-3227(01)00265-1

Limber, P. W., Patsch, K. B., and Griggs, G. B. (2008). Coastal sediment budgets and the littoral cutoff diameter: a grain size threshold for quantifying active sediment inputs. *J. Coast. Res.* 24, 122–133. doi: 10.2112/06-0675.1

Mantua, N. J., Hare, S. R., Zhang, Y., Wallace, J. M., and Francis, R. C. (1997). A Pacific interdecadal climate oscillation with impacts on salmon production. *Bull. Am. Meteorol. Soc.* 78, 1069–1079. doi: 10.1175/1520-0477(1997)078<1069:apicow>2.0.co;2

Masson-Delmotte, V., Schulz, M., Abe-Ouchi, A., Beer, J., Ganopolski, A., González Rouco, J., et al. (2013). "Information from paleoclimate archives," in *Climate Change 2013: The Physical Science Basis. Contribution of Working Group I to the Fifth Assessment Report of the Intergovernmental Panel on Climate Change*, eds T. F. Stocker, D. Qin, G.-K. Plattner, M. Tignor, S. K. Allen, J. Boschung, et al. (Cambridge: Cambridge University Press), 383–464. doi: 10.1017/cbo9781107415324.013

Nittrouer, C. A. (1999). STRATAFORM: overview of its design and synthesis of its results. *Mar. Geol.* 154, 3–12. doi: 10.1016/s0025-3227(98)00128-5

Nizou, J., Hanebuth, T. J. J., Heslop, D., Schwenk, T., Palamenghi, L., Stuut, J.-B., et al. (2010). The senegal river mud belt: a high-resolution archive of paleoclimatic change and coastal evolution. *Mar. Geol.* 278, 150–164. doi: 10.1016/j.margeo.2010.10.002

O'Connor, J. E., Duda, J. J., and Grant, G. E. (2015). 1000 dams down and counting. *Science* 348, 496–497. doi: 10.1126/science.aaa9204

Odigie, K. O., and Warrick, J. A. (2017). Coherence between coastal and river flooding along the California Coast. *J. Coast. Res.* 34, 308–317. doi: 10.2112/jcoastres-d-16-00226.1

Palinkas, C., and Nittrouer, C. (2006). Clinoform sedimentation along the Apennine shelf, Adriatic Sea. *Mar. Geol.* 234, 245–260. doi: 10.1016/j.margeo.2006.09.006

Palinkas, C. M. (2009). The timing of floods and storms as a controlling mechanism for shelf deposit morphology. *J. Coast. Res.* 25, 1122–1129. doi: 10.2112/08-1041.1

Puig, P., Palanques, A., and Guillén, J. (2001). Near-bottom suspended sediment variability caused by storms and near-inertial internal waves on the Ebro mid continental shelf (NW Mediterranean). *Mar. Geol.* 178, 81–93. doi: 10.1016/s0025-3227(01)00186-4

Reimer, P. J., Bard, E., Bayliss, A., Beck, J. W., Blackwell, P. G., Ramsey, C. B., et al. (2013). IntCal13 and Marine13 radiocarbon age calibration curves 0–50,000 years cal BP. *Radiocarbon* 55, 1869–1887. doi: 10.1016/j.dib.2018.10.040

Reynolds, L. C., and Simms, A. R. (2015). Late quaternary relative sea level in Southern California and Monterey Bay. *Quat. Sci. Rev.* 126, 57–66. doi: 10.1016/j.quascirev.2015.08.003

Reynolds, L. C., Simms, A. R., Ejarque, A., King, B., Anderson, R. S., Carlin, J. A., et al. (2018). Coastal flooding and the 1861–2 California storm season. *Mar. Geol.* 400, 49–59. doi: 10.1016/j.margeo.2018.02.005

Rosati, J. D., Dean, R. G., and Walton, T. L. (2013). The modified Bruun Rule extended for landward transport. *Mar. Geol.* 340, 71–81. doi: 10.1016/j.margeo.2013.04.018

Sallenger, A. H. Jr., Krabill, W., Brock, J., Swift, R., Manizade, S., and Stockdon, H. (2002). Sea-cliff erosion as a function of beach changes and extreme wave runup during the 1997–1998 El Niño. *Mar. Geol.* 187, 279–297. doi: 10.1016/s0025-3227(02)00316-x

Sanchez-Cabeza, J., and Ruiz-Fernández, A. (2012). 210Pb sediment radiochronology: an integrated formulation and classification of dating models. *Geochim. Cosmochim. Acta* 82, 183–200. doi: 10.1016/j.gca.2010.12.024

Schwing, F., Murphree, T., and Green, P. (2002). The evolution of oceanic and atmospheric anomalies in the northeast Pacific during the El Niño and La Niña events of 1995–2001. *Prog. Oceanogr.* 54, 459–491. doi: 10.1016/s0079-6611(02)00064-2

Steffen, W., Grinevald, J., Crutzen, P., and McNeill, J. (2011). The anthropocene: conceptual and historical perspectives. *Philos. Trans. R. Soc. Lond. A Math. Phys. Eng. Sci.* 369, 842–867. doi: 10.1098/rsta.2010.0327

Storlazzi, C., and Field, M. (2000). Sediment distribution and transport along a rocky, embayed coast: monterey peninsula and carmel bay, California. *Mar. Geol.* 170, 289–316. doi: 10.1016/s0025-3227(00)00100-6

Storlazzi, C. D., and Griggs, G. B. (2000). Influence of El Niño–Southern Oscillation (ENSO) events on the evolution of central California's shoreline. *Geol. Soc. Am. Bull.* 112, 236–249.

Storlazzi, C. D., and Reid, J. A. (2010). The influence of El Nino-Southern Oscillation (ENSO) cycles on wave-driven sea-floor sediment mobility along the central California continental margin. *Cont. Shelf Res.* 30, 1582–1599.

Stuiver, M., and Reimer, P. J. (1993). Extended 14 C data base and revised CALIB 3.0 14 C age calibration program. *Radiocarbon* 35, 215–230.

Syvitski, J. P., Vörösmarty, C. J., Kettner, A. J., and Green, P. (2005). Impact of humans on the flux of terrestrial sediment to the global coastal ocean. *Science* 308, 376–380.

Traykovski, P., Geyer, W. R., Irish, J., and Lynch, J. (2000). The role of wave-induced density-driven fluid mud flows for cross-shelf transport on the Eel River continental shelf. *Cont. Shelf Res.* 20, 2113–2140.

Warrick, J. A., and Farnsworth, K. L. (2009). Sources of sediment to the coastal waters of the Southern California Bight. *Geol. Soc. Am. Spec. Pap.* 454, 39–52.

Weight, R. W. R., Anderson, J. B., and Fernandez, R. (2011). Rapid mud accumulation on the central texas shelf linked to climate change and sea-level rise. *J. Sediment. Res.* 81, 743–764.

Wheatcroft, R., and Borgeld, J. (2000). Oceanic flood deposits on the northern California shelf: large-scale distribution and small-scale physical properties. *Cont. Shelf Res.* 20, 2163–2190.

Wheatcroft, R., Sommerfield, C., Drake, D., Borgeld, J., and Nittrouer, C. (1997). Rapid and widespread dispersal of flood sediment on the northern California margin. *Geology* 25, 163–166.

Wheatcroft, R. A. (1990). Preservation potential of sedimentary event layers. *Geology* 18, 843–845.

Wheatcroft, R. A., Goñi, M. A., Richardson, K. N., and Borgeld, J. C. (2013). Natural and human impacts on centennial sediment accumulation patterns on the Umpqua River margin, Oregon. *Mar. Geol.* 339, 44–56.

Willis, C. M., and Griggs, G. B. (2003). Reductions in fluvial sediment discharge by coastal dams in California and implications for beach sustainability. *J. Geol.* 111, 167–182.

Wright, L. D., and Nittrouer, C. A. (1995). Dispersal Of river sediments in coastal seas - 6 contrasting cases. *Estuaries* 18, 494–508.

Xu, J., Noble, M., and Eittreim, S. L. (2002). Suspended sediment transport on the continental shelf near Davenport, California. *Mar. Geol.* 181, 171–193.

Zhou, L., Liu, J., Saito, Y., Zhang, Z., Chu, H., and Hu, G. (2014). Coastal erosion as a major sediment supplier to continental shelves: example from the abandoned Old Huanghe (Yellow River) delta. *Cont. Shelf Res.* 82, 43–59.

Conflict of Interest Statement: The authors declare that the research was conducted in the absence of any commercial or financial relationships that could be construed as a potential conflict of interest.

frontiers in Earth Science

ORIGINAL RESEARCH
published: 31 May 2019
doi: 10.3389/feart.2019.00104

Late Quaternary Vegetation Development Following Deglaciation of Northwestern Alexander Archipelago, Alaska

*Thomas A. Ager**

Geosciences and Environmental Change Science Center, U.S. Geological Survey, Denver, CO, United States

The Cordilleran Ice Sheet covered most of southeastern Alaska during the Last Glacial Interval (LGI: Marine Isotope Stage 2). Ice began to recede from western Alexander Archipelago ~17,000 ± 700 yr BP. In this study, pollen analysis and radiocarbon dating of three sediment cores were used to reconstruct, for the first time, the postglacial development of vegetation in the northwestern Alexander Archipelago during the past ~15,240 cal yr. Hummingbird Lake (HL), on southwestern Baranof Island, yielded a sediment core with one of the longest dated records from southeastern Alaska. The earliest part of the HL pollen record (~15,240–14,040 yr BP) indicates that the earliest vegetation was pine (*Pinus contorta* subsp. *contorta*) parkland with willows (*Salix*), heaths (Ericaceae), sedges (Cyperaceae), grasses (Poaceae), herbs and ferns. Starting at ~14,040 yr BP, alder (*Alnus*) rapidly colonized the area as pine populations declined. By 11,400 yr BP, Sitka spruce (*Picea sitchensis*) colonized the area, and soon became the dominant conifer. Mountain hemlock (*Tsuga mertensiana*) also colonized the area by ~11,400 yr BP, followed by western hemlock (*Tsuga heterophylla*) at ~10,200 yr BP. By ~9200 yr BP, western hemlock had become the dominant tree species in the area. During the late Holocene yellow cedar (*Chamaecyparis nootkatensis*) became established. Two marine sediment cores were also analyzed for pollen, with the oldest core from Lower Sitka Sound, between Kruzof and Baranof Islands. The lower part of the core consists of interlayered tephras and freshwater lake muds that are estimated to be ~14,000 to 13,150 yr BP. Pollen evidence indicates that the early postglacial vegetation around Sitka Sound was pine parkland with alders and abundant ferns. Damage to vegetation around Sitka Sound by volcanic eruptions is suggested by abrupt, large shifts in percentages of alder and pine pollen, and fern spores in samples adjacent to tephra layers. A marine sediment core from Slocum Arm, a fiord on the western coast of Chichagof Island, has a basal age of ~10,000 yr BP. The pollen record is similar to the Holocene pollen record at Hummingbird Lake. The sequence of vegetation changes interpreted from the three northwestern Alexander Archipelago pollen records is similar to those from other well-dated sites in southeastern Alaska, although chronologies differ between sites.

Keywords: Alaska, late quaternary, deglaciation, lake sediments, marine sediments, vegetation, pollen analysis, radiocarbon dating

OPEN ACCESS

Edited by:
Dorothy M. Peteet,
Goddard Institute for Space Studies (NASA), United States

Reviewed by:
Rolf Walter Mathewes,
Simon Fraser University, Canada
Li Wu,
Anhui Normal University, China

***Correspondence:**
Thomas A. Ager
tomager75@gmail.com

Specialty section:
This article was submitted to Quaternary Science, Geomorphology and Paleoenvironment, a section of the journal Frontiers in Earth Science

Received: *30 October 2018*
Accepted: *24 April 2019*
Published: *31 May 2019*

Citation:
Ager TA (2019) Late Quaternary Vegetation Development Following Deglaciation of Northwestern Alexander Archipelago, Alaska. Front. Earth Sci. 7:104. doi: 10.3389/feart.2019.00104

INTRODUCTION

The vast conifer forests of present-day southeastern Alaska (**Figure 1B**) are part of the world's largest temperate rainforest that extends from northern California, along the Oregon, Washington, British Columbia (B.C.) and Gulf of Alaska coasts as far northwest as the Cook Inlet region (**Figure 1A**) in south-central Alaska (Heusser, 1960). This northeast Pacific coastal rainforest is not uniform in its composition, as the number of plant species diminishes with cooler, wetter climates at higher latitudes. Fewer species along the northern coasts is also a result of the time required for plants from distant locations to colonize areas that were buried under ice during the Last Glacial Interval (LGI), roughly equivalent to Marine Isotope Stage 2, ∼29,000–14,000 yr BP (Lisiecki and Raymo, 2005). Glacial ice extended from Puget Sound in Washington State northward and westward to the Alaska Peninsula and beyond, into the Aleutians during the LGI (Blaise et al., 1990; Kaufman and Manley, 2004). Many plant species that now grow in southeastern (SE) Alaska appear to have spread northward along the coast into the region perhaps from as far south as coastal areas of Washington State or refugia along the B.C. coast and its exposed continental shelf (Heusser, 1960, 1989; Luternauer et al., 1989; Barrie et al., 1994; Fedje and Josenhans, 2000; Lacourse et al., 2003; Lacourse, 2005; Lacourse and Mathewes, 2005; Mathewes and Clague, 2017). However, the early, rapid spread of some tree species, especially pine, during and following deglaciation suggests that some plant populations probably survived in refugia within SE Alaska, and the Queen Charlotte Islands (Haida Gwaii) of B.C. (**Figure 1B**), as well as on unglaciated areas of the adjacent exposed continental shelves, allowing plants to quickly colonize newly deglaciated lands in the region.

The modern conifer forests of southeastern Alaska are classified as perhumid temperate rainforest, with climate characterized by heavy precipitation and no dry season (Alaback and Pojar, 1997). This region extends southward to northern Vancouver Island in B.C. South of northern Vancouver Island, seasonal rainforests of the Pacific Northwest prevail with a summer dry season. Northwest of SE Alaska is another subregion: subpolar rainforest, which has a cooler climate and vegetation more subalpine in character, fewer tree species, and larger areas covered by wetlands, shrublands, muskeg and meadows (Alaback and Pojar, 1997). In spite of the distances involved in postglacial colonizing of SE Alaska, largely from southern seed sources, the modern flora of southeastern Alaska is extraordinarily rich, with at least ∼862 species and subspecies of known native vascular plants. That number represents ∼56% of the native vascular flora of the entire State of Alaska, according to Muller (1982), and species range maps in Hultén (1968) and Pojar and MacKinnon (1994). This species richness is remarkable, given that SE Alaska's present land area (94,175 km^2) represents only 6.2% of the land area of the State of Alaska. In addition to the rich vascular plant flora (coniferous and deciduous trees, shrubs, and low woody plants, graminoids, forbs, ferns and fern allies), there are 572 known species of mosses and liverworts, 425 species of lichens (Vitt et al., 1988), and over 230 known species of fungi (O'Clair et al., 1997).

The species richness of today's SE Alaskan vegetation, and the ancient appearance of its dense, conifer-dominated rainforests, laden with epiphytic lichens, mosses and fungi, seems at odds with the fact that massive glaciers from the Cordilleran Ice Sheet (CIS) to the east, and local glaciers within the Alexander Archipelago expanded during the LGI to fill all of the fiords with ice, and cover nearly all of the land areas in the region, as well as large areas of the adjacent continental shelf (Carrara et al., 2003, 2007; Kaufman and Manley, 2004). The history of colonization of SE Alaskan and B.C. coastal regions by plants and animals during and following deglaciation has been an intriguing subject for research since 1950. Palynological investigations and radiocarbon dating of postglacial peat and sediment cores have been conducted to reconstruct the chronology and stages by which the vegetation developed. Coastal forests similar to today's existed in the region during the last interglacial (MIS 5), as indicated by pollen analysis of an exposure of organic rich interglacial sediments from the Echo Section, near Lituya Bay (**Figure 1B**). The site was discovered by Worley (1980), and later was sampled and analyzed by Mann (1986) to obtain an informative pollen record. The most abundant pollen types from that interglacial site included *Pinus, Picea, Tsuga heterophylla*, *Tsuga mertensiana, Alnus,* Cyperaceae, and *Lysichiton americanum*, all of which are common in the present-day forests of the region. Interstadial vegetation (MIS 3) of Haida Gwaii in northern coastal B.C. has been reconstructed from pollen evidence and indicates that conifer species were present prior to 32,200 ± 370 yr BP, before the beginning of the LGI (Warner et al., 1984). Interstadial pollen types included fir (*Abies amabilis* was reported, but it may have been *Abies lasiocarpa*), *Picea*, *T. mertensiana*, *Pinus, Alnus, Salix,* Cyperaceae, Poaceae, various herbs as well as fern spores. These pre-LGI pollen records indicate that the vegetation that has developed in southeastern Alaska and coastal B.C. since the end of the last glaciation is composed of essentially the same key species as were present during Marine Isotope Stages 3 (interstadial) and 5 (interglacial).

This paper focuses on reconstructing the postglacial vegetation history of western coastal areas of northwestern Alexander Archipelago (**Figure 1B**), a large area of southeastern Alaska for which no dated pollen records have been published prior to this study. The area under investigation includes western Baranof and Chichagof Islands and adjacent marine waters, a region directly exposed to the full force of North Pacific storms. This investigation is based on pollen and spore analysis of radiocarbon-dated sediment cores from a coastal lake and two marine sediment cores from the region. These data were collected in order to reconstruct the stages and chronology of vegetation development, and to evaluate an area on the southwestern coast of Baranof Island that may have been a refugium where some plants and animals survived during the LGI. The idea that refugia for plants and animals existed along the western edge of the CIS has long been a subject of discussion and research (e.g., Heusser, 1960, 1989; Worley, 1980; Wheeler and Guries, 1982; Heaton et al., 1996; Heaton and Grady, 2003; Lacourse and Mathewes, 2005; Reimchen and Byun, 2005; Carrara et al., 2007). These investigations provide strong biological evidence for the existence of refugia in southeastern Alaska, composed

FIGURE 1 | (A) Inset map of Alaska showing Gulf of Alaska sites mentioned in text: A – Alaska Peninsula; S – Sanak Islands (Misarti et al., 2012); C – Cook Inlet; K – Kodiak Island (Peteet and Mann, 1994); P – Patton Seamounts marine coring sites (de Vernal and Pedersen, 1997; Méheust et al., 2018); E – EW0408-85JC marine coring site (Barron et al., 2009; Davies et al., 2011; Praetorius et al., 2016). **(B)** Map of southeastern Alaska showing geographic features and research locations discussed in text.

of terrestrial and marine ecosystems robust enough to support a genetically distinct population of brown bears, implying long-term isolation from other populations (Heaton et al., 1996).

The reconstruction of changing postglacial environmental conditions in coastal regions of the Gulf of Alaska are also highly relevant to understanding the challenges faced by the first maritime-adapted human colonists who began to reach the area by boat from the northwest Pacific region at some as-yet unknown time after deglaciation, but prior to the beginning of the Holocene (Dixon, 1999, 2001). Human skeletal remains found in the Shuká Káa site (formerly known as On Your Knees Cave) on northwestern Prince of Wales Island (**Figure 1B**) indicate that maritime-adapted humans were present in the Alexander Archipelago by ~10,300 yr BP, and probably much earlier (Dixon, 1999, 2001; Dixon et al., 2014; Carlson and Baichtal, 2015; Lesnek et al., 2018). A recent archeological discovery of human footprints preserved in buried beach sands on Calvert Island in northern coastal B.C. suggests that humans were present in the region at least as early as 13,000 yr BP (Mackie et al., 2018; McLaren et al., 2018). This paper provides evidence of the terrestrial

plant resources and climatic conditions faced by human colonists and their descendants in this dynamic region with its history of earthquakes, tsunamis, volcanic eruptions, rapid sea level changes, and changing climate, faunas, and vegetation. The changes in regional marine and terrestrial faunas during the past ∼17,000 years are recorded in rich fossil vertebrate faunas excavated from caves in southeastern Alaska (Heaton and Grady, 2003; Lesnek et al., 2018) and in Haida Gwaii, B.C. (Wigen, 2005).

Regional Geography and Climate

Southeastern Alaska extends from Dixon Entrance on the south, to Icy Bay (west of Yakutat Bay) to the northwest, a distance of 844 km (**Figure 1B**). Of the region's land area of 94,175 km^2, 12,500 km^2 is presently covered by glacial ice (Molnia, 2008). Present-day climate is maritime, with relatively mild winter temperatures, frequent North Pacific storms, heavy rainfall, especially in autumn and winter, frequent fog, and heavy winter snowfall in the mountains (**Table 1**). The Alexander Archipelago (**Figure 1B**) comprises over 1100 islands, which range in size from small rocky islets to Prince of Wales Island (**Figure 1B**), which is the third largest island in the United States (6674 km^2). The Coast Mountains on the mainland of SE Alaska and B.C. (**Figure 2**) and many of the larger islands (e.g., Chichagof, Baranof, Admiralty, Prince of Wales, Dall, and Revillagigedo) have rugged mountainous terrain, but the altitudes of most mountain chains on the islands are generally too low to support glaciers under present climate conditions. At present, glaciers cover only about 150 km^2 in the Alexander Archipelago, mostly on Chichagof and Baranof Islands (Molnia, 2008).

Modern Vegetation

Most of present-day southeastern Alaska up to ∼700 m altitude is blanketed by dense conifer forests (**Figure 3**), dominated by a few tree species: *T. heterophylla* (western hemlock), *Picea sitchensis* (Sitka spruce), *T. mertensiana* (mountain hemlock), and *Pinus contorta* subsp. *contorta* (shore pine), closely related to lodgepole pine (*P. contorta* subsp. *latifolia*). Also common is *Chamaecyparis nootkatensis* (yellow cedar). In southern Alexander Archipelago, *Thuja plicata* (red cedar), *A. lasiocarpa* (subalpine fir), *Taxus brevifolia* (Pacific yew), and *A. amabilis* (Pacific silver fir) occur, but are absent from northern southeastern Alaska (except for subalpine fir near the Juneau area) and played no role in the present study area's vegetation history. Deciduous trees are locally important, especially along streams, and include *Populus balsamifera* subsp. *trichocarpa* (black cottonwood), and *Alnus rubra* (red alder). The conifer forests of SE Alaska are interspersed with small to large areas of muskeg (peatlands), where mosses, sedges, heaths (Ericaceae), and slow growing or stunted conifer trees such as shore pines and mountain hemlock are found (**Figure 4**). Tree growth is often limited in muskeg terrain by waterlogged acidic soils, thick peat deposits, and low availability of nutrients. Muskeg generally forms on level or slightly sloping terrain in cool, wet climates. With increasing altitude in mountainous areas, the coastal forest of western hemlock-Sitka spruce transitions to a montane forest in which mountain hemlock trees become more abundant than spruce and western hemlock. Trees become smaller, are slower growing, and are interspersed with shrub thickets, especially Sitka alders (*Alnus viridis* subsp. *sinuata*). Mountain hemlocks become far more abundant at higher elevations in the subalpine zone and that species, along with less common Sitka spruce develop as low growing shrubs at the upper limits of tree growth (**Figure 5**; Heusser, 1989). Alpine tundra occurs above the altitudinal limits of tree growth (∼675–700 m), which has a discontinuous vegetation cover of mosses, lichens, cushion plants, prostrate woody shrubs, such as *Salix* (low willows), *Empetrum* (crowberry), *Phyllodoce aleutica* (mountain heather), *Cassiope mertensiana* (Merten's cassiope) and many other hardy plants that grow interspersed with barren bedrock, talus, and glacial deposits (Jaques, 1973; Heusser, 1989; O'Clair et al., 1997). The flora and vegetation of subalpine and alpine zones in SE Alaska are of particular interest, as the plants that are able to grow in those cooler, snowier environments with shorter growing seasons are most likely to have survived in refugia at much lower altitudes during the LGI when mean July temperatures were probably 4–5°C cooler near sea level than today (Heusser, 1989; **Table 1**). Subalpine vegetation is also heavily utilized by bears, Sitka deer, and other animals as a summer food source (O'Clair et al., 1997).

Previous Research on Vegetation History of Southeastern Alaska

Calvin J. Heusser began an ambitious project in 1950 to reconstruct the postglacial history of vegetation development of the Pacific coast conifer forests by analyzing pollen records from peat deposits scattered along the coasts between northern California northward to the Gulf of Alaska and sites as far west as the Aleutians. His investigations included numerous sites in southeastern Alaska and coastal B.C. (Heusser, 1952, 1954, 1960, 1965, 1985, 1989). Heusser's pioneering studies

TABLE 1 | Climate data for northern Alexander Archipelago and vicinity.

	Location			Mean temp (°C)			Mean annual precipitation (cm)	Years of record
Locality	Latitude (N)	Longitude (W)	Altitude (m)	January	July	Annual		
Sitka	57°04′	135°21′	3	1.2	13.3	7.1	217	1944–2016
Gustavus	58°24′	135°44′	12.2	–4.1	13.2	4.8	141.5	1949–2012
Juneau	58°22′	134°35′	3	–4	13.4	4.9	146.5	1936–2012

Data from Western Regional Climate Center (2018), Desert Research Institute (wrcc.dri.edu); accessed May 14, 2018.

occurred at a time when radiocarbon dating methods were under early development, and therefore few of Heusser's sites in the region had any age control. Those of Heusser's sites with radiocarbon age control usually had only a single date near the core bases (Heusser, 1960). Also, the reliance on peat deposits for sampling sites limited the time depth of most of the records obtained, as most peat deposits in the region are of Holocene age (Heusser, 1960). Nevertheless, his landmark publication remains an impressive contribution and a valuable source of information about the modern vegetation and the history of the North Pacific coastal rainforests.

Updating the record of vegetation history of southeastern Alaska following Heusser's pioneering research has proceeded slowly, beginning with reports of dated pollen records from a postglacial peat deposit near Lituya Bay (**Figure 1B**; Mann, 1983), Lily Lake near Haines (**Figure 1B**; Cwynar, 1990), a lake on Pleasant Island near Glacier Bay (**Figure 1B**; Hansen and Engstrom, 1996), an archeological site with a discontinuous Holocene pollen record (Hidden Falls) at Kasnyku Bay on the northeastern coast of Baranof Island (Holloway, 1989), a peat deposit on Mitkof Island (**Figure 1B**; Ager et al., 2010), a lake sediment deposit (Pass Lake) on central Prince of Wales Island (**Figure 1B**; Ager and Rosenbaum, 2009), and lake sediments and peat deposits from Heceta Island (**Figure 1B**; Ager, 2007). In northwestern Alexander Archipelago, previous studies are few, and include pollen records from peat deposits in the Sitka area, and near Suloia Lake on southern Chichagof Island (**Figure 1B**; Heusser, 1952, 1954, 1960). None of Heusser's sites from this region had radiocarbon age control, and in the case of the Sitka area sites, only a few conifer pollen types were recorded. Those records are probably no older than mid-Holocene age, based on comparison with records discussed in this paper. The Suloia Lake peat core pollen record from Chichagof island is likely of pre-Holocene age at the base of the core. This paper provides the missing history of dated, pollen-based vegetation histories for the northwestern archipelago, and then compares the region's history with well-dated records from other areas of SE Alaska.

FIGURE 2 | Juneau Icefield with its ice-filled valleys and scattered nunataks is a useful analog for what much of the Alexander Archipelago was like during the Last Glacial Interval (T. Ager photo).

FIGURE 3 | Temperate western hemlock-Sitka spruce coniferous rainforest in southeastern Alaska (T. Ager photo).

Glacial and Climate History

Reviews of glacial history of southeastern Alaska (Mann, 1986; Mann and Hamilton, 1995) emphasize how little was known about the region's glacial record as of the mid-1980s and mid-1990s. Since then, progress in interpreting the onshore history of the LGI has been limited (e.g., Briner et al., 2017; Lyles et al., 2017). Important new information derived from cosmogenic dating of erratic boulders and glacially scoured bedrock surfaces indicate that LGI glacial ice was somewhat more extensive in southwestern Alexander Archipelago than was depicted in maps by Carrara et al. (2003, 2007) and Kaufman and Manley (2004). Their studies indicate that deglaciation in that region was underway in that area by ∼17,000 ± 700 yr BP (Lesnek et al., 2018). The maximum extent of LGI ice in the archipelago appears to have occurred between ∼20,000–17,000 yr BP, based on a gap in dated vertebrate remains in cave deposits (Heaton and Grady, 2003; Lesnek et al., 2018). Farther west along the coast of Gulf of Alaska (GOA), glacial ice retreated from the continental shelf south of the Alaska Peninsula (**Figure 1A**) ∼17,000 yr BP based on radiocarbon dating of lake sediment cores from Sanak Island (**Figure 1A**) south of the peninsula (Misarti et al., 2012). On Kodiak Island (**Figure 1A**), investigations indicate that glacial ice retreat also occurred early: ∼16,700 yr BP (Peteet and Mann, 1994).

During the LGI the CIS vastly expanded from the Coast Mountains of SE Alaska to fill the numerous fiords with glacial ice (**Figure 2**). Expanding glaciers eventually overtopped many of the smaller, lower islands, especially in the eastern archipelago (e.g., Mitkof, Kupreanof, Zarembo, Gravina, Etolin, and Wrangell Islands). At its maximum LGI extent, the CIS was about the size of the present Greenland ice sheet (Clague, 1989). In many areas, the CIS and local ice from the mountains on western Alexander Archipelago islands expanded onto the continental shelf (Carrara et al., 2007), as it did along the northern and northeastern coasts of the Gulf of Alaska (Mann, 1986; Molnia, 1986). However, it is likely that some areas along the western margins of the Alexander Archipelago and parts of the adjacent subaerially exposed inner

FIGURE 4 | Muskeg (peatlands) with shore pines (*Pinus contorta* subsp. *contorta*) on Kruzof Island, northwestern Alexander Archipelago, southeastern Alaska (T. Ager photo).

FIGURE 5 | Upper subalpine zone vegetation with stunted mountain hemlock and Sitka spruce growing near its altitudinal limits, on Prince of Wales Island, southeastern Alaska (T. Ager photo).

continental shelf remained free of glacial ice cover (Heaton and Grady, 2003; Carrara et al., 2007). Such areas provided likely refugia for plants and animals. Other likely refugia have been identified in the Lituya Bay area (**Figure 1B**) north of the Archipelago (Heusser, 1960; Worley, 1980; Mann, 1983, 1986). Likely LGI refugia also existed on the exposed continental shelf east and south of Haida Gwaii in northern coastal B.C. (**Figure 1B**; Heusser, 1989; Lacourse et al., 2003; Lacourse and Mathewes, 2005).

GOA coastal areas and mountain ranges underwent significant isostatic crustal adjustments as a result of the massive ice load during the LGI, with the greatest crustal depression occurring along the mainland Coast Mountains and inner (eastern) islands of the archipelago where ice was thickest (Mann, 1986). Along the western margins of the archipelago, and farther south in the area of Haida Gwaii in B.C., crustal adjustments included forebulge development caused by westward lateral movement of upper mantle material from under the Coast Mountains that had subsided under the weight of thick glacial ice. The forebulge elevated coastal areas of the western archipelago and raised large areas of the inner continental shelf well beyond the areas that were exposed by at least –125 m of eustatic sea level lowering alone (Clague, 1983; Hetherington et al., 2004; Briner et al., 2017).

Important advances in glacial-deglacial history in the region have been made recently through detailed, well-dated paleoceanographic studies of a key marine sediment core from the northern GOA region (**Figure 1A**, Site E: Barron et al., 2009; Davies et al., 2011; Praetorius and Mix, 2014; Praetorius et al., 2015). A marine record spans the past ∼17,400 yr and was collected from the continental slope (core EW0408-85JC) at 59.5553°N, 144.1535°W, 682 m water depth). That record indicates that seawater salinities began to freshen from glacial meltwater by 16,650 ± 170 yr BP, but ice proximal glaciomarine sediments were still being deposited on the continental slope at that time. In that area, coastal glaciers that expanded onto the continental shelf, perhaps in part as floating ice shelves, persisted until ∼14,790 ± 380 yr BP, when glaciers apparently retreated onshore and into fiords (Davies et al., 2011). The retreat by glaciers to onshore positions coincides with the onset of the Bølling-Allerød warm interval (14,700–12,900 yr BP). The withdrawal of glaciers from coastal waters of the northern GOA coincides with the disappearance of ice-rafted debris (IRD) in marine core 85JC, indicating that icebergs from calving glaciers largely disappeared from the GOA after ∼14,700 yr BP (Praetorius and Mix, 2014). Sea surface temperatures in the GOA remained cold until after ∼16,000 yr BP, when they begin to warm, rising ∼4–5°C during the Bølling, cooled somewhat during the Allerød, and cooled more during the Younger Dryas (12,900–11,700 yr BP), then warmed ∼4–5°C again during the early Holocene (11,500–10,500 yr BP; Praetorius and Mix, 2014; Praetorius et al., 2015).

Deglaciation of the continental shelf near Haida Gwaii, B.C., began as early as ∼18,000 yr BP, and the lowlands of the islands were undergoing deglaciation by about that time (Barrie and Conway, 1999). The available records from the GOA indicate the timing of deglaciation in the western Alexander Archipelago by ∼17,000 ± 700 yr BP from cosmogenic dating of erratic boulders and ice-scoured bedrock surfaces. However, stagnating glacial ice in some valleys may have persisted for longer, e.g., 15,300 ± 600 yr BP on Baker Island in the southwestern archipelago (**Figure 1B**; Lesnek et al., 2018).

Studies of marine diatom and dinocyst assemblages in Gulf of Alaska sediment cores, including sites in the Patton Seamounts southeast of Kodiak Island (**Figure 1A**, site P) provide information about the extent and timing of sea ice during and after the LGI (de Vernal and Pedersen, 1997; Barron et al., 2009, 2016; Méheust et al., 2018). The marine microfossil assemblages indicate that LGI winter sea ice was very widespread in the Gulf of Alaska, probably lasting for ∼six months a year, and extending seaward from the Gulf of Alaska coastlines perhaps as far south as ∼52°N in central GOA (Méheust et al., 2018), and along the coasts of SE Alaska and probably B.C., as indicated by the presence of sea ice diatoms preserved in marine sediment records (Barron et al., 2009, 2016). Other evidence for coastal sea ice includes late

glacial-age vertebrate fossils of mammals preserved in caves in southeastern Alaska that include species associated with arctic sea ice, such as ringed seals (*Phoca hispida*) and arctic foxes (*Alopex lagopus*; Heaton and Grady, 2003; Lesnek et al., 2018). Winter sea ice disappeared from most of the Gulf of Alaska during the Bølling warm interval, starting ∼14,700 yr BP (Méheust et al., 2018), but persisted at least intermittently during winters, well into the Holocene in coastal areas, where cold winters and input of cool freshwater from runoff from rain and snow and glacial melting reduced local sea surface salinity, promoting winter sea ice development (Barron et al., 2009, 2016). Coastal sea ice was more widespread during the Younger Dryas cold interval (Barron et al., 2009) when summer sea surface temperatures dropped ∼4°C (Praetorius et al., 2015). The existence of winter-spring sea ice in fiords during and soon after deglaciation may have allowed animals to disperse over ice from island to island, although they are known to swim across marine waterways today in spite of strong currents and variable sea conditions. Sea ice history has implications for human colonization of Alaskan coastal regions, reducing winter mobility by boat, and making access to marine food resources more challenging. Colder temperatures during the Younger Dryas resulted in less productive marine ecosystems, reducing potential food resources, such as fish, shellfish and other intertidal faunas and floras (Hetherington and Reid, 2003; Davies et al., 2011).

Climate shifts within the Holocene began with early Holocene warming ∼11,500–10,500 (e.g., Pellatt and Mathewes, 1997; Praetorius et al., 2015), followed by cooling of the GOA between ∼10,500–8000 ka, followed by gradual warming (Praetorius and Mix, 2014). During the mid- to late Holocene, temperatures shifted between warmer and cooler intervals, during which several Neoglacial ice advances and retreats occurred in the mountains rimming the Gulf of Alaska region, with many glaciers reaching tidewater (McKenzie and Goldthwait, 1971; Heusser et al., 1985; Mann et al., 1998; Moss et al., 2007). The Neoglacial began in the Gulf of Alaska region ∼5600 yr BP and included the Little Ice Age that began ∼1350 AD and ended ∼1900 AD (Mann et al., 1998).

MATERIALS AND METHODS

The lake sediments in Hummingbird Lake (HL) were sampled during the summer of 2000 with a modified Livingstone piston corer (Aaby and Digerfeldt, 1986), using aluminum core tubes with an inside diameter of 5 cm. Sediment cores were taken in 1-m-long drives (or less), from an anchored platform with inflatable floats. Soon after the field season the sealed cores were extruded in the laboratory, described, and sampled for pollen analysis and radiocarbon dating. Samples for pollen analysis were collected at 2 to 10 cm intervals and varied in volume between 2 and 5 cm^3. Core samples were processed in the U.S. Geological Survey (USGS) Cenozoic Palynology Laboratory in Denver, Colorado, using pollen extraction methods modified from those described by Doher (1980) and Brown (2008). Processing treatments began with screening to remove coarse plant detritus > 150 μm, then washed in dilute HCl to remove carbonates, HF in a hot water bath to remove silicate minerals, then timed washes in Shultze solution (10% HNO_3 and potassium chlorate ($KClO_3$) to oxidize fine plant detritus remaining after sieving. A 5% solution of potassium hydroxide (KCl) was used to remove oxidized organic material without damaging pollen and spores. Pollen residues were mounted on glass slides in glycerine jelly. Pollen slides were examined with a transmitted light binocular microscope at magnifications of 400×, 630×, and occasionally 1000× (oil immersion). Pollen and spores were identified using a modern pollen reference slide collection at the USGS in Denver.

Core samples selected for radiocarbon dating, many of which consisted of detrital peat, were prepared at the USGS Radiocarbon Laboratory in Reston, Virginia, and dated by Accelerator Mass Spectrometry (AMS) at the National Science Foundation-Arizona dating facility in Tucson, Arizona, or at the Center for Accelerator Mass Spectrometry (CAMS), Lawrence Livermore National Laboratory in Livermore, California. The lowest sample in the HL core selected for AMS radiocarbon dating contained more silt than detrital peat, and the organic material used for dating that sample consisted of excess pollen concentrates resulting from the processing procedures for pollen analysis (Brown et al., 1989). Radiocarbon ages and their calibrations for the Hummingbird Lake core are presented in **Table 2**. The ^{14}C ages were calibrated using the IntCal13 dataset and CALIB 7.1 html (Stuiver and Reimer, 1993; Reimer et al., 2013). Ages are presented in calibrated years, yr BP (Before Present; 0 yr BP = 1950 A.D.), and uncertainties are given at the 95% (2-sigma) confidence level. In the event that multiple ranges were permitted during calibration, ages discussed in the text and shown in the figures are based on the mean of the ranges weighted by their probabilities and are presented without uncertainties. For example, an age of a single calibrated range would be given as 13,090 ± 100 yr BP, whereas it would be presented as ∼13,100 yr BP if multiple ranges were permitted.

Additional samples for pollen analysis and radiocarbon dating were collected from two cores obtained during the August–September 2004 oceanographic research cruise of the R/V Maurice Ewing. The cores were obtained with a jumbo piston corer with a 10 cm inside diameter, in single drives up to 18 m long. These cores, along with several others, were sampled at the Oregon State University marine core repository in Corvallis, Oregon. The generally rapid sedimentation rates in the marine cores allowed larger sampling intervals, sometimes 50 cm or more. In core EW0408-40JC, some sampling intervals in the lower part of the core were much closer in order to evaluate the influence of volcanic activity on vegetation changes. The radiocarbon chronologies for these two cores were developed by dating shell fragments, wood, and plant material, as discussed in Addison et al. (2010) for EW0408-40JC from lower Sitka Sound (**Figure 1B**), and in Barron et al. (2016) for EW0408-47JC in Slocum Arm (**Figure 1B**). Corrections for marine reservoir effect (MRE) and calibrations for the radiocarbon ages are presented in those publications. Pollen and spore percentage diagrams for the sites discussed in

TABLE 2 | Radiocarbon ages and calibrations for the Hummingbird Lake core, Baranof Island, Alaska.

Hummingbird Lake								
Still Harbor, SW Baranof Island, Alaska								
Core depth (cm)	**Radiocarbon age (1-sigma)**	**^{13}C**	**Calibrated range 2-sigma**			**Calibrated ^{14}C ages**	**Lab number**	**Material dated**
			Min	**Max**	***P***			
85	5340 ± 30	–25	6001	6210	0.98	6110 ± 100	WW-5688 (AA)	Peat
145	4265 ± 35	–25	4810	4878	0.88	∼4850	WW-4527 (CAMS)	Peat
			4706	4756	0.1			
175	5235 ± 35	–25	5916	6027	0.78	∼5980	WW-5689 (AA)	Peat
			6077	6117	0.12			
			6151	6176	0.06			
205	6580 ± 35	–25	7428	7517	0.87	∼7480	WW-4528 (CAMS)	Peat
			7536	7562	0.13			
235	7800 ± 35	–25	8511	8642	0.96	8580 ± 60	WW-5663 (CAMS)	Peat
245	8215 ± 30	–25	9077	9285	0.96	9180 ± 110	WW-5690 (AA)	Peat
285	9145 ± 35	–25	10232	10402	1	10320 ± 80	WW-4529 (CAMS)	Peat
325	10055 ± 35	–25	11392	11764	1	11580 ± 180	WW-4530 (CAMS)	Peat
355	10500 ± 60	–25	12366	12633	0.8	∼12460	WW-5691 (AA)	Peat
			12225	12357	0.15			
			12140	12212	0.06			
365	10985 ± 30	–25	12729	12962	1	12850 ± 110	WW-5692 (AA)	Peat
396	12660 ± 54	–27.6	14795	15246	1	15020 ± 230	WW-7457 (CAMS)	Pollen concentrate

CAMS: Samples for which ^{14}C ages were determined at the Center for Accelerator Mass Spectrometry, Lawrence Livermore National Laboratory. AA: Samples for which ^{14}C ages were determined at the NSF-Arizona Accelerator Mass Spectrometry Facility in Tucson, Arizona.

this paper were drafted using Tilia and TiliaGraph software (Grimm, 1991, 1993).

RESULTS

Hummingbird Lake Core

The longest and most complete late Quaternary pollen record currently available from northwestern Alexander Archipelago was obtained from Hummingbird Lake (informal name), near the northern shore of Still Harbor on the remote southwestern coast of Baranof Island (**Figures 1B**, **6**). The lake is located at 56.54931°N, 135.01652°W, at an altitude of 46 m. The lake has a surface area of 6.47 ha, and a maximum depth of 18 m. The lake formed in a trough between bedrock ridges and outcrops striking NW-SE. The water depth at the coring site was 15.2 m. The bedrock underlying the area and exposed in landslide scars is Sitka Graywacke of Late Jurassic to Early Cretaceous age (Loney et al., 1975). The lake was selected as a coring target from air photos because of its location within a suspected refugium, an area that does not appear to have been overridden by glacial ice during the LGI (Carrara et al., 2003, 2007). The northwest-southeast trending bedrock ridges within the suspected refugium may have diverted valley glaciers that were flowing from the mountains farther inland to the northwest. If this interpretation is correct, the diverted glaciers would have flowed into the Whale Bay glacier system (**Figure 1B**) rather than flowing directly southwest over a series of perpendicular sharp bedrock ridges to the (present) coast. During our brief ground surveys of the Still Harbor and Sandy Bay areas (**Figure 1B**), no glacial landforms, erratic boulders, or glacial deposits were observed in landslide scars and coastal exposures. During the LGI, the glacier within Whale Bay advanced onto the adjacent continental shelf, and glaciers to the south of Snipe Bay (**Figure 1B**) also reached part of the exposed inner shelf (Carrara et al., 2003, 2007). A large expanse of the subaerially exposed continental shelf south of Whale Bay glacial ice would likely have provided a significant refugium for plants and animals during the LGI (Carrara et al., 2003, 2007). The area of the exposed shelf would likely have been considerably larger than that depicted in Carrara et al. (2007), if the forebulge raised the shelf in this area.

The immediate area around HL has a present-day vegetation of mixed conifer coastal forest that is composed of *T. heterophylla, P. contorta,* subsp. *contorta,* and *C. nootkatensis. P. sitchensis* and *T. mertensiana* trees and *Alnus* shrubs were not observed in the immediate vicinity of the lake, but the pollen record from the lake indicates that those trees and shrubs are present in the area. Common shrubs observed in the lake area include *Menziesia ferruginea, Vaccinium* spp., *Empetrum nigrum*, and *Juniperus communis.* Aquatic and semiaquatic plants observed in the lake areas include *Nuphar polysepalum, Eriophorum russeolum, Sparganium angustifolium, Menyanthes trifoliata, Isoëtes, Potamogeton natans,* and *Carex* spp. Muskeg areas near the lake include numerous moss species including *Sphagnum* spp., along with Cyperaceae, mostly *Carex* spp., along with *Vaccinium* spp., *Kalmia polifolia, Ledum groenlandicum,*

FIGURE 6 | Hummingbird Lake with coring platform in distance. Also shown is hemlock-yellow cedar forest on steep slopes at Still Harbor, southwestern coast, Baranof Island (Paul Carrara photo).

Andromeda polifolia, Oxycoccus oxycoccus, Cornus canadensis, E. nigrum, Drosera rotundifolia, Gentiana douglasiana, Tofieldia glutinosa, Coptis trifoliata, and *Geum calthifolium.*

The lake sediments were sampled with a 5 cm-diameter piston corer to a total penetration of 450 cm below the lake bottom. The lowest 48 cm of sediments encountered could only be penetrated by percussion coring, using a cylindrical 10 kg hammer with an anvil attachment on a coring extension rod. The piston corer hit a hard layer at ∼450 cm core depth that may have been bedrock, which ended the sampling operations. The lowermost 48 cm of sediments fell out of the core tube when the piston corer was raised to the surface, but a small amount of sediment recovered indicates that the lost sediments were fine sand, perhaps eolian sand, perhaps from the terrain around Whale Bay that was probably deglaciated or in ice retreat. The recovered sediments from the 402 cm long Hummingbird Lake core consisted of 118 alternating layers of fine detrital peat, and coarser, more fibrous peat. Most of the coarse peat layers were 1–2 cm thick. Those coarse layers may represent rapid deposition during major rainstorm events that may have washed plant detritus into the lake from the surrounding steep upland slopes (**Figure 6**). Far fewer layers (3) of coarse peat occurred below 315 cm core depth, where the sediments contained more silt. The limited number of those coarser detrital peat layers in the lower part of the core may reflect less accumulation of plant detritus on the slopes adjacent to the lake during the first ∼4000 years of the record, or it may indicate fewer major rainfall or meltwater events during that period.

Hummingbird Lake Pollen Record

The pollen and spore record recovered from Hummingbird Lake (HL) is shown in **Figure 7** and **Supplementary Table S1**. Pollen sums (the total of all pollen grains counted in a single sample) exceeded 300 in all but two samples, and sums ranged from 217

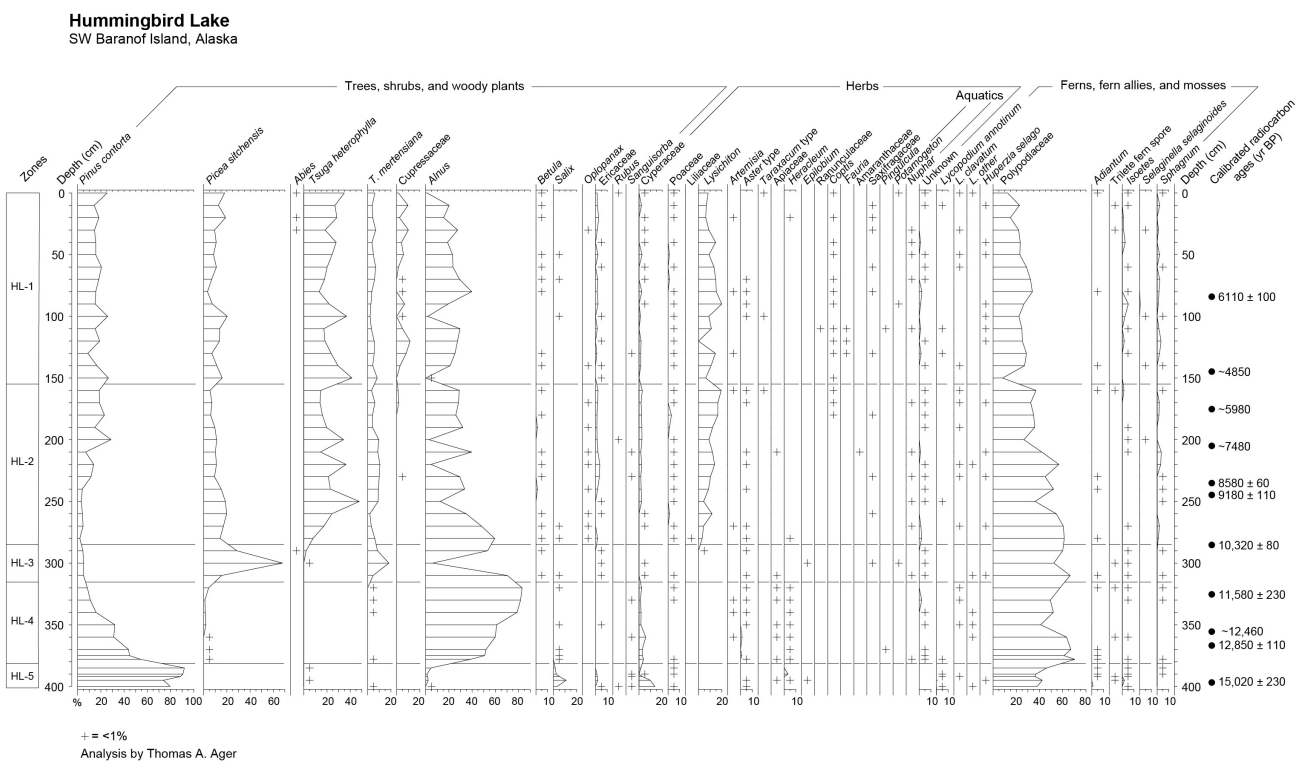

FIGURE 7 | Pollen and spore percentage diagram with calibrated radiocarbon ages for the Hummingbird Lake sediment core, from the southwestern coast of Baranof Island. Pollen data are shown in **Supplementary Table S1**.

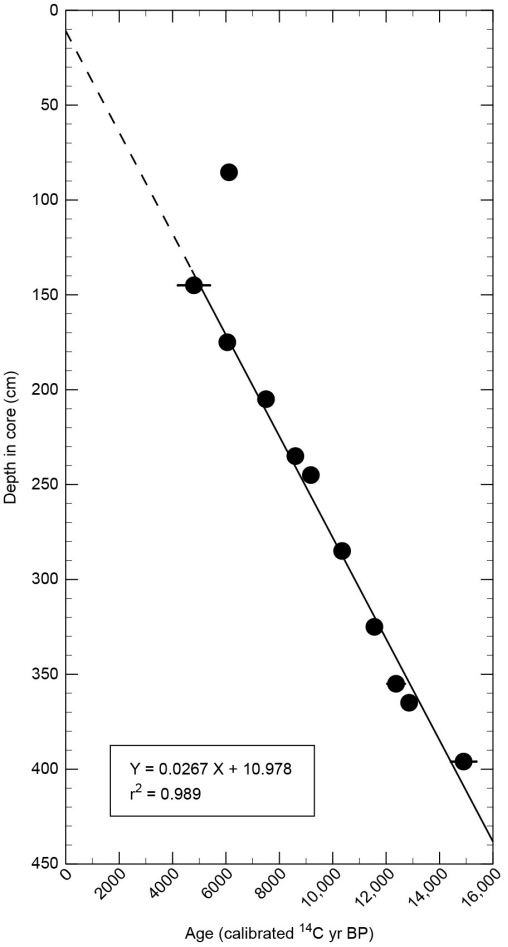

FIGURE 8 | Depth vs. calibrated radiocarbon sample age plot for the Hummingbird Lake core.

to 366 grains. The pollen plus spore sums ranged between 354 to 1184 grains. The pollen and spore percentage diagram is divided into five pollen assemblage zones, the boundaries of which were drawn where significant changes in pollen assemblages occur, such as the initial local arrival of pollen of a tree species, such as Sitka spruce. The chronology for the core is provided by 11 AMS radiocarbon-dated core samples (**Table 2**), all but one of which fall close to the regression line that indicates an average sedimentation rate (∼37.9 yr/cm) over the past ∼15,240 years (**Figure 8**). The uppermost calibrated radiocarbon age plots far from the regression line and is clearly anomalously old. It probably represents plant material that was eroded from older deposits on steep slopes adjacent to the lake and transported into lake sediments much younger than the dated material. That sample was not used to calculate the slope of the regression line and was not used for interpreting the core chronology.

Pollen Zone HL-5

Beginning with the lowest, and oldest pollen and spore assemblage zone (HL-5, 400–382 cm core depth; ∼15,240 to ∼14,040 yr BP), the dominant pollen and spore types include abundant *Pinus* pollen and fern spores, mostly of the Polypodiaceae type (monolete, psilate). Pollen types that are present in low percentages include *Salix,* Ericaceae, Cyperaceae, Poaceae, *Aster* type, *Heracleum* and other Apiaceae, and *Epilobium* type. *Isoëtes* microspores are the only aquatic plant fossils represented in HL-5 pollen samples. The oldest radiocarbon age obtained from the core within lower zone HL-5 is 15,020 ± 230 yr BP (**Table 2**). That radiocarbon sample was obtained from excess pollen and spore concentrates remaining after sample processing to obtain material for pollen analysis. Such pollen concentrates have been shown to be reliable material for AMS radiocarbon dating (Brown et al., 1989). The depth vs. age plot (**Figure 8**) shows that the lowermost dated sample from the HL core falls close to the regression line calculated for the core, and therefore the age is likely to be valid. The abundance of pine pollen (>75% of the pollen sum) in even the lowermost samples in Zone HL-5 suggests that pines were well established in the area before the extrapolated age of the base of the core (∼15,240 yr BP), and perhaps were growing within the hypothesized refugium on southwestern Baranof Island (Carrara et al., 2007) and probably on the adjacent subaerially exposed continental shelf. It is noteworthy that the calculated pollen accumulation rates for pine from a sediment core from an unnamed lake on Pleasant Island in the early postglacial (pre-13,000 yr BP) are much higher (up to ∼4000 grains cm^{-2} yr^{-1}) than at any time during the Younger Dryas cold interval (12,900–11,700 yr BP) that followed, or during the Holocene (Hansen and Engstrom, 1996). The earliest approximate age for pine at Hummingbird Lake (∼15,240 yr BP) predates the onset of the Bølling-Allerød (BA) warmer climate interval (∼14,700–12,900 yr BP). Pine populations may have been responding to the beginnings of ocean warming at ∼16,000 yr BP that preceded the BA warming in the Gulf of Alaska (Praetorius et al., 2015). The BA is recognized from Gulf of Alaska marine sediments as a warmer climate event, with some cooling events during the Allerød (Barron et al., 2009; Davies et al., 2011; Praetorius and Mix, 2014; Praetorius et al., 2015).

Two tephras were discovered in the lower part of the Hummingbird Lake core within Zone HL-5 and at the boundary between Zones HL-5 and HL-4. The upper, slightly younger tephra is from 378 to 381.6 cm core depth, and is light gray to white in color. The lower tephra is from 390.5 to 392.2 cm and is pinkish-gray in color. The approximate ages of the two tephras, calculated by interpolating between dated core samples are ∼13,760 yr BP for the upper tephra, and 14,600 yr BP for the lower tephra. Both tephra samples were analyzed by microprobe by John Westgate at University of Toronto, and he concluded that the upper tephra was rhyolitic in composition and came from one of the early postglacial eruptions from the Mount Edgecumbe volcanic field on Kruzof Island west of Sitka (Riehle et al., 1992a,b; Addison et al., 2010). The lower tephra is also of rhyolitic composition, but came from an unidentified source, perhaps from the Alaska Peninsula. Neither tephra layer is associated with changes in pollen and spore percentages that might indicate damage to vegetation as a result of the ash

deposition, in contrast to the record of EW0408-40JC, to be described below.

Zone HL-4

The age of Pollen Zone HL-4's lower boundary at 382 cm core depth is ∼14,040 yr BP (interpolated age), and the upper boundary is at 317 cm core depth, ∼11,330 yr BP (interpolated age) which is near the base of the Holocene. The pollen samples within this zone record an apparently rapid expansion by *Alnus*, probably Sitka alder (*A. viridis* subsp. *sinuata*) which is the most common alder shrub in southeastern Alaska today, often forming nearly impenetrable thickets along shorelines, in gullies, on avalanche scars, and on mountain slopes in the upper subalpine zone. Within HL-4, the rapid increase in alder pollen percentages coincides with a dramatic decline in pine pollen percentages. This may be a response to somewhat cooler climates during the Allerød, as suggested by paleoceanographic records from the Gulf of Alaska and the even colder conditions during the Younger Dryas cold interval (12,900–11,700 yr BP) that followed (Davies et al., 2011; Praetorius and Mix, 2014). *P. contorta* subsp. *contorta* grows most commonly in lowland areas of SE Alaska, but it is sometimes found growing in the cooler subalpine zone of southeastern Alaska, where such climatic conditions result in slow, stunted growth habit in conifers, and it is generally uncommon. *Alnus* shrubs, on the other hand, are more tolerant of colder climates, as indicated by their abundant growth in the upper subalpine zone in SE Alaska. Alder populations first began to expand during the Allerød (∼14,200–12,900 yr BP), but expanded much more during the Younger Dryas in sites across southeastern Alaska. Alder populations in eastern Canada, although the alder species are different than in southeastern Alaska, also expanded during the Younger Dryas (Mayle et al., 1993). Fern spores are abundant in HL-4 samples, and that may reflect their common occurrence within alder thickets and as colonizing plants in disturbed terrain. Pollen types present in HL-4 in low percentages include Cyperaceae, *Salix, Artemisia.* and *Heracleum* and other Apiaceae. Pollen of the aquatic plant *Nuphar* makes its first appearance within Zone HL-4. The only other aquatic plant represented in HL-4 is *Isoëtes* (quillwort), a spore-producing plant. Very low percentages of pollen of *P. sitchensis* occur in lower HL-4 samples and increase slightly near the top of the zone. This initial appearance of spruce pollen suggests that the species was probably present on southern Baranof Island as early as ∼12,400 yr BP, but was probably not yet present near Still Harbor. Its slight percentage increase in upper HL-4 samples suggests that spruce trees were approaching the Still Harbor area by ∼11,200 yr BP.

Another site sampled during this investigation on southwestern Baranof Island during the 2000 field season was a peat bog located 9.5 km south of Hummingbird Lake, near the north shore of Sandy Bay (**Figure 1B**) at 56.47657°N, 134.95691°W, at 18 m asl. The bog site was selected as a coring target from air photos of the area, when no suitable lakes were found to be accessible from the shores of Sandy Bay. We recovered a peat and lake sediment core 755 cm long that has a pollen record quite similar to that in Hummingbird Lake, but the record is somewhat younger at the base (∼14,600 yr BP). The Sandy Bay bog pollen record is not presented here, as it is quite similar to that from Hummingbird Lake. One unusual discovery from within the Sandy Bay core is worthy of mention, however. Three well-preserved seed cones of *P. sitchensis* were recovered from the Sandy Bay core. The stratigraphically lowest of the cluster of three cones (625–630 cm core depth) yielded a radiocarbon age of 10,000 ± 40 yr BP (WW-4387: calibrated age ∼11,500 ± 142 yr BP), near the beginning of the Holocene. The cone's position in that core coincides with a major rise in spruce pollen in the core sediments that enclosed the seed cone, and demonstrates that *Picea* was present in the Sandy Bay area, only slightly before it began to colonize the Still Harbor area ∼11,300 yr BP. Since conifers are wind pollinated, the presence of low percentages of pollen alone may not indicate that the trees grew at or very near the sampling site. The presence of macrofossils such as seed cones, needles, or stomatal cells derived from decomposed conifer needles (Hansen, 1995; Lacourse et al., 2012, 2016) provide convincing evidence of local presence. At Sandy Bay, the strongest evidence for its arrival locally comes from the presence of spruce seed cones coinciding with rising spruce pollen percentages. No spruce macrofossils were found in the HL core. At Cape Ball, on Graham Island in Haida Gwaii, B.C. (**Figure 1B**), Warner and Chmielewski (1987) recovered seed cones of spruce of latest Pleistocene and early Holocene age that had morphological characteristics of hybrids between *P. sitchensis* and *Picea glauca*. It is therefore possible that the early colonization of southeastern Alaska by spruce included such hybrids. However, spruce needles found in association with the seed cones at Cape Ball had characteristics of Sitka spruce (Warner and Chmielewski, 1987), so the possible presence of early postglacial spruce hybrids in the region remains uncertain.

Zone HL-3

Pollen Zone HL-3 in the Hummingbird Lake core spans core depths 315–285 cm, between ∼11,330 and 10,350 yr BP. The main features in the HL-3 pollen record are the rapid rise in spruce percentages (rising above 60% of the pollen sum in one sample), and the smaller rise in percentages of *T. mertensiana* (mountain hemlock) pollen. Mountain hemlock grows in southeastern Alaska from sea level to the upper subalpine zone, but greatly increases in abundance at higher altitudes. However, the trees become increasingly stunted at higher altitudes where there are deep winter snows and shorter, cooler growing seasons. Mountain hemlock develops low shrubby growth forms near its upper altitudinal limits of growth in the upper subalpine zone at ∼685 m in the Sitka area (Yehle, 1974). Trace amounts of mountain hemlock pollen in the oldest postglacial records available from southeastern Alaska suggest that it is likely to have survived in refugia in the region during the LGI. Its pollen is usually underrepresented in pollen samples (Heusser, 1960) so even small amounts of its pollen in lowland samples may indicate a significant population of the species in the area. Pollen percentages of mountain hemlock are generally much higher in subalpine zone records, reflecting the greater local abundance of those trees. *Alnus* pollen and Polypodiaceae type fern spores are also well represented in Zone HL-3. The abundance of alder pollen and fern spores suggests that the developing spruce

forests were growing in open stands or scattered denser stands, interspersed with alder shrublands rather than spruce trees covering most of the landscape. Pollen types represented in low percentages in Zone HL-3 include *Betula*, *Salix,* Ericaceae, Cyperaceae, *Aster* type, and Apiaceae. *Betula* (birch) shrubs or trees have not been found in the present-day vegetation anywhere on Baranof Island, but its pollen can be wind transported long distances. The shrub *Betula glandulosa* has been found growing on uplands of northern Chichagof Island and along the northern coast of Cross Sound, however (Viereck and Little, 2007), and that appears to be the closest known source of *Betula* pollen in the northwestern archipelago. The boreal forest paper birch tree, *Betula papyrifera*, has colonized some areas of western slopes of the Coast Mountains, particularly near Juneau, and is likely to have reached the coast from interior British Columbia along major rivers that flow through the mountains (e.g., the Taku River valley south of Juneau). It is possible that those trees were a source of some of the birch pollen that often shows up in trace amounts in pollen samples from across the region.

Zone HL-2

Zone HL-2 spans the time interval of 10,350 to ∼5000 yr BP, between core depths 285–155 cm. The main feature of the HL-2 pollen record is the evidence for colonization of the Still Harbor area by the conifer *T. heterophylla* (western hemlock), beginning ∼10,350 yr BP, and which appears to have become the dominant tree in the HL area by ∼9500 yr BP, when its pollen percentages first exceeded that of spruce. As seen from other pollen records in southeastern Alaska, western hemlock spread across most of southeastern Alaskan forest lands in the early Holocene, usually after spruce had become established, but soon became the dominant conifer in most areas. Whereas Sitka spruce is able to colonize barren ground successfully, western hemlock generally requires some organic material and moister soils to successfully develop seedlings that survive, and likely also benefit from the nitrogen added to soils by the alders that preceded it (Cooper, 1939; Lawrence, 1958). Most pollen records from southeastern Alaska that are old enough to record pre-Holocene and early Holocene vegetation histories show pine as the earliest tree to colonize, often with minor amounts of mountain hemlock, followed much later by Sitka spruce, then western hemlock (Heusser, 1960; Hansen and Engstrom, 1996; Ager and Rosenbaum, 2009; Ager et al., 2010). Zone HL-2 shows a significant increase in pine pollen percentages after ∼8000 yr BP, which may reflect the early onset of warmer, moister conditions in the region (Praetorius and Mix, 2014). Sitka spruce percentages decline gradually within HL-2, reflecting the growing dominance of western hemlock trees in the area. Alder pollen and fern spores remain abundant in HL-2, suggesting open or discontinuous conifer forests that did not crowd out the alders. The appearance of *L. americanum* indicates local swampy areas with organic rich soils along with some mineral soils in the vicinity of Hummingbird Lake throughout the past ∼10,000 yr. Skunk cabbage contributes to the paludification processes that contribute to the expansion of muskeg (peatland) vegetation, which often gradually replaces stands of conifer forest (Heusser, 1960).

Zone HL-1

Pollen Zone HL-1 pollen assemblages are quite similar to those in Zone HL-2. The zone extends from core depth 155 cm to the top of the core (lake floor), and spans the past ∼5000 yrs. The main difference between HL-2 and HL-1 pollen assemblages is that small amounts of Cupressaceae type pollen are present in HL-1. The cedar type pollen is most likely to have been derived from *C. nootkatensis* (yellow cedar), as yellow cedar is abundant in the Still Harbor area forests today. *T. plicata* (red cedar) is absent from the area, so the Cupressaceae pollen in HL-1 could not have come from that species. *J. communis* shrubs produce pollen that is very similar to that of yellow cedar and red cedar, and junipers do occur in the Still Harbor area, but they are low growing, tend to grow in muskeg areas, and are less likely than yellow cedar to contribute much pollen to the lake record. Cupressaceae pollen is often poorly preserved in sediments, or not at all, so it is often either unrepresented in pollen records, or is underrepresented. Therefore the postglacial history of Cupressaceae in coastal Alaska is very poorly known. Heusser (1952, 1954, 1960, 1965) did not record the presence of Cupressaceae type pollen in any of his many pollen diagrams. *P. sitchensis* pollen is slightly more abundant in HL-1 than in HL-2. Fern spores remain abundant in Zone HL-1. Pollen types that are present in low percentages include *Betula*, Ericaceae, Cyperaceae, Poaceae, *Artemisia*, *Aster* type, *Coptis*, *Nephrophyllidium crista-galli*, and Saxifragaceae. Aquatic plants represented by pollen include *Potamogeton* and *Nuphar*. The persistence of fairly abundant alder pollen in Zone HL-1 within an area that now has a widespread cover of conifer forest may result from alders colonizing shorelines, streambanks and landslide scars that are common on steep slopes in the area.

Lower Sitka Sound Core (EW0408-40JC)

Pollen samples from two marine sediment cores obtained during the 2004 oceanographic research cruise of the R/V Maurice Ewing were analyzed, in order to evaluate whether informative vegetation histories areas could be reconstructed from nearshore marine cores, for areas where no pollen records were available onshore. The analyses of pollen assemblages from the EW0408-40JC and 47JC cores represent the first attempts to reconstruct coastal terrestrial vegetation histories from marine sediment cores from the Gulf of Alaska region. It had been demonstrated previously that pollen analysis of marine deposits from an anoxic coastal inlet (Saanich Inlet) in southern Vancouver Island, British Columbia yielded high-quality records of coastal temperate rainforest history (Heusser, 1983; Pellatt et al., 2001). At another site in B.C., on the east coast of Moresby Island in Haida Gwaii, early postglacial freshwater lake deposits within an isolation basin in Logan Inlet was later inundated by marine waters as sea level rose. A 12-m long core was obtained from the Logan Inlet site, at a depth of ∼200 m below present sea level (Josenhans et al., 1997). Pollen analysis of the freshwater sediment portion of the Logan Inlet core (between 4 and 12 m depth) yielded a pre-Holocene record spanning ∼14,060–12,300 yr BP (Lacourse and Mathewes, 2005).

The first marine record from SE Alaska to be discussed here is from core EW0408-40JC, located at 56.98573°N, 135.47757°W,

in lower Sitka Sound (**Figure 1B**), 53 km NW of Hummingbird Lake. The jumbo piston core was collected from a water depth of 216 m. The core is 1145 cm in length, and consists of marine lithogenic mud in the upper ∼890 cm, and of freshwater lake muds interbedded with tephras and pyroclastic deposits below 900 cm core depth, representing the lower 245 cm of the core (Addison et al., 2010). The volcanic deposits were derived from multiple eruptions of volcanoes in nearby Kruzof Island's Mount Edgecumbe volcanic field (MEVF; **Figure 1B**; Riehle et al., 1992a; Addison et al., 2010). The pollen and spore percentage diagram from 40JC is shown in **Figure 9** and **Supplementary Table S1**. Calibrated radiocarbon ages are also shown in **Figure 9**. Pollen sums from 40JC samples ranged from 252 to 360 grains, with most sums more than 300 grains, while pollen plus spore sums ranged between 354 and 1049 specimens. Pollen preservation was good to excellent in 40JC samples.

The base of the 40JC core is undated because of the lack of organic material within the volcanic deposits at the base of the core, but in NE Gulf of Alaska marine cores, tephras consisting largely of lapilli were deposited between ∼14,300 and 13,300 yr BP, and that may represent the approximate age range of multiple early postglacial MEVF eruptions on Kruzof Island (Praetorius and Mix, 2014). The pollen assemblages in the lowermost Subzone L-2B include abundant alder pollen. In the previously described Hummingbird Lake core, alder pollen did not become abundant until after ∼14,040 yr BP, near the base of Zone HL-4. That ∼14,040 yr BP age provides an approximate maximum limiting age for the lowermost pollen samples in the 40JC core, assuming the timing of the alder population increase is about the same in both areas. Alders are prolific pollen producers, and alder pollen is readily transported by wind. Therefore it is unlikely that alder would be largely absent from 40JC's Subzone L-2B at the same time when alder was abundant at HL.

Sitka Sound was filled with glacial ice during the LGI (Kaufman and Manley, 2004), and therefore the volcanic deposits in the Sitka region must be younger than the time of local deglaciation, which may have been underway by ∼17,000 ± 700 yr BP in the western Alexander Archipelago

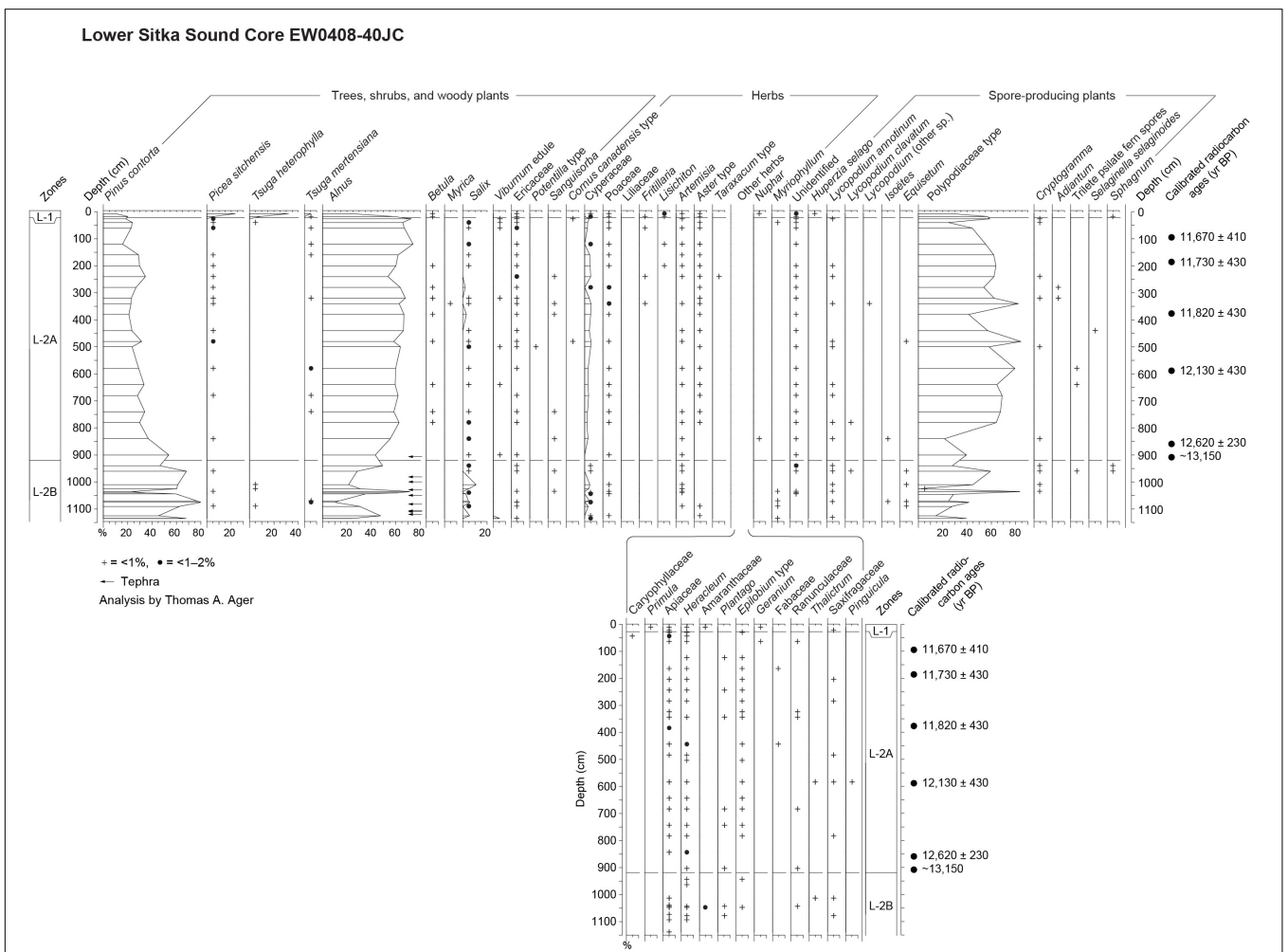

FIGURE 9 | Pollen and spore pollen percentage diagram with calibrated radiocarbon ages for Core EW0408-40 JC in Lower Sitka Sound. Pollen data are shown in **Supplementary Table S1**.

(Lesnek et al., 2018). In the Sitka area east of Kruzof Island, volcanic ash deposits 1–3 m thick overlie glacial till and bedrock (Yehle, 1974). The volcanic deposits recovered in 40JC do not represent the entire postglacial eruptive sequence, as a longer series of tephras have been described from an undated lake sediment core from Chichagof Island (Riehle et al., 1992b; Addison et al., 2010). The older tephras in the lower part of that Chichagof lake core included a basaltic andesite tephra that does not occur in 40JC, and was produced during an early stage of the eruption sequence (Addison et al., 2010).

Maximum global eustatic sea level lowering during the LGI was ∼125 m below present sea level (Fairbanks, 1989). The freshwater lake sediments discovered within the 40JC core are below 900 cm core depth, and the top of the core is 216 m below modern sea level. Therefore, the top of the freshwater lake sediments is now more than 225 m below present sea level, and ∼100 m below the approximate low stand global eustatic sea level position during the LGI. What remains unknown is the depth of the former lake, and the position and current depth of its paleoshoreline below present sea level, which could be used to calculate the amount of seafloor subsidence more accurately. It is likely that a crustal forebulge developed along the western margins of the Alexander Archipelago during LGI, as a westward lateral migration of mantle rocks responded to the massive weight of the thick ice in the CIS that depressed the Coast Mountains, as has been documented in the Haida Gwaii area (Clague, 1983, 1989). Since deglaciation, isostatic rebound has raised marine shell-bearing deposits up to 220 m along the west flank of the Coast Mountains (Mann, 1986). With rapid deglaciation of the western margins of the CIS and local glaciers ∼17,000 yr BP, the forebulge of mantle material migrated back eastward (Clague, 1983) and caused marine waters to flood the continental shelf in excess of that caused by postglacial eustatic sea level rise alone. This widespread submergence inundated the floor of lower Sitka Sound (Addison et al., 2010). Flooding of the freshwater lake by marine waters in what is now Sitka Sound occurred by ∼12,620 ± 230 yr BP, based on a marine shell date from above the lake sediments. This inundation of freshwater lake deposits in 40JC by rising sea level and crustal adjustments during and after deglaciation is very similar to the situation at the Logan Inlet core near Moresby Island in Haida Gwaii, in terms of present-day water depths, and where both deposits contain pollen and diatom records with overlapping ages with those in 40JC (Josenhans et al., 1997; Lacourse and Mathewes, 2005; Addison et al., 2010). The crustal adjustments during deglaciation included forebulge lateral migration, isostatic rebound, and perhaps major earthquakes caused by nearby fault movements along the Queen Charlotte-Fairweather Fault system on the outer shelf (Carlson et al., 1988). These events may have triggered the multiple volcanic eruptions on Kruzof Island soon after local deglaciation (Addison et al., 2010; Praetorius et al., 2016).

Core 40JC, Pollen Subzone L-2B

Pollen Assemblage Zone L-2B spans the lower part of 40JC from 900 to 1145 cm core depths. The Zone L-2A/L-2B boundary is marked by a dacitic tephra that is correlated with the dacitic tephra that has been dated on western Kruzof Island and Yakobi Island northwest of Chichagof Island (Beget and Motyka, 1998) at ∼13,150 yr BP (calibration range 13,050–13,250 yr BP). The lower end of the Zone L-2B (core base) is not dated, but the abundance of alder pollen within Zone L2B suggests that the core base is no older than the rise of alder pollen percentages in lower Zone H-4 in Hummingbird Lake (∼14,040 yr BP). Freshwater lake sediments (diatomaceous mud) are interbedded with tephras in Subzone L-2B. Freshwater diatoms in the lacustrine sediments in the lower part of 40JC were identified by Scott Starratt at the U.S. Geological Survey in Menlo Park, California (Addison et al., 2010).

The large abrupt shifts in percentages of pine, alder, and fern spores within Zone L-2B, as seen in the 40JC pollen diagram (**Figure 9**) are likely to be a result of widespread and repeated destruction of vegetation around Kruzof Island and the Sitka Sound coastal areas on Baranof Island during multiple eruptions, some of which may not be represented by tephras preserved in 40JC (Addison et al., 2010). Deposition of tephras at any location depends on the magnitude and duration of the eruptions, distance from the volcano, and wind directions at the time of the event. A total of nine tephras were identified within Subzone L-2B in the 40JC core between 900 cm and the core base at 1145 cm (left-pointing arrows mark positions of tephra layers in the *Alnus* column in **Figure 9**). The tephras were described by Addison et al. (2010). There are also dense layers of pyroclastic deposits in the lower part of the core, which probably prevented the heavily weighted jumbo piston corer from penetrating deeper.

Freshwater lake mud deposits from 40JC below ∼900 cm contained pollen and spore assemblages in Zone L-2B that indicate that the vegetation around the Sitka Sound area at the time of the eruptions was pine parkland with abundant alders and ferns, *Salix*, Ericaceae, Cyperaceae, and herbaceous plants such as *Artemisia, Aster*, Poaceae, Apiaceae, *Heracleum, Plantago*, *Epilobium,* and Saxifragaceae. Shallow water aquatic plants are represented by trace amounts of pollen of *Myriophyllum* and microspores of *Isoëtes*. Also present are spores of *Lycopodium annotinum* and *Equisetum*. This assemblage is similar, but not identical to Zone HL-4 in the Hummingbird Lake (∼14,040 to ∼11,330 yr BP). The percentages of pollen of pine, alder, and fern spores in HL-4 do not show the large variations as in 40JC's Zone L-2B. This suggests that the vegetation around Still Harbor was not significantly damaged by tephra deposition during the eruptions from the MEVF, a result of Still Harbor's remoteness from the volcanoes and its relatively unfavorable direction for wind transport of volcanic ash plumes from its source on Kruzot Island.

Core 40JC, Pollen Subzone L-2A

Pollen Subzone L-2A extends from ∼25 to 900 cm core depth, and spans the time interval between ∼11,400 to ∼13,150 yr BP. The record in this zone is dominated by abundant pollen of alder, pine, and fern spores, an assemblage quite similar to samples in Subzone L-2B, but the percentages of the dominant taxa differ enough to justify defining a separate zone. Pine percentages are generally 20% lower, while alder and fern spore percentages are generally 20–30% higher than in L-2B. Other pollen types that are present, but in low percentages, and include *Salix,* Ericaceae,

Cyperaceae, Poaceae *Artemisia, Aster* type, *Heracleum* and other Apiaceae, *Plantago, Epilobium* type, and other herbs, as well as *L. annotinum*. All of these plant types are present in the region today and are also present in Pollen Zone HL-4 from Hummingbird Lake. The sediments in Zone L-2B were deposited very rapidly (∼1.68 yr/cm), perhaps related to the subsidence of a crustal forebulge in Sitka Sound during or soon after deglaciation (Addison et al., 2010). The Zone L-2A pollen assemblages are quite similar to those in Hummingbird Lake's Zone HL-4, as in Zone L-2B. Assemblages are dominated by pollen of alder, somewhat declining pine, and abundant fern spores, and the chronologies of the two zones (HL-4 and L-2A) are quite similar. The abundance of alder pollen and fern spores suggests that the Sitka Sound area vegetation was probably heavily dominated by alder shrublands, in which ferns often grow as an understory.

Core 40JC, Pollen Zone L-1

Only two samples from the top of 40JC (**Figure 9**, 0–25 cm core depth) appear to be of Holocene age, but are undated, as no wood or shell fragments were found in those core sediments. The uppermost marine sediments at this site were dispersed by the impact of the jumbo piston corer, so some Holocene sediments were not recovered in this core. The abundance of pollen of western hemlock in the uppermost core sample suggests that it may have an age of <9800 yr BP, about the time when western hemlock first became fairly abundant at Hummingbird Lake. The lowermost sample in Zone L-1 contains spruce pollen but little western hemlock pollen, and it is therefore probably of very early Holocene age (∼11,500–10,000 BP). Pollen Zone L-1 samples also contain pollen of mountain hemlock, alder, and abundant fern spores (Polypodiaceae type). Minor taxa (low percentages) in Zone L-1 include Ericaceae, *Betula*, Cyperaceae, *Lysichiton*, *Artemisia* and *Aster*. The near-absence of Holocene sediments at this coring site may be a result of strong bottom currents, or because of entrapment of sediments in deep fiords on adjacent Baranof Island. The base of Pollen Zone L-1 is at ∼25 cm core depth. Since these early Holocene samples are undated, they are not used for vegetation reconstruction for the Sitka Sound region.

Slocum Arm Core (EW0408-47JC)

The 40JC record from lower Sitka Sound discussed above has only a short, undated Holocene pollen record (two samples near the top of the core). In order to fill in most of the missing marine Holocene record for the far northwestern edge of the Alexander Archipelago, pollen samples were analyzed from marine sediment core EW0408-47JC, collected from near the entrance to Slocum Arm, a fiord on the southern coast of Chichagof Island (**Figure 1B**). The jumbo piston coring site was located at 57.57546°N, 136.06297°W, at a water depth of 114 m. As with 40JC, core 47JC was collected during the 2004 cruise of the R/V Maurice Ewing, and was subsequently sampled by the author and resampled later by Jason Addison. The core is 1800 cm long, and spans most, but not all of the Holocene. The age of the base of the core is ∼10,000 yr BP. A detailed study of the paleoceanographic record of that core, based primarily on analysis of marine diatom and silicoflagellate assemblages, was reported by Barron et al. (2016). The calibrated AMS radiocarbon chronology reported in that publication is used here in the pollen diagram for 47JC (**Figure 10**). The chronology is based upon 12 calibrated radiocarbon dates on bivalve fragments, a wood sample, and detrital plant material. The radiocarbon ages of bivalve samples were adjusted for MRE, reducing the reported radiocarbon age by 735 years (Barron et al., 2016) prior to calibrating the dates. Pollen sums from analyzing the 47JC samples for this study ranged from 305 to 358 grains, while pollen plus spore sums ranged from 444 to 937 specimens.

Core 47JC, Pollen Zone SA-3

The pollen record from 47JC (**Figure 10** and **Supplementary Table S1**) is divided into three pollen and spore assemblage zones. A core sediment description is provided in Barron et al. (2016). The oldest Pollen Zone SA-3 is ∼10,000 yr BP at the base of the core at 1800 cm core depth, and its upper boundary is at 1740 cm core depth (∼9840 yr BP). That short core interval contains pollen assemblages dominated by pollen of Sitka spruce, alder, and fern spores. At Hummingbird Lake, which has a much longer record than 47JC, the base of the Sitka spruce-alder-fern zone (HL-3) began ∼11,300 yr BP and ended at ∼10,300 yr BP. This indicates that the arrival time of spruce in the Slocum Arm area is unknown, but the spruce dominance lasted longer than at HL. The local increase in spruce pollen in the lake coring site on Pleasant Island lake (**Figure 1B**) began at ∼10,500 yr BP (Hansen and Engstrom, 1996). Therefore the ∼10,000 yr BP date for the base of the 47 JC core should be considered a minimum age for spruce arrival locally. Pollen types present in low percentages in Zone SA-3 include *Pinus, Salix*, Ericaceae, *Viburnum*, *Rubus*, Cyperaceae, Poaceae, *Artemisia*, *Plantago* and other herbs. The abundance of alder pollen and fern spores suggests that the forest was probably more open than the denser western hemlock-Sitka spruce forest that exists today around Slocum Arm.

Core 47JC, Pollen Zone SA-2

Pollen Zone SA-2 extends from 1740 cm up to 900 cm core depth, representing the time interval of ∼9840 to ∼7850 yr BP (Barron et al., 2016). Zone SA-2 records the colonization of the Slocum Arm area by western hemlock, which became the dominant conifer pollen type by ∼8500 yr BP. Zone SA-2 is characterized by abundant pollen of Sitka spruce, western hemlock, alder, and fern spores. Low percentages of pine and mountain hemlock pollen indicate their presence in the area, but their local populations were probably small. Pollen types present in low percentages in SA-2 include *Betula, Salix,* Ericaceae, Cyperaceae, Poaceae, *Lysichiton*, and *Aster* type, plus other herbs.

Core 47JC, Pollen Zone SA-1

Pollen Zone SA-1 extends from 900 cm core depth to the top of core 47JC, representing the time interval of ∼7850 yr BP to near the present day. The upper ∼42 cm of core 47JC is missing from the impact of the piston corer as it penetrated the sediments (Barron et al., 2016). The missing sediments represents ∼54 years (Barron et al., 2016). The pollen assemblages in SA-1 differ little from those in SA-2 in terms of taxa present,

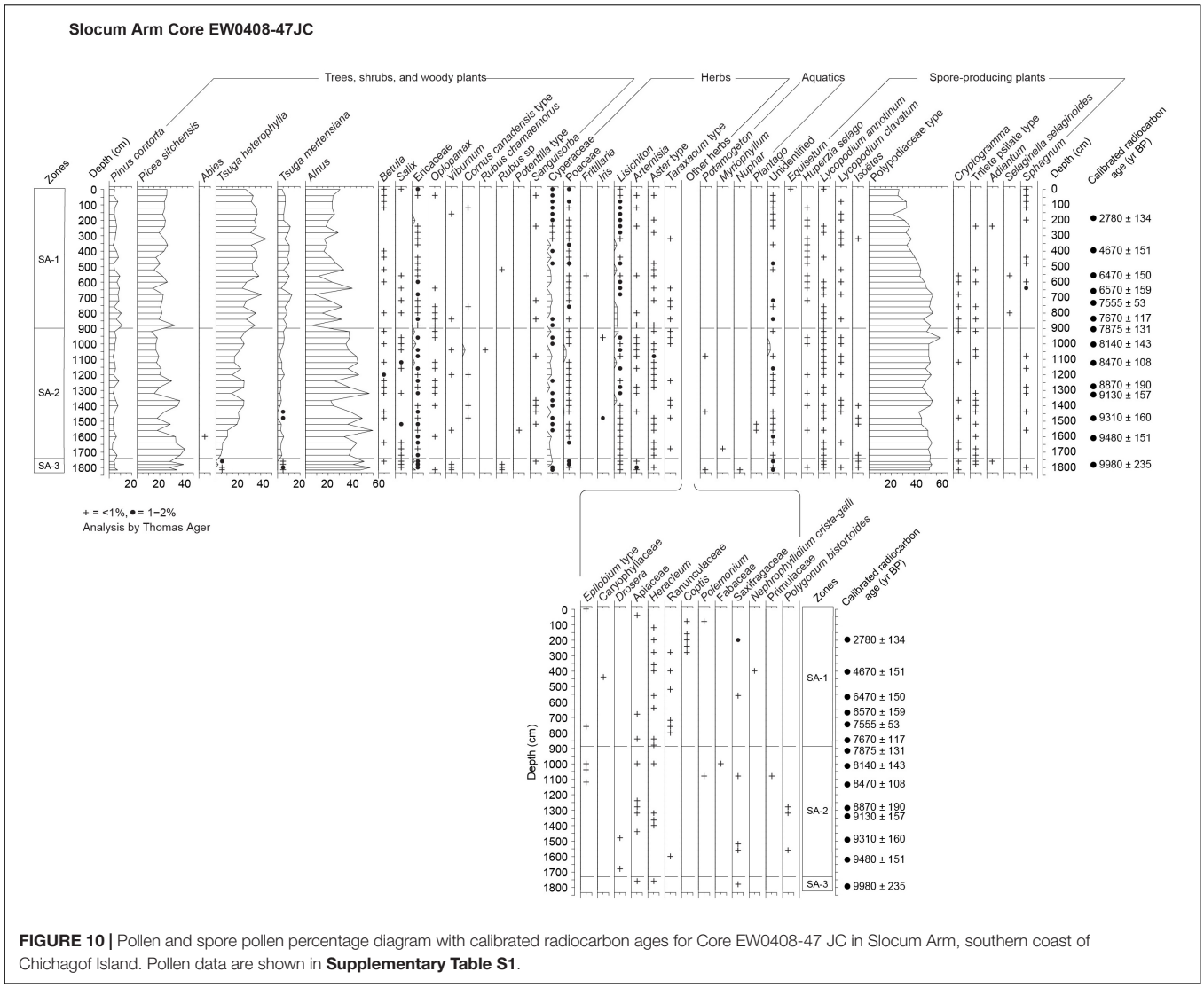

FIGURE 10 | Pollen and spore pollen percentage diagram with calibrated radiocarbon ages for Core EW0408-47 JC in Slocum Arm, southern coast of Chichagof Island. Pollen data are shown in **Supplementary Table S1**.

but relative abundances of some pollen types are significant enough to differentiate Zone SA-1 from SA-2. Spruce, western hemlock and mountain hemlock pollen percentages are all higher than in upper SA-2. Alder pollen percentages are generally lower than in SA-2, and fern spores decline in abundance within SA-1. These percentage changes suggest that a denser forest (more area with closed canopy and reduced alder shrublands) developed in the area during the past ∼7850 years. Pollen types that are present in low percentages within SA-1 include *Betula*, Ericaceae, Cyperaceae, Poaceae, *Lysichiton*, *Aster* type, and occasional occurrences of other herb taxa. The steep walls of Slocum Arm fiord do not favor the development of extensive muskeg terrain, and therefore limits the area where shore pines can grow. However, pine percentages are somewhat higher in SA-1, so there was apparently some expansion of the pine population after ∼7850 yr BP, perhaps linked to muskeg expansion in areas of low relief on the Khaz Peninsula, which forms the southern side of Slocum Arm fiord.

DISCUSSION

If deglaciation of northwestern Alexander Archipelago occurred ∼17,000 ± 700 yr BP, as indicated for the southwestern archipelago (Lesnek et al., 2018), then there may be an earlier stage in the vegetation history that has yet to be discovered in the Baranof-Chichagof Island area. Such very early, radiocarbon-dated postglacial histories are rare at present in southeastern Alaska, but two are known from widely separated locations: the Pleasant Island lake sediment core in Icy Strait (**Figure 1B**; ∼15,460 ± 360 yr BP, Hansen and Engstrom, 1996), and a lake sediment core from Heceta Island (**Figure 1B**; ∼16,700 ± 228 yr BP, Ager, 2007). These two early records indicate that lowland tundra developed in SE Alaska soon after local deglaciation. This tundra vegetation included willows, heaths, including *Empetrum* (crowberry), as well as sedges, grasses, various herbs, and ferns. Pine pollen occurs in both of these early postglacial tundra-dominated sites, indicating its local presence during or soon after local deglaciation.

The dated pollen records from Hummingbird Lake and the marine cores EW0408-40JC and EW0408-47JC provide the first dated vegetation histories for the far northwest coastal region of the Alexander Archipelago. The HL record serves as the key vegetation history for northwestern Alexander Archipelago. The pollen record from the lower HL core indicates a very early local abundance of pine pollen, and presumably local pine trees as early as ∼15,240 yr BP, several centuries before the onset of the Bølling warm event that began ∼14,700 yr BP, but during a time when sea surface temperatures were already beginning to warm (Davies et al., 2011). This early appearance of pine suggests that the hypothesized refugium on SW Baranof Island, where HL is located, and the adjacent subaerially exposed continental shelf (Carrara et al., 2007), may have supported a pine population during the LGI. Pine-fern-willow-sedge vegetation developed into alder-sedge-pine vegetation during the Allerød, when the pine population declined, with further substantial decline in pine occurring during the Younger Dryas cold event, while alder increased. Spruce and mountain hemlock, with alder and ferns became the dominant regional vegetation during the early Holocene warm event, followed by the colonization of the region by western hemlock by ∼10,000 yr BP. At Hummingbird Lake, pollen evidence indicates that yellow cedar trees colonized NW Alexander Archipelago by ∼5000 yr BP, although its pollen does not appear in the 47 JC Holocene record from Slocum Arm.

Plant Colonization of Deglaciated Terrain

The rapid colonization of southeastern Alaska during and after deglaciation by plants occurred as plant propagules were dispersed across large areas of barren terrain by various means. Spore-producing plants such as mosses, liverworts, fungi, lichens, ferns, and fern allies such as *Equisetum*, and Lycopodiaceae have a distinct advantage in dispersing their abundant microscopic spores by means of wind, as each spore (unlike pollen) has the potential for developing into a complete plant. Many vascular plants produce seeds adapted to wind transport, including *Salix, Populus, Dryas, Epilobium, Eriophorum, Betula, Alnus,* and most of the conifers (*Pinus, Picea, Tsuga, Chamaecyparis* and *Abies*). During gale-force North Pacific storms, most common in autumn and winter, some seeds that are ordinarily unlikely to be transported far from the parent plant are apparently carried much farther. In general, most conifer seeds are wind transported within 30–60 m of the source trees. Sitka spruce seeds are sometimes transported by wind up to 800 m from the parent trees (Harris, 1990), while western hemlock seeds are known to be transported up to 1600 m, but most hemlock seeds reach the ground within 610 m (Packee, 1990). Seeds of conifers (and other plants) are also wind transported on the surface of snowbeds (Lotan and Critchfield, 1990), and possibly on drifting sea ice. Plants that produce edible fruits and berries are aided in the rapid and relatively long-distance dispersal of their seeds by birds and over shorter distances by mammals. In southeastern Alaska birds and mammals disperse seeds of *Empetrum, Vaccinium, Rubus spectabilis, C. canadensis, Ribes, Oplopanax, Sorbus, J. communis,* and other plants. Migratory wildfowl feed on aquatic plants and carry seeds from lake to lake along their flight routes (e.g., *Nuphar, Potamogeton, Sparganium, Utricularia, Carex*). Given that humans have been present in southeastern Alaska and coastal B.C. for over 10,300 years (Dixon, 1999), and perhaps ≥ 13,000 years (Mackie et al., 2018; McLaren et al., 2018), plant propagules may have been transported by boat from island to island, perhaps inadvertently. During high water stages, streams carry plant detritus, including seeds, many of which germinate downstream (Jaques, 1973, and observations in Alaska by the author). Plants adapted to growing along coastal shorelines are apparently able to distribute their propagules through transport in marine waters, as suggested by the widespread distribution of coastal floras all across the Gulf of Alaska and beyond. Examples of such plants found along the coasts of the Gulf of Alaska include *Mertensia maritima, Zostera marina, Ruppia spiralis, Honckenya peploides, Stellaria humifusa, Fragaria chiloensis, Potentilla egedii, Lathyrus maritimus, Ligusticum scoticum, Plantago maritima* and others (Hultén, 1968). What is currently unknown is whether conifer seeds immersed in salt water will remain afloat, and viable, and if so, for how long? The Alaska Coastal Current flows northward along the continental shelf of southeast Alaska, then turns northwest and west to follow the Gulf of Alaska coast, carrying driftwood logs and rafts of plant detritus, including conifer cones. If seeds can survive such marine transport and deposition by high tides and waves on coastal beaches, it would be a rapid method of dispersal along the western coastline. As pointed out by Peteet (1991), viable conifer seed transport by sea is a testable idea that has yet to be studied experimentally.

The initial colonization of southeastern Alaska by pine trees during and soon after deglaciation raises some interesting questions. How were pines able to spread so rapidly over vast areas of newly deglaciated terrain, when under present-day conditions, they are largely restricted to open muskeg terrain, and are poor competitors where Sitka spruce and western hemlock trees are present? They are intolerant of shade and competition from other plant species (Heusser, 1960; Lotan and Critchfield, 1990), so their seedlings do not survive for long in mixed stands of spruce and hemlocks. In Glacier Bay, in northern southeastern Alaska (**Figure 1B**), a late Holocene (Little Ice Age) expansion of glaciers filled the entire bay to its entrance in Icy Strait by the mid-1700's, but since the late 1700s, glaciers have retreated over 100 km and exposed large tracts of barren bedrock, glacial till, and outwash deposits (Stowell, 2006). The conifer forests that survived just beyond the areas that had been buried under ice provided local seed sources for rapid colonization by plants as local ice receded. For more than a century, Glacier Bay has served as an outdoor laboratory for the study of plant succession, starting with recently deglaciated barren terrain of known ages, and involving repeat visits to study areas over decades to record floral and vegetation changes. In most cases, pioneer herbs such as dwarf fireweed, horsetails, willows, and mosses are initial colonizers of recently deglaciated terrain. These are soon followed by alders and cottonwoods, along with or followed by Sitka spruce and western hemlock (e.g., Cooper, 1931, 1939; Lawrence, 1958; Goldthwait et al., 1966). In a very few areas of outer Glacier Bay, pines have been observed to colonize glacial deposits, particularly in outwash sediments

near the entrance to the bay (Cooper, 1931). This suggests that shore pines can act as effective colonizers of barren deglaciated terrain, but perhaps only in the local absence, or near absence of competing conifers such as Sitka spruce and western hemlock trees. A lack of competition from other conifer species, along with its apparent advantage of having survived in the region in refugia during the LGI allowed pines to develop pine woodlands over most, if not all of lowland southeastern Alaska during and soon after deglaciation. **Figure 11** shows the earliest available calibrated radiocarbon ages for pines across the region. These dates should be considered minimal ages for the local appearance of pines at any given locality.

The history of Sitka spruce colonization in SE Alaska is more difficult to interpret, in that its earliest appearances in pollen records and a few macrofossil sites across much of southeastern Alaska are more varied than one might expect. The oldest occurrences of Sitka spruce pollen first occur in southwestern Alexander Archipelago at ∼13,600 yr BP on Heceta Island (**Figures 1B**, **11**; Ager, 2007), and at ∼13,200 yr BP at nearby Baker Island (**Figure 11**; Wilcox et al., 2016), assuming these early dates are accurate. This suggests possible refugia for spruce in the SW Alexander Archipelago or on the adjacent continental shelf. At most other sites in the region spruce first appears close to the beginning of the Holocene ∼11,600–11,300 yr BP or soon thereafter (**Figure 11**). Spruce was somewhat later arriving in the northeast, however, both at Pleasant Island (**Figure 1B**) and Lily Lake near Haines (**Figures 1B**, **11**) at ∼10,500 yr BP, suggesting a south to north migration from Mitkof Island of 240–300 km over a millennium (Ager et al., 2010), or a shorter west to east (∼80 km) migration from the outer coast (**Figure 1B**). Farther to the northwest, near Yakutat (**Figures 1B**, **11**), both pollen and macrofossil evidence indicate that spruce arrived in that area about 11,500 yr BP (Peteet, 1991), while at Hummingbird Lake and Sandy Bay on the SW coast of Baranof Island (**Figure 1B**), pollen and seed cones indicate that spruce was locally present at about the same time (∼11,300–11,500 yr BP). At Pass Lake on Prince of Wales Island (**Figure 1B**), pollen evidence suggests that spruce arrived there ∼11,500 yr BP (Ager and Rosenbaum, 2009).

Two spruce macrofossil records from northern Alexander Archipelago and Glacier Bay (**Figure 1B**) are seemingly out of place when compared with the available pollen records from the region. At Adams Inlet in Glacier Bay, a fossil seed cone identified as spruce yielded an unusually old date of ∼13,070 ± 370 yr BP. The cone was collected from an exposure of the early postglacial Forest Creek Formation (McKenzie and Goldthwait, 1971). If the cone was correctly identified, it would be a surprising discovery, given the absence of fossil spruce pollen in the region until about 3000 years later. A younger sample from the same Forest Creek Formation dated to ∼12,900 yr BP, and yielded a fossil pollen assemblage that included pine and alder, along with other shrubs and herbs, but with no spruce pollen. The absence of spruce pollen in that dated sample casts doubt upon the original identification of the older seed cone. The other report of early spruce in northern Alexander Archipelago is from a charred standing tree trunk buried by pyroclastic deposits on the southern coast of Kruzof Island. The charred wood was identified as spruce and was dated to ∼13,100 ± 91 cal yr BP (Baichtal, 2014). It is possible that spruce persisted in southeastern Alaskan refugia during the LGI, perhaps in small scattered populations, and perhaps producing little or no pollen for long intervals until climatic conditions more favorable for sexual reproduction developed. Fossil evidence in support of an early population of spruce producing little pollen has been reported from Hippa Island in Haida Gwaii (Lacourse et al., 2012) where spruce stomata derived from decomposed spruce needles are present 14,000–13,800 yr BP in samples containing very low percentages of spruce pollen. Also present were stomata of other conifer species that had not yet shown up in the pollen record (western hemlock, and red cedar (*T. plicata*). It is not yet understood how conifers are able to survive and persist without producing much, if any pollen for sexual reproduction (e.g., Peteet, 1991), although many conifers can reproduce vegetatively by layering of lower branches in contact with soil, as has often been observed near altitudinal and latitudinal treelines. Rapid expansion of spruce across much of SE Alaska during the early Holocene suggests that a climate threshold may have been crossed that allowed scattered *in situ* populations to quickly expand across the region. The early Holocene warming reported from marine records (Praetorius et al., 2015) and from studies of tree line fluctuations (Pellatt and Mathewes, 1997) may have been a triggering event for regionwide spruce expansion from scattered populations.

The calibrated radiocarbon dates that record the colonization of southeastern Alaska and Haida Gwaii by western hemlock during the early Holocene are more consistent than the postglacial spread of spruce when plotted on a map (**Figure 11**), with somewhat older dates for initial occurrences in the south, and with younger ages to the north, suggesting northward migration from southern sources. Summer temperatures that favor western hemlock reproduction and seedling survival tend to be warmer (≥11.3°C mean July temperature: Packee, 1990) than for Sitka spruce (∼8°C MJT: Heusser, 1989), and mountain hemlock (MJT probably ∼8°C). Western hemlock seedlings survive most often where alders and other nitrogen-fixing plants precede its arrival, adding nitrogen to soil and producing some organic material in the soil which provide a more favorable seed bed (Lawrence, 1958; Goldthwait et al., 1966). These factors of temperature and soil conditions may explain why western hemlock trees colonized southeastern Alaska centuries or more after Sitka spruce and long after alder shrubs were locally established.

In order to place the new records of late Quaternary vegetation history of NW Alexander Archipelago into a broader regional context, a comparison chart summarizing vegetation histories from the oldest, well-dated pollen records from the Alexander Archipelago, southeastern Alaska is shown in **Figure 12**. An additional comparison chart (**Figure 13**) summarizes vegetation histories from key sites in Haida Gwaii.

CONCLUSION

Deglaciation along the western edge of the Alexander Archipelago was underway by 17,000 ± 700 yr BP, and

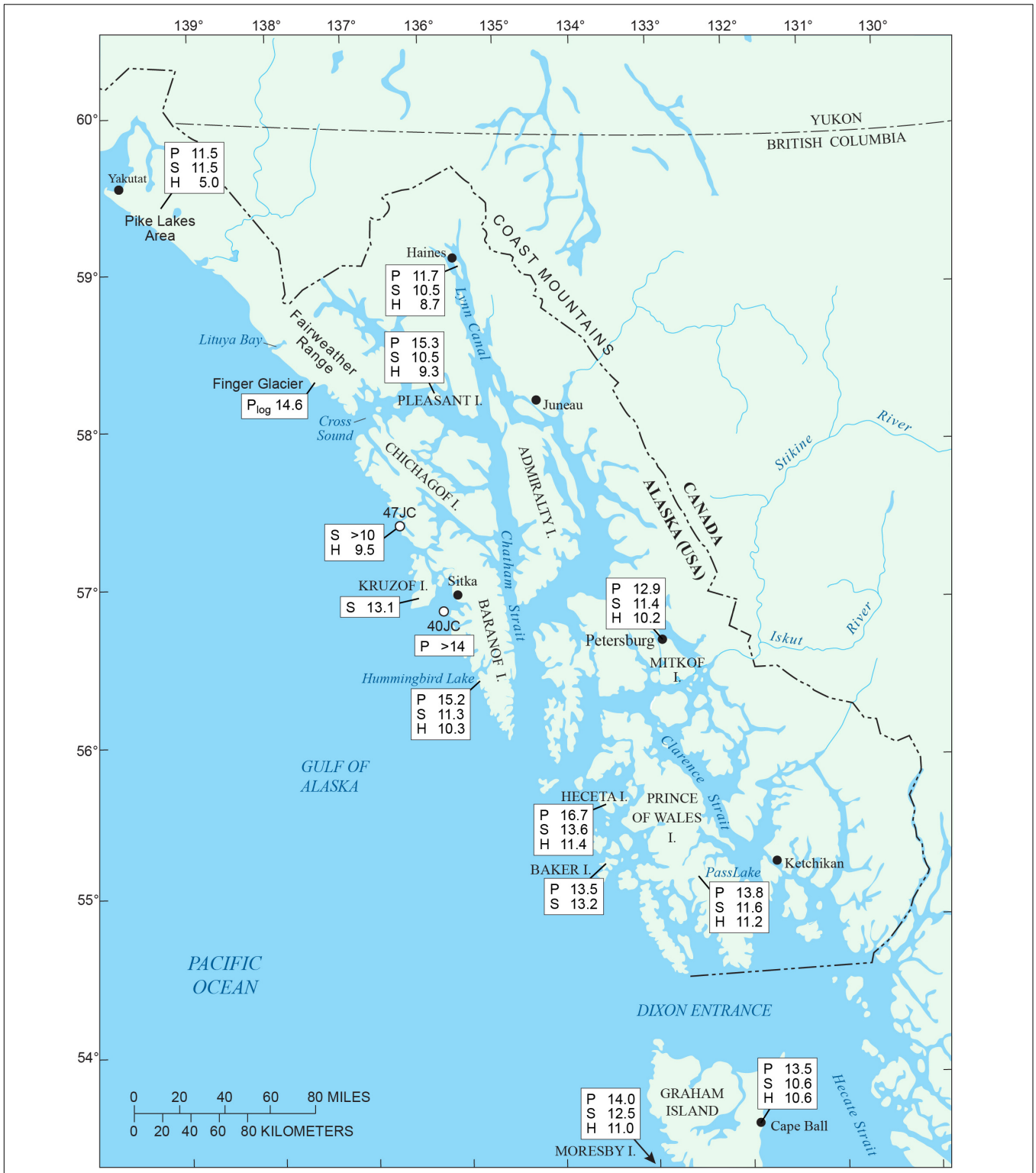

FIGURE 11 | Map of southeastern Alaska showing abbreviated calibrated 14C ages (yr BP × 1000) of earliest occurrences of shore pine: *Pinus contorta* ssp. *contorta* (P), Sitka spruce: *Picea sitchensis* (S), and western hemlock: *Tsuga heterophylla* (H). References for data sources: Yakutat area cores (Peteet, 1991); Finger Glacier pine log (Mann, 1986); Kruzof Island spruce tree trunk (Baichtal, 2014); 47JC marine sediment core (this paper); 40JC marine and freshwater lake sediment core (this paper); Hummingbird Lake core (this paper); Pleasant Island lake core (Hansen and Engstrom, 1996); Lily Lake core near Haines (Cwynar, 1990); Mitkof Island peat core (Ager et al., 2010); Pass Lake core, Prince of Wales Island (Ager and Rosenbaum, 2009); Baker Island lake core (Wilcox et al., 2016); Heceta Island lake core (Ager, 2007 and unpublished data); Cape Ball coastal exposure, Graham Island, Haida Gwaii (Queen Charlotte Islands) (Warner, 1984; Lacourse and Mathewes, 2005); Moresby Island/Hippa Island sites, Haida Gwaii (Fedje, 1993; Lacourse and Mathewes, 2005; Lacourse et al., 2012).

soon thereafter plants began to colonize newly exposed lands as the ice retreated to the east. Spore and seed sources for colonization are likely to have included refugia for plants along the western margins of the Alexander Archipelago and the adjacent inner continental shelf that had been subaerially exposed by eustatic sea level lowering during glaciation. Plants also spread from sources along the coasts of British Columbia and from areas of vegetated exposed B.C.'s continental shelf. Stages in colonization include early postglacial lowland herb-shrub tundra (known so far from only from two sites in SE Alaska), followed by pine parkland with ferns, shrubs, and herbs. The high percentages of pine pollen in sediments up to ∼15,240 yr BP at Hummingbird Lake suggest that pines were well established very early at that site, even before the onset of the Bølling warming that began ∼14,700 yr BP. This suggests that pine trees survived during the LGI in the local hypothesized refugium on the SW coast of Baranof Island and adjacent shelf (Carrara et al., 2003, 2007). Biological evidence for the existence of refugia in the western Alexander Archipelago and Haida Gwaii and adjacent shelf areas is strong, but as yet no suspected continuously ice-free refugium has been proven by pollen or other evidence dating to the LGI.

Pine parklands all across SE Alaska declined as alder shrub populations expanded during the Allerød and Younger Dryas. During the early Holocene, Sitka spruce populations expanded over most of SE Alaska, although fossil evidence indicates that earlier populations appear have existed in SW Alexander Archipelago and Haida Gwaii to the south. Western hemlock trees spread across SE Alaska centuries or more after the establishment of Sitka spruce populations. Western hemlocks soon became the dominant conifer tree species in the region, as it dominates most of the conifer forests today. Plant colonization may still be underway, as suggested by the presence of more tree species in coastal B.C. and southern Alexander Archipelago than in the north, although climatic limitations imposed by increasing latitude may explain some of this varied distribution of species. During the late Holocene, under generally wetter and cooler climates, the modern dense temperate conifer forests of SE Alaska developed, during which Cupressaceae (yellow cedar in the north, and yellow and red cedar in southern SE Alaska) became well established. Muskeg vegetation also

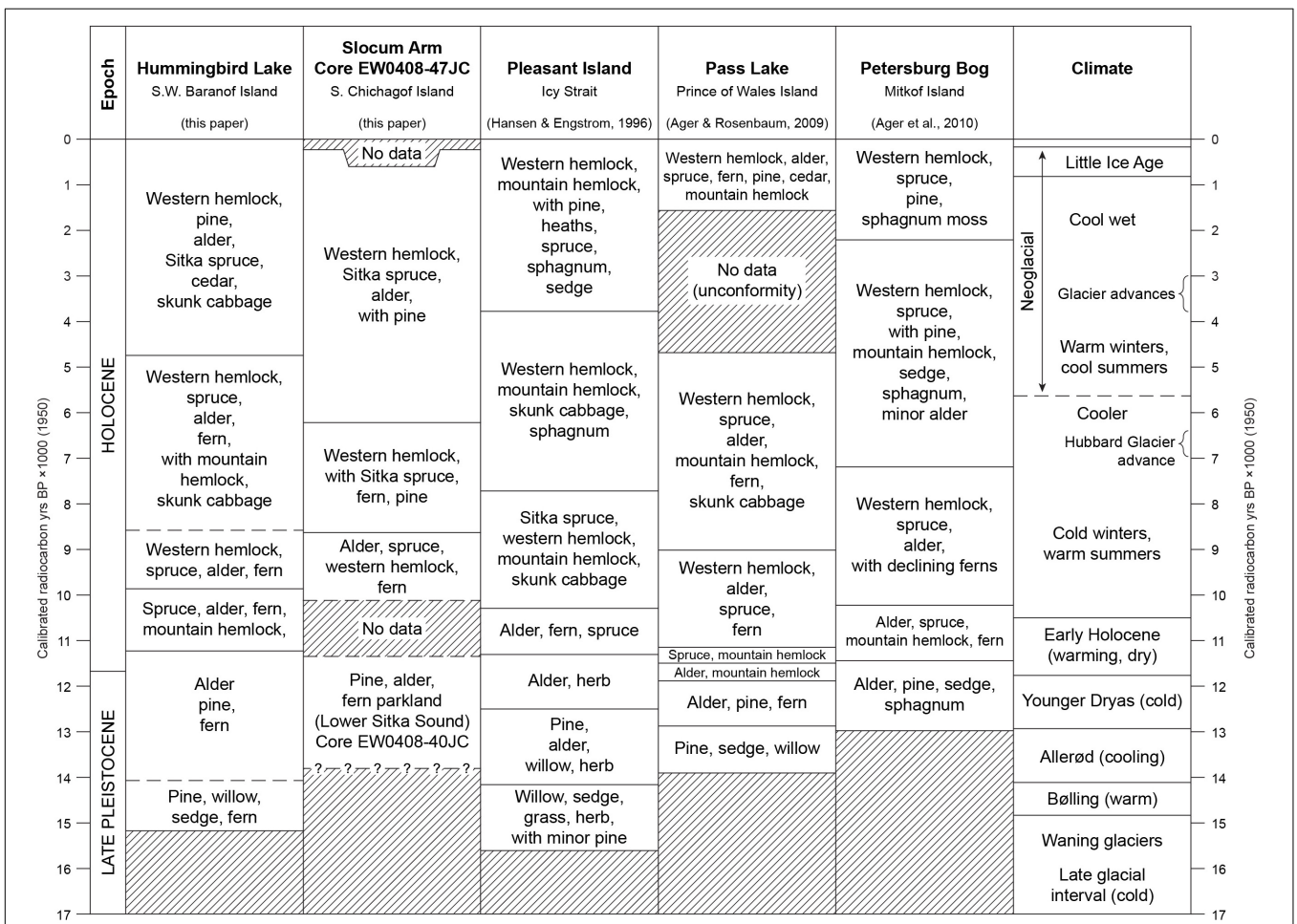

FIGURE 12 | Comparison chart of key vegetation histories from the Alexander Archipelago and vicinity, southeastern Alaska.

expanded in the late Holocene, at the expense of dense conifer forests.

Early Human Colonists in Southeastern Alaska

The western margins of the Alexander Archipelago were undergoing deglaciation by 17,000 ± 700 yr BP (Lesnek et al., 2018), but paleoceanographic evidence from the north-central coast of the GOA indicates the persistence of glaciers on the continental shelf, with calving icebergs, and sea ice for many months of the year (Méheust et al., 2018) until the beginning of the Bølling warm interval ∼14,700 yr BP. Large glaciers on the shelf along the northern coast would have posed a challenging obstacle for boat travel along that coast until after the onset of Bølling-Allerød (BA) warming (Davies et al., 2011). Coastal conditions during the Younger Dryas cooling would have been less favorable for human occupation, but the warmer early Holocene would have been more favorable for humans, as ocean productivity was relatively high, and with terrestrial ecosystems rapidly increasing in diversity of plants and animals. Vertebrate fossil assemblages from caves indicate that both marine and terrestrial mammals were present in southeastern Alaska before and during the BA and through the Holocene, along with fish, and birds, but the faunas changed through time in response to climatic and ecosystem changes both onshore and offshore (Heaton and Grady, 2003).

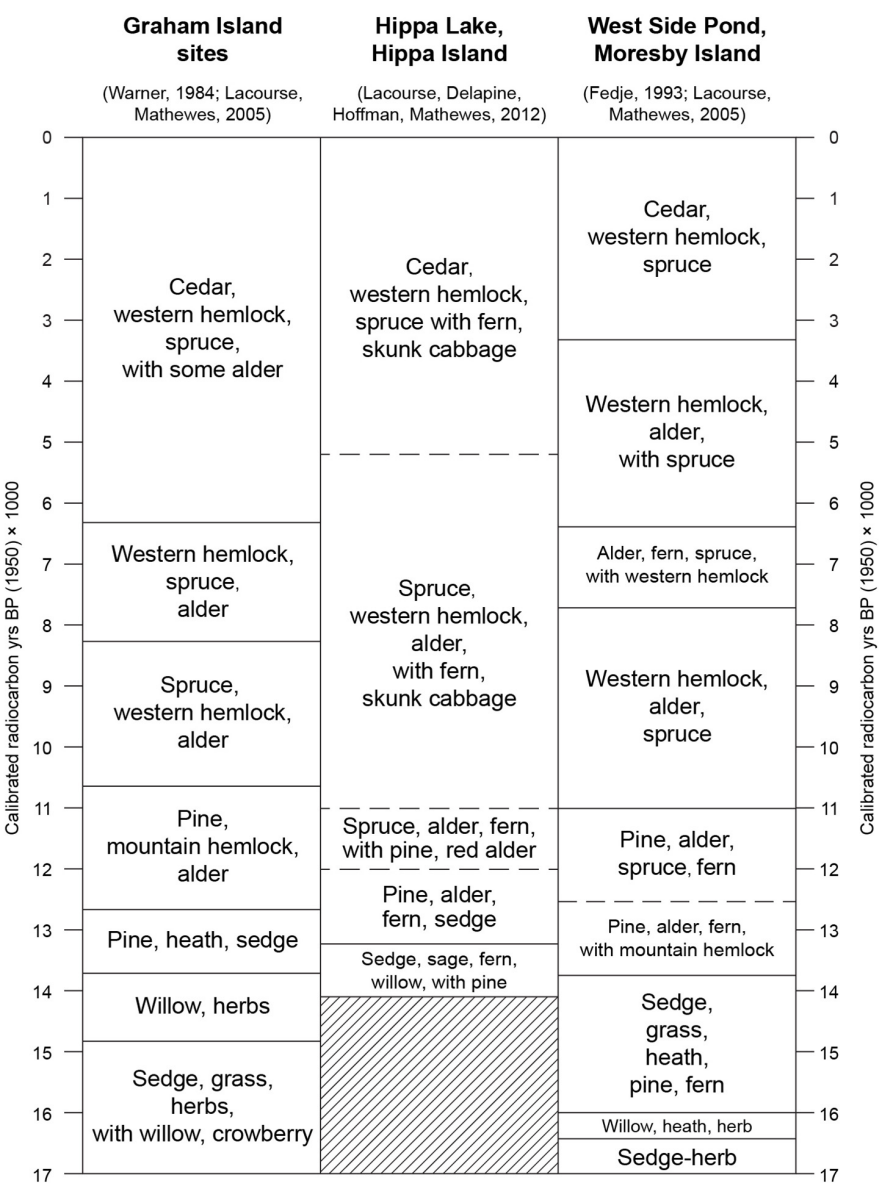

FIGURE 13 | Comparison chart of key vegetation histories from Haida Gwaii (Queen Charlotte Islands) in northern coastal British Columbia, Canada.

Human colonization of southeastern Alaska occurred at least as early as shortly before the beginning of the Holocene: e.g., Ground Hog Bay site east of Glacier Bay (Ackerman et al., 1979); Hidden Falls site, northeastern Baranof Island (Davis, 1996) and Shuká Káa [On Your Knees Cave]: Dixon (1999, 2001). Earlier human presence, perhaps ≥ 13,000 yr BP, is suggested by the recent discovery of dated human footprints preserved in buried beach sands from Calvert Island in central coastal B.C. and archeological evidence from other B.C. coastal sites (Mackie et al., 2018; McLaren et al., 2018). Numerous early Holocene archeological sites have been found recently in southern Alexander Archipelago (Carlson and Baichtal, 2015), indicating that a marine-adapted human population was well established in the region by that time. The paleoecological evidence from NW Alexander Archipelago suggests that pine parkland was well developed in that area at least as early as ∼15,240 yr BP. Pine and mountain hemlock trees would have provided potential sources of fuel, shelter, resin and perhaps material for boat building for human colonists, along with smaller wood from willow shrubs, and after about 14,000 yr BP, alder wood and bark. By earliest Holocene time, Sitka spruce was colonizing SE Alaska rapidly, providing another source of wood products, fiber, resin, and other products for human use.

AUTHOR CONTRIBUTIONS

TA conceived the project, collected the samples, analyzed the pollen samples, developed and interpreted the data, and wrote the manuscript.

FUNDING

This research was supported by the U.S. Geological Survey Land Change Science Program.

ACKNOWLEDGMENTS

Field investigations within Tongass National Forest were made possible through the cooperation and logistical support of the U.S. Forest Service, and the collaboration of Forest Service (FS) scientists Jim Baichtal and Michael Shephard during the 2000 summer field season, and Mary Stensvold during the 2007 and 2008 visits to Sitka. The USGS-FS field party that assisted in carrying loads and sampling Hummingbird Lake and Sandy Bay bog on SW Baranof Island included Larry Phillips, Paul Carrara, and Josh Beene (all from USGS) and Jim Baichtal and Michael Shephard (FS). The author especially thanks the U.S. Forest Service, Tongass National Forest, for arranging for boat transport to reach the remote SW coast of Baranof Island during a circumnavigation of Baranof Island aboard the Chugach Ranger, an historic wooden Forest Service vessel captained by Bob Kinville during the 2000 summer field season. John Westgate, University of Toronto, analyzed two tephra samples from Hummingbird Lake and one from Sandy Bay Bog (Addison et al., 2010). Ager's participation in the 2004 oceanographic research cruise of the R/V Maurice Ewing was at the invitation of Alan Mix, Oregon State University (OSU). Marine sediment cores obtained during the cruise were archived at the OSU marine core repository in Corvallis. Sampling of selected cores by the author during visits to the OSU core facility was expedited by core curators Bobbi Conard and Misti Weber. Pollen samples from Hummingbird Lake, Core EW0408-40JC and Core EW0408-47JC were processed in the U.S. Geological Survey's Cenozoic Palynology Laboratory in Denver, Colorado by Jeff Honke. Pollen diagrams were prepared by Rebecca Brice (USGS, Denver). Figures were prepared by computer graphics specialist Jeremy Havens. Samples of plant material and shell fragments collected from the three cores discussed in this paper were prepared for AMS radiocarbon dating at the U.S. Geological Survey Radiocarbon Laboratory in Reston, Virginia, by John McGeehin and his staff. AMS dating of those samples was done at the National Science Foundation-Arizona AMS facility in Tucson. Calibrations for the Hummingbird Lake radiocarbon samples were provided by Jeff Pigati (USGS Denver). The author also expresses appreciation to the reviewers Laura Strickland, RM, LW, and constructive comments from guest editor DP, and Specialty Chief Editor Steven L. Forman. Any use of trade, firm, or product names is for descriptive purposes only and does not imply endorsement by the U.S. Government.

SUPPLEMENTARY MATERIAL

The Supplementary Material for this article can be found online at: https://www.frontiersin.org/articles/10.3389/feart.2019.00104/full#supplementary-material

TABLE S1 | Raw pollen and spore counts for samples analyzed from Hummingbird Lake (Baranof Island), Core EW0408-40JC (Lower Sitka Sound), and Core EW0408-47JC (Slocum Arm Fiord, Chichagof Island, Alaska. Percentages calculated from these counts were used to construct the pollen and spore diagrams.

REFERENCES

Aaby, B., and Digerfeldt, G. (1986). "Sampling techniques for lakes and bogs," in *Handbook of Holocene Palaeoecology and Palaeohydrology*, ed. B. E. Berglund (Chichester: John Wiley & Sons), 181–194.

Ackerman, R. E., Hamilton, T. D., and Stuckenrath, R. (1979). Early cultural complexes on the Northwest Coast. *Can. Jour. Archaeol.* 3, 195–209.

Addison, J. A., Beget, J. E., Ager, T. A., and Finney, B. P. (2010). Marine tephrochronology of the Mt. Edgecumbe volcanic field, southeast Alaska, U.S.A. *Quat. Res.* 73, 277–292. doi: 10.1016/j.yqres.2009.10.007

Ager, T. A. (2007). Vegetation development on Heceta Island, southeastern Alaska during the Late Glacial and Holocene. *Geol. Soc. Amer. Abstr. Prog.* 39:17.

Ager, T. A., Carrara, P. E., Smith, J. L., Anne, V., and Johnson, J. (2010). Postglacial vegetation history of Mitkof Island, Alexander Archipelago, southeastern Alaska. *Quat. Res.* 73, 259–268. doi: 10.1016/j.yqres.2009.12.005

Ager, T. A., and Rosenbaum, J. G. (2009). "Late Glacial-Holocene pollen-based vegetation history from Pass Lake, Prince of Wales Island, Southeastern Alaska," in *Studies by the U.S. Geological Survey in Alaska, 2007*. U.S. Geological Survey Professional Paper 1760-G, eds P. J. Haeussler and J. P. Galloway, 1–19.

Alaback, P., and Pojar, J. (1997). "Vegetation from Ridgetop to Seashore," in *The Rain Forests of Home: Profile of a North American Bioregion*, eds P. K. Schoonmaker, B. von Hagen, and W. C. Wolf (Washington, D.C: Island Press), 69–87.

Baichtal, J. F. (2014). *The Buried Forest of Alaska's Kruzof Island: A Window Into the Past*. United States Department of Agriculture Blog Archives. Available at: https://www.usda.gov/media/blog/2014/03/07/buried-forest-alaskas-kruzof-island-window-past (accessed May 13, 2019).

Barrie, J. V., Conway, K. M., Mathewes, R. W., Josenhans, H. W., and Johns, M. J. (1994). Submerged late Quaternary terrestrial deposits and paleoenvironment of northern Hecate Strait, British Columbia continental shelf, Canada. *Quat. Internat.* 20, 123–129. doi: 10.1016/1040-6182(93)90041-d

Barrie, J. V., and Conway, K. W. (1999). Late Quaternary glaciation and postglacial stratigraphy of the northern Pacific margin of Canada. *Quat. Res.* 51, 113–123. doi: 10.1006/qres.1998.2021

Barron, J. A., Bukry, D., Addison, J. A., and Ager, T. A. (2016). Holocene evolution of diatom and silicoflagellate paleoceanography in Slocum Arm, a fjord in southeastern Alaska. *Mar. Micropaleontol.* 126, 1–18. doi: 10.1016/j.marmicro.2016.05.002

Barron, J. A., Bukry, D., Dean, W. E., Addison, J. A., and Finney, B. (2009). Paleoceanography of the Gulf of Alaska during the past 15,000 years: Results from diatoms, silicoflagellates, and geochemistry. *Mar. Micropaleontol.* 72, 176–195. doi: 10.1016/j.marmicro.200904.006

Beget, J. E., and Motyka, R. J. (1998). New dates on Late Pleistocene dacitic tephra from the Mount Edgecumbe volcanic field, southeastern Alaska. *Quat. Res.* 49, 123–125. doi: 10.1006/qres.1997.1945

Blaise, B., Clague, J. J., and Mathewes, R. W. (1990). Time of maximum late Wisconsin glaciation, west coast of Canada. *Quat. Res.* 34, 282–295. doi: 10.1016/0033-5894(90)90041-i

Briner, J. P., Tulenko, J. P., Kaufman, D. S., Young, N. E., Baichtal, J. F., and Lesnek, A. (2017). The last deglaciation of Alaska. *Cuad. Invest. Geográfica* 43, 429–448.

Brown, C. A. (2008). *Palynological Techniques*, 2nd Edn. Dallas, TX: Amer. Assoc. of Stratigraphic Palynologists Foundation.

Brown, T. A., Nelson, D. E., Mathewes, R. W., Vogel, J. S., and Southon, J. R. (1989). Radiocarbon dating of pollen by accelerator mass spectrometry. *Quat. Res.* 32, 205–212. doi: 10.1016/0033-5894(89)90076-8

Carlson, P. R., Bruns, T. R., and Plafker, G. (1988). Late Cenozoic offsets on the offshore connection between the Fairweather and Queen Charlotte faults off southeast Alaska. *Mar. Geol.* 85, 89–97. doi: 10.1016/0025-3227(88)90085-0

Carlson, R. J., and Baichtal, J. F. (2015). A predictive model for locating early holocene archaeological sites based on raised shell-bearing strata in Southeast Alaska. *Geoarchaeology* 30, 120–138. doi: 10.1002/gea.21501

Carrara, P. E., Ager, T. A., and Baichtal, J. F. (2007). Possible refugia in the Alexander Archipelago of southeastern Alaska during the late Wisconsin glaciation. *Can. J. Earth Sci.* 44, 229–244. doi: 10.1139/e06-081

Carrara, P. E., Ager, T. A., Baichtal, J. F., and Van Sistine, D. P. (2003). *Map of Glacial Limits and Possible Refugia in the Southern Alexander Archipelago, Alaska During the Late Wisconsin Glaciation*. United States Geological Survey Misc. Field Studies, Map 2424.

Clague, J. J. (1983). "Glacio-isostatic effects of the Cordilleran Ice Sheet, British Columbia, Canada," in *Shorelines and Isostasy*, eds D. E. Smith and A. G. Dawson (London: Academic Press), 321–343.

Clague, J. J. (1989). "Quaternary geology of the Canadian Cordillera," in *Quaternary Geology of Canada and Greenland: Geology of Canada 1*, ed. R. J. Fulton (Ottawa: Geological Survey of Canada), 17–96.

Cooper, W. S. (1931). A third expedition to Glacier Bay, Alaska. *Ecology* 12, 61–95. doi: 10.2307/1932934

Cooper, W. S. (1939). A fourth expedition to Glacier Bay, Alaska. *Ecology* 20, 130–155. doi: 10.2307/1930735

Cwynar, L. C. (1990). A late Quaternary vegetation history from Lily Lake, Chilkat Peninsula, southeast Alaska. *Can. Jour. Bot.* 68, 1106–1112. doi: 10.1139/b90-139

Davies, M. H., Mix, A. C., Stoner, J. S., Addison, J. A., Jaeger, J. A., Finney, B., et al. (2011). The deglacial transition on the southeastern Alaskan margin: meltwater input, marine productivity, and sedimentary anoxia. *Paleoceanography* 26:A2233. doi: 10.1029/2010PA002051

Davis, S. D. (1996). "Hidden Falls," in *American Beginnings: The Prehistory and Palaeoecology of Beringia*, ed. F. H. West (Chicago: University of Chicago Press), 413–424.

de Vernal, A., and Pedersen, T. F. (1997). Micropaleontology and palynology of core PAR87A-10: A 23,000 year record of paleoenvironmental changes in the Gulf of Alaska, northeast Pacific. *Paleoceanography* 12, 821–830. doi: 10.1029/97PA02167

Dixon, E. J. (1999). *Bones Boats & Bison: Archeology and the First Colonization of Western North America*. Albuquerque: University of New Mexico Press.

Dixon, E. J. (2001). Human colonization of the Americas: timing, technology, and process. *Quat. Sci. Rev.* 20, 277–299. doi: 10.1016/s0277-3791(00)00116-5

Dixon, E. J., Heaton, T. H., Lee, C. M., Fifield, T. E., Coltrain, J. B., Kemp, B. M., et al. (2014). "Evidence of maritime adaptation and coastal migration from Southeast Alaska," in *Kennewick Man: The Scientific Investigation of an Ancient American Skeleton*, eds D. W. Owsley and R. L. Jantz (Texas: Texas A&M University Press).

Doher, L. I. (1980). *Palynomorph Preparation Procedures Currently used in Paleontology and Stratigraphy Laboratories*. United States Geological Survey Circular 830.

Fairbanks, R. G. (1989). A 17,000-year glacio-eustatic sea level record – influence of glacial melting rates on the Younger Dryas event and deep ocean circulation. *Nature* 342, 637–642. doi: 10.1038/342637a0

Fedje, D. W. (1993). *Sea-Levels and Prehistory in Gwaii Haanas*. Ph.D. thesis, University of Calgary, Calgary.

Fedje, D. W., and Josenhans, H. (2000). Drowned forests and archaeology on the continental shelf of British Columbia. *Can. Geol.* 28, 99–102. doi: 10.1130/0091-7613(2000)028%3C0099%3Adfaaot%3E2.3.co%3B2

Goldthwait, R. P., Loewe, F., Ugolini, F. C., Decker, H. F., DeLong, D. M., Troutman, M. B., et al. (1966). *Soil Development and Ecological Succession in a Deglaciated Area of Muir Inlet, Southeast Alaska*. Columbus: Ohio State University Institute of Polar Studies.

Grimm, E. (1991). *TILIAGRAPH 2.0.b.5 (Computer Software)*. Springfield, IL: Illinois State Museum, Research and Collections Center.

Grimm, E. (1993). *TILIA v. 2.0 (Computer Software)*. Springfield, IL: Illinois State Museum, Research and Collections Center.

Hansen, B. C. S. (1995). Conifer stomate analysis as a paleoecological tool: an example from the Hudson Bay Lowlands. *Can. Jour. Bot.* 73, 244–252. doi: 10.1139/b95-027

Hansen, B. C. S., and Engstrom, D. R. (1996). Vegetation history of Pleasant Island, southeastern Alaska, since 13,000 yr BP. *Quat. Res.* 46, 161–175. doi: 10.1006/qres.1996.0056

Harris, A. S. (1990). "Picea sitchensis (Bong.) Carr.: Sitka Spruce," in *Silvics of North America*, Vol. 1, eds R. M. Burns and B. H. Honkala (Washington, D.C: U.S. Dept. of Agriculture Forest Service), 260–267.

Heaton, T. H., and Grady, F. (2003). "The late Wisconsin vertebrate history of Prince of Wales Island, southeast Alaska," in *Ice Age Cave Faunas of North America*, eds B. W. Schubert, J. I. Mead, and R. W. Graham (Bloomington: Indiana University Press), 17–53.

Heaton, T. H., Talbot, S. L., and Shields, G. F. (1996). An ice age refugium for large mammals in the Alexander Archipelago, southeastern Alaska. *Quat. Res.* 46, 186–192. doi: 10.1006/qres.1996.0058

Hetherington, R., Barrie, J. V., Reid, R. G. B., MacLeod, R., and Smith, D. J. (2004). Paleogeography, glacially induced crustal displacement, and late Quaternary coastlines on the continental shelf of British Columbia. *Can. Quat. Sci. Rev.* 23, 295–318. doi: 10.1016/j.quascirev.2003.04.001

Hetherington, R., and Reid, R. G. B. (2003). Malacological insights into the marine ecology and changing climate of the late Pleistocene-early Holocene Queen Charlotte Islands archipelago, western Canada and implications for early humans. *Can. Jour. Zool.* 81, 626–661. doi: 10.1139/z03-024

Heusser, C. J. (1952). Pollen profiles from southeastern Alaska. *Ecol. Monog.* 22, 331–352. doi: 10.2307/1948473

Heusser, C. J. (1954). Additional pollen profiles from southeastern Alaska. *Amer. Jour. Sci.* 252, 106–119. doi: 10.2475/ajs.252.2.106

Heusser, C. J. (1960). *Late Pleistocene Environments of North Pacific North America*. New York, NY: American Geographical Society.

Heusser, C. J. (1965). "A Pleistocene sketch of the Pacific Northwest and Alaska," in *The Quaternary of the United States*, eds H. E. Wright Jr. and D. G. Frey (Princeton: Princeton University Press), 469–483.

Heusser, C. J. (1985). "Quaternary pollen records from the Pacific Northwest Coast: Aleutians to the Oregon-California boundary," in *Pollen Records of Late-Quaternary North American Sediments*, eds V. M. Bryant Jr. and R. G. Holloway (Dallas: American Association of Stratigraphic Palynologists Foundation), 141–165.

Heusser, C. J. (1989). "North Pacific coastal refugia – the Queen Charlotte Islands in perspective," in *The Outer Shores*, eds G. G. Scudder, N. Gessler, and B. C. Skidegate (Washington, D.C: Islands Museum Press), 91–106.

Heusser, C. J., Heusser, L. E., and Peteet, D. M. (1985). Late-quaternary climate change on the American North Pacific coast. *Nature* 315, 485–487. doi: 10.1038/315485a0

Heusser, L. E. (1983). Palynology and paleoecology of postglacial sediments in an anoxic basin, Saanich Inlet, British Columbia. *Can. J. Earth Sci.* 20, 873–885. doi: 10.1139/e83-077

Holloway, R. G. (1989). "Analysis of botanical materials," in *The Hidden Falls Site: Baranof Island, Alaska*, ed. S. D. Davis (Anchorage, AK: Anthropological Assoc. Monograph Series), 61–92.

Hultén, E. (1968). *Flora of Alaska and Neighboring Territories*. Stanford: Stanford University Press.

Jaques, D. R. (1973). *Reconnaissance Botany of Alpine Ecosystems of Prince of Wales Island, Southeast Alaska*. master's thesis, University of Oregon, Eugene, OR.

Josenhans, H., Fedje, D., Pienitz, R., and Southon, J. (1997). Early humans and rapidly changing Holocene sea levels in the queen Charlotte Islands - Hecate Strait, British Columbia, Canada. *Science* 277, 71–74. doi: 10.1126/science.277.5322.71

Kaufman, D. S., and Manley, W. F. (2004). "Pleistocene maximum and late Wisconsin glacier extents across Alaska, U.S. A," in *Quaternary Glaciations – Extent and Chronology. Part II. North America: Developments in Quaternary Science, 2*, eds J. Ehlers and P. I. Gibbard (Amsterdam: Elsevier), 9–27. doi: 10.1016/s1571-0866(04)80182-9

Lacourse, T. (2005). Late Quaternary dynamics of forest vegetation on northern Vancouver Island, British Columbia, Canada. *Quat. Sci. Rev.* 24, 105–121. doi: 10.1016/j.quascirev.2004.05.008

Lacourse, T., Beer, K. W., and Hoffman, E. H. (2016). Identification of conifer stomata in pollen samples from western North America. *Rev. Palaeobot. Palynol.* 232, 140–150. doi: 10.1016/j.revpalbo.2016.05.005

Lacourse, T., Delepine, J. M., Hoffman, E. H., and Mathewes, R. W. (2012). A 14,000 year vegetation history of a hypermarine island on the outer Pacific coast of Canada based on fossil pollen, spores and conifer stomata. *Quat. Res.* 78, 572–582. doi: 10.1016/j.qres.2012.08.008

Lacourse, T., and Mathewes, R. W. (2005). "Terrestrial paleoecology of the Queen Charlotte Islands and the continental shelf: vegetation, climate, and plant resources of the coastal migration route," in *Haida Gwaii: Human History and Environment From the Time of Loon to the Time of the Iron People*, eds D. W. Fedje and R. W. Mathewes (Vancouver, B.C: Univ. of British Columbia Press), 38–58.

Lacourse, T., Mathewes, R. W., and Fedje, D. W. (2003). Paleoecology of late-glacial terrestrial deposits with in situ conifers from the submerged continental shelf of western Canada. *Quat. Res.* 60, 180–188. doi: 10.1016/s0033-5894(03)00083-8

Lawrence, D. R. (1958). Glaciers and vegetation in southeastern Alaska. *Amer. Sci.* 46, 88–122.

Lesnek, A. J., Briner, J. P., Lindqvist, C., Baichtal, J. F., and Heaton, T. H. (2018). Deglaciation of the Pacific coastal corridor directly preceded the human colonization of the Americas. *Sci. Adv.* 2018:eaar5040. doi: 10.1126/sciadv.aar5040

Lisiecki, L., and Raymo, M. (2005). A Pliocene-Pleistocene stack of 57 globally distributed benthic del 180 records. *Paleoceanography* 20:A1003. doi: 10.1029/2004P001003

Loney, R. A., Brew, D. A., Muffler, L. J. P., and Pomeroy, J. S. (1975). *Reconnaissance Geology of Chichagof, Baranof, and Kruzof Islands, Southeastern Alaska*. United States Geological Survey Professional Paper 792.

Lotan, J. E., and Critchfield, W. B. (1990). "Pinus contorta Dougl. Ex. Loud., Lodgepole Pine," in *Silvics of North America, Vol. 1, Conifers*, eds R. M. Burns and B. H. Honkala (Washington, D.C: U.S. Dept. of Agriculture Forest Service), 302–315.

Luternauer, J. L., Clague, J. J., Conway, K. W., Barrie, J. V., Blaise, B., and Mathewes, R. W. (1989). Late Pleistocene terrestrial deposits on the continental shelf of western Canada: evidence for rapid sea-level change at the end of the last glaciation. *Geology* 17, 357–360. doi: 10.1130/0091-7613(1989)017%3C0357%3Alptdot%3E2.3.co%3B2

Lyles, A. S., Baichtal, J. F., and Karl, S. M. (2017). *Deciphering Flow Path of Ice Across the Southern Alaska Panhandle Based on Geomorphological Interpretation and Field Data*. Geological Society of America Program and Abstracts 49,6.

Mackie, Q., Fedje, D., and McLaren, D. (2018). Archaeology and sea level change on the British Columbia coast. *Can. J. Archaeol.* 42, 74–91.

Mann, D. H. (1983). *The Quaternary History of the Lituya Bay Refugium, Alaska*. Ph.D. thesis, University of Washington, Seattle, WA.

Mann, D. H. (1986). "Wisconsin and Holocene glaciation of southeast Alaska," in *Glaciation in Alaska – The Geologic Record*, eds T. D. Hamilton, K. M. Reed, and R. M. Thorson (Anchorage: Alaska Geological Society), 237–265.

Mann, D. H., Crowell, A. L., Hamilton, T. D., and Finney, B. P. (1998). Holocene geologic and climatic history around the Gulf of Alaska. *Arctic. Anthro.* 35, 112–131.

Mann, D. H., and Hamilton, T. D. (1995). Late Pleistocene and Holocene paleoenvironments of the North Pacific Coast. *Quat. Sci. Rev.* 14, 449–471. doi: 10.1016/0277-3791(95)00016-i

Mathewes, R. W., and Clague, J. J. (2017). Paleoecology and ice limits of the early Fraser glaciation (Marine Isotope Stage 2) on Haida Gwaii, British Columbia, Canada. *Quat. Res.* 88, 277–292. doi: 10.1017/qua.2017.36

Mayle, F. E., Levesque, A. J., and Cwynar, L. C. (1993). Alnus as an indicator taxon of the Younger Dryas cooling in eastern North America. *Quat. Sci. Rev.* 12, 295–305. doi: 10.1016/0277-3791(93)90038-n

McKenzie, G. D., and Goldthwait, R. P. (1971). Glacial history of the last eleven thousand years in Adams Inlet, southeastern Alaska. *Geol. Soc. Amer. Bull.* 82, 1767–1782.

McLaren, D., Fedje, D., Dyck, A., Mackie, Q., Gauvreau, A., and Cohen, J. (2018). Terminal Pleistocene Epoch human footprints from the Pacific coast of Canada. *PLoS One* 13:e0193522. doi: 10.1371/journal.pone.0193522

Méheust, M., Stein, R., Fahl, K., and Gersonde, R. (2018). Sea-ice variability in the subarctic North Pacific and adjacent Bering Sea during the past 25 ka: new insights from IP25 and Uk'37 proxy records. *Arktos* 4:8. doi: 10.1007/s41063-018-0043-1

Misarti, N., Finney, B. P., Jordan, J. W., Maschner, H. D. G., Addison, J. A., Shapley, M. D., et al. (2012). Early retreat of the Alaska Peninsula Glacier Complex and the implications for coastal migrations of first Americans. *Quat. Sci. Rev.* 48, 1–6. doi: 10.1016/j.quascirev.2012.05.014

Molnia, B. F. (1986). "Glacial history of the northeastern Gulf of Alaska – A synthesis," in *Glaciation in Alaska – The Geologic Record*, eds T. D. Hamilton, K. M. Reed, and R. M. Thorson (Anchorage, AK: Alaska Geological Society), 219–235.

Molnia, B. F. (2008). *Glaciers of Alaska: Satellite Image Atlas of Glaciers of the World*. United States Geological Survey Professional Paper 1386-K.

Moss, M. L., Peteet, D. M., and Whitlock, C. (2007). "Mid-Holocene culture and climate on the northwest coast of North America," in *Climate Change and Cultural Dynamics: A Global Perspective on Mid-Holocene Transitions*, eds D. H. Sandweiss, K. Maasch, and D. Anderson (Amsterdam: Elsevier, Inc), 491–529. doi: 10.1016/b978-012088390-5.50019-4

Muller, M. C. (1982). *A Preliminary Checklist of the Vascular Plants of Southeastern Alaska*. United States Forest Service Wildlife and Fisheries Habitat Notes, Alaska Region, Administrative Document 112.

O'Clair, R. M., Armstrong, R. H., and Carstensen, R. (1997). *The Nature of Southeast Alaska: A Guide to the Plants, Animals, and Habitats*. Anchorage: Alaska Northwest Books.

Packee, E. C. (1990). "Tsuga heterophylla (Raf.) Sarg.: Western Hemlock," in *Silvics of North America, Vol. 1, Conifers*, eds R. M. Burns and B. H. Honkala (Washington, D.C: U.S. Dept. of Agriculture Forest Service), 613–622.

Pellatt, M. G., Hebda, R. J., and Mathewes, R. W. (2001). High-resolution Holocene vegetation history and climate from Hole 1034B, ODP leg 169S, Saanich Inlet, Canada. *Mar. Geol.* 174, 211–226. doi: 10.1016/s0025-3227(00)00151-1

Pellatt, M. G., and Mathewes, R. W. (1997). Holocene tree line and climate change on the Queen Charlotte Islands, Canada. *Quat. Res.* 48, 88–99. doi: 10.1006/qres.1997.1903

Peteet, D. M. (1991). Postglacial migration history of lodgepole pine near Yakutat. Alaska. *Can. J. Bot.* 69, 786–796. doi: 10.1139/b91-102

Peteet, D. M., and Mann, D. H. (1994). Late-glacial vegetational, tephra, and climatic history of southwestern Kodiak Island. Alaska. *Ecoscience* 1, 255–267. doi: 10.1080/11956860.1994.11682250

Pojar, J., and MacKinnon, A. (eds) (1994). *Plants of the Pacific Northwest Coast: Washington, Oregon, British Columbia, & Alaska*. Redmond: Lone Pine Publishing.

Praetorius, S. K., Mix, A., Jensen, B., Froese, D., Milne, G., Wolhowe, M., et al. (2016). Interaction between climate, volcanism, and isostatic rebound in Southeast Alaska during the last deglaciation. *Earth Planet. Sci. Lett.* 452, 79–89. doi: 10.1016/j.epsl.2016.07.033

Praetorius, S. K., and Mix, A. C. (2014). Synchronization of North Pacific deglacial hypoxic events linked to abrupt ocean warming. *Science* 345, 444–448. doi: 10.1126/science.1252000

Praetorius, S. K., Mix, A. C., Walczak, M. H., Wolhowe, M. D., Addison, J. A., and Prahl, F. G. (2015). North Pacific deglacial hypoxic events linked to abrupt ocean warming. *Nature* 527, 362–366. doi: 10.1038/nature15753

Reimchen, T., and Byun, A. (2005). "The evolution of endemic species in Haida Gwaii," in *Haida Gwaii: Human History and Environment from the Time of the Loon to the Time of the Iron People*, eds D. W. Fedje and R. W. Mathewes (Vancouver, B.C: University of British Columbia Press), 77–95.

Reimer, P. J., Bard, E., Bayliss, A., Beck, J. W., Blackwell, P. G., Bronk Ramsey, C., et al. (2013). IntCal13 and Marine13 radiocarbon age calibration curves 0-50,000 years cal BP. *Radiocarbon* 55, 1869–1887. doi: 10.1016/j.dib.2018.10.040

Riehle, J. R., Champion, D. E., Brew, D. A., and Lanphere, M. A. (1992a). Pyroclastic deposits of the Mount Edgecumbe volcanic field, southeast Alaska: eruptions of a stratified magma chamber. *Jour. Volcanol. Geotherm. Res.* 53, 117–143. doi: 10.1016/0377-0273(92)90078-r

Riehle, J. R., Mann, D. H., Peteet, D. M., Engstrom, D. R., Brew, D. A., and Meyer, C. E. (1992b). The Mount Edgecumbe tephra deposits, a marker horizon in southeastern Alaska near the Pleistocene-Holocene boundary. *Quat. Res.* 37, 183–202. doi: 10.1016/0033-5894(92)90081-s

Stowell, H. H. (2006). *Geology of Southeast Alaska: Rock and Ice in Motion*. Fairbanks: University of Alaska Press.

Stuiver, M., and Reimer, P. J. (1993). Extended 14C data base and revised CALIB 3.0 14C age calibration program. *Radiocarbon* 35, 215–230. doi: 10.1017/s0033822200013904

Viereck, L. A., and Little, E. L. Jr. (2007). *Alaska Trees and Shrubs*, 2nd edn. Fairbanks: University of Alaska Press.

Vitt, D. H., Marsh, J. E., and Bovey, R. B. (1988). *Mosses, Lichens & Ferns of Northwest North America*. Edmonton: Lone Pine Publishing.

Warner, B. G. (1984). *Late Quaternary paleoecology of eastern Graham Island, Queen Charlotte Islands, British Columbia, Canada*. Ph.D. thesis, Simon Fraser University, Burnaby, BC.

Warner, B. G., and Chmielewski, J. G. (1987). Biometric analysis of modern and late Pleistocene cones of Picea from western Canada. *New Phytol.* 107, 449–457. doi: 10.1111/j.1469-8137.1987.tb00196.x

Warner, B. G., Clague, J. J., and Mathewes, R. W. (1984). Geology and paleoecology of a mid-Wisconsin peat from the Queen Charlotte Islands, British Columbia, Canada. *Quat. Res.* 21, 337–350. doi: 10.1016/0033-5894(84)90073-5

Western Regional Climate Center (2018). *Recent Climate in The West*. Available at: wrcc.dri.edu (accessed May 14, 2018).

Wheeler, N. C., and Guries, R. P. (1982). Biogeography of lodgepole pine. *Can. J. Bot.* 60, 1805–1814. doi: 10.1139/b82-227

Wigen, R. J. (2005). "History of the vertebrate fauna in Haida Gwaii," in *Human History and Environment from the Time of Loon to the Time of the Iron People,"*, eds D. W. Fedje and R. W. Mathewes (Vancouver, B.C: University of British Columbia Press), 96–115.

Wilcox, P., Fowell, S. J., Bigelow, N. H., and Baichtal, J. F. (2016). *Increasing humidity during Younger Dryas revealed by palynological and sedimentological analysis of cores from Baker Island, southeast Alaska (Abstr) Annual Meeting, Denver, Colorado, Paper No. 73-75*. Boulder, CO: Geological Society of America.

Worley, I. A. (1980). "Ancient environments and age of non-glaciated terrain in southeastern Alaska," in *National Geographic Society Research Reports*, Vol. 12, eds P. H. Oehser, J. S. Lea, and N. L. Powars (Washington, DC: National Geographic Society), 733–747.

Yehle, L. A. (1974). *Reconnaissance Engineering Geology of Sitka and Vicinity, with Emphasis on Evaluation of Earthquake and Other Geologic Hazards*. United States Geological Survey Open-File Report 74-53, 104.

Conflict of Interest Statement: The author declares that the research was conducted in the absence of any commercial or financial relationships that could be construed as a potential conflict of interest.

frontiers in Earth Science

ORIGINAL RESEARCH
published: 06 August 2019
doi: 10.3389/feart.2019.00188

Dynamic Holocene Vegetation and North Pacific Hydroclimate Recorded in a Mountain Peatland, Moloka'i, Hawai'i

David W. Beilman[1], Charly Massa[1], Jonathan E. Nichols[2], Oliver Elison Timm[3], Russel Kallstrom[4] and Stephanie Dunbar-Co[4]*

[1] Department of Geography and Environment, University of Hawai'i at Mānoa, Honolulu, HI, United States, [2] Lamont-Doherty Earth Observatory, Columbia University, Palisades, NY, United States, [3] Department of Atmospheric and Environmental Sciences, University at Albany, Albany, NY, United States, [4] The Nature Conservancy, Moloka'i Program, Kualapu'u, HI, United States

The Hawaiian Islands are the only high land in a vast stretch of the North Pacific where past climatological and ecological processes can be reconstructed from terrestrial Earth system archives. We measured hydroclimatic proxies and carbon accumulation in an organic sediment core from the windward montane peatland Pēpē'ōpae on the Island of Moloka'i, Hawai'i using radiocarbon, leaf wax geochemistry, and stable isotopes of carbon and hydrogen in addition to historical pollen records. Following a period of soil development, substantial carbon accumulation began around 10 ka BP (thousands of years before present) under wet conditions. Peat formation was continuous but variable throughout the Holocene, including maxima in carbon accumulation around 9 and 3 ka and a minimum around 1.5 ka that has resulted in a belowground carbon storage today of 144 kg C m^{-2}. From this core we generated a new chronology for previously published pollen spectra from the study site and a Wetness Index that shows increases in dry-adapted taxa in upwind forests during periods of decreased carbon accumulation in the peatland. Shifts in the distribution of sedimentary *n*-alkane chain lengths in the context of 14 species of modern bog plant *n*-alkanes suggests litter inputs have been derived from a diverse plant community that changed in dominant species in response to climate. Hydrogen stable isotope ratios of sedimentary C_{29} *n*-alkanes show negative departures around 9 and 3 ka consistent with increases in storm-derived rainfall likely related to the position and strength of the northern jet stream. This study is the first to provide a continuous organic sedimentary record of links between hydroclimate, vegetation, and montane belowground carbon sequestration for this part of the North Pacific.

Keywords: tropical peatland, Hawai'i, Moloka'i, leaf wax, pollen, deuterium, Holocene

OPEN ACCESS

Edited by:
Lesleigh Anderson, United States Geological Survey, United States

Reviewed by:
Daniel B. Nelson, University of Basel, Switzerland
Nadia Solovieva, University College London, United Kingdom

****Correspondence:***
David W. Beilman
beilman@hawaii.edu

Specialty section:
This article was submitted to Quaternary Science, Geomorphology and Paleoenvironment, a section of the journal Frontiers in Earth Science

Received: *19 December 2018*
Accepted: *04 July 2019*
Published: *06 August 2019*

Citation:
Beilman DW, Massa C, Nichols JE, Elison Timm O, Kallstrom R and Dunbar-Co S (2019) Dynamic Holocene Vegetation and North Pacific Hydroclimate Recorded in a Mountain Peatland, Moloka'i, Hawai'i. Front. Earth Sci. 7:188. doi: 10.3389/feart.2019.00188

INTRODUCTION

Knowing the history of hydroclimatic change from a network of sites across the Pacific is important to understanding the external and internal drivers critical to the long-term future of rainfall in the region. Owing to their size, elevation, and isolation, the Hawaiian Islands are the sole location in the central Pacific for comparison to other important freshwater terrestrial proxy records across the

region. Despite a growing number of studies of past environments and climates that have studied pollen (e.g., Selling, 1948; Burney et al., 1995; Hotchkiss and Juvik, 1999; Crausbay et al., 2014), sediment geochemistry (Uchikawa et al., 2010; Crausbay et al., 2014), and sea surface temperatures (SSTs) (Lee and Slowey, 1999) much remains to be learned about hydroclimate change in Hawaiʻi and the north central Pacific. For example, the two synoptic atmospheric circulation patterns today that produce the most rainfall in Hawaiʻi are orographically lifted trade winds and so-called "Kona storms" (Chu et al., 1993), yet we do not know the long-term history of these patterns. It has been shown that drier leeward locations of the islands have experienced increasingly arid conditions over the last several thousand years (Uchikawa et al., 2010), but high quality Holocene records of hydroclimate from wet windward locations in Hawaii have not yet been developed in detail.

Montane freshwater peatlands in the Tropics are useful for reconstruction of climate and ecosystem change owing to their relatively widespread distribution and their high organic matter (OM) content for measurement of organic geochemical proxies and radiocarbon. While the largest tropical peatlands occur in rainforest lowlands of Southeast Asia (Page et al., 2011), Africa (Dargie et al., 2017), and South American Amazonia (Lähteenoja et al., 2013), low-latitude peatland ecosystems can also be found in mountainous terrain, where waterlogged soils are maintained in locally flat areas of heavy rainfall. Such ecosystems and organic deposits are found, for example, in Papua New Guinea (Hope, 2014), West Kalimantan (Anshari et al., 2004), South American Andes (Benavides et al., 2013) and the Guyana Highlands (Zinck and Huber, 2011) and various Pacific Islands (Rieley and Page, 2015). In the Hawaiian Islands, freshwater lakes and sediments are rare owing to steep and permeable volcanic terrain (Maciolek, 1969) but many small mountain peatlands are found on the main islands (Carlquist, 1970), long noted biogeographically for rare plants of cold evolutionary origins (e.g., Rock, 1913). In addition to holding archives of past hydroclimatic change, mountain peatlands in Hawaiʻi provide the opportunity for ecological reconstructions of OM cycling and carbon sequestration relevant to understanding long-term tropical peatland carbon dynamics in general, as well as processes affecting Hawaiʻi mountain forests.

In this paper, we reconstruct environmental changes in Hawaiʻi using carbon and leaf wax geochemistry in modern plant leaf tissue and in peat deposits from the Island of Molokaʻi. We also analyze previously published fossil pollen from East Molokaʻi and the Island of Maui. Other studies have reconstructed Holocene environment in Hawaiʻi from a dry, leeward coastal site (Uchikawa et al., 2010) and high elevations at the trade wind inversion layer (Burney et al., 1995; Crausbay et al., 2014). Our goal here is to develop a multi-proxy picture of hydroclimatic and ecological variations at a mid-elevation windward wet forest.

MATERIALS AND METHODS

Study Site and Field Collections

The Island of Molokaʻi (**Figure 1**), formed of two shield volcanoes in the Maui Nui group, is situated geographically in the middle of the main Hawaiian Archipelago. Molokaʻi is high (1506 m) for its size (673 km^2) owing in part to mass wasting events on its north shore (Moore et al., 1989), that have created some of the world's highest sea cliffs. The upper flows of the East Molokaʻi Volcanic Series are mugearitic basalt that are 1.3–1.5 Ma old (Macdonald et al., 1983). Wet rainforest on Molokaʻi, typically above 600 m (Jacobi, 1989), have wet soils and can form small open wetlands where topography flattens. Pēpēʻōpae is a montane peatland at 1310 m elevation, ∼11,550 m^2 in area, situated leeward of the western rim of Pelekunu Valley, 3.6 km northwest of the island's summit at Kamakou, and 5 km from the windward north coast (**Figure 1**). Estimates of mean monthly air temperature at the site ranges from 13 to 17°C, and mean annual rainfall is ∼3400 mm, about two-thirds of which falls during the rainy season from November to April (Giambelluca et al., 2014). Pēpēʻōpae was known to early botanists for its rare plants and thick deposits (Hillebrand, 1888; MacCaughey, 1916) and was a focus of the Hawaiian Bog Survey 1938 (Skottsberg, 1940) that resulted in the seminal palynological study of the Hawaiian Islands by Selling (1948).

Today, Pēpēʻōpae has an open vegetation and diverse community of sedges, dwarf woody plants, ferns, lycopods, and mosses in a gently sloping hummocky terrain (**Figure 1**; **Supplementary Table S2**). The peatland lacks pools, but temporary standing water can be found in small depressions. The site lies within the Kamakou Nature Preserve, granted to the Nature Conservancy in 1982, and within a network of protected areas covering more than one hundred acres of contiguous ecosystems.

A sediment core (PEP1) was raised from the upper part of Pēpēʻōpae (21° 7′ 8.6″N, 156° 54′ 2.3″ W, 1262m ASL) on May 28, 2013 using a Russian-style side-cut peat corer with a 50-cm long and 5-cm diameter barrel. Core sections were frozen within 3 h of collection, transferred frozen to the laboratory at the University of Hawaiʻi at Mānoa and stored at −20°C. Plant leaf tissue samples from 14 common bog species were collected at the site on May 14, 2018 (**Supplementary Table S1**). Leaf samples from multiple individuals were collected and composited from both the upper and lower areas of the main bog, resulting in duplicate measurements for each species. Tissues were frozen within 3 h of collection and freeze dried. A rainwater collector was made of a five-gallon plastic bucket with a funnel set in the lid and a 1-cm mineral oil layer to prevent evaporation, and was sampled opportunistically between May and December 2018.

Core Chronology

The age of organic carbon in the profile was determined based on the top of the core (assigned as the year of collection, 2013) and the radiocarbon (^{14}C) dating of peat samples. Subsamples for ^{14}C measurement were carefully removed from the center of core slices, dispersed in 18.0 MΩ water, and OM free of visible roots was hand-picked using a 50× Zeiss Stemi 2000 microscope. To remove exogenous organic carbon and inorganic carbon, OM samples were prepared by Acid-Base-Acid pretreatment and rinsed to circum-neutral pH before drying to constant mass at 65°C. Dry OM was combusted to CO_2 at 1000°C for 6 h in evacuated quartz tubes in the presence of copper oxide and

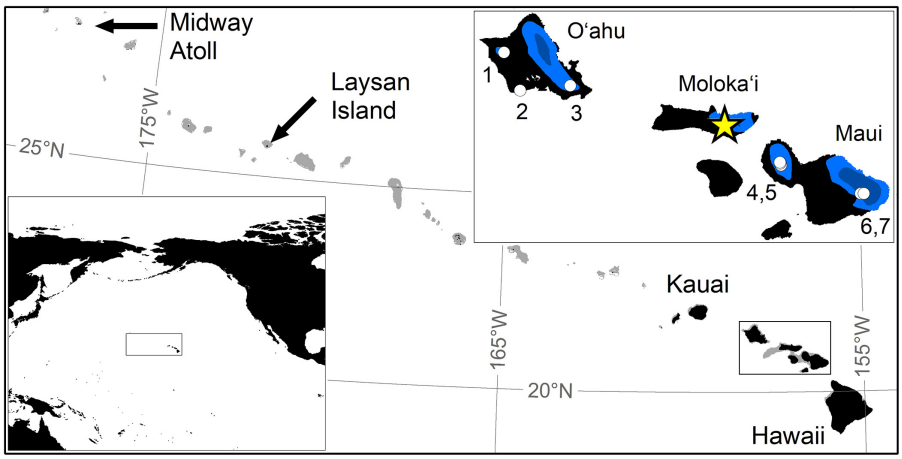

FIGURE 1 | Map of the North Pacific region and the study site. The Hawaiian Island chain in the North Pacific (inset) from Midway Atoll to the Island of Hawai'i with bathymetry to 130 m shown in gray. Islands of O'ahu and of the Maui Nui complex shown with annual rainfall over 1500 mm (blue) and 4000 mm (dark blue) with the location of the study site at Pēpē'ōpae (star) on the Island of Moloka'i and sites mentioned in the text (circles): (1) Ka'ala, (2) Kalaeloa and Ordy Pond (Uchikawa et al., 2010), (3) Ka'au Crater (Hotchkiss and Juvik, 1999), (4) and (5) summit and lowest bog Pu'u Kukui sites (Selling, 1948), (6) Wai'anapanapa Pond (Crausbay et al., 2014), and (7) Flat Top Bog (Burney et al., 1995).

silver powder. CO_2 ampules were graphitized and $^{14}C/^{12}C$ ratios determined at the Lawrence Livermore National Lab Center for Accelerator Mass Spectroscopy (LLNL-CAMS). The ^{14}C ages were calibrated to calendar years using the IntCal13 dataset (Reimer et al., 2013) and age-depth modeling was implemented in the R package BACON 2.3.4 (Blaauw and Christen, 2018).

Geochemistry

The PEP1 core was sliced frozen at 1-cm resolution on a band saw with a stainless steel blade. A 2–3 cm^3 subsample of known volume was dried at 100°C to constant mass to determine bulk density, and then homogenized with a Retsch MM200 ball mill and sieved at 250 μm. OM content was determined by loss-on-ignition of a 1–2 cm^3 subsample combusted in a muffle furnace at 550°C for 4 h. Elemental concentrations of carbon and nitrogen and the carbon stable isotope composition ($\delta^{13}C$ values reported in values of per mille vs. VPDB; Vienna Pee Dee Belemnite) of 2.4–15 mg subsamples (depending on OM content to target a consistent response) were loaded in tin capsules and determined by Elemental Analyzer (EA)-Cavity Ring-Down Spectrometer (CRDS) using a Costech ECS 4010 EA coupled to a Picarro G2201-i CRDS. Plant $\delta^{13}C$ and $\delta^{15}N$ values were determined by Isotope Ratio Mass Spectroscopy (IRMS) using an ECS 4010 coupled to a Thermo Scientific Finnigan Delta Plus XP at the Stable Isotope Laboratory at the University of Hawai'i at Mānoa. Long-term accuracy and precision of $\delta^{13}C$ and $\delta^{15}N$ is better than ±0.2‰.

Sedimentary *n*-alkanes were extracted from 2-cm thick composited samples from 31 depths in core PEP1. Plant leaf wax *n*-alkanes were extracted from ∼650 mg leaf samples. Total lipids were extracted by sonication in hexane and separated into four molecular fractions based on polarity using silica gel flash columns following the method of Nichols (2011) and Nichols et al. (2014) at the University of Hawai'i at Mānoa. Hydrocarbons were analyzed using an Agilent GC (Gas Chromatograph) equipped with programed temperature vaporization (PTV) inlet, 30 m DB-5 column, flame ionization detector (FID) and Agilent Mass Selective Detector (MSD). The oven temperature holds at 60°C for the first minute, ramps at 22°C min^{-1} to 200°C, ramps at 7.5°C min^{-1} to 320°C, and dwells for 10 min (Nichols et al., 2014). Hydrogen isotopes of individual *n*-alkanes were measured by GC-IRMS. Compounds eluting from the GC (column and program parameters same as above) were routed through a Thermo GC Isolink pyrolysis reactor at 1420°C. Compounds were pyrolized to hydrogen gas and routed through a Thermo Conflo IV continuous flow device to a Thermo Delta V Plus IRMS. Values of δ^2H are reported in per mille VSMOW. Absolute delta values are determined by comparison with certified reference standards (A. Schimmelmann, University of Indiana). Long-term mean analytical uncertainty of δ^2H measurements on individual alkanes is ±2‰. Analysis of *n*-alkanes was conducted at the Organic Geochemistry Laboratory at Lamont-Doherty Earth Observatory. Water isotope measurements of collected rainwater were made on a Picarro L20130-i at the University of Hawai'i Stable Isotope Biogeochemistry Lab.

Literature Forest Pollen and Peat Depth Data

Selling (1948; hereafter referred to as the OHS1948 data) produced microfossil diagrams for 14 peat cores from Kauai, Moloka'i, and Maui, which summarized relative pollen and spore abundances for 17 dominant genera. This seminal work includes 60 assemblages from a 330-cm core raised from Pēpē'ōpae in 1937 (Ser. 1; hereafter OHS1948-01) raised likely within 20 m of our core PEP1. We also included OHS1948 pollen from Pu'u Kukui on West Maui in our analysis (**Figure 1**). We digitized the pollen percent relative abundances for OHS1948-01 (Pēpē'ōpae) and OHS1948-33, -34, -60, and -80 (West Maui)

by scanning the published diagrams at high-resolution and generating data with PlotDigitizer 2.6.8. From Selling's (1948) original survey sketches, the 33 peat depths they measured along three transects at Pēpē'ōpae were also digitized. We established a chronology for OSH1948-01 based on correlations between pollen concentrations in OSH1948-01 and the carbon accumulation rate in PEP1.

Statistical Analysis

The percentage distributions of *n*-alkanes in plants and peat were summarized by calculating index values for average chain length (ACL) and the carbon preference index (CPI; Marzi et al., 1993). The ACL is a concentration-weighted average of chain lengths of odd-numbered chains between 17 and 35. A Principle Components Analysis (PCA) of odd-numbered *n*-alkane percentages in the 24 plant and 31 peat samples aided the interpretation of the contribution of leaf litter types to the sedimentary *n*-alkanes. The OSH1948 data was analyzed in two ways. First, we put the Pēpē'ōpae pollen assemblages in context of nearby OHS1948 data by ordinating assemblages from Pēpē'ōpae and sites on West Maui using orthogonalized Non-metric Multidimensional Scaling (NMDS) based on the Bray–Curtis dissimilarity measure. Second, we generated a climatic Wetness Index by scoring the 17 OHS1948 pollen genera by their habitat wetness (**Supplementary Table S3**) as provided by Wagner et al. (1996) and Palmer (2008) and a Weighted Average (WA) ordination to produce a Wetness Index value for each assemblage (Hotchkiss and Juvik, 1999). Multivariate analyses were run using PC-ORD (McCune and Mefford, 2016).

RESULTS

Core

Core PEP1 was 272 cm in total length and the peat section from the surface with living plants to a sharp interface with basal clay was 232 cm (**Figure 2**). The core consists of highly humified peat of high OM and carbon content (means of 97 and 53%, respectively) and low bulk density (mean of 0.11 g cm^{-2}). The $\delta^{13}C$ values of bulk peat ranged from −28.1 to −25.3‰. Eight radiocarbon measurements (**Supplementary Table S1**) show the age of OM at the clay-peat transition to be about 11.5 ka BP (thousands of years Before Present, where present is AD1950), with rapid peat formation occurring after ∼9.6 ka. Estimated carbon storage (carbon density per unit area) was 56 kg C m^{-2}

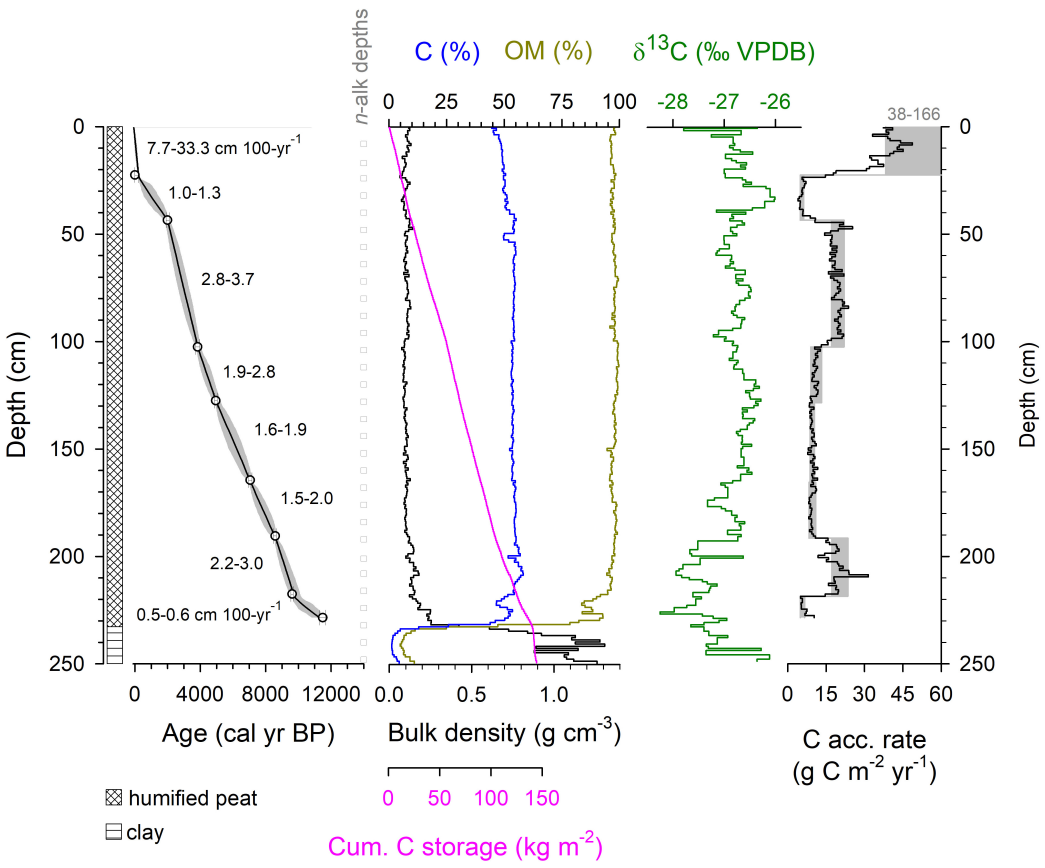

FIGURE 2 | Physical and carbon characteristics of bulk peat from core PEP1. The apparent carbon accumulation rate is calculated two ways: using the BACON-derived weighted average age of each contiguous 1-cm mid-point (black line) and using a linear interpolation between the minimum and maximum age of the 2-sigma calibrated range of each dated level (gray shading). Radiocarbon dates are provided in **Supplementary Table S1**.

at 100-cm depth, and 144 kg C m^{-2} for the entire profile (**Figure 2**). Peat depths at the site during the 1937 surveys ranged from 40 to 335 cm with a mean of 184 cm. An estimate for belowground carbon storage for the site, based on the mean peat carbon density (0.60 kg C m^{-3}; PEP1 average, this study), the mean peat depth (1.84 m; n = 33, Selling, 1948), and the peatland area (11,550 m^2), is 12.8 Mg C. The reconstructed rate of apparent carbon accumulation since 9.6 ka BP varied from 4.1 to 48.7 g C m^{-2} $year^{-1}$.

n-Alkane Distributions in Peat and Leaf Tissue

The relative abundance of n-alkane chain lengths (C_{15}–C_{37}) were quantified for both peat samples and modern plant samples from Pēpē'ōpae. The ACL of peat samples ranged from 26.4 to 30.4 with a median of 27.9 (**Figure 3**). In the modern leaf tissue samples, ACL ranged from 24.2 to 32.0 (**Supplementary Table S2**). Duplicate collection and measurement of plants from two areas of the study site showed that within-species variation was less typically than between species (**Supplementary Table S2**), although within-species variation was high in *Plantago pachyphylla*. CPI values of the peat samples (3–19) were within the range of the modern leaf values (2–24; **Figure 3**, **Supplementary Table S2**) but show an overall decreasing trend with depth. The PCA of the combined dataset of peat and leaf tissue had 56% of variation explained by the first two axes, PC1 and PC2, 41 and 15%, respectively, and axis scores for peat samples that fell within the range of leaf tissues (**Figure 4**). The PEP1 peat scores of PC1 are correlated linearly with ACL ($p < 0.0001$, $R^2 = 0.85$). Because flowering plants produce n-alkanes in far greater amounts than other plant types (Bush and McInerney, 2013) they dominate the sedimentary signal at Pēpē'ōpae, and we therefore do not over-interpret potential contributions of ferns, lycopods, and bryophytes based on n-alkane relative abundances.

Hydrogen Stable Isotope Values in Sedimentary *n*-Alkanes and Waters

Median values of δ^2H measured in the abundant C_{29} n-alkane in Holocene peat samples (>80% OM) ranged 26‰ from −164 to −202‰ VSMOW (**Figure 5**). Average values in the underlying clay layer were 44‰ more enriched than the mean Holocene peat value. The most depleted sedimentary n-alkane δ^2H values were observed ∼9.3 and ∼3.1 ka. A trend of overall increasing enrichment beginning around 9.3 ka reached a maximum value at 5 ka. To reconstruct the δ^2H value of peatland waters from sedimentary n-alkane values, we used values of apparent fractionation ($\varepsilon_{l/w}$) between modeled precipitation δ^2H values (Bowen and Revenaugh, 2003) and observed leaf wax values of tropical angiosperms between 30°S and 30°N in the database compiled by Sasche et al. (2012). No difference was observed between means of $\varepsilon_{l/w}$(± SD) for tropical dicots (−137 ± 30, n = 21) and monocots (−137 ± 19, n = 4), therefore we used a single value for $\varepsilon_{l/w}$(−137 ± 28) for all vascular plant types in this study. Reconstructed peatland water δ^2H values were between −22 and −48‰. The δ^2H value of rainwater collected at

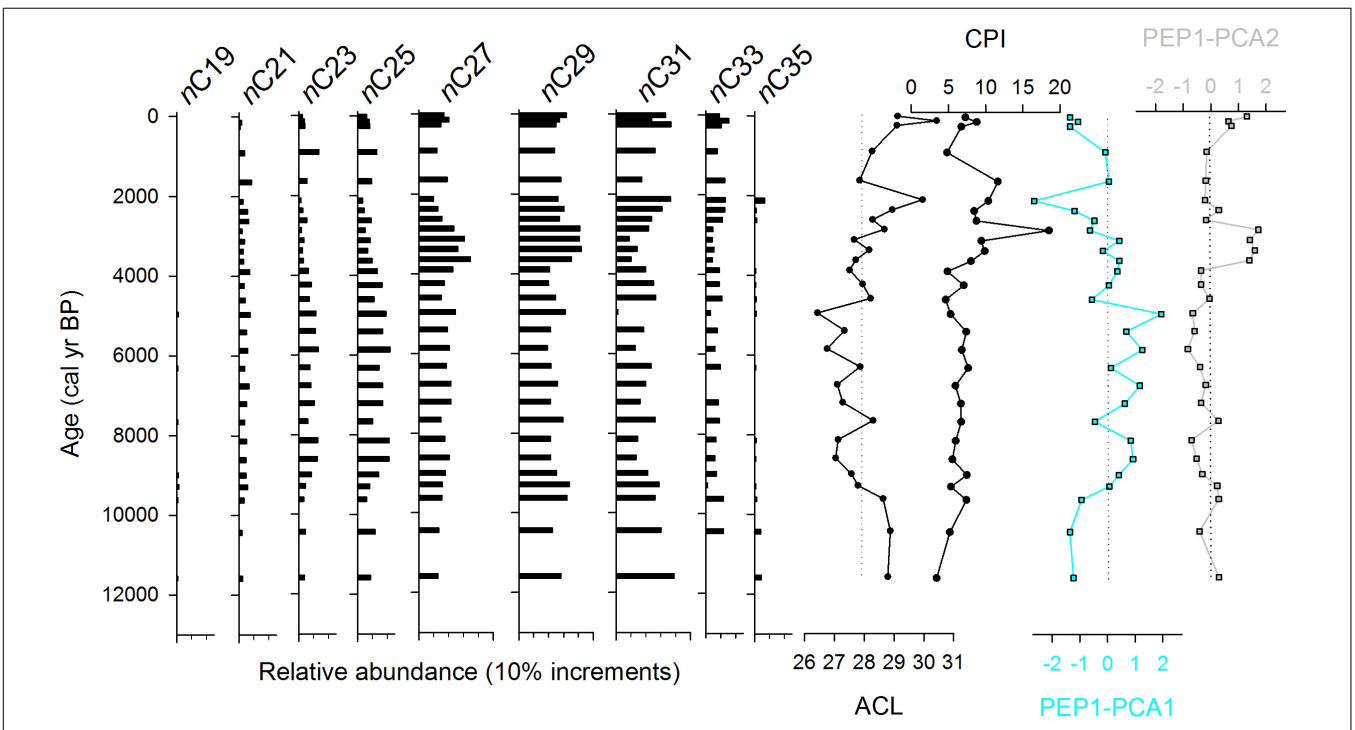

FIGURE 3 | Relative abundance of n-alkanes in 29 peat samples from core PEP1 including index values for average chain length (ACL) and the carbon preference index (CPI). PCA scores for the first two axes of an analysis of peat and leaf tissue distributions from the study site (**Figure 4**) are shown.

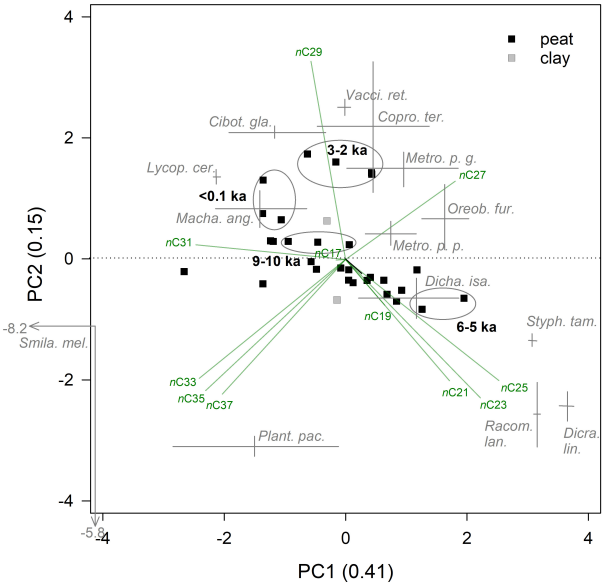

FIGURE 4 | Principle components analysis (PCA) of *n*-alkane relative abundances in sedimentary samples from core PEP1 and modern plant leaf tissue at Pēpē'ōpae explained 41 and 15% of the variance on PC1 and PC2, respectively. Scores for sedimentary samples (squares) show peat (solid, $n = 29$) or underlying clay (filled, $n = 2$). Ellipses show the region in biplot space of important periods in the mutli-proxy record (ka = thousands of years before present). Modern leaf tissue scores for dominant plant species at the study site ($n = 14$, **Supplementary Table S2**) are shown where the height and length of the crosses span the axis scores of duplicate composited plant collections.

Pēpē'ōpae was –8.6 to –15.6‰ ($n = 4$) which is within the range of values estimated by the OIPC (Bowen, 2018) for this location (−8 to −36‰) and those reported by Scholl et al. (2002) for windward East Maui (−7 to −22‰ VSMOW).

Forest Pollen

At the study site, dominant pollen types were present throughout the profile (**Supplementary Table S3**), showing that rainforest vegetation characterized by *Metrosideros* and *Cibotium* has been present throughout the Holocene, albeit with substantial shifts in abundance, and including changes in dry-adapted vegetation upwind (Selling, 1948). The two-dimensional NMDS had a final stress of 11.6 and scores for OHS-1948-01 pollen assemblages that fall within the range of scores from the other sites, showing an overall representativeness of upwind valley vegetation on East Moloka'i relative to similar elevations (1300–1700 m) on West Maui, but with some noteable differences. For example, the East Moloka'i Holocene pollen spectra is dominated more by *Metrosideros* and nearly absent is *Acacia* compared to rainforests on Pu'u Kukui (**Figure 6**). We developed a chronology for OSH1948-01, which was published before the development of radiocarbon dating, by assuming a common basal age with our core (**Supplementary Table S1**), an estimate for the uppermost OSH1948-01 sample at 25 cm (collected in 1938) based on the rate of near-surface accumulation in our core, and matching independent changes in total pollen abundance OHS1948-01 (**Supplementary Table S4**) with changes in sedimentation rate in PEP1. This approach assumes the rate of microfossil influx to the surface is relatively consistent on multi-centennial scales, and that the dominant influence on concentration is the rate of peat accumulation, i.e., the effect of microfossil concentration/dilution driven by the balance of plant production vs. OM decomposition. Specifically, the timing of two carbon accumulation minima in PEP1 were assigned to two pollen concentration maxima at 265 and 50 cm in OHS1948-01. An age-depth model was derived in BACON 2.3.4 (Blaauw and Christen, 2018) from these four temporal tie-points and a prescribed age uncertainty of ±100 year, and the ages of the mid-points of each sampled pollen depth is given in **Supplementary Table S4**. Drier pollen types were most abundant, and Wetness Index values were at their lowest, from 12–11, ∼5.5, and ∼1.5 ka (**Figure 7**).

DISCUSSION

Carbon Accumulation and Holocene Hydroclimate

Carbon accumulation at Pēpē'ōpae increased rapidly around 10 ka and continued without hiatus but with faster and slower periods until the present (**Figures 2**, **7**). The long-term capacity for this low-latitude peatland ecosystem to sequester carbon belowground is substantial (144 kg C m^{-2} total; 56 kg C m^{-2} to 1 m depth) compared to soil organic carbon storage in native mesic-wet forests in Hawai'i generally (18.7 kg C m^{-2} on average; Selments et al., 2017). Plant growth in tropical wetlands can be rapid, with NPP values between 560 and 2438 g C m^{-2} $year^{-1}$ (Sjögersten et al., 2014; sites with organic soils). Yet, mean Holocene tropical peat carbon accumulation rates are broadly similar to their cold region counterparts (∼5–60 g C m^{-2} $year^{-1}$; Yu et al., 2010) despite cold peatlands having substantially lower NPP. Anaerobic conditions below the water table are a key factor stabilizing peat OM (Clymo, 1984) although chemical recalcitrance may be important (Hodgkins et al., 2018), and in Hawai'i wet forest environments depress decomposition overall relative to drier conditions (Schuur, 2001). However, the rate of near-surface OM decomposition can be high in tropical peatlands (Chimner, 2004) when conditions promote soil carbon loss, i.e., when water tables are lowered (Kurnianto et al., 2015). In this way, we interpret changes in long-term carbon accumulation rate to reflect shifts in water table position and stability, with faster rates showing higher, stable water tables that promote the stabilization and sequestration of OM, and slower rates showing lower or variable water table conditions.

Multiple lines of evidence suggest wet conditions in Hawai'i around 10–9 and 3 ka BP. At Pēpē'ōpae, a carbon accumulation maximum around 9 ka occurs contemporaneously with an increase in the pollen-derived Wetness Index (**Figure 7**). The bulk $\delta^{13}C$ values during this period are more negative than any other time after 10 ka. Because plants that use the C3 photosynthetic pathway dominate higher mountain elevations in Hawai'i (Rundel, 1980; Edwards and Still, 2008) and all of the dominant plants at the site today are C3 (**Supplementary Table S2**), negative $\delta^{13}C$ departures are

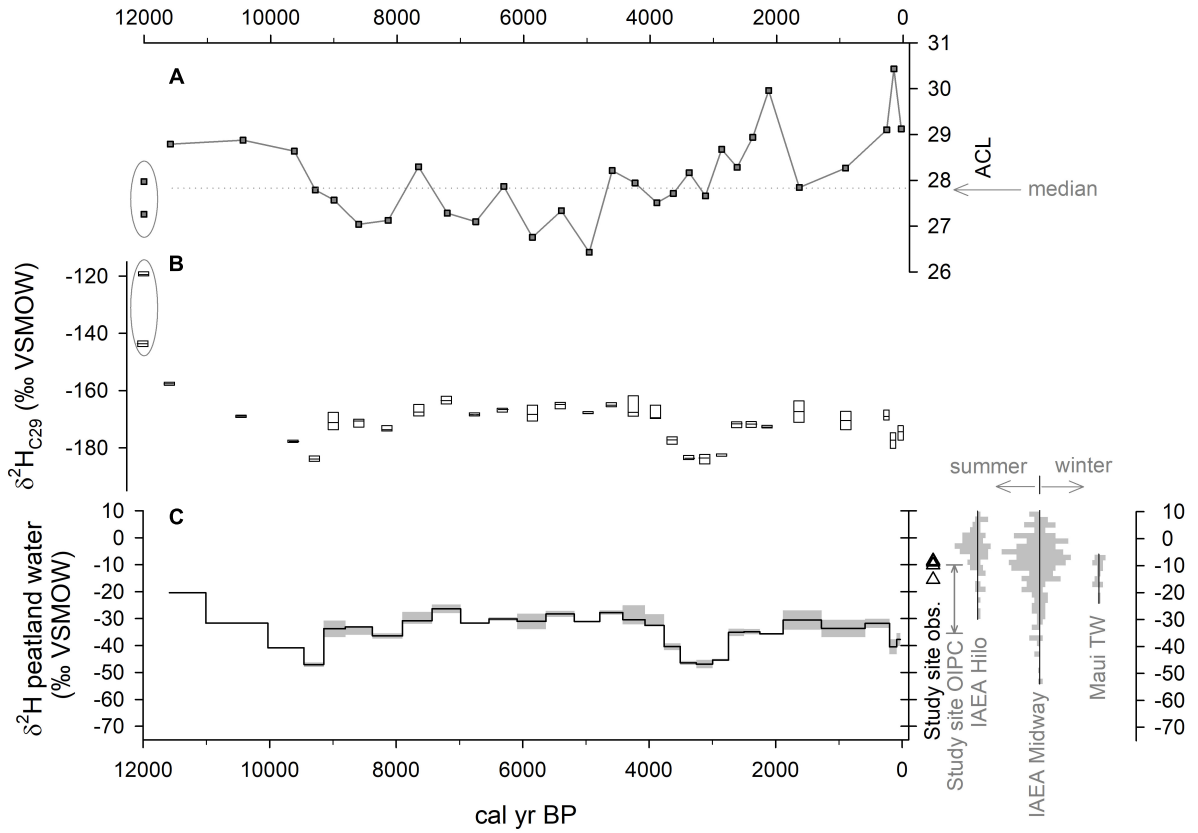

FIGURE 5 | Values for ACL, δ^2H of sedimentary leaf waxes, and reconstructed peatland water δ^2H in core PEP1. **(A)** ACL values. **(B)** δ^2H of nC_{29} where boxes are the interquartile range and horizontal lines show the median. **(C)** Reconstructed plant-available peatland water δ^2H values. Shown to the right are direct measurements of rainwater (triangles) as well as the seasonal range of modeled values for the study site from the online isotopes in precipitation calculator (OIPC). Also shown are distributions of seasonal IAEA monthly observations of δ^2H for Hilo and Midway (IAEA/WMO, 2018; **Figure 1**), and for windward East Maui (Scholl et al., 2002), where winter is November–April.

consistent with more-frequently open stomata in vascular plant leaves and lower water use efficiency during wet conditions. On the Island of Oʻahu, a pulse of wetter-than-present vegetation between 9 and 11 ^{14}C kyr BP in the Kaʻau Crater pollen record is reported by Hotchkiss and Juvik (1999). Around Kalaeloa on the leeward plain of Oʻahu, Uchikawa et al. (2010) suggest that the proportion of C_4 plants was at its Holocene minimum around this time. During the late Holocene, an increase in carbon accumulation at Pēpēʻōpae suggests wet conditions around 3.5–2 ka. This time period includes departures in the peat $\delta^{13}C$ values toward more negative values (**Figures 2**, **7**). On East Maui, the well-dated Holocene lake sediments from Waiʻānapanapa, show an abrupt increase in sedimentation rate at 3.2 ka (Crausbay et al., 2014) and the initiation of high-OM peat formation at Flat Top Bog by 2.3 ka (Burney et al., 1995).

Prolonged drier conditions lasting centuries have occurred at Pēpēʻōpae. The carbon accumulation rate was overall low between 8.5 and 4.5 ka. During this time, values of peat $\delta^{13}C$ increased and reached least-negative values around 5 ka, and the pollen Wetness Index decreased (**Figure 7**). This pattern matches the aridification of leeward Oʻahu over this same period, argued by Uchikawa et al. (2010) to be associated with the warming of eastern equatorial Pacific (EEP) Ocean waters, extended upper level westerly jet, fewer extratropical storms entering the Hawaiian sector, and thus diminished winter rainfall. Drying may have been widespread across the north-central Pacific region, as pond sediments on Laysan Island (**Figure 1**) also show a decrease in palm (*Pritchardia*) pollen around 5 ka (Athens et al., 2007), consistent with the "El Niño-like" response pattern in connection with the EEP positive SST anomalies. The apparent carbon accumulation rate at Pēpēʻōpae reached a Holocene minimum around 1.5–1 ka (**Figure 7**), which is a strong signal given its relatively young position in the upper part of the profile and far less time for decomposition than deeper levels of OM. Peat $\delta^{13}C$ values reach a maximum at this time consistent with greater water use efficiency of vascular plants under drier conditions and lower mountain humidity. Dry pollen types in OHS1948-01 (*Dodonea* and *Chenopodium*; **Figure 6**) increase in abundance around 1.5 ka that drive the Wetness Index to its Holocene minimum at this time (**Figure 7**). Thus, East Moloka'i experienced relatively dry Holocene conditions just before and during the earliest period of arrival of Polynesian settlers around 1 ka (Wilmshurst et al., 2011; Dye, 2015).

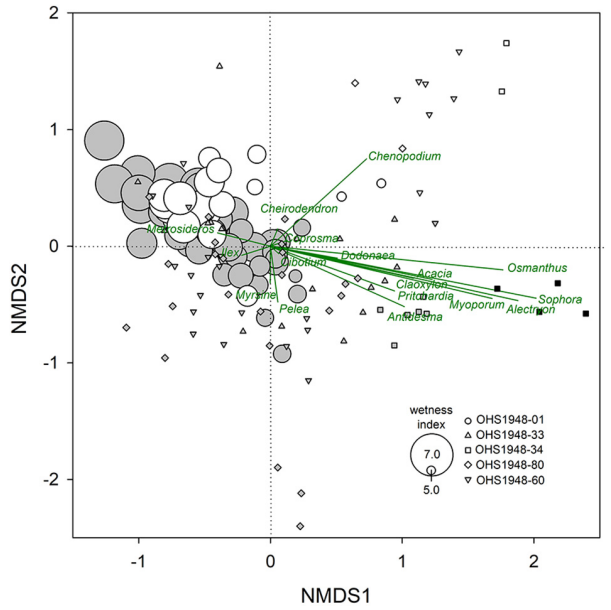

FIGURE 6 | Non-metric multidimensional scaling (NMDS) ordination of fossil pollen abundance from five sites in Maui Nui (Selling, 1948). Pēpē'ōpae (1262 m elevation) axis scores shown with symbol size scaled to values of the pollen Wetness Index (**Supplementary Table S3**, see section "Materials and Methods") and four sites from East Maui (**Figure 1**) near the summit (1703 m; OHS1948-33 and -34), a mid-elevation site (OHS1948-80), and a lowest bog (1390 m; OHS1948-60). Shading shows Selling (1948) original pollen Periods; the oldest Period 1 (black) drier vegetation with rain forest restricted, Period 2 (gray) with rain forest extended, and the youngest Period 3 (white) with drier vegetation.

Vegetation Change Evident in Geochemistry and Pollen

The few studies of montane peatland vegetation in Hawai'i describe peat derived from sedge litter, e.g., *Oreobolus* peat (Selling, 1948; Carlquist, 1970). However, the fossil leaf wax ACL in core PEP1 varied substantially from 26.4 to 30.4 (**Figure 3**) compared to the ACL of *Oreobolus furcatus* was 26.3–27.0. This variation in peat ACL suggests changes in contributions from various litter types rather than dominance by a single short-chain type such as *Oreobolus*. The similarity of ACL and CPI values between the modern leaf tissue and the peat samples also suggests that the leaf waxes of these plants are dominating the sedimentary *n*-alkanes, and that inputs from other sources like bacteria and algae biomass that have shorter chain lengths and CPI values (Bush and McInerney, 2013) are minor at Pēpē'ōpae.

Periods of rapid carbon accumulation during wet conditions around 9 and 3 ka, have PC1 axis scores around zero (**Figure 4**), consistent with a mixture of plant litter types from a diverse plant community. Of these wet periods, the peat samples from the 3–2 ka period have a greater abundance of C_{29} and more positive PC2 scores, suggesting greater inputs from *Cibotium* and *Vaccinium* leaf tissue and more *Metrosideros polymorpha* var. *glaberrina* (**Figure 4**). Crausbay et al. (2014) report that glabrous-leafed *M. polymorpha* (var. *macrophylla*) abundant in wet forests of Hawai'i have relatively long ACL (30.6 on average) compared to pubescent-leafed *M. polymorpha* (var. *incana*) growing in drier forests with shorter ACL (26.9 on average). Although the ACL values for the dwarf *M. polymorpha* varieties at Pēpē'ōpae are not as clearly separated (**Supplementary Table S2**), the period around 3 ka may have had more glabrous 'ōhi'a and been wetter than 9 ka BP. During drier conditions around 5 ka, the peat has abundant C_{21}–C_{25} (**Figure 4**) and among the shortest ACL values in the profile (**Figure 3**), possibly with more leaf litter from *Dicranopteris* ferns, *Styphelia* shrubs and small graminoids (*Oreobolus* and *Dichanthelium*; **Figure 4**). The *n*-alkane distributions suggest a vegetation that responded sensitively to wet vs. dry conditions with shifts in plant community abundance at Pēpē'ōpae, and that these shifts occurred on a multi-millennial scale.

At the mountain forest scale, vegetation composition in upwind valleys (e.g., Pelekunu and Wailau) observed in the OSH1948-01 pollen shows changes in the dominance of forest community species over the Holocene. Our chronology for OSH1948-01 shows the wetter-drier transition between Selling's (1948) Period 2 (wetter with rainforest extended) and Period 3 (drier vegetation) occurred around 4.3 ka. Selling's oldest Period 1 (drier vegetation with rainforest restricted) is not observed at Pepeopae, and thus must have occurred before 11.5 ka, and Period 2 can be viewed to have a minimum onset age of 11.5 ka. The NMDS analysis of OHS1948 pollen shows that the East Moloka'i and West Maui Period 2 and 3 pollen occupies generally the same ordination space. However, the East Moloka'i forests have been dominated more by *Metrosideros* over the Holocene with nearly absent *Acacia*, consistent with modern observations of a lack of *Acacia koa* forest on Moloka'i despite a suitable climate (Price et al., 2012). It is noteworthy that the overall composition of upwind forests did not dramatically change in East Moloka'i over the last 12,000 years, but changes in abundance and shifting dominance of forest species occurred multiple times. It is noteworthy that the dry vegetation of Selling's (1948) Period 1, evident in pollen in shallow peat at the summit of Pu'u Kukui, was substantially different (**Figure 6**). Although it is not dated, it is likely a dry episode(s) during the complex glacial period in Hawaii (Anslow et al., 2010) characterized by abundant dry-adapted genera (*Dodonaea* and *Chenopodium*) clearly separated from the rest of the pollen spectra (**Figure 6**).

The pollen Wetness Index values follow the wet–dry trend of the OHS1948 data along the first NMDS axis (**Figure 6**). Because the Index values are strongly affected by variations in the percentage contribution of dry taxa as well as the large variations in *Metrosideros*, it is possible that the pollen reflects internal ecosystem dynamics, or a combination of ecosystem and direct climate influences. Mueller-Dombois (1986) argued that the Holocene decreases in *Metrosideros* pollen abundance in East Moloka'i are driven by ecological forest dieback of like-aged cohorts. Our chronology for OHS1948-01 suggests that *Metrosideros* minima are separated by one or two thousand years (between 1100 and 2400 years) and do not seem truly cyclical. Although *M. polymorpha* trees in wet forests of Hawaii can be long-lived, e.g., Hart (2010) reports ^{14}C ages of mature trees between 100 and 600 years old, the return interval of

Metrosideros minima is substantially longer than the longest tree age, showing influence of some external factor such as climate perturbation (Boehmer et al., 2013). The Wetness Index can thus be interpreted in a hydroclimatic context.

Decreases in the pollen-derived Wetness Index tend to track increases in the ACL of PEP1 sedimentary *n*-alkanes (**Figures 3**, **7**), suggesting that peatland vegetation and ecosystem processes are similarly responsive as forests to changes in rainfall in Hawai'i. For example, the abrupt decrease in the Wetness Index around 2 ka is the period with the greatest ACL in PEP1. Peatland carbon cycling also appears to be sensitive to regional hydroclimate changes on this quasi-millennial scale, e.g., increases in the carbon accumulation rate around 9 and 3 ka. Although the apparent carbon accumulation rate is rather flat in the mid Holocene, it is possible that the dry conditions around 5 ka may have had a lowered water table for long enough that mineralization of organic carbon in deeper peat layers "erased" some of the record of previous carbon sequestration. Model experiments show that decomposition losses may be substantial in tropical peatlands when water tables drop for long periods (Kurnianto et al., 2015), and montane peatlands in Hawaii may also be sensitive to large carbon losses with drying. Sedimentary *n*-alkane CPI values theoretically decrease with greater microbial decomposition (Buggle et al., 2010). CPI values are low around 5 ka and are at their highest around 3 ka, consistent with increased decomposition and carbon loss during drier periods and depressed decomposition playing an important role for belowground carbon sequestration during wetter periods.

Holocene North Pacific Climate

Peat formation accelerated initially around 10 ka when wintertime insolation was generally at its minimum (**Figure 7**). Uchikawa et al. (2010) argued that this low top-of-atmosphere shortwave energy flux during early Holocene winter was a driver of cooler SST in the equatorial Pacific that weakened the Hadley circulation and diminished subtropical subsidence. The data from Pēpē'ōpae show the period between 10 and 8.5 ka was particularly wet and includes reconstructed peatland water δ^2H values that are relatively depleted (**Figure 5**). Monthly rain δ^2H values from sites at sea level at Midway Atoll and Hilo (**Figure 1**) in the Global Network of Isotopes in Precipitation (GNIP) database (IAEA/WMO, 2018) and at higher elevations (229–1295 m) on trade-wind-affected windward East Maui (Scholl et al., 2002) do not exhibit a strong seasonal pattern (**Figure 5C**). However, storm rain δ^2H values has been observed to be depleted relative to trade-wind rain in Hawai'i (Scholl et al., 1996), and thus storms may have increased during the period around 9 ka and been a driver of rapid peat accumulation. An enhanced temperature gradient between tropical and extratropical latitudes during the early Holocene, caused by larger negative temperature anomalies in the polar latitudes owing in part to remnant ice sheets, further suggests that storm activity and atmospheric heat transport from the subtropics to the high latitudes was enhanced. However, at Pēpē'ōpae the peat layer would have been relatively thin at this time, suggesting that summer (dry) season rainfall was also sufficient to maintain saturated soil conditions year-round in the absence of a thicker peat layer of low hydraulic conductivity that can buffer OM decomposition from summer drought conditions. Shifts in the ITCZ position in response to orbital forcing could have played a role for the overall water table balance during the Holocene (McGee et al., 2014; Reimi and Marcantonio, 2016).

A trend of aridification during the early Holocene has been observed in multiple proxy records in Hawai'i (e.g., Gavenda, 1992; Hotchkiss and Juvik, 1999). In our record from Pēpē'ōpae, the overall drying from 9 to 4.5 ka follows this trend where $\delta^{13}C$ is least negative, accumulation rates are diminished, and the Wetness Index is lowest at 5.5–4.5 ka (**Figure 7**). Uchikawa et al. (2010) argued this drying in Hawai'i was primarily a response to eastern tropical Pacific Ocean SST anomalies, resembling the present-day ENSO teleconnection mode. In that mechanism the anomalous warming in the eastern tropical Pacific (relative to the Pacific average SST trend) drives an atmospheric circulation response similar to that observed during the El Niño events in modern times.

Our interpretation of the general drying at Pēpē'ōpae is in that sense consistent with the previous model-based mechanisms (Uchikawa et al., 2010). In addition, we find new evidence for a trend toward isotopically heavier precipitation from the early to mid Holocene. The values of reconstructed peatland water δ^2H values in PEP1 reach peak enrichment during this interval (**Figures 5**, **7**). In modern-day climate, extratropical winter storms (Kona Lows and frontal systems) contribute isotopically depleted precipitation during the cold season, compared with the prevailing trade-wind induced precipitation (Scholl et al., 1996). Our data suggest the mid Holocene was most likely an era with decreased extratropical storm activity near the Hawaiian Islands. In modern times this is an analog to El Niño events (Chu and Chen, 2005; Elison Timm et al., 2011) and relates to circulation in the upper troposphere.

The position and strength of the upper level jet stream controls the path of synoptic storm systems across the Pacific. During El Niño years, a more intense and zonally extended jet north of Hawai'i steers storm systems and their fronts from the dateline toward the North American continent. Adopting this modern analog to the early to mid-Holocene trend depicts a relatively consistent picture. A positive eastern tropical Pacific SST anomaly trend induces a strengthening and eastward extension of the upper level jet, a more organized west to east propagation of synoptic storm systems, and with that fewer extratropical storms and fronts have the opportunity to develop rain-producing disturbances over Hawai'i. Further support comes from Risi et al. (2012); winter months with the most ^2H-enriched rain (the top three Januaries) over Moloka'i have a sea level pressure pattern characterized by a large and deep low-pressure center in the eastern North Pacific (**Figure 8**). Such pressure anomalies are tightly connected with an extension of the upper level westerly wind jets (Linkin and Nigam, 2008).

It is noteworthy that, relative to leeward coastal proxy sites, the wet windward location of Pēpē'ōpae can experience topographically induced trade-wind precipitation in all months, which can contribute substantially to annual totals. Therefore, the trends found in the isotopic proxy time series at Pēpē'ōpae could also reflect changes in the warm season (May–September).

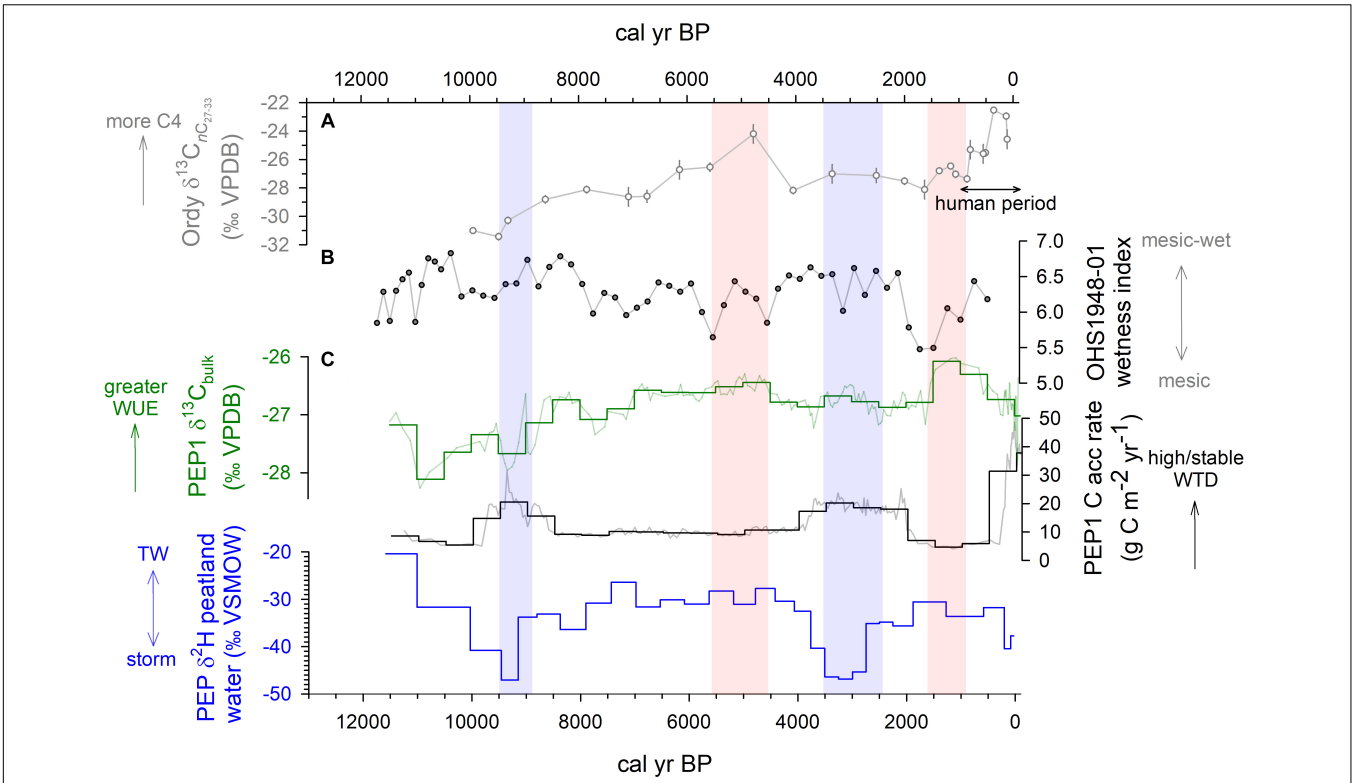

FIGURE 7 | Comparison of hydroclimate changes at Pēpē'ōpae and East Moloka'i and aridity changes on the leeward coastal plain of Oahu (**Figure 1**). **(A)** Variation in reconstructed abundance of C_4-photosynthesis plants in sediments of Ordy Pond, leeward O'ahu (Uchikawa et al., 2010). **(B)** A Wetness Index derived from fossil pollen in core OHS1948-01 (Selling, 1948) reflecting vegetation and habitat wetness in upwind valleys on east Moloka'i. **(C)** Data from core PEP1, including $\delta^{13}C_{bulk}$ shown as raw data and as mean values in 500-year bins, the rate of C accumulation shown in 500-year bins, and the reconstructed δ^2H values of plant-available water (**Figure 5**). Hydroclimate proxy interpretations include increases in C_3-plant water use efficiency (WUE), the stability of wetland water table depth (WTD), changes in the contribution from storm-derived vs. tradewind (TW) rain, and wetter periods (blue shading) and drier periods (red shading).

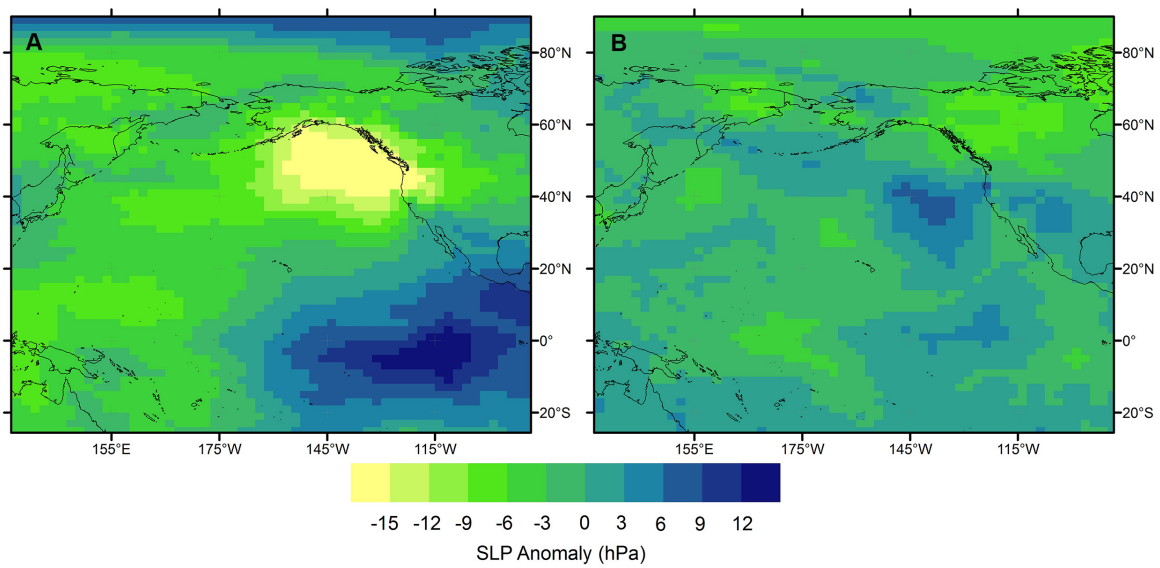

FIGURE 8 | Sea level pressure (SLP) anomalies in the North Pacific region averaged for the three January periods with the most enriched **(A)** and most depleted **(B)** δ^2H values of rainfall for the grid box spanning the islands of Maui Nui (Risi et al., 2012).

Although no seasonal differences are detectable in modern rainfall (**Figure 5C**) the warm season precipitation regime during the Holocene is less well understood. Interactions between tropical Pacific zonal SST gradients and interhemispheric tropical SST gradients affect not only the position of the Intertropical Convergence Zone in terms of shifts in the latitude position (Donohoe et al., 2013; McGee et al., 2014) but also the strength of the Hadley Cell circulation and potentially the meridional width of the Hadley circulation. All these factors could affect precipitation in Hawai'i during the warm season and thus play an important role in the hydroclimatic changes during the Holocene.

Our new data show that early Holocene aridification at Pēpē'ōpae was interrupted by wet conditions around 3 ka. It has been argued that the dominant climate forcing mechanism in the Pacific since about 4 ka has switched from external influence of insolation to internal influence by ENSO and PDO-like modes of circulation (Conroy et al., 2008; Anderson et al., 2016). Reconstructed peatland water δ^2H values decrease by more than 30‰ and reach a minimum around 3 ka (**Figure 7**), reflecting a shift toward more isotopically depleted extratropical/subtropical storms at the study site (Scholl et al., 1996). In the Risi et al. (2012) data set, cold months with the most ^{2}H-depleted rain (the bottom three Januaries) over Moloka'i show higher pressure to the northeast (**Figure 8**). The high pressure anomaly indicates an atmospheric pattern that can enhance storm activity west of the ridge. The decreased peatland water δ^2H values during the period around 3 ka suggest that wintertime North Pacific circulation shifted toward a retracted upper level westerly wind jet that enabled more frequent intrusion of extratropical storm activity into the central subtropical Pacific (Seager et al., 2010). Alternative mechanisms should be also considered, and ideally supported by model simulations, in the interpretation of these millennial scale regional signals, e.g., changes in the Hadley cell or Walker circulation impacts on summer precipitation. Finding ways to disentangle winter and summer precipitation signals from multivariate proxy data is a worthwhile goal for future research projects.

Hydroclimatic conditions at Pēpē'ōpae are generally drier after 2 ka. Reconstructed peatland water δ^2H values suggest tradewind-dominated rainfall, similar to rainfall values at the site today. The millennium preceding arrival of the first people in Hawai'i was drier than previous times with potentially an increased frequency of stronger Aleutian Low conditions in the North Pacific (Bailey et al., 2018). Recent analysis of rainfall observations since 1920 show an overall drying in Hawai'i, including East Moloka'i (Frazier and Giambelluca, 2017), that appears to be continuing an overall drying trend in Hawaii since 1500 (Diaz et al., 2016). The hydroclimate proxy data from Pēpē'ōpae suggest that this overall drying began as early as 2 ka BP.

CONCLUSION

The environmental proxy data from Pēpē'ōpae provide a high quality continuous record of Holocene ecological and hydroclimatic change from a windward mid-elevation wet forest in Hawai'i. The montane peatland is a carbon hot-spot today, storing 144 kg C m^{-2}, but has had a dynamic history of carbon accumulation. The distribution of *n*-alkanes in peat and modern plants suggests that leaf litter inputs in the peatland over time have not been static, but shifted among dominant plant types in response to climate. We generated a best-estimate chronology for a previously published but undated fossil pollen record from the site, that showed increases in dry-adapted taxa in upwind forests during periods of reduced carbon accumulation at Pēpē'ōpae. Wet hydroclimatic periods around 9 and 3 ka corresponded to negative departures in the hydrogen stable isotope ratios of sedimentary C_{29} *n*-alkanes, consistent with increases in storm-derived rainfall that promoted more stable water table levels. Multi-centennial dry periods have occurred since the mid-Holocene that lack a strong storm rain signal in leaf wax hydrogen stable isotope values. Varying contributions of storm rain to annual totals at the study site are likely tied to the strength and position of the upper level jet stream. This study is the first in Hawai'i to provide a continuous organic sedimentary record of links between hydroclimate, vegetation, and montane belowground carbon sequestration for this part of the North Pacific. Developing a network of sites across gradients in the Hawaiian Islands should be a research priority to better understand North Pacific circulation using the terrestrial proxy view from these isolated islands.

AUTHOR CONTRIBUTIONS

DB and OET acquired funding. DB, RK, and SD-C obtained the samples. DB, CM, and JN conducted the laboratory analyses. DB wrote the manuscript with input from all authors.

FUNDING

This work was supported by the National Science Foundation (United States) Grant AGS-1502984 to DB and AGS-1502951 to OET.

ACKNOWLEDGMENTS

Access to Pēpē'ōpae was made possible by The Nature Conservancy Moloka'i and Ed Misaki. We thank Axel Timmermann, Niklaus Schneider, Karl Hsu, and Derek Ford for their help in the field.

SUPPLEMENTARY MATERIAL

The Supplementary Material for this article can be found online at: https://www.frontiersin.org/articles/10.3389/feart.2019.00188/full#supplementary-material

Additional data can be found in the EarthChem library at: http://dx.doi.org/10.1594/IEDA/111334.

REFERENCES

Anderson, L., Berkelhammer, M., Barron, J. A., Steinman, B. A., Finney, B. P., and Abbot, M. B. (2016). Lake oxygen isotopes as recorders of North American Rocky Mountain hydroclimate: holocene patterns and variability at multi-decadal to millennial scales. *Glob. Planet. Change* 1377, 131–148. doi: 10.1016/j.gloplacha.2015.12.021

Anshari, G., Kershaw, A. P., van der Kaars, S., and Jacobsen, G. (2004). Environmental change and peatland forest dynamics in the Lake Sentarum area, West Kalimantan, Indonesia. *J. Quat. Sci.* 19, 637–655. doi: 10.1002/jqs.879

Anslow, F. S., Clark, P. U., Kurz, M. D., and Hostetler, S. W. (2010). Geochronology and paleoclimatic implications of the last deglaciation of the Mauna Kea Ice Cap, Hawaii. *Earth Planet. Sci. Lett.* 297, 234–248. doi: 10.1016/j.epsl.2010.06.025

Athens, J. S., Ward, J. V., and Blinn, D. W. (2007). Vegetation history of Laysan Island, Northwest Hawaiian Islands. *Pac. Sci.* 61, 17–37. doi: 10.1371/journal.pone.0136773

Bailey, H. L., Kaufman, D. S., Sloane, H. J., Hubbard, A. L., Henderson, A. C. G., Leng, M. J., et al. (2018). Holocene atmospheric circulation in the central North Pacific: a new terrestrial diatom and d18O dataset from the Aleutian Islands. *Quat. Sci. Rev.* 194, 27–38. doi: 10.1016/j.quascirev.2018.06.027

Benavides, J. C., Vitt, D. H., and Wieder, R. K. (2013). The influence of climate change on recent peat accumulation patterns in *Distichia muscoides* cushion bogs in the high-elevation tropical Andes of Columbia. *J. Geophys. Res. Biogeosci.* 118, 1627–1635. doi: 10.1002/2013jg002419

Blaauw, M., and Christen, J. A. (2018). *Rbacon: Age-Depth Modelling using Bayesian Statistics. R package version 2.3.4*. Available at: https://CRAN.R-project.org/package=rbacon

Boehmer, H. J., Wagner, H. H., Jacobi, J. D., Gerrish, G. C., and Mueller-Dombois, D. (2013). Rebuilding after collapse: evidence for long-term cohort dynamics in the native Hawaiian rain forest. *J. Veg. Sci.* 24, 639–650. doi: 10.1111/jvs.12000

Bowen, G. J. (2018). *The Online Isotopes in Precipitation Calculator, version 3.1*. Available at: http://www.waterisotopes.org

Bowen, G. J., and Revenaugh, J. (2003). Interpolating the isotopic composition of modern meteoric precipitation. *Water Resourc. Res.* 39:1299. doi: 10.1029/2003WR002086

Buggle, B., Wiesenberg, G. L. B., and Glaser, B. (2010). Is there a possibility to correct fossil *n*-alkane data for postsedimentary alteration effects? *Appl. Geochem.* 25, 947–957. doi: 10.1016/j.apgeochem.2010.04.003

Burney, D. A., DeCandido, R. V., Burney, L. P., Kostel-Hughes, F. N., Stafford, T. W., and James, H. F. (1995). A Holocene record of climate change, fire ecology and human activity from montane Flat Top Bog, Maui. *J. Paleolimnol.* 13, 209–217. doi: 10.1007/bf00682765

Bush, R. T., and McInerney, F. A. (2013). Leaf wax n-alkane distriubtions in and across modern plants: implications for paleoecology and cheotaxonomy. *Geochim. Cosmochim. Acta* 117, 161–179. doi: 10.1016/j.gca.2013.04.016

Carlquist, S. (1970). *Hawaii A Natural History*. New York, NY: The Natural History Press.

Chimner, R. A. (2004). Soil respiration rates of tropical peatlands in Micronesia and Hawaii. *Wetlands* 24, 51–56. doi: 10.1672/0277-5212(2004)024[0051:SRROTP]2.0.CO;2

Chu, P.-S., and Chen, H. (2005). Interannual and interdecadal rainfall variations in the Hawaiian Islands. *J. Clim.* 18, 4796–4813. doi: 10.1175/jcli3578.1

Chu, P.-S., Nash, A. J., and Porter, F. (1993). Diagnostic studies of two contrasting rainfall episodes in Hawaii: dry 1981 and wet 1982. *J. Clim.* 15, 2678–2689.

Clymo, R. S. (1984). The limits to peat bog growth. *Philos. Trans. Royal Soc. London B* 303, 605–654. doi: 10.1098/rstb.1984.0002

Conroy, J. L., Overpeck, J. T., Cole, J. E., Shanahan, J. M., and Steinitz-Kannan, M. (2008). Holocene changes in eastern tropical Pacific climate inferred from a Galapagos lake sediment record. *Quat. Sci. Rev.* 27, 1166–1180. doi: 10.1016/j.quascirev.2008.02.015

Crausbay, S., Genderjahn, S., Hotchkiss, S., Sachse, D., Kahmen, A., and Arndt, S. (2014). Vegetation dynamics at the upper reaches of a tropical montane forest are driven by disturbance over the past 7300 years. *Arct. Antarct. Alp. Res.* 46, 787–799. doi: 10.1657/1938-4246-46.4.787

Dargie, G. C., Lewis, S. L., Lawson, I. T., Mitchard, E. T. A., Page, S. E., Bocko, Y. E., et al. (2017). Age, extent, and carbon storage of the central Congo Basin peatland complex. *Nature* 542, 86–90. doi: 10.1038/nature21048

Diaz, H. F., Wahl, E. R., Zorita, E., Giambelluca, T. W., and Eischeid, J. K. (2016). A five-century reconstruction of Hawaiian Islands Winter Rainfall. *J. Clim.* 29, 5661–5674. doi: 10.1175/jcli-d-15-0815.1

Donohoe, A., Marshall, J., Ferreira, D., and McGee, D. (2013). The relationship between ITCZ location and cross-equatorial atmospheric heat transport: from the seasonal cycle to the Last Glacial Maximum. *J. Clim.* 26, 3597–3618. doi: 10.1175/jcli-d-12-00467.1

Dye, T. S. (2015). Dating human dispersal in remote oceania: a Bayesian view from Hawai'i. *World Archaeol.* 47, 661–676. doi: 10.1080/00438243.2015.1052845

Edwards, E. J., and Still, C. J. (2008). Climate, phylogeny and the ecological distribution of C4 grasses. *Ecol. Lett.* 11, 266–276. doi: 10.1111/j.1461-0248.2007.01144.x

Elison Timm, O., Diaz, H. F., Giambelluca, T. W., and Takahashi, M. (2011). Projection of changes in the frequency of heavy rain events over Hawaii based on leading Pacific climate modes. *J. Geophys. Res. Atmos.* 116:12.

Frazier, A. G., and Giambelluca, T. W. (2017). Spatial trend analysis of Hawaiian rainfall from 1920-2012. *Int. J. Climatol.* 37, 2522–2531. doi: 10.1002/joc.4862

Gavenda, R. T. (1992). Hawaiian quaternary paleoenvironments: a review of geological, pedological, and botanical evidence. *Pacific Sci.* 46, 295–307.

Giambelluca, T. W., Shuai, X., Barnes, M. L., Alliss, R. J., Longman, R. J., Miura, T., et al. (2014). *Evapotranspiration of Hawai'i*. Washington, DC: U.S. Army Corps of Engineers.

Hart, P. J. (2010). Tree growth and age in an ancient Hawaiian wet forest: vegetation dynamics at two spatial scales. *J. Trop. Ecol.* 26, 1–11. doi: 10.1017/s0266467409990320

Hillebrand, W. (1888). *Flora of the Hawaiian Islands*. Heidelberg: Carl Winter, 673.

Hodgkins, S. B., Richardson, C. J., Dommain, R., Wang, H., Glaser, P. H., Verbeke, B., et al. (2018). Tropical peatland carbon storage linked to global latitudinal trends in peat recalcitrance. *Nat. Commun.* 9:3640. doi: 10.1038/s41467-018-06050-2

Hope, G. S. (2014). The sensitivity of the high mountain ecosystems of New Guinea to climate change and anthropogenic impact. *Arct. Antarct. Alp. Res.* 46, 777–786. doi: 10.1657/1938-4246-46.4.777

Hotchkiss, S., and Juvik, J. O. (1999). A Late-Quaternary pollen record from Ka'au Crater, O'ahu, Hawai'i. *Quat. Res.* 52, 115–128. doi: 10.1006/qres.1999.2052

IAEA/WMO (2018). *Global Network of Isotopes in Precipitation. The GNIP Database*. Vienna: Agence Internationale de L"Energie Atomique.

Jacobi, J. D. (1989). *Vegetation Maps of the Upland Plant Communities on the Islands of Hawai'i, Maui, Moloka'i, and Lana'i. Technical Report* 68. Honolulu, HI: University of Hawai'i at Mānoa.

Kurnianto, S., Warren, M., Talbot, J., Kauffman, B., Murdiyarso, D., and Frolking, S. (2015). Carbon accumulation of tropical peatlands over millennia: a modeling approach. *Glob. Change Biol.* 21, 431–444. doi: 10.1111/gcb.12672

Lähteenoja, O., Flores, B., and Nelson, B. (2013). Tropical peat accumulation in Central Amazonia. *Wetlands* 33, 495–503. doi: 10.1007/s13157-013-0406-0

Lee, K. E., and Slowey, N. C. (1999). Cool surface waters of the subtropical North Pacific Ocean during the last glacial. *Nature* 397, 512–514. doi: 10.1038/17357

Linkin, M. E., and Nigam, S. (2008). The North Pacific Oscillation-west Pacific teleconnection pattern: mature-phase structure and winter impacts. *J. Clim.* 21, 1979–1997. doi: 10.1175/2007jcli2048.1

MacCaughey, V. (1916). Vegetation of the Hawaiian summit bogs. *Am. Bot.* 22, 45–52.

Macdonald, G. A., Abbot, A. T., and Peterson, F. L. (1983). *Volcanoes in the Sea: the Geology of* Hawaii: University of Hawaii Press.

Maciolek, J. A. (1969). Freshwater lakes in Hawaii. *Verhandlungen des Internationalen Verein Limnologie* 17, 386–391. doi: 10.1080/03680770.1968.11895863

Marzi, R., Torkelson, B. E., and Olson, R. K. (1993). A revised carbon preference index. *Org. Geochem.* 20, 1303–1306. doi: 10.1016/0146-6380(93)90016-5

McCune, B., and Mefford, M. J. (2016). *PC-ORD. Multivariate Analysis of Ecological Data. Version* 7.04. Gleneden Beach, OR: MjM Software.

McGee, D., Donohoe, A., Marshall, J., and Ferreira, D. (2014). Changes in the ITCZ location and cross-equitorial heat transport at the last glacial maximum, Heinrich Stadial 1, and the mid-Holocene. *Earth Planet. Sci. Lett.* 390, 69–79. doi: 10.1016/j.epsl.2013.12.043

Moore, J. G., Clague, D. A., Holcomb, R. T., Lipman, P. W., Normark, W. R., and Torresan, M. E. (1989). Prodigious submarine landslides on the

Hawaiian Ridge. *J. Geophys. Res. Solid Earth* 94, 17465–17484. doi: 10.1029/JB094iB12p17465

Mueller-Dombois, D. (1986). Perspectives for an etiology of stand-level dieback. *Annu. Rev. Ecol. Syst.* 17, 221–243. doi: 10.1146/annurev.ecolsys.17.1.221

Nichols, J. E. (2011). Procedures for extraction and purification of leaf wax biomarkers from peats. *Mires Peat* 7, 1–7.

Nichols, J. E., Peteet, D. M., Moy, C. M., Castañeda, I. S., McGeachy, A., and Perez, M. (2014). Impacts of climate and vegetation change on carbon accumulation in a south-central Alaskan peatland assessed with novel organic geochemical techniques. *Holocene* 24, 1146–1155. doi: 10.1177/0959683614540729

Page, S. E., Rieley, J. O., and Banks, C. J. (2011). Global and regional importance of the tropical peatland carbon pool. *Glob. Change Biol.* 17, 798–818. doi: 10.1073/pnas.1806003115

Palmer, D. D. (2008). *Hawai'i's Ferns and Ferns Allies*. Honolulu: University of Hawai'i Press.

Price, J. P., Jacobi, J. D., Gon, S. M. III, Matsuwaki, D., Mehrhoff, L., Wagner, W., et al. (2012). *Mapping Plant Species Ranges in the Hawaiian Islands - Developing a Methodology and Associated GIS layers: U.S. Geological Survey Open-File Report 2012–1192*. Reston, VA: United States Geological Survey, 34.

Reimer, P. J., Bard, E., Bayliss, A., Beck, J. W., Blackwell, P. G., Bronk Ramsey, C., et al. (2013). IntCal13 and MARINE13 radiocarbon age calibration curves 0-50000 years cal BP. *Radiocarbon* 55, 1869–1887. doi: 10.2458/azu_js_rc.55.16947

Reimi, M. A., and Marcantonio, F. (2016). Constraints on the magnitude of the deglacial migration of the ITCZ in the Central Equatorial Pacific Ocean. *Earth Planet. Sci. Lett.* 453, 1–8. doi: 10.1016/j.epsl.2016.07.058

Rieley, J., and Page, S. (2015). "Tropical peatland in the world," in *Tropical Peatland Ecosystems*, eds M. Osaki and N. Tsuji (Tokyo: Springer), 3–32. doi: 10.1007/978-4-431-55681-7_1

Risi, C., Noone, D., Worden, J., Frankenberg, C., Stiller, G., Kiefer, M., et al. (2012). Process-evaluation of tropospheric humidity simulated by general circulation models using water vapor isotopologues: 1. comparison between models and observations. *J. Geophys. Res.* 117:D05303. doi: 10.1029/2011JD016621

Rock, J. F. (1913). *The Indigenous Trees of the Hawaiian Islands*. Honolulu: Bibliolife DBA of Bibilio Bazaar II LLC, 547.

Rundel, P. W. (1980). The ecological distribution of C4 and C3 grasses in the Hawaiian Islands. *Oecologia* 45, 354–359. doi: 10.1007/BF00540205

Sasche, D., Billault, I., Bowen, G. J., Chikaraishi, Y., Dawson, T. E., Feakins, S. J., et al. (2012). Molecular paleohydrology: interpreting the hydrogen-isotopic composition of lipid biomarkers from photosynthesizing organisms. *Annu. Rev. Earth Planet. Sci.* 40, 221–249. doi: 10.1146/annurev-earth-042711-105535

Scholl, M. A., Gingerich, S. B., and Tribble, G. W. (2002). The influence of microclimates and fog on stable isotope signatures used in interpretation of regional hydrology: East Maui, Hawaii. *J. Hydrol.* 265, 170–184. doi: 10.1016/s0022-1694(02)00073-2

Scholl, M. A., Ingebritsen, S. E., Janik, C. J., and Kauahikaua, J. P. (1996). Use of precipitation and ground water isotopes to interpret regional hydrology on a tropical volcanic island: Kilauea volcano area, Hawaii. *Water Resour. Res.* 32, 3525–3537. doi: 10.1029/95wr02837

Schuur, E. A. G. (2001). The effect of water on decomposition dynamics in mesic to wet Hawaiian montane forests. *Ecosystems* 4, 259–273. doi: 10.1007/s10021-001-0008-1

Seager, R., Naik, N., Ting, M., Cane, M. A., Harnik, N., and Kushnir, Y. (2010). Adjustment of the atmospheric circulation to tropical Pacific SST anomalies: variability of transient eddy propagation in the Pacific-North America sector. *Q. J. R. Meteorol. Soc.* 136, 277–296. doi: 10.1002/qj.588

Selling, O. H. S. (1948). *Studies in Hawaiian Pollen Statistics*. Honolulu, HI: Bishop Museum Special Publication, 154.

Selments, P. C., Giardina, C. P., Jacobi, J. D., and Zhu, Z. (2017). "Baseline and projected future carbon storage and carbon fluxes in ecosystems of Hawai'i," in *Paper Presented at the U.S. Geological Survey Professional Paper 1834*, (Reston, VA: U.S. Geological Survey).

Sjögersten, S., Black, C. R., Evers, S., Hoyos-Santillan, J., Wright, E. L., and Turner, B. L. (2014). Tropical wetlands: a missing link in the global carbon cycle? *Glob. Biogeochem. Cycl.* 28, 1371–1386. doi: 10.1002/2014GB004844

Skottsberg, C. (1940). "Report on Hawaiian Bogs", in *Proceedings of the 6th Pacific Science Congress, IV*, (Berkeley: University of California Press), 659–661.

Uchikawa, J., Popp, B. N., Schoonmaker, J. E., Timmermann, A., and Lorenz, S. J. (2010). Geochemical and climate modeling evidence for Holocene aridification in Hawaii: dynamic response to a weakening equatorial cold tongue. *Quat. Sci. Rev.* 29, 3057–3066. doi: 10.1016/j.quascirev.2010.07.014

Wagner, W. L., Herbst, D. R., and Sohmer, S. H. (1996). *Manual of the Flowering Plants of Hawai'i: Revised Edition*. Honolulu: University of Hawai'i Press.

Wilmshurst, J. M., Hunt, T. L., Lipo, P., and Anderson, A. J. (2011). High precision radiocarbon dating shows recent and rapid initial human colonization of East Polynesia. *Proc. Natl. Acad. Sci. U.S.A.* 108, 1815–1820. doi: 10.1073/pnas.1015876108

Yu, Z., Loisel, J., Brosseau, D. P., Beilman, D. W., and Hunt, S. J. (2010). Global peatland dynamics since the last glacial maximum. *Geophys. Res. Lett.* 37:L13402. doi: 10.1029/2010GL043584

Zinck, J. A., and Huber, O. (2011). *Peatlands of the Western Guyanana Highlands, Venezuela*. Berlin: Springer-Verlag.

Conflict of Interest Statement: The authors declare that the research was conducted in the absence of any commercial or financial relationships that could be construed as a potential conflict of interest.

Advantages of publishing in Frontiers

OPEN ACCESS
Articles are free to read for greatest visibility and readership

FAST PUBLICATION
Around 90 days from submission to decision

HIGH QUALITY PEER-REVIEW
Rigorous, collaborative, and constructive peer-review

TRANSPARENT PEER-REVIEW
Editors and reviewers acknowledged by name on published articles

Frontiers
Avenue du Tribunal-Fédéral 34
1005 Lausanne | Switzerland

Visit us: www.frontiersin.org
Contact us: info@frontiersin.org | +41 21 510 17 00

REPRODUCIBILITY OF RESEARCH
Support open data and methods to enhance research reproducibility

DIGITAL PUBLISHING
Articles designed for optimal readership across devices

FOLLOW US
@frontiersin

IMPACT METRICS
Advanced article metrics track visibility across digital media

EXTENSIVE PROMOTION
Marketing and promotion of impactful research

LOOP RESEARCH NETWORK
Our network increases your article's readership